

Springer

Berlin

Heidelberg

New York

Hong Kong

London

Milan

Paris

Tokyo

Progress in Colloid and Polymer Science

Editors: F. Kremer, Leipzig and G. Lagaly, Kiel

Volume 123 · 2004

Trends in Colloid and Interface Science XVI

Volume Editors:

M. Miguel

H. D. Burrows



Springer

The series Progress in Colloid and Polymer Science is also available electronically (ISSN 1437-8027)

- Access to tables of contents and abstracts is *free* for everybody.
 - Scientists affiliated with departments/institutes subscribing to Progress in Colloid and Polymer Science as a whole also have full access to all papers in PDF form. Point your librarian to the LINK access registration form at <http://springeronline.com>
-

ISSN 0340-255X
ISBN 3-540-00553-6
DOI: 10.1007/b12337
Springer-Verlag, Berlin, Heidelberg,
New York

This work is subject to copyright. All rights are reserved, whether the whole or part of the material is concerned, specifically the rights of translation, reprinting, reuse of illustrations, recitation, broadcasting, reproduction on microfilm or in any other way, and storage in data banks. Duplication of this publication or parts thereof is permitted only under provisions of the German Copyright Law of September 9, 1965, in its current version, and permission for use must always be obtained from Springer-Verlag. Violations are liable for prosecution under the German Copyright Law.

Product liability: The publisher cannot guarantee the accuracy of any information about dosage and application contained in this book. In every individual case the user must check such information by consulting the relevant literature.

The use of general descriptive names, registered names, trademarks, etc. in this

publication does not imply, even in the absence of specific statement, that such names are exempt from the relevant protective laws and regulations and therefore free for general use.

Springer-Verlag Berlin Heidelberg New York a part of Springer Science + Business Media

<http://www.springeronline.com>

© Springer-Verlag
Berlin Heidelberg 2004

Typesetting: SPS, Chennai, India

Cover: Estudio Calamar,
F. Steinen-Broo, Pau/Girona, Spain

Printing: Mercedes Druck, Berlin,
Germany

Printed on acid-free paper
Printed in Germany

The fifteenth meeting of the European Colloid and Interface Society (ECIS) was held in the historic university city of Coimbra from 16th to 21st September 2001. This follows in the tradition of these annual meetings, which started in Como, Italy, in 1987. From the beginning these were intended as interdisciplinary meetings, with participation from chemists, physicists, life and materials scientists, both from academia and industry. The 15th meeting followed this tradition. There was a broad scientific programme, with sessions on *Self Assembly in Mixed Systems*, *Surface Modification*, *Biological and Biomimetic Systems*, *Theory and Modelling*, *New Techniques and Developments*, *Food and Pharmaceuticals*, *Dynamics at Interfaces* and *Mesoscopic and Mesoporous Systems*. In spite of the shadow of the tragic events of September 11th, the meeting attracted 340 participants from 34 countries. It was especially gratifying that our aim to encourage participation of younger scientists succeeded.

The meeting had a very strong scientific programme. We were particularly pleased to be host to the first *Rhodia* Colloid Prize Lecture, which was presented by Professor Kre Larsson of the University of Lund, Sweden. In addition there were 16 invited lectures, 62 oral presentations and 184 posters.

This special issue of *Progress in Colloid and Polymer Science* contains a selection of the contributions, all of which have been peer reviewed. We take this opportunity to thank all the colleagues who accepted to review these manuscripts. We also thank all the members of the scientific committee, the local organising committee and the sponsors who helped to make ECIS 2001 such a memorable meeting. Finally, we hope that you will enjoy reading the contributions to this special issue, which we feel highlights some of the important contemporary advances in the area of colloid and interface science.

Maria da Graça Miguel
Hugh D. Burrows

Miguel M da G, Burrows HD:	Preface	V
	Self Assembly in Mixed Systems	
Hungerford G, Real Oliveira MECD, Castanheira EMS, Burrows HD, Miguel M da G:	Transitions in Ternary Surfactant/alkane/water Microemulsions as Viewed by Fluorescence	1
Siegel S, Vollhardt D:	Phase Behaviour and Domain Structure of 9-Hydroxyhexadecanoic Acid Monolayers	5
Wright M, Kurumada K-i, Robinson BH:	Rates of Incorporation of Small Molecules into Pluronic Micelles	8
Kurumada K-i, Robinson BH:	Viscosity Studies of Pluronic 127 in Aqueous Solution	12
Bergström M, Eriksson JC:	Synergistic Effects in Binary Surfactant Mixtures	16
Chittofrati A, Pieri F, D'Aprile F, Lenti D, Maccone P, Visca M:	Perfluoropolyether Carboxylic Salts in Micellar Solution and O/W Microemulsions	23
Sobral AJFN, Lopes SH, Rocha Gonsalves AM d'A, Ramos Silva M, Matos Beja A, Paixão JA, L. Alte da Veiga L:	Synthesis and Crystal Structure of New Phase Transfer Catalysts Based on 1,8-diazabicyclo[5.4.0]undec-7-ene and 1,5-diazabicyclo [4.3.0]non-5-ene	28
Berlot I, Chevalier Y, Coche-Guérente L, Labbé P, Moutet J-C:	Interfacial and Micellar Behaviour of Pyrrole-Containing Surfactants	31
Persson G, Edlund H, Lindblom G:	Phase Behaviour of the 1-Monooleoyl- <i>rac</i> -glycerol/ <i>n</i> -octyl- β -D-glucoside/water System	36
Thuresson K, Antunes FE, Miguel MG, Lindman B:	The Association Between a Non-ionic Microemulsion and Hydrophobically Modified PEG. A Rheological Investigation	40
	Surface modification	
Esumi K:	Adsolubilization by Mixtures of Ionic and Nonionic Surfactants	44
Oliger P, Fischer A, Hebrant M, Tondre C:	Probe Entrapment by Vesicular Systems in Relation with the Properties of the Amphiphilic Film	48
Burrows HD, Kharlamov AA:	About Energy and Electron Transfer Processes in C ₆₀ / Phthalocyanine Films	52
	Biological and Biomimetic Systems	
Hato M, Minamikawa H, Salkar RA, Matsutani S:	Phase Behaviour of Phytanyl-chained Alkylglycoside/ Water Systems	56
Llères D, Clamme J-P, Dauty E, Behr J-P, Mély Y, Duportail G:	Oxidizable Cationic Detergent for Gene Therapy: Condensation of DNA and Interaction with Model Membranes	61

Ardhammar M, Lincoln P, Nordén B:	Orientation of Ruthenium Dipyridophenazine Complexes in Liposome Membranes Sensitive Controlled by Ligand Substituents	65
Airolidi M, Boicelli CA, Gennaro G, Giomini M, Giuliani AM, Giustini M, Paci E:	Cationic Microemulsion Hosting Polynucleotides: Effect of NaCl on Host and Guest	69
Santos MSCS, Lacerda SMV, Barbosa EFG:	Interactions of Selected Flavonoids with NaDS Micelles	73
Di Biasio A, Bordi F, Cametti C:	Salt-induced Aggregation in Cationic Liposome Suspensions	78
Céu Rei M, Coutinho PJG, Castanheira EMS, Real Oliveira MECD:	C ₁₂ E ₇ -DPPC Mixed Systems Studied by Pyrene Fluorescence Emission	83
Baptista ALF, Coutinho PJG, Real Oliveira MECD, Rocha Gomes JIN:	Lipid Interaction with Textile Fibres in dyeing Conditions	88
Hatzara E, Karatza E, Avramiotis S, Xenakis A:	Spectroscopic Mobility Probing Studies of Lecithin Organogels	94
	Theory and Modelling	
Hauck J, Mika K:	Self-assembly of Homogeneous Systems	98
Lawlor A, McCullagh GD, Zaccarell E, Foffi G, Dawson KA:	Interactions in Systems with Short-range Attractions and Applications to Protein Crystallisation	104
Boström M, Williams DRM, Ninham BW:	Specific Ion Effects: Why Colloid Science has Failed to Contribute to Biology	110
Martín-Molina A, Quesada-Pérez M, Galisteo-González F, Hidalgo-Álvarez R:	Charge Inversion of Latex Particles in Presence of Electrolyte	114
Moncho-Jordá A, Quesada-Pérez M, Martínez-López F, Hidalgo-Álvarez R:	Structure and Interaction Forces in Colloidal Monolayers	119
	New Techniques and Developments	
Kovalchuk NM, Vollhardt D:	Direct Numerical Simulation of the Mechanism of Surface Tension Auto-oscillation	123
Hrust V, Tomišić V, Kallay N:	Characterization of Aqueous Solutions of Ionic Surface Active Agents by Conductometry	127
González-Romero E, Fernández-Calvar B, Carlos Bravo-Díaz C:	Electrochemical Determination of the Stability Constant of an Aryl Radical with β -Cyclodextrin	131

Lehmann L, Kudryashov E, Buckin V:	Ultrasonic Monitoring of the Gelatinisation of Starch	136
Scheffold F, Romer S, Cardinaux F, Bissig H, Stradner A, Rojas-Ochoa LF, Trappe V, Urban C, Skipetrov SE, Cipellatti L, Schurtenberger P:	New Trends in Optical Microrheology of Complex Fluids and Gels	141
Briscoe WH, Horn RG:	Electrical Double Layer Interactions in a Nonpolar Liquid Measured with a Modified Surface Force Apparatus	147
Dynarowicz-Łatka P, Miñones Jr J, Kita K, Milart P:	The Utility of Brewster Angle Microscopy in Evaluating the Origin of the Plateau in Surface Pressure/Area Isotherms of Aromatic Carboxylic Acids	152
Brunner M, Bechinger C:	Colloidal Systems in Intense, Two-dimensional Laser Fields	156
Miñones Jr J, Dynarowicz-Łatka P, Seoane R, Iribarnegaray E, Casas M:	Brewster Angle Microscopy Studies of the Morphology in Dipalmitoyl Phosphatidyl Glycerol Monolayers Spread on Subphases of Different pH	160
	Food and Pharmaceuticals	
Peel LL, Lu JR:	The Interaction of C ₁₂ E ₅ with Olive Oil Films Studied by Neutron Reflection	164
Terreros Gomez A, Rubio Retama BJ, Lopez Ruiz B, Galera Gomez PA, Rueda Rodriguez C, Arias Garcia C, Lopez Cabarcos E:	Encapsulation of Alkaline Phosphatase in Polyacrylamide Microparticles Using the Concentrated Emulsion Polymerisation Method	169
Lopez F, Palazzo G, Colafemmina G, Cinelli G, Ambrosone L, Ceglie A:	Enzymatic Activity of Lipase Entrapped in CTAB/Water/Pentanol/ Hexane Reverse Micelles: a Functional and Microstructural Investigation	174
Kharlamov AA, Burrows HD:	Monitoring of the Aroma of Fruits at their Surface by Luminescence	178
Romsted LS, Zhang J:	Determining Antioxidant Distributions in Model Food Emulsions Development of a New Kinetic Method Based on the Pseudophase Model in Micelles and Opaque Emulsions	182
Wege HA, Holgado-Terriza JA, Cabrerizo-Vílchez MA:	Development of a Pressure-Controlled Pendant Drop Surface Balance. Study of Protein Adsorption Kinetics at the Solution-air Interface	188
Dziechciarek Y, van Soest JJG, Philipse AP:	Rheology of Starch-based Colloidal Microgels	194
Zoumpanioti M, Karavas E, Skopelitis C, Stamatidis H, Xenakis A:	Lecithin Organogels as Model Carriers of Pharmaceuticals	199

Rosmaninho R, Visser H, Melo L:	Influence of the Surface Tension Components of Stainless Steel on Fouling Caused by Calcium Phosphate	203
Pérez L, Infante MR, Angelet M, Clapés P, Pinazo A:	Glycerolipid Arginine-based Surfactants Synthesis and Surface Active Properties	210
	Dynamics at Interfaces	
Cuenca A:	The Role of Premicellar Assemblies and Micelles upon the Hydrolysis of 2-(2-fluorophenoxy)quinoxaline	217
Liu J, Palberg T:	Crystal Growth and Crystal Morphology of Charged Colloidal Binary Mixtures	222
Pontoni D, Narayanan T, Rennie AR:	Nucleation and Growth Kinetics of Colloidal Silica	227
Klich J, Paluch M:	Properties of Some Mixed Adsorption Films at the Water/Air Interface	231
Pieri R, Carignano G, Chittofrati A, D'Aprile F, Visca M:	Wetting of Low Energy Surfaces by Perfluoropolyether Carboxylic Salts in Aqueous Solution	236
	Mesoscopic and Mesoporous Systems	
Poncet-Legrand C, Petit L, Reculusa S, Mingotaud C, Duguet E, Ravaine S:	Dissymmetrical Gold Tagging on Spherical Silica Nanoparticles	240
Gzyl B, Paluch M:	Langmuir Monolayers of Lipids at the Water/air Interface	245
Fernández-Nieves A, Fernández-Barbero A, de las Nieves FJ:	Static Light Scattering from Fractal Aggregates of Microgel Particles	251
Valle-Delgado JJ, Molina-Bolívar JA, Galisteo-González F, Gálvez-Ruiz MJ:	Stabilisation of an Amphoteric Latex by Hydration Forces	255
Medebach M, Palberg T:	Flashing of Colloidal Crystals in Square Wave Electric Fields	260
Wette P, Schöpe H-J, Liu J, Palberg T:	Characterisation of Colloidal Solids	264
Uddin Md H, Yamashita Y, Furukawa H, Harashima A, Kunieda H:	Phase Behaviour of Poly(oxyethylene)-poly(dimethylsiloxane) surfactant (copolymer) with Water or Silicone Oil	269
Dugas V, Chevalier Y, Depret G, Nesme X, Souterand E:	The Immobilisation of DNA Strands on Silica Surface by Means of Chemical Grafting	275
Carretti E, Dei L, Baglioni P:	Aqueous Polyacrylic Acid Based Gels: Physicochemical Properties and Applications in Cultural Heritage Conservation	280

D. Bica
L. Vékás
M.V. Avdeev
M. Bălăsoiu
O. Marinică
F.D. Stoian
D. Susan-Resiga
G. Török
L. Rosta

Magnetizable colloids on strongly polar carriers – preparation and manifold characterization

D. Bica · L. Vékás (✉)
Laboratory of Magnetic Fluids,
Center for Fundamental and Advanced
Technical Researches,
Romanian Academy –Timisoara Branch,
24 Mihai Viteazu Bv. ,
Timisoara 1900, Romania
e-mail: vekas@flumag2.mec.utt.ro
Tel.: +40-256-221547
Fax: +40-256-221547

M.V. Avdeev · M. Bălăsoiu
Frank Laboratory for Nuclear Scattering –
Joint Institute for Nuclear Research,
141980 Dubna, Moscow Region, Russia

O. Marinică · F.D. Stoian
D. Susan-Resiga
National Center for Engineering of Systems
with Complex Fluids –
University Politehnica Timisoara,
Timisoara 1900, Romania

G. Török · L. Rosta
Budapest Neutron Center – Institute of
Solid State Physics and Optics,
Hungarian Academy of Sciences,
P.O. Box 49, 1525 Budapest, Hungary

Abstract The aim of this paper is to present methods applied to obtain and to investigate the properties of magnetic fluids on strongly polar carrier liquids, such as short-chain-length alcohols and water. The high degree of colloidal stability of these colloids is achieved by double-layer sterical stabilization of Fe_2O_3 and CoFe_2O_4 nanoparticles dispersed in the carrier liquid, the adequate choice and efficient adsorption of the surfactant(s) used being one of the key problems to be solved in each particular case, in order to obtain high-quality magnetic fluids. The samples were investigated using a vibrating-sample magnetometer, a rheo/magnetorheometer with various measuring cells, as well as by small-angle neutron scattering, in order to detect magnetic-field-

induced changes at the nanometric level and qualitative differences in the macroscopic behaviour of various samples. The conclusions refer to the dependence of the colloidal stability on the composition and volumic concentration of the magnetic fluid samples, as well as on the applied magnetic field.

Keywords Magnetic nanoparticles · Magnetic fluids · Preparations · Properties

Introduction

Magnetic fluids are a special category of colloids consisting of magnetic nanoparticles, such as Fe_3O_4 , CoFe_2O_4 , Co or Fe, stably dispersed in a carrier liquid. Owing to their high degree of colloidal stability, achieved by specific stabilization procedures, these colloids behave macroscopically as a homogeneous magnetizable liquid, even in strong and nonuniform magnetic fields. Consequently, these kinds of colloids, usually called magnetic fluids or ferrofluids, are smart colloidal systems, which manifest simultaneously fluid and magnetic properties. Macroscopically, the introduction of a controllable magnetic force into the fundamental hydrodynamic

equations for the quasihomogeneous magnetizable liquid medium gives rise to the magnetohydrodynamics of magnetic fluids, known also as ferrohydrodynamics and opens an entire field of new phenomena [1, 2, 3]. From a microscopic point of view, the interactions between magnetic nanoparticles have to be adequately controlled in order to ensure the required high colloidal stability of the system in various operating conditions.

In the case of sterically stabilized nanoparticles in various liquid carriers, the type and quality of surfactants used will determine the efficiency of particle surface covering and, consequently, the balance between attractive and repulsive interactions between particles. The attractive interactions may lead to various types of

aggregates, usually in the shape of linear chains quasi-parallel to the applied magnetic field, or droplike aggregates [3]. The agglomeration processes and the resulting agglomerates are not desired for most applications; therefore, the synthesis and complex characterization of magnetic fluids, based on their physicochemical properties, are among the main topics of current research. In the absence of agglomerates or when their volume fraction is negligible, the physical properties are determined by the particle volume fraction and the orientation of permanent magnetic moments of individual nanoparticles in the external magnetic field. This is mainly the case of low-volume-fraction/low-saturation-magnetization samples, which are less important for applications. For higher-volume fractions of magnetic nanoparticles, the interactions and the presence of agglomerates, even of temporary ones, cannot be neglected and detailed investigations on the microstructure as well as on the magnetic and flow properties of magnetic fluids [4, 5] are necessary for the proper design of any application [3]. The behaviour of magnetic fluids in the usually strong and nonuniform magnetic field conditions specific to many devices using magnetic fluids, for example, leakage-free rotating seals, is determined mainly by some essential features of the process of magnetic nanoparticle synthesis and of their dispersion/stabilization in various nonpolar and polar carrier liquids.

In this paper results are reviewed concerning the synthesis of high-concentration magnetic fluids, especially with polar carriers. The microstructural, magnetic and flow properties, determined by neutron scattering, vibrating-sample magnetometry and rheological/magnetorheological measurements, are comparatively analysed, with special regard to highly stable pentanol and weaker colloidal stability water-based samples.

Chemical synthesis of concentrated magnetic fluids

The main steps of the chemical coprecipitation/sterical stabilization procedures applied for magnetic nanoparticle/magnetic fluid synthesis are given in Refs. [6, 7, 8]. For the samples investigated in this work polar solvents, such as pentanol and water, were used as carrier liquids.

For magnetic fluids on polar organic solvents, a volatile hydrocarbon (e.g., kerosene, heptane, octane) was used as the primary dispersion medium for magnetite nanoparticles covered with a chemisorbed oleic acid monolayer as the first surfactant layer. The surfactant-covered magnetite nanoparticles were flocculated and transferred into an organic polar solvent (e.g., short-chain-length alcohols, diesters), using a secondary surfactant, such as dodecylbenzenesulphonic acid (DBS) or polymers [e.g. poly(isobutylsuccinimide)], depending on the properties of the carrier liquid.

As shown later, in the case of water and various organic polar carriers, the preparation process [6, 9, 10, 11, 12, 13, 14] is quite different from that developed for nonpolar organic carriers. Owing to specific difficulties encountered in stable dispersion of magnetic nanoparticles in the strongly polar water carrier, most of the preparation procedures were used for low-magnetization (100–200 G) samples. The preparation of alcohol-based magnetic fluids was first reported in Ref. [7] and implies a stabilization mechanism, different from that applied in the case of water carrier.

Polar magnetic fluids on organic carriers

The preparation process starts from a medium concentration (about 7% solid volume concentration), well-purified, light hydrocarbon (e.g., kerosen) based primary magnetic fluid. The magnetic nanoparticles are transferred into the desired polar carrier by a carrier liquid exchange procedure [1, 6, 14]. The magnetic nanoparticles from the primary magnetic fluid are reversibly flocculated using acetone, followed by magnetic decantation and elimination of the light hydrocarbon solvent. The magnetic nanoparticles, covered with a chemically adsorbed oleic acid monolayer, are then redispersed in the prescribed polar carrier, using an adequate secondary surfactant. For the purposes of the experimental investigations described in this paper, three pentanol-based samples were prepared, using DBS as the secondary, physically adsorbed surfactant. As it will be shown, all these samples have very good colloidal stability, including that with the highest saturation magnetization (sample 8, Table 1). The high degree of colloidal stability of pentanol-based magnetic fluids was first evidenced by ultracentrifugation/sedimentation velocity analysis [15].

This basic procedure produced good colloidal stability magnetic fluids on alcohol carriers of various chain lengths, as well as on other type of polar carriers, such as diesters, amines or ketones. It is worthwhile to note especially the series of C_3 – C_{10} alcohol-based magnetic fluids [8], the first ones with very high solid volume concentration (up to 20%)/magnetization (up to 900 G), as well as the strongly polar methyl ethyl ketone based magnetic fluid [10] of medium physical volume concentration (approx. 10%).

Water-based magnetic fluids

These types of magnetic fluids, owing to the strongly polar character of the carrier, have several particularities concerning their preparation procedures, as well as their colloidal stability and physical properties. The double-layer electrostatic stabilization mechanism [9] gives weakly stable and relatively low concentration magnetic fluids, which manifest phase-separation (droplike

Table 1 Magnetic fluid samples on water and pentanol carrier liquids

Number	Indicative/carrier	Stabilizing layers	Density (g cm ⁻³ at 20 °C)	Saturation magnetization (M at H_{\max}) (G)
1	Magnetic fluid/ water–CoFe ₂ O ₄	Lauric acid (double)	1.07	80
2	Magnetic fluid/water–Fe ₃ O ₄	Lauric acid (double)	1.08	80
3	Magnetic fluid/water–Fe ₃ O ₄	Lauric acid (double)	1.17	170
4	Magnetic fluid/water–Fe ₃ O ₄	Lauric acid (double)	1.31	300
5	Magnetic fluid/water–Fe ₃ O ₄	Lauric acid + dodecylbenzenesulphonic acid	1.07	80
6	Magnetic fluid/water–Fe ₃ O ₄	Lauric acid + dodecylbenzenesulphonic acid	1.17	180
7	Magnetic fluid/water–Fe ₃ O ₄	Lauric acid + dodecylbenzenesulphonic acid	1.24	235
8	Magnetic fluid/pentanol	Oleic acid + dodecylbenzenesulphonic acid	1.73	945
9	Magnetic fluid/pentanol	Oleic acid + dodecylbenzenesulphonic acid	1.43	600
10	Magnetic fluid/pentanol	Oleic acid + dodecylbenzenesulphonic acid	1.12	280

agglomerates) even in a low-intensity magnetic field [3]. Double-layer steric stabilization coupled with an electrostatic stabilization mechanism resulted in better colloidal stability and higher saturation magnetization water-based magnetic fluids prepared according to the methods in Refs. [8, 13].

The main steps of the various preparation procedures are summarized in what follows. The coprecipitation of Fe²⁺ (or Co²⁺) and Fe³⁺ ions was performed in conditions of excess concentrated NH₄OH (or NaOH) at approximately 80 °C. The resulting subdomain Fe₃O₄ (or CoFe₂O₄) nanoparticles were subjected to repeated washing/purification, as well as to double-layer surface covering, the first surfactant being chemisorbed, while the secondary one was physically adsorbed. For the water-based samples presented in Table 1 (samples 1–7), the lauric acid double layer and lauric acid (chemisorbed, first layer) with DBS (physically adsorbed, secondary layer) ensured the stable dispersion of magnetic nanoparticles in water. There are several differences between the procedure just described and those described in Ref. [12], especially concerning the type of surfactants and the stabilization procedures applied, which will be discussed in detail elsewhere [10].

Concerning the enhanced steric and electrostatic stabilisation mechanism, for example, the secondary DBS layer has the –SO₃⁻ groups oriented towards the dispersion medium forming a local electric field with hydrated NH₄⁺ ions around the particles. Consequently, the degree of stability of water-based magnetic fluids depends on the pH of the medium and the stabilization mechanism outlined earlier is specific only to water as the dispersion medium.

Magnetic properties

Magnetization curves can be used extensively for the study of both particle interactions and agglomerate formation,

processes which strongly influence the rheological and magnetoheological behaviour of magnetic fluids. Saturation magnetization, M_s , initial susceptibility (χ_i), full magnetization curves [$M = M(H)$ or $M/M_s(H)$], where H is the intensity of applied magnetic field] and magneto-granulometric analysis (mean magnetic diameter $\langle D_m \rangle$ and standard deviation σ), at various values of the volumic concentration of magnetic nanoparticles, give an insight into the microstructural characteristics of various samples to be compared [15, 16, 17, 18]. For example, the initial susceptibility is influenced by the particle diameter and the size distribution, particle interactions, the existence of preformed aggregates during the preparation process and aggregate formation at zero field or induced by the applied magnetic field. As it was shown in detail in Ref. [19], the comparison of the dependence of χ_i with the physical volume fraction, Φ , of magnetic nanoparticles for samples of different types of magnetic fluids reveals interesting microstructural aspects. The initial susceptibility in the framework of the thermodynamic perturbation theory (TPT) [20] is given by

$$\chi_i = \chi_{iL} \left(1 + \frac{1}{3} \chi_{iL} \right), \quad (1)$$

where

$$\chi_{iL} = \frac{\mu_0 \pi M_d^2 D_m^3 \Phi_m}{18 k_B T}. \quad (2)$$

Here $M = M_s L(\xi)$, with $\xi = \mu_0 m H / (k_B T)$, where M_d is the spontaneous magnetization of the particles, $\Phi_m = p_m \Phi$ is the “magnetic” volume fraction (Φ is the physical volume fraction, p_m is the proportionality factor and m is the magnetic moment of the particles), D_m is the magnetic diameter of the particles, $k_B T$ is the thermal energy and μ_0 is the permeability of a vacuum. Equations (1) and (2) show the strong influence of the mean “magnetic” volume/diameter of the particles as well as of the size distribution on the low-field part of the magnetization curve. In particular, particle agglomerates

which behave as large particles will determine this part of the magnetization curve.

Equation (1) may be extended in the framework of the same TPT for concentrated magnetic fluids, applying the second-order approximation [20]:

$$\chi_i = \chi_{iL} \left(1 + \frac{1}{3} \chi_{iL} + \frac{1}{144} \chi_{iL}^2 \right). \quad (3)$$

Composition details, in particular the quality of the surfactant used, influence particle agglomeration processes. The use of technical grade oleic acid (TOA) resulted in incomplete particle covering and a significant fraction of preformed agglomerates, which manifest themselves in the higher initial susceptibility values and in a nonlinear $\chi_i = \chi_i(\Phi)$ dependence [19]. In contrast, pure oleic acid (POA) monolayer stabilized hydrocarbon (transformer oil) based samples showed a negligible effect of the preformed agglomerates, owing to better adsorption of POA on the surface of the particles. Moreover, double-layer sterically stabilised pentanol magnetic fluids have a smaller initial susceptibility compared to TOA-stabilized samples of the same concentration and quasi-linear $\chi_i = \chi_i(\Phi)$ dependence, at least for small Φ values, i.e., agglomerates are practically absent in this case. This conclusion was supported by ultracentrifugation/sedimentation velocity tests [15] and by comparison with theoretical models [19], in particular with the second-order susceptibility formula obtained by Ivanov and Kuznetsova [20] in the framework of the TPT.

In this context, it is interesting to compare the nondimensional magnetization curves in the low-field region for two different kinds of polar samples. For a set of water-based samples of low and medium saturation magnetization (up to 300 G) and a very high magnetization (945 G) pentanol-based sample (Table 1) such a comparison is presented in Fig. 1. In spite of its high hydrodynamic volume fraction (approximately 0.6), the pentanol-based sample 8 shows the lowest initial susceptibility, i.e., the fraction of agglomerates is negligible compared to that evidenced for the water-based samples, with agglomerates, among them the diluted sample 1, having the greatest initial susceptibility.

The qualitative differences just outlined determined the choice of water-based samples, on the one hand, and the pentanol magnetic fluids, on the other hand, for further comparative investigations by small-angle neutron scattering (SANS).

SANS analyses of microstructural processes

The complex magnetic analyses of the magnetic fluids on polar and strongly polar carrier liquids evidence clear differences existing at the microstructural level between samples on organic polar carriers (e.g., alcohols) and water-based samples. It is expected that these differences

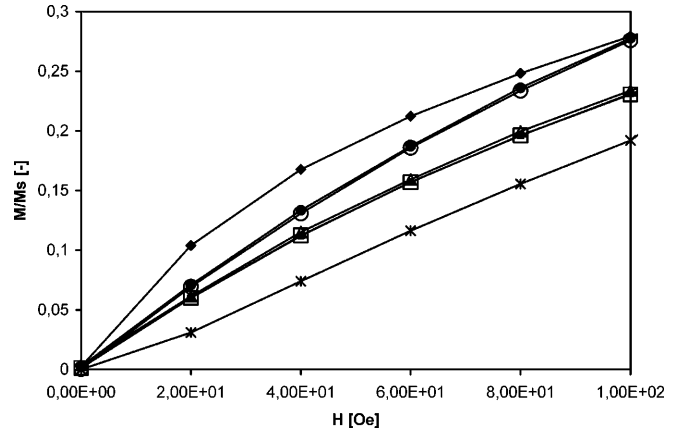


Fig. 1 Reduced magnetization curves for magnetic fluid samples at low magnetic fields: magnetic fluid/water- CoFe_2O_4 (sample 1) (*diamonds*); magnetic fluid/water- Fe_3O_4 (sample 2) (*triangles*); magnetic fluid/water- Fe_3O_4 (sample 3) (*open squares*); magnetic fluid/water- Fe_3O_4 (sample 4) (*filled squares*); magnetic fluid/water- Fe_3O_4 (sample 5) (*filled circles*); magnetic fluid/water- Fe_3O_4 (sample 6) (*open circles*); magnetic fluid/pentanol (sample 8) (*stars*)

will even increase when a strong magnetic field is applied to the samples.

SANS investigations proved to be very efficient in microstructural analysis of magnetic fluids, up to the highest volume fraction of magnetic nanoparticles. Recent experiments [21, 22, 23] conducted at the Budapest Neutron Center (BNC) (Research Institute for Solid State Physics and Optics, KFKI, Budapest) and at the Frank Laboratory of Neutron Physics (Joint Institute for Nuclear Research, Dubna), used various magnetic fluids on deuterated benzene, heavy water, water and pentanol. Among others, it was particularly evidenced that the effective thickness of the single surfactant shell of oleic acid in benzene-based ferrofluids decreases with the increase in particle concentration.

For a deeper insight into microstructural processes, SANS investigations were extended to detect microstructural changes in water- and pentanol-based magnetic fluids induced by the application of a strong magnetic field. The particle agglomerates were also followed after the field was turned off.

Water- and pentanol-based samples were especially selected taking into account the existing similarities (strongly polar, double sterically stabilized) and the significant differences concerning the colloidal stability of the two types of samples, as was pointed out in the previous sections.

The SANS experiments, described in detail in Ref. [24], were carried out on the small-angle diffractometer of the BNC, in a q range $0.19\text{--}5\text{ nm}^{-1}$. For each sample the measurements were made consequently in conditions “no field” (1200 s), “field on” (1200 s), “field off” (several expositions 1200 s each). The

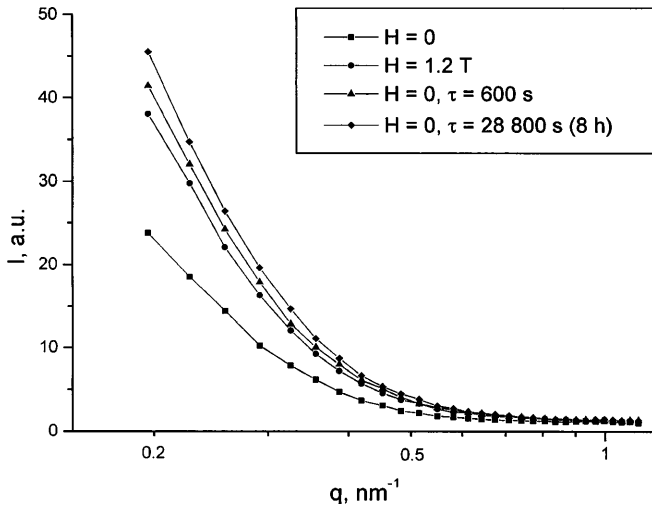


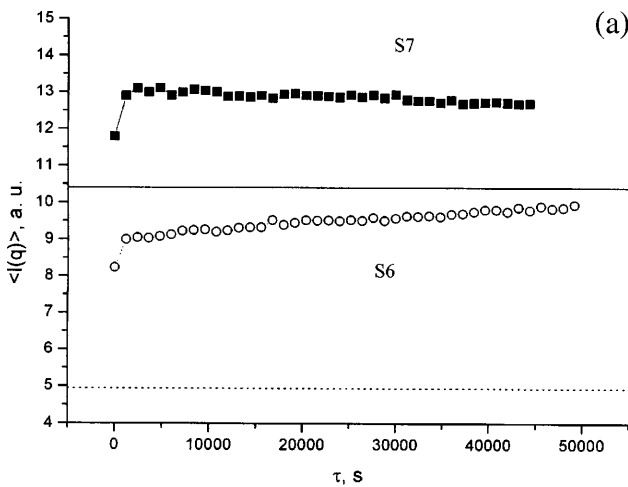
Fig. 2 Radially averaged scattering curves for sample water- Fe_3O_4 (sample 6) at different moments after demagnetization. Experimental errors do not exceed 5%

induction of the applied magnetic field was 1.2 T, at which practically all the samples saturate. The time of increase and decrease of the magnetic field was of the order of seconds. The temperature was maintained at 20 °C.

The possible anisotropy in the scattering patterns was analyzed according to the expression

$$I(q, \varphi) = A(q) + B(q) \sin^2 \varphi, \quad (4)$$

Fig. 3 Mean intensity $\langle I \rangle$ as a function of time τ after demagnetization for **a** water-based magnetic fluid samples 6 (S6) and 7 (S7) and **b** pentanol-based magnetic fluid sample 10 (S10). Horizontal lines in the graphs correspond to the mean intensity value of the initial ferrofluids before they are set in the magnetic field: applied field ($B = 1.2$ T) (squares); zero field ($B = 0$ T) (continuous line and broken line)



Water based magnetic fluids

where φ is the angle between the direction of the applied magnetic field and the scattering vector. For this purpose the averaging over φ was made in the 15° vicinity around $\varphi = 0^\circ$ and $\varphi = 90^\circ$, which allows one to separate $A(q)$ and $B(q)$ functions in Eq. (4). For the limiting cases, when the applied field is $H = 0$ and $H = H_\infty$, where H_∞ is the field corresponding to the saturation magnetization, the $A(q)$ and $B(q)$ functions are connected with the nuclear, $F_N(q)$, and magnetic, $F_M(q)$, scattering in the system as follows:

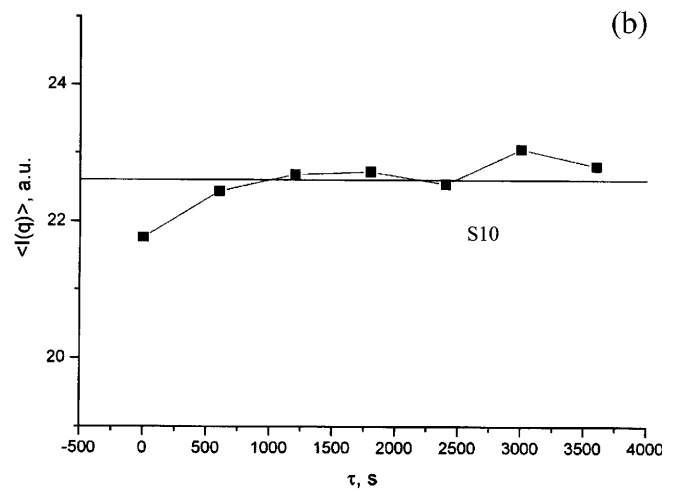
$$(H = 0) \quad A(q) = F_N(q) + 2/3 F_M(q), B(q) = 0; \quad (5)$$

$$(H = H_\infty) \quad A(q) = F_N(q), B(q) = F_M(q). \quad (6)$$

Magnetic-field-induced aggregation in the case of water-based sample 6 is illustrated by the radially averaged scattering curves given in Fig. 2 for different moments of the magnetization/demagnetization cycles. One can see that in contrast to the expected decrease in intensity as follows from Eqs. (4), (5) and (6) an increase appears when the sample is in the magnetic field, as well as after the magnetic field is turned off. The analysis of the anisotropy showed that the scattering is quite isotropic over the φ angle. The observed increase is a reflection of the aggregation in the system, whose effect is significantly more than that of the magnetic scattering.

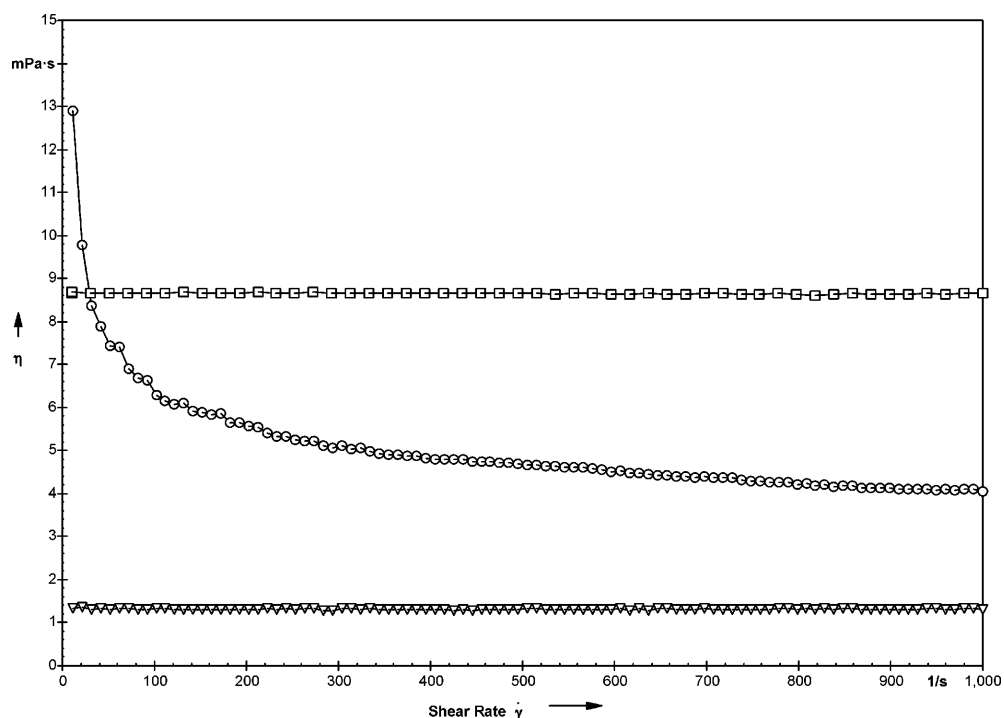
To follow the changes in the aggregation, the scattering intensity was averaged over a q interval of 0.2–0.7 nm^{-1} . The mean intensity over the indicated interval as a function of time is presented in Fig. 3 for the previously mentioned water-based sample, as well as for a pentanol-based reference sample of approximately the same magnetization. The mean intensity values corresponding to the initial stage of the samples, before the magnetic field was applied, are also shown (solid lines).

The field-induced agglomerate formation in the water-based samples is clearly evidenced by the large difference



Pentanol based magnetic fluid (S10)

Fig. 4 Shear-rate dependence of the viscosity for water-based and pentanol-based magnetic fluid samples: magnetic fluid/water- Fe_3O_4 (sample 2) (*triangles*); magnetic fluid/water- Fe_3O_4 (sample 7) (*circles*); magnetic fluid/pentanol (sample 10) (*squares*)



between the curves corresponding to “no field” (solid line) and “field off” stages. Comparatively, the pentanol-based sample practically does not show such changes. When the sample is in the magnetic field the scattering follows the behaviour according to changes in the magnetic scattering (Eqs. 4, 5, 6), while after the magnetic field is turned off it returns to the initial value. Thus, field-induced agglomeration processes in this fluid are negligible.

Rheological and magnetorheological behaviour

The flow properties of magnetic fluids are very important for almost any engineering or biomedical application; therefore, they have been investigated by many researchers. However, most of the works consider especially the behaviour of relatively dilute magnetic fluids, with negligible effects of particle interactions. A recent review of the theoretical and experimental results may be found in the book by Odenbach [4], which also offers a comprehensive analysis of the magnetorheological behaviour of concentrated magnetic fluids of high practical interest.

The viscosity of colloids is influenced by temperature, interactions between particles, concentration, shape and dimension of the particles and viscosity of the carrier liquid. Owing to the complex phenomena, there is no general formula for the viscosity of suspensions, in particular for magnetic fluids, but various approximating

relationships have been proposed, each one based on specific considerations and therefore with limited applicability [3, 25, 26, 27, 28].

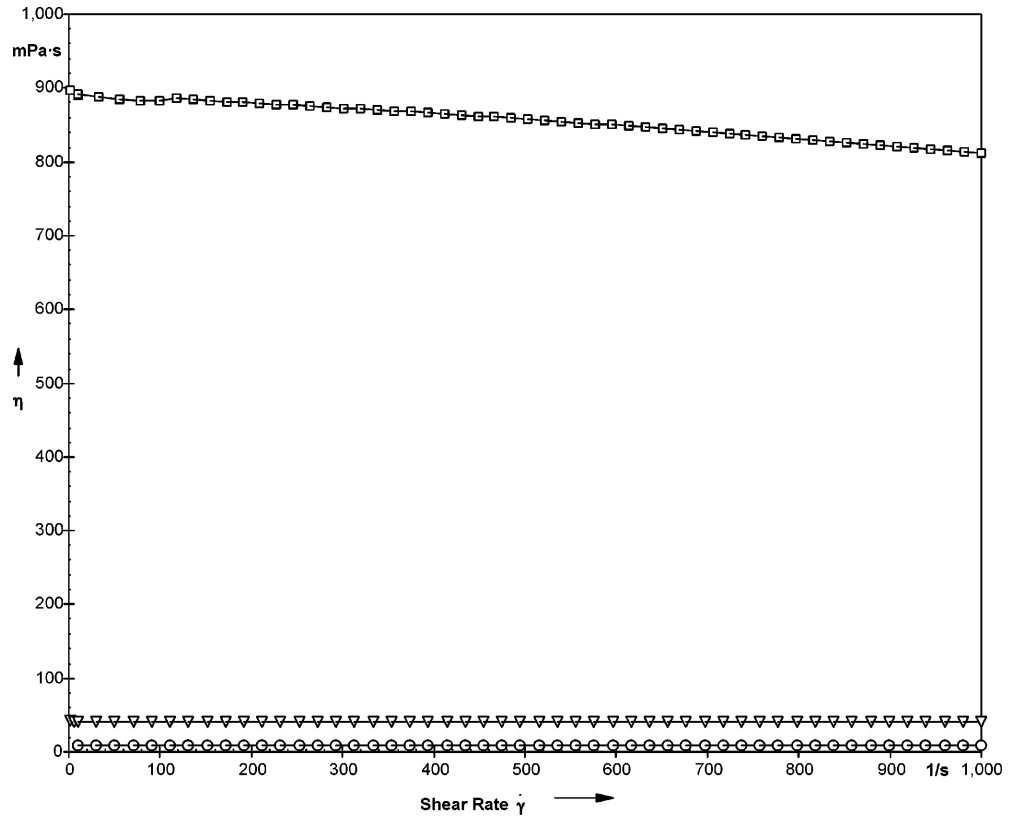
A thorough analysis [16, 17, 18, 25] of the hydrodynamic volumic fraction (ϕ_h) dependence of the viscosity (η) of mono-layer and double-layer sterically stabilized magnetic fluids of high colloidal stability evidenced that this is best described by the theoretical formula obtained by Chow [27]:

$$\eta = \eta_0 \left[\exp\left(\frac{2.5\phi_h}{1-\phi_h}\right) + \frac{A\phi_h^2}{1-A\phi_h^2\phi_x} \right] \quad (7)$$

As shown in Ref. [18], the overall fitted value of 3.78 for the interaction coefficient A for pentanol-based magnetic fluids, for the temperature range -10 to 70°C , is somewhat lower than the theoretical one ($A = 4.67$), most probably owing to the fact that Eq. (7) was obtained for nonmagnetic suspensions and it does not take into account dipolar interactions between magnetic nanoparticles, which become increasingly important at high packing fractions. Indeed, at temperature values over 50°C , the fitted values of A approach the theoretical one, because the increased thermal motion diminishes the influence of dipolar interactions.

Particle interactions and the formation of agglomerates produce important changes in the flow properties [4, 17, 18] compared to the flow behaviour of a highly stable magnetic fluid. Such qualitative differences between flow properties are easy to evidence in the case of water-based samples when compared to pentanol magnetic fluids.

Fig. 5 Shear-rate dependence of the viscosity of pentanol-based magnetic fluids of different saturation magnetization: magnetic fluid/pentanol (sample 10) (*circles*); magnetic fluid/pentanol (sample 9) (*triangles*); magnetic fluid/pentanol (sample 8) (*squares*)



Comparative diagrams are given in Figs. 4 and 5 for the shear-rate dependence of the viscosities of two water-based and three pentanol-based magnetic fluid samples (samples 2, 7, 8, 9, 10), determined with a PHYSICA MCR 300-type rheometer. The quantitative differences between the two kinds of samples illustrate the significance of their different microscopic makeup [4]. Indeed, in the case of water-based samples, Newtonian behaviour is observed only for the low-saturation-magnetization (below 100 G) sample, with a magnetic solid volume fraction below 2% (sample 2 with 80 G, Table 1). At higher magnetization (e.g., 235 G, sample 7), the influence of agglomerates, usually preformed during preparation, resulted in a strong shear-rate dependence of the viscosity, in particular a threefold decrease in the viscosity of sample 7 with increasing shear rate, up to $1,000 \text{ s}^{-1}$ (Fig. 4), compared to the practically constant viscosity values of samples 2 and 10. Note, that the pentanol-based sample 10 shows Newtonian behaviour, while the water-based sample 7, approximately of the same magnetic particle volume fraction (saturation magnetisation), has quite different, strongly non-Newtonian behaviour (Fig. 6).

A comparison is made concerning the rheological behaviour of the three pentanol-based samples 8, 9 and 10 in Fig. 5. The shear-rate dependence of the viscosity shows slightly non-Newtonian, shear-thinning behaviour

only in the case of the sample with the highest magnetization (sample 8), with the hydrodynamic volume fraction of the particles approaching the upper limit of approximately 0.6 [18]. Samples 9 and 10 are Newtonian.

$\frac{\eta(B) - \eta(0)}{\eta(0)} = f(B)$ curves determined with the cylindrical magnetorheological cell described in Ref. [18] clearly

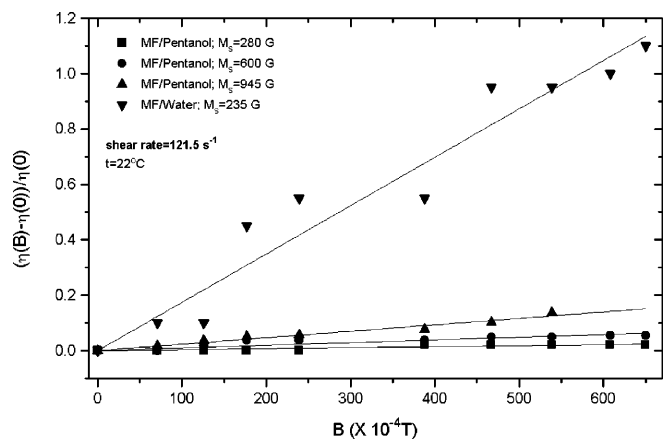


Fig. 6 The magnetoviscous effect for pentanol-based (samples 8, 9, 10) and water-based (sample 7) magnetic fluid (MF) samples at 121.5 s^{-1} shear rate

evidence the large differences existing between the water- and pentanol-based samples. Indeed, the magnetorheological effect in the case of water-based samples is large, $\frac{\eta(B)-\eta(0)}{\eta(0)} \approx 1$ which is not explainable in the framework of the rotational viscosity model valid only for highly dilute magnetic fluids, $\varphi \leq 0.05$ [4, 25]. At the same time, the highly stable pentanol samples, even at the highest magnetization (945 G), show a weak magnetorheological effect, $\frac{\eta(B)-\eta(0)}{\eta(0)} \approx 0.15$ and have practically Newtonian character, even under the influence of a magnetic field.

These results are in very good agreement with the low-field magnetization curves (Fig. 1) and denote that pentanol-based samples are practically free of agglomerates [8, 15, 19], even at high volumic concentration of magnetic nanoparticles (hydrodynamic volume fraction approximately 0.6), while the less concentrated water-based samples have an important fraction of preformed and field-induced agglomerates.

Conclusions

1. The surfactant double-layer steric stabilization procedure was used with good results for a large number of polar carrier liquids, in particular to obtain high-magnetization (up to approximately 950 G) samples on a pentanol carrier, as well as medium-magnetization (up to approximately 300 G) water-based magnetic fluids.
2. Manifold characterization, especially by vibrating-sample magnetometry, rheometry/magnetorheometry

and SANS, revealed different microstructural characteristics of water-based systems compared to pentanol-based samples, as well as the strong influence on the flow properties of preformed and field-induced agglomerates. SANS investigations of samples subjected to a strong magnetic field, characterized also by magnetization and (magneto)rheological measurements, proved to be an efficient method to correlate microstructural characteristics with the flow behaviour of concentrated magnetic fluids under the influence of an applied magnetic field.

3. In the case of less stable water-based samples the magnetorheological effect is much larger than that determined for high-concentration pentanol-based magnetic fluids of very good colloidal stability, in agreement with the mean neutron scattering intensity versus time curves which evidenced the presence of an important fraction of field-induced agglomerates in the case of water-based magnetic fluids.

Acknowledgements The permanent support of Prof. Ioan Anton, a member of the Romanian Academy, was of great help to develop and to perform the many investigations on the structure and flow properties of magnetic fluids presented in this paper. The financial support received through grant no. 87/2001–2002 of the Romanian Academy and through Project no. 37/2001 of the Romanian Space Agency, as well as through grant KFKI-CMRC ICA1-CT-2000–70029 and grant HAS-JINR,SANS Project 2002 of the Hungarian Academy of Sciences, is gratefully acknowledged. The opportunities offered by the scientific exchanges between the Romanian Academy and the Hungarian Academy of Sciences are also acknowledged. The authors are indebted to M. Rasa for careful reading of the manuscript.

References

1. Rosensweig RE (1985) *Ferrohydrodynamics*. Cambridge University Press, Cambridge
2. Blums E, Cebers A, Maiorov MM (1997) *Magnetic fluids*. de Gruyter, Berlin, Chap 7
3. Berkovski B, Bashtovoy V (eds) (1996) *Magnetic fluids and applications handbook*. Begell House, New York
4. Odenbach S (2002) *Magnetoviscous effects in ferrofluids*. Lecture notes in physics. Monographs: physics and astronomy, vol 71. Springer, Berlin Heidelberg New York
5. Vékás L, Bica D, Rasa M, Balau O, Potencz I, Gheorghe D (2001) In: Dascalu D, Paun G, Pincovski E, Topa V, Voicu V (eds) *Micro and Nanostructures*. Academiei Romane, Bucharest, pp 127–158
6. Bica D (1995) *Rom Rep Phys* 47:265–272
7. Bica D, Vékás L (1994) *Magn Hidrodin (Magnetohydrodynamics)* 30:194–196
8. Bica D, Vékás L, Rasa M (2002) *J Magn Magn Mater* 252:10–12
9. Massart R (1981) *IEEE Trans Magn* 17:1247
10. Bica D et al (in preparation)
11. Shimoizaka J (1979) *US Patent* 4,094,804
12. Shen L, Laibinis P E, Hatton TA (1999) *Langmuir* 15:447–453
13. Bica D (1985) *Romanian Patent RO* 90078
14. Bica D, Vékás L (2002) In: Sora I et al (eds) *Echipamente electroacustice pentru procesarea performanta În medii lichide*. Orizonturi Universitare Timisoara, Timisoara, chap 6 (in Romanian)
15. Donselaar LN, Philipse AP, Suurmond J (1997) *Langmuir* 13:6018–6025
16. Vékás L, Bica D, Gheorghe D, Potencz I, Rasa M (1999) *J Magn Magn Mater* 201:159–162
17. Vékás L, Rasa M, Bica D (2000) *J Colloid Interface Sci* 231:247–254
18. Vékás L, Bica D, Potencz I, Gheorghe D, Balau O, Rasa M (2001) *Prog Colloid Polym Sci* 117:104–109
19. Rasa M, Bica D, Philipse AP, Vékás L (2002) *Eur Phys J E* 7:209–220
20. Ivanov AO, Kuznetsova OB (2001) *Colloid J* 63:60–67
21. Avdeev MV, Bălăsoiu M, Bica D, Rosta L, Török Gy, Vékás L (2001) *Mater Sci Forum* 273–276:457–460
22. Aksenov V, Avdeev MV, Bălăsoiu M, Rosta L, Török Gy, Vékás L, Bica D, Garamus V, Kohlbrecher J (2002) *Appl Phys A* 74:943
23. Avdeev MV, Bălăsoiu M, Török Gy, Bica D, Rosta L, Aksenov V, Vékás L (2002) *J Magn Magn Mater* 252:86–88

-
24. Aksenov V, Avdeev MV, Bălăşoiu M, Bica D, Rosta L, Török G, Vékás L () Aggregation in non-ionic water-based ferrofluids by small-angle neutron scattering (to be published)
25. Balau O, Bica D, Koneracka M, Kopcansky P, Susan-Resiga D, Vékás L (2002) In: Bossis G (ed) Proceedings of 8th international conference on electrorheological fluids and magnetorheological suspensions, 9–13 July 2001, Nice, France, World Scientific, Singapore, pp 874–880
26. Vand V (1948) *J Phys Colloid Chem* 52:277–299
27. Chow TS (1994) *Phys Rev E* 50:1274–1279
28. Shliomis MI (1972) *Soviet Phys JETP* 61:2411–2418

Judit Hegyi
Ottó Horváth

Photocatalytic reduction of mercury(II) and simultaneous oxidative degradation of surfactants in titanium dioxide suspensions

Abstract Anionic dodecyl sulfate (DS^-) surfactant proved to be an efficient hole scavenger in the TiO_2 -mediated photocatalytic reduction of $\text{Hg}(\text{II})$ in aqueous solution. While oxygen did not affect the efficiency of mercury deposition in this system, chloride ions strongly hindered it, owing to the formation of anionic chloromercurate(II) complexes. Also pH significantly influenced the reduction of $\text{Hg}(\text{II})$: an increase of pH in the range 4.5–6.8 dramatically enhanced the efficiency. The presence of $\text{Hg}(\text{II})$ considerably accelerated the oxidative degradation of

dodecyl sulfate. This reaction was moderately promoted upon increasing the pH; thus, a neutral or a slightly basic reaction mixture was most suitable for simultaneous removal of $\text{Hg}(\text{II})$ and DS^- . Cationic cetyltrimethylammonium (CTA^+) detergent also acted as a hole scavenger but less efficiently than DS^- . Its photocatalytic degradation, however, was hindered by $\text{Hg}(\text{II})$.

Keywords Photocatalysis · Titanium dioxide · Mercury · Surfactants · Decontamination

J. Hegyi · O. Horváth (✉)
University of Veszprém,
Department of General and Inorganic
Chemistry, P.O. Box 158,
8201 Veszprém, Hungary
e-mail: otto@vegic.sol.vein.hu
Tel: +36-88-427915
Fax: +36-88-427915

Introduction

Much attention has been focused on the photocatalytic degradation of hazardous organic chemicals mediated by TiO_2 particles in aqueous suspensions [1, 2, 3, 4, 5, 6, 7, 8, 9, 10]. Wastewaters, however, contain considerable numbers of metal ions, which are generally nondegradable. Thus, the utilization of semiconductor catalysis has also been studied, although to a lesser extent, for decontamination of heavy-metal polluted waters [11, 12, 13, 14, 15, 16]. Under appropriate conditions quantitative removal of heavy-metal ions becomes possible with irradiated TiO_2 semiconductor particles [17, 18, 19]. Mercury is one of the most dangerous metals to be removed. It is used mainly in electrical equipment, catalysts, metallurgy, the paint and color industry, pharmaceuticals, and pesticides, etc. Its removal from wastewaters is of crucial importance because it is harmful to biological systems and can easily get into the food chain.

In TiO_2 -mediated photocatalysis, metal ions are deposited on the surface of semiconductor particles generally in a reduced, elemental form. The efficiency of this process can be affected by the presence or the absence of oxygen, the irradiation time, the pH of the system, and the concentration of the sacrificial electron donor. Most organic pollutants can serve as electron donors in this system. Several detergents belong to contaminants of our environment owing to their industrial and domestic use. Although they are not directly toxic, they hinder both the dissolution of atmospheric oxygen into natural waters and the sedimentation of floating particles. In this paper, a kinetic study of photoinduced reduction of $\text{Hg}(\text{II})$ using suspended TiO_2 catalyst is presented. The effects of pH, complexing agent, and sacrificial electron donors were studied. Two frequently used surfactants, cationic cetyltrimethylammonium (CTA^+) and anionic dodecyl sulfate, were also chosen as potential electron donors in order to realize simultaneous removal of mercury and oxidative degradation of surface-active pollutants.

Experimental

Reagents

HgCl₂ (reagent grade) was used as a source of Hg(II). TiO₂ (Fluka, predominantly in rutile form) served as a photocatalyst. Triply distilled water was used for the preparation of solutions containing 1×10⁻³ M Hg(II) to be reduced and 0.1 wt% TiO₂ suspended. Analytical grade ethanol, sodium dodecyl sulfate (SDS), and cetyltrimethylammonium bromide (CTAB) (Aldrich) were applied as electron donors in various concentration. NaOH and H₂SO₄ were utilized for adjusting the pH of the solutions to be irradiated.

Instruments

The experiments were carried out in a glass-jacketed reactor vessel filled with 60 cm³ (or, in some cases 180 cm³) of reaction mixture and wrapped with aluminium foil. A 125-W immersion-type medium-pressure mercury lamp was applied as a radiation source. The light intensity was determined by ferrioxalate actinometry [20] ($I_a = 1.5 \times 10^{-5}$ mol photons dm⁻³ s⁻¹ at 366 nm). A GBC UV-vis 911A spectrophotometer was used for the analysis.

Procedure

Photolysis of the reaction mixtures was carried out for various time intervals up to 20 min. Oxygen-free experiments were carried out by bubbling nitrogen through the reaction solution for 15 min prior to and throughout the experiment. Continuous mixing was provided with permanent gas flow (air or N₂) and a magnetic stirrer. The pH was adjusted using a glass electrode. All experiments were carried out with solutions thermostated to 22.0 °C.

Analysis

After the irradiation the samples were filtered through a syringe-driven filter unit (Millex, 25-mm diameter, 0.45-μm pore size). The photolyzed solution was analyzed for Hg(II) spectrophotometrically using halide ions as complexing agents. A 0.5-cm³ aliquot of the sample was taken and introduced into 2.5 cm³ 4 M NaCl solution in a 1-cm quartz cuvette. The absorbance of the chloromercurate(II) complexes formed was measured at 233 nm. This procedure could not be applied in the presence of CTAB. In that case Hg(II) was analyzed as iodo complex: 2 cm³ of the sample was mixed with 1 cm³ 0.001 M NaI solution in a 1-cm quartz cuvette. The absorbances of the halomercurate(II) complexes obeyed the Bouguer–Lambert–Beer law in the concentration range studied (0–7×10⁻⁴ M).

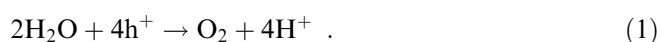
The concentration of the detergents was also determined photometrically. A 0.2-cm³ aliquot of the sample was diluted with distilled water to 100 cm³. In the case of SDS, 25 cm³ was added to the diluted sample from the following solution: 30 cm³ 1 g dm⁻³ methylene blue aqueous solution, 6.8 cm³ H₂SO₄ and 50 g NaHPO₄·H₂O were mixed and diluted with distilled water to 1 dm³. Chloroform (10 cm³) was also added to this mixture. Methylene blue and SDS form a complex which dissolves in chloroform (organic phase). After the extraction, the absorbance of the organic phase was measured at 652 nm in a 0.5-cm quartz cell. In the case of CTAB, (instead of methylene blue) methyl orange was used as a color agent in the same procedure, and the absorbance of the adduct formed was measured at 415 nm.

Results and discussion

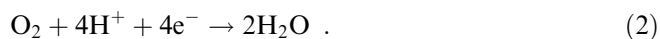
Theory

Bandgap excitation of semiconductor particles suspended in water causes electronic transitions from the valence band to the conduction band, leaving holes in the former. These electrons and holes then either migrate to the particle surface and become involved in redox reactions or they recombine and simply liberate heat.

Conduction-band electrons can serve as reductants, while holes are filled via oxidation reactions. The photogenerated hole (h⁺) can oxidize H₂O as an initial step:



The oxygen molecule, however, as an electron acceptor can chemically reverse this process:

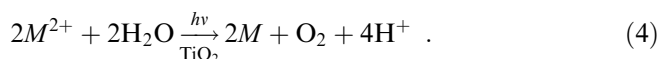


If the carrier fluxes owing to the oxidation and reduction reactions, Eqs. (1) and (2) are exactly balanced, there is no net chemistry, and O₂ has functioned as a short-circuiting agent for mediating the e⁻-h⁺ recombination process.

In pollutant destruction, either Eq. (1) or Eq. (2) constitutes half the conjugate reaction pair; the other half of the pair comprises the pollutant molecule or ion. Besides oxygen, any dissolved species with a reduction potential more positive than the conduction band of the photocatalyst can, in principle, consume electrons and complete the redox cycle. For example, with a toxic metal ion M²⁺



In this instance, Eqs. (1) and (3) form a conjugate pair, giving the overall reaction



The energetics of this reaction, Eq. (4), is determined by its Gibbs free-energy change (ΔG^0) [21]. If it is negative ($\Delta G^0 < 0$), the reaction is photocatalytic. In this case, the reduction of the metal ion is thermodynamically preferred, and the radiant energy simply serves to overcome the activation barrier for the process. If ΔG^0 for this reaction is positive, it is photosynthetic: the light drives the system in the thermodynamically uphill direction. Photoassisted reduction of metal ions is generally photosynthetic, except for metals with very positive potentials, i.e., when they have standard reduction potentials that are more positive relative to the O₂/H₂O redox couple. These reactions too can be made photocatalytic with the addition of appropriate hole

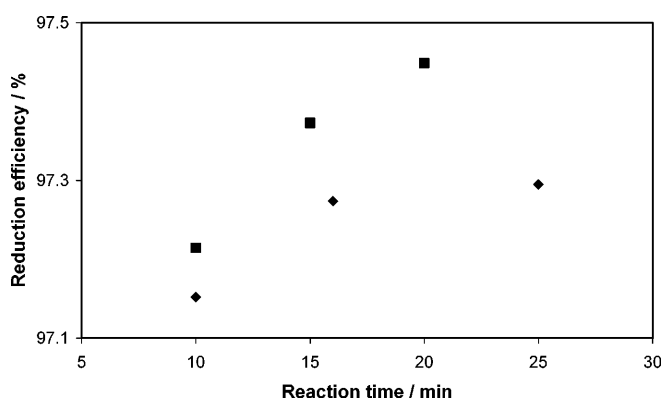


Fig. 1 Efficiency of Hg(II) reduction versus reaction time in the presence (diamonds) and absence (squares) of oxygen in the presence of 2.6×10^{-2} M ethanol

scavengers. Thus, the free-energy change for the overall process becomes negative.

Effect of oxygen on the photocatalytic reduction of Hg(II)

Although Hg(II) can be reduced by TiO₂-mediated photocatalysis in air-saturated aqueous solution without added hole scavengers, the reaction is relatively slow for practical application. However, in the presence of ethanol as a sacrificial electron donor, the reaction rate is significantly enhanced [22]. According to Eq. (2), besides Hg(II), O₂ can also act as an electron scavenger in this system; hence, the effect of dissolved oxygen had to be checked. The presence of oxygen can be expected to decrease the efficiency of the reduction of Hg(II) owing to the competition for the conduction-band electrons and possible promotion of reoxidation of the deposited mercury as experienced earlier in the absence of additional hole scavengers [17]. As shown in Fig. 1, the difference between the reduction efficiencies of air-saturated and deoxygenated systems is negligible (less than 0.5% after 15–20-min irradiation) in the presence of 2.6×10^{-2} M ethanol. Thus, application of efficient hole scavengers makes the deoxygenation superfluous in these reduction processes. Notably, the rate of the photoinduced reduction of mercury became very low above 90% deposition owing to the significant decrease in the actual reduction potential of Hg(II) according the Nernstian equation.

Effects of pH on the reduction of Hg(II)

The photocatalytic or photosynthetic nature of a system which does not contain an added hole scavenger can be determined by the comparison of the standard reduction

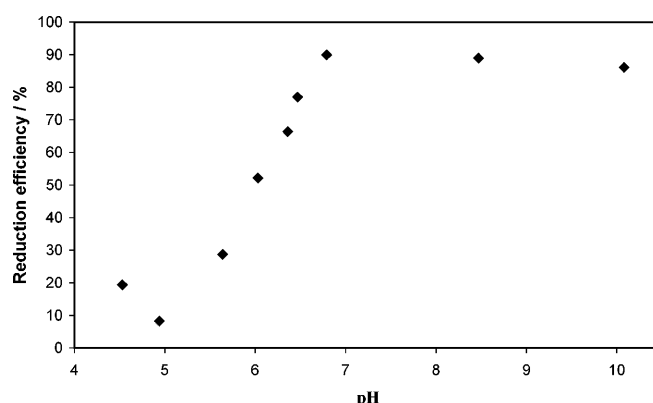


Fig. 2 Efficiency of Hg(II) reduction versus pH at 3-min reaction time in an air-saturated system

potential of the metal ion to be reduced to that of the O₂/H₂O couple. The latter, however, is rather pH-dependent, according to the Nernstian equation (at 25 °C) [23]:

$$E(\text{O}_2/\text{H}_2\text{O}) = (1.229 - 0.059\text{pH})\text{V} . \quad (5)$$

Besides, the potential of the conduction-band obeys a similar relationship [24]:

$$E(\text{CB}) = (-0.05 - 0.059\text{pH})\text{V} . \quad (6)$$

Thus, the pH is expected to strongly affect the efficiency of the reduction of Hg(II). Since the presence of effective hole scavengers levels the reduction efficiency, no added electron donors were used in the experiments on the pH effect. Preliminary results indicated that even after 3-min irradiation the air-equilibrated system reached an almost photostationary state. Thus, the efficiency of photoinduced reduction of Hg(II) was determined after 3-min photolysis at various pH values. As can be seen in Fig. 2, upon increasing the pH, a dramatic increase in the efficiency occurred in the range pH 5–6.5. Above this range a slight decrease can be observed in basic systems (down to pH 10).

The promoting effect of the increasing pH can partly be accounted for by the relationships described by Eqs. (5) and (6). Thus, the reducing potentials of both the water molecules (as hole scavengers) and the conduction-band electrons, toward Hg(II) species, are enhanced at decreasing acidity. These general tendencies, however, cannot unambiguously explain the characteristics of the plot in Fig. 2. The steep increase in a relatively narrow range of pH (5–6.5) might also be associated with the surface charge of the semiconductor particles, especially because the zero point of charge, pH_{zpc} , of TiO₂ (both anatase and rutile) is in the same range [25].

The slight decrease of the reduction efficiency in the basic solutions may also be caused by the surface charge, which is negative above pH_{zpc} . Since HgCl₂ molecules coordinates OH⁻ ions, the anionic mixed ligand

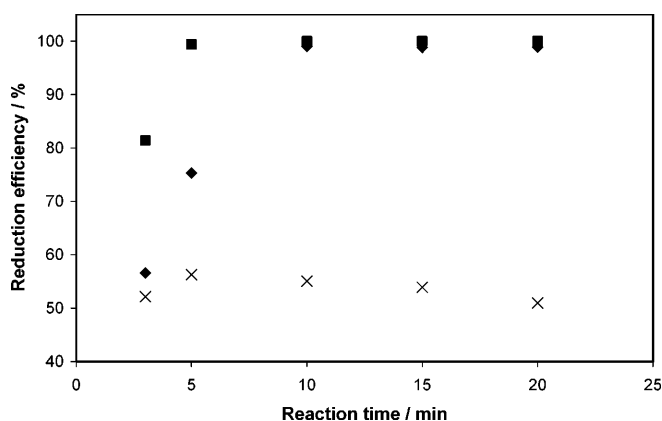


Fig. 3 Efficiency of Hg(II) reduction versus irradiation time at pH 6 without a hole scavenger (*crosses*), in the presence of 5×10^{-4} M sodium dodecyl sulfate (SDS) (*squares*) and 1×10^{-3} M ethanol (*diamonds*)

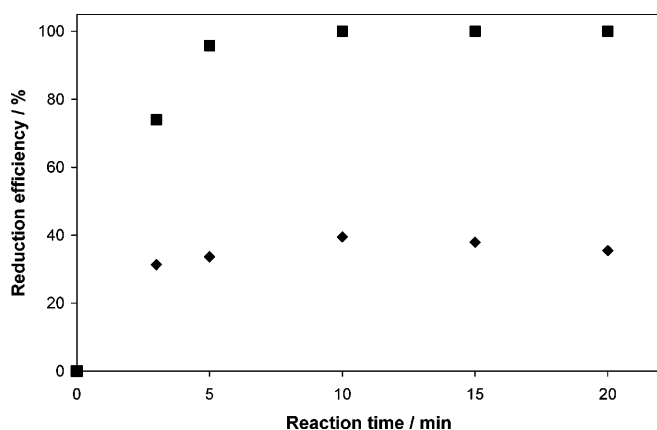


Fig. 4 Efficiency of Hg(II) reduction versus irradiation time in the absence (*squares*) and in the presence (0.1 M) (*diamonds*) of Cl^- , with 5×10^{-4} M SDS in both cases

halo-hydroxomercurate(II) complexes formed are hindered in the approach to the surface of the photocatalyst.

Effects of DS^- and chloride ions

DS^- proved to be a very good hole scavenger for the reduction of Hg(II). Its promoting effect is rather strong even at relatively low concentration. At pH 6, 5×10^{-4} M SDS speeds up the rate of the reaction more efficiently than 1×10^{-3} M ethanol does (Fig. 3). In both cases, the efficiency of the Hg(II) reduction approached 100% after 10-min irradiation, while in the absence of an added electron donor about 55% was reached, then a moderate decrease was also observed. The latter phenomenon was also experienced earlier [17], owing to the back-oxidation in air-saturated systems.

Addition of chloride ions to the system containing 5×10^{-4} M SDS as a sacrificial electron donor caused a dramatic decrease in the efficiency of the Hg(II) reduction. As Fig. 4 shows, the reduction efficiency does not exceed 40% in this case, while in the absence of Cl^- ions nearly 100% can be reached.

Besides, after 10-min, further irradiation resulted in a considerable decrease in the efficiency. The reason for this phenomena is similar to that of the effect of higher pH in basic solutions. The neutral HgCl_2 particles coordinate negatively charged ligands (Cl^- , in this case) and form anionic HgCl_3^- and (to a slightly lesser extent) HgCl_4^{2-} complexes. The negative charge of these species hinders the reduction of the metal center by the conduction-band electrons, even in the presence of added hole scavenger. Complex formation, as a chemical driving force, promotes the back-oxidation of the deposited mercury in the air-saturated system.

Photocatalytic degradation of DS^-

The results presented in the previous section clearly show that DS^- acts as an efficient hole scavenger in the TiO_2 -mediated photocatalytic reduction of Hg(II). Since in this photoelectrochemical process the number of charges involved in the reduction by conduction-band electrons and oxidation by valence-band holes must be equal, one can expect that the promoting effect is mutual, i.e., the presence of Hg(II) species enhances the photoassisted degradation of DS^- . In accordance with earlier studies [9], SDS can be degraded via photoinduced oxidation in air-saturated aqueous TiO_2 suspensions with no additives (Fig. 5). In the presence of 1×10^{-3} M HgCl_2 , however, the average rate of the SDS disappearance in this system became about 3 times higher than that without additives. This very strong enhancement indi-

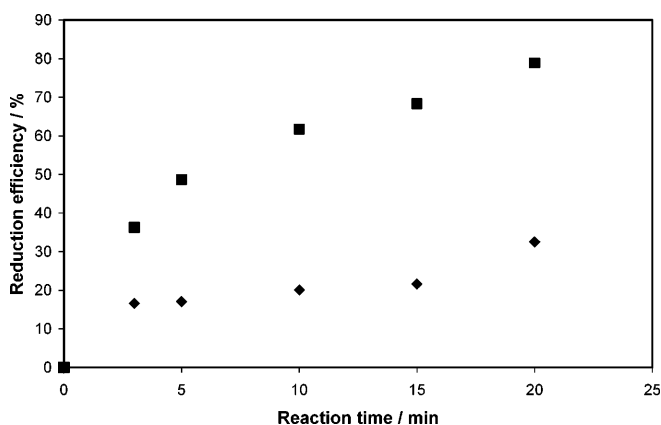


Fig. 5 Efficiency of dodecyl sulfate degradation versus irradiation time in the absence (*diamonds*) and in the presence (1×10^{-3} M) (*squares*) of HgCl_2 at pH 6

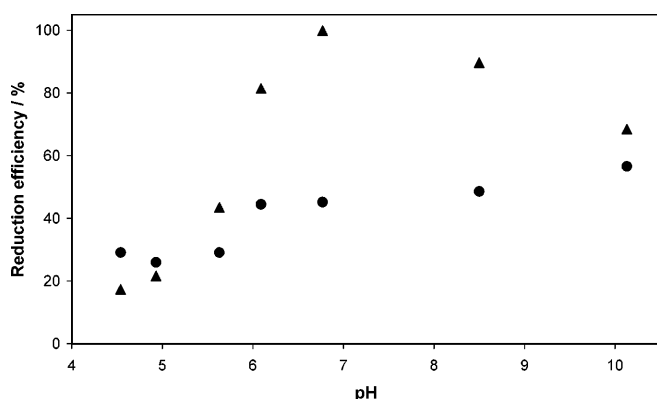


Fig. 6 Efficiency of Hg(II) reduction (*triangles*) and SDS degradation (*circles*) versus pH after 3-min irradiation (initial concentrations 1×10^{-3} M HgCl₂, 3×10^{-3} M SDS)

cates that these mutual promoting effects can be utilized in efficient simultaneous oxidative degradation of DS⁻ and reductive deposition of mercury in the same system.

Effects of pH on the Hg(II)–SDS system

On the basis of the previous results, it can be expected that one of the most crucial parameters for the effective simultaneous removal of mercury and degradation of SDS is the pH of the photocatalytic system. Thus, the effects of pH were also studied in mixtures containing both HgCl₂ and DS⁻. Since at some values of the pH the efficiency of the Hg(II) reduction levels off after 5- or 10-min photolysis of 60 cm³ reaction mixture, from the experimental series the results regarding the 3-min irradiation were taken for the efficiency versus initial pH plots. (In order to decrease the reaction rate and, thus, to increase the time resolution of the analysis, the experiments of this type were also carried out with 180 cm³ of reaction mixture, with the same light source. The same tendencies were observed, and the actual values of the efficiency after 9-min irradiation in this system were almost equal to those measured in the 60-cm³ mixtures after 3 min.) Besides, a significant change in pH was observed after a considerable conversion of the contaminants in most cases. Thus, experimental values regarding the earlier stage of the photolysis give more reliable information on the effects of the initial pH.

As shown in Fig. 6, the initial pH significantly affects the efficiency of Hg(II) reduction. Although the reaction mixtures contained added hole scavenger (SDS) of considerable concentration (3×10^{-3} M) in this case, the characteristics of the plot are very similar to those of the previous experiments without added sacrificial electron donor (Fig. 2). Only the absolute values of the efficiency are higher owing to the promoting effect of SDS. This phenomenon indicates that the influence of pH in the

reduction of Hg(II) in this system is mostly effective in the primary interaction between the Hg(II) species and the conduction-band electrons, affecting $E(\text{CB})$ and the charge of both the Hg(II) complex and the surface of the photocatalyst, and independent of the hole scavenger. Thus, the characteristics of this plot can be interpreted in the same way as in the case of Fig. 2.

The initial pH affects the efficiency of the SDS destruction, however, much less than that of the mercury deposition. Probably that is why the characteristics of the Hg(II) reduction plot did not change in the presence of DS⁻. A slight but continuous increase of the degradation efficiency can be observed upon increasing the initial pH. This phenomenon cannot be attributed to the change of the valence-band oxidation potential because it linearly decreases in accordance with the Nernstian equation (at 25 °C) [26]:

$$E(\text{VB}) = (3.15 - 0.059\text{pH})\text{V} . \quad (7)$$

The change of the surface charge of the photocatalyst cannot explain this tendency either because it becomes more and more negative upon increasing the pH, repulsing the anionic detergent. This indicates that adsorption of DS⁻ is mainly governed by the apolar hydrocarbon chain. A possible explanation for the pH effect on the SDS degradation can be found in the stoichiometry of the oxidation of the electron donors by the valence-band holes. As shown by Eqs. (1) and (8), consumption of each hole results in the formation of one proton in an aqueous system, no matter if water or DS⁻ is the hole scavenger.



In Eq. (8) $-\text{CH}_2-$ symbolizes one unit of the reducing hydrocarbon chain of SDS.

This interpretation is supported by the significant decrease of the pH during the photolysis, especially in the case of initial values of 4.5–8.5. In this range of the initial pH, after 20-min irradiation resulting in nearly 100% reduction of 1×10^{-3} M Hg(II), the final pH is 2.8–3.0. These changes are in accordance with the formation of about 2×10^{-3} M protons.

On the basis of the results shown in Fig. 6, a neutral or a slightly basic reaction mixture is most preferable for simultaneous photocatalytic decontamination of wastewaters containing Hg(II) and DS⁻. In such a medium, the rate of mercury deposition is maximum, while the rate of the SDS disappearance is acceptable, and also its efficiency reaches 100% within 20-min irradiation. Besides, nearly neutral solutions are favorable in environmental respects too.

Photocatalytic degradation of CTAB

In our earlier study with a high-pressure mercury lamp and 3 cm³ reaction mixtures, a slight promoting effect of

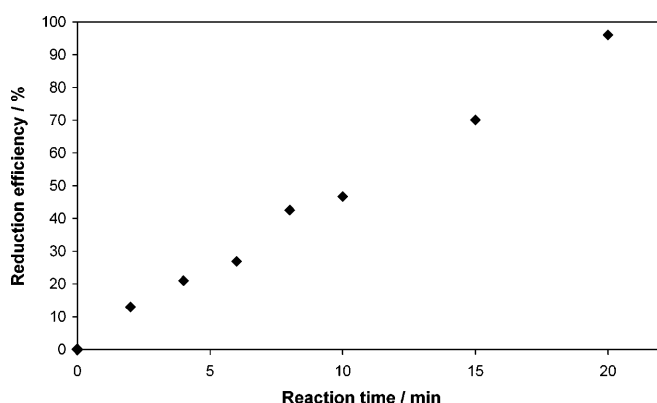


Fig. 7 Efficiency of Hg(II) reduction versus irradiation time in the presence of 0.01 M cetyltrimethylammonium bromide (CTAB)

the CTA^+ detergent on the photocatalytic reduction of Hg(II) was experienced [22]. Besides, CTAB proved to be a much less efficient hole scavenger than ethanol. Experiments in the present work using a 60-cm³ reactor with an immersion-type medium-pressure mercury lamp confirmed these observations. Addition of 0.01 M CTAB to the reaction mixture of pH 6 resulted in nearly 100% deposition of mercury after 20-min irradiation (Fig. 7). Deviating from the cases of no added hole scavenger or the SDS-containing system (Fig. 3), the reduction efficiency is a linear function of the irradiation time up to 20 min. Without added electron donor, the maximum efficiency is about 55%, while in the presence of SDS (only 5×10^{-4} M) 100% reduction is reached within 5 min. This clearly shows that the CTA^+ is a considerably less efficient hole scavenger than DS^- . This phenomenon might be associated with the charge of the electron donors.

The TiO_2 -mediated photocatalytic degradation of CTA^+ was also studied in this system. In the reaction mixture containing no Hg(II), the rate of the disappearance of the CTA^+ (on the basis of the degraded percentage versus reaction time plot, Fig. 8) was about twice as high as that of the DS^- under similar circumstances (Fig. 5). Moreover, considering the much higher initial concentration of CTAB (0.01 M), its photoassisted degradation proved to be rather efficient. The presence of Hg(II) (1×10^{-3} M HgCl_2), however, dramatically decreased the efficiency of the photodegradation of CTAB. In this system, the rate of the CTA^+ disappearance (on the basis of the initial linear section of the plots, up to 10-min reaction time) was diminished to one fifth of the value experienced in the absence of Hg(II) (Fig. 8). Although the absolute rate of the degradation is considerable even in this case, the strong hindering effect

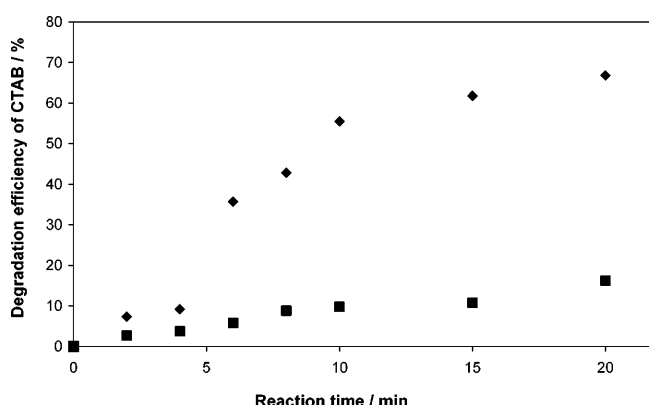


Fig. 8 Efficiency of the photocatalytic degradation of CTAB versus irradiation time in the absence (diamonds) and in the presence (squares) of Hg(II). Initial parameters pH 6, 1×10^{-3} M HgCl_2 , 0.01 M CTAB

of Hg(II) ought to be taken into account in the practical utilization of this simultaneous decontamination procedure. In order to elucidate the mutual effects experienced in the Hg(II)–CTAB system, further experiments are in progress.

Conclusion

Simultaneous removal of Hg(II) and surfactants was realized in TiO_2 -mediated photocatalysis. DS^- surfactant as an electron donor efficiently promoted the reduction of Hg(II) in aqueous solution. In the presence of added hole scavenger, oxygen did not affect the efficiency of mercury deposition, while chloride ions considerably hindered this process as a consequence of the formation of anionic chloromercurate(II) complexes. An increase of pH in the range 4.5–6.8 significantly enhanced the efficiency of the Hg(II) reduction. As a mutual effect, Hg(II) promoted the oxidative degradation of DS^- . This reaction was moderately accelerated upon increasing the pH. Thus, for simultaneous reduction of Hg(II) and oxidative destruction of DS^- , a neutral or a slightly basic reaction mixture was found to be most suitable. CTA^+ detergent also functioned as a sacrificial electron donor, although less efficiently than DS^- . Its photocatalytic degradation, however, was strongly reduced by Hg(II). Even so, simultaneous decontamination by TiO_2 -mediated photocatalysis can also be realized in this case.

Acknowledgement Support for this work by the Hungarian Ministry of Education (FKFP 0082/1999) is gratefully acknowledged.

References

1. Ollis DF (1985) *Environ Sci Technol* 19:480
2. Okamoto K, Yamamoto Y, Tanaka H, Tanaka M (1985) *Bull Chem Soc Jpn* 58:2015
3. Matthews RW (1986) *Water Res* 20:569
4. Matthewa RW (1988) *J Catal* 111:264
5. Terzian R, Serpone N, Minero C, Pelizetti E (1991) *J Catal* 128:352
6. Heller A, Brock JR (1994) In: Helz GR, Zepp RG, Crosby DG (eds) *Aquatic surface photochemistry*. Lewis, Boca Raton, pp 427–436
7. Hoffmann MR, Martin ST, Choi W, Bahnemann DW (1995) *Chem Rev* 95:69
8. Linsebigler AL, Guangquan L, Yates JT Jr (1995) *Chem Rev* 95:735
9. Lea J, Adesina AA (1998) *J Photochem Photobiol A* 118:111
10. Fujishima A, Rao TN, Tryk DA (2000) *J Photochem Photobiol C* 1:1
11. Curran JS, Domenech J, Jaffrezic-Renault N, Philippe R (1985) *J Phys Chem* 89:957
12. Borgarello E, Serpone N, Emo G, Harris R, Pelizetti E (1986) *Inorg Chem* 25:4499
13. Domenech J, Munoz J (1987) *Electrochim Acta* 32:1383
14. Herrmann J-M, Disdier J, Pichat P (1988) *J Catal* 113:72
15. Herrmann J-M, Guillard C, Pichat P (1993) *Catal Today* 17:7
16. Lau LD, Rodriguez R, Henery S, Manuel D (1998) *Environ Sci Technol* 32:670
17. Serpone N, Ah-You YK, Tran TP, Harris R, Pelizetti E, Hidaka H (1987) *Sol Energy* 139:491
18. Prairie MR, Evans LR, Stange BM, Martinez SL (1993) *Environ Sci Technol* 27:1176
19. Tennakone K, Wijayantha KGU (1997) *J Photochem Photobiol A* 113:89
20. Hatchard CG, Parker CA (1956) *Proc R Soc Lond A* 235:518
21. Rajeshwar K, Ibanez JG (1995) *J Chem Educ* 72:1044
22. Horváth O, Hegyi J (2001) *Prog Colloid Polym Sci* 211
23. Kobayashi T, Taniguchi Y, Yoneyama H, Tamura H (1983) *J Phys Chem* 87:768
24. Ward MD, White JR, Bard AJ (1983) *J Am Chem Soc* 105:27
25. Aguado MA, Cervera-March S, Giménez J (1995) *Chem Eng Sci* 50:1561
26. Chen D, Ray AK (2001) *Chem Eng Sci* 56:1561

Ottó Horváth
Tamás Marosvölgyi
József Vörös

Microenvironmental effects on equilibrium and photoredox chemistry of bromo complexes in reverse micelles

Abstract Kinetically labile bromo complexes are formed with main-group metal ions of s^2 and s^0 electron configurations both in homogeneous aqueous solutions and in water droplets inside reverse micelles. The local concentration of the Br^- ligand in the inner water pool can reach extremely high values if it is the counterion of the surfactant as in the case of cetyltrimethylammonium bromide (CTAB) dissolved in CH_2Cl_2 or CHCl_3 . Bromo complexes of the possibly highest coordination number are formed with Sb^{3+} ($n=6$), Bi^{3+} ($n=6$), and Pb^{2+} ($n=4$) in these systems at low water to surfactant molar ratio, W . Irradiation of these complexes results in ligand-to-metal charge-transfer (LMCT) reactions generating Br_3^- as an end product. The quantum yields for the overall processes

dramatically decrease upon increasing W in the CTAB/ CHCl_3 systems. This phenomenon can be attributed to a hydration effect enhancing the efficiency of the vibrational energy dissipation. In homogeneous aqueous solution of 0.1 M Br^- , the predominant coordination number of bromomercurate(II) complexes is 4, while inside aerosol-OT reverse micelles (at the same local concentration of the ligand) it is only 3, owing to the dehydration of the reactants of the same charge in the complex equilibrium. Upon UV excitation, these complexes also undergo a LMCT reaction producing elemental mercury and Br_3^- as end products.

Keywords Reverse micelles · Photoredox chemistry · Main-group metal ions · Bromo complexes · Ligand-to-metal charge-transfer reaction

O. Horváth (✉) · T. Marosvölgyi
J. Vörös
University of Veszprém,
Department of General and
Inorganic Chemistry, P.O. Box 158,
8201 Veszprém, Hungary
e-mail: otto@vegic.sol.vein.hu
Tel: +36-88-427915
Fax: +36-88-427915

Introduction

For kinetically labile complexes to exist in aqueous solutions the ligand needs to be in considerable excess [1, 2, 3, 4, 5]. Species with higher ligand numbers are generally formed in aprotic solvents of low coordination ability [6, 7, 8, 9, 10]. Application of reverse micelles, however, gives us the possibility to examine aqueous-phase complexes with different ligand numbers which do not exist in homogeneous aqueous solutions. In nonpolar solvents cationic surfactants, for example, cetyltrimethylammonium bromide (CTAB), form micelles, the outer sides of which consist of hydrophobic hydrocarbon

chains, while their inner sides are built up of the ionic groups of the tensides. Since the concentration of water in these systems is comparable with that of the surfactants, an extremely high local concentration of the counterions can be realized in the micro aqueous phase. If these ions (e.g., halides) are potential ligands, dissolution of appropriate metal ions can lead to the formation of complexes with high coordination numbers. In the case of kinetically labile complexes, different species exist in equilibrium, which can be influenced by the water-to-surfactant molar ratio, W . Since the charge density inside these micelles is extremely high, the activity of the ions in these aqueous microphases can significantly

differ from those in homogeneous aqueous solutions at similar concentrations. In a system containing reverse micelles, water molecules can exist in at least three different (micro) environments as proved by IR [11, 12, 13] and ^1H NMR [11, 14] studies: dissolved in the bulk of the organic solvent, directly adhered to the inner, hydrophilic surface of the micelle, and in a layer less linked to the micellar wall, but still strongly polarized.

These aqueous phase microreactors ensure special environments not only for the complex equilibria but also for the photo and thermal reactions taking place in them. The overall quantum yield of photoinduced reactions in homogeneous solutions is significantly determined by the fate of the products of the primary photochemical step. Namely, the competition between the recombination (back reaction) of the primary product pair and their escape from the solvent cage in which they formed. This competition can be strongly influenced by a micellar environment, especially because in most cases one reverse micelle contains (at appropriate concentrations) only one (if any) photoactive complex. Thus, for example, the dark reactions between the primary (or secondary) photochemical products (intermediates) and the ground-state complexes can be considerably hindered. The overall quantum yield can be significantly affected by this environment if the solubility of an intermediate or a final product is much higher in the organic bulk phase than in water. Then an in situ extraction can hinder the back reactions, and, thus, efficient photocatalytic systems can be realized.

The aim of our work was to study how the micro-environment inside the reverse micelles influence the formation and the photoinduced reactions of the bromo complexes of Bi(III), Pb(II), Sb(III), and Hg(II).

Experimental

Reagents

Analytical grade BiBr_3 , SbBr_3 , $\text{Pb}(\text{NO}_3)_2$, NaBr , LiBr , CTAB and aerosol-OT (sodium dioctyl sulfosuccinate, AOT) were used for the preparation of the solutions studied. Chloroform, dichloromethane, and isooctane of spectroscopic grade as well as Milli-Q water served as solvents. For removal of water traces in the organic solvents molecular sieves of 4-Å pore size were applied. The concentration of the surfactant was 0.1 M in the CTAB/ CH_2Cl_2 and 0.2 M in the CTAB/ CHCl_3 systems. Dichloromethane was used for the study of the equilibrium because it makes wider ranges of W possible. Chloroform, being less volatile, was applied for photolysis experiments, in some cases of which degassing was carried out. Microvolumes from aqueous stock solutions of the simple metal salts were introduced into 10 cm^3 of the micellar systems using Drummond micropipettes of 1–10 μl and homogenized. Perchloric acid (1:1) was used to acidify the stock solutions of Sb(III) and Bi(III) for prevention of hydrolysis. Bromomercurate(II) complexes were prepared in an AOT/isooctane system containing 0.0167 M surfactant. HgBr_2 was dissolved in 0.1 M NaBr solution then introduced into the micellar system. All experiments were carried out with solutions thermostated to

25.0 °C. Oxygen-free experiments were carried out by bubbling argon through the reaction solution for 45 min prior to the irradiation. During the photolyses, the reaction mixtures were continuously homogenized by magnetic stirring.

Instruments and procedures

Absorption spectra were recorded using a GBC 911/A UV–vis spectrophotometer. For most of the continuous-wave experiments an AMKO LTI photolysis apparatus (containing a high-pressure 200-W Xe–Hg lamp and a monochromator) was applied. For irradiation of bromomercurate(II) complexes ($\lambda_{\text{ir}} = 253.7\text{ nm}$), a low-pressure 16-W mercury-arc lamp was used. The light intensity was measured by ferrioxalate actinometry [15] and frequently checked by a thermopile. The experimental results were processed and evaluated by Quattro and Microsoft Excel programs on personal computers. The quantum yields for the formation of Br_3^- were determined from the initial rates of the photoinduced reactions, following the spectral changes.

Results and discussion

Spectra and equilibria

Bromo complexes of Sb(III), Pb(II), and Bi(III) were studied in cationic CTAB/ CH_2Cl_2 reverse micelles from the viewpoint of the absorption spectra and coordination number. Since the electronic spectra of the bromomercurate(II) complexes strongly overlapped with the spectrum of CTAB, these coordination compounds were investigated in the anionic AOT/isooctane micellar system. In some cases, for comparison, spectra were also recorded in homogeneous aqueous solutions. Equilibrium constants were not calculated for the micellar systems because the actual activities of the reactants cannot be determined in the aqueous microphase, although the formal concentrations and ionic strengths may be estimated.

Bromoantimonate(III) complexes

Sb(III) is strongly inclined to hydrolysis, hence SbBr_3 was introduced into the CTAB/ CH_2Cl_2 system after dissolution in 1:1 HClO_4 solution. For the same reason 1:1 HClO_4 solution was also used to adjust the water content. Even so, 5.2 was the maximum value of W realizable in this system. On the basis of the literature [16] the formation of SbBr_4^- and SbBr_6^{3-} complexes was expected, with characteristic bands at 334 and 359 nm, respectively. If solid SbBr_3 was dissolved in the water-free CTAB/ CH_2Cl_2 system, hexabromoantimonate(III) was unambiguously identified. If a strongly acidified solution of SbBr_3 was introduced, the formation of both SbBr_4^- and SbBr_6^{3-} was observed (Fig. 1). In the range of W studied (0.8–4.8), the hexacoordinated complex is the predominant species as indicated by the position of the longest-wavelength absorption band at 449–457 nm.

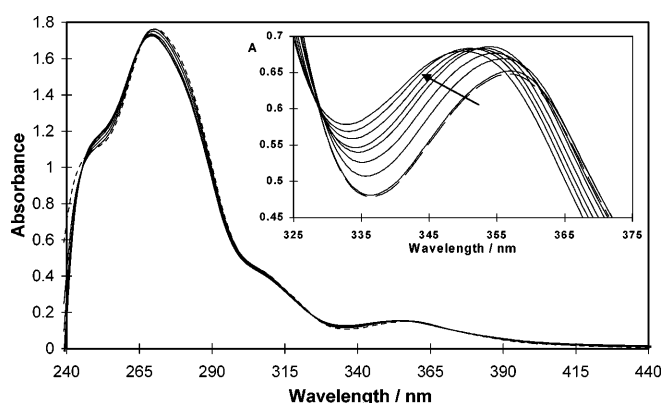


Fig. 1 Spectral change of a 0.1 M cetyltrimethylammonium bromide (CTAB)/CH₂Cl₂ system containing 1.5×10^{-4} M (in the inset 6×10^{-4} M) Sb(III) upon increasing the water-to-surfactant molar ratio, W , from 0.8 to 4.8, recorded in a 1-cm cuvette

Upon increasing the water content, the shifts of the band towards shorter wavelengths suggest moderate increases in the molar fraction of SbBr_4^- .

Bromobismuthate(III) complexes

Bromobismuthate(III) complexes in the CTAB/CH₂Cl₂ system could only be studied in a range of W even narrower than in the case of bromoantimonate(III) complexes because of the more effective hydrolysis. In this case, a stock solution of $\text{Bi}(\text{NO}_3)_3$ strongly acidified with HNO_3 was introduced into the micellar system. Above $W=2$, colloidal $\text{Bi}(\text{OH})_3$ or BiOBr appeared, impeding the spectrophotometric measurements. According to the literature [16, 17], in acetonitrile, the BiBr_4^- complex displays a characteristic band at 367 nm, while the longest-wavelength transition of BiBr_6^{2-} can be found at 384–387 nm. In homogeneous aqueous solution containing 6 M NaBr, absorption bands at 374 nm can be observed, indicating that both complexes exist in comparable concentrations in this system. The absorption spectra obtained in the CTAB/CH₂Cl₂ system show the longest-wavelength band at 382 nm (Fig. 2). This suggests that the predominant complex inside the CTAB reverse micelles is hexabromobismuthate(III), and its molar fraction only slightly decreased upon increasing the water content up to $W=2$.

Bromoplumbate(II) complexes

The formation of bromoplumbate(II) complexes in the CTAB/CH₂Cl₂ system can be studied in a rather wide range of W (0.94–19.01) because Pb^{2+} ions do not hydrolyze in neutral solution.

According to the literature [16], in acetonitrile, the longest-wavelength characteristic bands can be found at

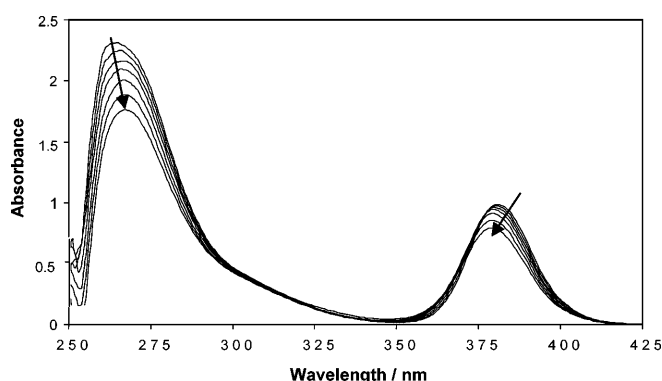


Fig. 2 Spectral change of a 0.1 M CTAB/CH₂Cl₂ system containing 2.0×10^{-4} M Bi(III) upon increasing W from 0.18 to 2.0, recorded in a 1-cm cuvette

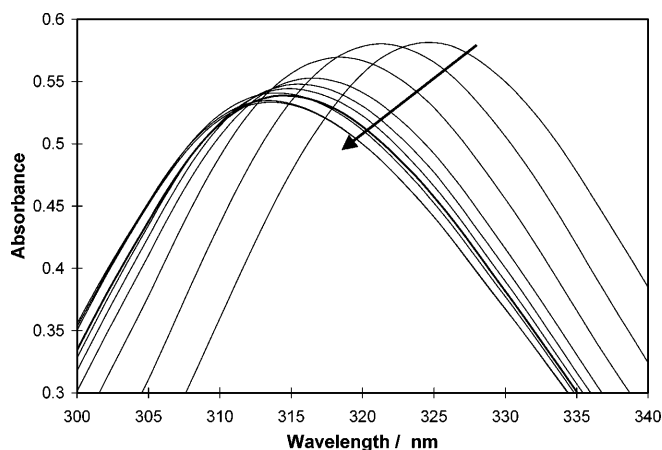


Fig. 3 Spectral change of a 0.1 M CTAB/CH₂Cl₂ system containing 2.5×10^{-4} M Pb(II) upon increasing W from 0.97 to 19.0, recorded in a 1-cm cuvette

306 and 343 nm for the PbBr_3^- and PbBr_4^{2-} complexes, respectively. In homogeneous aqueous solution containing 6 M NaBr, an absorption band at 303 nm can be observed, indicating that the tribromoplumbate(II) complex is predominant in this system.

In the CTAB/CH₂Cl₂ system, at low water content, the band maximum appears at 325 nm (Fig. 3). This suggests that both PbBr_3^- and PbBr_4^{2-} complexes exist in comparable concentration at $W=1.6$. Upon increasing the water content up to $W=19$, the band is slightly decreased and shifted to 313 nm, indicating that the tribromoplumbate(II) complex became the predominant species.

Bromomercurate(II) complexes

On the basis of the literature [18, 19, 20], the characteristic absorption bands for HgBr_3^- and HgBr_4^{2-} in water and methanol can be found at 262 and 250 nm,

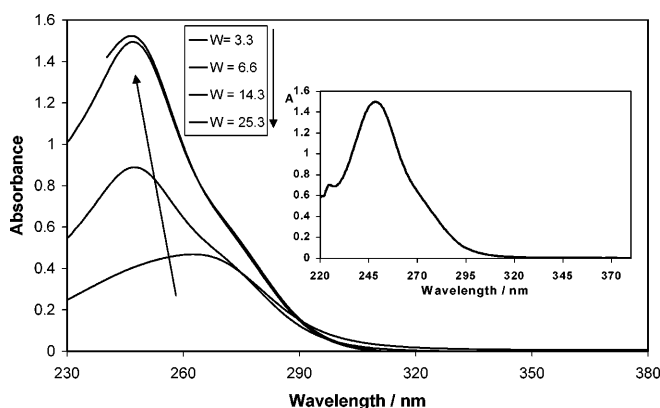


Fig. 4 Spectral change of a 0.0167 M aerosol-OT (AOT)/isooctane system containing 0.1 M (local concentration, inside the micelles) NaBr and 5×10^{-5} M Hg(II) upon increasing W from 3.3 to 25.3, recorded in a 1-cm cuvette. *Inset*: spectrum of a homogeneous aqueous solution containing 0.1 M NaBr and 5×10^{-5} M Hg(II)

respectively. The UV spectrum of an aqueous solution containing 0.1 M NaBr and 5×10^{-5} M HgBr_2 displays a band at 250 nm (Fig. 4, inset), indicating that almost 100% of Hg(II) exist as a tetrabromo complex. After introducing $10 \mu\text{l}$ 0.1 M NaBr solution containing 0.05 M HgBr_2 into 10 cm^3 of the AOT/isooctane system, the overall concentration of Hg(II) will be the same as in the previous case (5×10^{-5} M), while the local concentration of bromide in the aqueous microphases inside the reverse micelles remains 0.1 M. Thus, we can compare the complex formation in homogeneous aqueous solution and AOT reverse micelles at formally constant ligand concentration. At low W (3.3), the UV spectrum of the micellar system shows a band at 263 nm, exactly corresponding to the tris coordinated species (Fig. 4). Upon increasing W , and keeping the local concentration of bromide constant, a shift of the absorption peak to 250 nm can be observed, accompanied by a significant increase of the absorbance. This tendency unambiguously indicated that the distribution of Hg(II) in the equilibrium



is shifted towards the HgBr_4^{2-} species, and at $W=14.6$, practically all Hg(II) can be found in this form. This is confirmed by the fact that also the absorbance at this W or higher is equal to that measured in homogeneous aqueous solution. The micellar effect (at low W) can be attributed to the strong repulsion between the reactants in Eq. (1). The few water molecules in the core of the micelles are located at the hydrophilic headgroups of the surfactants; thus, they cannot efficiently hydrate the negatively charged HgBr_3^- and Br^- ions, hindering their reaction. At higher values of W , hydration of the reactants solubilizes them and reduces their repulsion, promoting the formation of HgBr_4^{2-} .

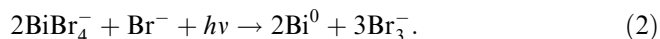
Photochemistry

The primary photoinduced reactions in the photoredox chemistry of metal complexes can be divided into two classes. In the primary step, electron transfer can take place from the metal center to a ligand (ligand-to-metal charge transfer, LMCT) or the surrounding solvent molecules (charge transfer to solvent), or, oppositely, from a ligand to the central metal (metal-to-ligand charge transfer). Such reactions were observed with coordination compounds of both transition-metal and main-group metal ions [21]. These complexes can be kinetically inert and labile as well. In the latter case, considerable ligand excess is necessary for the formation of complexes even with lower coordination numbers. Hydroxo and halo complexes are well-known examples of these compounds.

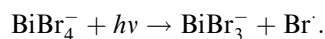
Main-group metal ions of s^0 and s^2 electronic configurations form kinetically labile complexes with halo ligands both in homogeneous aqueous solutions and in water droplets inside reverse micelles. Complexes of the s^0 metal ions are exclusively featured by LMCT reactions as with Pb(IV), Sb(V), and Hg(II) [8, 22, 23, 24]. The Hg(II) cation possesses a filled d subshell; thus, its chemical features are rather similar to main-group metal ions. In the case of the s^2 configuration, however, electron ejection (with oxidation of the metal center) can also occur, demonstrated by the example of hydroxo complexes of Sn(II), Tl(I), and Pb(II) [25, 26].

Bromobismuthate(III) complexes

The photochemical behavior of bromobismuthate(III) complexes was recently studied in acetonitrile solution [16]. The LMCT process was observed upon irradiation, leading to the formation of Br_3^- and (in the case of relatively high concentration of BiBr_4^- , 10^{-3} M) metallic bismuth as a result of the following overall reaction:



In the primary photochemical step of this process, Bi(II) and Br^\cdot are formed:



Rather high quantum yields were determined for the formation of Br_3^- : 0.45, 0.43, and 0.30 for 306-, 313-, and 366-nm excitations, respectively [16].

Our experiments were carried out with the 0.2 M CTAB/ CHCl_3 system containing 2×10^{-4} M Bi(III) ions. Thus, the concentration of the reverse micelles was about 10 times as high as that of the bromobismuthate(III) complexes. Hence, no formation of colloidal bismuth was expected during the photolysis. Irradiation of this system ($\lambda_{\text{ir}}=374 \text{ nm}$) also resulted in the formation of tribromide (Fig. 5, inset) as indicated by the increasing

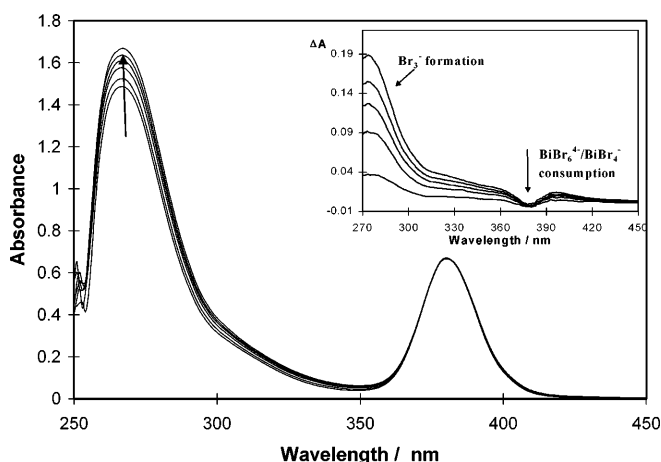


Fig. 5 Spectral change of a 0.2 M CTAB/CHCl₃ system containing 2.0×10^{-4} M Bi(III) after 0-, 30-, 70, 100-, 130-, and 160-s irradiation at 374 nm ($W=0.83$, $l=1$ cm). Inset: differential spectra obtained by subtraction of the 0-s spectrum

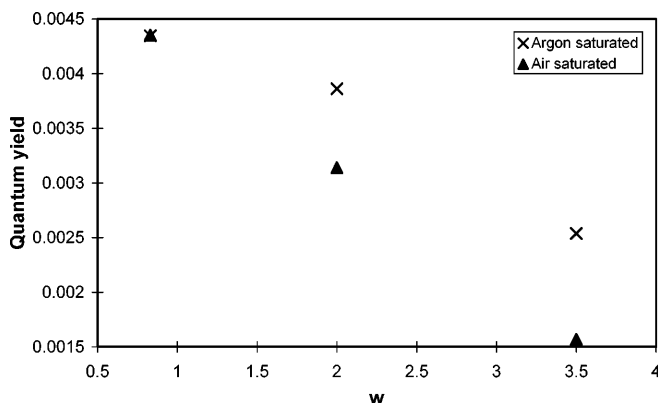


Fig. 6 Quantum yield for the formation of Br_3^- versus W for the photolysis of bromobismuthate(III) complexes in a 0.2 M CTAB/CHCl₃ system (2.0×10^{-4} M Bi(III), $\lambda_{\text{ir}} = 374$ nm)

absorbance at 270 nm. Besides, a slight decrease at 380 nm can also be observed, owing to the disappearance of BiBr_6^{3-} and (to a lesser extent) BiBr_4^- complexes. The quantum yields, Φ , determined for the Br_3^- formation in this system were 2 orders of magnitude lower than those obtained in acetonitrile. Upon increasing the water content in the W range 0.83–3.5, Φ decreased from 4.4×10^{-3} to 1.6×10^{-3} in aerated system (Fig. 6). Under oxygen-free circumstances (argon-saturated solution) a somewhat smaller decrease was experienced, but at the lowest W (0.83) the quantum yields were equal. This phenomenon suggests that at extremely high local concentration of Br^- dissolved oxygen cannot efficiently interact with the excited complexes or rather with the Bi(II) species formed in the primary photochemical step (Eq. 2). The reaction of O_2 with Bi(II) gives superoxide, which can oxidize Br^- to a bromine atom.

Notably, photolysis of bromobismuthate(III) complexes in homogeneous aqueous solutions (in 6 M NaBr or 11.3 M LiBr) resulted in no permanent chemical change. This fact is in accordance with the dependence of the quantum yield in reverse micelles on the water content. At higher W more water molecules can be associated with complexes in the first and second coordination spheres. Since water molecules have more vibrational movements than bromo ligands do, they can enhance the efficiency of the energy dissipation from the excited complex, diminishing the quantum yield of their photoinduced redox reaction. This interpretation is confirmed by the fact that Φ is 2 orders of magnitude higher in the very weakly coordinating CH₃CN than in the aqueous microphase inside the reverse micelles. Besides, in the Chapman layer, at the inner surface of the micelles, the efficient recombination of the Bi(II)–Br \cdot pair formed in the primary photochemical step may be hindered, promoting their escape to give stable end products. At higher W , the role of this effect is reduced because a lower and lower fraction of the complexes is located in the double layer.

Bromoplumbate(II) complexes

Similarly to the bromobismuthate(III) complexes, a recent investigation of PbBr_3^- complexes indicated that UV irradiation of their acetonitrile solution resulted in a LMCT reaction with the formation of colloidal metallic lead [16]. In our experiments, 8.3×10^{-5} M Pb(II) species were contained in the 0.2 M CTAB/CHCl₃ system. Thus, the concentration of the reverse micelles was about 25 times as high as that of the bromoplumbate(II) complexes. Hence, like the photolysis of the bismuth(III) complexes, no formation of colloidal lead was experienced. Irradiation of this system at 315 nm generated Br_3^- . Similarly to the case of bromobismuthate(III) complexes, the quantum yields for the tribromide formation decreased upon increasing the water content in the W range 0.5–3.5 (Fig. 7). In this system, however, the absolute values of Φ are much (1.5–2 orders of magnitude) higher, and are not appreciably affected by the presence of oxygen. The Φ versus W function is linear in the range studied, but is much steeper than the corresponding plots for the Bi(III) complexes. This tendency indicates that the primary photochemical step and the secondary dark reactions leading to the formation of Br_3^- are more effective for the bromoplumbate(II) complexes and the interactions with oxygen cannot efficiently compete with them. This also suggests that the recombination of the Pb(I)–Br \cdot pair formed in the primary photochemical step is much less efficient than in the case of bromobismuthate(III) complexes. In homogeneous aqueous solutions (11.3 M LiBr), however, no permanent chemical change was caused by the photolysis of bromoplumbate(III) complexes either. This fact

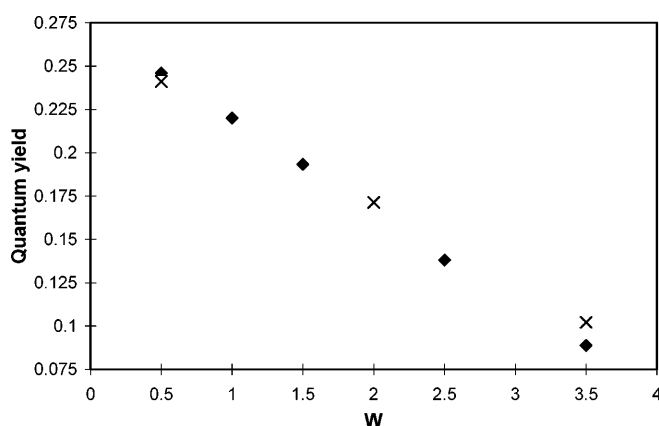


Fig. 7 Quantum yield for the formation of Br_3^- versus W for the photolysis of bromoplumbate(II) complexes in aerated (diamonds) and argon-saturated (crosses) 0.2 M CTAB/ CHCl_3 systems (8.3×10^{-5} M Pb(II) , $\lambda_{\text{ir}} = 315$ nm)

clearly shows that energy dissipation via coordinated water molecules very efficiently hinders the photoredox reaction of these complexes too.

Bromoantimonate(III) complexes

The photochemistry of bromoantimonate(III) complexes has not been investigated so far. In our work, SbBr_4^- and SbBr_6^{3-} complexes in the 0.2 M CTAB/ CHCl_3 system were photolyzed at 362 nm. In this case, 5 M H_2SO_4 was applied to hinder the hydrolysis of Sb(III) . Only experiments with air-saturated solutions were carried out. These coordination compounds also display LMCT photochemistry giving Br_3^- as an end product. In accordance with the cases of bromobismutate(III) and bromoplumbate(II) complexes, the quantum yield for the formation of tribromide decreased upon increasing the water content in a somewhat narrower range of W (Fig. 8). The Φ versus W plot is nearly linear. The order of magnitude of the quantum yield is between those for the Pb(II) and Bi(III) complexes. Also in this case, the effect of the water content on the efficiency of the photoredox reaction can be attributed to the enhanced relaxation of the excited-state complexes via coordinated solvent molecules. Besides, the efficient recombination of the $\text{Sb(II)}-\text{Br}^\bullet$ pair formed in the primary step may play a significant role.

Bromomercurate(II) complexes

The photochemistry of bromomercurate(II) complexes was studied in an AOT/isooctane system. Upon irradiation at 253.7 nm, in deoxygenated solution, the Hg^{2+} metal center was reduced to elemental mercury as the spectral change shows in Fig. 9. The absorption

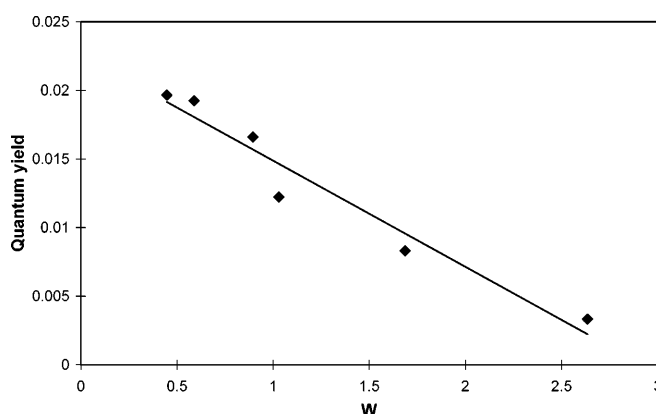


Fig. 8 Quantum yield for the formation of Br_3^- versus W for the photolysis of bromoantimonate(III) complexes in a 0.2 M CTAB/ CHCl_3 system (8.64×10^{-4} M Sb(III) , $\lambda_{\text{ir}} = 362$ nm)

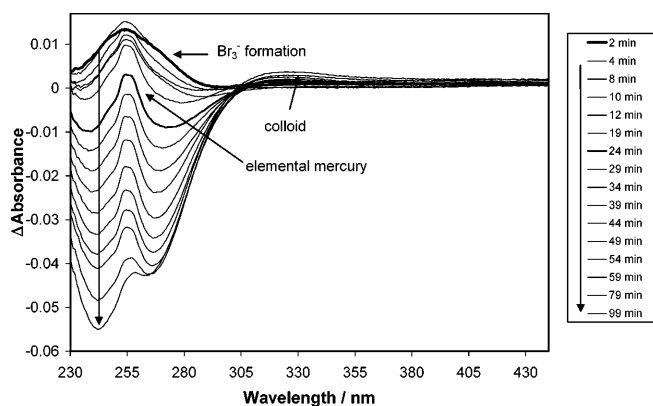


Fig. 9 Differential spectra of the 0.0167 M AOT/isooctane system containing 0.1 M (local concentration, inside the micelles) NaBr and 5×10^{-5} M Hg(II) , irradiated at 253.7 nm ($W = 3.3$, $l = 1$ cm). The spectrum belonging to $t = 0$ was subtracted from the original spectra recorded during the photolysis

spectrum of Hg^0 displays a characteristic double band at 253–257 nm [27]. The concentration of the elemental mercury in the system is apparently constant during the photolysis because of its extremely low solubility (10^{-7} M in water). This value was reached within several minutes, and Hg^0 produced in the subsequent period of the photolysis formed colloidal metal as indicated by the continuously increasing absorbance above 305 nm. The minimum quantum yield for the production of Hg^0 can only be estimated, $\Phi \approx 4.7 \times 10^{-4}$ at $W = 3.3$. The formation of Hg_2Br_2 may also have contributed to the colloidal absorption.

After 2-min irradiation, absorption by the Br_3^- ions generated was detected as a weak shoulder at 270 nm, but in the later period, the observation of this spectral feature is hampered by the decrease of the absorbance due to the consumption of the bromomercurate(II) complexes. Besides, the photochemically produced bromine may be extracted into the organic bulk phase.

W also affects the photoinduced processes in this system. At a high value of W (25.3), the rate of the colloid formation significantly increased owing to the generation of Hg_2OH_2 . Nevertheless, the quantum yield for the production of Hg^0 was equal to the value determined at low W (3.3). This suggests that the efficiencies of the primary photochemical (LMCT) reaction are about the same. Thus, the value of W influences the secondary dark reactions, especially the hydrolysis.

Conclusion

In the aqueous microphase of CTAB reverse micelles, SbBr_6^{3-} , BiBr_6^{3-} , and PbBr_4^{2-} complexes are formed at low W , while the corresponding predominant coordination numbers in homogeneous aqueous solutions of high bromide concentration are lower. If the ligand is the counterion of the cationic surfactant, its local concentration can be extremely high. Thus, at very low W , the inner aqueous phase is like a matrix, and the coordination sphere of a metal center is similar to that in crystals or aprotic solvents. In accordance with this conclusion, a hexabromocuprate(II) complex, which was identified earlier only in the solid phase [28], could also be produced in this system.

In the CTAB/ CHCl_3 systems, the bromo complexes of Pb^{2+} , Bi^{3+} , and Sb^{3+} undergo photoinduced LMCT reactions producing Br_3^- as an end product. Upon

increasing W , the quantum yields for the overall processes dramatically decrease. This tendency cannot be attributed to the moderate shift of the complex equilibria toward the species of lower coordination numbers. The main reason for this phenomenon may be the hydration effect enhancing the efficiency of the vibrational energy dissipation and the recombination of the primary pair formed in the photochemical step.

While in a homogeneous aqueous solution containing 0.1 M Br^- Hg(II) exists as HgBr_4^{2-} , inside AOT reverse micelles (at the same local ligand concentration) the predominant coordination number is 3. This interesting phenomenon can account for the dehydration of the reactants of the same charge in the complex equilibrium. UV photolysis of these complexes also results in a LMCT reaction producing elemental mercury and Br_3^- as end products. While the efficiency of the primary photochemical reaction does not seem to depend on W , the secondary processes are affected by the water content of the reverse micelles.

This study of bromo complexes clearly demonstrates that the microenvironment inside reverse micelles considerably influences both the complex equilibria and the efficiency of the photoinduced processes. In order to elucidate the micellar effects on the elementary steps of the photoredox reactions in these system, flash photolysis experiments are in progress.

Acknowledgement Support for this work by the Hungarian Ministry of Education (FKFP 0082/1999) is gratefully acknowledged.

References

- Horváth O, Stevenson KL (1989) *Inorg Chem* 28:2548
- Horváth O, Fendler JH, Stevenson KL (1993) *Inorg Chem* 32:227
- Becht A, Vogler A (1993) *Inorg Chem* 32:2835
- Stevenson KL, Dhawale RS, Horváth A, Horváth O (1997) *J Phys Chem* 101:3670
- Stevenson KL, Bell PB, Horváth O, Horváth A (1998) *J Am Chem Soc* 120:4234
- Nikol H, Vogler A (1991) *J Am Chem Soc* 113:8988
- Nikol H, Becht A, Vogler A (1992) *Inorg Chem* 31:3277
- Horváth O, Vogler A (1993) *Inorg Chem* 32:5485
- Horváth O, Mikó I (1997) *J Photochem Photobiol A* 114:95
- Horváth O, Mikó I (2000) *Inorg Chim Acta* 304:210
- Di Profio P, Germani R, Onori G, Santucci A, Savelli G, Bunton CA (1998) *Langmuir* 14:768
- Seno M, Sawada K, Araki K, Iwamoto K, Kise H (1980) *J Colloid Interface Sci* 78:57
- Novaki LP, Seoud OA, Lopes JCD (1997) *Ber Bunsenges Phys Chem* 101:1928
- Mandal AB, Wang L, Brown K, Verrall RE (1993) *J Colloid Interface Sci* 91:292
- Hatchard CG, Parker CA (1956) *Proc R Soc Lond A* 235:518
- Oldenburg K, Vogler A (1993) *Z Naturforsch* 48b:1519
- Mason WR (1999) *Inorg Chem* 38:2742
- Langmuir ME, Hayon E (1967) *J Phys Chem* 71:3803
- Griffiths TR, Anderson RA (1990) *J Chem Soc Faraday Trans* 86:1425
- Griffiths TR, Anderson RA (1991) *Inorg Chem* 30:1912
- Horváth O, Stevenson KL (1993) Charge transfer photochemistry of coordination compounds. VCH, New York
- Vogler A, Paukner A (1989) *Inorg Chim Acta* 163:207
- Vogler A, Paukner A, Kunkely H (1990) *Coord Chem Rev* 97:285
- Kunkely H, Horváth O, Vogler A (1997) *Coord Chem Rev* 159:85
- Horváth O, Stevenson KL, Vogler A (1999) *Radiat Phys Chem* 55:497
- Horváth O, Vörös J (2000) *Inorg Chem Commun* 3:191
- Mason WR (1988) *Inorg Chem* 22:147
- Roewer G, Kempe G (1976) *Wiss Z Tech Hochsch Leuna-Merseburg* 18:87

V. V. Kislyuk
M. M. Osipyonok
G. M. Strilchuk
P. M. Lytvyn
V. Z. Lozovski

Influence of particle size on luminescence spectra

Presentation at the 8th Conference on Colloid Chemistry

V. V. Kislyuk (✉) · G. M. Strilchuk
V. Z. Lozovski
Taras Shevchenko Kiev
National University,
Radiophysics Faculty,
Glushkov Prospekt 2/5,
03022 Kiev, Ukraine
e-mail: vkislyuk@univkiev.ua
Tel.: +38-44-2660522
Fax: +38-442655530

M. M. Osipyonok · P.M. Lytvyn
Institute of Semiconductor Physics,
National Academy of Sciences
of Ukraine, Prospekt Nauki 45,
03650 Kiev, Ukraine

Abstract Luminescent properties of particles are strongly sensitive to the local field that is dependent on the particle size. The particle size distribution, thus, determines the photoluminescence spectrum profile of a powder suspended in an aqueous medium. The distribution of the radii of CdS particles was determined during their sedimentation in water. Photoluminescence spectra were measured at room temperature in situ in particular time intervals. Photoluminescence was stimulated horizontally with a nitrogen pulsed laser (337 nm, 1 kW, 7–10 ns, 100 Hz) focused into a 0.25-mm²

spot and registered with a photon counter equipped with a coincidence circuit. The shift of the peak position to short wavelengths as well as the profile transformation, which was caused by dependencies of the sedimentation rate of CdS particles on their size, were detected.

Keywords Photoluminescence · CdS · Powder · Atomic force microscope

Introduction

Luminescence is attributed to electron transitions. The electron structure is strongly dependent on the local field. The luminescence from the bulk of a crystal is determined by the periodic potential, whereas the surface related to photon generation is influenced by the surface energy. If the size of the near-surface region is comparable to the bulk, the photons from both of them contribute to the resulting spectrum of the luminescence. When the particle sizes are small compared with the bulk exciton radius, quantum confinement effects are revealed, which have been studied extensively for various systems of small semiconductor crystals embedded in a dielectric matrix [1, 2, 3, 4]. At present the blueshift confinement is being studied intensively for zero-dimensional systems (quantum dots) of II–VI materials grown on a solid substrate owing to their possible practical application [5, 6, 7]. The more monodisperse the content,

the less the width of the overall spectral profile. The latter can be expanded into components corresponding to particles of different sizes. The spectral position of a component relates to the size and the intensity is proportional to the number of particles of a particular size. Apparently, a similar approach is applicable to particle size analysis in suspensions and colloid systems with particle sizes of the order of the optical wavelength (around 500 nm) or less.

We studied CdS particles suspended in water. The finest fraction of the powder extracted from the highest layers of the suspension after sedimentation is applied consequently for the fabrication of sintered CdS layers according to the method of Tomsen [8, 9]. The basic idea of the method is the binder material which is used for the recrystallization of the powdered layer of CdS or CdSe at higher temperature. This low-cost technology applicable for solar photovoltaics suffers from a lack of reproducibility owing to the wide range of the dispersivity, which

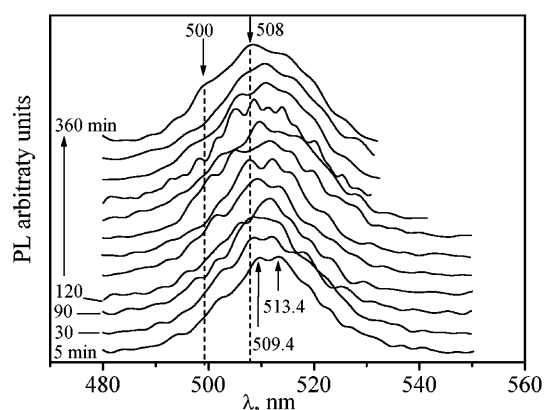


Fig. 1 Photoluminescence (PL) spectra registered in situ for 1 day from CdS particles suspended in water

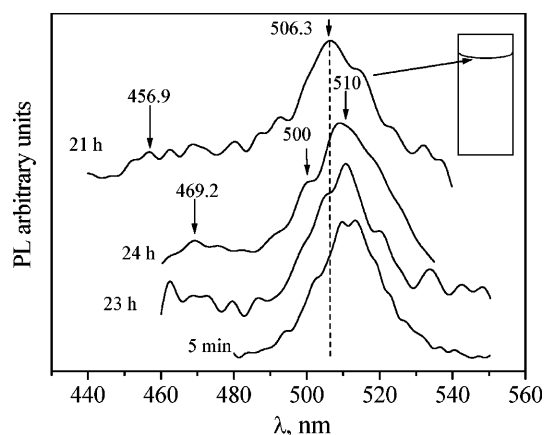


Fig. 2 PL spectra registered the day after sedimentation began, which corresponds to sedimentation for 21, 23 and 24 h. The curve for 21 h corresponds to luminescence from the surface force area

suppresses its large-scale application. The sedimentation of the powder to get the finest fraction is expected to avoid this shortcoming, luminescence spectroscopy being an effective method for express analysis of the size.

Experimental

Initially, 1 g CdS powder of high purity was mixed with distilled water and thoroughly milled in an agate mortar. Then it was dipped into a one l wide glass of distilled water. The suspension was mixed intensively for 2–4 min to make the particles uniformly distributed over the whole bulk of the glass. The suspension was allowed to settle for 150 min. A 2.5 ml sample of the suspension was collected with a syringe from 2-cm depth for a subsequent luminescent study in a quartz cell. The luminescence was stimulated with a nitrogen pulsed laser (337 nm, 7 ns, 100 Hz, 1 kW) focused into a 0.25-mm² spot at the highest water line. The spectrum was registered between 450 and 550 nm with a monochromator equipped with a photon counter and a coincidence circuit; the step was 0.2 nm and the counting time was 2–4 s. The scanning time did

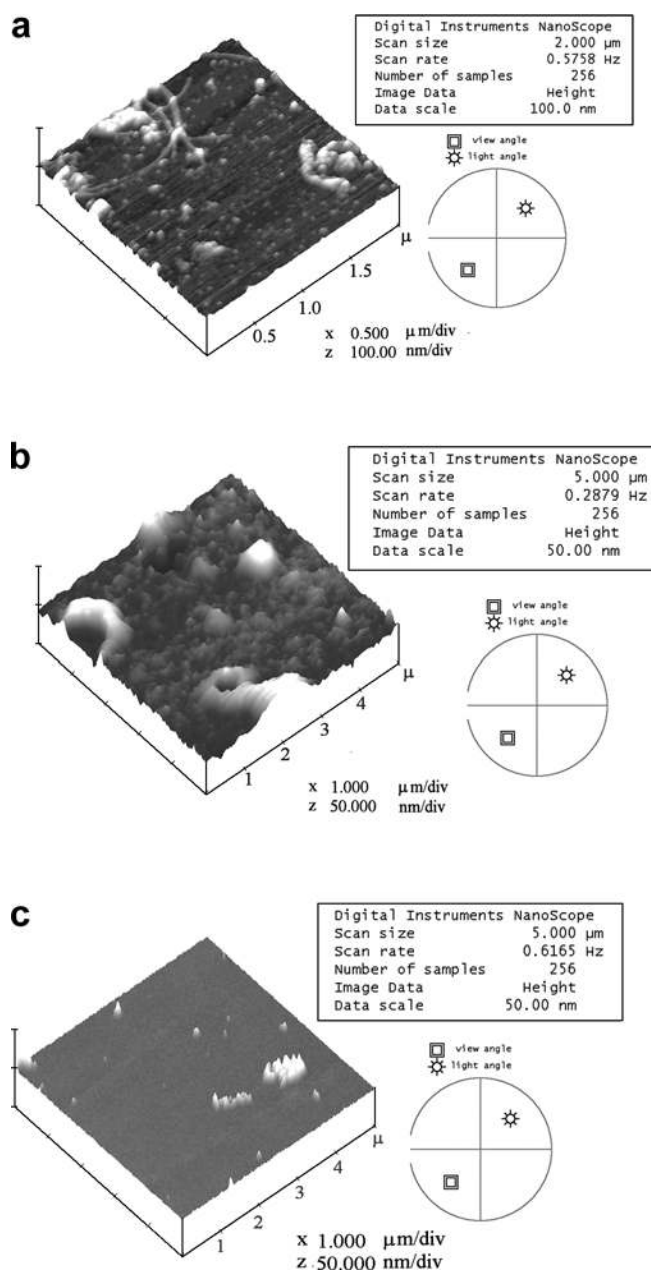


Fig. 3 Atomic force microscope images of the suspension drop extracted after a 2 h, b 2.5 h and c 3 h

not exceed 10 min. Initially, first three measurements for 5-, 30- and 90-min of sedimentation were made to adjust the proper interval. Then the spectra were registered for 1 day every 30 min and the next day in situ while the sedimentation proceeded. The curves were smoothed with a routine technique of fast Fourier transform filtering. All spectral profiles were normalized to the intensity at the maximum for better comparison.

The same procedure of the powder preparation was repeated for the microscope study to determine the particle size directly with an optical microscope and an atomic force microscope (AFM). Microscope images were made for samples extracted from the suspension settled in a wide glass for 2, 2.5 and 3 h.

Results and discussion

The luminescence spectra at various instants of time of sedimentation are presented in Figs. 1 and 2. The sedimentation gives rise to a widening of the short-wavelength wing of the profile (Fig. 1). Initially, there are two clear maxima, at 509.4 and 513.4 nm (curve for 5-min sedimentation). After 6-h sedimentation another maximum is revealed at near 500 nm. At the same time, in general, there are small changes in the long-wavelength wing in contrast to what is expected. This is, probably, attributed to the formation of complexes of smaller particles. Owing to the lower sedimentation rate of the small particles lateral diffusion is more efficient, and, thus, the probability of the complex formation at the same level increases. These assumptions agree with the microscope study which demonstrates that there are always particles of larger size. Even after 3-h sedimentation (Fig. 3c) there are still large particles in contrast to what was expected. AFM images demonstrate how nanoparticles form microscopic complexes. As the sedimentation proceeds the number of these complexes increases. Comparison of Fig. 3 shows that separate particles are rarer for longer sedimentation times. A new line at 469.2 nm appears the next day (Fig. 2, 23 and 24 h), which forms the basis for an assumption that the sedimentation rates of particles related to this line and those contributing to the 509–510-nm maximum differ essentially.

Of particular interest is the spectrum measured first on the next day (Fig. 2, 21 h). The maximum is shifted towards 506.3 nm. The water level lowered a little owing to evaporation. Since the optical adjustment was kept unchanged the beam stimulated

luminescence from the area of surface forces. After topping up the level (very slowly to avoid mixing) the spectrum had a maximum again at 510 nm. The area of surface forces, thus, either keeps small particles or contains a high nonuniformity of the local field which gives rise to changes of the photoluminescence spectrum compared to that measured from the bulk. photoluminescence of CdS particles in a dielectric medium is known to be strongly dependent on the local field even when its changes result from changes in the form of the particles [10].

Conclusion

The sedimentation can help in preparing a fine fraction of CdS powder; however small particles tend to form complexes, which correlates with the photoluminescence spectra of the suspension. The photoluminescence profile, thus, is an effective indicator of the dispersivity. The luminescence from the upper level of the surface forces differs substantially from that from the bulk, which can be attributed to

1. Different values of the local field in the near-surface region and in the bulk, which can give rise to the blueshift.
2. Different conditions for the complex formation. Their number is smaller in the surface region.

Acknowledgement The authors thank the organizers of the 8th Conference on Colloid Chemistry for supporting their participation in the meeting.

References

1. Rolo AG, Conde O, Gomes MJM (1998) *Thin Solid Films* 318:108
2. Okamoto S, Kanemitsu Y, Hosokawa H, Murakoshi K, Yanagida S (1997) *Solid State Commun* 105:7
3. Vlasov YA, Luterova K, Pelant I, Honerlage B, Astratov VN (1998) *Thin Solid Films* 318:93
4. Shen Q, Liang P, Zhang W (1995) *Opt Commun* 115:133
5. Kitamura K, Umea H, Jia A, Shimotomai M, Kato Y, Kobayashi M, Yoshikawa A, Takahashi K (2000) *J Cryst Growth* 214/215:680
6. Kurtz E, Shen J, Schmidt M, Grun M, Hong SK, Litvinov D, Gerthsen D, Oka T, Yao T, Klingshirn C (2000) *Thin Solid Films* 367:68
7. Behera SN, Sahu SN, Nanda KK (2000) *Indian J Phys* 74A:81
8. Thomsen SM, Bube RH (1955) *Rev Sci Instrum* 26:664
9. Thomsen S (1956) US Patent 765,385
10. Jaskolski W, Planelles J, Peris G (1999) *Physica E* 4:176

L. Körösi
K. Mogyorósi
R. Kun
J. Németh
I. Dékány

Preparation and photooxidation properties of metal oxide semiconductors incorporated in layer silicates

Abstract Various metal oxide semiconductor nanoparticles (TiO_2 , ZnO , SnO_2) were stabilized in the interlamellar space of clay minerals with a layered structure. In the first step, metal oxide/hydroxide nanosol particles were prepared by acidic hydrolysis, and the incorporation of the nanoparticles was next carried out between the layer silicates by a heterocoagulation method. Metal oxide semiconductor/layer silicate composites with large specific surface areas ($a_{\text{BET}}^s = 122\text{--}251 \text{ m}^2 \text{ g}^{-1}$)

were prepared with (TiO_2) and without calcination at 400°C (ZnO , SnO_2). The structure of these composites was characterized by X-ray diffraction measurements and their photocatalytic properties were determined in aqueous solutions, using salicylic acid as a test molecule.

Keywords Clay minerals · Semiconductors · Photocatalysis · X-ray diffraction · Nanocomposites

L. Körösi · K. Mogyorósi · R. Kun
J. Németh · I. Dékány
Department of Colloid Chemistry,
University of Szeged, 6720 Szeged,
Aradi v. t. 1, Hungary

I. Dékány (✉)
Nanostructured Materials Research Group
of Hungarian Academy of Sciences,
University of Szeged,
6720 Szeged, Aradi v. t. 1, Hungary
e-mail: i.dekany@chem.u-szeged.hu

Introduction

Titanium dioxide is the most extensively studied metal oxide semiconductor, discussed in many publications, which is primarily owing to its excellent photocatalytic properties and chemical stability [1, 2, 3, 4, 5, 6, 7, 8, 9]. It is utilized not only as a photocatalyst but also in solar cells and water splitting, because light induces charge separation on the surface of the semiconductor, resulting in the generation of electrons and holes on the surface. TiO_2 /montmorillonite samples were reported always in the literature using the mixing process of titania and clay mineral dispersions and hydrothermal heat treatment and/or calcination [1, 2].

Zinc oxide has similar photocatalytic properties, but it has satisfactory chemical stability only in neutral or alkaline media, whereas in acidic media it dissolves [10, 11]. Tin oxide is also a well-known photocatalyst as well as a preferred basic material for sensors [12, 13]. These may be prepared using classical colloid chemical methods, i.e. by converting the metal salts of the semiconductor into metal hydroxides by hydrolysis, followed by

calcination at $350\text{--}400^\circ\text{C}$. After the heat treatment, crystalline oxide semiconductors may be obtained, with particle sizes strongly dependent on the conditions of preparation.

When semiconductors are prepared for use as photocatalysts, it is very important that the particle size be in the range of a few nanometers, as in this case the sample has a large specific surface area and a high catalytic activity [1, 2, 8]. In the course of preparation, particles obtained by hydrolysis have to be stabilized in order to prevent coagulation. Materials earlier used for stabilization were surfactants and microemulsions. For example, metal hydroxide nanoparticles may be synthesized in the aqueous medium enclosed in the droplets of microemulsions of the water/oil type: the nanoparticles formed are protected from coagulation by the surfactant stabilizing the droplet, making possible the preparation of nanoparticles with diameters of $20\text{--}50 \text{ nm}$ [14, 15, 16, 17].

Nanoparticles may also be used for the preparation of nanofilms. SnO_2 nanoparticles were prepared by Ansari et al. [18] with the aim of developing sensors and by Vinodgopal et al. [19] for photooxidation. Nanoparticles

were stabilized by the addition of surfactants by Cao et al., who also generated multilayers from the particles prepared [15]. SnO_2 nanoparticles were also tested as efficient photocatalysts [20, 21, 22].

In the past few years we have used layer silicates for the stabilization of nanoparticles. This procedure is highly advantageous because, on the one hand, the nanoparticles obtained are free of organic stabilizers and, on the other hand, the particle size is easily controlled and usually does not exceed 2–5 nm. The reason for this is that, owing to steric reasons, particles larger than 2–5 nm do not remain between the lamellae [3, 4, 5, 23, 24, 25]. Another reason why stabilization of nanoparticles within the interlamellar space of layer silicates is important is that, owing to intercalation of nanoparticles, the specific surface area of the nanostructured semiconductor/layer silicate composite is fairly large ($150\text{--}350\text{ m}^2\text{ g}^{-1}$) and the composite will therefore act as a good adsorbent, promoting adsorption of the organic molecules used for photooxidation in the interlamellar space and in the micropores of the composite [1, 2, 4, 5].

Experimental

Materials

Titanium(IV) isopropoxide (tetraisopropyl orthotitanate, Fluka Chemika, pract.), hydrochloric acid (Reanal, pro anal.), sodium hydroxide (Reanal, puriss.) and 2-propanol (Reanal, puriss.) were used as received. Similarly, a commercial sample of P25 Degussa TiO_2 (25 wt% rutile, 75 wt% anatase) was used as a well-known photocatalytic reference material. Zinc(II) chloride (Reanal, pro anal.), ZnO (Reanal, puriss.), $\text{SnCl}_4 \cdot 5\text{H}_2\text{O}$ and SnO_2 (Reanal, pro anal.) were used as received.

Sodium montmorillonite (EXM-838, Süd-Chemie; containing montmorillonite particles smaller than $2\text{ }\mu\text{m}$ in diameter) and synthetic hectorite (Optigel SH, Süd-Chemie) were used as layered silicates.

Water was purified by a Milli-Q water ion-exchange system (Millipore) to give a resistivity of $18\text{ M}\Omega\text{ cm}$.

Methods

Preparation of TiO_2 /layered silicate (montmorillonite) nanocomposite

Titanium dioxide nanoparticles were prepared by hydrolysis of titanium(IV) alkoxides and subsequent heat treatment. In a typical preparation 320 ml 54.3 vol/vol% titanium(IV) tetraisopropoxide/

2-propanol mixture was added dropwise to purified 660 ml Milli-Q water under vigorous stirring over 20 min to yield a milky white dispersion. Subsequent to the addition of 18 ml concentrated hydrochloric acid the dispersion was stirred at $50\text{ }^\circ\text{C}$ for 12 h. During the stirring the dispersion became a transparent homogeneous sol (pH 1.25, 5.2 wt/vol% and the streaming potential of the particles $\zeta = +35\text{ mV}$). In this state the sol has positively charged nanoparticle aggregates with $d_{\text{DLS}} = 49.5 \pm 7.0\text{ nm}$, measured by dynamic light scattering (DLS), which coagulate in a montmorillonite suspension ($\zeta = -1,540\text{ mV}$) wherein the lamellae are negatively charged (Fig. 1). The sodium montmorillonite suspension (1.0 wt/vol%) and the diluted TiO_2 sol (1.0 wt/vol%) were mixed in different ratios in order to prepare the nanocomposite samples with variable TiO_2 content. The heterocoagulation products were kept at room temperature for 20 h, washed and centrifuged. The wet, solid precipitates were dried at $50\text{ }^\circ\text{C}$. The calculated TiO_2 content – after adding different amounts of TiO_2 nanosols to montmorillonite suspensions – in the nanocomposites were 20, 33 and 50 wt%. The shorthand notations of these samples are $\text{TiO}_2/\text{M}/\text{H}20$, $\text{TiO}_2/\text{M}/\text{H}33$, $\text{TiO}_2/\text{M}/\text{H}50$, in which the support material and the preparation method are indicated (M represents montmorillonite and H represents the heterocoagulation method). The $\text{TiO}_2/\text{M}/\text{H}50$ sample was calcinated at $400\text{ }^\circ\text{C}$ for 4 h ($\text{TiO}_2/\text{M}/\text{H}50\text{C}$).

Preparation of ZnO /layered silicate nanocomposite

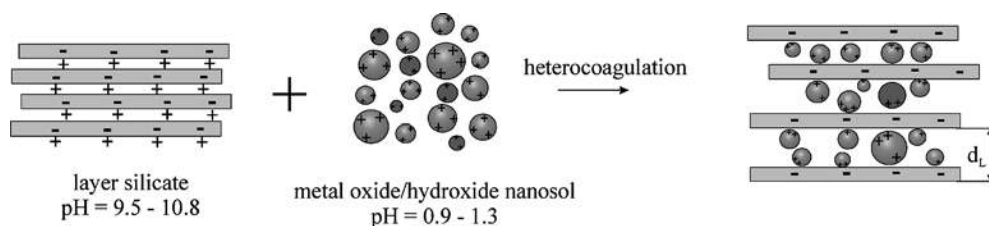
In this approach separately prepared positively charged $\text{Zn}(\text{OH})_2$ sols ($\zeta = +507\text{ mV}$) were coagulated with negatively charged sodium hectorite platelets (Fig. 1).

The following method was used for the heterocoagulation of ZnO hectorite composites. ZnCl_2 (1.50 g) was dissolved in 1.5 ml distilled water and subsequent to dissolution 4.0 ml aqueous 1.0 M NaOH was quickly introduced to produce $\text{Zn}(\text{OH})_2$ in the reaction. The crude precipitate was homogenized by ultrasonication and diluted with distilled water to 100 ml. The appropriate amount of the $\text{Zn}(\text{OH})_2$ nanosol was mixed with the 1 wt/vol% hectorite suspension ($\zeta = -1,530\text{ mV}$), and the heterocoagulated wet product was washed, dried and calcinated at $400\text{ }^\circ\text{C}$ for 3 h. The shorthand notations of these samples are $\text{ZnO}/\text{Hec}/\text{H}41\text{C}$ (41 wt% ZnO), $\text{ZnO}/\text{Hec}/\text{H}53\text{C}$ (53 wt% ZnO) and $\text{ZnO}/\text{Hec}/\text{H}80\text{C}$ (80 wt% ZnO).

Preparation of SnO_2 /layered silicate nanocomposite

The sols needed for the photocatalysis were prepared in aqueous solution according to the reaction of $\text{SnCl}_4 \cdot 5\text{H}_2\text{O}$ and NaOH. Due care was taken for selecting the initial concentrations of the precursors since it is this parameter which determines the relative saturation of the incipient crystals and hence the size of the nanoparticles. The most stable nanosol (pH 0.80, $\zeta = +8\text{ mV}$, $d_{\text{DLS}} = 267.6 \pm 54.2\text{ nm}$) was prepared by the dropwise addition of aqueous NaOH solution (1.057 g in 50 ml water) to $\text{SnCl}_4 \cdot 5\text{H}_2\text{O}$ solution (4.75 g in 50 ml water) followed by 5-min homogenization by ultrasonication. The dispersions of the SnO_2 particles so

Fig. 1 Schematics illustrating the layer silicate and metal oxide–hydroxide sol heterocoagulation



produced were used for the preparation of the photocatalytic montmorillonite and hectorite nanocomposites.

The tin hydroxide layer silicate nanocomposites were prepared by heterocoagulation (Fig. 1); the positively charged nanoparticles were attracted to the negatively charged silicate layers. Montmorillonite (1.0 wt/vol%, pH 9.49; $\xi = -1,540$ mV) and hectorite (1.0 wt/vol%, pH 10.78, $\xi = -1,530$ mV) were employed. The shorthand notations of these samples are SnO₂/M/H14C (14 wt% SnO₂), SnO₂/M/H26C (26 wt% SnO₂), SnO₂/M/H41C (41 wt% SnO₂), SnO₂/Hec/H31C (31 wt% SnO₂) and SnO₂/Hec/H50C (50 wt% SnO₂).

Measurement methods

The average particle diameter (d_{DLS}) of the metal oxide/hydroxide nanosols was determined using a SEMATech 633 DLS apparatus (He–Ne laser, 5 mW).

X-ray diffraction (XRD) measurements were performed with a Philips PW 1820/1830 diffractometer, (Cu K α = 0.1542 nm, 40 kV, 30 mA, in the 1–30° (2 θ) regime for solid powder samples). The basal distances, d_L , were calculated from the first (001) Bragg reflections by using the PW 1877 automated powder diffraction software. The standard deviation of the d_L values was established to be ± 0.01 nm in the 1–10° (2 θ) range, and ± 0.001 nm in the 20–30° (2 θ) range. The average diameters of the particles, D , were obtained by means of the Scherrer equation [$D = k\lambda/\beta\cos\Theta$, where β is the line broadening ($\beta = \beta_s - \beta_0$, where β_s and β_0 are the half-widths of the XRD peak of the sample and of the silicon standard), k is related to the crystallite shape, and α and Θ are the radiation wavelength and Bragg angle, respectively]. A single-crystal silicon standard ($\beta_0 = 0.105^\circ$, 2 θ) was used for calibration.

Specific surface areas of nanocomposites and metal oxide samples were determined by a Micromeritics gas adsorption analyzer (Gemini type 2375) at 77 ± 0.5 K in liquid nitrogen. Prior to measurements the samples were pretreated in a vacuum at 120 °C for 2 h. The sample vessel was loaded with about 0.1–0.7 g of samples. The adsorption isotherms were analyzed by means of the Brunauer–Emmett–Teller (BET) equation.

The streaming potential values of particles in aqueous dispersions were determined using a Müttek PCD 02 particle charge detector.

Analysis of the samples after photooxidation was carried out using a UVIKON 930 UV–VIS dual-beam spectrophotometer. The degradation of model pollutant (salicylic acid) was monitored by UV–VIS measurement.

Photocatalytic experiments were made in a 400-ml thermostated batch reactor (25 ± 0.1 °C) equipped with an immersion-type UV lamp (high-pressure mercury lamp, 150 W, 240–580 nm). In our experiments the surrounding of the lamp with a glass filter allowed a considerable proportion of the high-energy photons ($\lambda < 310$ nm) to be filtered out.

Results and discussion

X-ray diffractograms of the air-dried TiO₂/montmorillonite samples are presented in Fig. 2. The reflection at $d_L = 1.25$ nm, characteristic of the original sodium montmorillonite, is shifted towards smaller angles after the heterocoagulation process, indicating that the lamellae of the clay mineral are pillared by TiO₂ nanoparticles ($d_L = 3.40$ – 3.98 nm). The peak intensity of nonpillared sodium montmorillonite sheets decreases gradually on increasing the amount of TiO₂ added. The diffractogram of the TiO₂/M/H50 sample

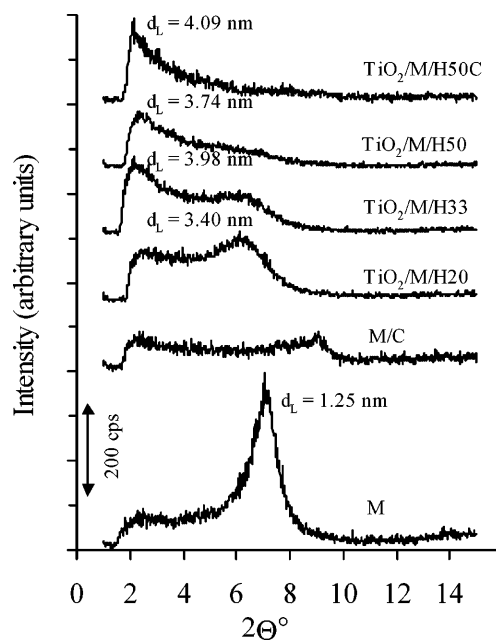


Fig. 2 X-ray diffraction (XRD) patterns of TiO₂/montmorillonite nanocomposites containing different amounts of TiO₂

does not show any significant change as a result of calcination (at 400 °C for 4 h, TiO₂/M/H50C), and the basal spacing is only slightly affected ($d_L = 3.74$ – 4.09 nm). The average size of TiO₂ pillars – calculated from the measured basal distance and the thickness of a TOT layer ($D_{TiO_2} = d_L - d_{TOT}$; $d_{TOT} = 0.96$ nm) – was around 3 nm which is somewhat smaller than the TiO₂ particle diameter calculated from the line broadening of the observed reflection at 25.3° (2 θ) corresponding to the pure anatase phase ($D_{TiO_2} = 4.3$ nm).

Increasing the amount of TiO₂ led, of course, to increased specific surface areas of 27.5, 171.4, 219.7 and 250.7 m² g^{−1} in sodium montmorillonite, TiO₂/M/H20, TiO₂/M/H33 and TiO₂/M/H50 samples, respectively. The calcination increased the amount anatase in the TiO₂/M/H50 sample, although growth of the nanoparticles was not observed.

The catalytic efficiency of the TiO₂/montmorillonite was tested on the photooxidation of salicylic acid. A photocatalyst suspension (0.1 wt/vol%) was prepared in 0.15 mM salicylic acid solution. Irradiations for 1 h were performed and samples were withdrawn after 5, 10, 20, 30, 40, 50 and 60 min irradiation. Aliquots of the samples irradiated for various durations were centrifuged and particles interfering with photometry were removed by filtration through a sieve with 0.2 μ m pore size. Changes in salicylic acid concentration taking place as the reaction progressed were monitored by spectrophotometry at 297 nm (Fig. 3). The initial equilibrium concentration of salicylic acid was lowered by the adsorption of molecules on the oxide surface before irradiation [see the difference

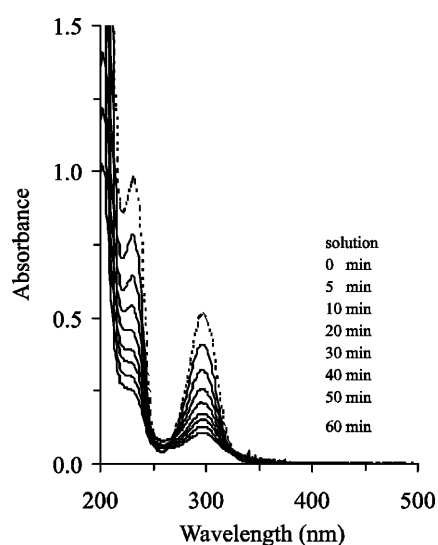


Fig. 3 UV-VIS spectra of the salicylic acid solution during UV-irradiation using $\text{TiO}_2/\text{M}/\text{H50}$ photocatalyst ($c_{\text{SA},0} = 0.15 \text{ mM}$, 0.1 wt/vol\% catalyst content)

between the absorption spectrum of the solution (dashed line) and the supernatant of the suspension at zero irradiation time]. The initial equilibrium concentration was calculated as 100% in each case. The photocatalytically decomposed amounts of salicylic acid are shown using different TiO_2 /montmorillonite nanocomposites in Fig. 4 and Table 1. The direct photolysis of the organic compound was observed (31%) in the UV-irradiation process. The amount of salicylic acid removed was very similar in sodium montmorillonite suspension (0.1 wt/vol\%) after 1 h. The highest rate of organic compound degradation was measured in the case of $\text{TiO}_2/\text{M}/\text{H50}$ nanocomposite. The calcination did not increase the photocatalytic efficiency of this catalyst. Taking account of the correction of direct photolysis, the specified decomposition rates were 103.5 , 108.1 , 84.0 and $40.5 \mu\text{mol h}^{-1} \text{ g}^{-1} \text{ TiO}_2$ by use of $\text{TiO}_2/\text{M}/\text{H20}$, $\text{TiO}_2/\text{M}/\text{H33}$, $\text{TiO}_2/\text{M}/\text{H50}$ and P25 Degussa TiO_2 ,

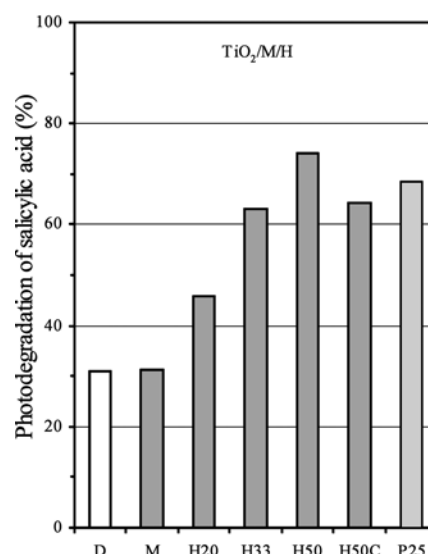


Fig. 4 Photodegradation of salicylic acid in the photocatalytic process after 1 h using different catalysts containing anatase. (*D* direct photolysis without catalyst, *M* sodium montmorillonite, $\text{TiO}_2/\text{M}/\text{H20}$, H33 $\text{TiO}_2/\text{M}/\text{H33}$, H50 $\text{TiO}_2/\text{M}/\text{H50}$, H50C $\text{TiO}_2/\text{M}/\text{H50C}$, *P25* Degussa P25 TiO_2 ; in 0.1 wt/vol\% suspension)

respectively. This maximum at 33 wt% TiO_2 content is probably caused by the diminished accessible surfaces for the chemisorption of salicylic acid on TiO_2 particles; this is one of the most important parameters [8]. The amounts adsorbed before irradiation were 60.8 , 60.7 and $22.9 \mu\text{mol g}^{-1} \text{ TiO}_2$ on $\text{TiO}_2/\text{M}/\text{H33}$, $\text{TiO}_2/\text{M}/\text{H50}$ and Degussa P25 TiO_2 , respectively.

In the case of $\text{ZnO}/\text{hectorite}$ nanocomposites similar X-ray diffractograms were observed (Fig. 5) with basal distances in the range 4.0 – 4.5 nm . The amount of salicylic acid decomposed increased with increasing ZnO content (46.2 – 70.8%) (Fig. 6, Table 1). The maximal specific amount of salicylic acid removed after 1 h as $168 \mu\text{mol g}^{-1} \text{ ZnO}$ can be found at 41 wt% ZnO content in hectorite.

Table 1 The photocatalytic efficiency of the catalysts containing TiO_2 or ZnO nanoparticles (310–390 nm)

Sample	Semiconductor content (wt%)	α_{BET}^a ($\text{m}^2 \text{ g}^{-1}$)	Amount of salicylic acid removed after 1 h (%)	Amount of salicylic acid removed after 1 h (mmol g^{-1} semiconductor)
Ref. P25 TiO_2	100	42.9	68.5	0.087
$\text{TiO}_2/\text{M}/\text{H20}$	20	171.4	45.8	0.336
$\text{TiO}_2/\text{M}/\text{H33}$	33	219.7	63.1	0.249
$\text{TiO}_2/\text{M}/\text{H50}$	50	250.7	74.2	0.177
$\text{TiO}_2/\text{M}/\text{H50C}$	50	–	64.2	0.166
Ref. ZnO	100	–	88.4	0.133
$\text{ZnO}/\text{O}/\text{S100C}$	100	–	76.9	0.120
$\text{ZnO}/\text{Hec}/\text{H41C}$	41	–	46.2	0.168
$\text{ZnO}/\text{Hec}/\text{H53C}$	53	–	47.5	0.134
$\text{ZnO}/\text{Hec}/\text{H80C}$	80	–	70.8	0.133

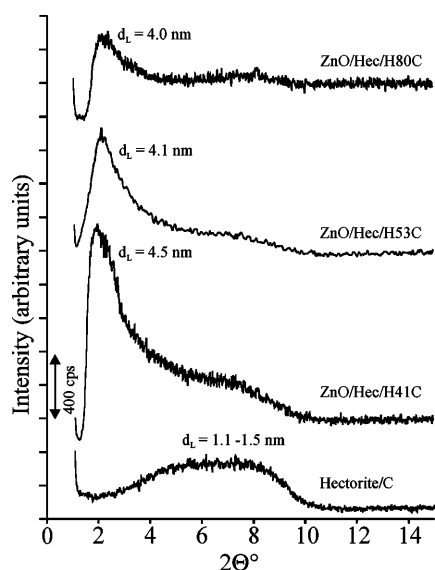


Fig. 5 XRD patterns of ZnO/hectorite nanocomposites containing different amounts of ZnO

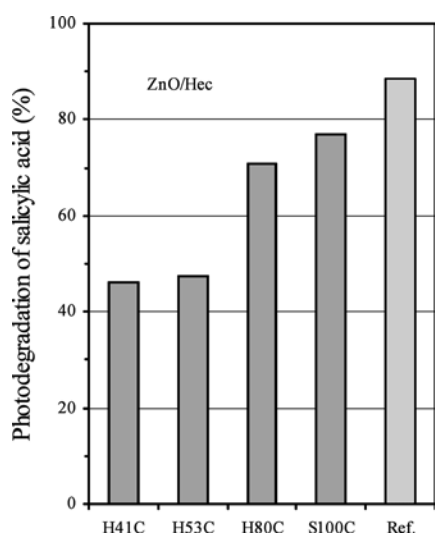


Fig. 6 Photodegradation of salicylic acid in the photocatalytic process after 1 h using different catalysts containing ZnO. (H41C ZnO/Hec/H41C, H53C ZnO/Hec/H53C, H80C ZnO/Hec/H80C, S100C ZnO nanoparticle powder dried at 100 °C, Ref. reference ZnO; in 0.1 wt/vol% suspension)

XRD spectra recorded for SnO₂/montmorillonite nanocomposites are presented in Fig. 7. The figure demonstrates that intercalation of nanoparticles among the silicate layers indeed occurred, as the peak intensity of the basal spacing characteristic of montmorillonite gradually decreases and, in the presence of SnO₂, the values of the basal distances fall in the range $d_L = 2.7$ – 6.6 nm. Nanocomposites with hectorite are shown in Fig. 8: intercalation of nanoparticles is amply

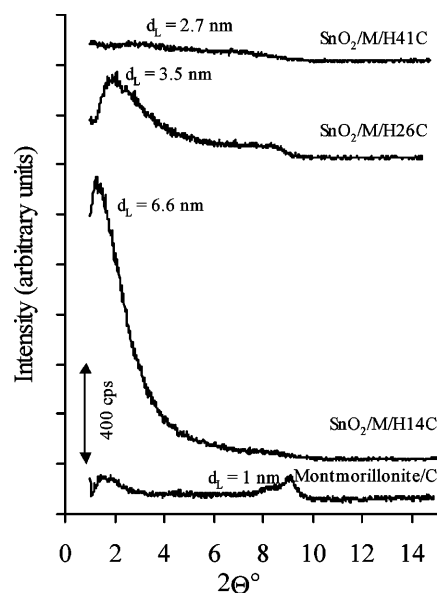


Fig. 7 XRD patterns of SnO₂/montmorillonite nanocomposites containing different amounts of SnO₂

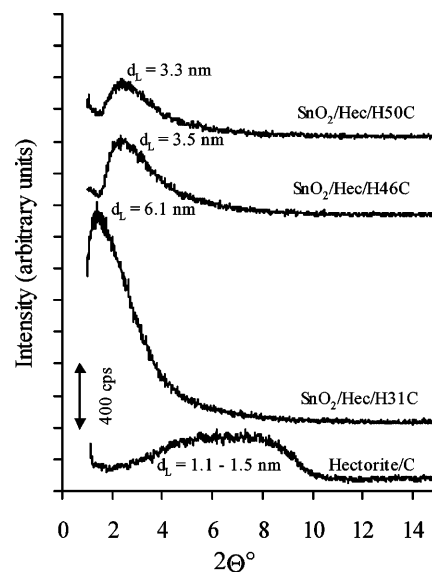


Fig. 8 XRD patterns of SnO₂/hectorite nanocomposites containing different amounts of SnO₂ after calcination at 400 °C

demonstrated by the disappearance of the broad reflection characteristic of hectorite and the appearance of the new hectorite/SnO₂ reflections. The values of the Bragg reflections range from 3.3 to 6.1 nm (Table 2). The average particle diameter of SnO₂ in the SnO₂/montmorillonite sample as determined by transmission electron microscopy is $d = 5.5 \pm 1.5$ nm.

In the case of SnO₂/montmorillonite catalysts calcinated at 400 °C, there are no significant differences

Table 2 The photocatalytic efficiency of the catalysts containing SnO₂ nanoparticles (310–390 nm)

Sample	SnO ₂ content (wt%)	a_{BET}^s (m ² g ⁻¹)	Amount of salicylic acid removed after 1 h (%)	Amount of salicylic acid removed after 1 h (mmol g ⁻¹ SnO ₂)
Ref. SnO ₂	99.9	6.0	15.0	0.023
SnO ₂ /M/H14C	14.4	126.8	45.3	0.472
SnO ₂ /M/H26C	26.0	121.7	43.0	0.248
SnO ₂ /M/H41C	40.9	121.8	41.6	0.153
SnO ₂ /Hec/H31C	30.6	142.3	76.3	0.374
SnO ₂ /Hec/H50C	50.3	137.3	68.5	0.206

between the efficiencies of degradation (Fig. 9, Table 2). From the two different supports used, montmorillonite has the more significant screening effect; its photooxidation efficiency is therefore lower. In other words, organic matter is more efficiently degraded by hectorite, owing to the weaker screening effect of the mineral.

The efficiency of photooxidation is also influenced by the calcination temperature, through structural changes. Degradation of salicylic acid during 60 min irradiations was studied in 0.1 wt/vol% suspensions of SnO₂/Hec/H50C samples calcinated at 80–600 °C (Fig. 10). The curve describing the effect of calcination temperature on the efficiency of the catalysts has a maximum. In order to interpret this result, one has to take into account that the higher calcination temperature is, the higher the SnO₂ content of the sample will be (this statement holds only up to the termination of the hydroxide–oxide conversion), which is also unambiguously proven by XRD measurements. It should be noted, that on this basis at

80–400 °C the designation “SnO₂/Hec/H50C” (indicating 50 wt% SnO₂ content) is inexact, because the mass of SnO₂ cannot be precisely calculated from the Sn⁴⁺ content of the sample, as in this temperature range most of it is present in the form of hydroxide. Catalysis is less effective in the presence of the hydroxide–oxide form; when the heat-treatment temperature is increased over an optimal value (about 300–400 °C), however, coarsening of the particles and a drastic change in the support structure will come about, greatly reducing catalytic efficiency.

The photodegradation profiles of salicylic acid are shown on different reference semiconductor and semiconductor/clay mineral nanocomposite photocatalysts in Fig. 11. As can be seen, the highest photodegradation rate was observed when using of the SnO₂/Hec/H50C sample after 1 h irradiation, although the initial degradation rate was higher in the case of ZnO/Hec/H80C and TiO₂/M/H50 samples.

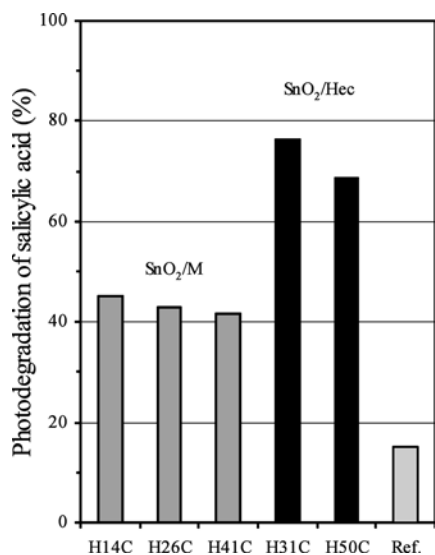


Fig. 9 Photodegradation of salicylic acid in the photocatalytic process after 1 h using different catalyst supports of montmorillonite (*M*) and hectorite (*Hec*) containing SnO₂. (*H14C* SnO₂/M/H14C, *H26C* SnO₂/M/H26C, *H41C* SnO₂/M/H41C, *H31C* SnO₂/Hec/H31C, *H50C* SnO₂/Hec/H50C, *Ref.* reference SnO₂; in 0.1 wt/vol% suspension)

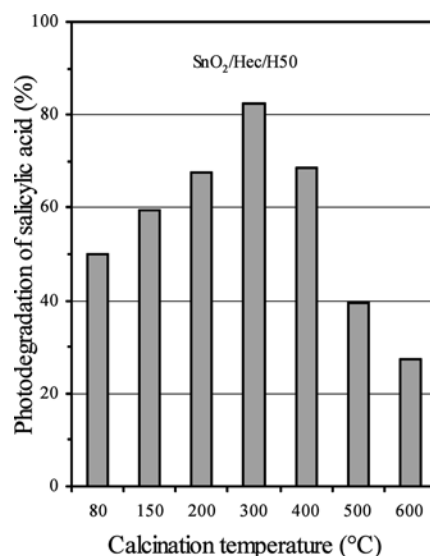


Fig. 10 Photodegradation of salicylic acid in the photocatalytic process after 1 h using SnO₂/Hec/H50 nanocomposite calcinated at different temperature in 0.1 wt/vol% suspension

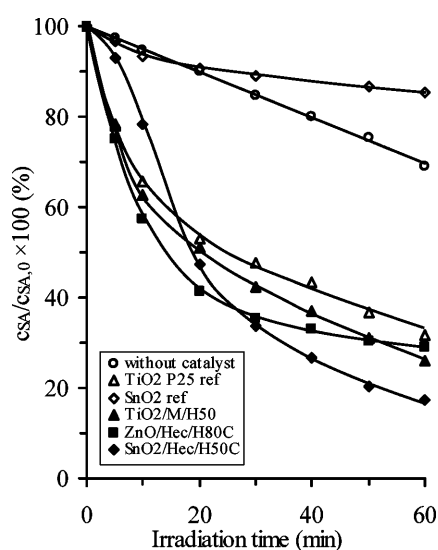


Fig. 11 Photodegradation profiles of salicylic acid on different reference semiconductor and semiconductor/clay mineral nanocomposite photocatalysts ($c_{SA,0} = 0.15$ mM, 0.1 wt/vol% catalyst content)

Conclusions

Clay mineral intercalated TiO_2 nanoparticles containing the anatase phase were prepared by a heterocoagulation process without any heat treatment. The observed photodegradation rate of salicylic acid on TiO_2 /montmorillonite nanocomposites was similar than that determined on P25 Degussa TiO_2 . Different measurement methods (XRD and BET) indicated the incorporation of ZnO and SnO_2 nanoparticles also into montmorillonite and hectorite clay minerals. The most effective photocatalysts were found with 50 wt% semiconductor content owing to the stabilization of 3–5-nm sized nanoparticles causing the optimal UV light absorption on the semiconductor/layer silicate composite with high specific surface area.

Acknowledgements The authors thank the Hungarian National Scientific Fund (OTKA T 034430) for scientific support and J.H. Fendler for helpful discussions.

References

- Ding Z, Zhu HY, Lu GQ, Greenfield PF (1999) *J Colloid Interface Sci* 209:193–199
- Ooka C, Akita S, Ohashi Y, Horiuchi T, Suzuki K, Komai S, Yoshida H, Hattori T (1999) *J Mater Chem* 9:2943–2952
- Dékány I, Szűcs A, Mogyorósi K, Király Z (2000) *Mol Cryst Liq Cryst* 341:361–368
- Mogyorósi K, Dékány I, Fendler JH (2003) *Langmuir* (in press)
- Mogyorósi K, Németh J, Dékány I, Fendler JH (2001) *Prog Colloid Polym Sci* 117:88–93
- Tunesi S, Anderson M (1991) *J Phys Chem* 95:3399–3405
- Minero C, Catozzo F, Pelizzetti E (1992) *Langmuir* 8:481–486
- Tomkiewicz M, Dagan G (1993) *J Phys Chem* 97:12651–12655
- Regazzoni AE, Mandelbaum P, Matsuyoshi M, Schiller S, Bilmes SA, Blesa MA (1998) *Langmuir* 14:868–874
- Bahnemann DW, Kormann C, Hoffmann MR (1987) *J Phys Chem* 91:3789–3798
- Spanhel L, Anderson MA (1991) *J Am Chem Soc* 113:2826–2833
- Yamazoe N, Kurokawa Y, Seiyama T (1982) *Chem Lett* 12:1899–1902
- Santos LRB, Larbot A, Persin M, Santilli CV, Pulcinelli SH (1998) *JSol-Gel Technol* 13:805–811
- Song K, Kim J (1999) *J Colloid Interface Sci* 212:193–196
- Cao L, Huo L, Ping G, Wang D, Zeng G, Xi S (1999) *Thin Solid Films* 347:258–262
- Song K, Kim J (1999) *J Colloid Interface Sci* 212:193–196
- Kim D, Oh S, Lee J (1999) *Langmuir* 15:1599–1603
- Ansari SG, Borojerdian P, Sainkar SR, Karekar RN, Aiyer RC, Kulkarni SK (1997) *Thin Solid Films* 295:271–276
- Vinodgopal K, Kamat PV (1995) *Environ Sci Technol* 29:841–845
- Sukharev V, Kershaw R (1996) *J Photochem Photobiol A* 98:165–169
- Tennakone K, Senadeera GKR, Perera VPS, Kottegoda IRM, De Silva LAA (1999) *Chem Mater* 11:2474–2477
- Nutz T, Haase M (2000) *J Phys Chem B* 104:8430–8437
- Kiricsi I, Pálkó I, Tasi G, Hannus I (1984) *Mol Cryst Liq Cryst* 244:149–154
- Dékány I, Turi L, Galbács G, Fendler JH (1999) *J Colloid Interface Sci* 213:584–591
- Dékány I, Nagy L, Turi L, Király Z, Kotov NA, Fendler JH (1996) *Langmuir* 12:3709–3715

Justus Simiyu
Bernard O. Aduda
Julius M. Mwabora

Anthocyanin-sensitized nanoporous TiO₂ photoelectrochemical solar cells prepared by a sol–gel process

J. Simiyu · B. O. Aduda
J. M. Mwabora (✉)
Department of Physics,
University of Nairobi,
P.O. Box 30197-001009 PO,
Nairobi, Kenya
e-mail: mwabora@uonbi.ac.ke
Tel.: +254-2-4441552
Fax: +254-2-4449616

Present address: J. Simiyu
International Science Programme,
Uppsala University, Box 549,
751 21 Uppsala, Sweden

Abstract Photoelectrochemical solar cells comprising a colloidal TiO₂ photoelectrode and sensitized with anthocyanin pigments, delphinidin purple and cyanidin 3,5-diglucose extracted from *Hibiscus sabdariffa* and *Ribes nigra* plants, respectively, have been fabricated. A sunlight-to-electricity conversion efficiency of 3.16% under simulated solar light was obtained with the cell sensitized with the delphinidin purple dye.

Open-circuit photovoltages of 0.2–0.3 V and short-circuit photocurrents of 15–30 mA/cm² were obtained, which points to efficient charge-carrier injection at the semiconductor/electrolyte interface. The cells also showed a high activation energy of between 0.3–0.5 eV.

Keywords Photoelectrochemical · Dye sensitization · Nanoporous

Introduction

Colloid science combined with electrochemistry and semiconductor physics has recently gained great interest in solar energy applications [1, 2], revealing intriguing features of solar energy conversion systems that are responsible for optimal performance. Features such as surface thermodynamics of the colloids, electronic properties of the semiconductor and the electrochemical positioning of the band edge potential of the electrolyte, well-matched and stable dyes have been studied with the view of optimizing the efficiency of solar cells [3]. Semiconductors with colloidal suspensions have been prepared for many materials, mainly oxides of Ti, Zn and Ag and sulphides of Zn, Cd, Pb and Cu [4], each used to form an assembly of thin, transparent and porous films whose inner surface area is enormous, with the colloidal particles constituting the network being in electronic contact thereby allowing electric charge percolation through the films. These semiconductors though exhibiting good electrical properties for solar cells are not sensitive to visible light. This has led to studies in the field of dyes to perform sensitization. The dye that has been found to give the best performance in terms of charge

transfer is the ligand-based ruthenium-complex dye RuL₂(μ-CN), where L is the complex 2,2'-bipyridine-4,4'-dicarboxylic acid ligand [2]. This dye is however very expensive and is not cost-effective in large-scale applications.

Studies into cheaper dyes, mainly naturally occurring, have been motivated by this fact that the ruthenium-complex dye is not cost-effective. On such naturally occurring plant pigments is anthocyanin, studied in this review. Anthocyanin pigment is a known visible-light trapper [5] that undergoes charge excitation and upon complexation with a metal oxide semiconductor like TiO₂, a charge-transfer process occurs. The charge-transfer mechanism in anthocyanins is mainly ligand-centered [6]. This is due to the presence of O and OH sites that perform complexation with TiO₂.

The charge-transfer process in dye sensitization follows the reaction path shown in Fig. 1 [6]. Upon illumination, the sensitization dye molecule (S) (Fig. 1) in its ground state is excited (S^{*}) (reaction 1) and injects an electron into the conduction band of the TiO₂ semiconductor (reaction 2); as a result the excited dye becomes oxidized (S⁺). The injected electron travels through an external load and is collected at the counterelectrode,

where it is then accepted by the redox couple I_3^-/I^- present in the electrolyte (reaction 3) hence reducing the oxidized dye to the ground state, consequently completing the cycle. The dye is then available for excitation again.

In the type of dye-sensitized solar cell, the dye and the semiconductor perform the processes of light absorption and charge separation, respectively, unlike the case of p-n junction type solar cells where the semiconductor performs both processes. This sensitization process minimizes losses due to recombination at the semiconductor/electrolyte interface (reaction 4). Since the electron transport in photoelectrochemical (PEC) cells is purely due to kinetic effects surfaces with structural defects do not therefore cause recombination and can be used in contrast to conventional solar cells [3]. That is the electron injection occurs anywhere in the cell and the time for electron recombination has been studied by flash photolysis and has been found to be very much longer than for electron injection [6].

In this paper, we report on the current–voltage (I – V) characteristics and conversion efficiency of PEC cells comprising a colloidal TiO_2 photoelectrode and sensitized with plant-derived anthocynin dyes. These investigations were carried out alongside those using cells sensitized with a ruthenium-complex dye for comparative studies. The activation energy of the cells and UV–vis transmittance of the sensitized TiO_2 photoelectrodes were examined.

Experimental

The colloidal solution of TiO_2 was prepared from Degussa P25 (Degussa, Germany) following the method described by Nazee-ruddin et al. [7]. The paste was coated on 1×2-cm conducting glass substrates (Pilkington Kappa Energy, 18 Ω) using the doctor-blade technique [1] and sintered at 450 °C using a heat gun (Bosch, Switzerland) for a duration of 30 min.

Anthocyanin pigments of delphinidin purple (Dp) and cyanidin 3,5-diglucose (C35D) were extracted from anthocyanin-containing *Hibiscus sabdariffa* and *Ribes nigra*, respectively, following the method described by Smestad [6] for extraction of anthocyanins. Fresh young leaves of *H. sabdariffa* were ground in a mortar and pestle with 3 ml methanol as the solvent. The dark-brown

methanol solution obtained was filtered into a dark bottle (using hyperfine filter paper) and more of the hibiscus leaves were cut and immersed in the solution. Reagent grade sodium nitrate (10 ml, 0.1 M, Aldrich, UK) was added to the solution and more methanol was added to make 100 ml Dp (10:90 NaNO_3 to methanol). The filtered extract was passed through a Sephadex LH 20 column in methanol. Ten fractions of the dye were extracted with a volume of about 5 ml each. The dye was then ready for sensitization but more was stored under refrigeration (5 °C) for as long as it would be used. Sensitization was accomplished by immersing the sintered photoelectrodes at 80 °C in the dyes for between 24 and 72 h. The ruthenium-complex dye was used as supplied (Fluka, Germany), and spectroscopic ethanol was used as the solvent.

A spectrum analyzer (Spectro 320, Instrument Systems, Germany) was used to study the optical transmission characteristics (in the visible spectrum) of the dyes and of the dye-sensitized photoelectrodes. The I – V characteristics, and hence efficiency, were obtained using a locally made manual I – V measuring apparatus with a 500 Ω linear potentiometer as the variable load. Simulated light (Phillips Electric, Japan) of 1,000 W/m^2 incident radiation was used. The overall conversion efficiency was determined from the relationship

$$\eta = \left(\frac{V_{OC} J_{SC}}{P_{IN}} \right) FF, \quad (1)$$

where V_{OC} , J_{SC} and P_{IN} are the open-circuit photovoltage, the short-circuit photocurrent density and the input power, respectively. These are measurable quantities, while FF is the fill factor and is obtained from the maximum power triangle on the I – V curve. The activation energy was studied using the relationship between the photovoltage and surface temperature in open-circuit mode.

Results and discussions

Dye extracts of Dp and C35D showed broad transmission minima ranging from 450 to 550 nm. However upon sensitization with TiO_2 , the troughs shifted towards the blue (Fig. 2). This is an expected observation because upon sensitization with metal oxide semiconductors, anthocyanins change their structures from the quinoidal form to the stabler flavilium form, which has an absorption peak in the blue [5].

The samples exhibited I – V characteristics of an ideal solar cell (Fig. 3). The overall conversion efficiencies were 3.16% for Dp, 2.97% for C35D and 4.84% for RuL. The low efficiency in anthocyanin-sensitized cells was mainly attributed to the nature of charge transfer in anthocyanins as mentioned earlier that the nature of charge transfer is ligand-based.

The activation-energy studies showed a linear relationship between open-circuit photovoltages and temperature, with Dp having 0.47 eV, while C35D had 0.39 eV (Fig. 4). A comparative study on the ruthenium dye gave a higher value of 0.52 eV for the activation energy. These results are in agreement with Eq. (2) [8], i.e.

$$V_{OC} = \frac{mkT}{e} + \frac{E_{f,red} - E_{cb}}{e}, \quad (2)$$

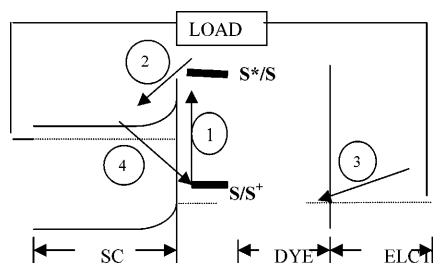


Fig. 1 Band structure and operational principle of a dye-sensitized solar cell [7]

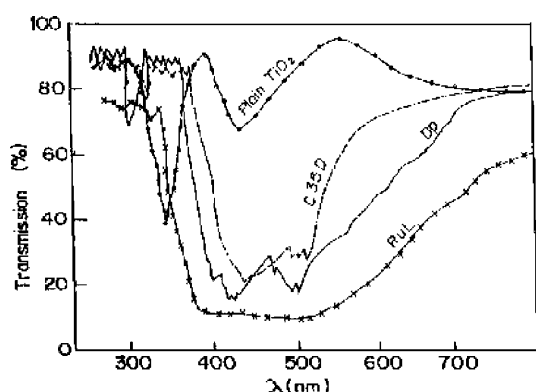


Fig. 2 Transmission characteristics of TiO_2 photoelectrodes sensitized with a ruthenium complex (*RuL*), delphinidin purple (*Dp*) and cyanidin 3,5-diglucose (*C35D*) dyes

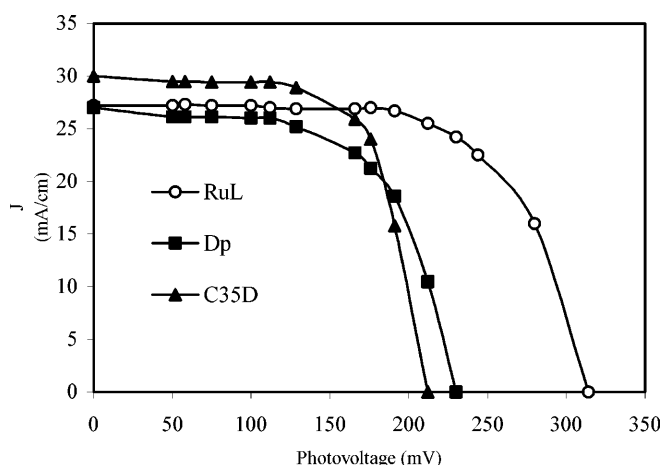


Fig. 3 I - V characteristics of *RuL*, *Dp* and *C35D* dye-sensitized solar cells

where extrapolation of the temperature to 0 K gives the value of the activation energy ($E_{f,\text{red}} - E_{\text{cb}}$). $E_{f,\text{red}}$ is the Fermi level of the electrolyte, E_{cb} is the semiconductor conduction band level, k is the Boltzmann constant, e is the electron charge and m is the ideality factor, which is in this case is assumed to be unity [8].

The differences in the activation energy for cells sensitized with *RuL*, *Dp* and *C35D* could be due to the differences in the final energy gaps created when the dyes complex with TiO_2 . The results also imply that the activation energy depends on the position of the semiconductor conduction band energy level (E_{cb}) and the Fermi level of the electrolyte media ($E_{f,\text{red}}$). The electrolyte medium provides the cation for the reaction in PECs, for which when the temperature changes, the radius of the cation changes, giving a varying potential drop in the Helmholtz layer of the cell [8].

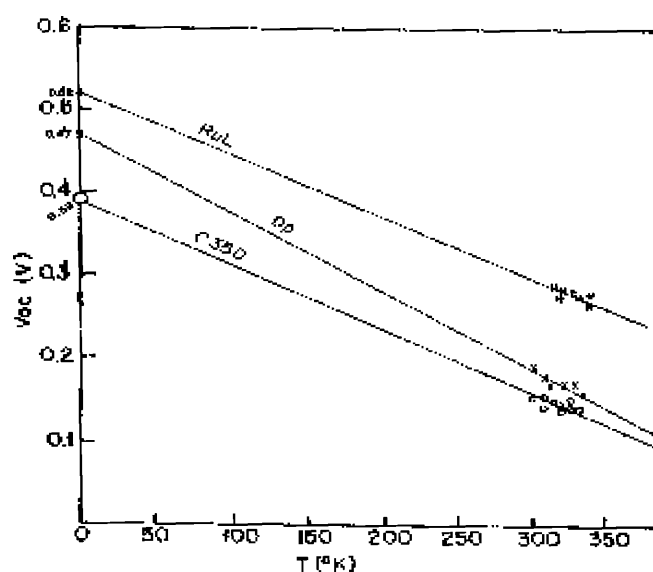


Fig. 4 Activation energy for TiO_2 solar cells sensitized with *RuL*, *Dp* and *C35D* dyes

The activation energy in the case of a PEC solar cell represents the minimum energy an excited electron needs to acquire in order to have a back reaction at the semiconductor–electrolyte interface. The back reaction occurs when an iodine molecule in the electrolyte traps an electron from the semiconductor conduction band to produce an iodide ion and an iodine surface-adsorbed atom. The adsorbed iodine again captures an electron from the conduction band to form an iodide ion instead of the electron traveling through the external circuit. From the results illustrated in Fig. 4, *Dp* presented a higher activation energy compared to *C35D*, which implies that it probably experienced less back reaction during illumination.

Conclusion

Sensitization of nanoporous TiO_2 photoelectrodes has been demonstrated by application of anthocyanin-based sensitization dyes. The dyes (*Dp* and *C35D*) have been found to exhibit characteristics of a good sensitizer, i.e. broad absorption maximum in the visible spectrum, effecting charge separation, and have shown high activation energies. This study has demonstrated the possibility of utilizing cheap sensitization dyes in place of the expensive traditional ruthenium-complex dye.

Acknowledgements This work was made possible by assistance from the International Programs in Physical Sciences, Sweden, through provision of research materials and equipment. The authors are grateful to Duke Orata and Francis Amugune of the Departments of Chemistry and Botany, respectively, University of Nairobi, for various contributions on their subjects.

References

1. Li Y, Hagen J, Dietrich H, Otschik P, Winfred S (1999) Sol Energy Mater Sol Cells 56:167
2. Grätzel M, O'Regan B (1991) Nature 353:737–739
3. Andreas K (1994) Solar cells based on dye-sensitized nanocrystalline TiO₂ electrodes. PhD thesis no. 1214, Ecole Polytechnique Federale de Lausanne, Switzerland
4. Hagfeldt A, Gratzel M (1995) Chem Rev 95:49–68
5. Coulson J (1980) Dev Food Colors 1:189
6. Smestad G (1998) Sol Energy Mater Sol Cells 55:157–178
7. Nazeeruddin MK, Kay A, Rodicho I, Humphry-Baker R, Muller E, Liska P, Vlachopoulos N, Grätzel M (1993) J Am Chem Soc 115:6382
8. Liu Y, Hagfeldt A, Xiao X-R, Lindquist S-E (1998) Sol Energy Mater Sol Cells 55:267–281

Makoto Suzuki

Actomyosin motor mechanism: affinity gradient surface force model

M. Suzuki
Graduate School of Engineering,
Tohoku University, Aoba-yama 02,
Sendai City 980-8579, Japan
e-mail: msuzuki@material.tohoku.ac.jp
Tel.: +81-22-217-7303
Fax: +81-22-217-7303

Abstract Actomyosin is a natural nanomachine which generates a force up to 5 pN per skeletal myosin motor domain and moves at a speed of $10 \mu\text{m s}^{-1}$. The working stroke per skeletal myosin motor domain per ATP hydrolysis was evaluated as at least 60 nm by Yanagida et al. (1985 *Nature* 316:366–369) which lead to the loose coupling model of Oosawa and Hayashi (1986 *Advances in Biophysics* 22:151–183). A dynamic change of the surface hydrophobicity of the myosin motor domain during the ATP hydrolysis

reaction was demonstrated by Suzuki et al. (1997 *Biophysical Journal* 72:18–23). This paper describes a linear motor model for actomyosin based on an affinity gradient surface force and affinity transition of the protein surface. This model explains the magnitude of the driving force and the force–velocity relation of Edman (1988 *Journal of Physiology* 404:301–321) and has the potential to explain long-powerstroke movement, which were hardly understood by well-known swinging-crossbridge models.

Introduction

A skeletal muscle fiber generates a tensile force as high as 0.5 MPa within 0.1 s. This force and the response speed enable animals to have quick and dexterous movement. Actomyosin is a motor protein complex which converts the chemical energy of ATP hydrolysis into mechanical work; therefore, it is the molecular engine of muscle fiber. F-actin is a linearly polymerized filament of G-actin (M_w 42,300) which is 5 nm in diameter. Myosin filament is a bipolar bundle of myosin molecules which have a tail and two identical motor domains called S1 which bind with ATP and hydrolyze it, and then drive the actin filament at $10 \mu\text{m s}^{-1}$ at no load. This speed is high enough to produce most of an animal's movement. The crystal structures of actin and myosin were solved by Kabsch et al. [1] and Rayment et al. [2], respectively. The actomyosin complex model is shown based on electron micrograph analysis in Fig. 1 [2]. The S1 domain can generate a force as high as 5 pN [3]. The ATP hydrolysis

rate (actin-activated ATPase rate) of S1 is 10 s^{-1} in solution. An in vitro motility experiment by Harada and Yanagida [4] showed that a short F-actin of 40-nm length can slide at $6 \mu\text{m s}^{-1}$, which is caused by only a few S1. Assuming that at most ten S1 molecules acted on a 40-nm F-actin and that the ATP hydrolysis rate is 10 s^{-1} , the F-actin filament must travel at 60 nm per ATP hydrolysis reaction. It is 12 times longer than G-actin and 4 times longer than S1. It is much longer than the distance shown by the structural change of the S1 molecule [5].

Bases of the new driving mechanism

To construct a driving model of actomyosin satisfying the facts just noted, we consider that F-actin cannot be only a rail of S1 and that it should act as an active device to carry S1 for a long distance using a part of the energy transferred from the S1–ATP complex. How can such an energy transfer be possible? What is the high energy state

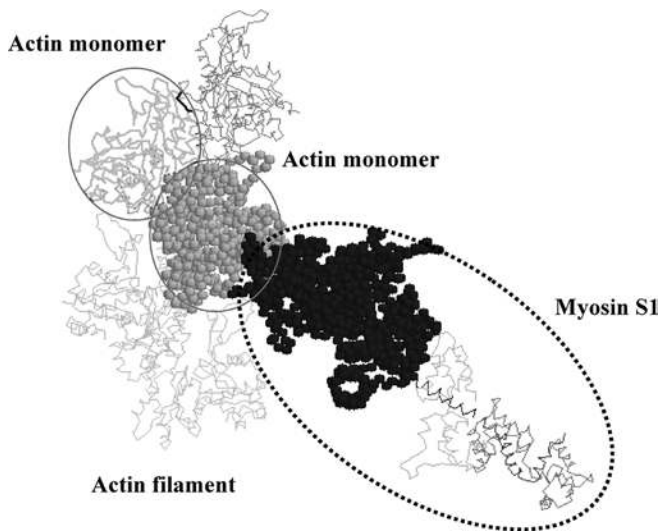


Fig. 1 Actomyosin complex reproduced from the Protein Data Base file: 1alm

of the protein molecule? To discuss these problems we here start from the basic energetics.

ATP is called a high-energy molecule because of its unstable structure between β -P (phosphorus) and γ -P. By hydrolysis reaction of ATP the chemical energy may be used to break a considerable number of secondary bonds between the nucleotide and the protein or in the inside of the protein. Breaking such secondary bonds corresponds to an enthalpy increase. It is not preferable in nature. But at the step from the M.ATP complex state to the M.ADP.Pi complex state $\Delta H > 0$, $\Delta S > 0$ and $\Delta C_p < 0$ was observed by calorimetric study [6]. It suggested a hydration decrease around the hydrophobic moieties. In water ATP molecules dissociate very slowly at neutral pH. There is a large energy barrier. How can the energy barrier be reduced in a protein molecule?

One solution was given by dielectric analysis of myosin S1 solution [7]. The study showed a 8% reduction of the hydrophobic hydration number of 1,400 per S1, which is proportional to the hydrophobic surface area [8, 9] of an S1 molecule at the M.ADP.Pi state and hydrophobicity recovery at the M.ADP state. The surface of S1 at the M.ADP.Pi state is less hydrophobic than that at the M.ADP state (Fig. 2). In addition a liquid chromatographic study [10] showed the surface hydrophobicity decrease of S1 in the presence of ATP. Thus, $\Delta S > 0$ at the step from the M.ATP state to the M.ADP.Pi state was explained by dehydration of the protein, and ΔH is compensated by $-T\Delta S$. The position of such a hydrophobicity change is considered to be the actin binding site as discussed previously [7].

The mechanism of hydrophobic dehydration from M.ATP to M.ADP.Pi can be understood as the secondary bond breaking inside the protein with ATP (which

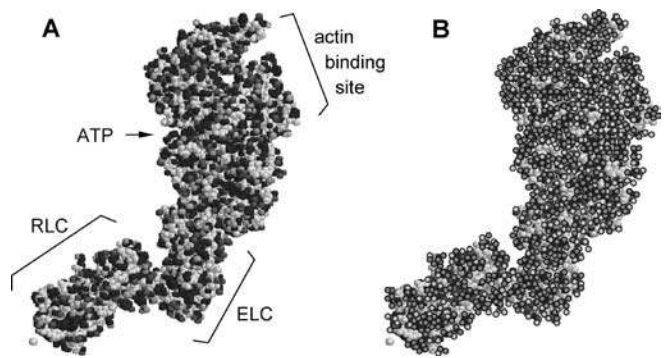


Fig. 2a, b Image of hydration structure of myosin motor domain. **a** Oxygen (red), nitrogen (green), hydrocarbons (gray), CONH bonds (black). **b** Water on polar atoms (cyan), water on hydrophobic atoms (violet)

corresponds to $\Delta H > 0$) and is promoted by hydrophobic interaction at the surface of S1 (which corresponds to $\Delta S > 0$). Such a hydrophobicity change of the protein surface upon some chemical reaction may be a rather general mechanism in protein–protein interactions.

We extend this idea to the actin myosin interaction. Through the interface between F-actin and myosin S1 some energy of the ATP hydrolysis may be transferred to actin and cause a structure change in the actin surface. Here we propose a new theory of force generation of actomyosin based on the idea of hydrophobicity transition of the protein surface [11].

Affinity gradient force

Let us consider a hydrophobic substrate in water. When a protein molecule with a surface-exposed hydrophobic area approaches the substrate the protein molecule (P) can attach to the substrate (S) with contact area A and diameter L . Let the free-energy change of contact be ΔG_c . If ΔG_c is negative the interaction is attractive (positive affinity). So we define the surface affinity to P as $-\Delta G_c$. Consider a plane S, surface of which has positive affinity to P, then the contact free-energy change is $\Delta G_{c1} (< 0)$. If the affinity of P to S became negative by some stimulation, such as by chemical reaction or light irradiation, the contact free-energy change is $\Delta G_{c2} (> 0)$. If the stimulation was made on the left half surface of the center position of P, P should translocate toward the right. The free-energy change of the translocation is $[\Delta G_{c1} - \Delta G_{c2}]$. Then the driving force, F , is written as

$$F = (\Delta G_{c2} - \Delta G_{c1})/L.$$

This consideration can be extended to a general substrate surface having hydrophobic moieties and polar or ionic groups. Extending this equation to a continuum form by introducing $\Delta G_c(x)$, the equation is written as

$$F = -\partial\Delta G_c(x)/\partial x,$$

where x is the center position of P and the surface affinity of S to P varies continuously as a function of x . ΔG_c is also a function of other parameters, such as temperature and the ionic strength of the solution.

The S surface can be stimulated by energy transfer from P which undergoes chemical reaction such as ATP hydrolysis. In actomyosin the chemical energy of ATP hydrolysis is first released in myosin S1 and finally transferred to actin to pull the load. It is important to note that the energy transferred from S1 to one actin molecule just interacting is not necessarily all of the hydrolysis energy of one ATP, which is about $20kT$. This idea gives a physical image of the loose coupling model proposed by Oosawa and Hayashi [12].

Linear motor model

Based on the affinity gradient force introduced earlier we constructed a linear motor model. X is the left-edge position of the motor (S1) on the x -axis, which is the long axis of F-actin. We put the lattice length as d . The contact length, L , is a function of ΔG_c . When the surface of F-actin at $X < x < X + d$ is stimulated to have negative affinity to S1 [$\Delta G_{c2}(>0)$], F is generated. Using a molecular friction coefficient, γ , and a load, F_w , the equation of motion of X becomes

$$dX/dt = (F - F_w)/\gamma.$$

We introduce a time constant τ for the transition of the surface affinity ($-\Delta G_c$) when a stimulation A was applied,

$$\begin{aligned} \partial\Delta G_c/\partial t &= (A - \Delta G_c)/\tau, \quad \min(\Delta G_c) = \Delta G_{c1}, \\ \max(\Delta G_c) &= \Delta G_{c2}, \end{aligned}$$

where $A = A_0 u(x, X)$, and $u(x, X) = 0$ for $x < X - d$ and $X + 2d < x$, $u(x, X) = 1$ for $X < x < X + d$, $u(x, X) = (x - X - d)/d$ for $X - d < x < X$, and $u(x, X) = (X + 2d - x)/d$ for $X + d < x < X + 2d$, and

$$F = -(L/L_0)\partial\Delta G_c/\partial x,$$

where

$$\begin{aligned} L &= L_0 \quad \text{for } \Delta G_c < \Delta G_{c1}/n \text{ or } \Delta G_c > \Delta G_{c2}/n, \\ L &= L_0/n \quad \text{for } \Delta G_{c1}/n < \Delta G_c < \Delta G_{c2}/n. \end{aligned}$$

Here and n were introduced to realize a sharp transition of the surface force.

The force-velocity relation of the present linear motor model using affinity gradient force and the experimental data on a muscle fiber given by Edman [13] are shown in Fig. 3. The parameters used in the model were $n=6$, $\gamma = 1.15 \mu\text{N s m}^{-1}$, $[\Delta G_{c2} - \Delta G_{c1}]/(L_0) = 3 \text{ pN}$, $d = 1 \text{ nm}$, $\tau = 80 \mu\text{s}$ and $A_0 = \Delta G_{c2}$, which gave a sliding speed around $5 \mu\text{m s}^{-1}$. The experimental contraction velocity

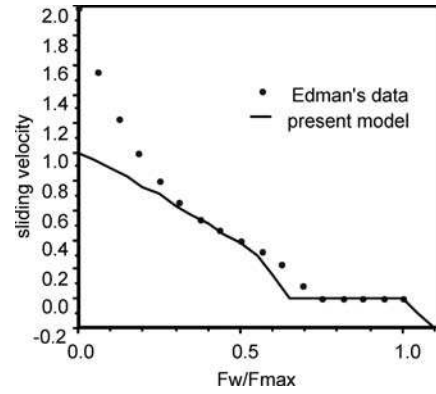


Fig. 3 Force-velocity relation

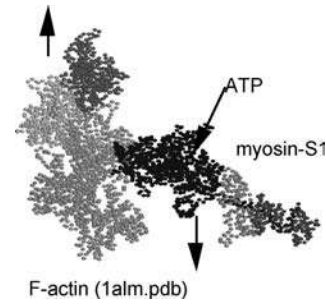


Fig. 4 Moving direction of actomyosin

is approximately hyperbolic and becomes zero above $F_w = 0.65F_{\max}$. The present model could predict the feature, especially the sudden decrease above $F_w = 0.6F_{\max}$, although there is a deviation at low force. The muscle fiber property is the integration of many small units which react randomly to cause such a hyperbolic feature.

The magnitude of the driving force

The possible driving force by this model can be estimated from the contact free energy-change, ΔG , which is close to the interfacial tension from 5 to 50 mJm^{-2} . The value of 50 nm^{-2} corresponds to the interface between water and liquid hydrocarbon. Using the contact area between F-actin and S1 of 5 nm^2 and the contact width $L = 2 \text{ nm}$, which are just possible values as shown in Fig. 2, we obtain a force of more than 10 pN calculated by $[\Delta G_{c2} - \Delta G_{c1}]/L = [5 \text{ mJm}^{-2} \times 5 \text{ nm}^2]/2 \text{ nm}$. This value is close to the experimental value of 5 pN given by Ishijima et al. [3]

Conclusion

From a hydration study with microwave dielectric spectroscopy the protein surface changes its surface

hydrophobicity during the ATP hydrolysis reaction by myosin S1. Extending this idea to a protein–protein complex, i.e. actomyosin complex, when a S1-hydrolyzing ATP interacts with F-actin the surface hydrophobicity of F-actin may be modulated. Then the affinity between S1 and F-actin can be modified in an asymmetrical manner along the F-actin axis because of the arrow structure of actin filaments. The linear motor model

using the affinity gradient surface force and surface transition of F-actin by interacting with the myosin motor domain S1 and ATP could explain the experimental facts, such as the order of the generated force of 5pN and the force–velocity relation of muscle fiber.

Acknowledgements The author thanks Dr. Kodama and Dr. Yanagida for helpful discussions. This work was supported by the Ministry of Education and Science, grant no. 11167203.

References

1. Kabsch W, Mannherz HG, Suck D, Pai EF, Holmes KC (1990) *Nature* 347:37–44
2. Rayment I et al (1993) *Science* 261: 58–65
3. Ishijima A, Harada Y, Kojima H, Funatsu T, Higuchi H, Yanagida T (1994) *Biophys Res Commun* 199:1057–1063
4. Harada Y, Yanagida T (1987) *Nature* 326:805–808
5. Suzuki Y, Yasunaga T, Ohkura R, Wakabayashi T, Sutoh K (1998) *Nature* 396:380–383
6. Kodama T (1985) *Physiol Rev* 65:467–551
7. Suzuki M, Shigematsu J, Fukunishi Y, Harada Y, Yanagida T, Kodama T (1997) *Biophys J* 72:18–23
8. Suzuki M, Shigematsu J, Fukunishi Y, Kodama T (1997) *J Phys Chem B* 101:3839–3845
9. Yokoyama K, Kamei T, Minami H, Suzuki M (2001) *J Phys Chem B* 105:12622–12627
10. Gopal D, Burke M (1997) *Biochemistry* 35:506–512
11. Suzuki M (1994) *Polym Gels Networks* 2:279–287
12. Oosawa F, Hayashi S (1986) *Adv Biophys* 22:151–183
13. Edman KAP (1988) *J Physiol* 404:301–321

Erzsébet Szabó-Bárdos
Hajnalka Czili
Katalin Megyery-Balog
Attila Horváth

Photocatalytic oxidation of oxalic acid enhanced by silver and copper deposition on a TiO₂ surface

Abstract Photooxidation of oxalic acid over a TiO₂ surface in the presence of Ag⁺ and Cu²⁺ ions was studied. Reduction of metal ions and oxidation of oxalic acid were followed under irradiation of aqueous suspensions of pH 2.5–3.5. It has been demonstrated that, after the completion of silver deposition, the small metal particles on the TiO₂ surface enhance the efficiency of the semiconductor by a factor of 5 for the photooxidation of oxalic acid. The photoreduction of Cu(II) also occurs. Although a small fraction of Cu(II) is reduced and deposited on TiO₂ under photolysis in the presence of oxygen, the photooxidation of oxalic acid is more effective in this

system than has been found for Ag-deposited TiO₂. The quantum yields for photooxidation of oxalic acid have been determined at various wavelength between 350 and 420 nm. These data demonstrate that the deposition of either Ag or Cu on the TiO₂ surface results in a shift of 1,200 cm⁻¹ in the band gap to lower energies and a considerable increase in the efficiency of photo-oxidation owing to the efficient separation of photogenerated holes and electrons.

Keywords Heterogeneous photocatalysis · TiO₂ · Reduction of silver(I) and copper(II) · Oxidation · Oxalic acid

E. Szabó-Bárdos · H. Czili
K. Megyery-Balog · A. Horváth (✉)
University of Veszprém,
Department of General and Inorganic
Chemistry, P.O. Box 158,
8201 Veszprém, Hungary
e-mail: attila@vegic.sol.vein.hu
Fax: +36-88-427915

Introduction

Heterogeneous photocatalysis based on excitation of semiconductor particles such as TiO₂ is extensively investigated for various purposes, including solar energy conversion and storage and mineralization of toxic pollutants [1, 2, 3, 4]. The advantages of the use of TiO₂ as a photocatalyst are its electronic and optical properties, chemical stability and nontoxicity [5, 6, 7, 8]. However, it absorbs UV light; hence, only a small fraction of the solar energy can be utilized by this practically white semiconductor. Therefore, in order to extend the absorption spectrum of TiO₂ into the visible range methods such as doping or loading with simple transition metals have been employed [9, 10, 11]. Although the photoresponses of these modified TiO₂ particles are shifted to longer wavelengths than

the band gap energy of the pure semiconductor it is of importance to note that in most cases the photocatalytic activity of the UV-excited particles seemed to be reduced. It has been concluded that in these cases the loading or doping of metals results in the formation of defective sites in the crystal lattice accelerating the recombination of the photoexcited electrons and holes [10, 12]. Recently this conclusion has been confirmed by femtosecond probe-and-pump diffuse reflectance spectroscopy of metal-loaded TiO₂ using various metals (V, Cr, Fe, Co, Mo and W) [13]. On the other hand, it has also been demonstrated that copper loading increases the efficiency of photocatalytic oxidation of acetic acid.

Our preliminary investigations indicated that the rate of photooxidation of oxalic acid is influenced by various transition metal ions (e.g. Co²⁺, Ni²⁺, Cu²⁺, Ag⁺) and

a considerable enhancement has been observed in the presence of Cu^{2+} and Ag^+ . In a very recent paper we reported the results obtained by light-induced oxidation of oxalic acid over a TiO_2 surface in the presence of silver(I) [14]. It has been demonstrated that addition of Ag^+ to the suspension prepared by aqueous solution of oxalic acid and TiO_2 resulted in typical photoconversion versus time curves consisting of two different sections. In the first section the reduction of the metal ions occurs with a relatively slow oxidation of the substrate. This period is followed by the rapid photooxidation of the oxalic acid.

In the present contribution we compare the effects of Cu^{2+} and Ag^+ on photooxidation of oxalic acid over a light-excited TiO_2 surface. It is demonstrated that the photoreduction of both metal ions on the surface of the semiconductor results in an increase in the photoactivity of the catalyst for oxidation of oxalic acid. The action spectra obtained by measurements performed using various wavelengths for irradiation of the samples containing bare TiO_2 and Ag-loaded TiO_2 and TiO_2 with added Cu^{2+} respectively clearly demonstrate the small decrease in the band gap energy of the metal-loaded semiconductor related to pure TiO_2 and the considerable increase in the rate of photooxidation of the oxalic acid over metal-deposited TiO_2 .

Experimental

Materials

The titanium dioxide sample used in all experiments was Degussa P25, mainly anatase, with a specific surface area of $50 \text{ m}^2 \text{ g}^{-1}$. Solutions of Ag^+ and Cu^{2+} were prepared by Ag_2SO_4 and $\text{CuSO}_4 \cdot 5\text{H}_2\text{O}$ (Reanal pure reagent grade), respectively. Oxalic acid and KMnO_4 were purchased from Reanal. The initial pH of the reaction mixture was adjusted by H_2SO_4 and NaOH of pure reagent grade. The other materials were also reagent grade and were used without further purification. The high-purity water used in the experiments was double-distilled and then purified with a Milli-Q system.

The photoreactor and the photocatalytic experiments

The large-scale (3 dm^3) photochemical reactor used for irradiation of the heterogeneous reaction mixture with a light source (40 W , $\lambda_{\text{max}} = 350 \text{ nm}$) was described in a previous paper [14]. In order to measure the action spectrum of bare TiO_2 and its metal-loaded derivatives an AMKO LTI system consisting of a 200-W high-pressure Xe-Hg arc lamp and a monochromator [15] was applied. Incident light intensity was determined with a thermopile calibrated by ferrioxalate actinometry. Typical illuminations were carried out using 1-cm quartz cuvettes. The reaction mixtures were purged by Ar and air respectively. The initial concentration of the oxalic acid was varied between 5×10^{-3} and $2 \times 10^{-2} \text{ M}$. The initial concentration of Ag_2SO_4 was varied between 0 and $3 \times 10^{-4} \text{ M}$, while that of CuSO_4 was increased up to $6 \times 10^{-4} \text{ M}$. The concentration of TiO_2 was adjusted to 1 g dm^{-3} .

Analyses

Before and after irradiation 4 cm^3 samples were taken through the septum with a syringe and immediately transferred to centrifuge tubing. The solid phase of the sample was separated by centrifugation at 6,000 rpm for 10 min. The concentration of the oxalic acid was determined by classical permanganometry using an aliquot of the clear liquid sample. The concentration of silver ions was determined by a potentiometric method [14] using a chloride-ion-selective electrode (Radelkis OP-271/1) and Ag/AgCl as the reference electrode. The concentration of the copper ions of the aqueous phase was determined by atom absorption spectroscopy using a Zeiss AAS 30 spectrophotometer. The absorption of $20 \mu\text{l}$ samples was determined at 324.8 nm.

Results and discussion

Typical variations in the concentration of oxalic acid in the large-scale photoreactor under irradiation of aqueous TiO_2 suspension at various conditions are depicted in Fig. 1. The photooxidation of oxalic acid occurs upon illumination under air with a moderate rate resulting in nearly linear decrease in the concentration of the substrate. Addition of either silver(I) sulfate or copper(II) sulfate to the suspension provides a considerable increase in the efficiency of the photo-reaction after the typical induction period. The induction period is rather short (around 8–10 min) in the presence of silver(I), while it is longer for the reaction mixture containing copper(II) ions (around 20 min).

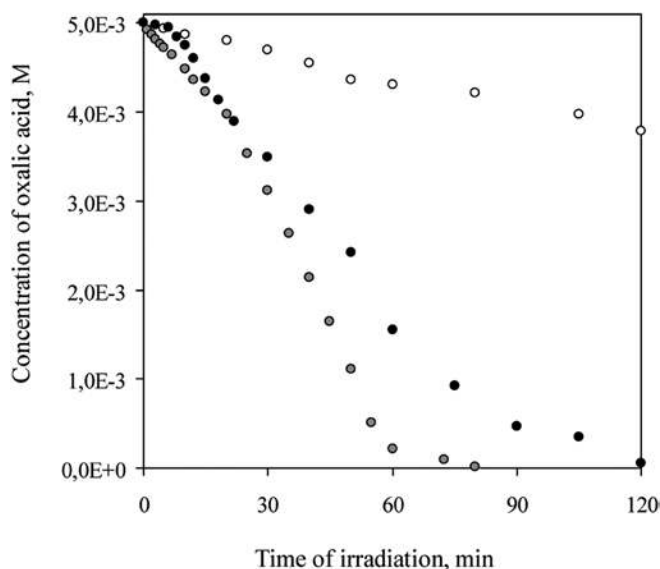
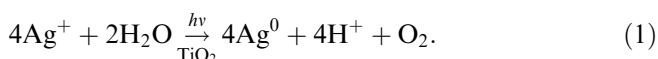


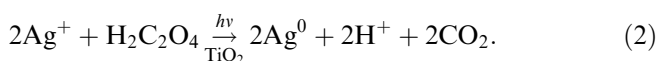
Fig. 1 Photooxidation of oxalic acid ($c_0 = 50 \times 10^{-3} \text{ M}$) at various conditions using aqueous suspension of TiO_2 (1 g dm^{-3}): none (open circles), $[\text{Ag}^+]_0 = 2 \times 10^{-4} \text{ M}$ (dark circles), $[\text{Cu}^{2+}]_0 = 2 \times 10^{-4} \text{ M}$ (shaded circles)

Reduction of metal ions in the induction period

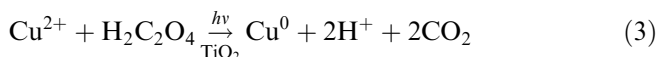
As pointed out in a previous paper [14] the electron scavenging by the oxygen at the surface of the excited semiconductor particle cannot compete efficiently with the electron transfer to the silver ion from the $\{e^-; h^+\}$ pair; hence silver is reduced and deposited on the surface of the semiconductor particles either in the absence or in the presence of oxygen. In aqueous suspension of TiO_2 and silver(I) salts the hole is trapped by the water molecule adsorbed on the semiconductor particle, resulting in a decrease in the pH of the reaction mixture [14, 16]:



The oxalic acid is a sacrificial electron donor; hence, under irradiation of the suspension containing Ag_2SO_4 and oxalic acid in excess the photoreduction of silver is rapidly completed in the induction period according to the following stoichiometry:



The reductive deposition also occurs in the presence of CuSO_4 as indicated by the change in the color of TiO_2 to pale grayish-purple. However, it should be noted that while under irradiation in the air-saturated reaction mixture the silver deposition is essentially complete in the induction period (Fig. 2); the decrease in the concentration of copper ions in the liquid phase is less than 1×10^{-5} M. The data also indicate that the photooxidation of oxalic acid in the presence of oxygen is more efficient in the copper-sensitized system than in the silver-sensitized reaction even in the induction period at an initial metal ion concentration of 2×10^{-4} M (Fig. 1). The photoreduction of the metal ions has also been investigated in an Ar-saturated reaction mixture. In this condition the rate of silver deposition is the same as observed for air-saturated reaction mixtures and the reaction occurs according to Eq. (1). However, as already pointed out, the decrease in the concentration of copper in the liquid phase is pretty small in the presence of oxygen, whereas the photoreduction of copper(II) is very rapid and it is practically complete when the photolysis is performed in the Ar-saturated system (Fig. 2) according to the following equation:



The reductive deposition of copper on the TiO_2 is also indicated by a change in the color of the semiconductor particles from white to purple. When this process has been completed the photooxidation of oxalic acid has also finished and then the concentration of oxalic acid does not change even under prolonged irradiation. When

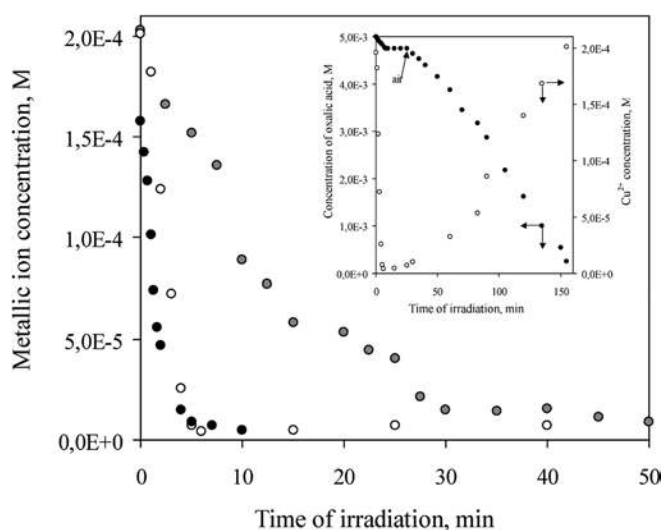
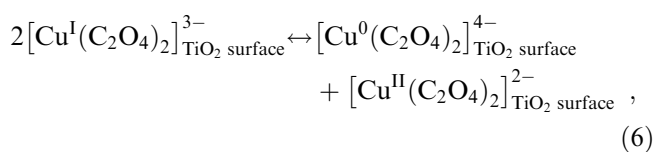
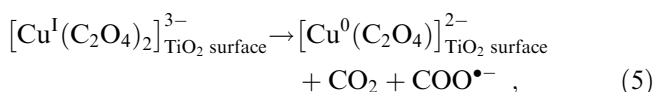
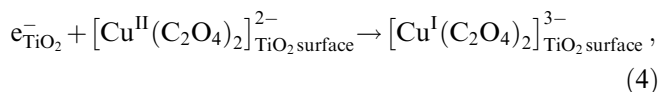


Fig. 2 Metal deposition on a TiO_2 surface under irradiation of different systems: Silver deposition under irradiation of the reaction mixture purged by air in the large-scale photoreactor ($I_0 = 4.86 \times 10^{-6}$ mol photon $\text{dm}^{-3} \text{s}^{-1}$) (dark circles), copper deposition under irradiation of the reaction mixture purged by argon in the large-scale photoreactor ($I_0 = 4.86 \times 10^{-6}$ mol photon $\text{dm}^{-3} \text{s}^{-1}$) (open circles), copper deposition under irradiation of the reaction mixture at 360 nm in a 1-cm cuvette using air for stirring the suspension ($I_0 = 2.85 \times 10^{-5}$ mol photon $\text{dm}^{-3} \text{s}^{-1}$) (shaded circles). The inset shows the concentration of Cu^{2+} (open circles) and that of $\text{H}_2\text{C}_2\text{O}_4$ (dark circles) under irradiation of the reaction mixture: $[\text{H}_2\text{C}_2\text{O}_4]_0 = 5 \times 10^{-3}$ M, $[\text{Cu}^{2+}]_0 = 2 \times 10^{-4}$ M, TiO_2 (1 g dm^{-3}). The irradiation was performed under Ar for 25 min and then under air

this purple suspension is purged with air instead of Ar the photooxidation of oxalic acid begins again. At the same time an increase in the concentration of Cu^{2+} in the liquid phase is observed. In addition the purple TiO_2 particles turn pale and finally white as expected because the oxygen readily oxidizes the deposited copper even in the dark as demonstrated by Yamazaki et al. [17]. Our data indicate that the photooxidation of oxalic acid is more efficient for the copper-sensitized reaction than in the presence of silver even in the induction period. In order to explain the different nature of the two systems it is reasonable to consider the difference in the redox potentials of the metallic couples ($\text{Ag}^+/\text{Ag}^0 = +0.779$ V, $\text{Cu}^+/\text{Cu}^0 = +0.521$, $\text{Cu}^{2+}/\text{Cu}^0 = +0.34$) and the formation constant of the surface complex of various forms of metallic species. Owing to the redox potentials and the energy level of the conduction band of TiO_2 the driving force for electron transfer from the excited semiconductor to the metallic ion decreases in the following order $\text{Ag}^+ \rightarrow \text{Ag}^0$, $\text{Cu}^+ \rightarrow \text{Cu}^0$ and $\text{Cu}^{2+} \rightarrow \text{Cu}^+$, which is in accordance with the observed efficient and complete reduction of silver(I) to silver. In addition, at least two electron-transfer steps are required in the reaction mixture containing copper(II) instead of the one-electron reduction of silver(I). In the systems investigated at the initial concentration of oxalic acid (5×10^{-3} M) and at the

pH of the reaction mixture (pH~3) the dominant species of the metal ions are $[\text{Ag}^+(\text{C}_2\text{O}_4)]^-$ and $[\text{Cu}^{\text{II}}(\text{C}_2\text{O}_4)_2]^{2-}$, respectively. TiO_2 has a positive charge (isoelectric point of the Degussa P25 is 6.6) in these conditions. Hence a higher value for surface complex formation is expected for the copper(II) complex than for the silver complex owing to the higher negative charge of $[\text{Cu}^{\text{II}}(\text{C}_2\text{O}_4)_2]^{2-}$ than $[\text{Ag}^+(\text{C}_2\text{O}_4)]^-$. However, it has been found that approximately 20% of the silver species is adsorbed on the TiO_2 surface [the concentration of the silver(I) in the liquid phase is around $1.6 \times 10^{-4} \text{ M}$] either in the presence or in the absence of oxalic acid, while the initial concentration of the copper(II) species in the liquid phase is nearly the same as the analytical concentration of copper before irradiation. This suggests that the surface complex of silver formed on TiO_2 particles is more stable than that of $[\text{Cu}^{\text{II}}(\text{C}_2\text{O}_4)_2]^{2-}$. Hence instead of electrostatic interaction some electronic effect dominates the surface complex formation. In addition, it is reasonable to suppose a very similar surface complex formation from aqua and oxalato complexes of silver(I), such as $\text{TiO}_2 \cdots \text{Ag}^+$.

The primary electron transfer from the excited TiO_2 to the $[\text{Cu}(\text{C}_2\text{O}_4)_2]^{2-}$ adsorbed on the surface of the semiconductor is followed by rapid intramolecular electron transfer from one of the coordinated oxalate ligands to the copper(I) metal center or by intermolecular electron transfer between two copper(I) complexes adsorbed on adjacent sites [17]:



Because of the HC_2O_4^- adsorbed on the TiO_2 surface it readily transfers electron to the hole:



hence one photogenerated $\{h^+; e^-\}$ can oxidize two oxalic acid molecules according to the reactions in Eqs. (4), (5), (6) and (8). The reduced copper species, either Cu^0 or Cu^{I} , can readily undergo oxidation in the air-saturated reaction mixture in the dark as was demonstrated by Yamazaki et al. [17]. These processes

with the reaction scheme including Eqs. (4), (5), (6), (7) and (8) provide a longer induction period for the copper-catalyzed system than that using silver ions. We also demonstrated that the Cu^{II} species are reduced very rapidly and completely under irradiation in the Ar-saturated reaction mixture (Fig. 2). On the other hand, the concentration of copper(II) in the aqueous phase slightly decreases in the induction period, and then it achieves a constant value when the reaction mixture has been circulated by air. So, at the end of the induction period the concentrations of both the copper(II) ions in the liquid phase and the amount of the copper deposited on the surface of the semiconductor particles achieve steady-state values depending on the analytical (total) concentration of copper species, the concentration of TiO_2 and that of the sacrificial electron donor in excess and on the pressure of the oxygen and the light intensity. In principle, a dry purple copper-loaded semiconductor sample can be obtained by illumination of the reaction mixture followed by its separation under an inert atmosphere using N_2 or Ar and it can be investigated by methods such as transmission electron microscopy to identify the copper species deposited under illumination. However, the results of these investigations cannot be considered as the assignment of the copper species deposited during photolysis under air because the colors of the reaction mixtures obtained by irradiation under air and nitrogen respectively are different. Hence it is reasonable to assume various species of reduced copper, such as Cu^0 , $[\text{Cu}^0(\text{C}_2\text{O}_4)_2]^{4-}$ and $[\text{Cu}^{\text{I}}(\text{C}_2\text{O}_4)_2]^{3-}$, at the surface of the TiO_2 sample irradiated under air. The influence of oxalic acid concentration on copper(II) concentration achieved at the end of induction period and the effect of light intensity are shown in Fig. 3.

Photooxidation of oxalic acid over metal-deposited TiO_2

Figure 1 demonstrates that the rate of photooxidation of oxalic acid is enhanced just after the silver deposition has been completed. The considerable increase in this process can be assigned as an indication of the change in the mechanisms of the light-induced reaction. Namely, while the reaction mixture has the same electron donor (oxalic acid) in the induction period and in the second stage of photooxidation it is the dissolved oxygen which acts as an electron acceptor instead of Ag^+ after the silver deposition. The product of the primary electron transfer from the excited silver-loaded TiO_2 initiates further redox reactions, resulting in the oxidation of the substrate. It has been concluded that the formation of the excited oxygen atom has a crucial role according to the following reactions [14, 18, 19]:

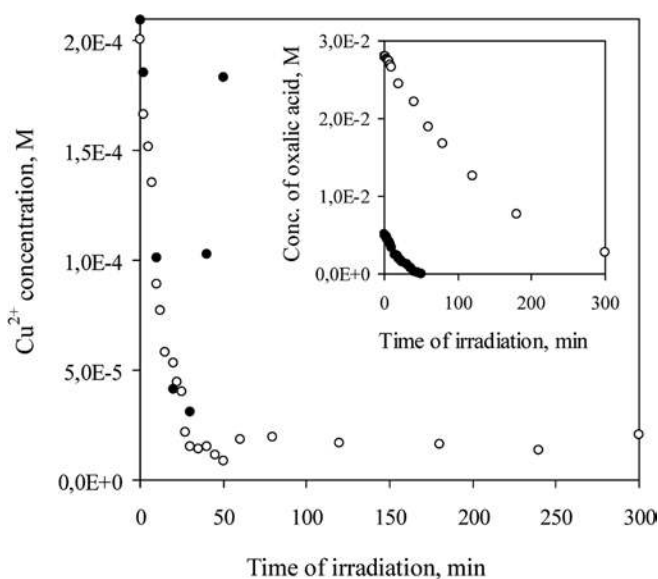
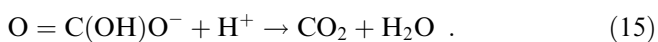
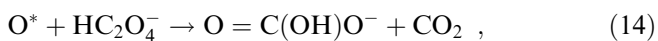
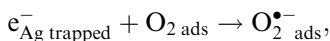
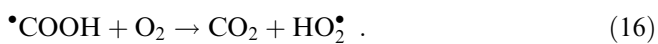


Fig. 3 The effect of oxalic acid concentration on the efficiency of copper deposition: concentration of copper in the aqueous phase of the reaction mixture at $[\text{H}_2\text{C}_2\text{O}_4]_0 = 5 \times 10^{-3} \text{ M}$ (dark circles) and $[\text{H}_2\text{C}_2\text{O}_4]_0 = 2 \times 10^{-2} \text{ M}$ (open circles), respectively. The inset shows the concentration of oxalic acid at $[\text{H}_2\text{C}_2\text{O}_4]_0 = 5 \times 10^{-3} \text{ M}$ (dark circles) and $[\text{H}_2\text{C}_2\text{O}_4]_0 = 2 \times 10^{-2} \text{ M}$ (open circles), respectively

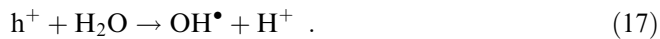


The electron transfer from oxalic acid to the photo-generated hole resulted in a $\bullet\text{COOH}$ radical (Eq. 8). This radical can also react with dissolved oxygen producing HO_2^{\bullet} :

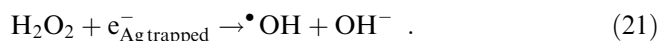
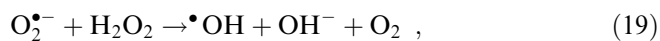
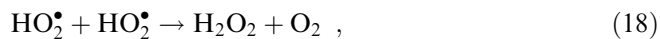


The concentration of $\bullet\text{COOH}$ is expected to be lower than the concentration of the oxygen molecules at the surface; hence, the efficient recombination of $\bullet\text{COOH}$ via bimolecular reaction with another $\bullet\text{COOH}$ to oxalic acid can be excluded. In a recent study, Hashimoto et al. [20] pointed out that the quantum yield of hole formation at the surface of the excited semiconductor particle is higher by nearly 3 orders of magnitude (5.7×10^{-2}) than the

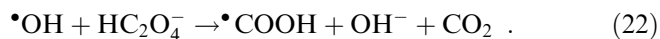
quantum yield for $\bullet\text{OH}$ radical formation due to the electron transfer from the water molecules (7×10^{-5}). Therefore, the oxalic acid is expected to be a more efficient electron donor than the water adsorbed at the surface of the semiconductor and it is reasonable to suppose that the yield of $\bullet\text{OH}$ according to the following reaction is very small:



On the other hand, reactions of the peroxy radicals formed by the reaction in Eq. (16) result in $\bullet\text{OH}$:



The hydroxyl radical readily oxidizes HC_2O_4^- [21]:



It has been concluded that the enhanced activity of silver-modified TiO_2 can be attributed to

1. The shift in the absorption spectrum of the semiconductor to the longer wavelength resulting in an increase of the absorbed light fraction.
2. The efficient separation of the light-generated $\{h^+; e^-\}$ pair via trapping of electrons by the metallic silver deposition.
3. The increase in the probability of the formation of the excited oxygen atom playing a crucial role in the oxidation of oxalic acid, which leads to the following stoichiometry according to the reactions in Eqs. (9), (11), (12), (13), (14) and (15):



The photooxidation of oxalic acid after the induction period has been found to be more efficient for the reaction mixture containing copper species than has been observed over silver-deposited TiO_2 . The rate of this photoreaction is higher by a factor of 1.8 for the copper-catalyzed system than that measured with silver at the same analytical concentration ($2 \times 10^{-4} \text{ M}$) of the metal ions.

In order to reveal the difference in the mechanism of silver- and copper-enhanced photooxidation we decided to investigate the influence of the analytical concentration of the metal ions and to measure the action spectrum of both systems between 350 and 450 nm. The effect of metal concentration is depicted in Fig. 4. The data clearly demonstrate that silver is more efficient than copper at relatively low metal concentrations. On the other hand, at metal concentrations higher than $5 \times 10^{-5} \text{ M}$ the rate of photooxidation of oxalic acid is more rapid in

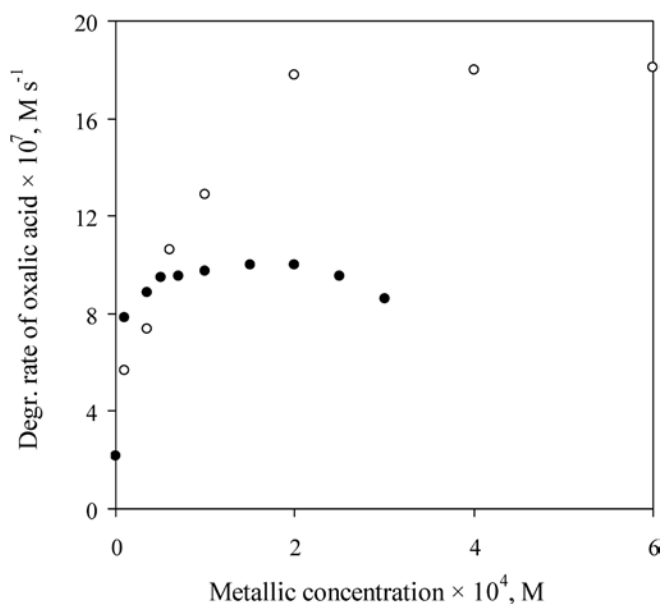


Fig. 4 The effect of the initial metal ion concentration on the rate of photooxidation measured after the induction period in reaction mixtures containing $1 \text{ g dm}^{-3} \text{ TiO}_2$ and $5 \times 10^{-3} \text{ M}$ oxalic acid before irradiation: for silver (dark circles) and for copper (open circles)

the presence of copper than in the reaction mixtures containing silver. For solutions containing silver a maximum in the rate is achieved at $1 \times 10^{-4} \text{ M}$ $[\text{Ag}^+]_0$ and this rate is constant up to $[\text{Ag}^+]_0 = 2 \times 10^{-4} \text{ M}$. Finally, the reaction rate slightly decreases above $[\text{Ag}^+]_0 = 2 \times 10^{-4} \text{ M}$. It should be noted that similar phenomena were observed by Sclafani et al. [22] when the effect of silver deposits on the photocatalytic activity of TiO_2 samples for oxidation of 2-propanol was studied. As the silver deposition was completed in our systems at the end of induction period a given fractional coverage of the surface by silver particles is obtained that depends on the ratio of the initial concentration of silver and TiO_2 concentration. It is reasonable to conclude that the maximum in the efficiency of the photooxidation is achieved at a defined average size of Ag^0 deposits and at a characteristic size distribution of Ag^0 species.

The rate of photooxidation increases moderately at low initial copper(II) concentration, then it levels off and finally a limiting value is achieved at $[\text{Cu}^{2+}]_0 = 2 \times 10^{-4} \text{ M}$. As already pointed out, the limiting rate of the photooxidation of oxalic acid is higher by a factor of 1.8 than the rate determined at optimum concentration of silver. Comparing the action spectra of TiO_2 and $\text{TiO}_2\text{-Ag}$ and $\text{TiO}_2\text{-Cu}$ systems, respectively, (Fig. 5) one can conclude that

1. The metal deposition (either silver or copper) results in a shift of $1,200 \text{ cm}^{-1}$ to lower energy in the band gap.
2. The metal-loaded TiO_2 has higher activity than the bare semiconductor.

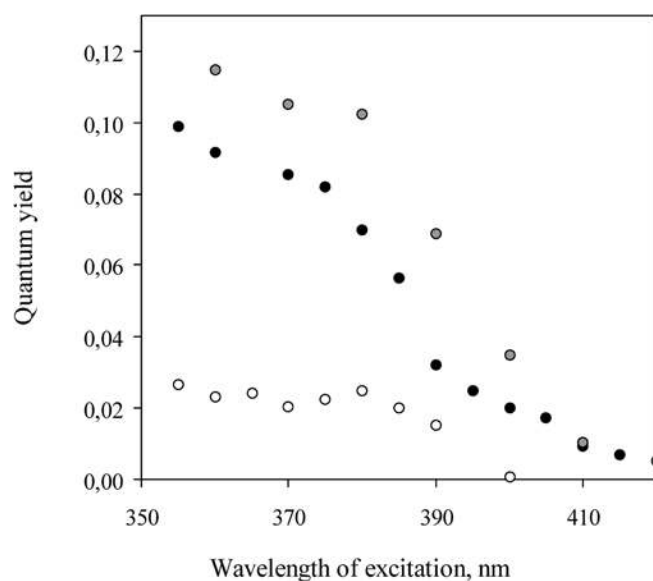


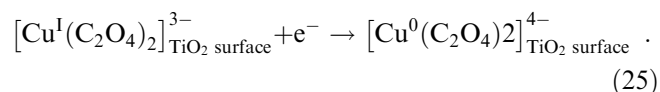
Fig. 5 Action spectra of TiO_2 (open circles), silver-deposited TiO_2 (dark circles) and copper-deposited TiO_2 (shaded circles)

3. The copper-modified TiO_2 has the highest activity within the wavelength range investigated.

Copper(0) deposited on the surface can act as an electron trap similarly to $\text{Ag}(0)$, resulting in efficient separation of $\{h^+; e^-\}$. In addition the nanosized metal particles accumulate electrons; hence, the reaction with molecular oxygen is expected to be very fast:



This reaction is followed by those in Eqs. (12), (13), (14) and (15), resulting in oxidation of oxalic acid. The electron scavenging by Cu(I) species such as $[\text{Cu}^{\text{I}}(\text{C}_2\text{O}_4)_2]^{3-}_{\text{surface}}$ results in Cu(0) according to the next reaction which is followed by that in Eq. (7).



On the other hand, in the presence of oxygen, the oxidation also takes place either in the dark or under illumination of the reaction mixture; hence, the efficient electron scavengers are regenerated by oxidation of Cu^0 . It should be noted that this reaction is faster in the irradiated reaction mixture than in the dark. It suggests that radicals such as $\bullet\text{OH}$ and O^{\bullet} formed by light-initiated reactions and with relatively high oxidation potentials can oxidize Cu(0) and Cu(I) species. So, competition for these species between oxalic acid and reduced forms of copper is expected. This is confirmed by the experiments performed at various oxalic acid concentration at constant light intensity and at the same initial concentration of oxalic acid and at different light

intensities. The thermal oxidative dissolution of silver deposited on a TiO_2 surface is a very slow process, while the same reaction for copper is fast. It should be noted that both reactions are sensitive for concentration of oxalic acid. The thermal oxidation is rather effective in systems containing copper species. This process ensures the regeneration of very good electron scavengers such as Cu(II) and Cu(I) species.

Conclusion

Simultaneous photoinduced reduction of metal ions (Ag^+ and Cu^{2+}) and oxidation of oxalic acid in excess was studied and compared using TiO_2 at pH 2.5–3.5. The reduction of Ag^+ was found to be completed within several minutes, resulting in nanosized silver species on

the surface of TiO_2 particles. This silver-modified TiO_2 proved to be more effective as a photocatalyst for photooxidation of oxalic acid than pure TiO_2 particles. Although the reduction of copper(II) complexes is found to be not complete, hence only a fraction of copper is deposited to the TiO_2 surface under irradiation in the presence of oxygen, the photoinduced oxidation of oxalic acid has an even higher efficiency than that found for silver-deposited TiO_2 . These observations are interpreted by the electron-transfer processes of two steps: photoinduced reduction of Cu^{2+} and Cu^+ and thermal and photoinduced oxidation of Cu^0 and Cu^+ in the presence of oxygen. It has been demonstrated that the deposition of these metals on the surface of TiO_2 results in a shift of $1,200\text{ cm}^{-1}$ in the band gap to lower energies and a considerable increase in the efficiency of the primary electron transfer owing to the efficient charge separation.

References

1. Courbon H, Pichat J (1984) *J Chem Soc Faraday Trans I* 80:3175
2. Fox MA, Dulay MT (1993) *Chem Rev* 93:341
3. Anpo M, Yamashita H (1996) In: Anpo M (ed) *Surface photochemistry*. Wiley, Chichester, p 117
4. Ollis DF, Al-Ekabi H (eds) (1993) *Photocatalytic purification, and treatment of water and air*. Elsevier, Amsterdam
5. Pelizzetti E, Serpone N (eds) (1986) *Homogeneous and heterogeneous photocatalysis*. Reidel, Dordrecht
6. Chiavella M (ed) (1988) *Photocatalysis and environment. Trends and applications*. Kluwer, Dordrecht
7. Pelizzetti E, Serpone N (eds) (1989) *Photocatalysis. Fundamentals and applications*. Wiley, New York
8. Kamat PV (1993) *Chem Rev* 93:267
9. Yamashita H, Harada M, Ichihashi Y, Anpo M (1998) *J Phys Chem B* 102:10707
10. Serpone N, Lawless D (1994) *Langmuir* 10:643
11. Ohno T, Tanigawa F, Fujihara K, Izumi S, Matsumura M (1999) *J Photochem Photobiol A* 127:107
12. Luo Z, Gao QH (1992) *J Photochem Photobiol A* 63:367
13. Ikeda S, Sugiyama N, Pal B, Marci G, Palmisano L, Noguchi H, Uosaki K, Ohtani B (2001) *Phys Chem Chem Phys* 3:267
14. Szabó-Bárdos E, Czili H, Horváth A (2003) *J Photochem Photobiol A* 154:195
15. Horváth O, Mikó I (2000) *Inorg Chim Acta* 304:210
16. Ilisz I, László Z, Dombi A (1999) *Appl Catal A* 180:25
17. Yamazaki S, Iwai S, Yano J, Taniguchi H (2001) *J Phys Chem A* 105:11285
18. Hermann JM, Disdier J, Mozzanega MN, Pichat P (1979) *J Catal* 60:369
19. Pichat P, Disdier J, Hermann JM, Vaudano P (1986) *Nouv J Chim* 10:545
20. Ishibashi K-i, Fujishima A, Watanabe T, Hashimoto K (2000) *J. Photochem Photobiol A* 134:139
21. Buxton GV, Greenstock CL, Helman VP, Ross AB (1988) *J Phys Ref Data* 17:743
22. Sclafani A, Mozzanega MN, Pichat P (1991) *J Photochem Photobiol A* 59:181

Ralf Zimehl
Torsten Textor
Thomas Bohners
Eckhard Schollmeyer

Smart textiles – when colloid chemistry bears a challenge

Abstract Functional coatings from inorganic–organic hybrid materials were deposited on polyethylene films and technical polyester fabrics. The differently modified inorganic–organic hybrids were based on 3-glycidyloxypropyltrimethoxysilane (GPTMS) and bisphenol A (BPA). The GPTMS–BPA hybrids were modified by UV-active components. The modification was performed by filling of the inorganic organic network with zinc oxide nanoparticles to create UV-protective technical laminates or with light-sensitive dyestuffs to produce fabrics with self-adapting colorations, respectively. Although fabrics which have been modified by inorganic–organic

coating possess several advantages they are prone to insufficient wear resistance and insufficient long-term stability. Other limitations for a common application of the so-called smart materials is the lack of suitable feedback loops; these have to be integrated into the interactive fabrics for them to become really smart ones. The latter argument can be regarded as the most important reason why smart textiles even nowadays remain a real challenge for colloid chemistry and textile engineering.

Keywords Organically modified ceramic · Sol–gel process · Textile Tunable coating · UV absorption

R. Zimehl (✉) · T. Textor · T. Bohners
E. Schollmeyer
Deutsches Textilforschungszentrum
Nord-West e.V., Adlerstrasse 1,
47798 Krefeld, Germany
e-mail: info@dtnw.de
Tel.: +49-2151-8430
Fax: +49-2151-843143

Introduction

The textile industry still constitutes one of Europe's most relevant industrial sectors for both the economy and society. The very latest trend in textile and linked industries is to create miscellaneous new products which possess the potential of interacting with the surrounding environment through active feedback. This class of new interactive material is termed intelligent textile structures or smart textiles. In order to make interactive fabrics available at the industrial level it is necessary to apply a multidisciplinary approach. The route to develop and optimise multifunctional material involves in the same way textile engineering and colloid chemistry. The complexity of the production process for modern composite materials is a real challenge to textile engineering but the fundamentals of interfacial and colloid science are indispensable to characterise and control the

properties of auxiliary materials, which are often applied in the form of dispersions and emulsions. Furthermore, underneath the economic and technological fulfilment, certain toxicological and ecological limits comes more and more into focus and may drastically change the group logistics overnight.

In the Deutsche Textilforschungszentrum Nord-West (DTNW) at Krefeld an interdisciplinary team of physicists, colloid and interfacial chemists, textile engineers and biologists have joined together and accepted the challenge to create tailor-made materials with new and unexpected properties. Intense research is presently aimed at new methods for surface modification in order to establish improved or new properties. An innovative method for textile finishing is the modification of fibre material with a thin coating of inorganic–organic hybrid materials, that combines the advantages of organic polymers and

ceramics [1, 2, 3]. A new perspective is offered on the background of recent work in the sol–gel technique [4, 5]. Organically modified ceramics, which are made by sol–gel processing, combine qualities of ceramics and synthetic polymers and have immense potential for creative modifications of the surface of fabrics with little technical effort and at moderate temperatures. These materials are derived from silica alkoxides that are modified with one organic group. This group consists of, for example, a hydrocarbon chain with functional epoxy, methacrylic or thiol groups. In the presence of certain amounts of water, under basic or acidic conditions these alkoxides undergo a hydrolysis reaction and partly condense to form transparent sols. The sols can be further modified by mixing with other metal alkoxides or dispersing nanosized metal oxides and dyestuffs, respectively. The sols can be applied by common methods, for example, dipping, spraying or knife coating. In a following curing step the condensation of the hydrolysed silicon alkoxides can be completed by simultaneously cross-linking the functional groups. Therefore the curing temperatures are very moderate. Depending on the organic modification, the final curing of the coating can be carried out with UV radiation as well and in contrast to ceramic processing the resulting three-dimensional networks are built from organic and inorganic domains. In this study we point at new strategies for the application of these tailor-made coatings to satisfy the increasing demands for functional and highly specialised textiles.

Experimental

Materials

The coating experiments were carried out with polyethylene foil (layer thickness 0.1 mm, Goodfellow) and technical polyester fabric (layer thickness 0.15 mm, 80 g m⁻²). Prior to the treatment, the carriers were extracted with ethanol and petroleum ether.

Chemicals

The inorganic–organic hybrids were synthesised from organically modified alkoxy silane 3-glycidoxypropyltrimethoxysilane (GTPMS, ≥ 97%, ABCR) and bisphenol A (BPA, Fluka). For catalysing the cross-linking reaction of the epoxy groups 1-methylimidazol (≥ 99%, ABCR) was chosen. To create UV-sensitive inorganic–organic coatings the GPTMS–BPA hybrid sols were modified with zinc oxide (Sachotech Mikro-Zinkoxid, Sachtleben, particle sizes 5–10 nm) and 1,3-dihydro-1,3,3-trimethylspiro[2H-indol-2,3'-(3H)-naphth(2,1-b)(1,4)oxazin] (Photorom I, Aldrich), respectively.

Preparation of the sols

The sols discussed in this article are based on GPTMS–BPA. One mole of GPTMS was prehydrolysed with 1.5 mol water (0.01 M hydrochloric acid) and stirred for at least 2 h

to build the basis sol. To the prehydrolysed GPTMS sol BPA was added in a molar ratio of 0.5 and was dissolved under stirring.

To prepare UV-protective inorganic–organic coatings the GPTMS–BPA hybrid sols were immediately mixed with zinc oxide dispersions of appropriate concentration. Before mixing the zinc oxide particles were dispersed in acidic water with a high-speed homogeniser (Ultra-turrax T25, IKA) and exposure to ultrasound. Finally the complete sol was diluted either with ethanol (10 vol%) or with water.

To prepare the UV-sensitive coatings prehydrolysed GPTMS–BPA sols with only 30 mol% BPA were used. Photorome I was dissolved with the help of a small amount of surfactant up to a final dyestuff concentration of 0.05 mol l⁻¹.

In both cases the catalyst for activating the cross-linking reaction of the epoxy group, 1-methylimidazol, was added (at a concentration 1 of 5% relative to the final GPTMS content in the sol) just before the coating process.

Coating processes

The wet-coatings of polyethylene foil with the different inorganic–organic hybrid materials were done by simply dipping hydrophilised polyethylene sheets into the activated sols. The wet-coated polyethylene specimens were dried in a stove (Memmert) adjusted to about 100 °C.

The coating of the technical polyester fabrics was carried out by a padding process with a lab padder (Mathis). The coated fabrics were tightened on a pin tenter heat setter (Labcoater LTE-S, Mathis) and dried for about 1 h. The drying temperature for the technical polyester fabric was always below 120 °C.

Results and discussion

UV protective coatings by filling with nanoparticles

Textile materials with a high absorption coefficient for UV radiation are very important nowadays and are of increasing interest for protection from the sun. Therefore different types of inorganic–organic hybrid materials were tested in a first simple screening experiment for their optical properties. Hydrophilised polyethylene sheets were coated with the different hybrid materials by simple dip-coating. After drying, the specimens were investigated by UV–vis spectrophotometry. Bare polyethylene sheets and polyethylene sheets covered with GPTMS–BPA hybrid material are clear with a distinct yellow shade. The specimens do not reveal significant absorption in the UV–vis spectrum (Fig. 1). On the other hand GPTMS–BPA filled with 10 mol% ZnO results in yellowish to white shaded coatings with an increased absorption in the UV-A, UV-B and UV-C, but the light absorption is still low in the visible region above 400 nm. By further increasing of the degree of filling of the hybrid coating the optical properties change from a semitransparent white shaded to a turbid and milky white appearance. The UV–vis spectrum of an opaque GPTMS–BPA hybrid filled with 30 mol% ZnO clearly reveals the increased

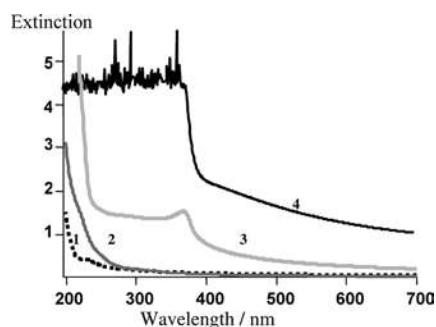
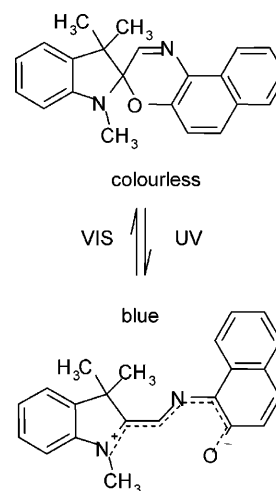
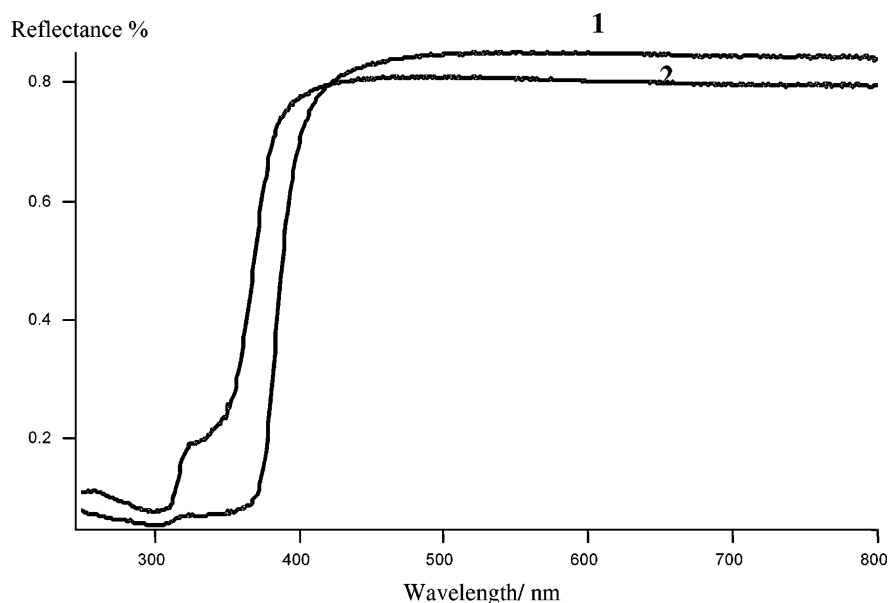


Fig. 1 Transmission UV-vis spectra of polyethylene sheets: 1 uncoated polyethylene, 2 3-glycidyloxypropyltrimethoxysilane (GPTMS)-bisphenol A (BPA) coated polyethylene, 3 GPTMS-BPA filled with 10 mol% ZnO on polyethylene, 4 GPTMS-BPA filled with 30 mol% ZnO on polyethylene

absorption of light in the region from 200 to 700 nm (Fig. 1).

In further experiments the UV filtering potential of polyester fabrics covered by semitransparent GPTMS-BPA hybrids filled with different mole percentages of ZnO was investigated. Some results from reflectance measurements in the UV-vis region for polyester fabrics are depicted in Fig. 2. For the sake of comparison the spectra of the bare polyester fabric and the polyester material coated by GPTMS-BPA hybrids with 10 mol% ZnO are plotted. Again the polyester material coated with the inorganic-organic hybrids clearly reveals the enhanced adsorption of UV in the region of 300–400 nm.

Fig. 2 Reflectance UV-vis spectra of uncoated polyester fabrics (1) and a the same polyester sample coated by GPTMS-BPA hybrids filled with 10 mol% ZnO (2)



Scheme 1 The reversible rearrangement of 1,3-dihydro-1,3,3-trimethylspiro[2*H*-indol-2,3'-(3*H*)-naphth(2,1-*b*)(1,4)oxazin] (Photocrom I) triggered by UV irradiation

UV-responsive coatings by incorporating tunable dyestuffs

To create an adaptive coating we functionalised the GPTMS-BPA based inorganic-organic hybrid by the addition of UV-tunable dyestuffs. Here we present some results obtained with Photocrom I. The molecules of Photocrom I reversibly rearrange their constitution upon UV irradiation (Scheme 1). The rearrangement of the molecules is accompanied by a colour change from colourless to blue. Because of the reversibility of the

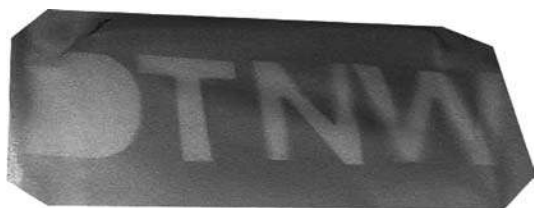


Fig. 3 Photograph of a polyester fabric coated by GPTMS-BPA hybrids filled with Photorem I. The photograph was taken after the UV irradiation had been stopped. The fabric under the letters *DTNW* was protected from UV exposure

colour change of Photorem I the dyestuff molecules may provide a UV quantum trap if the molecules are integrated in a long-lasting coating. For this purpose the UV-tunable dyestuff was added to a sol from GPTMS-BPA which was then deposited on a technical polyester fabric by dip-coating. After drying the functionalised fabric was exposed to UV radiation. A picture of the photochrome coating after the UV illumination is presented in Fig. 3. The blue area of the coating was exposed to the UV radiation, while the white writing on the coating was covered with the letters *DTNW*. To give a more quantitative view of the UV absorption and colour change of the incorporated dyestuff we performed measurements with a self-constructed dual photometer. With this equipment the functionalised fabric can be illuminated with a xenon lamp radiating light from the UV-C region up to the visible region. For the recording of the absorption spectrum the specimen was illuminated by a filtered xenon lamp with a cutoff at 400 nm. This means that no light having a wavelength below 400 nm passes the filter system. A processed spectrum obtained from this kind of experiment is depicted in Fig. 4. It can be clearly deduced from the difference spectrum that there is attenuated absorption in the orange and red regions of the spectrum recorded without UV filtering. Thus it is proven that the reversible UV switching of the

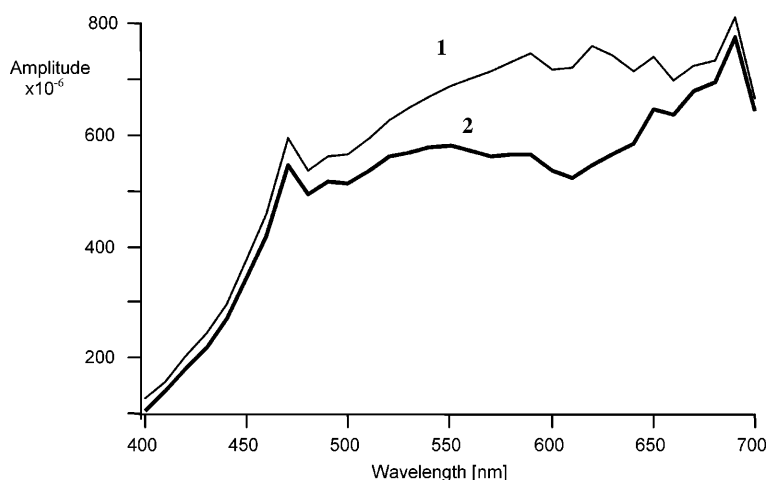
dyestuff molecules is still operative even if they are incorporated into the inorganic organic network of the coating.

Conclusion

The coating of flat or slightly curved surfaces with organically modified ceramics and inorganic-organic hybrid materials was intensively investigated in the last few years. For textile materials composites promise wide possibilities for a creative surface design and for the introduction of functionality. Several applications are already used commercially, for example, for the hydrophilic and hydrophobic coating of technical textiles or to improve the wear resistance of glass fibres.

In this contribution we have demonstrated that additional interesting properties are conceivable by suitable modifications of the coating material. Examples given were properties giving protection from the sun and self-adapting coloration. But many more applications have been suggested in the literature. By adequate coatings transdermal therapy systems could be created by incorporating drugs that are released by the inorganic-organic networks over an adjustable period of time and in therapeutically advisable dosages. Moreover, adjustable magnetic features can be created by the modified inorganic-organic hybrids. Nevertheless fabrics which have been modified by inorganic-organic coating have several disadvantages. One of the restrictions is the insufficient wear resistance and long-term stability. Other limitations for a common application of the so-called smart materials is the lack of suitable feedback loops; these have to be integrated into the interactive fabrics for them to become really smart ones. The latter argument can be regarded as the most important reason why smart textiles even nowadays remain a real challenge for colloid chemistry and textile engineering.

Fig. 4 Transmission UV-vis spectra of polyester fabrics modified by GPTMS-BPA hybrids filled with Photorem I. Spectrum 1 was obtained when the UV filter was turned on, whereas spectrum 2 was obtained when the UV filter was turned off



Acknowledgements We thank the Forschungskuratorium Textil e.V. for funding this research project (AiF-nos. 10954N and 12000N). The project was funded with financial resources of the Bundesministerium für Wirtschaft und Technologie with a grant from the Arbeitsgemeinschaft industrieller Forschungsvereinigungen “Otto von Guericke” e.V.

References

1. Nass R, Schmidt H (1990) J Non-Cryst Solids 121:329–333
2. Schmidt H (1994) J Non-Cryst Solids 178:302–312
3. Nass R, Arpac E, Glaubitt W, Schmidt H (1990) J Non-Cryst Solids 121:370–374
4. Knittel D, Textor T, Bahners T, Schollmeyer E (1998) UMIST conference: textiles engineered for performance, Manchester 20–22 April 1998, pp 1–13
5. Textor T, Bahners T, Schollmeyer E (1999) Melliand Textilber 10:847–848

A. Agod
G. Tolnai
N. Esmail
Z. Hórvölgyi

Compression of nanoparticulate arrays in a film balance: computer simulations

A. Agod · G. Tolnai · Z. Hórvölgyi (✉)
Budapest University of Technology and
Economics, 1521 Budapest, Hungary
e-mail: zhorvolgyi@mail.bme.hu
Tel.: +36-1-463-2911
Fax: +36-1-463-3767

N. Esmail
Concordia University,
Department of Mechanical
and Industrial Engineering,
de Maisonneuve Blvd. W.,
H549 Montreal,
Quebec H3G 1M8, Canada

Present address: G. Tolnai
Department of Nanostructures and
Surface Modification, CRC HAS,
P.O.B. 17, 1525 Budapest, Hungary

Abstract The structure and surface pressure of compressed monolayers consisting of silica nanoparticles at the water–air interface have been studied by means of molecular dynamics computer simulations. The simple “hexagonal array of monodisperse particles” model overestimates the range of the repulsive interparticle potentials between the nanoparticles in a monolayer. On the basis of the results of the simulation we proposed a method to assess the error of the estimation. We also investigated the relevance of

the rate of compression in terms of the structure formation and the simulated surface pressure–area isotherms, and considered a possible collapse mechanism based on the different potential energies of the ejected particles.

Keywords Molecular dynamics · Computer simulation · Film balance · Stöber silica · Nanoparticles · Collapse mechanism

Introduction

Monolayers of nanoparticles at liquid–fluid interfaces have attracted considerable attention over several decades [1, 2, 3, 4, 5, 6, 7, 8, 9, 10, 11, 12, 13, 14, 15, 16, 17]. Among others, the examinations focused on thin-layer preparation [10, 18, 19, 20, 21, 22, 23], emulsion stabilisation [15, 24] and particle characterisations [25, 26, 27]. The Stöber silica (synthesised by controlled hydrolysis of tetraethylorthosilicate in ethanol in the presence of ammonia and water) [28] has many advantageous properties for model investigations. The nearly spherical particles show a narrow size distribution and are compact above a certain particle size (around 20 nm diameter) [29]. The particles, on the one hand, show partial wettability and, on the other hand, form a weakly cohesive two-dimensional dispersion at the water–air interface [10, 14]. All that makes them suitable to determine the total repulsive interparticle energies in a film balance by measuring the effective surface tension of the monoparticulate layer [30, 31, 32, 33, 34, 35, 36].

Computer simulation of the compression of nanolayers is a powerful tool to gain a better insight into the structure formation and particle ordering in two dimensions [37, 38]. It is also applicable to confirm model assumptions, or to assess the error of the oversimplified calculations concerning the layer properties or the interparticle energies.

The purpose of this work is to study the structure and the surface pressure of compressed noncohesive monolayers consisting of silica nanoparticles at the water–air interface. We employ molecular dynamics computer simulations to analyse the pressure–area (Π – A) isotherms and to show that the use of the “hexagonal array of monodisperse particles” model can lead to a significant overestimation of the particle–particle (p–p) distances calculated from the Π – A isotherms. We also examine the relevance of the rate of compression in terms of the structure formation of the layer and the isotherms. Finally, we consider a collapse mechanism based on the different potential energy of the ejected particles.

In the next part of the paper we survey the experimental methods and the model calculations.

Experimental methods and calculations

Particle size measurements

A JEOL JEM-100 CX II transmission electron microscope (TEM) was used to assess the particle size and shape. The sample was deposited on a Formvar film-coated carrier grid. The size distribution of the sample was determined by measuring the diameters of around 500 spherical particles. For demonstration, a TEM image of the particles is shown in Fig. 1. The size distribution of the sample investigated (average diameter of 44 nm) is depicted in Fig. 2.

We determined the average diameter (\bar{d}), the average cross-section (\bar{A}) and the average volume (\bar{V}) from the size distribution. The number of the particles at the interface, Z , was determined from the total mass of the spread particles, m_{tot} , as follows:

$$Z = m_{\text{tot}} / (\rho \bar{V}), \quad (1)$$

where $\rho = 2,060 \text{ kg/m}^3$ is the density of a silica particle [39].

Film balance experiments

A laboratory-built Wilhelmy film balance was used to determine the Π - A isotherms of monolayers at $23 \pm 1^\circ\text{C}$ ambient temperature. The sols used for spreading were prepared by diluting the silica suspensions with chloroform (1 vol alcosol and 2 vol chloroform); this was then homogenised in an ultrasonic bath for 10 min. An appropriate amount of sol was spread on the surface of the water in the film balance. After evaporation of the spreading liquid, the Π - A isotherms were obtained at a rate of 3.35 cm/min of the moving barrier (corresponding to $33.5 \text{ cm}^2/\text{min}$). The film balance experiments were repeated five times to assess the reproducibility.

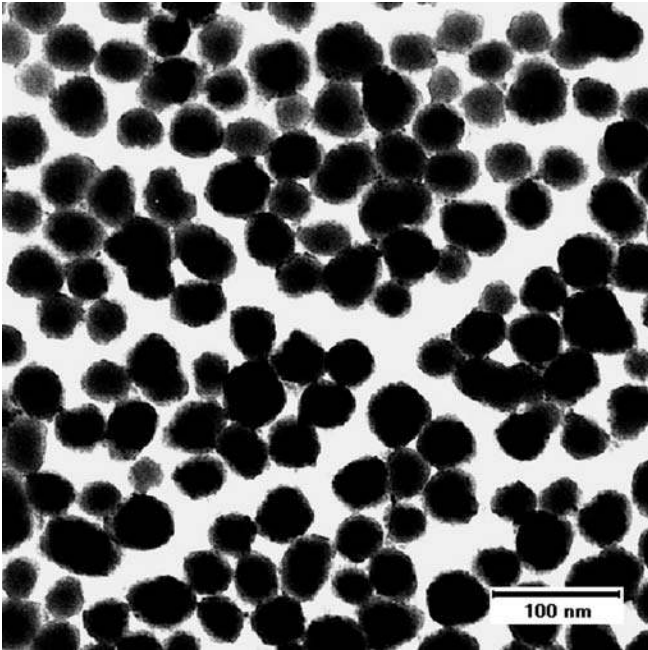


Fig. 1 Transmission electron microscope image of the particles (magnification 80,000)

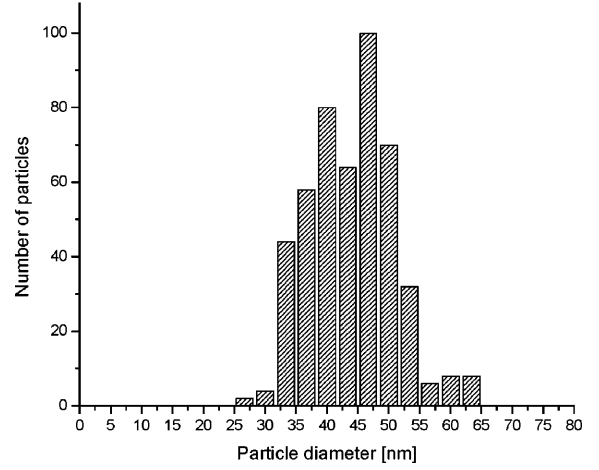


Fig. 2 The size distribution of the sample

Determination of the total interparticle repulsion energies by the analysis of the Π - A isotherms

The total pair-interaction energies were calculated by integrating the Π - A isotherms assuming a hexagonal array of stabilised particles during compression and that only the first-neighbour interactions are significant. (Later, we will show that these assumptions cause significant differences in determining the range of repulsion, but as a first approximation we use these pair-potentials in the simulation.):

$$V_T = -\frac{1}{3} \int_{A_\infty}^{A_H} \Pi(A') dA'. \quad (2)$$

where A' is the area for a single particle in the monolayer and A_H is the area for a particle at an interparticle distance of H . H relates to A_H as follows:

$$H = \sqrt{\frac{2A_H}{\sqrt{3}}} - \bar{d}. \quad (3)$$

For the calculation of A_H , the total number of spread particles (Z) and the area of the layer (A) are required:

$$A_H = \frac{A}{Z}. \quad (4)$$

We get the first approximation of the total pair-interaction energy as a function of H by the comparison of Eqs. (2), (3) and (4). To be able to use the experimentally obtained potential function, $V_T(H)$, for shorter distances than the interparticle separations at the collapse of the layer, the data were fitted with an exponential function. The fitting seemed to be reasonable, as shown in Fig. 3.

Computer simulation

We used the results of a molecular dynamics simulation to interpret the Π - A isotherms. The evolution of the many-particle system can be described by integrating Newton's equations of motion. To integrate the differential equation system we used the leapfrog method [40]. The simulation of the compression was performed for 1,000 particles in a rectangular cell with periodic boundary conditions. The size distribution of the particles could be set

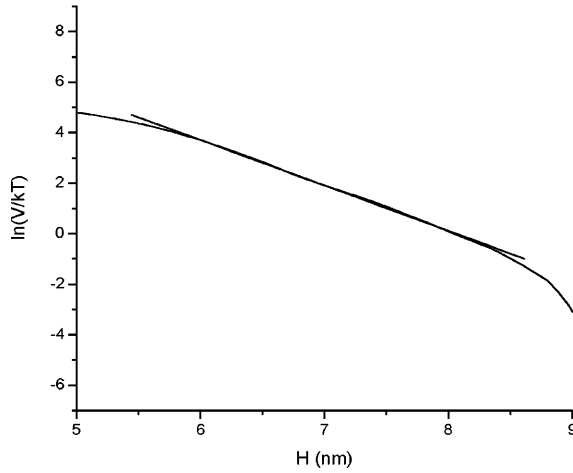


Fig. 3 Exponential fit of the experimentally obtained potential function

according to the experimentally measured values. The p-p interactions were derived from the experimentally obtained isotherms in the manner described in the previous section. The interaction potential is independent of the size of the particles, and depends only on the distance between the closest points of the surfaces of the particles. We applied a potential cutoff, i.e. if the potential obtained from the experiments was less than $0.1 kT$ we used $V=0$.

The compression of the layer was simulated by decreasing the area of the simulation cell by 0.5% (either in an isotropic or in an anisotropic manner) and by rescaling the positions of the particles proportionally after every compression step. A time step size of 10^{-11} s was used in the numerical integration of the equations of motion. It took about $M=800$ time steps to achieve (quasi) equilibrium in a compression step. (The problem of choosing M is considered in more detail in the Structure formation section.) Since the real experiments were performed at ambient temperature we rescaled the velocity of the particles to keep $\frac{1}{2} \sum_{i=1}^N m_i v_i^2 = NkT$ constant (m_i is the mass of the i th particle). The surface pressure of the layer was derived from the virial theorem [40]:

$$\Pi = n \frac{\left\langle \sum_{i=1}^N m_i v_i^2 + \sum_{(i,j)} \vec{F}_{ij} \cdot \vec{r}_{ij} \right\rangle}{2N} = \frac{NkT}{A} + \frac{1}{2A} \left\langle \sum_{(i,j)} \vec{F}_{ij} \cdot \vec{r}_{ij} \right\rangle, \quad (5)$$

where $\vec{r}_{ij} = \vec{r}_i - \vec{r}_j$ is the separation between the centres of mass of particles i and j (i, j), are the interacting pairs, \vec{F}_{ij} is the force between particles i and j (derived from the interaction potential), $n = \frac{N}{A}$, v_i is the velocity of particle i , k is the Boltzmann constant, and T is the ambient temperature.

Results

Previously, it was found that the collapse pressure and the calculated contact angles of hydrophobic particles significantly depend on the number of spread particles [41]. The effect was attributed to a surface pressure gradient along the cohesive particulate layer. More moderated mass-dependence, as expected, was found for smallest hydrophobic silica particles [41]. In order to

take this effect into consideration, we measured the Π - A isotherms by spreading different numbers of particles. The experimentally obtained Π - A isotherms are shown in Fig. 4. As can be seen, the collapse pressure increases with a decreasing number of particles.

Analysis of Π - A isotherms: p-p interactions and distances

For noncohesive or weakly cohesive particulate films the contact cross-sectional area, A_k , [42] can be related to the characteristic length of repulsion or the p-p distances at the secondary energy minimum [27, 36]. To determine A_k , a line was fitted to the most steeply rising part of the Π - A isotherms (see the leftmost isotherm in Fig. 4) at the surface pressure of $2 \text{ mN/m} < \Pi < \Pi_c - 2 \text{ mN/m}$ (Π_c is the collapse pressure) and the intersection of the fitted line and the horizontal axis (A) gives the parameter, A_k . Dividing A_k by Z , the total number of particles in the boundary layer, one gets this parameter for an individual sphere, A_1 .

As a first approximation we assumed that the layer consists of monodisperse particles and is ordered in a perfect hexagonal lattice; thus, one spherical particle occupies area A_0 , where A_0 relates to A_1 as Eq. (6) shows:

$$A_0 = A_1 \frac{\pi}{2\sqrt{3}}. \quad (6)$$

Comparing the values of A_0 and \bar{A} (the mean cross-sectional area of a single particle calculated from the size distribution function), we found in every case that $A_0 > \bar{A}$. This can be attributed to two reasons:

1. The aforementioned assumption (monodisperse particles in perfect hexagonal order) is not correct; the lattice imperfections cause lower maximum coverage than $\frac{\pi}{2\sqrt{3}}$ (Fig. 5).
2. Significant repulsion exists among the particles.

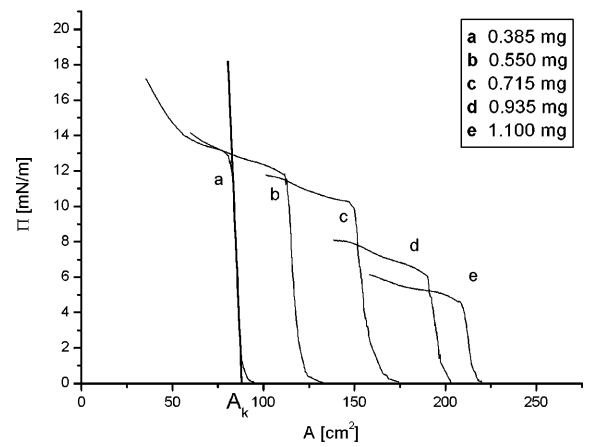
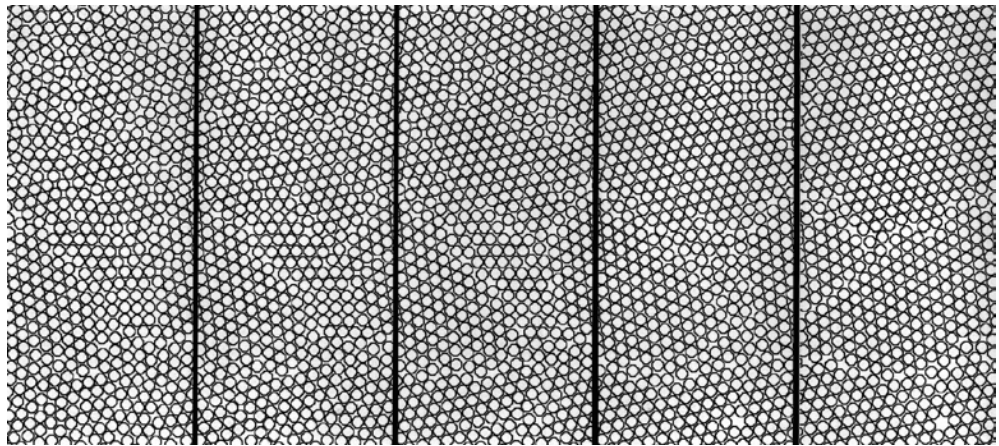


Fig. 4 Characteristic isotherms for different masses of spread particles

Fig. 5 Simulation of the compression of randomly situated monodisperse particles. The maximum surface coverage is lower than in perfect hexagonal order owing to the lattice defects. Domain structure formation can be observed



If merely the repulsion caused the difference between A_0 and \bar{A} , the range of the repulsion, H_L , could be calculated as follows (Fig. 6):

$$H_L = 2 \left(\sqrt{\frac{A_0}{\pi}} - \sqrt{\frac{\bar{A}}{\pi}} \right). \quad (7)$$

In order to clarify the effect of the model assumptions (perfectly hexagonal array of monodisperse spheres) on the calculated range of repulsion, we carried out computer simulations.

If every particle had cross-sectional area \bar{A} and formed a perfectly hexagonal array during the simulated compression, we got the experimentally obtained isotherm (Fig. 7, first isotherm), with the same A_k and range of repulsion (Fig. 8). If the particles were “scattered” randomly onto the surface with real polydispersity (set according to the experimental size distribution function), the simulation resulted in a different isotherm with a larger A_k (Fig. 7, second isotherm), from which a larger range of repulsion was obtained (Fig. 8). We determined the p-p interaction from this latter isotherm in the same manner as in the previous case and made a new run with this pair-potential applying random scattering of polydisperse particles. We got a new isotherm (Fig. 7, third isotherm) and a larger range of repulsion (Fig. 8). By repeating the previous steps and plotting the H_L values against the steps, we got a nearly linear function (Fig. 8). By extrapolating this function to the zeroth step, a more correct value could be obtained for the range of

repulsion. So, with knowledge of the systematic error of the evaluation procedure, the values of the range of separation can be corrected.

By making the determinations for different numbers of spread particles, we got a corrected function for the range of repulsion dependence (Fig. 9).

The observed dependence of the range of repulsion on the number of spread particles can be attributed to the previously mentioned surface pressure gradient along the layer that manifests itself in a gradient of the surface concentration of the particles. Hence, the characteristic lengths of repulsion could be determined by extrapolating the H_L values in Fig. 9 to zero particles.

Structure formation

To investigate the relevance of the rate of compression in terms of the simulated isotherms and the structure of the



Fig. 6 Schematic picture of a particle to illustrate A_1 , A_0 , \bar{A} and H_L

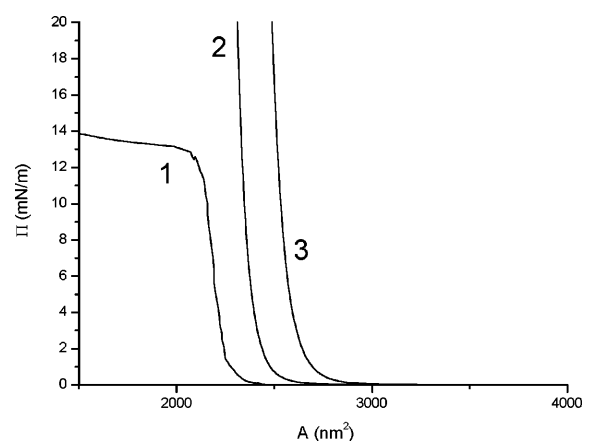


Fig. 7 The original isotherm (1), the first simulated isotherm obtained by employing the interaction potential from the original one (2) and the second simulated isotherm obtained by employing the interaction potential from the first simulated one (3)

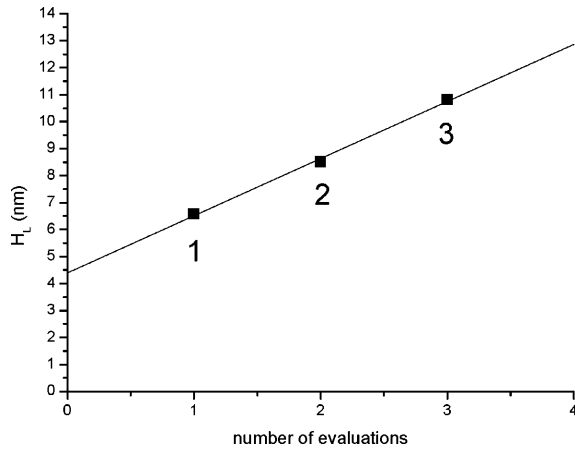


Fig. 8 Range of the repulsion between particles calculated from the original isotherm (1), from the first simulated isotherm (2) and from the second simulated isotherm (3)

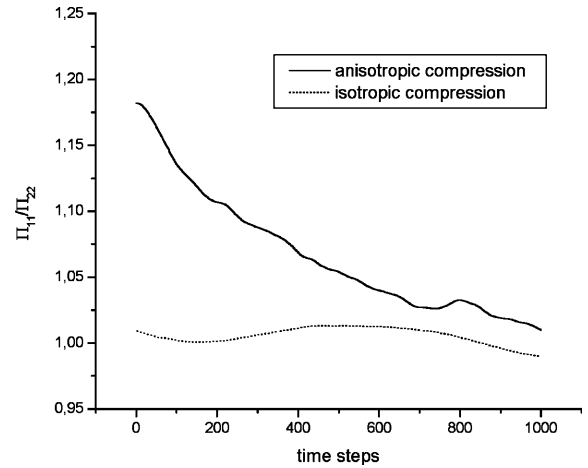


Fig. 10 The quotient of the diagonal elements of the pressure tensor versus the time steps after performing a compression step

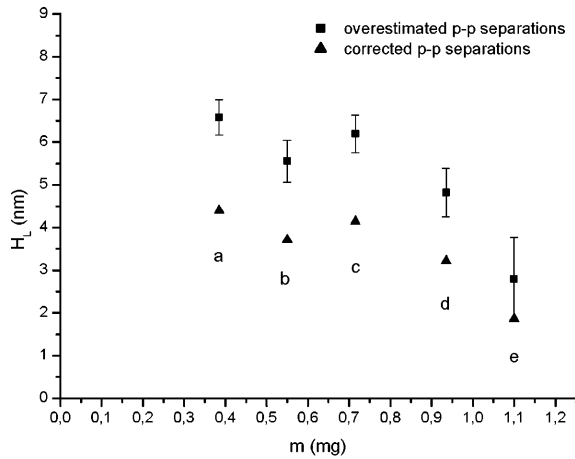


Fig. 9 Overestimated (*squares*) and corrected values (*triangles*) of the range of repulsion between the particles as a function of the total mass of the spread particles

layer, we carried out simulations. Note that the relaxation times of the system in the simulation and in the real experiments are different because the manner of the compression differs in the simulation from a real film balance experiment. (The size of the simulation cell is decreased and the positions of the particles are proportionally rescaled.)

During a slow compression the particles have enough time to reach their local equilibrium positions, whereas the fast compression of the layer leads to nonequilibrium structure formation. In the course of the determination of the range of repulsion between the particles, we let the system reach a (quasi) equilibrium after every compression step. With a time step size of 10^{-11} s one compression step took about $M=800$ time steps. To determine this value of M ,

we followed the quotient of the diagonal elements (Π_{11}/Π_{22}) of the pressure tensor (Eq. 8) after performing an anisotropic compression step (Fig. 10). (Monitoring the autocorrelation function of the surface pressure resulted in similar relaxation times.)

$$\Pi_{xy} = n \frac{\left\langle \sum_{i=1}^N m_i v_{ix} v_{iy} + \sum_{(i,j)} F_{ijx} r_{ijy} \right\rangle}{2N} \quad (8)$$

In our film balance the layer is compressed anisotropically, i.e. only in one direction; the simulation, however, allowed us to investigate isotropic compression too. If we let the systems reach local equilibrium between two compression steps, we did not find significant differences either in the structures or in the isotherms between isotropic and anisotropic compressions. However, if the systems were compressed much faster (we did not let them reach local equilibrium, i.e. Π_{11}/Π_{22} was significantly greater than 1 during the anisotropic compression), the A_k value of the anisotropically compressed system was found to be greater. This implies that the relaxation time of the monolayer is greater if it is compressed in an anisotropic manner. In Fig. 5, it was already demonstrated that monodisperse particles form a domain structure. In this context $\Pi_{11}/\Pi_{22} > 1$ indicates that the domains are ordered in a rhombohedral lattice, as was visualized by Aveyard et al. [43].

We found that the rapidity of the compression has an impact on the domain sizes. The more time was given to the particles to get closer to a local equilibrium configuration the bigger the domains that formed. The structures of slowly ($M=800$) and faster ($M=100$) compressed layers are compared in Fig. 11. The lighter shade of grey implies the particle's higher potential energy calculated from the pair-interactions.

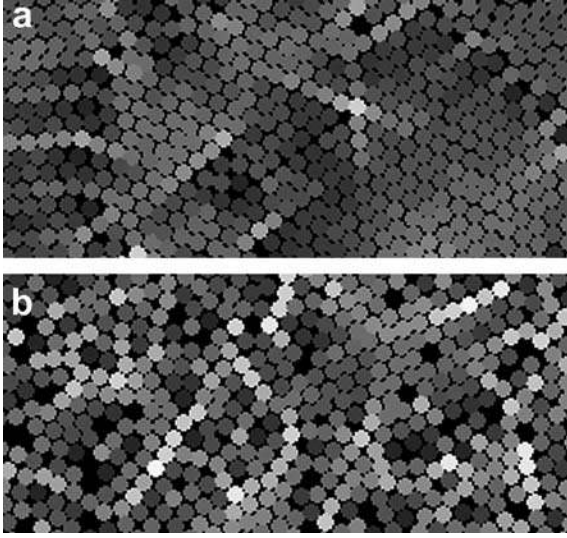


Fig. 11 Simulated structures of monolayers of monodisperse particles: **a** slow compression, **b** fast compression), The *lighter shade of grey* implies the particle's higher potential energy calculated from the pair interactions

Removing particles from the interface (a possible collapse mechanism)

The Π - A isotherms in the real experiments were not reproducible if the layer was compressed beyond the collapse point; this fact refers to the irreversible removal of the particles from the interface. Aveyard and coworkers [43, 44] indicated that the buckling of the layer has to be taken into account during the collapse. However, in their experiments the collapse pressure reached the surface tension of the interface, whereas in our experiments Π_c was found to be much lower than the surface tension of the water–air interface (Fig. 4), so the monolayer can be considered planar and the two-dimensional simulation is applicable.

In the simulation the particles were allowed to leave the water–air interface (simply by eliminating them from the system) if their potential energy exceeded the adhesion work attributed to a single sphere immersed in water to its equilibrium depth (Eq. 9).

$$V_i = \sum_j V_T(r_{ij}) > \gamma_{wa} R_i^2 \pi (1 - \cos \theta)^2, \quad (9)$$

where V_i is the potential energy of the i th particle arising from the p–p interactions, γ_{wa} is the water–air surface tension, R_i is the radius of the i th particle and θ is its water contact angle.

If monodisperse particles were used in the simulation, the particles at the edges of the domains (at lattice defects) left the interface first, as can be seen in Fig. 11 from the potential-energy distribution map. In this collapse mechanism the simulated isotherms showed

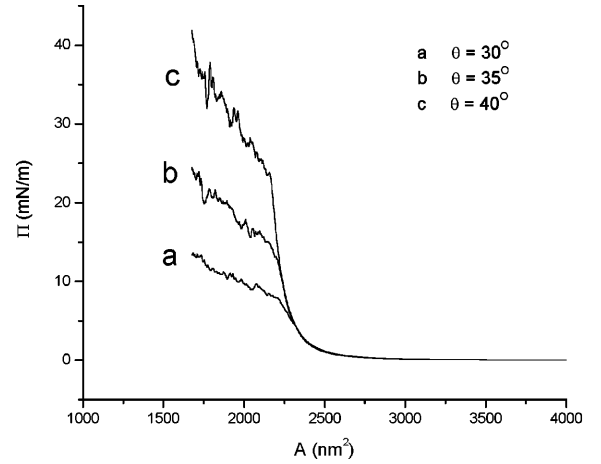


Fig. 12 Simulated isotherms of polydisperse spheres. The water contact angle of the surface of the particles was set to 30° (*a*), 35° (*b*) and 40° (*c*)

similar breakdown to the experimentally gained isotherms.

Simulated isotherms of polydisperse systems with different contact angles (30°, 35°, 40°) are presented in Fig. 12. The collapse pressure of the simulated layer was close to the value obtained in the real experiments (Fig. 4) if the water contact angle was set to $\theta = 35^\circ$. Thus, in this manner the contact angle of the surface of the particles can be estimated.

The experimentally obtained isotherms rose after the onset of the collapse (Fig. 4), and the simulation reproduced this behaviour. The increasing surface pressure of the layer during the collapse is a consequence of the different potential energy of the particles owing to the inhomogeneous layer structure.

Conclusions

We have presented molecular dynamics simulations of the compression of colloidal Stöber silica nanoparticles in a film balance. We showed that the compression of polydisperse and randomly situated nanoparticles at the water–air interface results in greater A_k , i.e. lower coverage at the onset of the steeply rising part of the surface pressure than that of monodisperse particles in a perfect hexagonal lattice. In consequence, those methods, which assumed perfect hexagonal order of the particles during the compression of the layer, overestimated the range of the interaction between the particles. We proposed a method to assess and correct the error of the monodisperse particles in hexagonal lattice assumption. The method suggested was applied to evaluate the range of repulsion between hydrophilic silica particles from their experimentally obtained Π - A isotherms.

We considered the relevance of the rate of compression in terms of the structure and the simulated isotherms. In the case of monodisperse particles the slower compression resulted in bigger domains.

By ejecting the particles from the interface if their potential energy exceeded the adhesion work, the simulation reproduced the breakdown of the surface pressure

after the onset of the collapse of the layer and allowed us to estimate the contact angle of the particles.

Acknowledgements This work was supported by the European Community – Access to Research Infrastructure action of the Improving Human Potential Programme (contract no. HPRI-CT-1999-00026) and OTKA (T 023080 and T030457).

References

- Skjeltorp AT (1987) *Phys Rev Lett* 58:1444
- Meakin P (1988) *Adv Colloid Interface Sci* 28:249
- Roussel JF, Camoin C, Blanc R (1989) *J Phys (Paris)* 50:3259
- Robinson DJ, Earnshaw JC (1992) *Phys Rev A* 46:2045
- Williams DF, Berg JC (1992) *J Colloid Interface Sci* 152:218
- Kralchevsky PA, Nagayama K (1994) *Langmuir* 10:23
- Hidalgo-Álvarez R, Martin A, Fernandez A, Bastos D, Martinez F, de las Nieves F (1996) *J Adv Colloid Interface Sci* 67:1
- Hansen PHF, Bergström L (1999) *J Colloid Interface Sci* 218:77
- Ghezzi F, Earnshaw JC (1997) *J Phys Condens Matter* 9:L517
- Tolnai Gy, Csempesz F, Kabai-Faix M, Kálmán E, Keresztes Z, Kovács AL, Ramsden JJ, Hórvölgyi Z (2001) *Langmuir* 17:2683
- Wolert E, Setz SM, Underhill RS, Duran RS (2001) *Langmuir* 17:5671
- Schwartz H, Harel Y, Efrima S (2001) *Langmuir* 17:3884
- Hansen PH, Rödner S, Bergström L (2001) *Langmuir* 17:4867
- Szekeres M, Kamalin O, Schoonheydt RA, Wostyn K, Clays K, Persoons A, Dékány I (2002) *J Mater Chem* 12:3268
- Levine S, Bowen BD (1993) *Colloids Surf A* 70:33
- Aveyard R, Clint JH (1995) *J Chem Soc Faraday Trans* 91:2681
- Aveyard R, Beake BD, Clint JH (1996) *J Chem Soc Faraday Trans* 92:4271
- Meldrum FC, Kotov NA, Fendler JH (1994) *J Phys Chem* 98:4506
- Kotov NA, Meldrum FC, Wu C, Fendler JH (1994) *J Phys Chem* 98:2735
- Yi K, Hórvölgyi Z, Fendler JH (1994) *J Phys Chem* 98:3872
- Fendler JH, Meldrum FC (1995) *Adv Mater* 7:607
- Fulda KU, Tieke B (1997) *Supramol Sci* 4:265
- Xu H, Goedel WA (2002) *Langmuir* 18:2363
- Binks BP (2002) *Curr Opin Colloid Interface Sci* 7:21
- Aveyard R, Binks BP, Fletcher PDI, Rutherford CE (1994) *Colloids Surf A* 83:89
- Hadjiiski A, Dimova R, Denkov ND, Ivanov IB, Borwankar R (1996) *Langmuir* 12:6665
- Hórvölgyi Z, Németh S, Fendler JH (1996) *Langmuir* 12:997
- Stöber W, Fink A, Bohn EJ (1968) *Colloid Interface Sci* 26:62
- Bailey JK, McCartney ML (1992) *Colloids Surf* 63:151
- Schuller H (1967) *Kolloid Z Z Polym* 216–217:380
- Sheppard E, Tcheurekdjian NJ (1968) *Colloid Interface Sci* 28:481
- Doroszowski A, Lambourne RJ (1971) *Polym Sci Part C* 34:253
- Garvey MJ, Mitchell D, Smith AL (1979) *Colloid Polym Sci* 257:70
- Clint JH, Taylor SE (1992) *Colloids Surf* 65:61
- Olugebefola SC, Park SY, Banerjee P, Mayes AM (2002) *Langmuir* 18:1098
- Tolnai Gy, Agod A, Kabai-Faix M, Kovács LA, Ramsden JJ, Hórvölgyi Z (2003) *J Phys Chem B* 107:11109
- Sun J, Stirner T (2001) *Langmuir* 17:3103
- Fenwick NID, Bresme F, Quirke N (2001) *J Chem Phys* 114:7274
- Kabai-Faix M (1996) *Magy Kem Foly* 102:33
- Rapaport DC (1995) *The art of molecular dynamics simulation*. Cambridge University Press, Cambridge
- Máté M, Fendler JH, Ramsden JJ, Szalma J, Hórvölgyi Z (1998) *Langmuir* 14:6501
- Hórvölgyi Z, Németh S, Fendler JH (1993) *Colloids Surf A* 71:327
- Aveyard R, Clint JH, Nees D, Paunov VN (2000) *Langmuir* 16:1969
- Aveyard R, Clint JH, Nees D, Quirke N (2000) *Langmuir* 16:8820

Erzsébet Hild
Tímea Seszták
Dávid Völgyes
Zoltán Hórvölgyi

Characterisation of silica nanoparticulate layers with scanning-angle reflectometry

Abstract Scanning-angle reflectometry using p-polarized laser light is a sensitive in situ method to characterize the structure of very thin surface layers when the reflectance is scanned around the Brewster angle of the substrate. Monolayers of silica particles (of size 40 nm and of different hydrophobicity) on the water surface were investigated with this method. We used both a uniform-layer model to evaluate the measured reflectance curves and a “gradient refractive index layer” approximation. The uniform-layer approximation yields both an effective refractive index and a layer thickness, but it breaks down when the layer is strongly inhomogeneous, i.e. the size of particles is comparable with the wavelength and/or the refractive index of the particles differs much from that of the host material. At the air–water interface, the particles are partially submerged

in the liquid phase and partially surrounded by air, so there is a steep refractive index change inside the layer. We elaborated a model which takes in depth inhomogeneity into account, and the structure parameters, such as the immersion depth, the particle diameter, the nearest-neighbour distance and the surface coverage, were determined by fitting the theoretical reflectivity to the measured reflectance curves. The effective refractive index of the hydrophilic layers was considerably higher than that of the hydrophobic ones, and that proved to correlate with the immersion depth of the particles. The parameters also changed with the applied surface pressure.

Keywords Scanning-angle reflectometry · Reflectance of inhomogeneous layers · Layer of silica nanoparticles · Stöber silica

E. Hild · T. Seszták · D. Völgyes
Z. Hórvölgyi (✉)
Budapest University of Technology
and Economics,
Department of Physical Chemistry,
Budafoki út 6-8, 1111 Budapest,
Hungary
e-mail: zhorvolgyi@mail.bme.hu
Tel.: +36-1-4632911
Fax: +36-1-4632911

Introduction

Scanning-angle reflectometry (SAR) together with Brewster-angle microscopy (BAM) [1, 2] are powerful tools for the investigation of very thin layers of nanoparticles deposited or spread on the surface of a bulk material. Both reflectance methods are nondestructive and can be applied in situ, and can be realized by the same optical setup. They use the special property of p-polarized light waves: that the reflectance of a perfectly abrupt, smooth interface between the medium of incidence and a

semi-infinite bulk is zero at the Brewster angle. Any deviation of abruptness – a rough interface or an interfacial layer – increases the reflectance. In a BAM device, the sample is illuminated with a p-polarized laser light beam incident exactly at the Brewster angle. The clean substrate appears dark, while anything added onto the surface appears as light or bright spots. SAR, on the other hand, measures reflectivity as a function of the angle of incidence, $R(\theta)$, near the Brewster angle. The reflectance curves are compared to that of the clean surface, which exhibits a minimum; this minimum shifts,

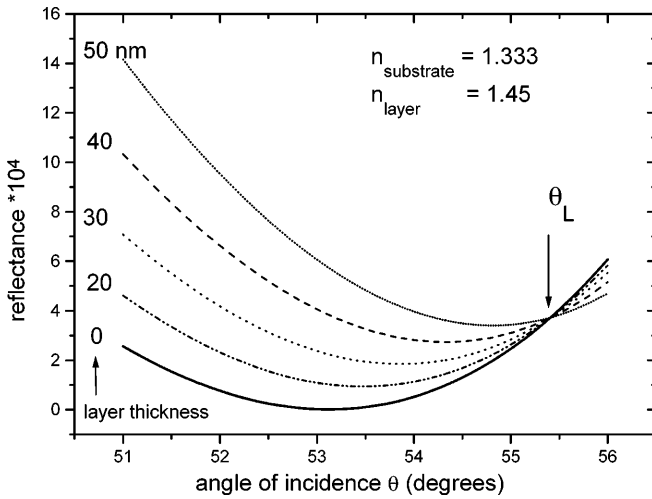


Fig. 1 Simulated $R(\theta)$ curves of homogeneous silica layers on a water surface, at different thickness values for p-polarized laser light, $\lambda = 632.8$ nm. Note that the reflectance is the same as that of the substrate at the angle θ_L

the minimum reflectance increases if an interface layer is present (Fig. 1). Even layers of few tens of nanometers thick cause well-detectable changes in the shape of the $R(\theta)$ curves.

The question is how to extract reliable information about the structure of an interfacial layer formed by nanoparticles and about the particles themselves from the reflectance measurements. The simplest method of evaluation is when one approximates the interface between the two phases with a homogeneous layer and finds the effective refractive index, n_{eff} , and thickness, d_{hom} , that correspond most closely to the measured reflectance curve. This approach is valid for nanoparticulate layers if the particles are small compared to the wavelength and their refractive index does not differ much from that of the host material [3]. For particles of size comparable with the wavelength, the light scattering must be taken into account [4]. Even for particles considerably smaller than the wavelength and where light scattering is negligible, the uniform-layer model breaks down when there are considerable refractive index differences between the components of the interfacial layer. For this case we present a method which still assumes that the layer is continuous with respect to the light wave and it is laterally homogeneous, but takes in-depth inhomogeneity into account, i.e., approximates the interface with a layer of gradient refractive index.

The optical models

Reflectance in the uniform-layer model

The reflectance of a homogeneous layer on semi-infinite substrate can be easily derived on the basis of thin-layer

optics. The interfaces between air–layer and layer–substrate are characterized by the Fresnel reflectance coefficients r_{01} and r_{12} ,

$$r_{ik} = \frac{q_i - q_k}{q_i + q_k}, \quad \text{with} \quad q_i = \frac{\sqrt{n_i^2 - n_0^2 \sin^2 \theta}}{n_i^2}, \quad (1a)$$

where n_0 , n_1 and n_2 are the refractive indices of air, the layer and the substrate, respectively, and θ is the angle of incidence. The phase change of the light wave of wavelength λ in the layer of thickness d is δ ,

$$\delta = 2\pi \cdot d / \lambda \cdot \sqrt{n_i^2 - n_0^2 \sin^2 \theta}, \quad (1b)$$

and the formula for the reflectance is

$$R = \frac{r_{01}^2 + r_{12}^2 + 2r_{01}r_{12} \cos 2\delta}{1 + r_{01}^2 r_{12}^2 + 2r_{01}^2 r_{12}^2 \cos 2\delta}. \quad (1c)$$

Calculated reflectance curves are shown in Fig. 1 for silica layers on a water substrate. The layer thickness varied from 10 to 50 nm, and the refractive index values [5] $n_1 = 1.45$ and $n_2 = 1.333$ were used for silica and water, respectively. The reflectance of the uncovered substrate is $R_s = r_{02}^2$, and this is zero at the Brewster angle of the substrate material,

$$\theta_B = \arctan(n_2/n_0). \quad (2)$$

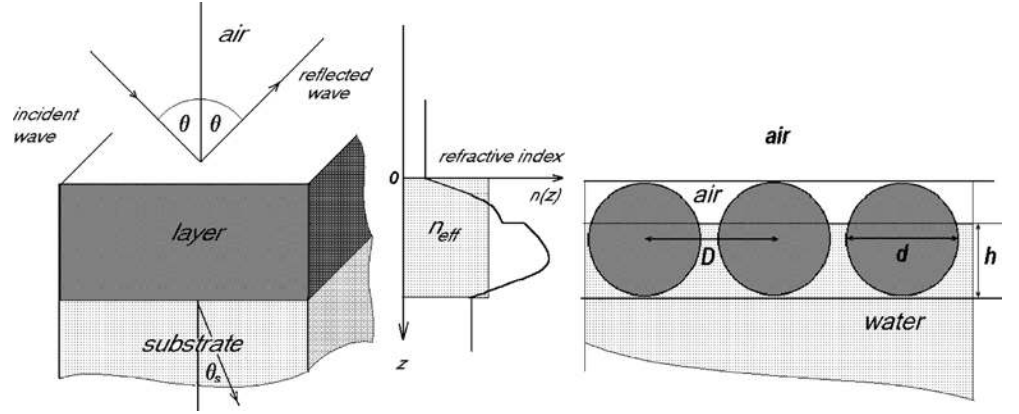
All the reflectance curves in Fig. 1 intersect at a certain angle, where the reflectance is the same as that of the bare substrate. This is the Brewster angle of the layer material, θ_L , where the reflection coefficient of the air–layer interface vanishes; $r_{01} = 0$. This fact provides us with a simple tool to estimate the effective refractive index of the layer, n_{eff} , comparing the reflectance curve of the system to that of the bare substrate, and finding the angle of intersection θ_L ,

$$n_{\text{eff}} = n_0 \tan \theta_L. \quad (3)$$

The gradient-layer model

We constructed a simplified model for the monolayer of silica particles, shown in Fig. 2: The particles are assumed to be spherical and of uniform size and are arranged hexagonally at the air–water interface (the x,y -plane). The silica spheres are partially submerged in water. That means that the water–air interface is inside the layer; h is the immersion depth. The particle diameter is d ; the distance between the particle centers is D . The layer thickness was assumed to be equal to the particle diameter. We also allowed partial coverage of the water surface by layer domains, i.e. the measured reflectance, R_m , was assumed to be a combination of reflectance from the layer, R , and that from the bare substrate, R_s :

Fig. 2 Optical model for the monolayer of spherical particles



$$R_m = \gamma R + (1 - \gamma) R_s . \quad (4)$$

The whole system was considered laterally homogeneous, but in-depth inhomogeneity was taken into account by a z -dependent refractive index function, $n(z)$. The refractive index function can be approximated by a suitable effective medium approach [6], by calculating the refractive index at a depth z from the volume fraction of the components at that depth and from their bulk refractive indexes.

In the regular hexagonal arrangement, the volume fraction of silica at depth z is

$$\alpha = \frac{2\pi}{D^2\sqrt{3}}z(d - z) . \quad (5)$$

The refractive index function has been derived both from the Lorentz–Lorenz formula,

$$\frac{n_{\text{eff}}^2 - 1}{n_{\text{eff}}^2 + 2} = \alpha \frac{n_s^2 - 1}{n_s^2 + 2} + (1 - \alpha) \frac{n_h^2 - 1}{n_h^2 + 2} , \quad (6)$$

and from the Bruggeman formula [6],

$$\alpha \frac{n_s^2 - n_{\text{eff}}^2}{n_s^2 + 2n_{\text{eff}}^2} + (1 - \alpha) \frac{n_h^2 - n_{\text{eff}}^2}{n_h^2 + 2n_{\text{eff}}^2} = 0 , \quad (7)$$

where n_s is the refractive index of silica, n_h is the refractive index of the host material, which is air for $0 < z \leq (d - h)$ and is water for $d > z > (d - h)$.

The optical model is also shown in Fig. 2. The interfaces are parallel to the x, y -plane, the system is assumed to be laterally homogeneous, but the refractive index changes in the direction normal to the interfaces, and this change is abrupt at the water–air interface inside the layer. If the thickness of the layer (d) is much less than the wavelength, the most convenient way to calculate the reflectance is in terms of the optical admittance.

The (relative) optical admittance is defined by the ratio of the tangential magnetic, H_t , to the tangential electric, E_t , field components, which are continuous throughout the system [7, 8]:

$$\Gamma = -\sqrt{\frac{\mu_0}{\epsilon_0}} \frac{H_t}{E_t} . \quad (8)$$

For p-polarized light, Γ satisfies the following first-order differential equations (λ is the wavelength of the incident light, θ is the angle of incidence, $n(z)$ is the z -dependent refractive index and n_0 is the refractive index of the medium of incidence):

$$d\Gamma/dz = -2\pi i/\lambda \left[\left(1 - \frac{n_0^2 \sin^2 \theta}{n^2(z)} \right) \Gamma^2 - n^2(z) \right] . \quad (9)$$

The optical admittance of a single traveling wave in a homogeneous medium of refractive index n_i is called the wave admittance of that medium, η_i . For a p-polarized light wave,

$$\eta_i = -\frac{n_i}{\sqrt{\left(1 - \frac{n_0^2 \sin^2 \theta}{n_i^2} \right)}} . \quad (10)$$

The reflectivity of the system is expressed by the surface value of $\Gamma(z)$ and the wave admittance of the incident wave:

$$R = \left| \frac{\eta_0 - \Gamma(0)}{\eta_0 + \Gamma(0)} \right|^2 . \quad (11)$$

As there is only one single traveling wave in the substrate, $\Gamma(d) = \eta_s$. Starting from this boundary condition, and solving the differential equation numerically for $z = 0$, the reflectivity can be calculated if the $n(z)$ function is known.

In order to find if the uniform-layer approximation can be used in our gradient-layer model, we simulated the $R(\theta)$ curves of the layer of 40-nm-diameter particles, calculating $n(z)$ from the volume fraction (Eq. 5) and the Lorentz–Lorenz formula (Eq. 6) (using the refractive index values 1.450 for silica, 1.333 for water and 1.000 for air), and evaluated these simulated reflectance curves by the uniform-layer method. The results are shown in Fig. 3. It is evident that the uniform-layer method can

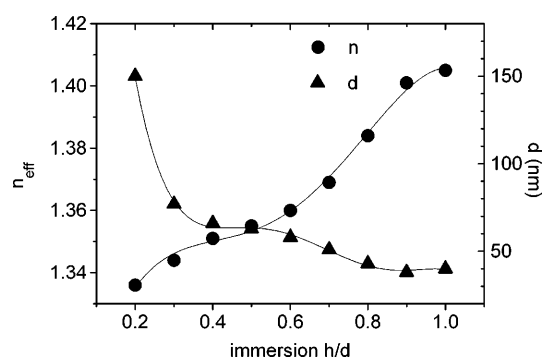


Fig. 3 Refractive index and layer thickness data obtained for the monolayer of particles when evaluated using the uniform-layer model ($d = D = 40$ nm)

result in quite erroneous thickness data when the particles float high, because of the strong inhomogeneity of the refractive index inside the layer.

Experimental

Instruments

The construction of our homemade SAR instrument is shown in Fig. 4. The source is a 17-mW polarized-beam He-Ne laser, (Melles Griot, $\lambda = 632.8$ nm) and a PD200 silicon photodiode (Edmund Industrial Optics) is used as a detector. The same setup can be used in BAM arrangement, replacing the detector with a charge-coupled-device video camera. In the vertical arrangement

shown, the source arm and detector arm move simultaneously, driven by a Little Step-U unipolar stepper motor. The layers were investigated using a Wilhelmy film balance. The whole measurement – control of the motors, setting the angle, collecting data – is fully computer controlled.

Materials

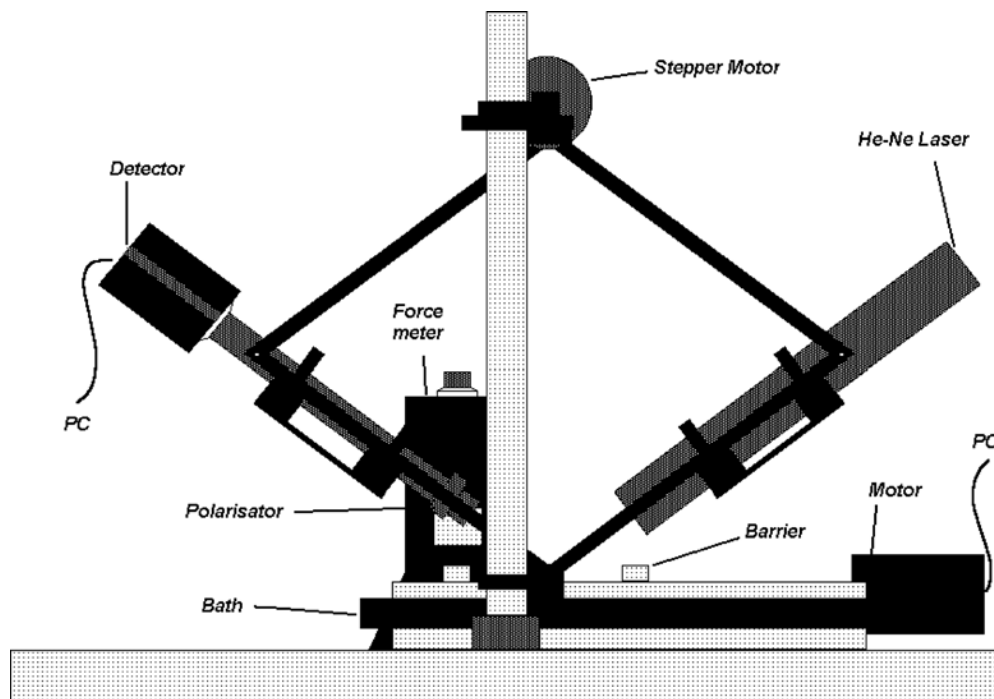
The silica nanoparticles of about 40-nm diameter were produced by the Stöber method [9] from ethanol, ammonium hydroxide and tetraethyl orthosilicate. One kind of sample was used as formed, (hydrophilic sample), the other was surface-treated by trimethylsilyl-*N,N*-dimethylcarbamate, in order to render the particles hydrophobic. The samples were used from the alcossols. The solid content of the sols was determined from the amount of solid residuum after evaporating the solvent at 80 °C. The diameter of the particles was determined from the transmission electron microscope (TEM) image of layers transferred on Formvar-coated grids. Details of sample preparation and characterization have been described in previous papers [10, 11].

Measurements

The silica particles were spread onto the water surface in the trough of the Wilhelmy film balance from a 1:2 mixture of the alcossol and chloroform (ultraresin-analyzed > 99.8%, J.T. Baker), after homogenizing the mixture in an ultrasonic bath for 10 min. We used distilled water purified with a Millipore Milli-Q filtration system.

Prior to the reflectance measurements, surface pressure–surface area isotherms were measured (Fig. 5) and the collapse of the layer was determined. [10, 11]. The amount of silica spread onto the water surface was 0.59 mg in the case of the hydrophilic samples and 0.53 mg in the case of the hydrophobic ones. The area of the trough was 250 cm²; the isotherms were taken at the rate of 33.5 cm²/min from 230 to 25 cm². The reflected light intensity was

Fig. 4 Measuring setup: scanning-angle reflectometry/Brewster-angle microscopy instrument and Wilhelmy film balance



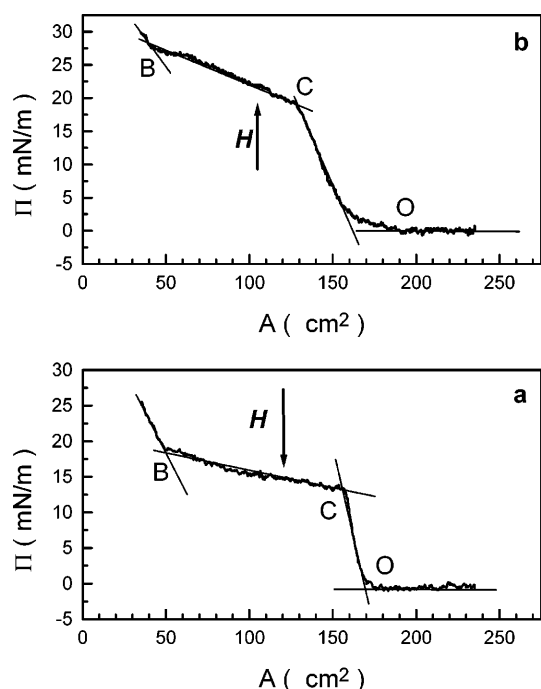


Fig. 5 Typical isotherm of **a** a hydrophilic and **b** a hydrophobic surface layer. *O* is the starting point of the rising segment of the isotherm at $\Pi = 0$, *C* is the collapse point of the two-dimensional gel structure, *B*–*C* is the range of irreversible structural changes when the particles are removed from the interface, *B* is the point where the nanoparticulate layer breaks up and *H* denotes the minimal area of the monolayer in a hexagonal arrangement of the particles

measured around 53.1° , the Brewster angle of water, at 0.1° or 0.05° steps (Fig. 6). First the reflectance curve of pure water was scanned, then the layer was spread and the moving barrier of the film balance was set to the desired surface pressure, and then the reflectance curve of the layer was measured. Twenty measurements were taken at each angle and the data were averaged. The angles, averaged data and standard deviations were stored in the measurement data file for further processing. All measurements were performed at room temperature, $22 \pm 1^\circ\text{C}$. The evaluation results are presented in Table 1 and in Fig. 7.

Evaluation and results

We evaluated the measured intensity versus angle curves by applying a Levenberg–Marquardt curve-fitting procedure to fit the theoretical reflectance to the experimental data. In the calculations, the following refractive index values were used: 1.000 for air, 1.333 for water and 1.450 for silica [11]. First we converted the measured intensity curves (Fig. 6) to reflectance, using the water curve for calibration. The light intensity reflected from the bare water surface is

$$I_w = I_0 + Ar_{02}^2(\theta + \Delta),$$

where I_0 is the residual intensity, A is the amplification, Δ is the angle shift and r_{02} is the Fresnel reflection

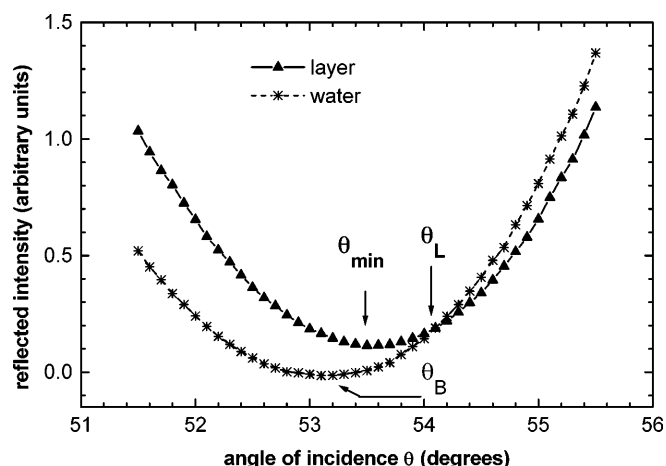


Fig. 6 Typical measured reflectance curves: reflected intensity versus angle of incidence both for water and for the spread layer. θ_B is the Brewster angle of the water substrate; θ_L is the same for the layer. In the frames of the homogeneous model, n_{eff} and d_{hom} can be obtained by a fitting procedure, but n_{eff} can be calculated also from the intersection of the two curves ($n_{\text{eff}} = \tan \theta_L$) and the thickness can be estimated from the position of minimal reflectance, θ_{min}

coefficient (Eq. 1a) of water. The $R(\theta)$ curves were obtained from the $I_R(\theta)$ data by using the parameters of the water curve that had been measured just before spreading the layer onto the water surface.

The corrected reflectance curves were evaluated using both the uniform-layer and the gradient-layer models. The results of those measurements, which were taken along the OC segment of the isotherm (Fig. 5), were averaged and the averaged values are collected in Table 1. The pressure dependence, where it was significant, is presented in Fig. 7a–c.

Results from the uniform-layer model

The parameters obtained with this model were the effective refractive index, n_{eff} , and the layer thickness, d_{hom} . The n_{eff} values were systematically higher for the hydrophilic layers than for the hydrophobic ones. The higher refractive index in the hydrophilic case can be explained by the deeper submergence of these particles, so the volume fraction of water over that of air was higher for them than for the hydrophobic ones. On the other hand, we obtained layer thickness data which were coherent with the particle diameter only for the hydrophilic particles, and they appeared much higher than the diameter for the hydrophobic ones. Both kinds of particles had to form monolayers below the collapse point, as the occupied surface was well below the theoretical area for hexagonal arrangement (denoted by *H* in Fig. 5); thus, the average thickness of 76 nm for hydrophobic case in Table 1 lacked any physical meaning. On the other hand, such high thickness values could have resulted from the inhomogeneity, as shown in

Table 1 Averaged fitting results obtained for the structure parameters along the OC segment of the isotherms. Distance between nearest neighbours, D , particle diameter, d , surface coverage, γ , immersion depth, h ; all from the gradient-layer model. Effective

refractive index, n_{eff} , diameter, d_{hom} ; both from the uniform-layer method. Diameter obtained from the transmission electron microscope images, d_{TEM}

Parameters	Hydrophilic				Hydrophobic			
	Lorentz–Lorenz		Bruggeman		Lorentz–Lorenz		Bruggeman	
	Mean	Standard deviation	Mean	Standard deviation	Mean	Standard deviation	Mean	Standard deviation
h/d	0.84	0.06	0.86	0.06	0.53	0.04	0.54	0.08
d/D	0.95	0.06	0.92	0.06	0.94	0.01	0.91	0.03
γ	0.96	0.06	0.96	0.06	0.97	0.02	0.90	0.04
d (nm)	42	2	43	2	44	2	47	3
n_{eff}	1.381 ± 0.004				1.345 ± 0.003			
d_{hom} (nm)	41 ± 2				76 ± 27			
d_{TEM} (nm)	43 ± 5				44 ± 5			
Collapse (mN/m)	13 ± 2				20 ± 1			

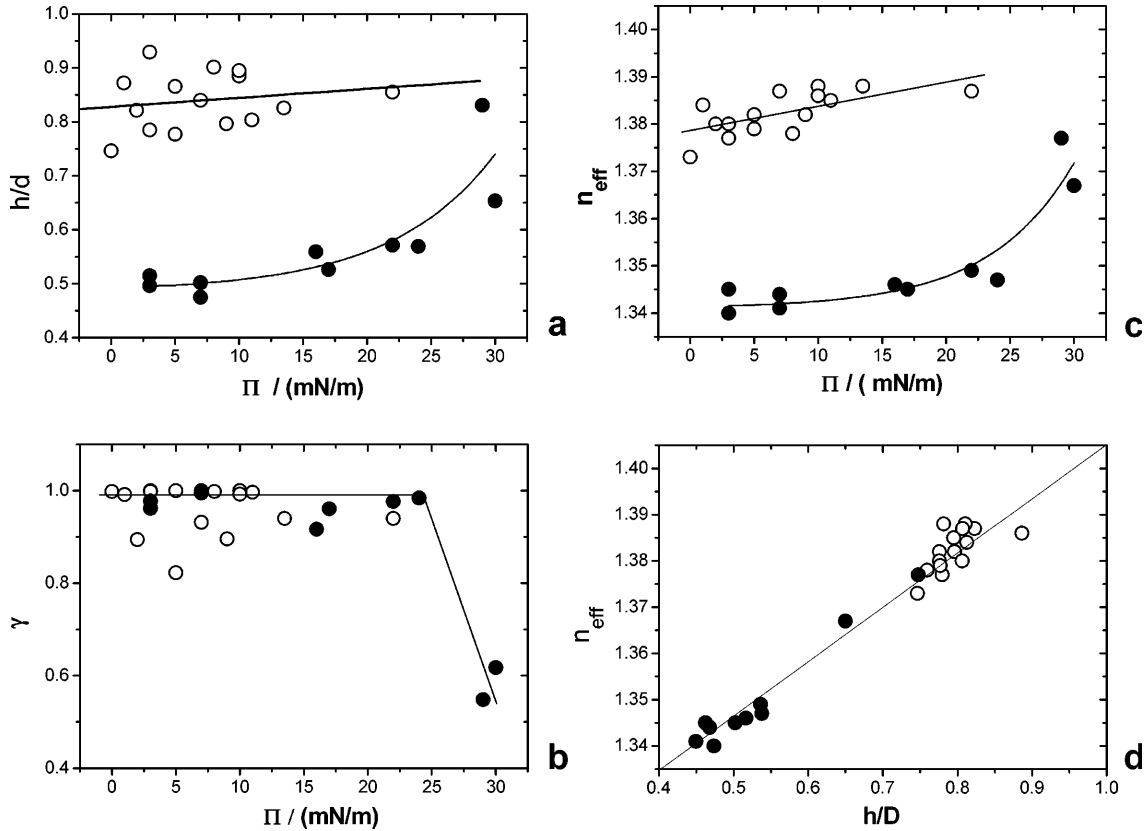


Fig. 7 Correlation among the layer parameters (immersion depth, h , particle diameter, d , distance between the centers of nearest neighbours, D , surface coverage, γ), n_{eff} and the surface pressure, Π : **a** immersion of particles versus surface pressure; **b** surface coverage versus surface pressure; **c** the change of the effective refractive index with compression; and **d** correlation between the effective refractive index and the rate of silica in the layer that is submerged in water. Hydrophobic particles (closed circles), hydrophilic particles (open circles)

Fig. 3. So we had to use the model that took inhomogeneity inside the layers into account.

Results with the gradient-layer model

With this model, the structure parameters h (immersion depth), D (distance between nearest neighbors), γ (surface

coverage) and d (particle diameter) were obtained by the fitting procedure. It is expected that the model should yield steady layer thickness values which correspond to the particle diameter and do not change with compression. Every reflectance curve was evaluated using both the Lorentz–Lorenz and the Bruggeman formulae (Eqs. 6, 7) to determine the effective refractive index function $n(z)$, but the latter one resulted in thickness values which changed systematically with surface pressure. The data we obtained from the measurements along the OC segment of the isotherms were averaged and both the mean values and the standard deviations are shown in Table 1, together with the TEM diameter of the particles and the collapse pressures.

The parameters h , D , γ and also n_{eff} exhibited some slight variations with the surface pressure, especially those of hydrophobic layers and above collapse. The dependence of the parameters on the surface pressure is shown in Fig. 7a–c, and Fig. 7d presents the correlation between the parameters obtained both from the uniform-layer model and from the gradient-layer one.

Conclusions

The results shown in Table 1 and Fig. 7 prove the applicability of our model – a gradient refractive index layer, where the local refractive index is determined from the volume fraction of the constituents by the Lorentz–Lorenz formula, as the fitted layer thickness corresponded to the particle diameter (Table 1) – and the other results were also consistent with the expectations both about the behavior of the particles and the structure of the interfacial layer.

The hydrophilic particles appeared to float deeper in the water phase than the hydrophobic ones, as was expected, and the immersion (h/d) of the hydrophobic particles increased slightly with compression before reaching the collapse pressure, and abruptly above it (Fig. 7a). The surface coverage γ did not change significantly with increasing surface pressure throughout the isotherms, except around the breaking point B (Fig. 7b) in the hydrophobic case, where it fell abruptly.

The effective refractive index obtained from the uniform-layer method proved to be a useful parameter to characterize the interfacial layer between water and air. It was found to be higher for the hydrophilic particles than for the hydrophobic ones, and it increased with the applied surface pressure (Fig. 7c). The variation of the effective refractive index was found to correlate with the immersion depth of the particles and their packing density (h/D), as expected of a valid optical model (Fig. 7d).

Figure 7c reflects that the layers of hydrophobic particles exhibited similar refractive index values that had been characteristic of the hydrophilic ones when the hydrophobic layer was compressed near to point B on the isotherm (Fig. 5b). That could mean that when the layer structure broke up (see also Fig. 7b), the fragments of the broken layer might have sunk deeper in the water phase (Fig. 7a), but these experimental results need further confirmation.

Acknowledgements The authors thank Márta Kabai-Faix for helpful advice concerning sample and layer preparations, Attila L. Kovács for the TEM measurements and Péter Lucz for help with the optical work. This work was supported by the Hungarian National Scientific Foundation for Research (OTKA T023080) and by grant FKFP 0532/2000.

References

1. Schaaf P, Déjardin P, Schmitt A (1987) *Langmuir* 3:1131
2. Mann EK, van der Zeeuw EA, Koper GJM, Schaaf P, Bedeaux D (1995) *J Phys Chem* 99:790
3. van der Zeeuw EA, Sagis LM, Koper GJM, Mann EK, Haarmans MT, Bedeaux D (1996) *J Chem Phys* 105:1646
4. Mann EK, Heinrich L, Voegel JC, Schaaf P (1996) *J Chem Phys* 105:6082
5. van Blaadren A, Vrij A (1992) *Langmuir* 8:2921
6. Boyd RV, Gehr RJ, Fischer GL, Sipe JE (1996) *Pure Appl Opt* 5:505
7. Jacobsson R (1965) In: Wolf E (ed) *Progress in optics*, vol 5. North Holland, Amsterdam, pp 247–286
8. Hild E, Evans MW (1986) *J Appl Phys* 59:1822
9. Stöber A, Fink E, Böhm J (1968) *Colloid Interface Sci* 26:63
10. Tolnai G, Csémpesz F, Kabai-Faix M, Kálmán E, Keresztes Z, Kovács AL, Ramsden JJ, Hórvölgyi Z (2001) *Langmuir* 17:2683
11. Seszták T (2001) *Fabrication and investigation of nanostructural layers* (in Hungarian). Thesis. Budapest University of Technology and Economics

Jean-François Hochepped
Ana Paula Almeida de Oliveira

Controlled precipitation of zinc oxide particles

Abstract The scope of this work consisted of precipitating directly zinc oxide particles from zinc nitrate and zinc sulphate solutions using sodium hydroxide at pH 10.5, 2 h and 25 or 60 °C. For the zinc nitrate system, the effect of additives at 25 °C, such as sodium sulphate and sodium dodecyl sulphate, was also investigated. Precipitated powders were characterized in terms of their crystalline structure (X-ray diffraction), morphology and size (scanning electron microscopy, transmission electron microscopy). Precipitation in distilled water with zinc nitrate produced homogeneous star-type particles (1 μ m) composed of assembled 30-nm crystallites at 25 °C and ellipsoidal and spherical particles (100 nm to 1 μ m) at 60 °C. On the other hand, for the zinc sulphate system at 25 °C, several different morphologies were obtained as ellipsoids (250 \times 800 nm),

half ellipsoids (250 \times 350 nm), fibres (40 \times 700 nm) and unshaped particles (700 nm), whilst half ellipsoids (100 nm) were precipitated as well as smaller particles (25–60 nm) at 60 °C. The investigation of the additive effect showed that precipitation from zinc nitrate solution in the presence of sodium sulphate led to half ellipsoids with a size range from 100 to 300 nm. In contrast, the addition of sodium dodecyl sulphate resulted in a mixture of morphologies that included half ellipsoids (150–200 nm), asymmetrical and symmetrical ellipsoids, as well as small particles of 30 nm. This study evidenced the effect of additives on morphology and size control of submicrometric particles constituted of assembled nanocrystallites.

Keywords Zinc oxide · Chemical synthesis · Particle morphology · Self-assembly · Additives

J.-F. Hochepped
A.P. Almeida de Oliveira (✉)
Ecole des Mines de Paris,
CENERG/SCPI, 60 Bd. Saint Michel,
75272 Paris Cedex 06, France
e-mail: oliveira@paris.ensmp.fr
Tel.: +33-1-40519425
Fax: +33-1-43265910

Introduction

Among ceramic materials, ZnO plays an important role owing to its diverse applications, such as catalysis [1, 2], electronic devices (gas sensors, varistors, semiconductors) [3, 4, 5], luminescent devices [6, 7], solar cells [8] pigments [9] and components for the pharmaceutical [10, 11] and cosmetic industries.

In the literature, several processes are available for the synthesis of colloidal metallic oxides, including ZnO [12, 13, 14, 15, 16, 17, 18, 19]. Among them, controlled precipitation may be considered as one of the principal

methods owing to its capacity of producing large quantities of ceramic oxides in a reproducible approach. On the other hand, several studies [9, 12, 16, 17] have shown that intermediate compounds are obtained by precipitation. Consequently, a thermal decomposition step is necessary to achieve pure ZnO. This additional action can be considered as the major constraint of the precipitation process for ZnO synthesis.

The properties required for a specific application are intimately related to some powder characteristics, such as purity, chemical composition, particle size and morphology. Precipitated powder characteristics are

controlled by several physicochemical parameters, such as pH, temperature and precipitation time. It is also well known that the nature of the metal salt and the presence of an additive may modify the particle shape and size. Söhnle and Garside [20] suggested that the role of admixtures is quite different according to their nature. Generally, inorganic materials are incorporated into the crystal lattice during precipitation and this may cause disturbance of the lattice. On the other hand, organic additives may selectively adsorb on different crystal faces, changing their growth rate. At present, better understanding of the influence of anions/additives–oxide surface interactions on nucleation and crystal growth is the subject of intensive research because it could allow synthesis of powders with a particular shape and size.

The present work focuses on direct synthesis of ZnO from zinc nitrate and zinc sulphate solutions by controlled precipitation with sodium hydroxide at pH 10.5, 2 h and 25 or 60 °C. For the zinc nitrate system, at 25 °C, the effect of additives (sodium sulphate, SS, and sodium dodecyl sulphate, SDS) on the precipitated powder phase, the morphology and the particle size is also discussed.

Experimental

Precipitation procedures

Zinc nitrate $[\text{Zn}(\text{NO}_3)_2 \cdot 6\text{H}_2\text{O}]$ and zinc sulphate $[\text{ZnSO}_4 \cdot 7\text{H}_2\text{O}]$, both with 99% purity, were adopted as the source materials for the zinc species. NaOH with 97% purity was employed as a base for all experiments. SS ($\text{Na}_2\text{SO}_4 \cdot 10\text{H}_2\text{O}$) and SDS $[\text{H}_3(\text{CH}_2)_{11}\text{OSO}_3\text{Na}]$ with 99 and 98% purity, respectively, were chosen as the additives to be evaluated. All reagents were purchased from Prolabo.

The precipitation procedure consisted previously of preparing two solutions: solution A – 0.1 mol $\text{Zn}(\text{NO}_3)_2$ or ZnSO_4 dissolved in 0.2 dm³ distilled water – and solution B – 0.2 mol NaOH in 0.2 dm³ distilled water.

Solutions A and B were injected by a double jet at a rate of 1.68 dm³·h⁻¹ into a closed standard double-walled, water-jacketed,

thermostated (25 or 60 °C) hemispheric reactor ($V = 1.5 \text{ dm}^3$) filled with 0.6 dm³ distilled water or a solution containing 0.2 mol SS or 0.2 mol SDS. The insides of the reactor were composed of four Teflon baffles to reduce the vortex into the vessel, a four 45°-tilted blade propeller stirring at 500 rpm, a pH combination electrode, and a glass probe for temperature measurements. The pH of the reaction system was adjusted to 10.5 with a 1 mol·dm⁻³ NaOH solution and the temperature was recorded using a Radiometer PHM290 pH controller coupled with a computer.

After the reagents had been added, the mixture was stirred for 2 h at regulated pH and temperature. The precipitate was washed with distilled water, frozen and, subsequently, vacuum-dried.

Characterisation techniques

X-ray powder diffraction (XRD) patterns were recorded using a Bruker D8 diffractometer in θ – θ configuration, with $\text{Co K}\alpha$ radiation ($\lambda = 1.789 \text{ \AA}$) and equipped with a position-sensitive detector. XRD was used to identify the compounds present in the precipitated powders and to estimate their crystallite size, L , using the Scherrer formula:

$$L(hkl) = \frac{0.9\lambda}{\Delta(hkl) \cos \theta}, \quad (1)$$

where λ is the X-ray wavelength, θ is the Bragg's angle and Δ is the full width of the diffraction line (hkl) at half the maximum intensity.

A scanning electron microscope (SEM, Zeiss Leo 982) and a transmission electron microscope (TEM, Philips EM430, operating at 300 kV) were used to investigate the particle morphology and size.

Results and discussion

The experimental conditions and a summary of some characterization results for all the precipitation tests are presented in Table 1.

Crystalline structure

XRD analysis (Fig. 1) showed that pure ZnO was obtained directly from aqueous precipitation with

Table 1 Experimental conditions and characterization results

Test	Zinc salt	T (°C)	Additive	Precipitated product	Morphology and particle size
1	$\text{Zn}(\text{NO}_3)_2$	25	–	ZnO	Starlike: 1 μm
2	$\text{Zn}(\text{NO}_3)_2$	60	–	ZnO	Ellipsoidal + spherical: 100 nm–1 μm
3	ZnSO_4	25	–	ZnO	Ellipsoidal: 250 nm \times 800 nm; half-ellipsoidal: 250 nm \times 350 nm; fibres: 40-nm diameter
4	ZnSO_4	60	–	ZnO	Half-ellipsoidal: 70 nm \times 100 nm; small particles: 25–60 nm
5	$\text{Zn}(\text{NO}_3)_2$	25	SS	ZnO	Half-ellipsoidal: 100 nm \times 200 nm, 200 nm \times 450 nm
6	$\text{Zn}(\text{NO}_3)_2$	25	SDS	ZnO	Half-ellipsoidal: 80 nm \times 200 nm; ellipsoidal: 120 nm \times 350 nm; asymmetrically ellipsoidal

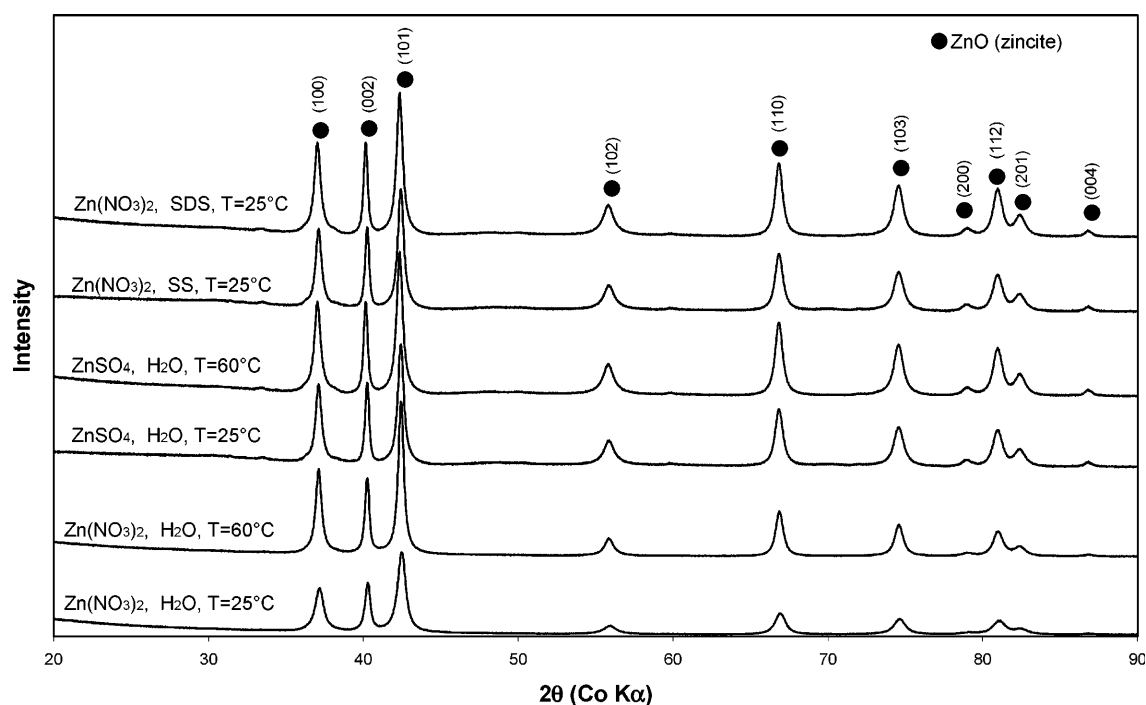


Fig. 1 X-ray diffraction patterns of ZnO powder prepared by double-jet precipitation with NaOH (pH 10.5, 2 h) for different experimental conditions

NaOH; therefore, no further thermal decomposition process was required. The diffraction peaks were in accordance with the JCP index [21] related to zincite, ZnO (P63mc, cell parameters $a=b=3.24982$ Å and $c=5.20661$ Å).

The crystallite size was estimated for the (100), (002) and (101) diffraction lines. For the zinc nitrate system in distilled water at 25 °C, the crystallite sizes calculated for the (100) and (101) directions were almost the same (16–17 nm); however, for the (002) direction the value was 27 nm, which indicated a preferential growth along the c -axis, leading to slightly elongated crystallites. Similar behaviour was noted at 60 °C, where the crystallite sizes in the (100) and (101) directions were between 22 and 25 nm, while along the (002) direction the size was 31 nm. These results revealed that ZnO precipitated powders had an orientation-dependent crystallite size in these experimental conditions. An increase of crystallite size with increasing temperature was also stated.

For the zinc sulphate system in distilled water, similar results were obtained for ZnO powders precipitated at 25 and 60 °C with 21–23-nm crystallite size for the (100) and (101) directions and 32–33 nm for the (002) direction. As for the previously studied system, ZnO crystallites exhibited preferential growth along the c -axis. On the other hand, the precipitation temperature had no effect on the crystallite size.

In the presence of additives (SS or SDS) for the zinc nitrate system, the difference between the crystallite sizes calculated for the (100) and (101) directions and (002) direction was also evident. They varied from 14–18 nm for the first two directions to 26 nm for the latter at 25 °C. No significant influence of the additives on the crystallite size was verified.

Morphology and particle size

Zinc nitrate system in distilled water

At 25 °C, starlike particles around 1 µm in size were formed (Fig. 2a). This morphology was also observed by Komarneni et al. [13] for 0.1 mol dm⁻³ Zn(NO₃)₂, pH 12 adjusted with NaOH. The authors attributed this morphology to the use of microwaves (50 °C, 15 min). Considering our results, one can suppose that other parameters are responsible for the formation of a starlike morphology.

It was noted that starlike particles were formed from oriented ZnO crystallites, creating star branches. These crystallites, as confirmed by crystallite size measurements, were elongated along the c -axis. The assembly of the crystallites might result from the polar behaviour of ZnO crystals in relation to this axis. The polarity of ZnO crystals has already been studied by Li et al. [22], Wander and Harrison [23] and Wander et al. [24]. The importance of dipolar effects in the alignments of particles and eventual further growth has been evidenced for other materials [25]. Besides, according to Collier et al. [26],

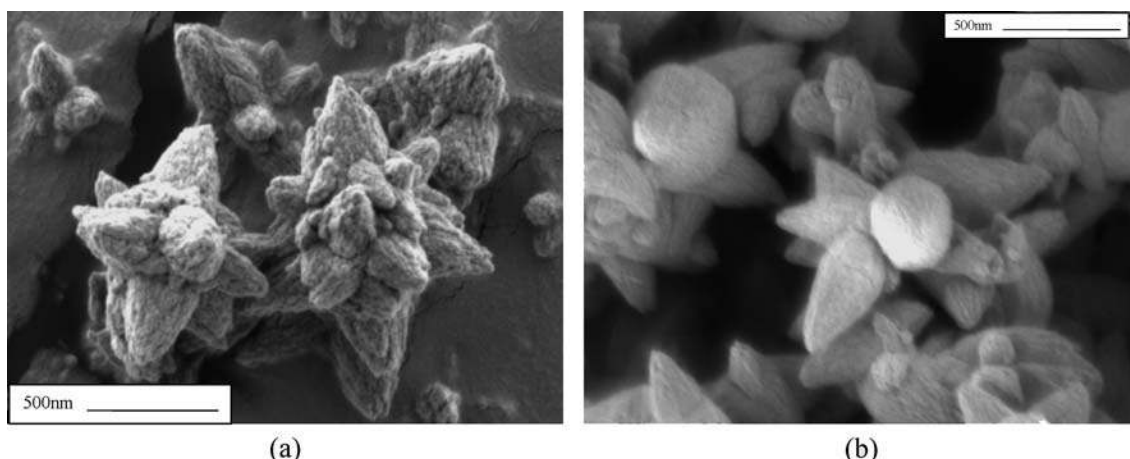
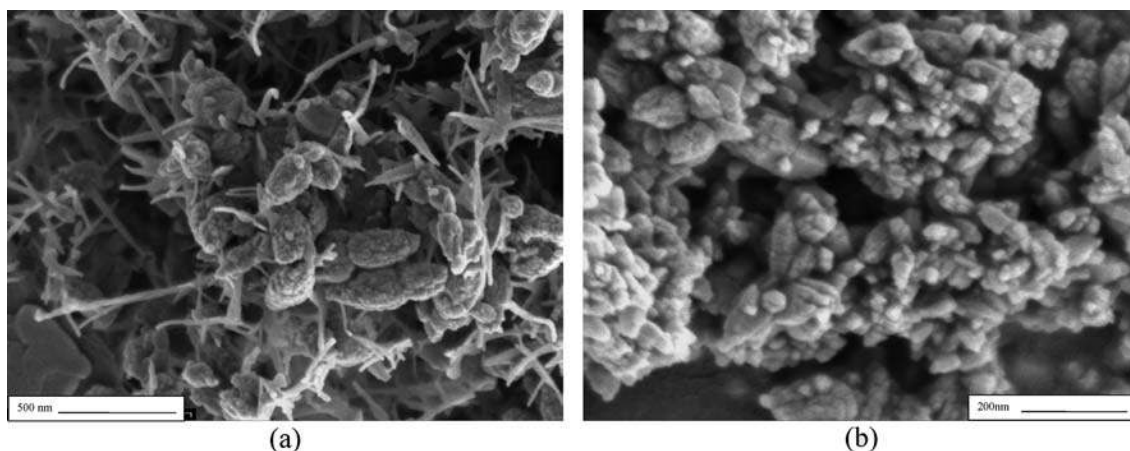


Fig. 2 Scanning electron microscope (SEM) micrographs of ZnO particles precipitated from $\text{Zn}(\text{NO}_3)_2$ and NaOH solutions in distilled water at pH 10.5, 2 h and **a** 25 °C, **b** 60 °C

despite the randomness of the collision of particles in solution, the realignment of crystals may occur owing to the high interfacial energy involving misaligned crystals. It is noteworthy that isotropic structures constituted of self-assembled ZnO nanocrystallites were observed by Rodriguez-Paez et al. [12], nevertheless these agglomerates were obtained by a rather indirect process with washing and thermal treatment as important stages to obtain the final product.

The precipitation test performed at 60 °C (Fig. 2b) led to ellipsoids and occasionally to spherical particles; however, no more stars were observed. The sample was clearly less homogeneous than at lower temperature, with the particle size varying from 100 nm to 1 μm . The presence of isolated small particles indicated that a temperature rise led to a reduction in the particle size and a limitation of particle organisation into a more complex starlike morphology.

Fig. 3 SEM micrographs of ZnO particles precipitated from ZnSO_4 and NaOH solutions in distilled water at pH 10.5, 2 h, and **a** 25 °C, **b** 60 °C



Zinc sulphate system in distilled water

At 25 °C, the powder precipitated from zinc sulphate solution was very heterogeneous, presenting some traditional morphologies, like half ellipsoids (250 nm \times 350 nm) and ellipsoids (250 nm \times 800 nm), both constituted by crystallites grouped in a preferential orientation, as well as 40-nm-diameter fibres of various lengths (Fig. 3a). The fibre structures for ZnO particles are usually synthesised by a thermal evaporation process [27, 28].

A drastic modification of the particle morphology was observed at 60 °C (Fig. 3b). Small particles from 20 to 60 nm were the major constituents of the precipitated powder. More rarely, some half ellipsoids of 100 nm could be found. The temperature effect for the zinc sulphate system was more intense than that observed for the zinc nitrate system; there was a sharp reduction in particle size owing to the temperature increase.

Zinc nitrate system in the presence of additives

The purpose of investigating zinc oxide precipitation from zinc nitrate solution in sulphate medium at 25 °C

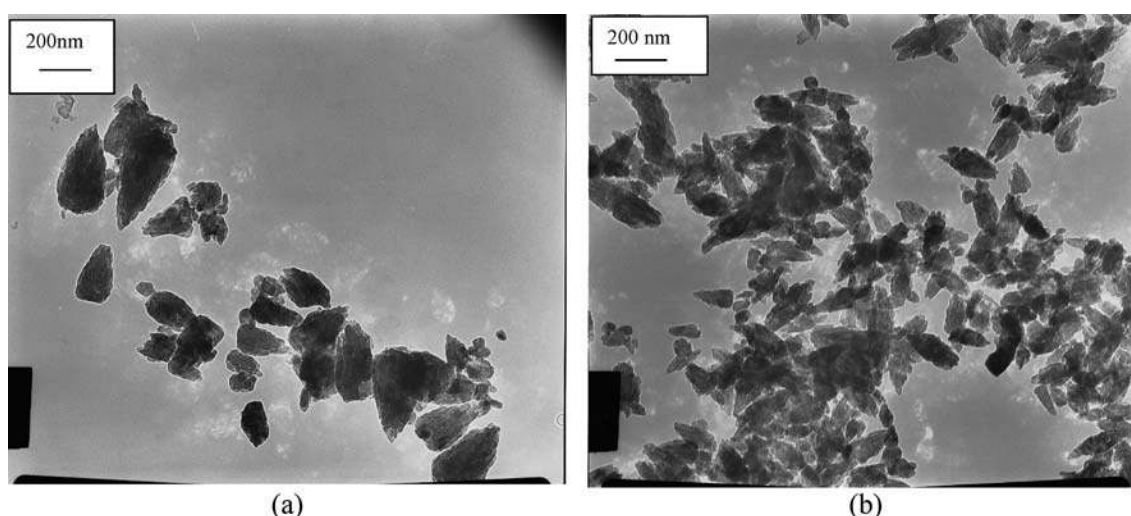


Fig. 4 Transmission electron microscope micrographs of ZnO particles precipitated from $\text{Zn}(\text{NO}_3)_2$ and NaOH solutions in the presence of **a** sodium sulphate and **b** sodium dodecyl sulphate at 25 °C, pH 10.5, 2 h

was to evaluate its capacity for hindering the assembly of nanocrystals into particles. Hence some clues on their formation mechanisms are expected to be gained from a comparison among the different system configurations studied in this work.

In the presence of SS, a pure ZnO phase was precipitated with a half-ellipsoid morphology (200×450 nm) at 25 °C (Fig. 4a). The presence of SS led to a substantial modification of the particle shape and size, considering the results obtained for precipitation from zinc nitrate solution in distilled water (Fig. 2a). In fact, SS limited particle growth as evidenced by the precipitation of particles with a less complex morphology and a considerably reduced size. Hence the system is roughly like zinc sulphate precipitation with more hindering of self-assembly, probably owing to the ionic strength effect.

SDS forms direct micelles in the bath. The surface of the micelles, formed by polar groups, constitutes a charged interface that may have an influence on precursor nucleation (favoured sites), on phase transformation (modification of zinc hydroxide surface reactivity by surfactants) and on ZnO nanocrystallites assemblies (adsorption of surfactant molecules on the crystallites faces).

Figure 4b shows that, in the presence of SDS, particles were precipitated with several morphologies, such as half ellipsoids ($80 \text{ nm} \times 200 \text{ nm}$), asymmetrical ellipsoids composed of differently sized half ellipsoids and, finally, symmetrical ellipsoids ($115 \text{ nm} \times 350 \text{ nm}$) whose previously smaller half was totally grown. Many 30-nm-diameter particles were observed near these almost complete ellipsoids. Hence, the building of

ellipsoids could result from self-assembly of these nanoparticles into half ellipsoids, followed by germination and growth of a second half at the base.

A comparison between the two additives employed in this work revealed few but instructive differences. SDS was efficient in reducing the particle size and producing asymmetrical ellipsoids, whereas SS was rather efficient in producing a unique half-ellipsoidal shape.

Conclusions

Direct precipitation of ZnO was possible for all the system configurations investigated in this work at pH 10.5 and 2 h. In other words, no thermal treatment was adopted.

The particles are always constituted by the assembly of ZnO nanocrystallites, which were around 50% longer along the *c*-axis than perpendicularly. The elongation and the well-known polarity effects along the *c*-axis might explain the formation of self-assembled elongated structures by dipolar interactions, leading to stars with six (or more) branches.

The nature of the salt produced significant variations in the morphology and size of the ZnO particles. In distilled water, at 25 °C, homogeneous well-shaped starlike particles of $1 \mu\text{m}$ were produced with zinc nitrate, while a heterogeneous product composed of relatively smaller ellipsoidal, half ellipsoids and fibres was obtained with zinc sulphate.

The presence of additives allowed the synthesis of smaller particles and a considerable change in shape with many poorly shaped particles from half to full ellipsoids. Probably, additives adsorbed on crystallites limited the assembly into bigger particles. These particles could be seen as the embryos of micrometre starlike particles. The use of growth-inhibiting agents allowed a description of the star birth and growth through the stages

formation of a half ellipsoid with a few nanocrystals, germination of the second half, growth of an ellipsoid, and germination and growth of star branches from the separation between the two halves.

Acknowledgements. The authors thank the precious collaborations of François Grillon during SEM sessions and Marie-Hélène Berger during TEM investigations. A.P.A gratefully acknowledges CAPES for financial support.

References

- Gouvêa CAK, Wypych F, Moraes SG, Durán N, Nagata N, Peralta-Zamora P (2000) *Chemosphere* 40:433
- Elseviers W, Verelst H (1999) *Fuel* 78:601
- Degen A, Kosec M (2000) *J Eur Ceram Soc* 20:667
- Look DC, Reynolds DC, Sizelove JR, Jones RL, Litton CW, Cantwell G, Harsch WC (1998) *Solid State Commun* 105:399
- Wrzesinski J, Fröhlich D (1998) *Solid State Commun* 105:301
- Fujihara S, Naito H, Kimura T (2001) *Thin Solid Films* 389:227
- Lorenz C, Emmerling A, Fricke J, Schmidt T, Hilgendorff M, Spanhel L, Müller G (1998) *J Non-Cryst Solids* 238:1
- Keis K, Bauer C, Boschloo G, Hagfeldt A, Westermarck K, Rensmo H, Siegbahn H (2002) *J Photochem Photobiol A* 148:57
- Sigoli FA, Davolos MR, Jafelicci M Jr (1997) *J Alloys Compd* 262–263:292
- Yamamoto O (2001) *Int J Inorg Mater* 3:643
- Akiyama H, Yamasaki O, Kanzaki H, Tada J, Arata J (1998) *J Dermatol Sci* 17:67
- Rodriguez-Paez JE, Caballero AC, Villegas M, Moure C, Durán P, Fernández JF (2001) *J Eur Ceram Soc* 21:925
- Komarnemi S, Bruno M, Mariani E (2000) *Mater Res Bull* 35:1843
- Lu C-H, Yeh C-H (2000) *Ceram Int* 26:351
- Chen D, Jiao X, Cheng G (2000) *Solid State Commun* 113:363–366
- Reverchon E, Della Porta G, Sannino D, Ciambelli P (1999) *Powder Technol* 102:127
- Lu C-H, Yen C-H (1997) *Mater Lett* 33:129
- Lim BP, Wang J, Ng SC, Chew CH, Gan LM (1998) *Ceram Int* 24:205
- Zhao X, Zheng B, Li C, Gu H (1998) *Powder Technol* 100:20
- Söhnle O, Garside J (1992) *Precipitation: basic principals and industrial applications*. Butterworth-Heinemann, Oxford
- Joint committee on powder diffraction standards. Powder diffraction file, card no 36–1451, Swarthmore, PA
- Li W-J, Shi E-W, Zhong W-Z, Yin Z-W (1999) *J Cryst Growth* 203:186
- Wander A, Harrison NM (2000) *Surf Sci Lett* 457:L342
- Wander A, Schedin F, Steadman P, Norris A, McGrawth R, Turner TS, Thornton G, Harrison NM (2001) *Phys Rev Lett* 86:3811
- Tang Z, Kotov N, Giersig M (2002) *Science* 297:237
- Collier AP, Hetherington CJD, Hounslow MJ (2000) *J Cryst Growth* 208:513
- Yao BD, Chan YF, Wang N (2002) *Appl Phys Lett* 81:757
- Hu JQ, Ma XL, Xie ZY, Wong NB, Lee CS, Lee ST (2001) *Chem Phys Lett* 344:97

Pál Joó

Porosity and permeability of clay films: an electrochemical survey

P. Joó
University of Debrecen,
Department of Colloid and Environmental
Chemistry, P.O. Box 31,
4010 Debrecen, Hungary
e-mail: joopal@tigris.klte.hu
Fax: +36-5251-2938

Abstract Clay-modified electrodes can provide an efficient method for studying the porosity of negatively charged, layered structures, i.e., swollen clay films. Diffusion transport processes of electroactive solute probes within hydrophilic and hydrophobized montmorillonite clay films have been studied. Cyclic voltammetry was performed in a three-electrode cell. Results regarding film permeability, the structure of the porous aerogel–hydrogel, the effect of layer thickness as well as the role

of the porosity on the diffusion have been presented. The kinetics of the hydration–dehydration, swelling–shrinking, i.e., the break-in/leach-out processes, and the effect of hydrophobization have been demonstrated. The rate constants of porosity-dependent macrodiffusion and microdiffusion have also been calculated.

Keywords Porosity · Permeability · Clay-modified electrodes · Diffusion · Kinetics

Introduction

There is little doubt that fertility- and productivity-affecting features of soils, such as liquid and electrolyte household management, i.e. the capacity to take up, hold, and pass liquids, ventilation, sorptional capacity, and the transport of dissolved substances, are highly dependent upon the structure and permeability of soil component colloid aggregates [1, 2]. Accordingly, the structure and permeability of mineral component clays are important factors [3].

The structure of “polyanion” particles of a particular montmorillonite may be different depending on the nature of the inherent cation – Na^+ , Ca^{2+} , or H^+ . The cations, apart from causing electroneutrality, provide different extents of adhesion for the layers within the particles, which results in differences in intramolecular swelling. Na montmorillonite has a greater swelling ability compared to either Ca montmorillonite or the naturally occurring H montmorillonite (the latter after acidic rainfall). These are also the factors that determine the water-holding and permeating characteristics of the soil.

In our recent publications [4, 5] we discussed results concerning ion and molecule mobility in cationic montmorillonite film modified electrodes hydrophobized with aliphatic and aromatic quaternary ammonium compounds. We also described experiences with independent measurements by electrochemical and radiochemical methods on transport processes in humate containing montmorillonite and bentonite thin layers [6]. We interpreted the results as consequences of changes in structure which lead to changes in porosity and diffusional transport [7, 8, 9]. The present paper approaches the role of film thickness, and the kinetics of the swelling of films (porodine xerogels) at different levels of hydrophobization, and also the kinetics of the penetration and release of probe molecules.

Experimental

Montmorillonite-modified electrodes were prepared by applying 10–40 μl of Na/Ca/H montmorillonite sol (Department of Colloid Chemistry, Jozsef Attila University of Arts and Sciences, Szeged, Hungary) in 10/20 μl portions onto the surface of Beckman platinum disk electrodes ($A=0.2\text{ cm}^2$), followed by

12-h drying/gelling at room temperature. (Cation-exchange capacity 0.80 ± 0.05 mEq g⁻¹; montmorillonite content 2 g 100 cm⁻³.) The dry montmorillonite content of the films was 2–8 mg cm⁻²; thickness 2–8 μm. Different extents of hydrophobization were reached by soaking hydrophilic Na montmorillonite modified electrodes in aqueous surfactant solutions of different concentration for different amounts of time. (The method is similar to that used in redox indicator dye modification [10, 11, 12].)

Hydrophobization was accomplished with the following:

1. Aliphatic quaternary ammonium compounds: hexadecylcetyltrimethylammonium bromide (CTAB); dodecyltrimethylammonium bromide (DTAB).
2. *N*-Alkylpyridinium compounds: hexadecylcetylpyridinium bromide (CPB); hexadecylcetylpyridinium chloride (CPC).
3. A Gemini-type compound (two carbon hydrogen chains connected to a neutral molecule segment or spacer, via ionic groups): (*p*-Phenyldimethyl)bis(octadecyldimethylammonium) dibromide, as in Scheme 1.

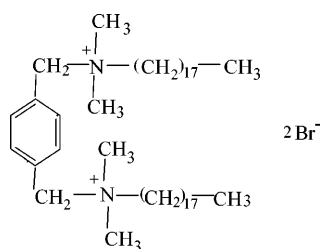
Cyclic voltammetry was done with a computer-assisted Elektroflex EF 427B potentiostat (Hungary). The measuring cell was unispaceous, comprising three electrodes, the atmosphere contained pure nitrogen, and the temperature was 25°C.

Results and discussion

The role of layer structure and thickness

The montmorillonite clay mineral is a 2:1 type aluminum hydrosilicate, made from tetraeder–octaeder–tetraeder layers [13]. Xerogel films of dried sols display various extents of permeability for probe molecules or ions that are to be oxidized–reduced on the surface of the Pt carrier electrode (insulating >> conducting films), following particle swelling (xerogel >> liogel films). Particle movement within the porous structure montmorillonite layer can take place in the “maze” of interaggregate macropores and mesopores (or interim) pores (i.e. in the gaps between particles), and inside the aggregates/particles: in the interlamellar spaces – utilizing intraparticle capillaries, or charged micropores.

Transport can be characterized by the cyclic voltammetric peak current, I_p , and the relative current, R , [14] – the ratio of I_p and $I_{p,b}$, the peak current value of the unmodified (bare) Pt electrode. The value of R is given by the Randles–Sevcik formula:



Scheme 1

$$R = \frac{I_p}{I_{p,b}} = \frac{A' D_{\text{clay}}^{1/2} C_{\text{clay}}}{A D_{\text{sol}}^{1/2} C_{\text{sol}}}, \quad (1)$$

where A is the area of the bare Pt electrode (centimeters squared), A' is the area of the modified electrode (i.e. the “free” area of the montmorillonite-film covered Pt electrode, also meaning the surface cross-sectional area of the capillary-system electrode), D_{clay} and D_{sol} are diffusion coefficients of the probe particle in the clay film and in the solution (centimeters squared per second), and c_{clay} and c_{sol} are concentrations in the film and in the solution. Understanding that $c_{\text{clay}} = \kappa c_{\text{sol}}$ [14], where κ is the partition coefficient of the probe particle between the solid and soluble phases, and $D_{\text{clay}} = \tau D_{\text{sol}}$ (τ is the tortuosity of the film) [15, 16, 17], leads to the simplification of Eq. (1). τ , on the other hand, is characteristic of the effective distance of the intralayer movement, l_{eff} , and is also dependent on the thickness of the coherent film, l : $\tau = l_{\text{eff}}/l$ [17]. $\tau = 1$ in dubious cases and when films are of ordered structure or when the pore system is oriented at a right angle to the electrode.

If $A'/A = \Theta$, where Θ is the surface porosity (centimeters squared centimeters squared) of the film, Eq. (1) is given [14] as

$$R = \kappa \Theta \tau^{1/2}. \quad (2)$$

Cyclic voltammetric features of montmorillonite-modified electrodes with clay minerals of different pore structure depend on l and the polarization rate, v , at a given probe particle. Cyclic voltammograms of a film made from 40 μl H montmorillonite ($l = 4$ μm), taken at different values of v , with 1,4-benzoquinone probe molecules, are shown in Fig. 1.

The gross redox reaction is $Q + 2H^+ + 2e^- \rightleftharpoons QH_2$.

The values of I_p and $I_{p,b}$ in 1–4-μm-thick Na montmorillonite layers as a function of the square root of the v are displayed in Fig. 2. The redox reaction is $Fe(CN)_6^{3-} + e^- \rightleftharpoons Fe(CN)_6^{4-}$.

The value of $I_{p,b}(A)$ at 25 °C is given by the Randles–Sevcik equation [18] as follows:

$$I_{p,b} = (2.69 \times 10^5) n^{3/2} A (D_i)_{\text{sol}}^{1/2} (c_i^*)_{\text{sol}} v^{1/2}, \quad (3)$$

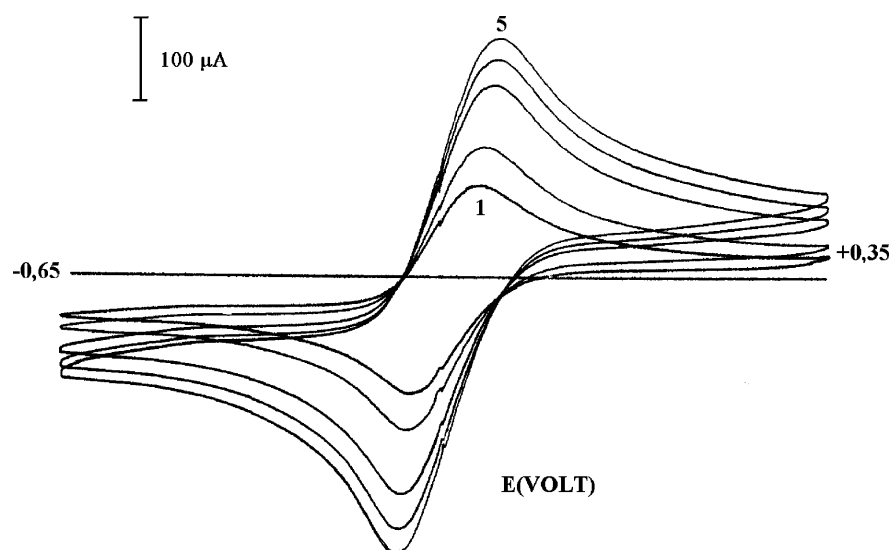
where n is the stoichiometric number of electrons that react in the gross redox reaction of the probe particles and v is the rate of polarization (volts per second).

For clay-modified electrodes

$$I_p = (2.69 \times 10^5) n^{3/2} A' (D_i)_{\text{clay}}^{1/2} (c_i^*)_{\text{clay}} v^{1/2}. \quad (4)$$

The slope of the lines in Fig. 2, given by Eqs. (3) and (4), can be interpreted by Eq. (2), and reflects the effect of structure (porosity). The figure also reveals that while the slope stays constant at varying thickness values, and $\kappa \Theta \tau^{1/2}$ is also constant, because $(D_i)_{\text{clay}}$ and A' are constant, the value of the peak current decreases at increasing thickness, when the rate of polarization is the

Fig. 1 Cyclic voltammograms of a H montmorillonite film in 0.1 mol dm^{-3} NaCl solutions of $5 \times 10^{-3} \text{ mol dm}^{-3}$ 1,4-benzoquinone, at different polarization rates (1:10, 2:20, 3:50, 4:80, 5:100 mV s^{-1})



same. This can also be observed in Fig. 3 for Ca montmorillonite.

The increase in thickness is thought not to cause a change either in the value of κ (with a value of 1 for nonbinding probe particles) or in Θ . The effect can be connected to τ , the tortuosity of the film. The thicker the film the less organized the structure, with more cardlike, more tortuous construction, containing more cross-links. This leads to a change in l_{eff}/l and τ , and peak currents decrease.

The kinetics of swelling–shrinking, break-in–leach-out processes

The intramolecular, interlayer (“crystalline” and “osmotic”) swelling/hydration properties of clay minerals and the formation of the gel structure have a basic practical value. Accordingly, studies of these features have long been in focus with unchanged intensity [14, 19, 20, 21].

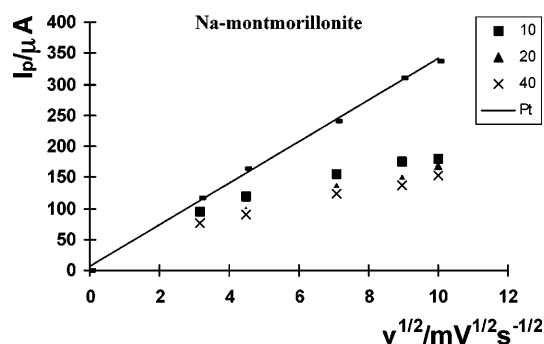


Fig. 2 $I_{p,c}$ peak currents in Na montmorillonite in 0.1 mol dm^{-3} NaCl solutions of $1 \times 10^{-2} \text{ mol dm}^{-3}$ Fe(CN)_6^{3-} , as the function of the square root of the polarization rate, at different thickness values (i.e. at different volumes of the applied clay sol: $V=0, 10, 20, 40 \mu\text{l}$)

These studies can successfully be done by utilizing methods of electrochemistry, more specifically, cyclic voltammetry [12]. Following a few potential cycles, voltammograms characteristic of the steady state and of the “total electrochemical activity” take shape. These are indicators of the saturation concentration of dissolved molecules within the film, representing the result of wetting, hydration, swelling, and liosorption – to be summarized as break-in.

Further cycles will cause no difference in the curve in the case of stable films with adequate adhesion and chemical properties. Leach-out, the inverse of the described process, can be studied by cycling the saturated film in a solution which contains no probe molecules. Probe molecules “squeeze” out water from the pore system during break-in, while the same effect is made by water during leach-out – it spaces out the electrolyte and the probe molecules. We find that the direction of transport is reversed if we compare the two processes: the soluble phase–gaps–capillaries (into the swelling/swollen film) during break-in; capillaries–gaps–the soluble phase

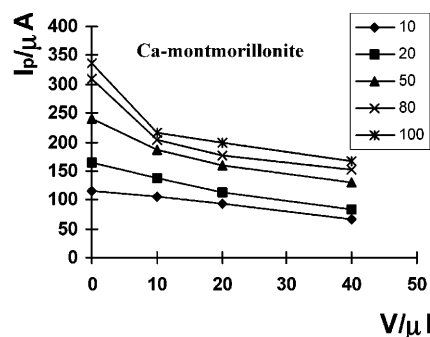
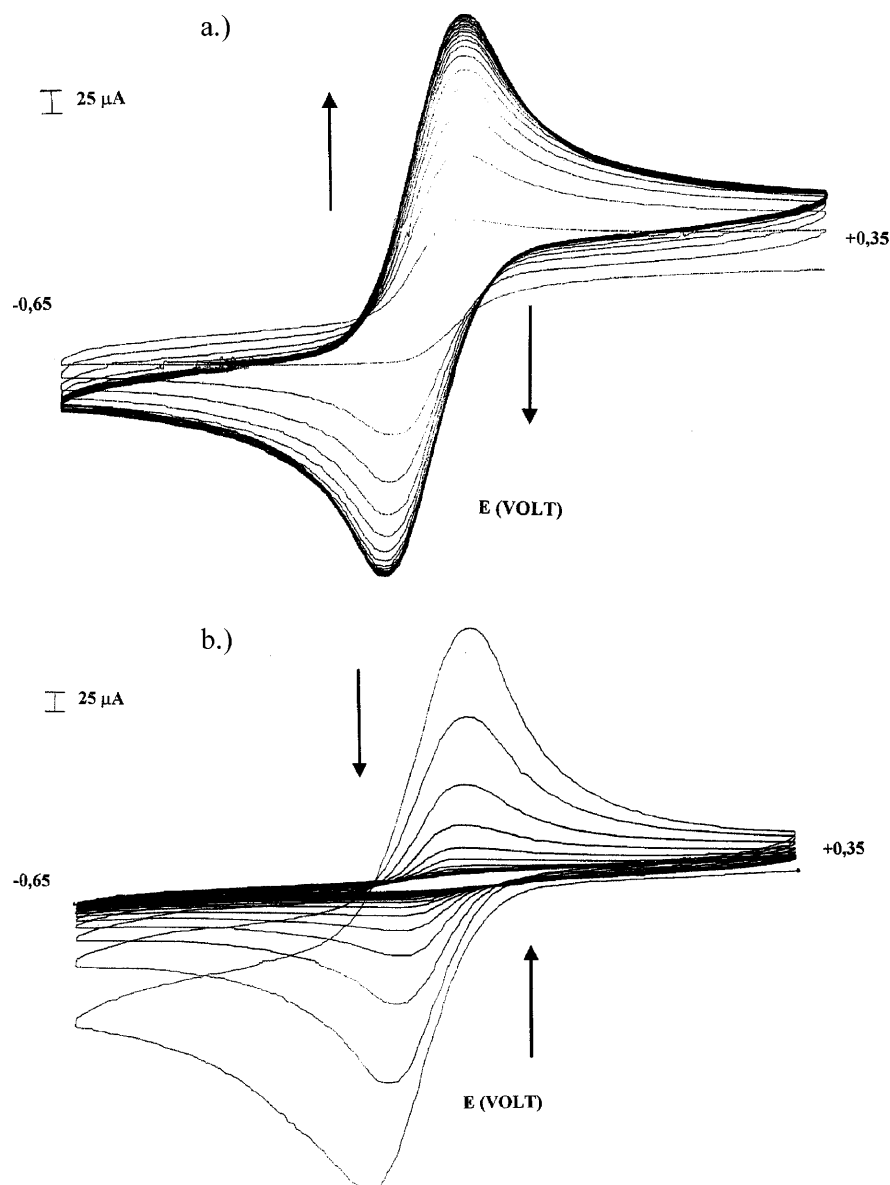


Fig. 3 $I_{p,c}$ measured for Ca montmorillonite films of various thickness (prepared from varying volumes of the sol), at various rates of polarization ($v=10, 20, 50, 80, 100 \text{ mV s}^{-1}$)

Fig. 4 **a**) Cyclic voltammograms of the break-in process. (Na - montmorillonite modified electrode after soaking in a $1 \times 10^{-3} \text{ mol dm}^{-3}$ hexadecylpyridinium bromide solution; in **a**) $5 \times 10^{-3} \text{ mol dm}^{-3}$ 1,4-benzoquinone/ 0.1 mol dm^{-3} NaCl solution system. $\nu = 50 \text{ mV s}^{-1}$). **b**) Cyclic voltammograms of the leach-out process (the same system as in **a**, $\nu = 70 \text{ mV s}^{-1}$)



(out of the film) in leach-out. Cyclic voltammograms of a Na montmorillonite modified electrode after soaking in $1 \times 10^{-3} \text{ mol dm}^{-3}$ CPB solution in a $5 \times 10^{-3} \text{ mol dm}^{-3}$ 1,4-benzoquinone/ 0.1 mol dm^{-3} NaCl solution system are shown in Figs. 4 and 5. The speed of break-in, in the hydration/swelling equilibrium, is expressed by the amount of adsorbed material over a constant period of time. This speed gradually decreases while the porous layer is getting saturated, and reaches zero at total saturation. The following equation is relevant:

$$\frac{dI_p}{dt} = K(I_{(p)s} - I_p) \quad (5)$$

where I_p is the peak current [18], proportional to the amount of substance reaching the Pt-electrode surface in a given time, $I_{(p)s}$ is the peak current proportional to the

amount of substance reaching the surface until the onset of the steady state; and k is the break-in rate constant, which is calculated from the integral of the equation as follows (if $t = 0$, then $I_p = 0$; and if $t = \infty$, then $I_p = I_{(p)s}$):

$$-kt = \ln\left(1 - \frac{I_p}{I_{(p)s}}\right) \quad (6)$$

As for leach-out (when the probe molecules diffuse out from the film) and in which case (if $t = 0$, then $I_p = I_{(p)s}$; and if $t = \infty$, then $I_p = 0$):

$$k't = \ln\left(1 - \frac{I_p}{I_{(p)s}}\right) \quad (7)$$

The rate constants can be computed from the slopes of speed curves (e.g. shown in Fig. 6, based on the data of

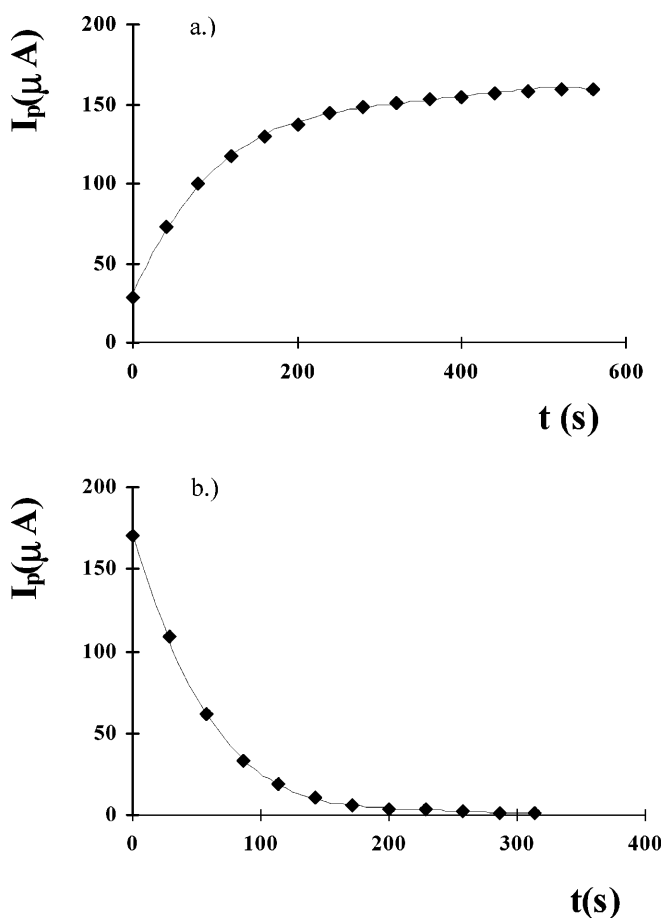


Fig. 5 **a** $I_{p,b}$ as a function of time, calculated from the cyclic voltammograms of break-in (the system is unchanged from Fig. 4a). **b** $I_{p,b}$ as a function of time, calculated from the cyclic voltammograms of leach-out (the system is unchanged from Fig. 4a)

Fig. 5). These investigations were done with hydrophilic Na montmorillonite films and that were hydrophobized to various extents with cationic surfactants, applying 1,4-benzoquinone probe molecules (film layer thickness 8 μm).

Hydration and swelling determine the speed of break-in or leach-out in films with no preliminary soaking (“air wet” films), while the speed determinant in swollen or shrunk films is the forming microstructure. The data in Fig. 6 and Table 1 indicate that break-in is described by one process, while leach-out is described by three subprocesses of different speed values. Gaps saturate rapidly, thus only one speed constant is sufficient to describe the process. Nevertheless, we lack data concerning the saturation of the capillary system (the intraparticle micropores). The pore system saturates slowly, micropores are the last to go, and then $I_p \approx I_{(p)s}$. In contrast, leach-out is the summary of three processes: the outflow from micropores, mesopores, and macropores, with speed values of increasing character in the order mentioned. The equation for break-in is

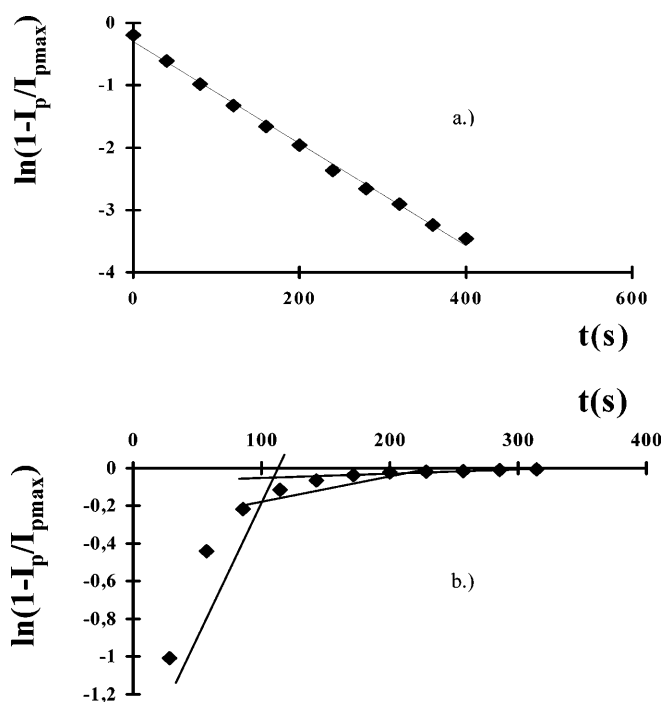


Fig. 6 **a** The kinetic curve of break-in, calculated from the data of Fig. 5a. **b** The kinetic curve of leach-out, calculated from the data of Fig. 5b

$$I_{(p)s} - I_p = I_{(p)s} \exp(-kt) \quad (8)$$

and that for leach-out (as a result of the superposition of subprocesses; in analogy with the kinetic equation for coupled reactions [22, 23]) is

$$I_{(p)s} - I_p = A_1 \exp(-k_1 t) + A_2 \exp(-k_2 t) + A_3 \exp(-k_3 t) \quad (9)$$

D_1 and D_2 are the diffusion coefficient of “macro” diffusion (via gaps) and D_3 is the diffusion coefficient for “micro” diffusion (via capillaries) [24, 25]. The exact physical interpretation of constants A_1 , A_2 , and A_3 has not been acknowledged so far.

Leach-out is a rapid process compared to break-in, owing to an already formed and constant pore structure.

Kinetic measurement data provide information about diffusional transport via macropores, mesopores, and micropores, and thus characterize pore structure. Increasing the period of presoaking resulted in increased swelling and permeability, which led to the increased speed of leach-out (i.e. macrodiffusion, characterized by k_1 and k_2), in similarity with break-in. The effects of hydrophobization with surfactants are also relevant: rate constants are higher than those for no soaking and no hydrophobization.

An additional observation is that the aliphatic or aromatic nature of the polar group and also the length of the anions and the apolar carbon chains played a secondary role in transport and are more likely to cause

Table 1 Rate constants of break-in and leach-out processes in hydrophobized Na montmorillonite ($v = 100 \text{ mV s}^{-1}$)

Soak in	Soak-in time (min)	Number of cycles	Break-in	Leach-out		
			$k \times 10^2 \text{ (s}^{-1}\text{)}$	$k_1 \times 10^2 \text{ (s}^{-1}\text{)}$	$k_2 \times 10^3 \text{ (s}^{-1}\text{)}$	$k_3 \times 10^4 \text{ (s}^{-1}\text{)}$
Hexadecylcetylpyridinium bromide (10^{-3} M)	10	1	0.9	2.3	0.8	3.3
		2	0.7	1.6	3.5	6.3
		3	2.2	1.3	2.3	6.4
		4	1.4	1.7	3.5	5.6
Gemini (10^{-5} M)	10	1	1.5	3.3	4.3	9.2
		2	1.4	3.4	5.7	10.8
		3	1.4	3.0	5.3	10
Gemini (10^{-5} M)	5	1	1.4	2.0	3.1	7.9
		2	1.6	1.9	3.4	8.0
		3	1.2	2.2	3.8	9.0
Gemini (10^{-6} M)	10	1	1.7	2.9	4.8	6.7
		2	1.4	1.8	3.3	4.7
		3	1.4	2.2	5.2	5.6

differences in the case of microdiffusion (transport via mesopores and micropores).

The data in Table 1 were taken uniformly at $v = 100 \text{ mV s}^{-1}$. This results in comparability between CPB and Gemini hydrophobization.

Reproducibility being a major concern, we repeated break-in and leach-out voltammograms after each primary measurement. Break-in was steadily represented by one speed constant and leach-out by three. The type of the surfactant – whether it was an aliphatic quaternary ammonium salt (CTAB, DTAB), an *N*-alkylpyridinium compound (CPC, CPB), or a Gemini tenside – left its mark on the parameters of hydrophobization, pore structure – and as a result – the permeability of the film.

Conclusions

Cyclic voltammetry offers a special possibility to study the permeability of thin clay films using clay-modified electrodes. The kinetics of the break-in/leach-out (hydration–dehydration, swelling–shrinking) processes depends on the structure of the porous aerogel–hydrogel and on the layer thickness of the film. The rate constants of structure-dependent macrodiffusion and microdiffusion can be calculated, and – to the best of our knowledge – this cyclic voltammetric determination of rate constants of the elementary processes is unique in the literature.

References

- Sposito G (1989) Chemistry of soils. Oxford University Press, New York
- De Boodt MF, Hayes MHB, Herbillon A (1990) Soil colloids and their associations in aggregates. Plenum, New York
- Filep G (1999) Soil chemistry: processes and constituents. Akad, Budapest
- Joó P, Fitch A (1996) Magy Kem Foly 102:25
- Joó P, Fitch A (1997) Magy Kem Foly 103:365
- Antal K, Joó P (1999) Magy Kem Foly 105:49
- Joo P, Fitch A (1996) Environ Sci Technol 30:2681
- Joo P, Fitch A, Park S-H (1997) Environ Sci Technol 31:2186
- Joo P, Antal K (1998) Colloids Surf A 141:365
- Joó P, S Nagy N (1993) Kem Kozl 76:119
- Joó P (1990) Colloids Surf 49:29
- Joo P (1998) Colloids Surf A 141:337
- van Olphen H (1977) An introduction to clay colloid chemistry, 2nd edn. Wiley, New York
- Fitch A, Du J, Gan H, Stucki JW (1995) Clays Clay Miner 43:607
- Lakatos I, Lakatosné-Szabó J (1995) Magy Kem Foly 101:517
- Dullien FAL (1992) Porous media: fluid transport and pore structure, 2nd edn. Academic, New York
- Lakatos I, Lakatosné-Szabó J (1996) Magy Kem Foly 102:276
- Bard AJ, Faulkner LR (1980) Electrochemical methods. Fundamental and applications. Wiley, New York
- Chang F-RC, Skipper NT, Sposito G (1995) Langmuir 11:2734
- Grandjean J (1997) J Colloid Interface Sci 185:554
- Mohan KK, Fogler HS (1997) Langmuir 13:2863
- Imre L (1937) Trans Faraday Soc 33: 571
- Kónya J, Kovács Z, Joó P, Mádi I (1972) Acta Phys Chim Debrecina 18:203
- Yiacoumi S, Tien C (1995) J Colloid Interface Sci 175:347
- Varro T (1991) Colloids Surf 54:61

Krisztina László
Katalin Marthi
Etelka Tombácz
Erik Geissler

Morphology and acid–base properties of porous carbon derived from poly(ethylene terephthalate) by nitric acid treatment

K. László (✉)
Department of Physical Chemistry,
Budapest University of Technology and
Economics, 1111 Budapest, Hungary
e-mail: klaszlo@mail.bme.hu

K. Marthi
Research Group for Technical Analytical
Chemistry, Hungarian Academy of
Sciences, Department of General and
Analytical Chemistry,
Budapest University of Technology and
Economics, 1111 Budapest, Hungary

E. Tombácz
Department of Colloid Chemistry,
Szeged University, 6721 Szeged, Hungary

E. Geissler
Laboratoire de Spectrométrie Physique
CNRS UMR 5588,
Université J. Fourier de Grenoble,
B.P. 87,
38402 Saint Martin d'Hères,
France

Abstract Activated carbon prepared from poly(ethylene terephthalate) was treated with nitric acid at ambient temperature and at the boiling point of the suspension. The morphology of the products was investigated by scanning electron microscopy, nitrogen adsorption observations and by small-angle X-ray scattering. The effect of acidic treatment on acid–base surface properties was studied by quasi-equilibrium potentiometric acid–base titration. It is found that the morphology of the products obtained after low-temperature treatment is similar, but high-temperature acid treatment induces a major reduction both in the surface area and in the fine pore structure. The intrinsic microporous

character of the original carbon, however, is conserved. Both for the morphology and for the surface chemistry, the temperature of the treatment is more important than its duration. Nevertheless, while the morphology is affected significantly only at high temperature, the acid–base properties are modified in all the acidic treatments.

Keywords Activated carbon · Chemical treatment · Adsorption · Scanning electron microscopy · Small-angle X-ray scattering · Quasi-equilibrium acid-base titration

Introduction

The surface activity of carbon is affected not only by the porosity but also by the chemistry of the surface. Introduction of heteroatoms either into the graphene sheet or into the edge of the turbostratic layers may strongly influence the adsorption properties or the catalytic activity. Heteroatoms such as hydrogen, oxygen, nitrogen, halogens, sulfur, and phosphorus form nonstoichiometric stable surface compounds. Oxygen complexes formed when activated carbon is treated with various oxidative chemicals are the most frequent and most important among these surface groups.

The oxidizing agent, its concentration, the temperature and the time of the treatment influence the chemistry of the surface obtained. The oxidative treatment may,

however, affect the morphology of the carbon structure as well. The aim of this paper is to reveal the effect of concentrated nitric acid treatment on both the morphology and the acid–base properties of an activated carbon prepared from poly(ethylene terephthalate) (PET).

Experimental

Sample preparation

Activated carbon (APET) was prepared from PET pellets [1, 2]. This activated carbon was treated with concentrated nitric acid at room temperature (RT) and at the boiling point (BP) of the carbon–acid suspension for 3 and/or 6 h. The acidic samples were then washed with distilled water and extracted in a Soxhlet apparatus until neutral pH was obtained. The samples were dried at ambient temperature.

Table 1 Sample preparation

Sample	Acidic treatment		Extraction with water	Yield (%)
	Temperature	Duration (h)		
APET2002	–	–	–	–
APET2002 V	–	–	+	100
APET2002 H3SEN	Room temperature	3	+	100
APET2002 M3SEN	Boiling point	3	+	94.5
APET2002 H6SEN	Room temperature	6	+	110

The preparation and the notation of the carbon samples are listed in Table 1.

Morphology of the carbons

Scanning electron microscopy

Surface morphology investigations were performed using a JEOL 5500 electron microscope in low-vacuum mode with a secondary electron detector. The accelerating voltage was 20 kV and the working distance 20 mm. The magnification is indicated on each image. The samples were fastened to the copper sample holder by double-sided adhesive carbon.

Low-temperature nitrogen adsorption

Nitrogen adsorption/desorption isotherms were measured at 77 K and evaluated using a Quantachrome Autosorb-1 computer-controlled apparatus. (Quantachrome, Boynton Beach, FL, USA) The apparent surface area was derived using the Brunauer–Emmett–Teller (BET) model, $S_{a,BET}$. The total pore volume, $V_{p,tot}$, was calculated from the amount of nitrogen vapor adsorbed, V_{ads} , at a relative pressure close to unity, on the assumption that the pores are then filled with liquid nitrogen. The average pore radius, r_p , was derived from the total pore volume and the BET surface area on the basis of uniform cylindrical pores. The micropore volumes, $V_{mp,t}$ and $V_{0,DR}$, were computed by the Dubinin–Radushkevich (DR) and t methods (Halsey), respectively. The characteristic energy, E_0 , was derived from the DR plot as well with $\beta = 0.34$. The slit size, L_0 , was derived from the relation $L_0(\text{nm}) = 10.8/(E_0 - 11.4)$, proposed by Stoeckli for pores with $L_0 < 1.8\text{--}2.0$ nm.

Pycnometry

The AUTOSORB-1 was used to determine the true density of the samples with helium gas.

Small-angle X-ray scattering

Small angle X-ray scattering (SAXS) measurements were made on the BM2 beam line at the European Synchrotron Radiation Facility, Grenoble, France. To cover the wide q range required ($0.01 < q < 10 \text{ nm}^{-1}$), two different incident X-ray energies, 7.9 and 16 keV, were selected, with sample–detector distances between 30 cm and 2.10 m. A two-dimensional charge-coupled device detector was used (Princeton Instruments), with exposure times between 1 and 50 s, depending on the sample and the q range explored. Corrections were made for the detector dark counts and for background scattering from the mica windows of the sample cell.

Characterization of acid–base properties

The “fully automatic” [3, 4] quasi-equilibrium acid–base titration was performed under a CO_2 -free atmosphere using NaCl back-

ground electrolyte. Carbon (0.15–0.25 g) was suspended in 50 ml 0.01 M NaCl solution. Solutions were prepared from fresh Millipore water. The washed and hot water extracted carbon samples were immersed in the aqueous electrolyte solution and ultrasonicated for 15 min, then stirred and bubbled with purified nitrogen for 1 h. The initial pH was measured before the titration. A laboratory-developed computer-controlled titration system (GI-MET1) consisting of 665 Dosimat (Metrohm) burettes, nitrogen bubbling, a magnetic stirrer, and a high-performance potentiometer was used. The equilibrium criterion for continuation of the titration was conditioned by the pH stability of the suspension and arbitrarily set as $\Delta\text{pH min}^{-1} < 0.012$. A Radelkis OP-0808P (Hungary) combination pH electrode was calibrated for three buffer solutions to check the Nernstian response. The concentration dependence of the hydrogen ion activity was determined from a background electrolyte solution titration, so that the electrode output could be converted directly to hydrogen ion concentration instead of activity.

The detailed description of the titration procedure for surface charge characterization of amphoteric solid particles is given elsewhere [5]. The reversibility of the titration was tested in a cycle of forward and backward titrations starting at the initial pH of the carbon suspension ($\text{pH} \sim 8.5$ for original APET and $\text{pH} \sim 4.5\text{--}2.7$ for the acid-treated APET samples), going down to pH 3 then up to pH 10, and finally returning to the lower pH limit. NaOH (0.1 M) and HCl (0.1 M) solutions were used in forward and backward titrations, respectively. Titration cycles were completed within 2–8 h, depending on the samples. The specific amount of net proton surface excess (Δn^σ , millimoles per gram), i.e. the difference between the surface excess amounts of H^+ ($n_{\text{H}^+}^\sigma$) and OH^- ($n_{\text{OH}^-}^\sigma$) was derived directly from the initial and equilibrium concentrations of the solute [6]. The values of $n_{\text{H}^+}^\sigma$ and $n_{\text{OH}^-}^\sigma$ were calculated at each point of the titration, and $\Delta n^\sigma = n_{\text{H}^+}^\sigma - n_{\text{OH}^-}^\sigma$ was plotted as a function of the equilibrium pH.

Results and discussion

Morphology of the carbons

According to the adsorption/desorption isotherms in Fig. 1, the carbons have a microporous structure. The ratio of the microporosity exceeds 90%, except for the M3SEN sample. The boiling water extraction results in a small increase in the surface area and all relevant parameters, probably by removing water-soluble tarlike plugs from the pores.

The RT acidic treatments, as illustrated in the scanning electron microscope (SEM) images (Fig. 2), do not affect significantly the surface structure of the sample either on a macroscopic scale or at the nanometre

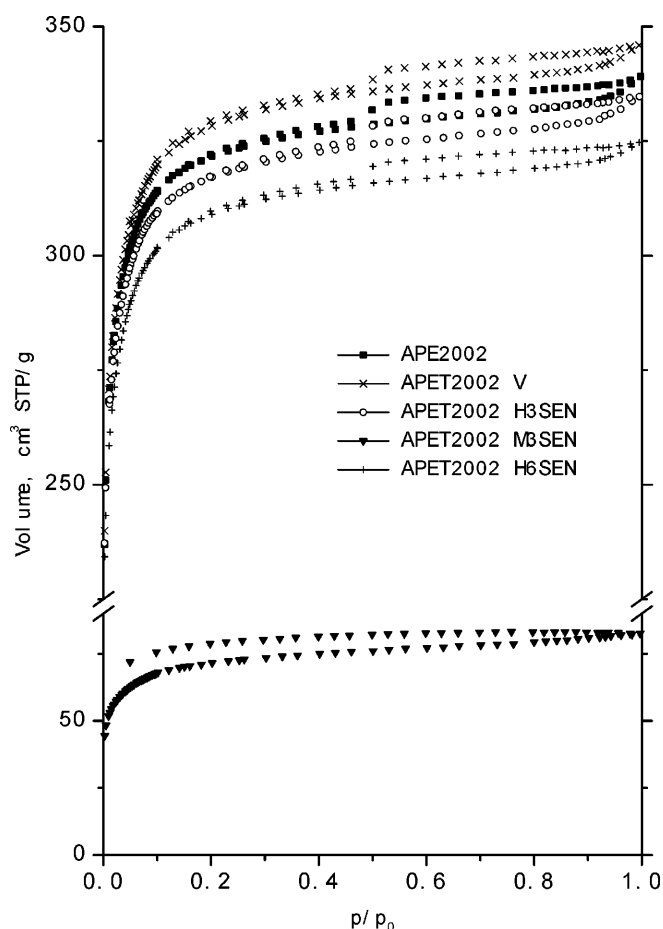


Fig. 1 Low-temperature nitrogen adsorption/desorption isotherms of the carbon samples

scale, as reflected by the images (Fig. 2b, c, e) and the isotherms. However, a small but systematic decreasing trend was observed in the surface area and the pore volumes (both total and micro), as the duration of the acid treatment was increased. The hysteresis loops reveal the interconnected pore structure of the polymer carbons.

The temperature of the treatment is more important than its duration. The carbon obtained after the BP treatment has a much more fractured surface (Fig. 2d) and a significantly reduced surface area. The fraction of micropores falls below 80%. The heavy damage to the pore structure is also reflected in the low-pressure hysteresis, observed only in this carbon. The lower helium density of the sample M3SEN reported in Table 2 is an additional sign of a severely weakened skeleton.

If the trends in the pore size and the micropore volume data are compared, it may be concluded that the acid first affects the walls of the wider pores (macropores and mesopores), as these are more accessible.

The SAXS response, in a double-logarithmic representation, of the activated carbon APET2002, prior to the washing stage, is shown in Fig. 3. Various regions in this curve can be discerned, corresponding to different structural features. In region a, the curve displays quasi-linear behaviour with slope approximately -2.7 , which is perhaps indicative of dense clusters of aggregates with a fractal-like arrangement. The radius of gyration of the clusters is, however, too large to be resolved in these measurements. Region b displays an apparent slope of -3.5 , implying that the surfaces of the component aggregates are rough. Closer inspection, however, shows that this scattering feature is made up of a Porod power-law component, $I(q) = Kq^{-4}$, from the smooth surfaces of the aggregates [7], plus a constant term. From the value of K , an estimate can be made of the surface area associated with the aggregates, $s_a/Vd \sim 18 \text{ m}^2 \text{ g}^{-1}$, where the subscript refers to the aggregates. For spherical aggregates this value is equivalent to a radius $r = 3V/s_a \sim 85 \text{ nm}$. This result corresponds to the external surface of the aggregates. The next feature at higher q in Fig. 3, the plateau region at c, defines a spatial scale over which the density of the material is virtually uniform, while the shoulder at d reveals the presence of finer-scale structures, i.e. pores, the radius of gyration of which is approximately 0.6 nm . Spatial correlation among pores is the cause of the flattened response of the curve in region c.

The wide-angle X-ray scattering spectra of these APET samples (not shown here) display extremely low crystallinity, as well as total absence of crystalline order in the c -axis.

The SAXS spectra for the set of acid-treated samples are shown in Fig. 4. For V, H3SEN and H6SEN, the X-ray responses are similar, with small but systematic differences. Sample M3SEN is, however, significantly different from the others. The entire low- q region has slope -4 , characteristic of smooth surfaces [7]. The absence of any curvature at low q makes it difficult to define with confidence the numerical value of the specific surface area. However, on the basis of a plausible assumption about the lower cutoff limit, it is found to be of the same order as in the other samples.

For all samples, the shoulder at $2\text{--}3 \text{ nm}^{-1}$, when plotted in a Guinier representation, yields an apparent radius of gyration of the pores, R_G , close to 0.6 nm , with the exception of M3SEN, where $R_G \sim 0.52 \text{ nm}$. The next slope at high q , beyond this shoulder, is associated with surface scattering from the pores, but is partly masked by an additional component due to stacking disorder, i.e. the internal structure of the carbon phase. The apparent slope of this feature (-2.5) is sometimes assumed to be simply separable into a Porod law [7] plus a constant C [8]; thus,

$$I(q) = Kq^{-4} + C \quad (1)$$

Fig. 2a–e Scanning electron microscope image of the original, the water-treated and the acid-treated carbon samples

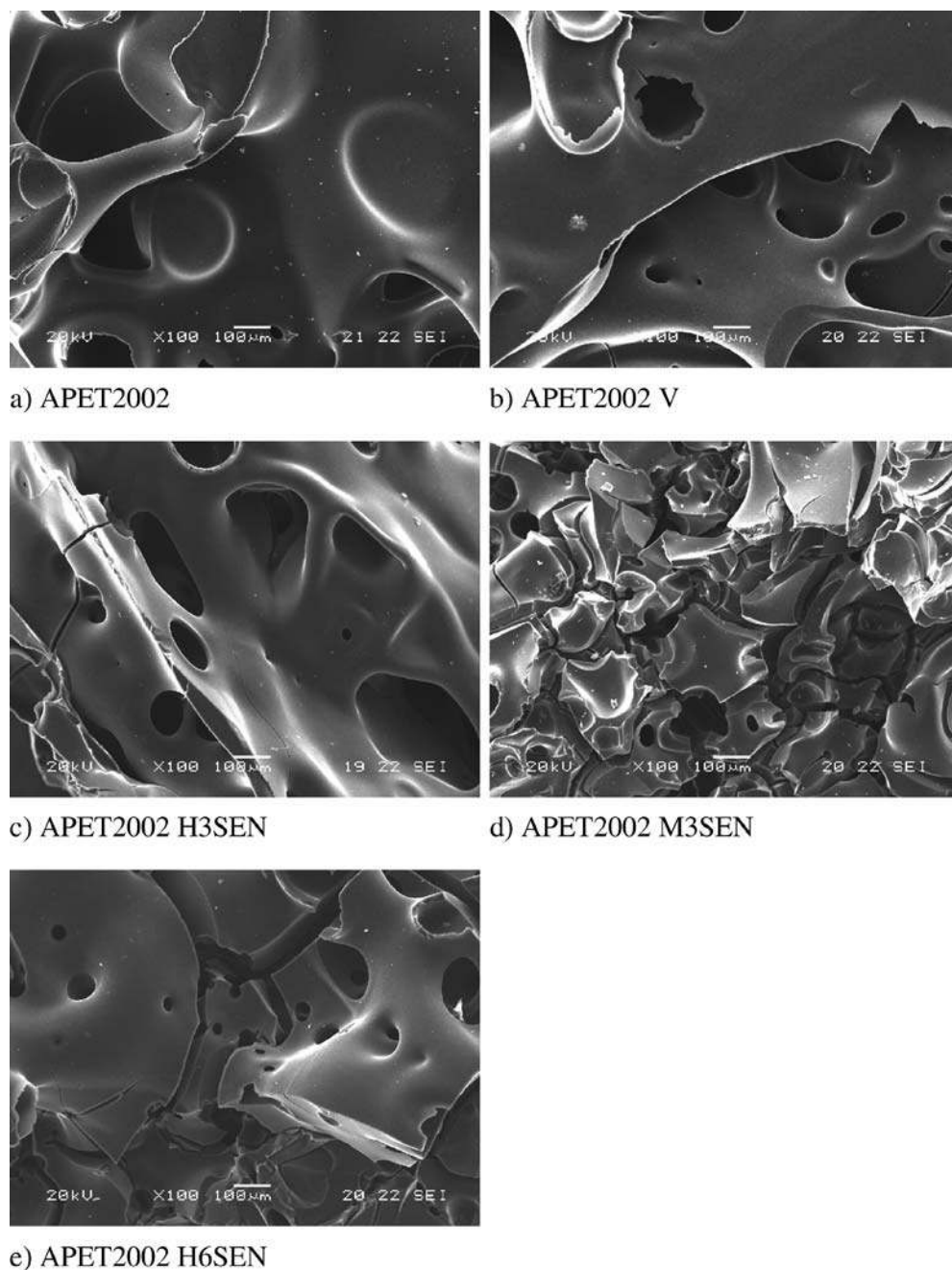


Table 2 Surface characterization from low-temperature nitrogen adsorption data

Sample	$S_{a,BET}$ ($m^2 g^{-1}$)	$V_{p,tot}$ ($cm^3 g^{-1}$)	r_p (nm)	$V_{mp,t}$ ($cm^3 g^{-1}$)	V_{DR} ($cm^3 g^{-1}$)	E_0 ($kJ mol^{-1}$)	L_0 (nm)	$V_{mp,t}/V_{p,tot}$
APET2002	1,214	0.53	0.87	0.49	0.50	20.5	1.19	0.93
APET2002 V	1,241	0.54	0.86	0.50	0.51	20.3	1.21	0.93
APET2002 H3SEN	1,197	0.52	0.87	0.49	0.49	21.2	1.10	0.94
APET2002 M3SEN	273	0.13	0.94	0.10	0.11	16.8	2.02	0.79
APET2002 H6SEN	1,165	0.50	0.86	0.47	0.48	21.4	1.08	0.93

Fig. 3 Small-angle X-ray scattering (SAXS) response of activated carbon sample APET2002, prior to washing and acid treatment. The various regions of the response are designated by *letters*

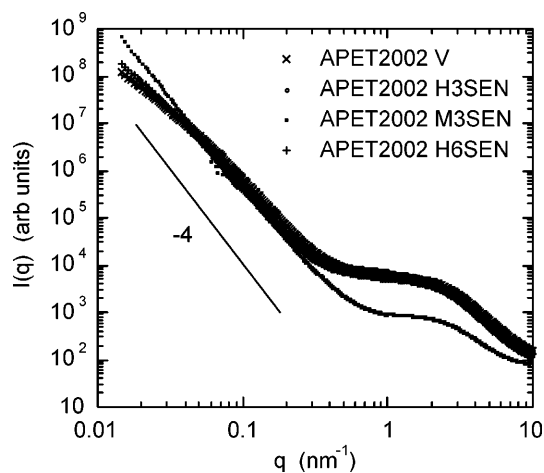
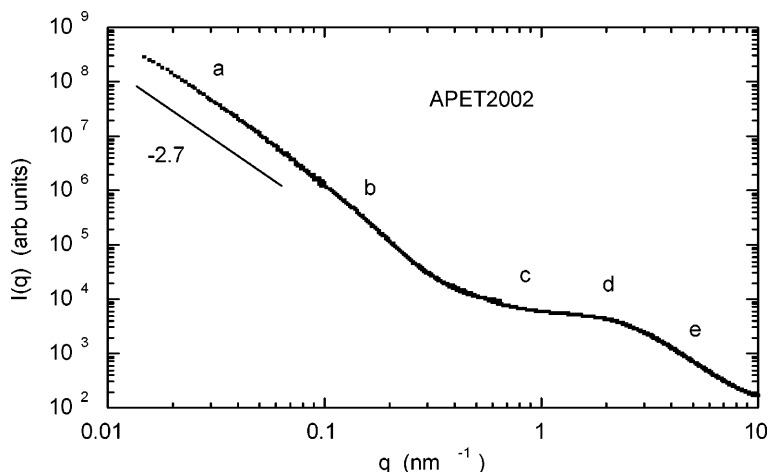


Fig. 4 SAXS spectra for APET samples after different exposures to nitric acid

To obtain the X-ray determination of the total surface area, the Porod formalism is used [7]:

$$\frac{s_x}{V} = \frac{\pi\phi(1-\phi)Kq^4}{\int_0^\infty [I(q) - C]q^2 dq}, \quad (2)$$

in which the volume fraction of carbon is $\phi = d/d_0$, d being the macroscopic sample density and d_0 the helium

density of the activated carbon. Estimates of the integral in the denominator of Eq. (2) can be controversial owing to effect of the restricted observed q range on the limits of the integral. Here, the integral was extrapolated to infinity using Eq. (1), while at the low- q limit, which contributes weakly to the integral, the intensity was taken to be a constant. The resulting SAXS specific surface areas $S_x = s_x/Vd$ are listed in Table 3.

In interpreting the data of Table 3, an uncertainty arises in connection with the component C describing the background from the fine-scale structure of the carbon in Eq. (1). The assumption that C is independent of q implies that the internal structure of the material surrounding the holes displays disorder only at higher q , an assumption whose validity is dubious. While different models for the subtraction term will modify the numerical value of the specific surface area, the entire difference between S_x and the surface area measured by nitrogen adsorption, $S_{a,BET}$, cannot be attributed to this uncertainty. The inherent difference between the results of these measurements comes from the presence of closed pores, i.e. cavities inside the bulk material that offer reduced, or variable, access to probe gas molecules.

It is important to bear in mind that X-ray determinations of surface areas in finely structured materials such as carbon are strongly model-dependent, owing to the contribution to the scattering from the internal structure of the carbon phase. An alternative procedure

Table 3 Density and small-angle X-ray scattering data

Sample	Pore volume (cm ³ g ⁻¹)	d_0 (g cm ⁻³)	ϕ	d (g cm ⁻³)	S_x (m ² g ⁻¹)	$S_{a,BET}/S_x$	R_G (nm)
APET2002	0.53	2.03	0.48	0.98	2380	0.510	0.58
APET2002 V	0.54	1.74	0.52	0.90	2500	0.497	0.59
APET2002 H3SEN	0.52	1.97	0.47	0.93	2310	0.518	0.66
APET2002 M3SEN	0.13	1.50	0.84	1.26	870	0.315	0.52
APET2002 H6SEN	0.50	1.92	0.51	0.98	2150	0.542	0.62

Table 4 pH values of suspensions of carbon samples (around 4×10^{-3} g cm $^{-3}$) immersed in 0.01 M NaCl solutions under CO $_2$ -free conditions

Sample	pH
APET2002 V	8.51
APET2002 H3SEN	4.43
APET2002 M3SEN	2.70
APET2002 H6SEN	4.04

for calculating S_x , that based on the Debye–Anderson–Brumberger (DAB) approach [9, 10], yields values that are roughly 30% higher than those listed in Table 3 (except for M3SEN, which is 90% greater). The values of S_x found in this way thus exceed the calculated surface area of a graphene layer. This discrepancy stems from the unphysical assumption in the DAB model that the internal structure of the carbon phase is uniform.

Table 3 shows that boiling nitric acid (sample M3SEN) dramatically reduces both d_0 and the specific surface area, detected both in SAXS (S_x) and N $_2$ adsorption ($S_{a,BET}$). RT nitric acid treatment produces a weaker trend: $S_{a,BET}$ hardly decreases with increasing reaction time, while the ratio $S_{a,BET}/S_x$ increases moderately. The radius of gyration of the cavities displays a weak maximum after 3-h exposure to nitric acid at RT. For the sample treated in boiling nitric acid for 3 h, however, a significant drop in the value of R_G is recorded.

We conclude that the acid first attacks accessible pores, thereby enlarging them. As the reaction advances, intervening walls dissolve and these regions merge, with resulting loss of pore character and reduction in free surface area. At later stages, only regions with inaccessible pores remain intact. In boiling nitric acid, the whole process is accelerated. For sample M3SEN, since regions with accessible pores have been preferentially removed, the ratio of the accessible surface area to the total surface area decreases ($S_{a,BET}/S_x$ in Table 3) as the surface area decreases. This picture is consistent with the initial increase in R_G , followed by a subsequent decrease. It is also consistent with the continuous increase in pore size observed in the adsorption measurements, where inaccessible pores are not detected.

Characterization of acid–base properties

The effect of acidic treatment on acid–base surface properties was studied by quasi-equilibrium potentiometric acid–base titration. The initial pH values of the carbon suspensions are summarized in Table 4.

The measured pH values differ significantly from the pH of dilute NaCl solution in which the carbon samples were immersed (pH 6.8) owing to the protolytic

processes taking place during immersion of powder samples. The activation of carbonized PET results in a basic surface character [2], and hence the pH of the immersion solution of sample V increases. This activated carbon sample can be classified as H-type, while all the acid-treated samples are L-type [11], because of the opposite shift in the pH of the H3SEN, M3SEN and H6SEN suspensions. The pH of the M3SEN suspension was particularly acidic. The low pH in the carbon suspensions indicates H $^+$ release from the acid-treated samples, which probably originates from the dissociation of acidic groups formed on the carbon surface during oxidative treatment. The acidic pH in the suspensions of oxidized carbon samples may, however, be caused by the acidic impurities remaining in the samples even after exhaustive extraction with hot water.

The powdered carbon samples were titrated under carefully controlled conditions in a cycle of forward and backward titrations to test the reversibility of surface protolytic processes. The range of the titration was limited between pH 3 and 10. The proton-binding isotherms, i.e. the pH-dependence of the net proton surface excess amount ($\Delta n^\sigma = n_{H^+}^\sigma - n_{OH^-}^\sigma$, mmol/g) calculated from the material balance of H $^+$ /OH $^-$, are shown in Fig. 5.

It can be seen that chemical oxidization, especially the hot treatment, has a significant effect on the proton-binding isotherms of treated samples in comparison with the untreated sample. Since positive values of net proton surface excess amount indicate acid consumption (proton binding) and negative ones mean consumption of base solution (release of protons or binding of hydroxyl ions) in the carbon suspensions, the pronounced shift of the curves from the positive to the negative region shows an entire change in acid–base properties of treated samples owing to the chemical oxidization of active carbon. A better comparison of samples (H3SEN and H6SEN) treated with concentrated HNO $_3$ at ambient temperature for 3 and 6 h with the untreated carbon is provided by Fig. 6.

A characteristic feature of the curves in both Figs. 5 and 6 is the existence of hysteresis loops. The upward and downward curves do not coincide, i.e. acid–base processes taking place in the direction of increasing and decreasing pH are not reversible. Similar hysteresis loops have been reported previously [12]. In every case the H $^+$ adsorption curves (decreasing pH due to acid addition) run below the H $^+$ desorption curves (increasing pH due to base addition), but no clear ionic strength dependence ever appeared. During upward titration starting from pH \sim 3 the desorption of bound H $^+$ ions (the uppermost H $^+$ desorption curves in each titration cycle in Fig. 6) is promoted by the addition of base titrant, since neutralization reaction takes place (H $^+$ + OH $^-$ = H $_2$ O). However, the diffusion of reactant OH $^-$ ions within the micropores of carbon samples seems to be hindered and

Fig. 5 Proton-binding isotherms of the washed and acid-treated powder samples in 0.01 M NaCl solution. APET2002 V (squares); APET2002 H3SEN (triangles); APET2002 H6SEN (circles). From initial pH down to pH~3 (open symbols); from pH~3 up to pH~10 (black symbols); from pH~10 back to pH~3 (grey symbols). APET2002 M3SEN from pH~ up to pH~10 (black diamonds); back to pH~3 (open diamonds)

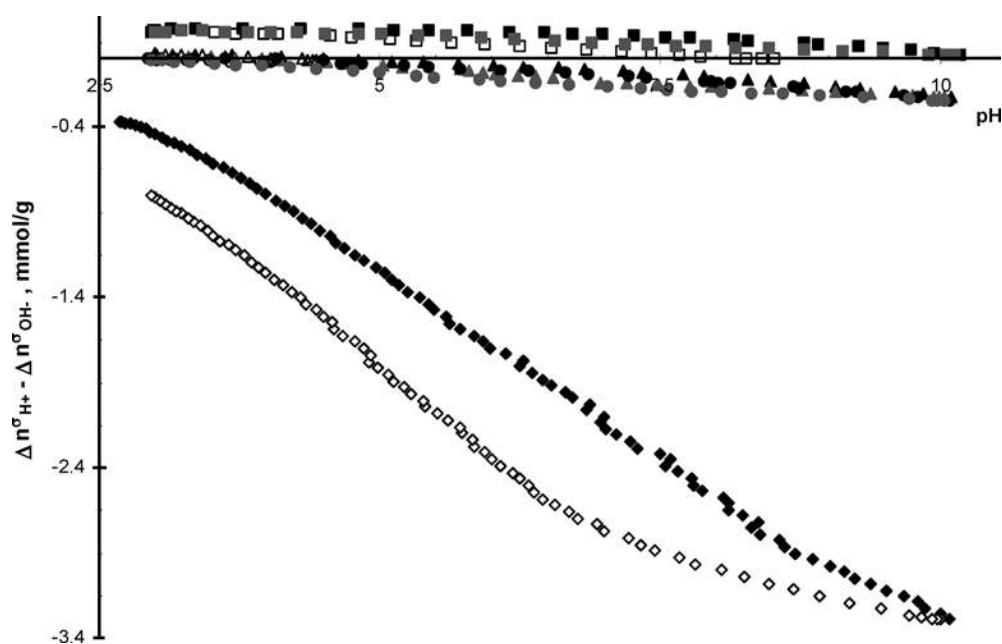
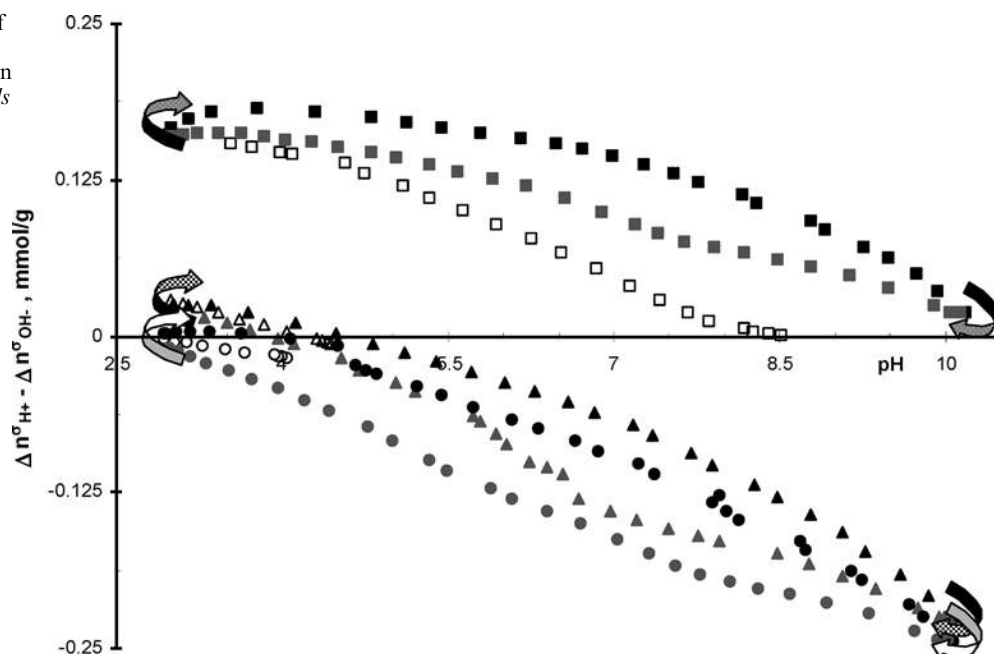


Fig. 6 Proton-binding isotherms of the washed and room temperature treated powdered carbon samples in 0.01 M NaCl solution. For symbols see Fig. 5



influences the acid–base titration results even in finely powdered samples.

Comparison of the proton-binding isotherms of treated samples with that of the untreated carbon reveals a pronounced difference, probably owing to the complete change of surface functional groups. However, the presence of residual acidic impurities cannot be excluded. The positive values of the net proton surface excess amount over the range of pH studied here indicate a significant accumulation of protons on the surface of the

untreated sample. It can be attributed to various surface protonation reactions or H^+ adsorption processes. Surface sites with basic character can be protonated, resulting in the formation of positive charges [13]. For example, as the graphitic part of the surface is significant, the π electrons of the graphite planes are of great importance. They may act as Lewis basic sites accepting protons [14], according to



Such active sites are randomly distributed on the carbon surface, and mutually influence each other. For example, the electron-localizing effect of the heteroatomic functional groups present in the activated samples may considerably decrease the basic strength of the π electrons. The proton-transfer reactions may be accompanied by a simultaneous redox transformation [14]. The negative values of the net proton surface excess amount, however, certainly prove the presence of acidic groups developed in strongly oxidative conditions. These chemically bound acidic groups release protons leaving behind negatively charged surface sites in the deprotonation process. The surface dissociation increases with increasing pH. Further investigation is necessary to verify the surface-charging process of these carbon samples. Surface protolytic processes would be confirmed only if both the protonation and the deprotonation processes are enhanced with increasing salt concentration. Such enhancement is a signature of surface charging, since the charges formed are located on the solid surface. A local electrostatic field develops in which these surface charges are compensated by the ionic cloud of the electrolytes (charge-screening effect) [15]. In this way, with increasing salt concentration, more and more charges can develop on the surface owing to surface protolytic reactions. Surface-charging processes can be assumed only if this characteristic ionic strength dependence occurs. When titration results display no ionic strength dependence, however, the acid–base consumption can originate from acidic or alkaline impurities or dissolution of a solid matrix [5].

Conclusions

In this study gas adsorption, SEM, SAXS and surface titration methods were used to characterize the mor-

phology of porous carbons that had been subjected to nitric acid treatment.

Surface functionalization in the early stages of acid treatment, where the structure of the carbon is only weakly affected, does not notably affect the morphological properties, as shown by adsorption, SEM and SAXS results. The ratio of the surface area measured by gas adsorption to that measured by SAXS, $S_{a,BET}/S_x$, corresponds to the fraction of open pores. The value of this parameter, approximately 50%, exhibits a weak increase with reaction time. Treatment in boiling nitric acid, however, leads to a dramatic loss both in surface area and in the fraction of open pores, as well as a significant change in the density and the morphology.

The chemical oxidization, especially the hot treatment affects the acid–base properties. The existence of hysteresis loops in the up and down titrations stems from the hindered diffusion of reactant OH^- ions in the micropores. Surface dissociation increases with increasing pH; however, further investigation is necessary to confirm the presence of surface-charging process.

Both for the morphology and for the surface chemistry, the temperature of the treatment is more important than its duration. Nevertheless, while the morphology is affected significantly only at high temperature, the acid–base properties are modified by all the acidic treatments.

Acknowledgements This research was supported by the Széchenyi NRDP no. 3/043/2001 and the Hungarian National Research Fund (OTKA, grant no. T 025581). The experimental work of Emese Fülöp and György Bosznai is gratefully acknowledged. We are grateful to the European Synchrotron Radiation Facility, Grenoble, for access to beamline BM2.

References

1. László K, Bóta A, Nagy LG (2000) Carbon 38:1965
2. László K, Tombácz E, Josepovits K (2001) Carbon 39:1217
3. Contescu A, Contescu C, Putyera K, Schwarz JA. (1997) Carbon 35:83
4. Lopez-Ramon MV, Stoeckli F, Moreno-Castella C, Carrasco-Martin F (1999) Carbon 37:1215
5. Tombácz E, Szekeres M (2001) Langmuir 17:1411
6. Everett DH (1986) Pure Appl Chem 58:967.
7. Porod G (1982) In: Glatter O, Kratky O (2002) Small angle X-ray scattering. Academic, London, pp 17–52
8. Bóta A, László K, Nagy LG, Copitzky T (1997) Langmuir 13:6502
9. Debye P, Bueche RM (1949) J Appl Phys 20:518
10. Debye P, Anderson HR, Brumberger H (1957) J Appl Phys 28:679
11. Mattson JS, Mark HB (1971) Activated carbon: surface chemistry and adsorption from solution. Dekker, New York, p 25
12. László K, Josepovits K, Tombácz E (2001) 25th biennial conference on carbon, 14–19 July, Lexington, KY, USA. CD-ROM of extended abstracts
13. László K, Josepovits K, Tombácz E (2001) Anal Sci 17:1741
14. Contescu A, Vass M, Contescu C, Putyera K, Schwarz JA (1997) Carbon 36:247
15. Lyklema J (1991) Pure Appl Chem 63:895

Szilvia Papp
Rita Patakfalvi
Imre Dékány

Synthesis and characterization of noble metal nanoparticles/kaolinite composites

Abstract Silver, palladium, and rhodium nanoparticles were prepared by heterogeneous nucleation in the interlamellar space of a layered kaolinite support. Disaggregation of the lamellae of nonswelling kaolinite was achieved by intercalation of dimethyl sulfoxide. The kaolinite was suspended in various metal precursor solutions and the adsorbed metal cations were reduced with NaBH_4 . The diameter of the silver particles (4–10 nm) prepared in this way depends on the initial Ag^+ concentration. Palladium and rhodium particles were stabilized by polymers and by the lamellae of kaolinite. The effect of the molecular mass and the concentration of the polymers on the size of the particles

formed was studied using neutral poly(vinylpyrrolidone). The effect of the concentration of the precursor was also examined. The average particle size fell in the range 1–3 nm, depending on the stabilization method used and the concentration of precursor ions. Interlamellar incorporation of nanoparticles was monitored by X-ray diffraction, and was verified by transmission electron microscopy and small-angle X-ray scattering.

Keywords Metal nanoparticles · Kaolinite · Adsorption · Transmission electron microscopy · X-ray diffraction · Small-angle X-ray scattering

I. Dékány (✉)
Department of Colloid Chemistry,
University of Szeged,
Aradi v. t. 1, 6720 Szeged,
Hungary
e-mail: i.dekany@chem.u-szeged.hu
Tel: +36-62-544-211
Fax: +36-62-544-042

S. Papp · R. Patakfalvi · I. Dékány
Nanostructured Materials Research
Group of the Hungarian
Academy of Sciences,
University of Szeged,
Aradi v. t. 1, 6720 Szeged,
Hungary

Introduction

In the past few years a great variety of methods have been devised for the preparation of particles in the nanosize range (1–50 nm) and the methods are described in the literature. A common feature of these methods is the protection of the primary particles from coagulation. An important role is played by stabilizing agents protecting the nanoparticles formed from aggregation, making possible the preparation of particles with a diameter measuring no more than a few nanometers [1, 2, 3, 4]. The most commonly used stabilizing agents are surfactants and polymers, with the help of which sols containing particles of subcolloid size are synthesized. The most widely used colloid chemical preparation method is synthesis in the droplets of microemulsions,

because droplet size may be controlled in the size range of a few times ten nanometers [5, 6, 7, 8].

Layer silicates are also eminently suitable for the preparation of particles with a diameter of a few nanometers on the surface and in the interlamellar space of clays in aquatic suspensions. Particle growth in the interlamellar space is sterically hindered.

Metal particles are most conveniently grown on the clay mineral surface by displacing the exchangeable cation by precursor transition-metal cations and by subsequent reduction. Au and Ag clusters were obtained in laponite clay mineral of synthetic origin by Aihara et al. [9] using this method with sodium borohydride as a reducing agent. Silver nanoparticles are widely used as photosensitive components [10], as catalysts [11], in photocatalysis [12], and in surface-enhanced Raman

spectroscopy [13]. In addition, they are easily detected by the characteristic absorption maximum in the visible range [14]. The most common methods were summarized by Heard et al. [15]: reduction by NaBH_4 , or ethylenediaminetetraacetic acid, preparation according to Carey Lea, or radiolysis. The colloidal sols obtained by these methods were compared in terms of particle size, absorption spectra, and particle shape. Silver hydrosols and organosols stabilized by surfactants and sols stabilized by reverse micelles were also prepared by NaBH_4 reduction [16].

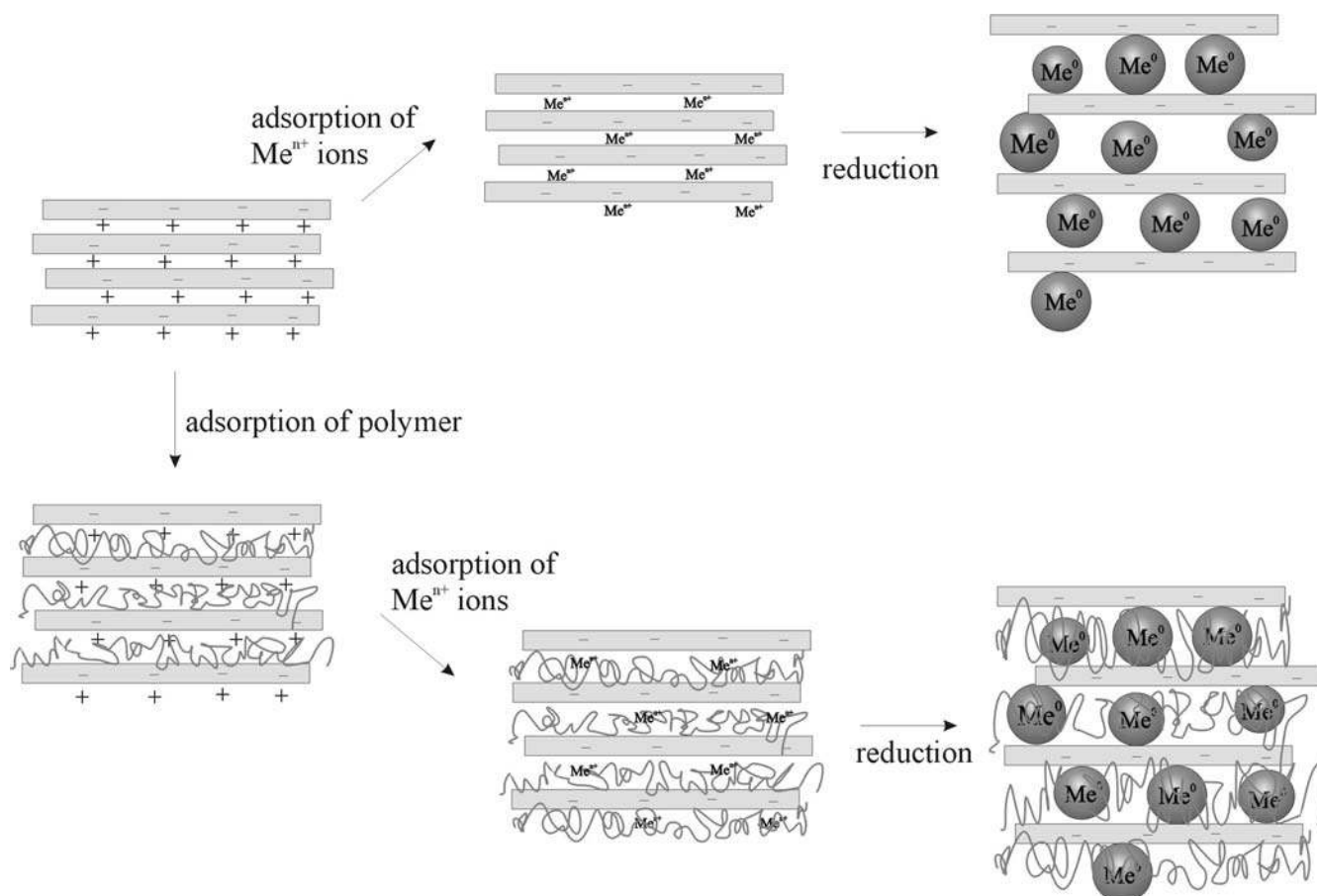
In our earlier works the adsorption layer at the solid/liquid interface was employed as a “nanophase reactor” for the generation of nanocrystalline metal particles and for their stabilization in the presence of the clay mineral [17]. The procedure consists of adsorbing the precursor ions of the nanocrystalline material in the interfacial adsorption layer of solid particles dispersed in the liquid phase and the synthesis is carried out in the adsorption layer by introducing the reducing agent. The nanoparticles can be grown attached to the surface, in well-controllable number and size between the silicate layers.

In view of the powerful stabilizing effect of polymers, we set out to test the joint stabilizing effect of the polymer/clay mineral complex in the preparation of Pd^0 nanoparticles. We showed that monodisperse particles can be obtained, the size of which depends on polymer and precursor ion concentrations and on the chemical nature of the reducing agent used [18].

Hiari et al. [19] generated rhodium nanosols stabilized by poly(vinyl alcohol), poly(vinylpyrrolidone), and poly(methyl vinyl ether) by alcohol reduction under reflux. Busser et al. [20] prepared nanosols by alcohol and hydrogen reduction and studied the strength of coordination between rhodium ions and various polymers.

In the present work, heterogeneous nucleation procedures for the preparation of monodisperse metal nanoparticles are described (Fig. 1). These methods share the common characteristics of using an aqueous medium and regulating particle growth and preventing aggregation by the addition of various polymers. The effect of the molecular mass and the concentration of the polymers on the size of the particles and their adsorption on the surface of kaolinite supports were studied. The particle size was determined by transmission electron microscopy (TEM) and the metal/

Fig. 1 Schematic picture of metal nanoparticle preparation



polymer/clay mineral composites were characterized by X-ray diffraction.

Materials and methods

The metal precursor silver nitrate (Reanal, purity 99.9%), palladium(II) chloride, rhodium(III) chloride hydrate (purity 98%), and the reducing agent sodium borohydride (purity 99%) were obtained from Aldrich. A polymer was used to stabilize the Pd and Rh nanoparticles: poly(*N*-vinyl-2-pyrrolidone) (PVP, K-30, average molecular weight 4×10^4 g, Fluka).

A fine fraction ($d \leq 2 \mu\text{m}$) of kaolinite (Zettlitz, Germany) was used as a support for the preparation of nanoparticles. Disaggregation of the kaolinite lamellae in water was brought about by the intercalation of dimethyl sulfoxide (DMSO) (Reanal, puriss.) at 65°C and 24 h in suspension (20 g kaolinite per 100 cm^3 DMSO) under stirring. The redundant DMSO was removed by sedimentation with repeated washes with methanol (Reanal, a.r.) and decanting for 5 days.

X-ray diffraction (XRD) measurements were taken on a Philips PW-1830 diffractometer, Cu K α radiation ($\lambda = 0.154 \text{ nm}$) being used at 40 kV and 25 mA between $2\theta = 1\text{--}15^\circ$. The basal distances, d_L , were calculated from the first (001) Bragg reflections through the PW 1877 automated powder diffraction software.

Small-angle X-ray scattering (SAXS) was measured using the same radiation as in the case of XRD. The primary beam was directed through a Ni filter into a compact Kratky camera, type KCEC/3, in which the width of the beam was 20 mm and its thickness $80 \mu\text{m}$. The measurements were done in a vacuum. The intensity of the scattered radiation was measured by a proportional detector (slit width $100 \mu\text{m}$) controlled by a PW 1710 microprocessor and scattering data controlling software, in an angle range of $2\theta = 0.05\text{--}7^\circ$.

Transmission electron micrographs were made with a Philips CM-10 transmission electron microscope with an accelerating voltage of 100 kV. The particle size distribution was determined by using the UTHSCSA Image Tool program.

Preparation of noble metal nanoparticles

The theoretical silver contents of the samples were 0.5, 1.0, 1.5, 2.0, and 5.0% Ag/kaolinite. Various amounts of disaggregated kaolinite were suspended in 10^{-3} M AgNO_3 aqueous solution. The concentration of the kaolinite aqueous suspensions varied in the range 0.2–1.2 g kaolinite per 100 cm^3 solution. The suspension was stirred for 24 h at room temperature. Freshly prepared $4 \times 10^{-2} \text{ M}$ NaBH_4 solution was next added under constant stirring to achieve an AgNO_3 -to- NaBH_4 molar ratio of 1:4. After the addition of the reducing agent, stirring was continued for another hour, the suspension was centrifuged, twice washed in distilled water, and dried in an oven at 50°C .

Pd/kaolinite and Rh/kaolinite composite were prepared, directly by reduction of Pd^{2+} and Rh^{3+} ions previously adsorbed in the $\text{CH}_3\text{OH}/\text{DMSO}/\text{kaolinite}$ system and on the other by applying a polymer to ensure binding nanoparticles to the lamellae and steric stabilization. Different polymers of 0.005–0.2 w/v% concentration were adsorbed on the kaolinite at

1.0 w/v% dispersion concentration from an aqueous solution and this was followed by adsorption and reduction of precursor ions. Intercalation complexes of polymer/kaolinite were prepared by this method in aqueous solution at various concentrations of PVP by polymer adsorption at room temperature in a 24 h reaction at constant stirring. Kaolinite samples containing different amounts of rhodium (0.5–2.0 w/v%) were obtained by NaBH_4 reduction at a Rh^{3+} -to- NaBH_4 ratio of 1:12.

Results and discussion

Disaggregation of kaolinite in DMSO can be conveniently monitored by XRD (Fig. 2). The kaolinite lamellae open up and the original basal spacing of $d_L = 0.72 \text{ nm}$ increases to 1.12 nm as a result of the intercalation of DMSO (Fig. 2).

After the adsorption of Ag^+ ions, the peak characteristic of disaggregated kaolinite disappears, because residual DMSO leaves the interlamellar space unhindered. At the same time, the original (001) reflection of kaolinite reappears, although its intensity is low.

After reduction of adsorbed metal ions a new Bragg reflection is observed at smaller 2θ angles ($d_L = 4.28 \text{ nm}$ for 1% Ag/kaolinite) (Fig. 2). It is proven by these increased d_L values that, in the course of ion exchange, Ag^+ ions are bound not only on the edges and the external surface of kaolinite but also in the interlamellar space. In these samples the intensities of the reflections are considerably lower, whereas their half-widths are larger than those of undoped clay minerals: the highly

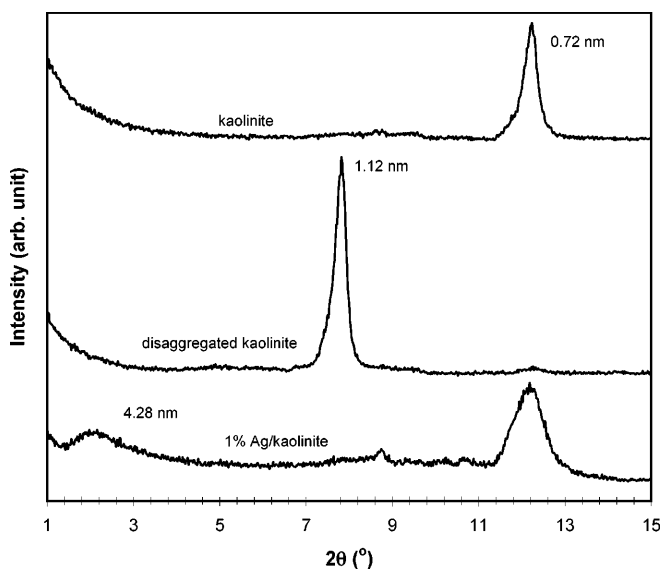
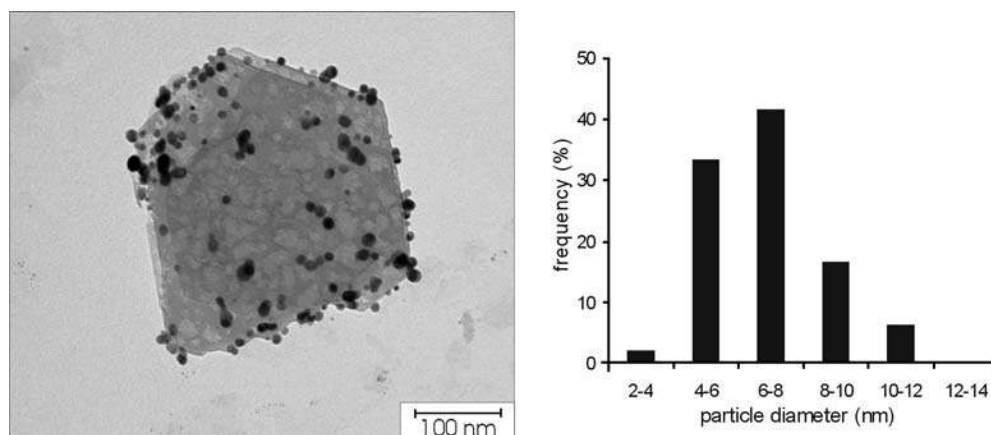


Fig. 2 X-ray diffraction (XRD) patterns of kaolinite, disaggregated kaolinite, and 1% Ag/kaolinite

Table 1 Structural parameters of kaolinite, disaggregated kaolinite, and silver/kaolinite samples

	Kaolinite	Disaggregated kaolinite	Ag/kaolinite				
Ag content (%)	–	–	0.5	1.0	1.5	2.0	5.0
d_L (nm)	0.72	1.12	4.58	4.28	4.24	4.39	4.95
d_{ave} (nm)	–	–	5.6	7.1	7.6	8.3	10.5
K_p (cps nm ⁻³)	59.59	57.02	75.26	86.56	98.41	91.58	101.83
l_c (nm)	45.11	41.62	41.22	38.83	39.35	37.93	34.59

Fig. 3 Transmission electron microscope (TEM) image and particle size distribution of 1.5% Ag/kaolinite

ordered parallel lamellar structure of kaolinite is disrupted by particle formation

The size distribution of the silver nanoparticles formed was determined by TEM measurements (Table 1, Fig. 3). Although particle growth is restricted by the dimensions of the interlamellar space, particles larger than limiting sizes are still observed (d_{TEM} = 5.6–10.5 nm). Consequently, these particles must have formed on the external surface of the clay mineral.

As the metal content is increased, the average size of the nanoparticles is also seen to increase: $d_{ave(TEM)}$ = 5.6 nm for the sample containing 0.5% Ag/kaolinite, whereas $d_{ave(TEM)}$ = 10.5 nm for the 5% Ag/kaolinite sample.

Changes in the structural properties of kaolinite and the presence of Ag nanoparticles on the support may also be detected by SAXS experiments. The intensity of X-ray scattering is enhanced by the higher electron density of the metal nanoparticles located on the surface; therefore, the intensity is seen to increase with increasing silver content. Differences between the samples are also confirmed by the Porod representation (Fig. 4) [21, 22, 23]. The intersections yield the values of the tail-end constants, K_p , for each sample. The value of this constant, proportional to the magnitude of the interfaces of the individual phases, tends to increase with increasing silver content. Its value is 57.02 cps nm⁻³ for disaggregated kaolinite and it increases to 101.83 cps nm⁻³ in the sample containing 5% silver. The value of the correlation

length, l_c , calculable from K_p is decreased as a consequence of Ag⁰ particle incorporation.

Palladium and rhodium nanoparticles were prepared on kaolinite at different metal contents and at different metal/polymer monomer ratios. We studied polymer incorporation between the disaggregated kaolinite lamellae. When the aqueous PVP solution was contacted with kaolinite a broadened peak of d_L ~ 3.6 nm was

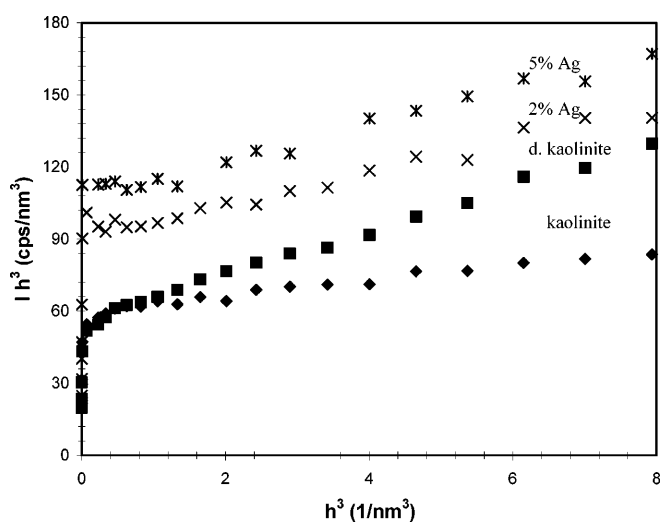
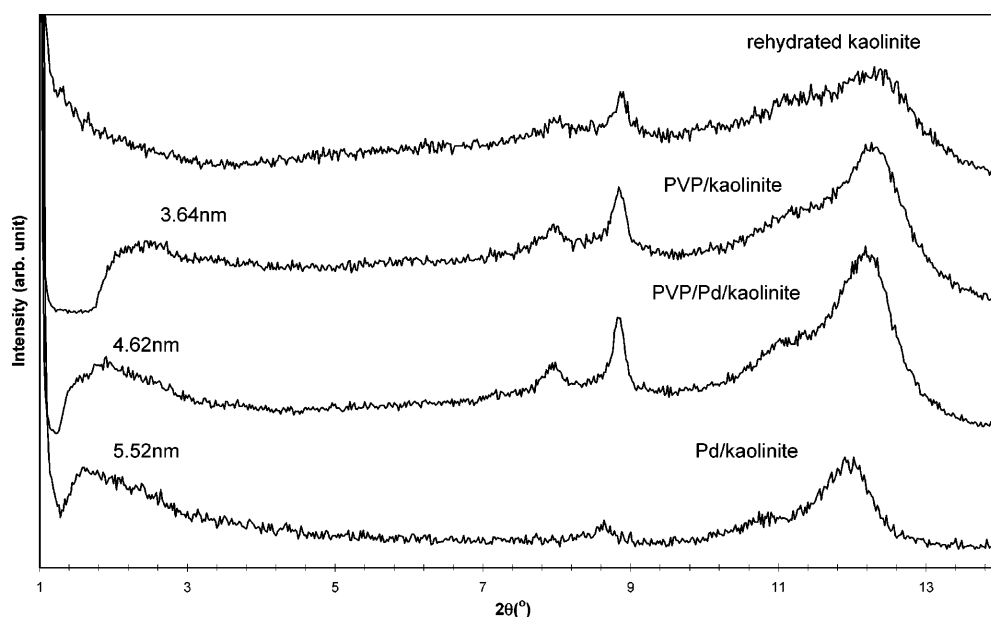
**Fig. 4** The Porod representation of the small-angle X-ray scattering (SAXS) curves for Ag/kaolinite samples

Fig. 5 XRD patterns of rehydrated kaolinite, poly(*N*-vinyl-2-pyrrolidone) (PVP)/kaolinite, PVP/Pd/kaolinite, and Pd/kaolinite



observed (Fig. 5). From the evidence of the diffractograms, the macromolecules are incorporated between the kaolinite lamellae (Table 2). The formation of Pd clusters in the interlamellar space of the PVP/kaolinite system was indicated by a shift of reflection from $d_L = 3.6$ to $d_L = 4.6$ nm. The TEM picture of the sample shows nearly spherical particles measuring 2–6 nm (Fig. 6). Kaolinite samples containing palladium were prepared without PVP stabilization. The Pd⁰/kaolinite samples prepared in the aqueous system yielded comparatively large palladium clusters of polydisperse size distribution (2–5 nm) covering densely the lamellae. Increasing the palladium content not only increased the particle size but also broadened the polydispersity. In each case, even at high metal contents, the palladium particles remained noncrystalline without distinct crystal shapes. The incorporation of the particles increases the basal spacing according to the XRD patterns. When the particle size is increased the peak is shifted to smaller angles (2.2→13).

When rhodium particles protected by polymers are grown, a new peak appears at $d_L \sim 2.7$ nm in all cases. PVP was applied at different Rh-to-PVP monomer ratios (1:1, 1:5, 1:20). When the amount of PVP added is increased, the structure is diluted to an increasing extent,

the relative intensity of the peak appearing at smaller angles increases, and the peak is shifted to 4.02 nm (Fig. 7). At a Rh-to-monomer ratio of 1:20, as much as 60% of the structure is opened up. When the metal content is increased (0.5–2%) at a Rh-to-PVP monomer ratio of 1:1, out of the two basal spacing values indicating two different initial particle sizes it is the intensity of the peak appearing at larger angles that is increased. At 2% metal content the peaks are no longer separable. TEM pictures show that the average particle size was somewhat reduced by higher precursor and polymer concentrations ($d_{ave} = 1.4 \rightarrow 1.1$ nm), whereas increasing molecular mass resulted in the formation of larger particles ($d_{ave} = 1.2 \rightarrow 1.9$ nm) (Fig. 8). Kaolinite samples with 0.5–2.0% rhodium content were also prepared without polymer stabilization. In the samples containing 0.5 and 1.0% Rh, over 40% of the structure of kaolinite was transformed due to intercalation, a result never achieved with either polymer (Table 3, Fig. 9).

The nanostructures of the composites containing palladium and rhodium were also studied by SAXS measurements (Fig. 10). The values of K_p increased with increasing metal content. The values for the silver/kaolinite and palladium/kaolinite composites are nearly the same (86.56, 89.12 cps nm⁻³) at the same metal

Table 2 Basal spacing and particle size of palladium/kaolinite samples

Poly(<i>N</i> -vinyl-2-pyrrolidone) content (%)	0	0	0	3.8
Pd content (%)	0.5	1.0	2.0	1
d_{L1} (nm)	4.04	5.52	6.87	4.62
d_{L2} (nm)	—	—	3.01	—
d_{L3} (nm)	0.73	0.73	0.74	0.72
d_{ave} (nm)	4.86	6.02	10.09	4.66

Fig. 6 TEM image and particle size distribution of medium molecular weight PVP-protected Pd⁰ kaolinite (1.0% Pd)

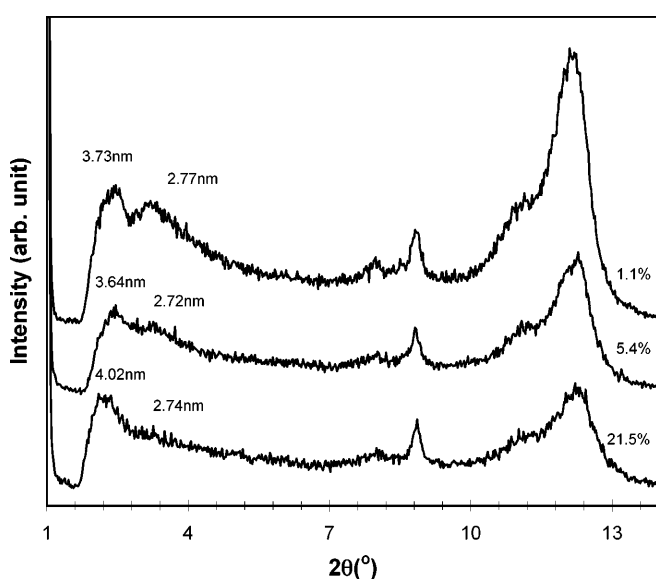
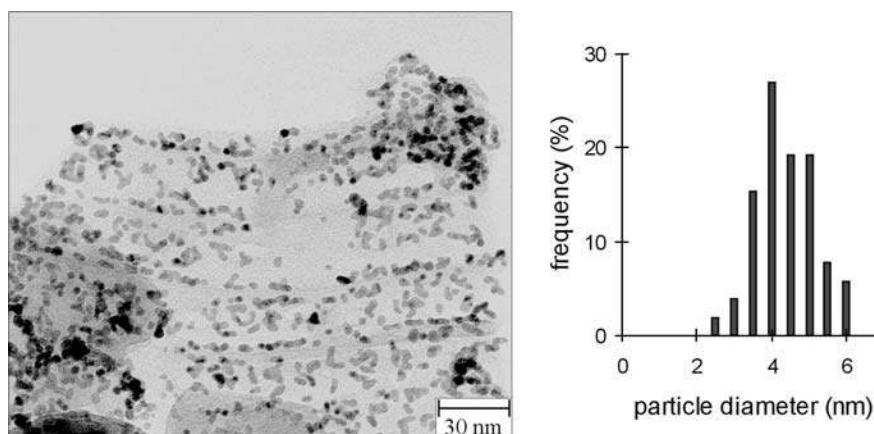


Fig. 7 XRD patterns of the PVP-protected Rh⁰ kaolinite showing Rh⁰ nanoparticles intercalated in the interlamellar space at different polymer content

content. When rhodium particles are intercalated into the kaolinite lamellae K_p is increased significantly (230.31 cps nm⁻³). The increase of the quantity of small rhodium particles in the sample yielded increased intensity of the scattered radiation. The correlation length calculable from K_p is decreased slightly with increasing metal content.

Conclusion

Noble metal/kaolinite composites were prepared in aqueous dispersions. The particles formed were stabilized with polymers and the lamellae of clay minerals. Silver nanoparticles were prepared on disaggregated kaolinite. It was proven by the change in basal spacing of kaolinite that a fraction of the nanoparticles was formed in the interlamellar space. However, the particle sizes obtained by TEM show that larger particles were also generated and that these are located on the external surfaces and on the edges. Both TEM and XRD measurements show that the average size of the silver

Fig. 8 TEM image and particle size distribution of Rh⁰ kaolinite (0.5% Rh)

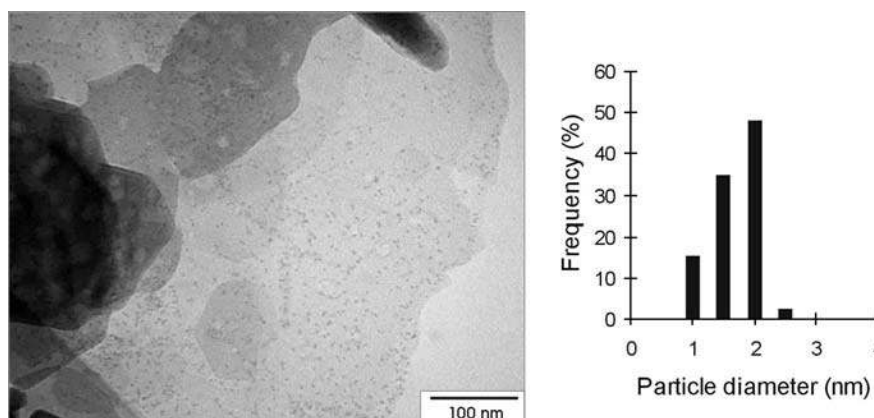
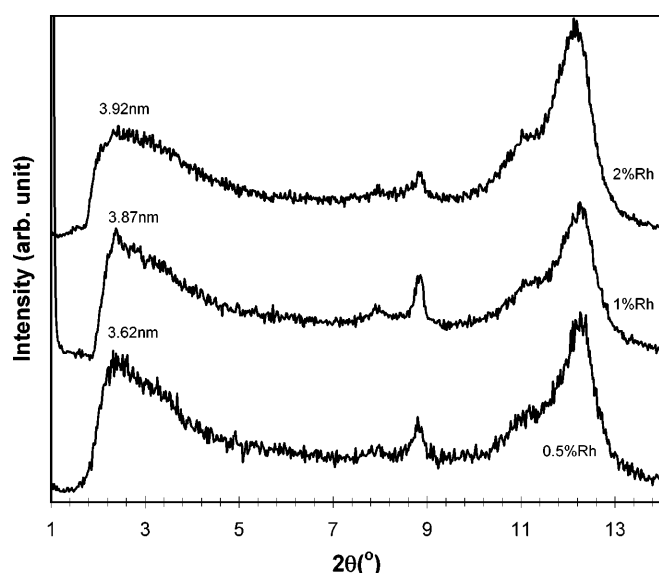
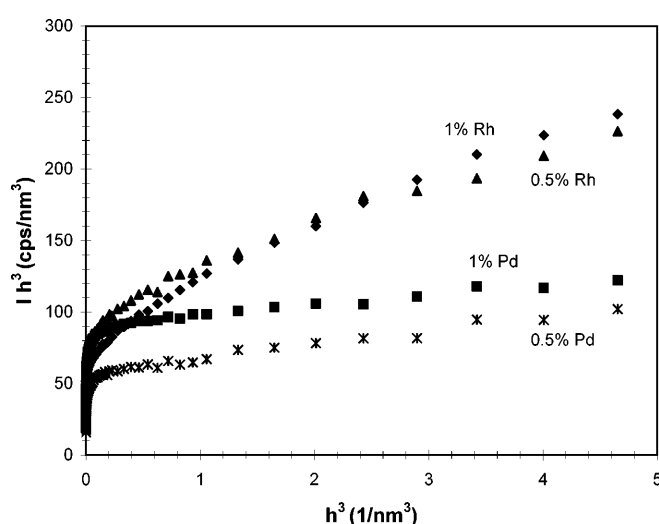


Table 3 Basal spacing and particle size of rhodium/kaolinite samples

Poly(<i>N</i> -vinyl-2-pyrrolidone)/kaolinite					
Polymer content (%)	0.54	1.08	2.16	5.39	21.5
d_{L1} (nm)	3.78	3.78	3.44	3.64	3.73
d_{L2} (nm)	—	—	—	—	—
d_{L3} (nm)	0.72	0.72	0.73	0.73	0.73
Poly(<i>N</i> -vinyl-2-pyrrolidone)/Rh/kaolinite					
Rh-to-monomer molar ratio	1:1	1:1	1:1	1:5	1:20
Rh content (%)	0.5	1.0	2.0	1.0	1.0
d_{L1} (nm)	3.92	3.73	3.78	3.65	4.03
d_{L2} (nm)	2.79	2.77	—	2.72	2.74
d_{L3} (nm)	0.72	0.73	0.73	0.73	0.72
d_{ave} (nm)	1.37	1.45	1.15	1.42	1.11
Rh/kaolinite					
Rh content (%)	0.5	1.0	2.0		
d_{L1} (nm)	3.62	3.69	3.92		
d_{L2} (nm)	—	—	—		
d_{L3} (nm)	0.72	0.72	0.73		
d_{ave} (nm)	1.41	1.34	1.1		

**Fig. 9** XRD patterns of Rh⁰ kaolinite showing Rh⁰ nanoparticles intercalated in the interlamellar space at different Rh⁰ content

particles formed increases with increasing initial Ag⁺ precursor ion concentration. The Rh and Pd contents were varied between 0.5 and 2.0% on the kaolinite surface. Interlamellar incorporation of nanoparticles was confirmed by XRD in every case. There is a huge difference between the structure of the mineral supplemented with only polymer or only metal and that of

**Fig. 10** The Porod representation of the SAXS curves: **a** NaBH₄ prepared Pd⁰ kaolinite and **b** Rh⁰ kaolinite

the three-component system (polymer/metal/kaolinite) which displays a new reflection at about 2.7–2.8 nm. It was established by TEM experiments that, depending on the stabilization method employed and the concentration of the precursor ions, the average particle size falls in the range 1–2 nm.

Acknowledgements The authors thank for the financial support of the Hungarian National Scientific Found (OTKA M036688).

References

1. Schmid G (1992) *Chem Rev* 92:1709
2. Esumi K, Suzuki A, Aihara N, Usui K, Torigoe K (1998) *Langmuir* 14:3157
3. Fink J, Kiely CJ, Bethell D, Schiffrin DJ (1998) *Chem Mater* 10:922
4. Reetz MT, Helbig W (1994) *J Am Chem Soc* 116:7401
5. Berkovich Y, Ganti N (1997) *Colloids Surf* 128:91
6. Fan C, Jang L (1997) *Langmuir* 13:3059
7. Trickot YM, Fendler JH (1984) *J Am Chem Soc* 106:7359
8. Your HC, Baral S, Fendler JH (1988) *J Phys Chem* 92:6320
9. Aihara N, Torigoe K, Esumi K (1998) *Langmuir* 14:4945
10. Hailstone RK (1995) *J Phys Chem* 99:4414
11. Claus P, Hofmeister H (1999) *J Phys Chem B* 103:2766
12. Tada H, Teranishi K, Inubushi Y, Ito S (2000) *Langmuir* 16:3304
13. Nickel U, Castell A, Pöpl K, Schneider S (2000) *Langmuir* 16:9087
14. Henglein A (1993) *J Phys Chem* 97:5457
15. Heard SM, Grieser F, Barraclough CG, Sanders JV (1983) *J Colloid Interface Sci* 93:545
16. Pal T, Sau TK, Jana NR (1998) *J Colloid Interface Sci* 202:30
17. Dékány I, Turi L, Szücs A, Király Z (1998) *Colloids Surf A* 141:405
18. Papp S, Szücs A, Dékány I (2001) *Appl Clay Sci* 19:155
19. Hirai H (1979) *J Macromol Sci Chem* A13:633
20. Busser GW, Ommen JG, Lercher JA (1999) *J Phys Chem B* 103:1651
21. Glatter O, Kratky O (1982) *Small-angle X-ray scattering*. Academic, New York
22. Guinier A, Fournet G (1955) *Small-angle scattering of X-rays*. Wiley, New York
23. Schmidt PW, Avnir D, Levy D, Hohn A (1991) *J Chem Phys* 94:1474

Lajos Rácz
Béla Pukánszky Jr
András Pozsgay
Béla Pukánszky

Polyamide 6/montmorillonite nanocomposites: effect of interaction on structure and properties

Abstract Polyamide 6 hydrophobic clay composites were prepared from two organophilized montmorillonites and from a nontreated layered silicate. An ω -amino acid and an aliphatic amine were used for treatment to assure coupling and weak interaction of the components, respectively. Homogenization was carried out by melt-mixing, followed by injection molding to prepare specimens for composite testing. Matrix and silicate structures were characterized by X-ray diffraction, while the melting and crystallization characteristics of polyamide were determined by differential scanning calorimetry. Tensile properties, impact strength and heat deflection temperatures were determined as a function of the layered silicate content. The results obtained confirmed published results that layered sili-

cates promote the formation of the γ modification of polyamide. Partial exfoliation was achieved with both fillers, the extent of which differed slightly in the two cases. The mechanical properties of the composites depend very much on the type of organic compound used for the treatment of the layered silicate. An analysis of the results proved that although many factors change both with the type of treatment and filler content, the dominating factor determining composite properties is interfacial interaction. Changing interfacial adhesion determines micromechanical deformation processes and the overall performance of the composites.

Keywords Nanocomposites · Structure · Mechanical properties

Lajos Rácz · Béla Pukánszky Jr
András Pozsgay · Béla Pukánszky (✉)
Department of Plastics
and Rubber Technology,
Budapest University of Technology
and Economics,
P.O. Box 91, 1521 Budapest, Hungary

L. Rácz · B. Pukánszky Jr · A. Pozsgay
B. Pukánszky
Institute of Chemistry,
Chemical Research Center,
Hungarian Academy of Sciences,
P.O. Box 17, 1525 Budapest,
Hungary

Introduction

The increased interest in nanocomposites started with the development of layered silicate polyamide 6 (PA6) nanocomposites at Toyota [1, 2, 3]. The composites had high stiffness, increased heat distortion temperature and acceptable impact strength compared to polyamide (PA). They offered 25% weight saving and a better balance of properties than traditional glass fiber reinforced PA composites [3]. Since then numerous studies have been carried out on nanocomposites prepared from PA [1, 2, 3, 4, 5, 6, 7, 8, 9, 10, 11, 12, 13, 14, 15, 16, 17, 18, 19, 20, 21, 22, 23], but also on composites with various polymers

as matrix materials [16, 17, 19, 24, 25, 26]. However, since the introduction of PA6 nanocomposites, further technical or commercial success was not achieved: the properties of most nanocomposites do not match predictions and expectations.

The success of PA nanocomposites is mainly due to the good adhesion between the modified layered silicate and the PA matrix. Good interaction is achieved by the chemical coupling of the components. PA nanocomposites can be prepared by intercalation of a monomer in the galleries of the clay and in situ polymerization or by the exfoliation of the silicate layers during processing. ω -amino acids are used in both cases for the

organophilization of the silicate and for monomer as well. The amine is attached to the surplus negative charges at the clay surface by an ionic bond, while the acid takes part in polymerization or coupling [1, 2, 3, 4, 5, 6]. The introduction of the silicate changes the crystalline structure of the polymer: evenly distributed clay particles modify properties considerably. Numerous studies investigated the exfoliation of layered silicates in PA [1, 3, 5, 10, 11, 17], the crystalline [4, 5, 7, 10, 12, 15, 20, 23] and phase structure [2, 3, 5, 6, 16] of the composite, the gallery structure of the dispersed silicate [1, 3, 5, 11, 16, 17], rheological [3, 11, 12] and mechanical [2, 3, 8, 9, 10, 11, 12] properties and many other issues [11, 14, 16, 18, 22]. However, in spite of its significance, limited attention has been paid to the effect of interfacial interactions on the structure and properties of PA nanocomposites.

As a consequence, the goal of our study was to prepare layered silicate nanocomposites from montmorillonites organophilized not only with an ω -amino acid, but also with alkylammonium salts and protonated amines [27, 28, 29, 30, 31]. The use of the two dissimilar modifiers was expected to lead to significant differences in the interaction of the clay and the polymer matrix. The effect of interfacial adhesion on exfoliation and on the structure and properties of the nanocomposites prepared were determined and are discussed in this paper. Less attention is paid to changes in the crystalline morphology of the PA matrix.

Experimental

Danamid E grade polycaprolactame produced by Zoltek, Hungary, was used as a matrix material. Three different layered silicates were homogenized with the matrix to prepare the composites: Nanofil 784 organophilized with an ω -amino acid for improved interaction (specific weight around 1.8 g/cm³, medium particle size 3 μ m, loss on ignition around 20%); Nanofil 948 treated with an aliphatic amine (specific weight around 1.4 g/cm³, medium particle size 36 μ m, loss on ignition around 45%), which was expected to result in decreased interfacial adhesion; and a bentonite clay (Majorbenton B), which was not coated, for comparison. Nanofil layered silicates were supplied by Süd Chemie, Germany. The filler content of the composites varied in a relatively wide range; they contained 0, 0.5, 1, 1.5, 2, 3, 5, 7 and 10 vol% silicate. The components were homogenized by extruding them twice on a Rheomex S 3/4" single-screw extruder driven by a Haake Rheocord EU 10 V unit. The set temperatures of the extruder were 220–240–250 °C, while the screw speed was 50 rpm. The pellets produced were injection molded to dog-bone-type tensile specimens using a Battenfeld BA 250 CD machine at 220–230–250–260 °C set temperatures; the temperature of the mold was kept at 60 °C.

The crystalline structure of the polymer and the gallery structure of the fillers were studied by X-ray diffraction (XRD) experiments using a Phillips PW 1830/PW 1050 with Cu K α radiation at 40 kV and 35 mA. The melting and crystallization characteristics of the PA matrix were determined by differential scanning calorimetry measurements using a PerkinElmer DSC 7 apparatus. The measurements were carried out on about 5 mg samples with 10 °C/min heating and cooling rate in two runs between 50 and 300 °C. The results reported in the paper were obtained in the second runs. The

actual filler content of the composites was determined by thermogravimetric analysis using a PerkinElmer TGA6. The heat deflection temperature was measured using a Ceast 6505 apparatus at 1.82 MPa loading. The stiffness, E , was determined on injection-molded specimens at 0.5-mm/min cross-head speed and 50-mm gauge length. The tensile yield stress, σ_y , yield strain, ε_y , tensile strength, σ , and elongation at break, ε , were calculated from force versus deformation traces recorded on the same specimens at 50-mm/min cross-head speed. The impact resistance of the composites was determined by a standard notched three-point bending test on specimens with dimensions 80×10×4-mm at 60-mm span, 0.8-mm notch depth and 2.9-m/s impact rate.

Results

The results of the experiments are discussed in two main subsections. Exfoliation, gallery structure and its effect on the crystallization of the polymer is presented in the first, while the most important properties of the composites are shown in the subsequent section. The relation of the structure and properties as well as the effect of interfacial interactions on properties are discussed in a separate section.

Structure

The exfoliation of a layered silicate in a polymer is usually estimated by the disappearance of the XRD peak characteristic for the montmorillonite and with the help of transmission electron microscope micrographs. XRD patterns of the composite containing 1 and 5 vol% of the silicate treated with the ω -amino acid are presented in Fig. 1. The diffractogram of the neat filler is also plotted

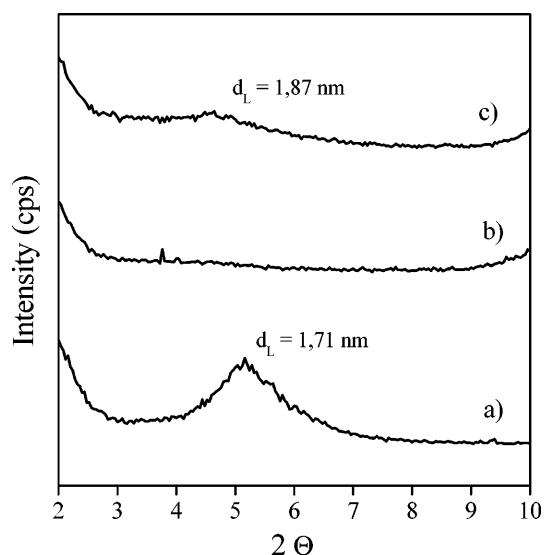


Fig. 1 X-ray diffraction (XRD) pattern of the layer silicate coated with ω -amino acid (a) and those of nanocomposites containing it at 1 vol% (b) and 5 vol% (c)

for comparison. At 1 vol% filler content the characteristic scattering of the organoclay is absent, which indicates complete exfoliation. On the other hand, the scattering peak appears in the diffractogram of the composite containing the filler at 5 vol%, although at low intensity. The peak shifted towards lower 2θ , indicating the further separation of the galleries. However, the increase in gallery distance is about 0.25 nm, which is smaller than the thickness of one aliphatic chain [26, 32, 33]. The presence of the scattering peak characteristic for the clay and the change of gallery distance indicate partial rather than complete exfoliation of the silicate.

Similar relations are reflected by the XRD patterns presented in Fig. 2. The traces were recorded on composites containing the bentonite treated with an aliphatic amine. The diffractogram of the neat organoclay is presented as a reference again. This latter diffractogram exhibits three peaks which usually appearing when silicates are well ordered and contain a considerable amount of surfactant. No peak can be observed in the XRD pattern of the composite containing 1 vol% of the silicate, while two relatively low intensity peaks can be detected in the diffractogram of the composite prepared with 5 vol% filler. The two diffuse peaks indicate again changing gallery structure without the strong ordering of the layers. On the other hand, interfacial interaction does not seem to influence the exfoliation process; a similar structure seems to develop in both cases.

The scattering intensity can be determined quantitatively by the integration of the area under the

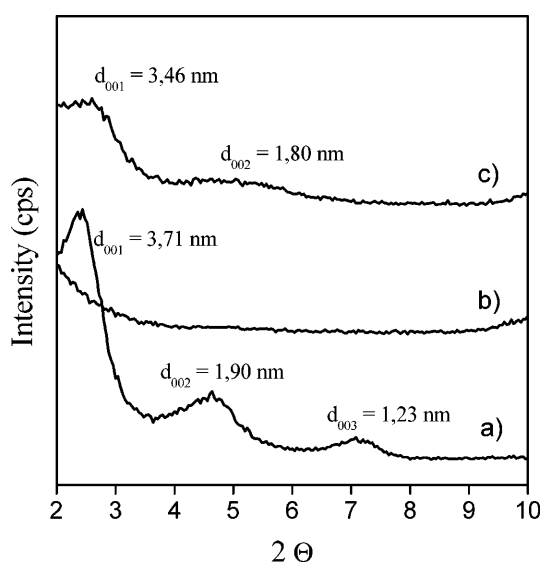


Fig. 2 XRD diffractograms of clay treated with an aliphatic amine (a) and those recorded on nanocomposites containing it at 1 vol% (b) and 5 vol% (c)

corresponding peaks. Intensities characterizing the silicate were measured on the two sets of composites and they are presented in Fig. 3 as a function of composition. The increase in intensity with filler content supports our assumption that the silicates exfoliated only partially. The extent depends on filler content as shown by the nonlinear composition dependence. The clay treated with aliphatic amine seems to exfoliate better, since its scattering intensity is significantly lower in the composite than that of the filler coated with the ω -amino acid. However, we must be aware of the fact that the scattering intensity depends on a lot of factors, including composition, orientation and regularity of the layers; thus the quantitative evaluation of XRD patterns is difficult.

Layered silicates were shown to nucleate PA and to promote the formation of the γ modification of the polymer [4, 7, 15, 20]. Nucleation also influences the rate of crystallization and crystallinity, i.e. the morphology of the polymer matrix changes considerably as a result of the introduction of the silicate. Similar phenomena were also detected in polypropylene and a study proved that organophilization decreased the nucleating effect of the clay owing to changes in particle and gallery structure [24, 25]. Nucleation depends on surface energetics and topology; thus, changes in either lead to a modification of the crystallization process and the structure of the polymer. The crystallization temperature of PA is presented as a function of composition in Fig. 4. The nontreated silicate does not change the nucleation of the polymer or it has a slight nucleating effect at most. On the other hand, the crystallization temperature decreases considerably in the presence of the two organophilic clays, the effect being stronger for the filler treated with

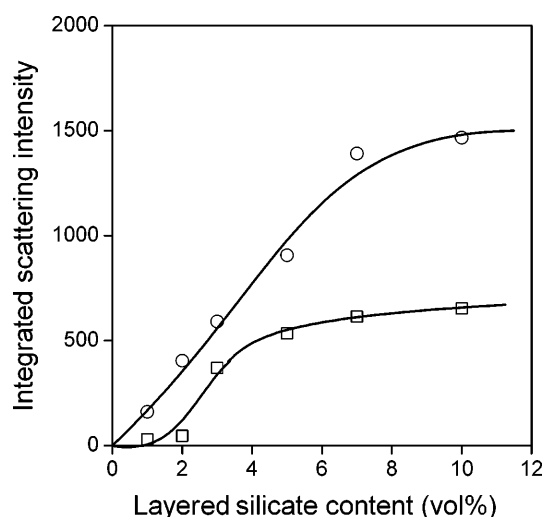


Fig. 3 Effect of the type of the treatment and the filler content on the intensity of the XRD scattering peak characterizing the clay. Changing extent of exfoliation. Amino acid (circles), aliphatic amine (squares)

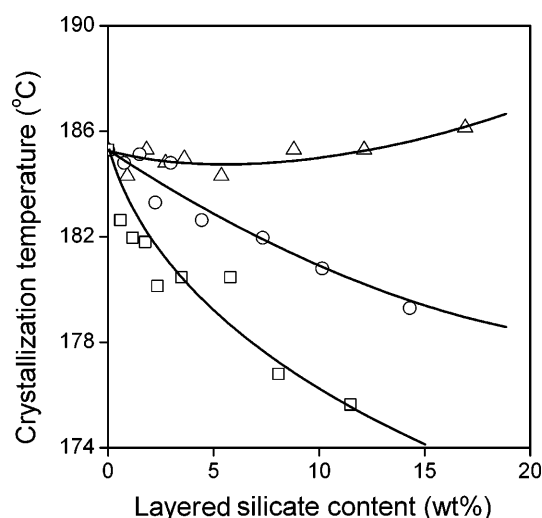


Fig. 4 Influence of organophilization and filler content on the crystallization peak temperature of polyamide (PA). Nontreated (triangles), amino acid (circles), aliphatic amine (squares)

the aliphatic amine than for the one coated with the amino acid. The decrease can be explained by confinement, decreasing surface energy, changing particle morphology, etc.; further study is needed to explain the observation unambiguously. The different extent of exfoliation also shown by Fig. 3 and changing interaction are definitely factors to be taken into account; thus, we may conclude that they considerably influence the structure and, therefore, also the properties of layered silicate nanocomposites.

Properties

Changes in stiffness are often used to draw conclusions about the structure of nanocomposites, the degree of intercalation and component interaction. On the other hand, the modulus should depend on interaction only slightly since it is measured at very low, principally zero, deformation. As a consequence, decreased mobility of the chains should have only a slight influence on the measured property [34]. Moreover, in heterogeneous polymer systems, interfaces may separate under the effect of an external load, a fact often neglected during the evaluation of mechanical properties. Debonding leads to a three-component system containing voids, which has a decreased modulus. The Young's modulus of the three sets of composites is presented in Fig. 5. Amino acid treatment increases stiffness considerably, while coating the clay with the aliphatic amine decreases it compared to the nontreated silicate. XRD indicated a larger extent of exfoliation for the clay treated with the aliphatic amine; thus, the most probable reason for the relative changes in the modulus is the different interaction of the

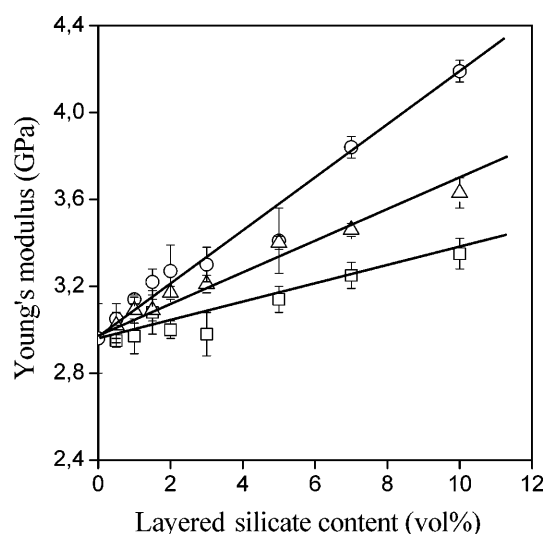


Fig. 5 Composition dependence of the stiffness of PA composites. Effect of the chemical structure of the coating agent. The symbols are the same as in Fig. 4

components. Both decreased mobility, in the case of the aliphatic acid treated filler, or debonding leads to the modification of stiffness. The overall crystallinity and the polymorphic composition of the matrix do not differ significantly enough in the three sets of composites to warrant such differences in stiffness. We must assume that the orientation of the particles is also approximately the same, since sample preparation occurred under the same conditions. Practically the same relationships are reflected in Fig. 6, in which the heat deflection of the composites is plotted against filler content. Both sets of results indicate that interfacial interactions play an

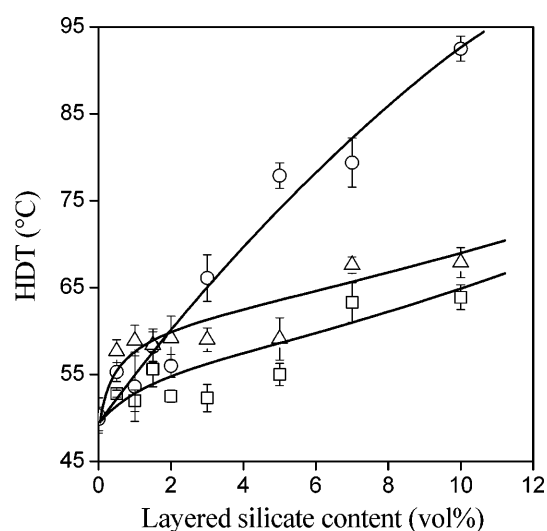


Fig. 6 Effect of the type of treatment and the filler content on the heat deflection temperature (HDT) of PA composites. The symbols are the same as in Fig. 4

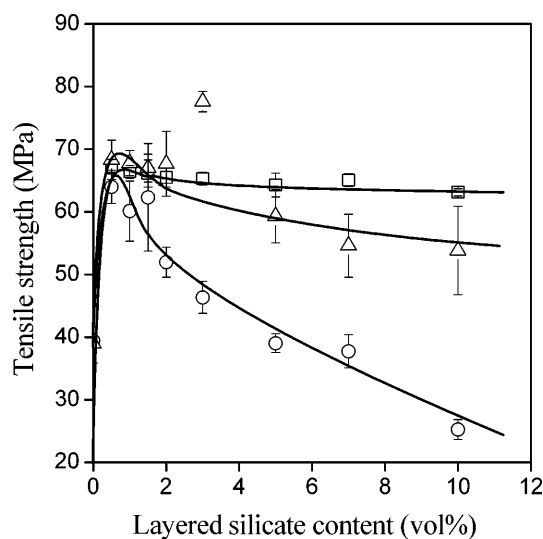


Fig. 7 Variation in the tensile strength of PA composites as a function of the filler content and the type of surface coating, respectively. The symbols are the same as those in Fig. 4

important role in the determination of composite properties.

This statement is strongly corroborated by Fig. 7, which presents the composition dependence of the tensile strength. Composite strength is determined by the relative load-bearing capacity of the components, as well as by failure initiation and propagation [35, 36]. Stress transfer depends on the size of the interacting surfaces and on the strength of the interaction [36]. The former is determined by exfoliation, while the latter by adhesion and the type of coating. The amino acid treated filler might have exfoliated to a lesser extent, but it is attached to the matrix firmly by covalent bonds. Decreased mobility of the chains leads to increased stiffness and larger sensitivity to failure initiation and the strength decreases rapidly with increasing filler content. The surface energy of the nontreated filler is high; thus, adhesion as well as the anisotropy of the particles lead to reinforcement. Increased filler content decreases the strength because of increasing stiffness, debonding and changing orientation. Although the interacting surfaces might be largest in composites containing the particles coated with the aliphatic amine, interfacial interaction is weakest in this composite. The combined effect of a large surface and weak interaction leads to the composition dependence shown in Fig. 7. The importance of interfacial interactions is further emphasized by the relations presented in Fig. 8. The figure shows the effect of treatment and filler content on the impact resistance of the composites. Impact strength decreases drastically for composites containing the bentonite covered by the amino acid, but less significantly for the nontreated filler, and improves considerably in the presence of the silicate coated with the aliphatic amine. Neither changing

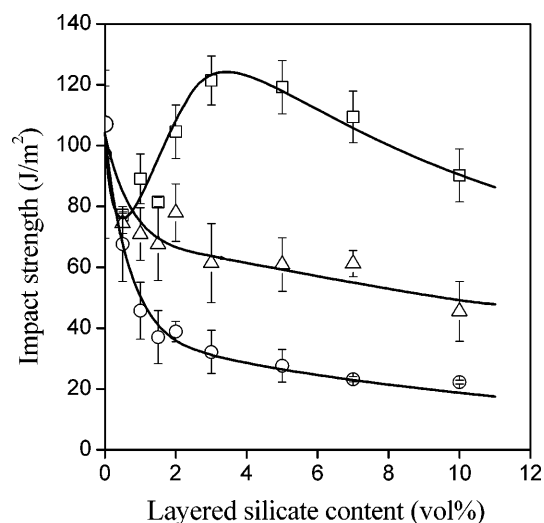


Fig. 8 Drastic differences in the impact resistance of PA composites as an effect of surface coating and composition. The symbols are the same as in Fig. 4

crystalline morphology nor different exfoliation justify such drastic changes in composite properties. The only reasonable explanation is offered by the effect of interaction; changing interfacial adhesion leads to different micromechanical deformation processes and energy absorption. Weak adhesion caused by the treatment with the apolar compound leads to increased debonding, which consumes energy and increases the impact resistance. The extent of debonding is much smaller in the composite containing the nontreated filler with high surface energy, while the attachment of the matrix to the filler through covalent bonds completely eliminates this process.

Discussion

The experimental results showed that the presence of the layered silicate considerably modified the structure and all the properties of PA. In the previous sections numerous factors were mentioned, all of which influence composite properties to a lesser or a greater extent. Since more than one factor changes simultaneously, the identification of the determining one is difficult. The extent of exfoliation, dispersion of the silicate layer, gallery structure, crystallinity and crystal modification, orientation of the silicate layers, skin-core structure and interfacial interactions all play a role in the determination of composite properties. Although on the basis of the available information we cannot define the effect of the previously mentioned factors on the properties quantitatively, we may draw conclusions about their influence by the thorough consideration of experimental data and other available information.

The crystalline structure of the polymer changes considerably in the presence of the silicate and all changes depend on the bentonite content. However, the relative amount of γ modification and the crystallinity change the same way in the presence of the two organophilic silicates used in this study; the nontreated filler behaves somewhat differently. The only dissimilar effect appears in the nucleation of the composites; a lower crystallization temperature results in thinner lamellae and a softer matrix. This could explain the smaller modulus of the composite containing the filler coated with the aliphatic amine, but this small effect does not justify the drastic differences in other mechanical properties. Changing the crystalline structure does not seem to be the factor determining the properties of the nanocomposites studied.

The extent of exfoliation, dispersion, gallery structure and orientation of the filler also influence composite properties. The XRD patterns presented in Figs. 1 and 2 indicate considerable, but not complete, exfoliation, which is further supported by Fig. 3. Moreover, this latter figure indicates better delamination of the filler coated with the aliphatic amine than for that treated with the amino acid. This observation leads to two conclusions: exfoliation depends mainly on treatment, but properties depend also on other factors. The exact degree of exfoliation and the difference in it in the two sets of composites is difficult to judge, since the quantitative evaluation of the XRD patterns is rather uncertain. We assume that considerable exfoliation takes place during processing and that the different behavior of the two sets of composites is not determined by its extent. The orientation of the particles takes place during processing as shown both by the XRD patterns and by the composition dependence of the properties, but we assume that it is similar in the three sets of composites owing identical processing conditions.

All the experimental results indicate the dominating role of interfacial interactions in the determination of composite properties. In the previous section we enumerated the results supporting this statement. Interfacial interactions can be estimated quantitatively by a simple model developed for the description of the composition dependence of composite properties [35, 36]. The evaluation of mechanical properties according to the model leads to a parameter (B), which is proportional to the effective load-bearing capacity of the dispersed phase. Since the model assumes the homogeneous dispersion of the second phase in the matrix, it also gives information about the effect of structural factors, like orientation and aggregation. Since the model has been described elsewhere [35, 36], we omit its detailed discussion here. The tensile strength of the PA composites is plotted in the linear representation suggested by the model in Fig. 9. Plotting reduced strength as a function of filler content (ϕ) should yield straight lines, the slope of which is

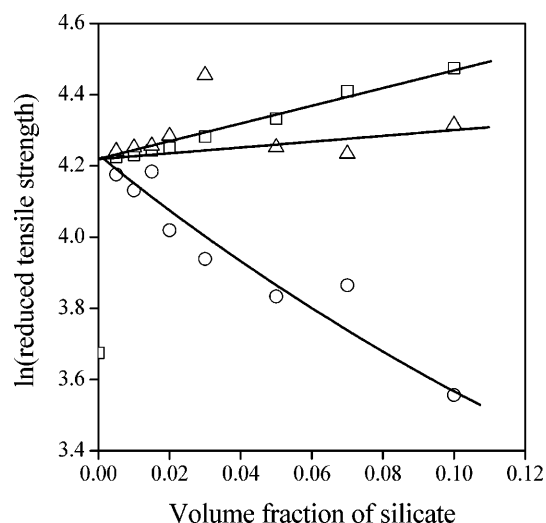


Fig. 9 Effect of interfacial interactions on the strength and deformation mechanism of PA nanocomposites. Reinforcement and failure initiation. The symbols are the same as in Fig. 4

proportional to the load-bearing capacity of the dispersed phase. In the absence of other effects this is directly related to interfacial adhesion [36, 37, 38]. Figure 9 presents a strange picture. The intersection of all three correlations differs considerably from the reduced strength of the neat polymer. The effect can be caused by the orientation of the dispersed phase [39] or by a change in the deformation mechanism [35]. Consideration of all properties, including elongation at break, indicates that the shift in the intersection is caused by the orientation of the particles. Moreover, its very similar value corroborates our assumption that orientation is similar for all three fillers. The reduced strength values fall on a perfectly straight line for the nanocomposite containing the silicate treated with the aliphatic amine, which indicates good dispersion and the validity of the model. The combined effect of the size of the interfacial area, which is large, and the strength of interaction, which is weak, determines the slope of the line. The large interface of the exfoliated clay results in a moderate reinforcing effect of this silicate in spite of the weak interaction. The smaller slope of the nontreated filler and the large scatter of the points are caused by the relatively small surface area of the particles and their possibly inhomogeneous dispersion. In principle the $\ln \sigma_{red}$ versus ϕ correlation cannot have a negative slope and the result obtained for the silicate treated with the amino acid clearly supports our earlier statement that strong interaction leads to a change in the deformation mechanism. High stiffness and low mobility of the polymer chains attached to the clay surface result in brittle fracture and the role of failure initiation becomes dominating. These considerations clearly prove that interfacial interaction is one of the most important factors determining the properties of layered silicate

nanocomposites and much more attention must be paid to it than before.

Conclusions

The results obtained on two sets of PA nanocomposites containing silicates with different organophilization confirmed published results that layered silicates promote the formation of the γ modification of PA. Partial exfoliation was achieved with both fillers, the extent of which differed slightly in the two cases. The mechanical properties of the composites depend very much on the type of organic compound used for the treatment of the silicate. Stiffness and heat deflection temperatures increased with composition, the tensile strength increased compared to the neat polymer, but its composition dependence was completely different in the two cases. Deformability decreased with increasing filler content, while the composition dependence of the impact resistance was very dissimilar in composites containing

the two organophilized silicates and the nontreated filler. The impact strength decreased with filler content for the filler coated with the amino acid and also for the nontreated filler, while it showed extremes in its composition dependence for composites containing the silicate covered by the aliphatic amine. An analysis of the results proved that although many factors change both with the type of treatment and with the filler content, the dominating factor determining composite properties is interfacial interaction. Changing the interaction determines the micromechanical deformation processes and the overall performance of the composites. Although the explanation given satisfies all the results, some of the statements need further study and confirmation.

Acknowledgements The authors greatly appreciate the help of István Sajó in the execution and evaluation of the XRD measurements. The National Fund for Scientific Research (OTKA T 30579) and the Varga József Fund of the Faculty of Chemical Engineering at the Budapest University of Technology and Economics are greatly appreciated for financial support of the research.

References

- Usuki A, Kojima Y, Kawasumi M, Okada A, Fukushima Y, Kurauchi T, Kamigaito O (1993) *J Mater Res* 8:1179–1184
- Kojima Y, Usuki A, Kawasumi M, Okada A, Fukushima Y, Kurauchi T, Kamigaito O (1993) *J Mater Res* 8:1185–1189
- Okada A, Usuki A (1995) *Mater Sci Eng C* 3:109–119
- Wu TM, Liao CS (2000) *Macromol Chem Phys* 201:2820–2825
- Varlot K, Reynaud E, Kloppfer MH, Vigier G, Varlet J (2001) *J Polym Sci Part B Phys* 39:1360–1370
- Medellin-Rodriguez FJ, Burger C, Hsiao BS, Chu B, Vaia R, Phillips S (2001) *Polymer* 42:9015–9023
- Lincoln DM, Vaia RA, Wang ZG, Hsiao BS, Krishnamoorti R (2001) *Polymer* 42:9975–9985
- Yang F, Ou Y, Yu Z (1998) *J Appl Polym Sci* 69:355–361
- Masenelli-Varlot K, Reynaud E, Vigier G, Varlet J (2002) *J Polym Sci Part B Phys* 40:171–283
- Liu L, Qi Z, Zhu X (1999) *J Appl Polym Sci* 71:1133–1138
- Fornes TD, Yoon PJ, Keskkula H, Paul DR (2001) *Polymer* 42:9929–9940
- Wu TM, Chen EC, Liao CS (2002) *Polym Eng Sci* 42:1141–1150
- Ji XL, Jing JK, Jiang W, Jiang BZ (2002) *Polym Eng Sci* 42:983–993
- Shelley JS, Mathet PT, DeVries KL (2001) *Polymer* 42:5849–5858
- Liu X, Wu Q (2002) *Eur Polym J* 38:1383–1389
- LeBaron PC, Wang Z, Pinnavaia TJ (1999) *Appl Clay Sci* 15:11–29
- Vaia RA, Price G, Ruth PN, Nguyen HT, Lichtenhan J (1999) *Appl Clay Sci* 15:67–92
- Cheng LP, Lin DJ, Yang KC (2000) *J Membr Sci* 172:157–166
- Alexandre M, Dubois P (2000) *Mater Sci Eng* 28:1–63
- Vasanthan N, Murthy NS, Bray RG (1998) *Macromolecules* 31:8433–8435
- Krishnamoorti R, Yurekli K (2001) *Curr Opin Colloid Interface Sci* 6:464–470
- Shelley JS, DeVries KL (2002) *Exp Mech* 42:178–181
- Liu LX, Wu QJ, Zhang QX, Mo ZS (2002) *Polym Bull* 48:381–387
- Pozsgay A, Papp L, Fráter T, Pukánszky B (2001) *Prog Colloid Polym Sci* 117:120–125
- Pozsgay A, Fráter T, Papp L, Sajó I, Pukánszky B (2002) *J Macromol Sci Part B Phys* 41:1249–1265
- Pozsgay A, Fráter T, Százd L, Müller P, Sajó I, Pukánszky B (2003) *Eur Polym J* 40:27–36
- Dékány I, Szántó F, Nagy LG (1985) *J Colloid Interface Sci* 103:321
- Dékány I, Szántó F, Weiss A, Lagaly G (1985) *Ber Bunsenges Phys Chem* 89:62–67
- Dékány I, Szántó F, Nagy LG (1986) *J Colloid Interface Sci* 109:376
- Dékány I, Szántó F, Nagy LG (1988) *J Colloid Interface Sci* 266:82–96
- Patzkó Á, Dékány I (1993) *Colloids Surf A* 71:299–307
- Lagaly G, Weiss A (1971) *Kolloid Z Z Polym* 243:48–55
- Lagaly G, Weiss A (1971) *Kolloid Z Z Polym* 248:968
- Pukánszky B (1995) In: Karger-Kocsis J (ed) *Polypropylene: structure, blends and composites*, vol 3. Chapman and Hall, London pp 1–70
- Pukánszky B (1990) *Composites* 21:255–262
- Pukánszky B, Turcsányi B, Tüdös F (1988) In: Ishida H (ed) *Interfaces in polymer, ceramic, and metal matrix composites*. Elsevier, New York, pp 467–477
- Pukánszky B, Fekete E, Tüdös F (1989) *Makromol Chem Macromol Symp* 28:165–186
- Demjén Z, Pukánszky B, Nagy J (1998) *Composites* 29A:323–329
- Pukánszky B, Belina K, Rockenbauer A, Maurer FHJ (1994) *Composites* 25:205–215

Katalin Sinkó
Anna Neményi

Effect of Al- and Si-containing precursors on the structures formed by sol–gel methods

Abstract The main aim of the present work was to study the effect of various Al- and Si-containing precursors on the gel structures prepared by sol–gel methods. The purpose of the investigations of the effect of aluminum nitrate, chloride, and isopropoxide was to form a homogeneous aluminosilicate gel structure with high Al incorporation and to get optically clear, bulk gel samples. The selection of aluminum acetate and sodium metasilicate has been realized considering the point of view of environmental protection and industry. The chemical bond systems have been investigated by ^{27}Al and ^{29}Si (cross-polarization) magic-angle spinning nuclear magnetic resonance spectroscopy and

Fourier transform IR spectroscopy. Small-angle X-ray scattering measurements were used for the study of supramolecular structures. The high Al content and the special structure of the samples provide the aluminosilicate systems prepared by new sol–gel methods with new, unique properties (e.g. piezoelectricity, high porosity, low density, and low thermal conductivity) that are not obtainable with conventional Al- and Si-containing ceramics or glasses.

Keywords Sol–gel method · Al- and Si-containing precursors · Small-angle X-ray scattering · Al and Si magic-angle-spinning nuclear magnetic resonance

K. Sinkó (✉) · A. Neményi
Department of Inorganic Analytical
Chemistry, L. Eötvös University,
1117 Budapest, Hungary
e-mail: sinkokata@ludens.elte.hu
Tel.: +36-12090555
Fax: +36-1-2090602

Introduction

Aluminosilicate amorphous materials as porous ceramics with high surface areas and small pore sizes may be exploited in applications such as filtration, separation, catalysis, and chromatography [1]. Aluminosilicate aerogels may be used to produce highly efficient catalysts owing to their high surface area and chemical reactivity [2, 3, 4]. Coatings represent the most current commercial application of sol–gel technology. The aluminosilicate coatings provide the substrates with greater mechanical strength and with greater electric and thermal insulating properties [5, 6]. By applying the sol–gel technique, aluminosilicate fibers can be drawn [7, 8].

The purpose of the present work was to prepare homogeneous aluminosilicate systems with as high as

possible aluminum content, i.e. higher aluminum content than can be achieved by traditional high-temperature melting methods. (This value is about 10% in a conventional glass or ceramic product. Above 10% Al content, phase separation occurs during cooling [9, 10, 11].) In previous work, we prepared optically clear, homogeneous aluminosilicate gels in one step from tetraethoxysilane (TEOS) and aluminum nitrate $[\text{Al}(\text{NO}_3)_3 \cdot 9\text{H}_2\text{O}]$ in an organic medium at 80 °C [12, 13]. Using this preparation method, a 0.53 molar ratio of bonded $\text{Al}/(\text{Si} + \text{Al})$ could be achieved as the highest incorporated aluminum amount in the homogeneous gel structures. The xerogels and aerogels prepared by normal or supercritical drying from the aluminosilicate alcogels or hydrogels show significant piezoelectric properties [14]

and porosity controllable and variable over a wide range.

The influence of the various Al- and Si-containing starting materials was studied in this work on the structure obtained by the sol-gel process. The selection of aluminum nitrate and aluminum chloride ($\text{AlCl}_3 \cdot 6\text{H}_2\text{O}$) as inorganic Al precursors was motivated by their low price, good chemical resistance in air, solubility in alcohols, and their controllable hydrolysis. Aluminum isopropoxide is the most often applied Al precursor according to the sol-gel literature [1]. Aluminum isopropoxide provided a reference for the evaluation of the research data. The other representative of organic Al precursors was aluminum acetate $[\text{Al}(\text{OH})(\text{OOCCH}_3)_2]$ and was applied regarding the point of view of environmental protection. The use of sodium silicate (commercial water glass solution) was supported by its low price.

Experimental

Gel preparation

Preparation from aluminum isopropoxide and TEOS

Owing to the very fast hydrolysis of aluminum isopropoxide, TEOS should be dissolved separately and prehydrolyzed in ethanol at 75 °C. The time of prehydrolysis was varied from 0 to 3 h. Aluminum isopropoxide $[\text{Al}(\text{OCHCH}_3\text{CH}_3)_3]$ and H_2O were added to the solution of TEOS. A homogeneous, optically clear gel formed in a few minutes at 60 °C. (The molar ratios applied were $\text{Al}/\text{Si}=1$, $\text{ethanol}/\text{Si}=25$, and $\text{H}_2\text{O}/\text{Si}=6$.)

Preparation from inorganic Al salts and TEOS

TEOS and aluminum nitrate (or aluminum chloride) were dissolved in 1-propanol and heated with reflux at about 80 °C to obtain clear homogeneous gels. The compositions used in these experiments were 1 mol TEOS, 1 mol aluminum nitrate, 6 or 20 mol 1-propanol, and 0–100 mol water. The gelation was performed by applying reflux for 10–11 h. In a closed system this same process took 20–22 h at 80 °C [12].

Preparation from basic aluminum acetate and TEOS

The application of aluminum acetate in a sol-gel process is a difficult task owing to its poor dissolution in water or alcohols. Basic aluminum acetate can be dissolved only in strongly acidic ($\text{pH} \leq 1$) or basic ($\text{pH} \geq 11$) media. The required pH values were obtained with solutions of HNO_3 , HClO_4 , or NaOH . At $\text{pH} \approx 1$, an optically clear, homogeneous gel sample formed in 24 h at 75 °C, after being mixed with an alcoholic solution of TEOS (molar ratio $\text{Al}/\text{Si}=1$, $\text{ethanol}/\text{Si}=20$). While at $\text{pH} \approx 11$, strongly opaque but homogeneous hybrid gels occurred in a few minutes even at 25 °C.

Preparation from sodium silicate and aluminum nitrate

The 45 wt/wt% commercial solution of water glass must be diluted in order to avoid the phase separation caused by addition

of aluminum nitrate (aluminum nitrate hydrolyzes acidic). An acidic solution ($\text{pH} \approx 1$) of around 4 w/w% is needed in order to get a clear solution of sodium silicate and aluminum nitrate (molar ratio of $\text{Al}/\text{Si}=1$, $\text{HNO}_3/\text{Si}=0.8$). After the evaporation of surplus solvent, gels formed in 24 h even at 25 °C. On decreasing the acidity by addition of NaOH solution (up to pH 3 and 5), a considerably opaque gel sample was obtained at 75 °C.

Drying processes of alcogels and hydrogels

The wet gels can be dried under ambient or supercritical pressure to obtain xerogels or aerogels, respectively. Using a very slow drying process under ambient pressure, compact, optically clear, glasslike, bulk samples formed without any cracks or with small cracks. A faster drying method resulted in broken samples. The wet gels were also dried under supercritical conditions. After washing with methanol, the gels were washed with liquid carbon dioxide for 2–3 days at 284 K, 6.0–7.0 MPa. After completion of the solvent-exchange process, the temperature in the autoclave was gradually raised to 313 K, while the pressure was kept at 10 MPa. Opaque, fragile aerogel samples were obtained.

Characterization methods

^{27}Al and ^{29}Si magic-angle-spinning (MAS) NMR measurements were performed at room temperature, using a BRUKER AVANCE DRX-500 NMR spectrometer (11.70 T). A 52-mm BB{1H} cross-polarization (CP)/MAS probehead was employed with a 7- and 4-mm $\text{ZrO}_2/\text{Kel-F}$ rotor. In the case of ^{27}Al measurements, after a 1- μs X pulse (the flip angle was about 16° for the major contribution of the $(1/2, -1/2)$ transition in the observed centerband and the well-determined signal response to the radio-frequency pulse) 4,096 data points were acquired in 31 ms, followed by 1-s relaxation delay. 128 fast induction decays were accumulated. The typical spectral width was 65,360 Hz (501 ppm), the line broadening parameter was 50 Hz, and each real spectrum comprised 2,048 data points. All NMR spectra were recorded at MAS conditions to reduce the nuclear quadrupolar interactions to the second-order quadrupole shift level. The spinning speed was 12 kHz. The ^{27}Al chemical shifts were recorded with respect to $\text{Al}(\text{H}_2\text{O})_6^{3+}$ as an external reference. In the case of ^{29}Si measurements, after a 3.5- μs X pulse (the flip angle was about 47°) data points were acquired for 65 ms, followed by 30-s relaxation delay. The typical spectral width was 29,762 Hz (299.5 ppm), the line broadening parameter was 30 and 100 Hz, and each real spectrum comprised 4,096 data points. The spinning speed was 5 kHz.

The IR spectra were recorded with a BRUKER IFS 55 FT-IR spectrometer over the range 400–4000 cm^{-1} using the standard KBr method.

For the small-angle X-ray scattering (SAXS) measurements, we used a 12-kW X-ray generator and a pinhole X-ray camera with variable distances from the sample to the two-dimensional detector (20.5–98.5 cm). The gels were covered in vacuum-tight foil to prevent drying during the measurements. The two-dimensional spectra were corrected for parasitic pinhole scattering, as well as for the foil scattering, and were then radially averaged to obtain the scattered intensity, $I(q)$, as a function of the scattering vector,

$$q = 4\pi \sin \theta / \lambda, \quad (1)$$

where λ is the incident X-ray wavelength (1.54 Å) and 2θ is the scattering angle between the incident and diffracted beams. The curves were interpreted on the basis of the Guinier law and the fractal theory [15, 16].

Results

^{27}Al and ^{29}Si MAS NMR Spectroscopy

The evaluation of ^{29}Si (CP) MAS NMR for gel samples is not a routine task. We made a distinction between the bonds of $\text{Si}-\text{O}-\text{Al}_{\text{tetrahedron}}$ and $\text{Si}-\text{O}-\text{Al}_{\text{octahedron}}$ using our NMR measurements and the NMR literature. The peak of the Al atoms bonded tetrahedrally in the silica network can be identified at about -105 ppm (Fig. 1). This peak is missing on the curve for pure silica gel. According to the literature the signal of $\text{Si}(\text{OSi})_4$ appears at about -110 ppm [17, 18]. Changing the group of OSi for OH or for OAl groups causes shifts of -10 and -5 ppm, respectively [19]. The signal of octahedrally bonded Al atoms can be associated with the peak at about -90 ppm. However, the peak of $\text{Si}(\text{OSi})_2(\text{OH})_2$ can also be found at about -90 ppm [17]. The establishment of the NMR data for the octahedral Al atoms can be proved by the Si NMR data for layer silicates (kaolinite and montmorillonite). In the Si NMR spectra for layer silicates, the signal of Si bonds can be observed at -92 to -93 ppm. As is well known, the Si atoms in the layer silicates are connected to one or two octahedral Al atoms, through oxygen atoms. Using the CP technique, the signals of the bonds with a lot of hydrogen atoms in their surroundings increase strongly, and the peaks of $\text{Si}(\text{OSi})_4$ and $\text{Si}(\text{OSi})_3(\text{OAl})$ decrease. The greatest number of OH groups could be detected by NMR in the samples prepared from aluminum isopropoxide. The Si NMR data for aluminosilicate samples prepared from aluminum acetate or sodium silicate in an acidic medium show a negligible number of bonded Al atoms in the gel networks. The NMR curves verify the considerably higher Al incorporation into the silica structure in the cases of aluminum isopropoxide and nitrate precursors.

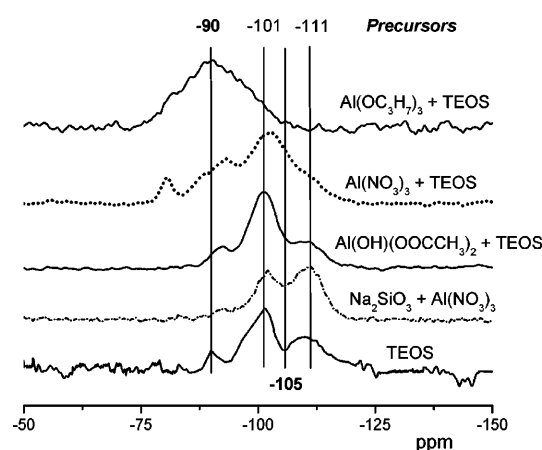


Fig. 1 ^{29}Si cross-polarization (CP) magic-angle-spinning (MAS) NMR curves for aluminosilicate and silica alcogels and hydrogels prepared from various precursors in acidic media

The results of Si NMR can be well proved by Al NMR spectra (Fig. 2). The shoulder at about 4 ppm and the peak at about 55 ppm indicate the octahedrally and tetrahedrally bonded Al atoms, respectively. The data for Al incorporation in the gel networks are presented in Table 1. The data were calculated by deconvolutions with Lorentz curves from Al NMR data and were checked by measurements of the Al concentration in the solution resulting from a washing step of the gel samples with water.

Of the parameters investigated the prehydrolysis time of TEOS influenced most intensively the bond systems. The rate of the tetrahedrally bonded Al atoms decreased as a result of the longer prehydrolysis time (Table 2) and the condensation reaction of Si atoms became more characteristic. The Si NMR measurements showed that the peak of $\text{Si}(\text{OSi})_3(\text{OH})$ at about -100 ppm increases (Fig. 3).

A significant difference can be found in the structure of the samples prepared from aluminum acetate in acidic and basic conditions. (Basic aluminum acetate can be dissolved only in strongly acidic, $\text{pH} \leq 1$, or basic, $\text{pH} \geq 11$, aqueous solutions.) Under acidic conditions, the Al incorporation is very low; however, at $\text{pH} \geq 11$, all the Al is tetrahedrally bonded in the gel structure (Fig. 4). The Si NMR curve also indicates a special structure for the gel sample obtained in basic solution (Fig. 5). Only a wide peak can be observed at -85 ppm and this belongs to the bond of $\text{Si}(\text{OSi})_{0-2}(\text{OAl})_{2-4}$ [19]. The peaks of $\text{Si}(\text{OSi})_4$ and $\text{Si}(\text{OSi})_3(\text{OH})$ are missing, hence proving the high Al incorporation and a compact structure of large particles.

The samples prepared from water glass and aluminum nitrate also prove the dependence of Al incorporation on the pH of the gelling solutions. The acidic medium

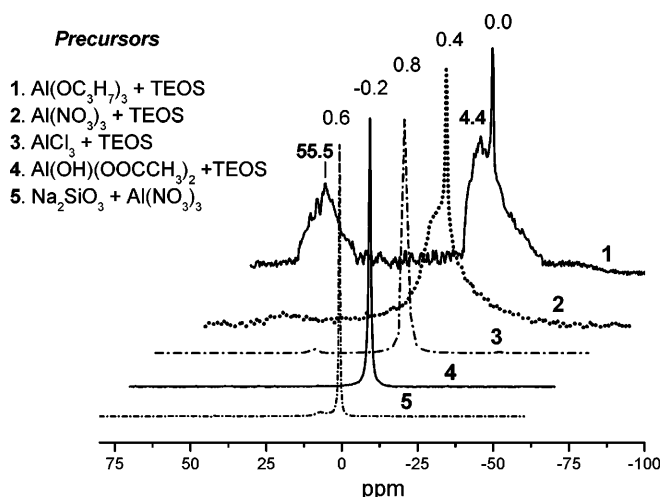


Fig. 2 ^{27}Al MAS NMR spectra for aluminosilicate alcogels and hydrogels prepared from various precursors in acidic media. The x-axis is shifted by about -10 ppm

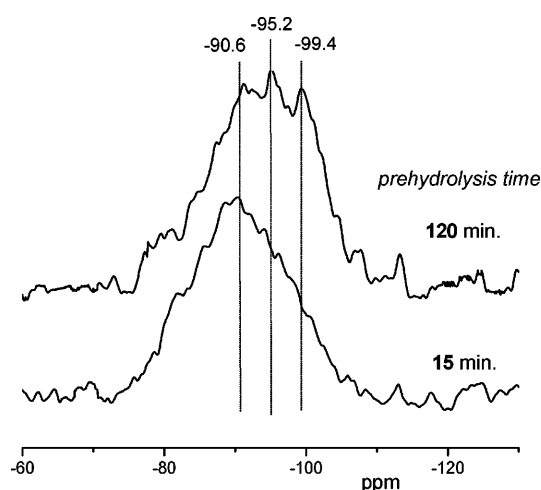
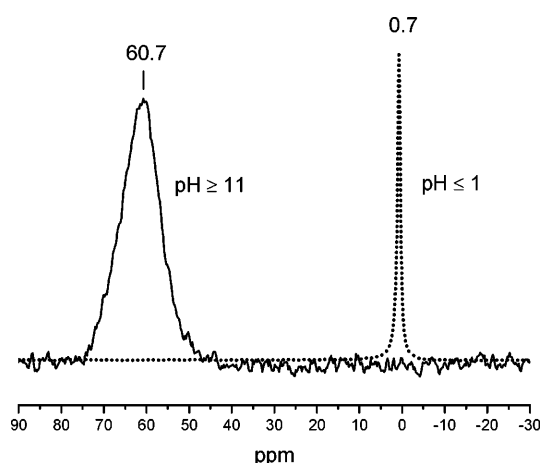
Table 1 Al content of hydrogels and alcogels prepared from various precursors

Precursors	Nonbonded Al ions (≈ 0 ppm) (%)	Octahedrally bonded Al (4–5 ppm) (%)	Tetrahedrally bonded Al (50–55 ppm) (%)
$\text{Al}(\text{OC}_3\text{H}_7)_3$	5–20 ^a	45–60 ^a	25–40 ^a
$\text{Al}(\text{NO}_3)_3$	25–55 ^a	40–65 ^a	2–5 ^a
AlCl_3	95–100	0–5	–
$\text{Al}(\text{OH})(\text{Ac})_2$ pH ≤ 1	98–100	0–2	–
Na_2SiO_3 pH ≤ 1	98–100	0–2	–

^a The values depend on the preparation conditions

Table 2 Al content of alcogels prepared from aluminum isopropoxide with different prehydrolysis times

Prehydrolysis time of tetraethoxysilane (min)	Nonbonded Al ions (≈ 0 ppm) (%)	Octahedrally bonded Al (4–5 ppm) (%)	Tetrahedrally bonded Al (50–55 ppm) (%)
15	7 ± 3	55 ± 10	38 ± 5
120	$15 \pm 3\%$	60 ± 10	25 ± 5

**Fig. 3** ^{29}Si CP MAS NMR curves for aluminosilicate alcogels prepared from aluminum isopropoxide with different prehydrolysis times of tetraethoxysilane (TEOS)**Fig. 4** ^{27}Al MAS NMR spectra for aluminosilicate hydrogels prepared from aluminum acetate in media of various pH

considerably hinders the condensation reactions of Al atoms (Table 3). This effect could be experienced using any precursor. Si MAS NMR measurements also indicate a difference in the number of Al atoms bonded in the silica network (Fig. 6). The NMR signals at about -105 and -95 ppm are missing on the curve for the sample prepared at pH 1, while the unambiguous presence of these peaks can be observed on the other curve of pH 5, proving the greater Al incorporation.

IR spectroscopy (Fourier transform IR)

The results of IR measurements supported the NMR data. The IR spectra of samples produced from aluminum isopropoxide and nitrate are parallel to each other, verifying their very similar bond systems (Fig. 7). Only the vibrational bands at $1,384\text{ cm}^{-1}$ assigned to nitrate ions show a little difference in the intensity owing to the lower nitrate (HNO_3) content of the sample obtained from isopropoxide. The stretching vibrational band for

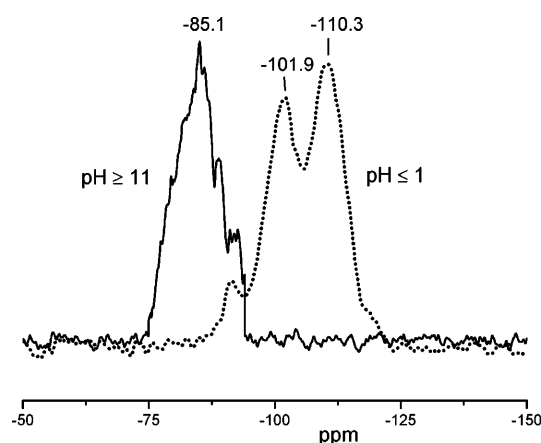
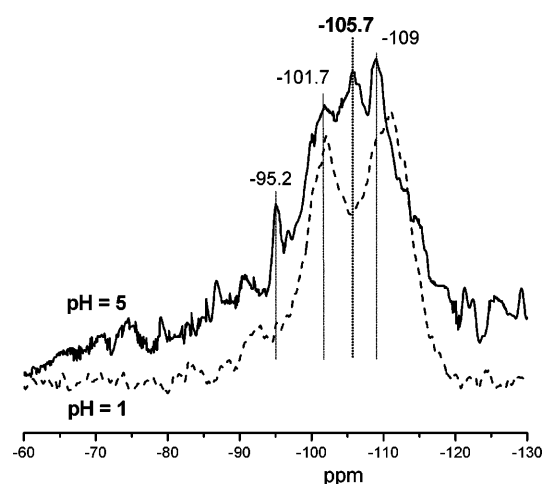
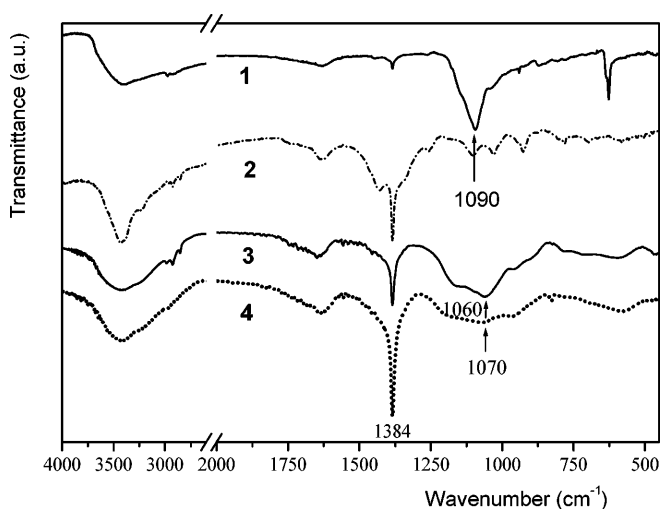
**Fig. 5** ^{29}Si CP MAS NMR curves for aluminosilicate hydrogels prepared from aluminum acetate in media of various pH

Table 3 Al content of hydrogels prepared from water glass in media of different pH

pH of medium	Nonbonded Al ions (≈ 0 ppm) (%)	Octahedrally bonded Al (4–5 ppm) (%)	Tetrahedrally bonded Al (50–55 ppm) (%)
1	99 ± 1	1 ± 1	–
3	93 ± 7	3 ± 1	4 ± 2
5	70 ± 7	18 ± 5	12 ± 5

**Fig. 6** ^{29}Si CP MAS NMR curves for aluminosilicate hydrogels prepared from sodium metasilicate in media of different pH**Fig. 7** IR spectra for aluminosilicate alcogels and hydrogels prepared from various precursors in acidic media. $\text{Al}(\text{OH})(\text{OOCCH}_3)_2 + \text{TEOS}$ (1); $\text{Na}_2\text{SiO}_3 + \text{Al}(\text{NO}_3)_3$ (2); $\text{Al}(\text{OC}_3\text{H}_7)_3 + \text{TEOS}$ (3); $\text{Al}(\text{NO}_3)_3 + \text{TEOS}$ (4)

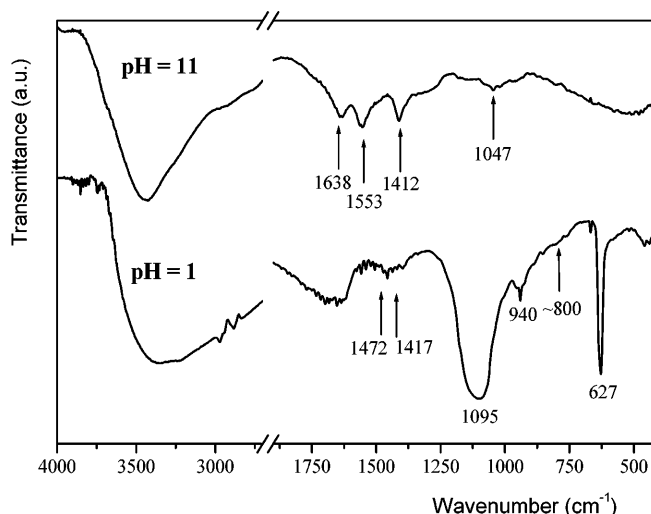
Si–O–Si at $1,090\text{ cm}^{-1}$ is shifted to lower wavenumbers ($1,060\text{--}1,070\text{ cm}^{-1}$) and is broadened by the presence of Si–O–Al bonds. Our measurements prove the dependence of the shift on the degree of Al incorporation. The greater the number of bonded Al atoms, the larger the

degree of the shift is (Fig. 7, Table 1). In the spectrum for the gel sample of water glass, the vibrational band at $1,090\text{ cm}^{-1}$ is shifted to $1,085$ and $1,078\text{ cm}^{-1}$ by increasing the pH from 1 to 3 and 5, respectively.

The IR spectra for samples prepared from aluminum acetate also show a significant difference in the function of pH (Fig. 8). The new absorption maximum at 627 cm^{-1} on the curve for the sample prepared in an acidic medium can be interpreted as Al–O stretching vibrations of condensed octahedral AlO_6 , which forms a separate phase from the silica network. The absorption band at 627 cm^{-1} disappears after washing the gel sample with water. The band of Si–O–Si can be found at $1,095\text{ cm}^{-1}$, similarly to that of pure silica gel. The IR spectrum of the sample obtained in basic conditions differs strongly from that for other aluminosilicate gel samples. The position of the peak for the Si–O–Al bond is at a low wavenumber, at $1,047\text{ cm}^{-1}$, corresponding to the Al NMR result, which indicates 100% Al incorporation. The vibrational bands at $1,412$ and $1,553\text{ cm}^{-1}$ can be associated with the acetate groups coordinated to Al atoms [20].

SAXS measurements

The scattering data of the gel samples formed from aluminum isopropoxide and nitrate correspond to each

**Fig. 8** IR spectra for aluminosilicate hydrogels prepared from aluminum acetate in media of various pH

other. The curves show a homogeneous gel structure in the range of SAXS (Fig. 9). These aluminosilicate alcogel samples can be characterized by a fractal structure. The linear region on the log-log plot with a slope of about -2.0 indicates a mass fractal. The gel structures obtained from aluminum isopropoxide or nitrate are very similar to that of pure silica alcogel. The incorporated Al atoms modify the elementary units rather than the fractal structure [13].

On the SAXS curves for samples of water glass, aluminum acetate, and aluminum chloride, broad distortions can be seen in the larger q ranges owing to the scattering of nonbonded Al ions. The nonbonded but partly hydrolyzed Al ions can form associates connected by weak hydrogen bonds. This assumption can be proved by a washing step. The nonbonded Al ions in weak associates can be removed by water. In the SAXS curve, the distortions are missing after the washing (Fig. 10). The associates hinder the formation of a fractal structure. After washing, the fractal character becomes dominant instead of the random structure (Fig. 10). On increasing the pH, the fractal network turns into a more compact structure. This structure is built up by aggregates rather than fractals. The scattering data show less homogeneity for the sample prepared in strongly basic medium (Fig. 10). The SAXS measurements gave the same results for the gel samples of sodium silicate.

Discussion

Aluminum isopropoxide

Aluminum isopropoxide as precursor of the sol-gel technology can be characterized by the following: homogeneous, optically clear gel samples can be

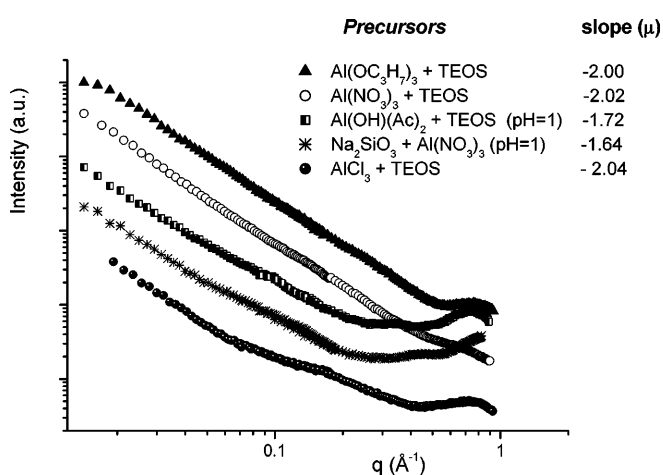


Fig. 9 Small-angle X-ray scattering (SAXS) curves for aluminosilicate alcogels and hydrogels prepared from various precursors in acidic media

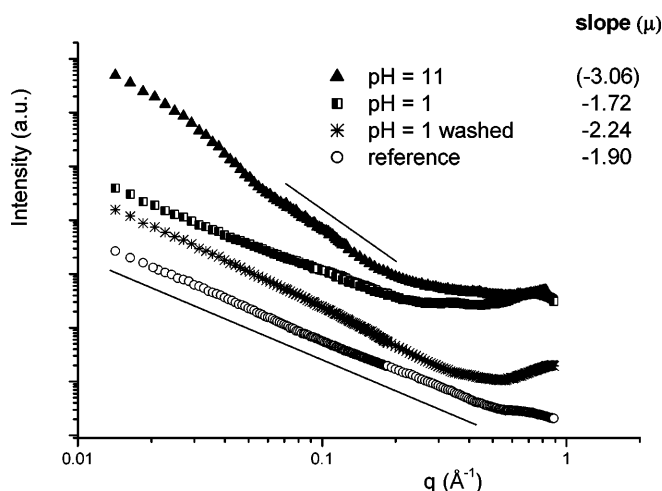


Fig. 10 SAXS curves for aluminosilicate hydrogels prepared from aluminum acetate in media of various pH. Silica alcogel provides as reference

obtained directly from an organic solution of aluminum isopropoxide and TEOS. The highest Al incorporation (70–90% of the Al content) could be achieved by the application of aluminum isopropoxide compared to the other Al precursors. Owing to the very fast hydrolysis of aluminum isopropoxide in an aqueous solution, TEOS should be prehydrolyzed in alcohol at 75 °C. The chemical composition and the time of prehydrolysis were optimized. Without prehydrolysis of TEOS, a homogeneous gel could not be obtained, because aluminum isopropoxide formed a separate phase. At a longer prehydrolysis time, Si-containing units formed and the Al atoms were incorporated on the surface of elementary units rather than in the inside. At shorter times the number of tetrahedrally bonded Al atoms increased in the inside of the units. Using 15 min, the highest Al incorporation could be detected. The prehydrolysis time regulates the Al incorporation. The optimal molar ratio of water-to-Si was 7. By using less water, the Al incorporation decreased, the surplus water (molar ratio of water/Si > 7) did not effect the bond system. Ethanol proved to be the best organic medium, while when using other alcohols the optical clearness of the gels was reduced.

The network obtained from aluminum isopropoxide can be characterized by a smaller degree of cross-linking. The NMR signal of $>\text{Si}(\text{OH})_2$ is the most intense (Fig. 1), however, the peak of $\equiv\text{Si}(\text{OH})$ is dominant in the curve for the pure silica network owing to the higher number of cross-linking connections. The condensation reactions of Si atoms become weaker in the presence of aluminum isopropoxide. The gel samples prepared from aluminum isopropoxide can be characterized by high porosity. (The Brunauer–Emmett–Teller specific surface area of aerogel prepared from isopropoxide is $832 \text{ m}^2 \text{ g}^{-1}$, while from nitrate it is $710 \text{ m}^2 \text{ g}^{-1}$.) This

looser structure containing a lot of OH groups results in faster aging of the gel network than can be observed in the gel sample obtained from aluminum nitrate.

Aluminum acetate

Environmental protection is the most important advantage of applying aluminum acetate as organic Al precursor. The acetate anions can escape as CO₂ and H₂O molecules during the heat treatment. An optically clear gel structure was obtained in a strongly acidic medium; however, the Al incorporation was negligible in the network. The structure is dominated by the silica network. The nonbonded Al ions form weak associates inserted in the silica network. Very high Al incorporation could be achieved in basic conditions, but the gel samples were strongly opaque owing to the larger aggregates, which build up the compact gel structure.

Inorganic Al salts

Aluminum sulfate cannot be used for gel preparation directly from solutions because of its very low solubility in alcohol or in aqueous solutions of any pH. However, optically clear gels can be obtained from both aluminum chloride and nitrate with TEOS; aluminum chloride is less suitable for sol-gel processes than aluminum nitrate. The number of bonded Al atoms was much lower in the chloride-containing gels than in the nitrate-containing gels. The very low Al incorporation resulted from the acid medium. The gel structure obtained from aluminum chloride is dominated by the silica fractal network strongly deformed by the nonbonded Al content. In addition, in the case of aluminum chloride, a washing step is needed to remove the anions.

Aluminum nitrate proved to be the best Al inorganic precursor [12, 13]. Aluminum nitrate shows good solubility in water and alcohol; it hydrolyzes strongly to produce an acidic medium required for the gelation. Thus, catalysis is not needed in this process. The hydrolysis speed of aluminum nitrate is closer to that of TEOS than that of aluminum alkoxides. Owing to spontaneous decomposition of the nitrate during gelation, the pH increases continuously during the process, supporting the hydrolysis and condensations reactions. Owing to the decomposition of nitrate ions, a washing step is unnecessary in order to remove the anions. However, the disadvantage of applying aluminum nitrate resulted from the nitrate content, which escapes as nitrous gases during the gelation and heat treatment. Apart from aluminum isopropoxide, aluminum nitrate resulted in the highest Al incorporation (50-70% of the Al content). However, the dried gel samples have a fractal structure and large porosity; their aging processes

are very slow. In a closed system the gel samples retain their structures even for several years.

Sodium metasilicate

The use of sodium metasilicate as a starting material in the sol-gel method is motivated by its lower price compared to TEOS. In order to get a homogeneous solution of sodium silicate and aluminum nitrate, an acidic medium was needed. The hydrolysis of Al ions begins only at pH ≥ 3 and the condensation reactions become dominant at pH ≥ 5 . An optically clear gel sample could be prepared at pH 1, but the Al incorporation was negligible in the network. As a maximum 30% incorporation of Al was achieved at pH 5. On increasing the pH above 5, phase separation occurred in the experimental conditions. On the basis of MAS NMR and SAXS measurements, it can be expected that the structure is built up from larger aggregates with a fractally rough surface.

Conclusion

A homogeneous gel network can be prepared by a simple sol-gel method, directly from Al- and Si-containing solutions. In many cases, much greater Al incorporation could be achieved in the gel structure using this method than can be obtained by a traditional melting process (10%).

Aluminum nitrate proved to be the best Al precursor in the sol-gel process. Using it resulted in one of the greatest Al incorporations, its application was very easy, a washing step and catalysis were not needed, and the gel samples obtained aged very slowly. The new sol-gel method provides aluminosilicate materials with new structures (e.g. fractals) and new properties (e.g. piezoelectricity or a wide range of variable porosity). The disadvantage of the use of aluminum nitrate is the release of nitrous gases noxious to the environment.

The highest Al incorporation could be detected in the samples prepared from aluminum isopropoxide. Its fast hydrolysis and high price are some disadvantages.

Regarding environmental protection, the most important advantage of the use of aluminum acetate is that acetate can very easily escape as CO₂ and H₂O molecules. For industrial applications only the samples prepared in basic conditions should be taken into consideration. The same can be concluded about the application of the samples prepared from sodium metasilicate (water glass solution). The price gives some preference to sodium silicate over TEOS.

Acknowledgement This work was supported by T 038228 and T 043636 OTKA funds.

References

1. Brinker CJ, Scherer GW (1990) Sol-Gel science. Academic, Boston, pp 839–870
2. López T, Bosch P, Gómez RJ, Basaldella E, Kikot A, Pereyra E (1991) React Kinet Catal Lett 43:461
3. López T, Bosch P, Asomoza M, Gómez RJ (1992) Catalysis 133:247
4. Fricke J (1986) Aerogels. Springer, Berlin Heidelberg New York, pp 22–24
5. Nogami M, Moriya Y (1977) J Jpn Ceram Soc 85:59
6. Dislich H (1971) Angew Chem Int Ed Engl 10:363
7. Kamiya K, Sakka S, Tashiro N (1976) J Jpn Ceram Soc 84:614
8. Klein LC (1988) Sol-gel technology for thin films, fibers, preforms, electronics, and specialty shapes. Noyes, Park Ridge, pp 382–390
9. Selvaraj U, Komarneni S, Roy R (1990) J Am Ceram Soc 73:3663
10. Lacka M, Beier W, Stock L (1989) Glastechn Ber 62:320
11. Chakrabarti S, Pramanik PJ (1990) Mater Sci Lett 9:1135
12. Sinkó K, Mezei R (1998) J Non-Cryst Solids 231/1–2:1
13. Sinkó K, Mezei R, Zrínyi M (2001) J Sol-Gel Sci Technol 21:147
14. Sinkó K, Fél K, Rohonczy J, Hüsing N (2001) Smart Mater Struct 10:1078
15. Emmerling A, Petricevic R, Beck A, Wang P, Scheller H, Fricke J (1995) J. Non-Cryst Solids 185:240
16. Fratzl P, Vogl G, Klaumünzer K (1993) J Appl Crystallogr 26:820
17. Stone WEE, El Shafei GMS, Sanz J, Selim SA (1993) J Phys Chem 97:10127
18. Luan Z, Cheng C, Zhou W, Klinowski J (1995) J Phys Chem 99:1018
19. Eckert H (1994) Solid State NMR 33:125
20. Ross SD (1972) Inorganic infrared and Raman spectra, McGraw-Hill, London

J. Dredán
I. Antal
I. Rácz
S. Marton

Interfacial behaviour of pharmaceutical excipients

Abstract Since drug release from dosage forms has importance for absorption from the gastrointestinal system, physicochemical characterisation of pharmaceutical systems is essential during the development of an optimal formulation with high efficacy and quality. Interfacial parameters of several pharmaceutical excipients were studied regarding their possible modifying effect on drug release from the dosage form. Measured data on water adsorption, wetting contact angle, and surface tension of pharmaceutical systems

were evaluated to characterise the interfacial behaviour during the dissolution of the active ingredient. The results demonstrated that the drug liberation process markedly depends on the wettability of the dosage form. The action of added excipients was investigated by applying the Weibull distribution as a mathematical model for dissolution kinetics and using a two-factor, three-level factorial experimental design to evaluate the effect of critical phenomena, such as water uptake and surface tension

J. Dredán (✉) · I. Antal · I. Rácz
S. Marton
Institute of Pharmacy,
Semmelweis University, Högyes E. str.7,
1092 Budapest, Hungary
e-mail: drejud@hogyes.sote.hu
Tel.: +36-1-2170914
Fax: +36-1-2170914

Introduction

The therapeutical effectiveness and biological availability of a drug from a solid dosage form implies its release and dissolution from a formulation into biological fluids, crossing of membrane barriers towards systemic circulation before reaching the site of action [1, 2]. Dosage forms serve as carrier systems for the active substance and they influence both the intensity and the duration of action by influencing the fate of the drug molecule in the body through the processes of the liberation, absorption, distribution, metabolism, elimination model (LADME).

The liberation and absorption processes can be rate-determining steps. The liberation process can be characterised by the dissolution rate of the drug from the solid particles [3, 4]; hence, the surface phenomena at the solid/liquid interface play an important part in drug delivery [5, 6].

The understanding of interfacial phenomena at the surfaces has improved significantly in the past decade

[7, 8]. The drug release processes are mediated by the presence of surface interactions between the fluid and a substrate (solid surface) and highly depend on the physical and chemical properties, such as wetting and solubility [9].

Several excipients are commonly applied in the pharmaceutical industry to produce new drug delivery systems. These inactive ingredients may influence the interfacial phenomena of the drug carrier system, the behaviour of which determines both the efficacy and the quality of the pharmaceutical preparation.

In this work we deal mainly with the first two steps of the LADME model that are influenced by interfacial parameters, namely with the liberation of the drug from the dosage form and with the characteristics influencing the absorption through biological membranes, respectively.

The objective of the present work was to study modifying effects of excipients on drug liberation in connection with their physical and chemical character-

istics, such as interfacial tension of solid and liquid phases, wetting contact angle of the solid phase and – a calculated quantity – the adhesion tension of the solid particles.

Materials and methods

Model drugs as medical compounds were chosen with different chemical characteristics, such as acids – Aspirin –, some with alkaline character – Theophylline, Ibuprofen – and salts – potassium chloride, sodium salicylate (USP 23, each).

Among the film-forming polymers we studied some methacrylic acid and methacrylate copolymers, Eudragits (USP 23, Röhm Pharma), and cellulose derivatives, such as Metolose (Shin-Etsu Chemical Co.). Nonionic surface-active agents (polysorbates, USP 23, Cremophors, BASF) were added to modify both the surface characteristics and the drug release. Adeps Solidus (hard fat, *Adeps neutralis*, Eur. P., a mixture of mono-, di- and triglycerides of the saturated fatty acids $C_9H_{19}COOH$ – $C_{17}H_{35}COOH$) and poly(ethylene glycol) (M_w 1,540, Eur. P) were applied as suppository bases. Excipient Ludipress (BASF) was used as direct tablet compression aid.

For surface tension, contact angle and water uptake measurements thin-film samples were prepared from coating polymers with surfactant addition. Aqueous solutions of different surfactants were also studied. Coated particle samples were prepared for drug release studies. The surface characteristics of some active ingredients in compressed form were monitored.

Determinations of surface tension, contact angle and water uptake

The surface tension of the samples was determined by a DuNouy ring method using a KSV Sigma 70 tensiometer (Braumann, Germany). The equipment is useful for determination the dynamic surface tension of liquids, the wetting contact angle and the water uptake or swelling of solid samples.

In vitro drug release studies

For the determination of dissolution profiles of the samples the rotating-paddle method of USP 23 at 100 rpm was used (PTW2 dissolution test apparatus, Pharmatest Apparatebau, Hainburg). The studies were conducted in 900 ml dissolution media. The dissolution of potassium chloride was continuously monitored with a digital pH meter (Radelkis OP 211/1, Budapest), equipped with a chloride-selective electrode.

The experimental media applied in the studies were purified and distilled water and artificial gastric and enteric juices, in some cases with enzyme addition. The temperature of the measurements was 37 °C for better simulation of the physiological conditions.

Scanning electron microscopy studies

The surface characteristics of samples were studied with a scanning electron microscope (JEOL JSM-25, JEOL, Japan) after gold vacuum coating. Samples of three different stages of dissolution were monitored as follows: intact samples before dissolution, a sample at the introductory stage of the process, and a sample after the dissolution experiment. A magnification of $\times 450$ was applied.

Results and discussion

Pharmaceutical formulators often meet the problem of low water solubility of the drugs. The water uptake [7] process of Ibuprofen, a non-steroid anti-inflammatory drug, after compression of the powder into a tablet and in the solid dispersion prepared by melting is shown in Fig. 1.

Solid dispersions are often used to enhance water solubility [6, 7]. The melting process causes physical changes in the surface structure of the material, the crystals of the drug suffer destruction, and they turn into an amorphous form. This statement can be justified by the results of differential scanning calorimetry examinations.

In this case it can be seen that not only the amount of adsorbed water was increased, but the rate of the process also increased.

The pharmaceutical industry in the last decade prepared tablets mainly by direct compression, using special excipients. It is a more economic and simpler method for preparing tablets than compression of the drugs following wet granulation. Most drugs can be compacted in this way. These excipients have different physical characteristics. The wetting contact angle values of different drugs compacted with a Ludipress were compared with the solubilities of the drugs. A significant connection was found between these parameters (Table 1).

A suppository dosage form is widely used for administration of drugs having irritative character or that suffer decomposition in the first pass process by the liver. Two types of suppository base materials are applied, hydrophilic and lipophilic types. The wetting

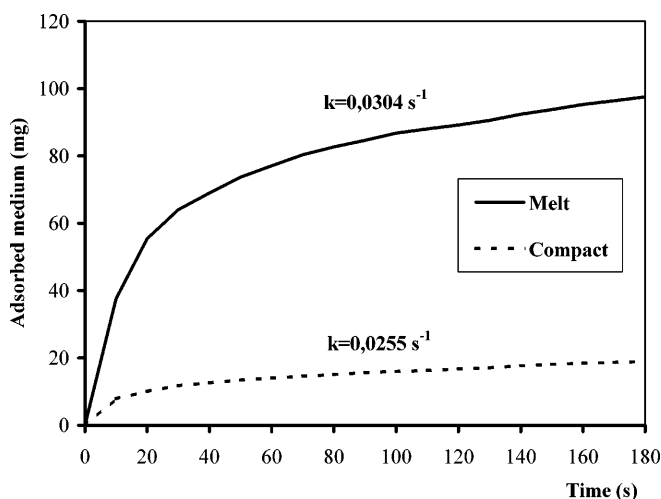


Fig. 1 Liquid adsorption of Ibuprofen samples prepared by melting and compression. The first-order rate constants of adsorption can be seen

Table 1 Relation between the wetting contact angles of samples and solubilities of the drugs

Sample	Solubility (% w/w)	Contact angle (degrees) Excipient		
		Poly (ethylene glycol) 1540	Adeps 50	Ludipress
Salicylic acid	0.33	64 74 (in saturated solution)	87	59
Sodium salicylate	117.65	18	46	44
Theophylline	0.83	76	102	74
Ibuprofen compact	Practically insoluble			83
Ibuprofen melt	15			51

contact angle values of film samples of drugs incorporated into suppository base materials are also shown in Table 1. The adhesion tension curves of these film samples significantly differ in the cases of application of suppository bases of different hydrophilic character.

The lipophilic base material Adeps Solidus showed decreased wetting ability, with a significantly large area under the curve compared with the hydrophilic poly(ethylene glycol) 1540. This shape of the curve of the latter is characteristic for the samples dissolving in the applied medium (Fig. 2).

Surface-active agents are not absolutely inert excipients – enough to take into consideration their haemolytic effect [2] – so determination of the minimal necessary concentration to achieve a desirable effect is of great importance. On the basis of physicochemical studies their drug release modifying influence can be predicted with a good approach. For this estimation surface tension and contact angle measurements can be applied, the latter gives a certain minimum value at the optimal concentration, above which the effect of the surfactant does not alter in stress proportion. This may be connected to the critical micelle concentration or the critical association concentration of the surfactant solutions, where the surfactant molecules saturate the surface and further surface tension decrease cannot be achieved. The adhesion tension values of the aqueous solutions of

surfactants showed a significant minimum value at the concentration optimum (Fig. 3), and were determined by the Wilhelmy plate method with the KSV Sigma 70 tensiometer. First the surface tension of the solutions was measured, and then the dynamic contact angle of the solutions was determined [8].

From the extrapolated buoyancy slope the contact angle can be calculated:

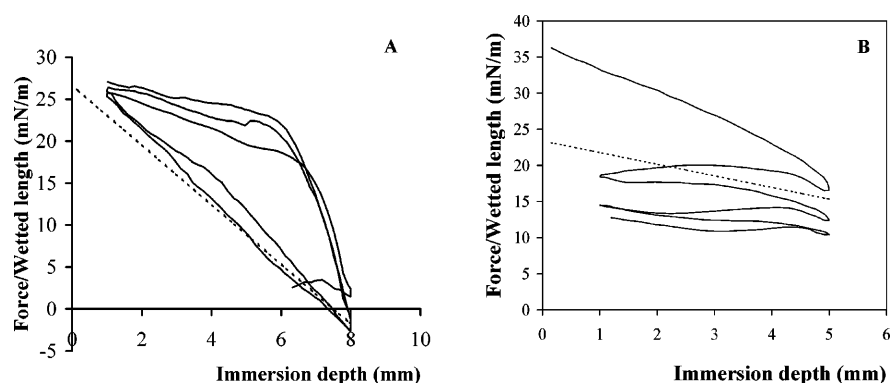
$$\cos\theta = f/p\gamma_{LV} \quad (1)$$

where θ is the contact angle, f is the force measured on the balance, p is the perimeter of the plate and γ_{LV} is the surface tension (interfacial free energy between the liquid and vapour) of the surfactant solution. The surface tension of water was 72.8 mN/m, the contact angle was 51.49°, and the adhesion tension, τ_0 , calculated by Eq. (2) was 45.33 mN/m [9]:

$$\tau_0 = \gamma_{LV}\cos\theta \quad (2)$$

Cremophor A25, a cetomacrogol, is a surfactant with hydrophilic character; its contact angle values were measured in aqueous solution do not alter significantly above 0.2% concentration, in accordance with the dissolution characteristics of the embedded samples.

Potassium chloride is a useful material in fighting diseases and it alters the normal ion milieu of the body, but it has a dangerous side effect: it may cause ulceration

Fig. 2 Adhesion tension curves of film samples prepared by embedding 20% w/w sodium salicylate into **a** lipophilic and **b** hydrophilic suppository bases

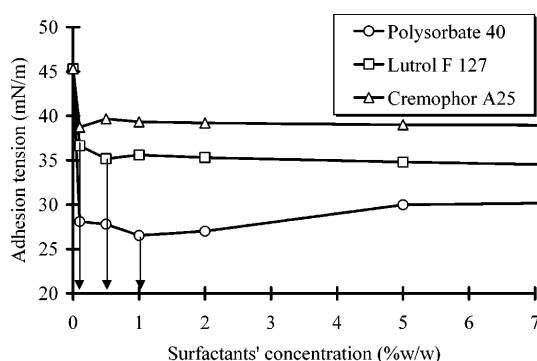


Fig. 3 Drug release curves of potassium chloride microcapsules with different core-to-wall ratios prepared by an embedding technique

of the stomach. That is the reason why it should be applied in coated form, for example, embedded into molten white beeswax. The dissolution curves of microcapsules prepared by a melt-embedding technique are shown in Fig. 4 for different core-to-wall ratios. A significant correlation exists there between the ratio of the lipophilic compound and the wetting character (Table 2). As the difference in solid/liquid interfacial character increases, the wetting contact angle values increase; meanwhile the drug release rate decreases.

The wall material has lipophilic character, so the release curves are S-shaped, with an expressed lag-time period. To describe the release patterns of the nondisintegrating lipophilic matrices the Rosin–Rammler–Bennett–Sperling–Weibull distribution function (Eq. 3) [10] was used:

$$M_t/M_\infty = 1 - \exp\left\{-[(t - t_0)/\tau_d]^\beta\right\} \quad (3)$$

where M_t is the dissolution (percentage) at time t (minutes), M_∞ is the dissolution (percentage) at infinite

Core/wall ratios:

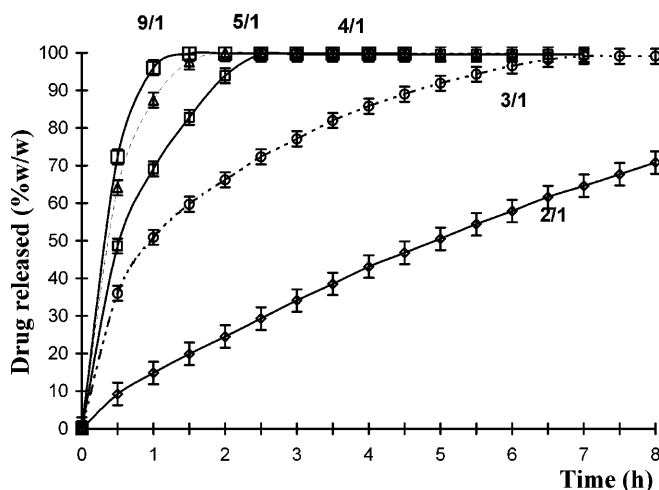


Fig. 4 Calculated adhesion tension values of aqueous surfactant solutions with different concentrations

Table 2 Wetting dynamic contact angle values of white beeswax coated potassium chloride microcapsules with different core-to-wall ratios and dissolution parameters of the Weibull distribution function (the medium for the wetting and dissolution measurements was distilled water)

Sample core-to-wall ratio	Wetting contact angle θ (degrees)	τ_d (min)	β
9:1	61	23	0.9876
5:1	73	28	1.2536
4:1	80	50	1.1789
3:1	86	84	1.2099
2:1	88	393	1.3301

time, t_0 is the lag time (minutes) of the drug dissolution, β is the shape parameter of the curve, and τ_d is the time when 63.2% of M_∞ has been dissolved.

The computer package Microsoft Excel 7.0 was applied for the nonlinear parameter estimation to minimise the squares of the residuals. The higher β values ($\beta > 1$) demonstrate that mainly the initial period of the release process slows down and refer to parallel running processes, such as disintegration, diffusion, with a rate close to that of the dissolution. In this case these shape parameter values refer to the parallel running processes such as drug dissolution and diffusion (Table 2).

The members of the polysorbate group surfactants are the most widely used surfactant excipients, despite their haemolytic side effect. These sorbitane–lipoic acid ester–poly(ethylene glycol) ethers mixed with waxes decrease the wetting contact angle (Table 3); in consequence they increase the water solubility of film samples, so a higher level of bioavailability can be achieved. The scanning electron microscope photographs of samples taken at different stages of the dissolution process (Fig. 5) justify the presence of pores in the coating layer. The guiding mechanism of drug release in this case is the diffusion of the drug solution through these pores (holes); the values $\beta > 1$ demonstrate it.

Table 3 Characteristic dissolution time (τ_d) and shape parameter values of potassium chloride embedded in white beeswax, containing surfactants at 10% w/w concentration and surface tension of aqueous solutions of surfactants and contact angles of free film samples prepared by melting from wax together with surfactants

Surfactant	τ_d (min)	β	γ (mN/m) (aqueous solution)	θ (degrees) (free film)
Polysorbate 20	27.4	0.9868	31.7	83
Polysorbate 40	35.2	1.2668	31.9	77
Polysorbate 60	40.6	1.1950	33.0	81
Polysorbate 80	58.9	1.2513	34.5	85

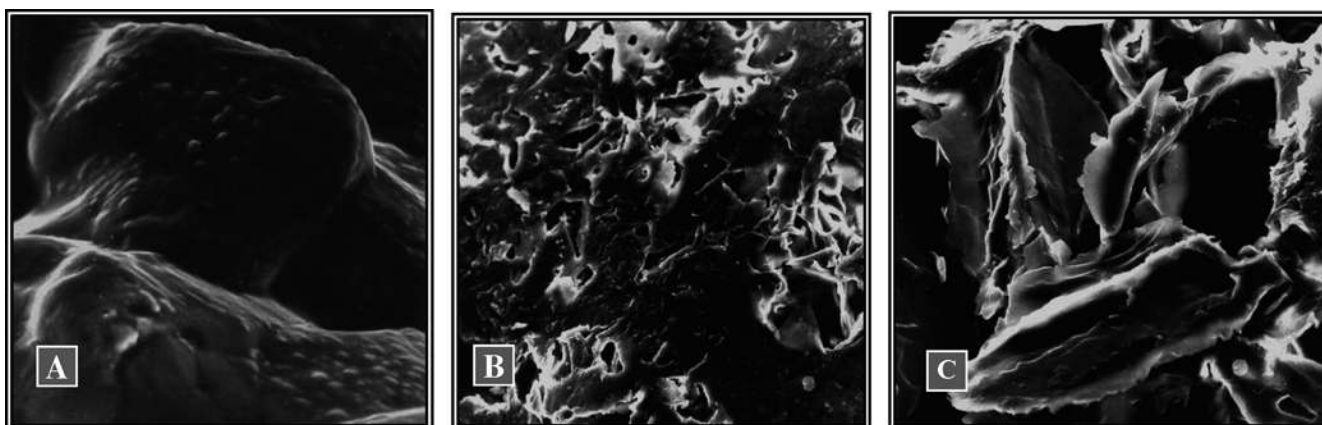


Fig. 5 Scanning electron microscope photographs of potassium chloride samples embedded into Cremophor A25 surfactant containing white beeswax **a** before dissolution, **b** after 1 h, and **c** at the end of the dissolution process. Magnification $\times 450$

The mean dissolution time (τ_d) determined by the Weibull distribution function was shortened as the surface tension of the surfactant aqueous solution decreased (Table 3). In accordance with the contact angle decreasing, greater water uptake can be observed, parallel to the drug release rate increasing.

A two-factor, three-level face-centered central composite design [11] was applied to construct a second-order polynomial model describing the effect of formulation factors on the product characteristics. The levels for each parameter are represented by a minus sign for the lower level, a plus sign for the higher level and by zero for the base level.

A BASIC (Microsoft visual Basic professional edition 3.0) language computer program was developed for the multiple regression analysis. The expected form of the polynomial equation is as follows:

$$y = b_0 + b_1x_1 + b_2x_2 + b_{11}x_1^2 + b_{22}x_2^2 + b_{12}x_1x_2, \quad (4)$$

where y is the response, x are the factors, and b parameters denote the coefficients characterising the main (b_1, b_2), the quadratic (b_{11}, b_{22}), and the interaction (b_{12}) effects.

On the basis of the results, it can be concluded that the influencing effect on the release rate of the adhesion tension of film samples is similar to the adhesion tension of the aqueous solution of surfactants: coefficient of

film-sample factor 37.53, of solution-sample factor 31.95. Since the interaction coefficient (b_{12}) is 4.02×10^{-18} , no important coherence between the two factors examined was found.

The importance of the water uptake of the samples is not so expressed: constant of water-uptake factor was 22.69. The interaction coefficient of the water uptake and the wetting contact angle of film samples of 1.24 indicates the existence of a slight relation between them. The surface tension decreasing effect of surfactant aqueous solutions does not influence significantly the drug release rate; the constant of this factor was -1.24.

The two-factor, three-level face-centered central composite design was applied successfully for describing the effect of formulation factors on the product characteristics.

Conclusions

The physical characteristics of the formulated samples of drugs are useful to predict the drug release, liberation, and dissolution conditions. The characteristics of samples simulating the dosage forms are important for proper evaluation of the results.

The study of the interfacial behaviour of formulated samples results in good prediction possibilities for the practice of pharmaceutical technology.

The results verify that to achieve higher bioavailability, formulating a solid dispersion from a poorly water soluble drug, or applying surfactants in the dosage form, would be the solution for the solubility difficulties.

References

1. Thull R (2002) *Biomol Eng* 19:1–8
2. De Bartolo L, Morelli S, Bader A, Drioli E (2002) *Biomaterials* 23:2485–2497
3. Musko Z, Bajdik J, Pintye-Hodik K, Szabo-Revesz P, Kelemen A, Erös I (2002) *Pharm Ind* 64(11): 1194–1198
4. Law BM (2001) *Prog Surf Sci* 66:159–216
5. Muster TH, Prestidge CA, Hayes RA (2001) *Colloids Surf A* 176:253–266
6. Mitragotri S (2000) *Pharm Res* 17
7. Zerrouk N, Chemtob C, Arnaud P, Toscani S, Dugue J (2001) *Int J Pharm* 225:49–62
8. Machiste EO, Buckton G (1996) *Int J Pharm* 145:197–201
9. Naylor LJ, Bakatselou V, Rodríguez-Hornedo N, Weiner ND, Dressman JB (1995) *Eur J Pharm Biopharm* 41:346–353
10. Carstensen JT (1977) *Pharmaceutics of solids and solid dosage forms*. Wiley, New York, pp 63–76
11. Franz RM, Browne JE, Lewis AR (1996) In: Liebermann HA, Rieger MM, Banker GS (eds) *Pharmaceutical dosage forms. Disperse systems*, 2nd edn. Dekker, New York, pp 437–519

Rita Földényi
Imre Czinkota
Tímea Ertli

Presentation of multistep isotherms formed at the adsorption of herbicides

R. Földényi (✉) · T. Ertli
Department of Environmental Engineering
and Chemical Technology,
University of Veszprém,
P.O. Box 158, 8201 Veszprém,
Hungary
e-mail: foldenyi@almos.vein.hu
Tel.: +36-88-422022
Fax: +36-88-425049

I. Czinkota
Department of Soil Science
and Agricultural Chemistry,
Szent István University,
Páter Károly u. 1., 2103 Gödöllo,
Hungary

Abstract The soil as an adsorbent has various active sites leading to rather complicated adsorption mechanisms with environmental pollutants, like pesticides. According to earlier results the chloroacetanilide type herbicides as solutes resulted in two-step isotherms on soils and quartz. This phenomenon has not been observed yet concerning trace compounds in the environment. In this case the so-called distributed reactivity model is used, suggesting that the total sorption is given as the sum of the local adsorption isotherms. The adsorption of isoproturon (urea-type herbicide) and prometryn (*s*-triazine type herbicide) was studied on quartz at different pH values,

leading to similar – multistep – isotherms generated by chloroacetanilide compounds. These plots were compared to the classification suggested by Giles. If the formation of different associates is supposed the following adsorption equation can be derived. Its applicability is proved by the fitting of the isotherms of herbicides having different structures. This isotherm equation can be used widely for environmental as well as for (other) colloidal systems.

$$q = \sum_{i=1}^s \left[\frac{q_{Ti} K_i (c - b_i + |c - b_i|)^{n_i}}{2^{n_i} + K_i (c - b_i + |c - b_i|)^{n_i}} \right]$$

Keywords Adsorption · Herbicides · Multistep isotherms · pH · Quartz

Introduction

Isotherms for adsorption of organic solutes were classified by Giles et al. [1] into four main groups (S, L, H and C) used generally not only for well-defined but even for such heterogeneous adsorbents like the soil [2, 3]. While pesticide adsorption is characterized according to the main groups of this system, the isotherms are generally described either by the Freundlich or by the Langmuir equation [2, 4].

Earlier studies with chloroacetanilide-type herbicides resulted in two-step isotherms which might be classified into the so-called subgroups of Giles [5, 6]. In this case the commonly used equations are not well fitted to the points and a new equation is needed. It can be widely applied for multistep isotherms, which is demonstrated

here by the adsorption of two different compounds: isoproturon and prometryn on quartz.

Experimental

Materials

Isoproturon (99.21%) was provided by Nitrokémia 2000, while prometryn (99.0%) was provided by ÉMV.

Quartz (particle size less than 0.5 mm, Brunauer–Emmett–Teller surface area $0.24 \text{ m}^2 \text{ g}^{-1}$) was prepared from sand collected at Fehérvársurgó (Hungary). The sand sample (1 kg) was mixed with 1 mol l^{-1} hydrochloric acid (2 l) and was left to stand overnight. The solid phase was separated and washed with deionized water until a sample of the aqueous phase gave no reaction with silver nitrate reagent. The quartz obtained was dried at 105°C .

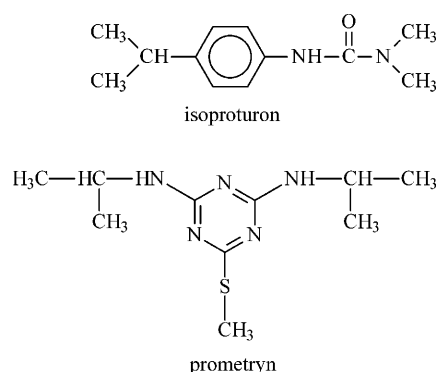


Fig. 1 The structure of the herbicides investigated

Sodium chloride, sodium dihydrogen phosphate and disodium hydrogen phosphate were obtained from the Reanal Chemical Co. (Hungary). High-performance liquid chromatography (HPLC) grade acetonitrile was purchased from Spektrum 3D (Hungary).

Methods

Static equilibrium experiments were carried out in 0.1 mol l^{-1} NaCl– 0.01 mol l^{-1} phosphate buffer solution at 25°C . Quartz (4 g) was left to stand in 5 ml of the buffered solution (pH 5, 7, 8) for 24 h at room temperature and then 65 ml of the herbicide in appropriate buffer solution ($10\text{--}300 \mu\text{mol l}^{-1}$) was added. The suspension was shaken for 1 h and then separated using a centrifuge ($3,000 \text{ min}^{-1}$). The aqueous phase was filtered and then analyzed by HPLC. The standard solutions for calibration were the same as were used in the static equilibrium experiments.

HPLC conditions

Chromatographic separations were made by using a MERCK LaChrom HPLC system equipped with a LiChrospher 100 column filled with $5\text{-}\mu\text{m}$ RP-18 packing material ($125 \text{ mm} \times 4 \text{ mm}$) and with a programmable UV detector. Samples ($10 \mu\text{l}$), injected by the autosampler, were eluted as follows. Isoproturon: eluent 60% acetonitrile, 40% water; flow rate 0.7 ml min^{-1} ; $\lambda = 240 \text{ nm}$. Prometryn: eluent 65% acetonitrile, 35% water; flow rate 1 ml min^{-1} ; $\lambda = 228 \text{ nm}$.

Results and discussion

Isoproturon is an urea-type herbicide, while prometryn is a triazine-type herbicide (Fig. 1) and both contain more nitrogen atoms with different basicity.

These chemicals can be present in various forms influenced by the hydrogen ion concentration of the medium. They are able to participate in hydrogen bonding, and isoproturon might form even salts in basic solutions [7, 8]. Therefore the adsorption of these compounds was carried out at different pH, leading to multistep isotherms on quartz (Figs. 2, 3).

In the system of Giles et al. [1] curves having not more than two steps can be found; however, they can be

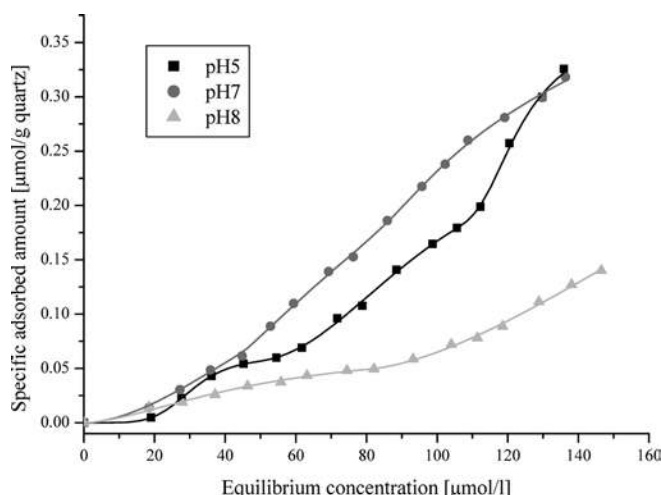


Fig. 2 Adsorption isotherms of isoproturon on quartz from 0.1 mol l^{-1} NaCl– 0.01 mol l^{-1} phosphate buffer solution at different pH at 25°C

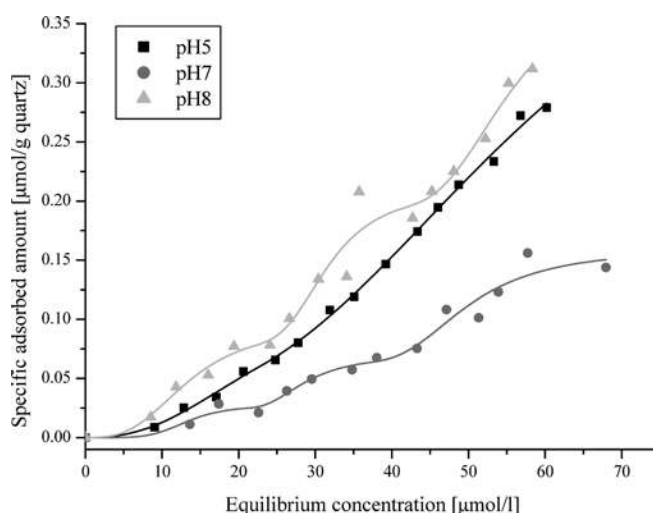


Fig. 3 Adsorption isotherms of prometryn on quartz from 0.1 mol l^{-1} NaCl– 0.01 mol l^{-1} phosphate buffer solution at different pH at 25°C

classified according to the nature of the slope of the initial portion of the isotherm. Considering this classification isoproturon formed an L-type isotherm (L3) at pH 8 and an S-type isotherm at pH 5 and 7, where the exact subgroups are difficult to determine (Fig. 2). This problem is caused by the three steps of the curves which are well-defined at pH 5. Similarly, prometryn resulted in three-step isotherms at pH 7 and 8 (main group is S) but at pH 5 an S2 curve is generated (Fig. 3).

The phenomena can be better clarified if the points of the isotherms are fitted by the new equation presented in the following.

The equation of the multistep isotherm

In the system the reaction in Eq. (1) is assumed:



where S represents the empty sites of the soil surface, A is the solute, SA_n is the surface complex, and $n \geq 1$: a noninteger number representing the average degree of association of the solute molecules

The equilibrium constant of the reaction is

$$K = \frac{[SA_n]}{[S][A]^n}. \quad (2)$$

where $[S]$, $[A]$, and $[SA_n]$ are the equilibrium concentrations of S , A , and SA_n , respectively.

$$[S]_T = [S] + [SA_n] \quad (3)$$

and

$$[S] = [S]_T - [SA_n], \quad (4)$$

where $[S]_T$ is the available total concentration of the surface sites.

After the substitution of $[S]$,

$$K = \frac{[SA_n]}{([S]_T - [SA_n])[A]^n}, \quad (5)$$

$$[SA_n] = \frac{[S]_T K [A]^n}{1 + K [A]^n}. \quad (6)$$

and

$$q = \frac{q_T K [A]^n}{1 + K [A]^n}, \quad (7)$$

where q and q_T are the surface concentrations of $[SA_n]$ and $[S]_T$, respectively.

If associates form above a certain concentration limit of the solute, the concentration variable $[A]$ is replaced by the following relationship:

$$[A] = \frac{c - b + |c - b|}{2}, \quad (8)$$

where c is the controlled value of the equilibrium concentration of solute and b is the critical concentration limit of associates.

If $b = 0$ the control variable is given by the concentration of the nonassociated solute ($c = [A]$) and associates can be formed only on the surface. If $b > 0$ associates can be formed either on the surface or in the solution and the concentration of these associates appears in Eq. (7):

$$q = \frac{q_T K \left(\frac{c - b + |c - b|}{2} \right)^n}{1 + K \left(\frac{c - b + |c - b|}{2} \right)^n}, \quad (9)$$

$$q = \frac{q_T K (c - b + |c - b|)^n}{2^n + K (c - b + |c - b|)^n}. \quad (10)$$

Equation (10) is the first step of the isotherm.

Similarly to the multisite Langmuir [9] or to the so-called distributed reactivity model which allow the addition of various isotherm equations [10] the multistep isotherm is calculated as the sum of the i steps:

$$q = \sum_{i=1}^s \left[\frac{q_{Ti} K_i (c - b_i + |c - b_i|)^{n_i}}{2^{n_i} + K_i (c - b_i + |c - b_i|)^{n_i}} \right], \quad (11)$$

where q_{Ti} is the adsorption capacity, K_i is the equilibrium constant, b_i is the critical concentration limit, and n_i is the average degree of association of the i th step of the curve.

Table 1 Calculated parameters of Eq. (11) for the adsorption isotherms of isoproturon and prometryn on quartz at different pH from 0.1 mol l⁻¹ NaCl–0.01 mol l⁻¹ phosphate buffer at 25 °C

Parameters	Isoproturon			Prometryn		
	pH 5	pH 7	pH 8	pH 5	pH 7	pH 8
q_{T1} ($\mu\text{mol g}^{-1}$)	0.06	0.26	0.07	0.13	0.03	0.09
q_{T2} ($\mu\text{mol g}^{-1}$)	0.22	0.42	0.5	0.38	0.04	0.12
q_{T3} ($\mu\text{mol g}^{-1}$)	0.12	0.03	—	—	0.09	0.18
K_1 ($\text{l } \mu\text{mol}^{-1}$) ^{n₁}	1.5×10^{-8}	3.2×10^{-4}	1.4×10^{-3}	3.5×10^{-4}	1.5×10^{-6}	3.6×10^{-4}
K_2 ($\text{l } \mu\text{mol}^{-1}$) ^{n₂}	2.5×10^{-4}	2.0×10^{-3}	1.5×10^{-4}	4.3×10^{-4}	8×10^{-3}	8.4×10^{-4}
K_3 ($\text{l } \mu\text{mol}^{-1}$) ^{n₃}	3.9×10^{-4}	1.0×10^{-5}	—	—	1.3×10^{-3}	7.0×10^{-4}
b_1 ($\mu\text{mol l}^{-1}$)	0	0	0	0	0	0
b_2 ($\mu\text{mol l}^{-1}$)	49.1	45.2	81.9	22.6	21.4	21.6
b_3 ($\mu\text{mol l}^{-1}$)	105.4	70.2	—	—	37.0	41.3
n_1	5.26	1.83	1.68	2.48	5.18	3.06
n_2	2.10	1.11	1.72	2.05	2.36	3.05
n_3	2.75	3.33	—	—	2.56	2.72
χ^2	1.0×10^{-5}	1.0×10^{-5}	5.0×10^{-6}	3.0×10^{-5}	3.0×10^{-4}	4.8×10^{-4}
R^2	0.9995	0.9996	0.9982	0.9981	0.9716	0.9838

The experimental points were fitted by Eq. (11) rather well as can be seen in Figs. 2 and 3. The parameters are summarized in Table 1. The calculation was carried out by using the nonlinear least squares curve fitting procedure of the “Origin” scientific graphing and analysis software.

The parameters in Table 1 show that the points were fitted only once by a two-step and twice by a three-step isotherm equation for both herbicides. This is in accordance with the discussion given earlier concerning the form of the isotherms.

Between the concentration limit values $b_1 = 0$ and $b_2 > 0$ (first step) the adsorption is governed by the surface – adsorbed solute interactions and the surface complex is formed. It has a rather high number of associates, which is emphasized at pH 5 for isoproturon and at pH 7 for prometryn. Since in these cases the adsorption capacity (q_{T1}) is low and the initial portion of the isotherms belong to the S group of Giles, vertical orientation of the molecules can be supposed on the surface [1]. Further steps of the curves are formed owing to the interaction between the solute and adsorbed solute molecules, resulting in three layers. Similar phenomena can be observed for isoproturon at pH 7 (here, however, q_{T1} is relatively high) and for prometryn at pH 8.

Two-step isotherms were generated in two cases: at pH 8 by isoproturon an L-type curve and at pH 5 by prometryn an S-type curve were formed. Giles suggested for L-type curves that molecules are oriented

horizontally on the surface [1]. This is possible in the case of isoproturon, which has the lowest degree of association for the first step at pH 8.

The adsorption, however, is pH-dependent for both types of herbicides; this is better emphasized by the parameters calculated for isoproturon. It is supported by the b_2 values of prometryn at every pH investigated as well as by the rather high concentration limit of isoproturon at pH 8.

Since quartz has a neutral siloxane surface that functions as a very weak Lewis base [11] under basic conditions the possibly negatively charged isoproturon is adsorbed in lower amounts than at neutral as well as at acidic pH and the adsorption must be governed by hydrophobic interactions.

Conclusion

The adsorption of isoproturon and prometryn herbicides is influenced by the pH, leading to curves having more steps. The new multistep isotherm equation was successfully applied under different conditions independent of the system used. The parameters calculated can help in the clarification of rather complicated adsorption mechanisms.

Acknowledgement. This research was funded by the Hungarian research program KAC (no. K0440802001).

References

1. Giles CH, MacEwan TH, Nakhva SN, Smith D (1960) *J Chem Soc* 1960:3973
2. McBride MB (1994) *Environmental chemistry of soils*. Oxford University Press, New York, p 342
3. Green RE (1975) In: Guenzi WD (ed) *Pesticides in soil and water*. American Society of Agronomy. Madison, pp 3–36
4. Weber WJ Jr, McGinley PM, Katz LE (1991) *Water Res* 25:499
5. Lengyel Zs, Földényi R (2001) <http://dx.doi.org/10.1065/espr2001.12.103>
6. Czinkota I, Földényi R, Lengyel Zs, Marton A (2002) *Chemosphere* 48:725
7. Stevenson FJ (1994) *Humus chemistry. Genesis, composition, reactions*. Wiley, New York, pp 465–469
8. Lopez A, Mascolo G, Földényi R, Passino R (1996) *Water Sci Technol* 34:351
9. Wolt JD (1994) *Soil solution chemistry. Applications to environmental science and agriculture*. Wiley, New York, p 169
10. Weber WJ Jr, McGinley PM, Katz LE (1992) *Environ Sci Technol* 26:1955
11. Johnston CT, Tombácz E (2002) In: Dixon J, Schulze D (eds) *Soil mineralogy with environmental applications*. SSSA book series 7. SSSA, Madison, pp 37–67

G. Horányi
P. Joó

Distinction between electrostatic and specific adsorption of anions on (hydr)oxide/electrolyte interfaces by application of a radiotracer technique

G. Horányi (✉)
Institute of Chemistry,
Chemical Research Center,
Hungarian Academy of Sciences,
P.O. Box 17, 1525 Budapest, Hungary
e-mail: hor34@ludens.elte.hu
Tel: +36-1267-0820
Fax: +36-1266-3899

P. Joó
Department of Colloid and Environmental
Chemistry, University of Debrecen,
P.O. Box 31, 4010 Debrecen, Hungary

Abstract On the basis of the comparative radiotracer study of the adsorption of sulfate and pertechnetate ions on γ - Al_2O_3 , it is shown that the application of the radiotracer technique allows us to distinguish specific and nonspecific adsorption without the knowledge and the use of quantitative data as to the extent of the adsorption or the

surface area of the adsorbent. It is demonstrated that the study of the adsorption of the TcO_4^- ion offers a tool for the investigation of electrostatic effects at the Al_2O_3 /electrolyte interface.

Keywords Radiotracer technique · Specific adsorption · Nonspecific adsorption · Anions · γ - Al_2O_3

Introduction

In a series of previous publications [1, 2, 3, 4, 5, 6, 7, 8, 9, 10, 11] adsorption of anions on various oxide/electrolyte interfaces was studied by the radiotracer technique. The application of the radiotracer technique for the study of the adsorption phenomena occurring at the oxide/solution interphase was prompted on the basis of the following argumentation:

1. We have little direct in situ (microscopic) information on the specific adsorption of charged species (ions) at the oxide/aqueous solution interface in strong acid media despite the fact that the role of the surface chemistry of the metal (hydr)oxide/solution interface is well documented [12, 13, 14, 15, 16].
2. Most of the (macroscopic) methods used in colloid chemistry for the investigations at the oxide/solution interface are far from being able to follow in situ the adsorption phenomena and to study the effect of various parameters on the adsorption without disturbing the original experimental conditions.

The radiotracer technique elaborated for the study of electrode surfaces [11] offers a unique possibility of solving this problem using metal oxides in the form of a

powder in contact with the solution phase containing various labeled anions.

Experimental

The experimental technique and setup for the radiotracer study of sorption processes (involving powdered sorbents) are described and surveyed in Refs. [1, 2, 3, 4, 5, 6, 7, 8, 9, 10]. Details concerning the experimental conditions characteristic for the study of sulfate adsorption on γ - Al_2O_3 can be found in Ref. [3].

The very principle of the method used in the present study is the measurement of radiation intensity originating from adsorbed species on a powdered oxide layer sprinkled on a thin plastic foil that serves simultaneously as the window for radiation measurement. The measurements were carried out at ambient temperature in an Ar atmosphere by bubbling Ar in the solution phase and letting it through the gap between the bottom of the measuring cell and the detector. Labeled H_2SO_4 was used (Amersham, specific activity $200 \text{ MBq mmol}^{-1}$) for the preparation of the solutions, mostly in perchlorate-supporting electrolyte. Pertechnetate from Amersham was used for the preparation of solutions containing TcO_4^- ions. (The E_{max} of the β radiation emitted by ^{99}Tc is 0.292 MeV).

A commercial neutral Al_2O_3 powder was used (Merck, 1077, particle size $0.063\text{--}0.200 \text{ mm}$). The specific surface area of the oxide powder, determined by the N_2 -Brunauer-Emmett-Teller method was $156 \pm 9 \text{ m}^2 \text{ g}^{-1}$, while by a methylene blue adsorption method $17 \pm 3 \text{ m}^2 \text{ g}^{-1}$ was obtained.

Results and discussion

Specific adsorption of anions induced by the protonation of the oxide surfaces

In order to get information concerning the specific interaction of radiolabeled anions with oxide surfaces the adsorption of the labeled species present in low concentration was studied in the presence of a great excess of a supporting electrolyte [2, 3, 4, 5, 8]. The problem of the distinction between specific and nonspecific adsorption is discussed in the next section. In this section the effect of the protonation of the surface on the anion adsorption is considered on the basis of data obtained from the pH-dependence of the adsorption. The pH-dependence of the adsorption of labeled sulfate ions at various oxide surfaces in the presence of a great excess of ClO_4^- ions is shown in Fig. 1. (For the sake of comparison the extent of adsorption is given on a relative scale. For experimental details see previous communications [2, 3, 4, 5, 8].)

The shapes of these curves are very similar. This type of behavior was interpreted [2, 3, 4, 5, 8] in terms of the protonation of the oxide surface characterized by the equilibrium formulated by the equation



where X is a surface site. According to the assumptions, the specific adsorption of anions takes place on the protonated surface sites. Considering Eq. (1) in the case of equilibrium,

$$k_a K c_{\text{H}^+} (1 - \theta_{\text{H}^+}) - k_d \theta_{\text{H}^+} = 0 \quad (2)$$

where k_a and k_d are the rate constants of adsorption and desorption, respectively, and

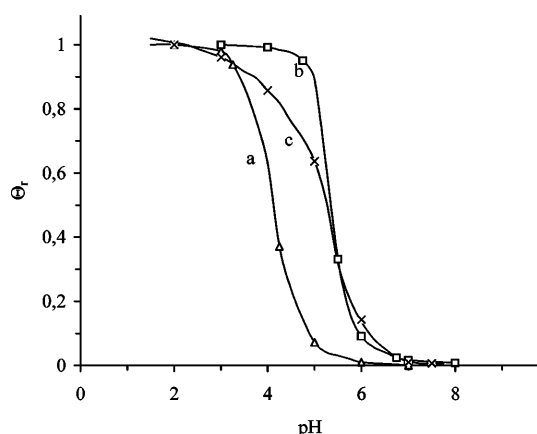


Fig. 1 pH-dependence of the adsorption of sulfate ions on *a* hematite, *b* $\gamma\text{-Al}_2\text{O}_3$, *c* CuO in $0.5 \text{ mol dm}^{-3} \text{ NaClO}_4$ and $5 \times 10^{-4} \text{ mol dm}^{-3}$ labeled H_2SO_4 . For the sake of comparison the relative coverage values, θ_r , are given

$$K c_{\text{H}^+} = \frac{\theta_{\text{H}^+}}{(1 - \theta_{\text{H}^+})} \quad (3)$$

where $K = \frac{k_a}{k_d}$ is the proton equilibrium constant and θ_{H^+} is the coverage with respect to the protonated surface sites. For

$$\frac{\theta_{\text{H}^+}}{1 - \theta_{\text{H}^+}} = 1 \quad (4)$$

$$\log K = \text{pH} \quad (5)$$

Thus, one can estimate the value of the protonation equilibrium constant from the data presented in Fig. 1. By plotting these data according to the relationship

$$-\log \left(\frac{\theta_{\text{H}^+}}{1 - \theta_{\text{H}^+}} \right) = \log K + \text{pH} \quad (6)$$

linearity can be found as shown in Fig. 2 in the case of hematite.

The simple model suggested for the case of the adsorption of labeled sulfate species cannot be unambiguously applied for other anions. For instance, in the case of phosphate anions the pH-dependence of the adsorption of phosphate ions goes through a maximum as shown in Fig. 3 for the case of $\gamma\text{-Al}_2\text{O}_3$ and hematite [5].

In the following for the sake of simplicity the results obtained with labeled SO_4^{2-} and TcO_4^- using $\gamma\text{-Al}_2\text{O}_3$ are presented.

Comparison of SO_4^{3-} (HSO_4^-) and TcO_4^- adsorption on $\gamma\text{-Al}_2\text{O}_3$

On the basis of preliminary studies we arrived at the conclusion that in the case of TcO_4^- ions the role of the specific adsorption at Al_2O_3 can be neglected. (Tc emits

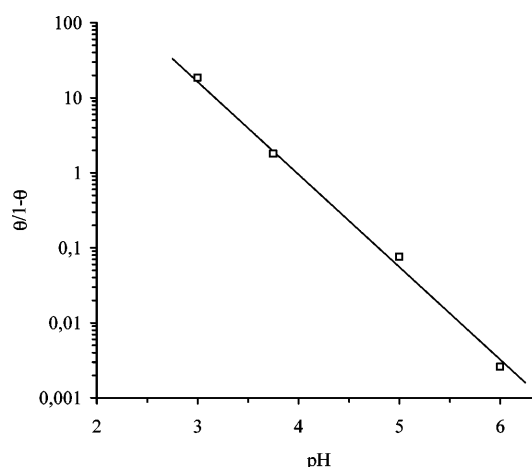


Fig. 2 $-\log \theta/(1 - \theta)$ versus pH from data obtained for the pH-dependence of the adsorption of sulfate ions on hematite

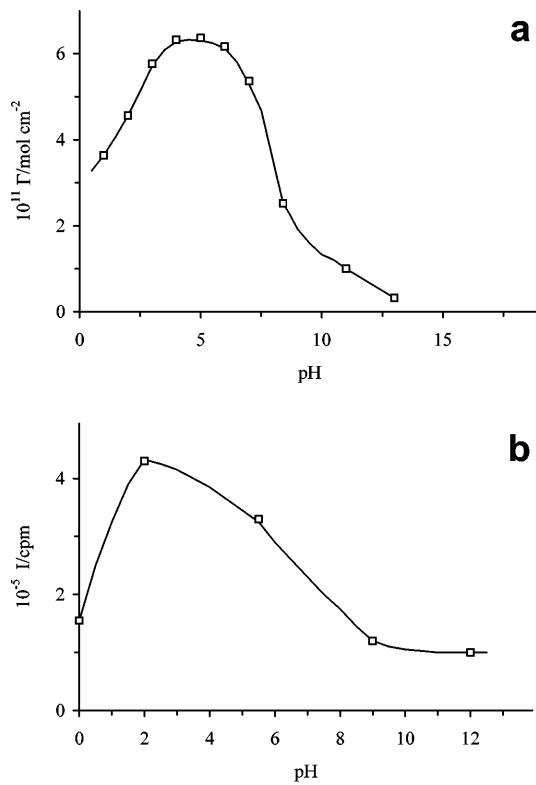


Fig. 3 **a** pH-dependence of the adsorption of labeled phosphate species ($c = 3 \times 10^{-4} \text{ mol dm}^{-3}$ in $0.5 \text{ mol dm}^{-3} \text{ NaClO}_4$) on $\gamma\text{-Al}_2\text{O}_3$. **b** The pH-dependence of the adsorption of labeled phosphate species ($c = 3 \times 10^{-4} \text{ mol dm}^{-3}$ in $0.5 \text{ mol dm}^{-3} \text{ NaClO}_4$) on hematite

soft β -radiation.) Therefore, it could be an ideal model for the investigation of nonspecific adsorption by the radiotracer technique and to compare its behavior with sulfate species considered as a representative of anions involved in specific adsorption. (Unfortunately, labeled ClO_4^- ions are not available for tracer studies.) ClO_4^- and NO_3^- can be considered as “inert” anionic components of the supporting electrolytes.

It follows from the considerations outlined in the previous section that the charge-determining species on the Al_2O_3 surface in acidic media are the protons. Denoting the surface excess concentration of protons bound to the surface by $\Gamma_{\text{H}^+}^b$, the charge balance characterizing the double layer as a whole should be

$$F\Gamma_{\text{H}^+}^b = F \sum Z_i \Gamma_i, \quad (7)$$

where Γ_i denotes the surface excess concentration of ionic components (cations and anions as well) believed to be present in the solution side of the double layer.

In the presence of two anions with equal charge, for instance, $|z_i| = 1$ for the case of nonspecific adsorption, according to the Gouy–Chapman theory, the following relationship can be given:

$$\frac{c_1}{c_2} = \frac{\Gamma_1}{\Gamma_2}, \quad (8)$$

where c_1 and c_2 are the concentrations of the anions in the bulk solution phase. The same applies for two cations.

For the sake of simplicity in the following a system containing two cations and anions, namely Na^+ , H^+ , ClO_4^- , and TcO_4^- , is considered and the corresponding Γ values are denoted Γ_{Na^+} , $\Gamma_{\text{H}^+}^b$, $\Gamma_{\text{ClO}_4^-}$ and $\Gamma_{\text{TcO}_4^-}$, respectively. For the solution phase the following conditions will be considered:

$$c_{\text{TcO}_4^-} \ll c_{\text{ClO}_4^-}; \text{ thus } c_{\text{Na}^+} + c_{\text{H}^+} \approx c_{\text{ClO}_4^-}. \quad (9)$$

$\Gamma_{\text{H}^+}^b$ is the total surface excess of protons determinable by thermodynamic means that can be conceived as composed of two components:

$$\Gamma_{\text{H}^+}^b = \Gamma_{\text{H}^+}^b + \Gamma_{\text{H}^+}^s, \quad (10)$$

where $\Gamma_{\text{H}^+}^s$ is the (negative) surface excess of protons in the solution side of the double layer. For the cations and anions in the solution side of double layer the following equations can be given:

$$\frac{\Gamma_{\text{H}^+}^s}{\Gamma_{\text{Na}^+}} = \frac{c_{\text{H}^+}}{c_{\text{Na}^+}} \quad \text{and} \quad \frac{\Gamma_{\text{ClO}_4^-}}{\Gamma_{\text{TcO}_4^-}} = \frac{c_{\text{ClO}_4^-}}{c_{\text{TcO}_4^-}}. \quad (11)$$

Both $\Gamma_{\text{H}^+}^s$ and Γ_{Na^+} are negative surface excesses in the case of protonated i.e., positively charged surfaces.

The electroneutrality of the whole system requires

$$\Gamma_{\text{H}^+}^b + \Gamma_{\text{Na}^+} = \Gamma_{\text{ClO}_4^-} + \Gamma_{\text{TcO}_4^-}. \quad (12)$$

Taking into consideration Eq. (11) we obtain

$$\Gamma_{\text{H}^+}^b + \Gamma_{\text{Na}^+} \left(1 + \frac{c_{\text{H}^+}}{c_{\text{Na}^+}} \right) = \Gamma_{\text{TcO}_4^-} \left(1 + \frac{c_{\text{ClO}_4^-}}{c_{\text{TcO}_4^-}} \right) \quad (13)$$

and

$$\Gamma_{\text{H}^+}^b + \Gamma_{\text{Na}^+} \left(\frac{c_{\text{H}^+} + c_{\text{Na}^+}}{c_{\text{Na}^+}} \right) = \Gamma_{\text{TcO}_4^-} \left(\frac{c_{\text{TcO}_4^-} c_{\text{ClO}_4^-}}{c_{\text{TcO}_4^-}} \right). \quad (14)$$

Considering the conditions given in Eq. (9),

$$\Gamma_{\text{H}^+}^b + \Gamma_{\text{Na}^+} \frac{c_{\text{ClO}_4^-}}{c_{\text{Na}^+}} = \Gamma_{\text{TcO}_4^-} = \frac{c_{\text{ClO}_4^-}}{c_{\text{TcO}_4^-}} \quad (15)$$

and

$$\Gamma_{\text{H}^+}^b = c_{\text{ClO}_4^-} \left(\frac{\Gamma_{\text{TcO}_4^-}}{c_{\text{TcO}_4^-}} - \frac{\Gamma_{\text{Na}^+}}{c_{\text{Na}^+}} \right). \quad (16)$$

In the first approximation assuming that the term $\Gamma_{\text{Na}^+}/c_{\text{Na}^+}$ can be neglected, we obtain

$$\Gamma_{\text{TcO}_4^-} = \frac{\Gamma_{\text{H}^+}^b c_{\text{TcO}_4^-}}{c_{\text{ClO}_4^-}}. \quad (17)$$

It may be seen in Fig. 1 that a limiting value of the proton sorption ($\Gamma_{H^+}^L$) is attained at pH values under 3.

Thus at $\text{pH} < 3$ the following equation can be given:

$$\Gamma_{\text{TcO}_4^-} = \Gamma_{H^+}^L \frac{c_{\text{TcO}_4^-}}{c_{\text{ClO}_4^-}}. \quad (18)$$

However, even the application of this simplified relationship for the case of nonspecific adsorption encounters significant difficulties owing to the very nature of the system. These problems are as follows:

1. In order to protonate the Al_2O_3 surface HClO_4 should be added to the solution phase; consequently ClO_4^- ions will appear in the solution phase.
2. On shifting of the pH to a preselected low value, for instance, to pH 3, the concentration of HClO_4 (ClO_4^- ions) should be about $10^{-3} \text{ mol dm}^{-3}$. In the case of nonspecific adsorption of labeled species (TcO_4^-) present in concentration $10^{-4} \text{ mol dm}^{-3}$ the extent of its adsorption will be strongly influenced by the ClO_4^- ions.

This is well reflected by the results shown in Fig. 4. Starting from a neutral aqueous solution in contact with Al_2O_3 powder containing solely the labeled species and gradually adding HClO_4 to the solution phase the count rate goes through a maximum. The initial increase is connected with the protonation of the surface; however, the further increase of the HClO_4 concentration leads to a decrease in the adsorption, indicating that more and more ClO_4^- will be involved in the formation of the solution side of the double layer.

A more convincing result can be obtained starting from a fixed pH value and increasing the concentration of ClO_4^- ions by addition of NaClO_4 . This is shown in Fig. 5.

Considering the very fact that

$$\Gamma_{\text{TcO}_4^-} = \alpha N, \quad (19)$$

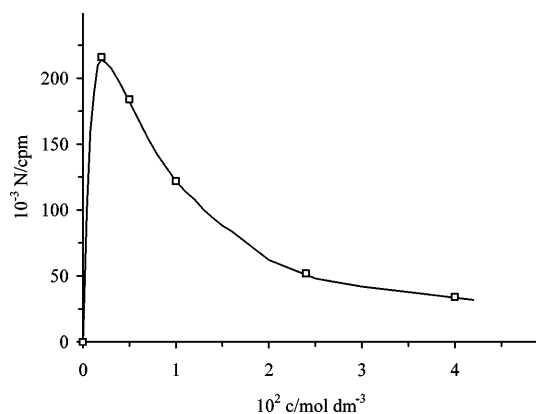


Fig. 4 Effect of the addition of HClO_4 on the radiation intensity originating from TcO_4^- ions (present in $2 \times 10^{-4} \text{ mol dm}^{-3}$) adsorbed on $\gamma\text{-Al}_2\text{O}_3$ (4 mg cm^{-2}) starting from a neutral solution without supporting electrolyte

where α is a proportionality factor and N is the radiation intensity measured as the count rate, Eq. (18) can be given in the following form:

$$N = \frac{B}{c_{\text{ClO}_4^-}}, \quad (20)$$

where

$$B = \frac{\Gamma_{H^+}^L c_{\text{TcO}_4^-}}{\alpha}. \quad (21)$$

By plotting N against $(c_{\text{ClO}_4^-})^{-1}$ the relationship presented in Fig. 6 is obtained. The proportionality found between N and $(c_{\text{ClO}_4^-})^{-1}$ furnishes firm evidence of the nonspecific adsorption.

A further important observation supporting this view is the proportionality of the count rate with the concentration of TcO_4^- at a fixed pH and ClO_4^- values as shown in Fig. 7.

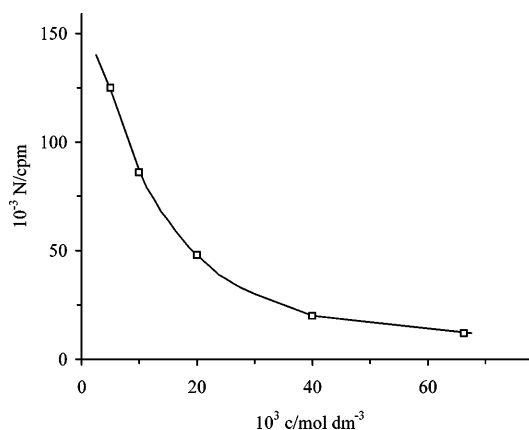


Fig. 5 Influence of the addition of NaClO_4 on the count rate originating from adsorbed TcO_4^- species starting from a solution containing $5 \times 10^{-3} \text{ mol dm}^{-3}$ HClO_4 ($\text{pH} \approx 2.5$) and $2.5 \times 10^{-4} \text{ mol dm}^{-3}$ TcO_4^-

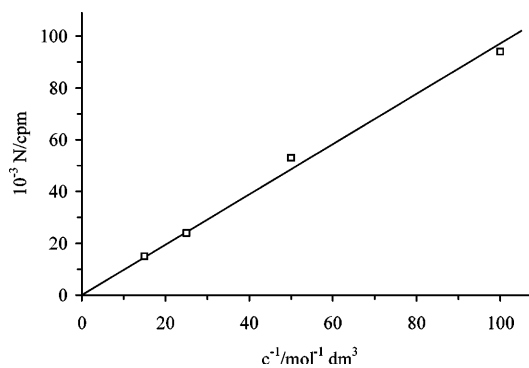


Fig. 6 Count rate versus c^{-1} for data reported in Fig. 5

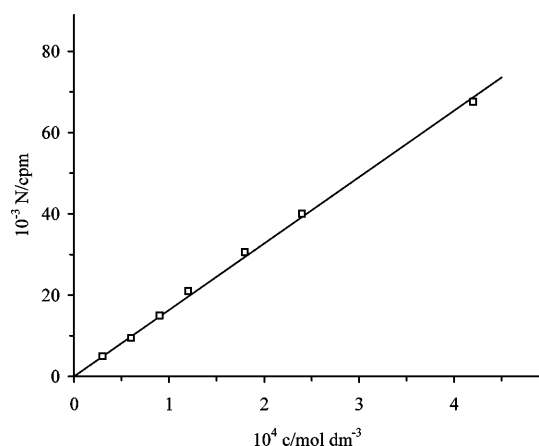


Fig. 7 Proportionality of the count rate with the concentration of TcO_4^- in the presence of $6 \times 10^{-2} \text{ mol dm}^{-3}$ NaClO_4 and HClO_4 at pH 2

In contrast to the results presented here quite different behavior was found for labeled sulfate species as reported in a previous communication [3]. The concentration of ClO_4^- ions did not exert significant influence on the adsorption of sulfate species in accordance with the assumption that specific adsorption takes place. Similar results can be obtained with other anions, for instance, with NO_3^- ions as shown in Fig. 8. In the case of Fig. 8a the effect of addition of HNO_3 on the extent of sulfate adsorption is shown. It may be seen from Fig. 8 that there is no decrease in the surface concentration of sulfate species following the addition of ClO_4^- or NO_3^- ions in concentrations 1 and 2 orders of magnitude higher than that of the sulfate ions as shown by parts 2 and 3 in Fig. 8b (compare this behavior with that presented in Fig. 4); however, a decrease in the adsorption can be observed at high total concentration of HNO_3 (part 4). (This decrease could be connected with the significant change of ionic strength in the solution.)

On the other hand, the modification of the solution side of the double layer following the addition of sulfate ions to the solution phase can be well demonstrated. On adding no labeled sulfate to the solution phase in a concentration negligible in comparison with that of ClO_4^- and H^+ ions the adsorption of TcO_4^- species decreases dramatically. This is shown in Fig. 9.

Starting from a supporting electrolyte NaClO_4 and HClO_4 ($6 \times 10^{-2} \text{ mol dm}^{-3}$) at pH 2 containing $5 \times 10^{-4} \text{ mol dm}^{-3}$ TcO_4^- the addition of $1.5 \times 10^{-3} \text{ mol dm}^{-3}$ nonlabeled H_2SO_4 results in an almost complete displacement of TcO_4^- ions, indicated by the significant decrease of the count rate. It is evident that the same happens simultaneously with ClO_4^- ions as both anions are in the solution side of the double layer. This observation can be considered as further proof of the specific adsorption of sulfate species. The positive charge of protons on the surface is now compensated by sulfate

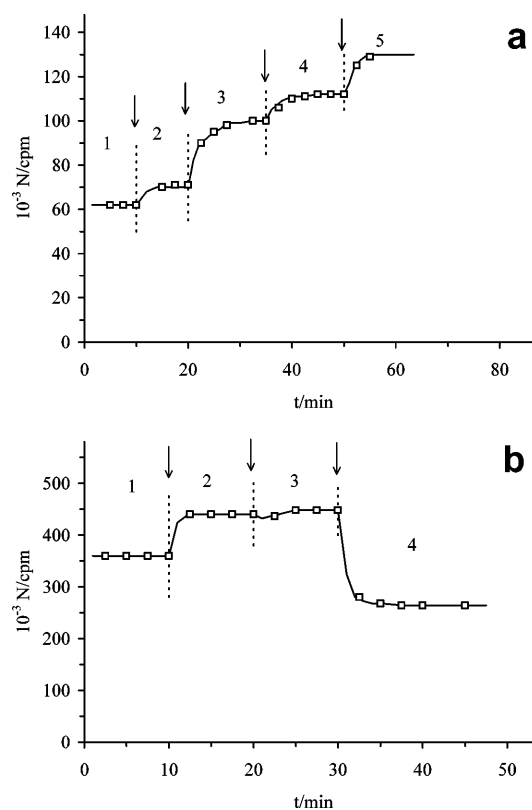


Fig. 8 a Effect of HNO_3 on the count rate originating from adsorbed sulfate species. Starting solution 0.5 mol dm^{-3} KNO_3 and $3 \times 10^{-4} \text{ mol dm}^{-3}$ labeled H_2SO_4 . Addition of HNO_3 0 (1), 5×10^{-4} (2), 2×10^{-3} (3), 4×10^{-3} (4), $1 \times 10^{-2} \text{ mol dm}^{-3}$ (5). **b** Effect of ClO_4^- and NO_3^- ions on the adsorption of labeled sulfate species dissolved in water in the absence of supporting electrolyte. $3 \times 10^{-4} \text{ mol dm}^{-3}$ H_2SO_4 (1), + $2 \times 10^{-3} \text{ mol dm}^{-3}$ HClO_4 (2), + $1 \times 10^{-2} \text{ mol dm}^{-3}$ KNO_3 (3), + 1 mol dm^{-3} HNO_3 (4)

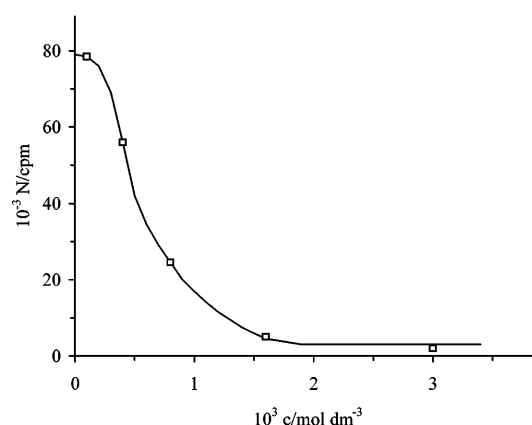


Fig. 9 Effect of the concentration of nonlabeled sulfate species on the count rate originating from TcO_4^- ions present in the solution side of the double layer. Supporting electrolyte NaClO_4 and HClO_4 ($6 \times 10^{-2} \text{ mol dm}^{-3}$), pH 2, $5 \times 10^{-4} \text{ mol dm}^{-3}$ TcO_4^-

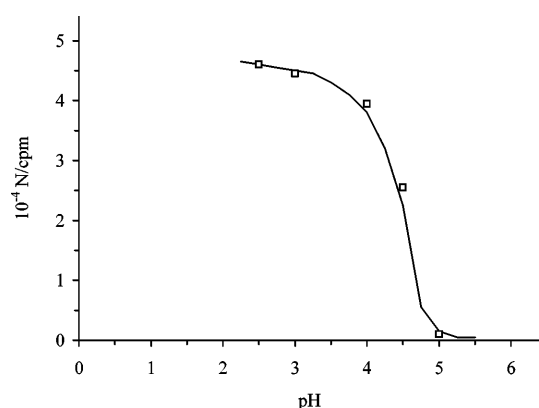


Fig. 10 pH-dependence of the count rate originating from TcO_4^- ions. Supporting electrolyte $5 \times 10^{-2} \text{ mol dm}^{-3} \text{ NaClO}_4$, $3 \times 10^{-5} \text{ mol dm}^{-3} \text{ TcO}_4^-$

species forming surface complexes on the protonated sites.

On the basis of these experimental results a suggestion can be made for the application of the radiotracer technique for the study of the double layer formed at protonated Al_2O_3 using TcO_4^- as an indicator species characterizing the behavior of the solution side of the double layer.

It follows from the considerations outlined previously that the formation of the double layer at the $\gamma\text{-Al}_2\text{O}_3$ /electrolyte interface at $\text{pH} < 7$ is connected with the protonation of the surface sites. Thus starting from a neutral solution containing $5 \times 10^{-2} \text{ mol dm}^{-3} \text{ NaClO}_4$ and $3 \times 10^{-5} \text{ mol dm}^{-3} \text{ TcO}_4^-$ no adsorption of TcO_4^- on the Al_2O_3 sample can be observed. Gradual addition of HClO_4 in a concentration of 1–2 orders of magnitude less than that of NaClO_4 allows us to determine the pH-dependence of the adsorption of TcO_4^- (at least in the pH range between 7 and 2). This is shown in Fig. 10. The curve presented in Fig. 10 is very similar to curve a in Fig. 1; thus, it furnishes the information on the protonation equilibrium of the $\gamma\text{-Al}_2\text{O}_3$ surface, i.e., the

radiation intensity originating from TcO_4^- can be a measure of the degree of protonation.

Assuming that the adsorption of both ClO_4^- and TcO_4^- is nonspecific at a given protonation and ClO_4^- concentration, the total negative charge involved in the solution side of the double layer (neglecting the negative adsorption of Na^+ ions) can be given by

$$Q = -F\Gamma_{\text{TcO}_4^-} - \left(1 + \frac{c_{\text{ClO}_4^-}}{c_{\text{TcO}_4^-}}\right) = -F\alpha N \left(1 + \frac{c_{\text{ClO}_4^-}}{c_{\text{TcO}_4^-}}\right). \quad (22)$$

On the other hand, the changes caused by specific adsorption of anions in the solution side of the double layer can also be followed through the measurement of TcO_4^- adsorption. Specifically adsorbed anions depending on the extent of their adsorption compensate the positive charge of a protonated surface; therefore, the negative charge on the solution side, i.e., the surface excess concentration of nonspecifically adsorbed anions, should decrease. This effect is well demonstrated by the curve presented in Fig. 9.

Conclusion

It follows from the results presented here that the main features characterizing specific and nonspecific adsorption occurring at $\gamma\text{-Al}_2\text{O}_3$ /electrolyte interfaces can be easily distinguished by the radiotracer technique using TcO_4^- as the indicator species. The main advantage of the application of the radiotracer technique is that the main tendencies governing the adsorption processes can be explored without the knowledge and the use of quantitative data as to the extent of the adsorption or the surface area of the adsorbent.

Acknowledgement Financial support from the Hungarian Scientific Research Fund and the Ministry of Environmental Protection is acknowledged (OTKA grant T 031703).

References

- Joó P, Horányi G (2000) *J Colloid Interface Sci* 223:308
- Horányi G, Joó P (2000) *J Colloid Interface Sci* 227:206
- Horányi G, Joó P (2000) *J Colloid Interface Sci* 231:373
- Horányi G, Joó P (2001) *J Colloid Interface Sci* 243:46
- Horányi G, Joó P (2002) *J Colloid Interface Sci* 247:12
- Horányi G, Joó P (2001) *Prog Colloid Polym Sci* 117:27
- Kálmán E, Horányi G (2002) *J Solid State Electrochem* 6:253
- Horányi G (2002) *J Solid State Electrochem* 6:463
- Horányi G, Gáncs L (2002) *J Solid State Electrochem* 6:485
- Horányi G, Joó P (2000) *Russ J Electrochem* 36:1189
- Horányi G (2002) In: Hubbard AT (ed) *Encyclopedia of surface and colloid science*. Dekker, New York, pp 4423–4437
- Sposito G (1984) *Surface chemistry of soils*. Oxford University Press, New York
- Schindler PV, Stumm W (1987) In: Stumm W (ed) *Aquatic surface chemistry: chemical processes at the particle–water interface*. Wiley, New York, pp 83–110
- Dzombak DA, Morel FMM (1990) *Surface complexation modeling. Hydrous ferric oxide*. Wiley, New York
- Stumm W (1992) *Chemistry of the solid–water interface*. Wiley, New York
- Stumm W (1996) *Aquatic chemistry*, 2nd edn. Wiley, New York

Éva Kiss
József Szalma
Zsófia Keresztes
Erika Kálmán
Miklós Mohai
Imre Bertóti

Adhesional stability of cadmium arachidate Langmuir–Blodgett layers

É. Kiss (✉)
Department of Colloid Chemistry,
L. Eötvös University, P.O. Box 32,
1518 Budapest 112, Hungary
e-mail: kissevak@ludens.elte.hu
Tel.: +36-1-2090555/1308
Fax: +36-1-2090602

J. Szalma
Department of Physical Chemistry,
L. Eötvös University, P.O. Box 32,
1518 Budapest, Hungary

Z. Keresztes · E. Kálmán
Department of Surface Chemistry
and Corrosion Research,
Chemical Research Centre,
Budapest, Hungary

M. Mohai · I. Bertóti
Research Laboratory for Materials
and Environment Chemistry,
Chemical Research Centre,
Budapest, Hungary

Abstract Two-layer Langmuir–Blodgett films of cadmium arachidate were deposited onto hydrophobic glass plates. The adhesional stability of the films has been studied by wetting tension measurements, X-ray photoelectron spectroscopy (XPS), and atomic force microscopy (AFM). Partial detachment of the Langmuir–Blodgett layer while immersing the plate repeatedly into water or aqueous electrolyte solutions was deduced from the increase in the wettability and the decrease in the surface tension of the immersion liquid. Surface coverages obtained from XPS data and shown by AFM images are in agreement with the expectation based on tensiometric measurements of arachidate release from the substrate. AFM investigations

revealed a distinct difference in the structure of the layer depending on whether water or an aqueous solution of NaCl and CaCl₂ was applied in the stability test, providing evidence for the dissolution or the detachment type of the removal of the Langmuir–Blodgett film. The contact of a sessile droplet with the Langmuir–Blodgett film induced no detectable change in the contact angle or the surface tension of the liquid, demonstrating the role of a moving contact line in the degradation of the Langmuir–Blodgett film.

Keywords Langmuir–Blodgett films · Cadmium arachidate · Adhesional stability · Wettability · Atomic force microscopy

Introduction

Langmuir–Blodgett (LB) films are molecularly ordered layers of amphiphatic molecules on a solid support. The special, well-defined layer structure offers the potential of its use in fields such as electronics, microlithography, biosensors, and corrosion protection [1, 2, 3, 4, 5]. The stability of LB films under various conditions has been and still is a crucial issue in practical applications [6, 7, 8, 9, 10], although the possible change of LB layers in an aqueous environment has obtained less attention [11, 12, 13, 14].

It was confirmed earlier [6, 15, 16] that salt-based LB films are fairly stable under high-vacuum conditions,

while a slow decomposition of lead arachidate films was detected on X-ray irradiation. In the present work, the well-defined and widely investigated cadmium salt of arachidic acid was chosen as the material of the LB film. Two layers of cadmium arachidate were deposited onto a hydrophobic support. The adhesional stability of that film was studied by wettability and surface tension measurements, atomic force microscopy (AFM), and X-ray photoelectron spectroscopy (XPS). The aim was to get information on the adhesional properties of two-layer LB films, which might be relevant for possible applications of such layers themselves or in their use as film-forming material in which to build functional molecules.

Experimental

Sample preparation

Substrate

Silica glass slides (20×40×0.16 mm, Menzel-Gläser, Germany) were cleaned in freshly prepared persulfuric acid (volume ratio of concentrated sulfuric acid to hydrogen peroxide, 30 w/v% solution = 2:1) for 2 h and were then washed thoroughly with double-distilled water and dried in a vacuum. The glass plates were silylated in the gas phase with trimethylchlorosilane (Sigma) in a closed chamber at 140 °C for 2 h. After rinsing with diethyl ether, ethanol (to remove physically adsorbed silane molecules [17]) and water, the samples were dried in a vacuum for overnight. The wettability of these hydrophobic surfaces is characterised by advancing ($\Theta_A = 96.8 \pm 1.4^\circ$) and receding ($\Theta_R = 73.5 \pm 1.0^\circ$) water contact angles.

LB films

Arachidic acid (eicosanoic acid, 100 μg , $\text{CH}_3(\text{CH}_2)_{18}\text{COOH}$, Merck, purity above 99 %) dissolved in chloroform was spread onto the aqueous solution of cadmium chloride ($5 \times 10^{-4} \text{ mol dm}^{-3}$) in a Teflon-coated aluminium Langmuir trough. The pH of the subphase was 5.8 or it was set to 6.7 by adding NaHCO_3 . Following the cadmium arachidate formation at the interface and the evaporation of the organic solvent the floating monolayer was compressed up to the transfer pressure and expanded three times to obtain a close-packed structure at the interface, indicated by the reproducible isotherm. Vertical transfer of the monolayer onto the solid support producing a classical Y-type bilayer was performed by film-lifting at constant surface pressure ($\pi_c = 3 \times 10^{-2} \text{ N m}^{-1}$) controlled by a Wilhelmy-type surface tension sensor. The dipping speed was 20 mm min^{-1} for the deposition in both directions. The salts and other reagents were of analytical grade and also fulfilled the surface-active purity requirement [18].

Methods

Stability studies

The adhesional stability of the LB film was tested by immersion experiments measuring the wettability of the layer by a tensiometric method. The dynamic wettability during the immersion and emersion of the plate perpendicularly to the liquid surface was calculated from the capillary force acting at the liquid/air contact line. Advancing and receding contact angles were measured at a velocity of 10 mm min^{-1} . The standard deviation of the contact angle was generally less than 2° , mainly determined by the reproducibility of the surfaces. The immersion liquids were water and aqueous solution of NaCl or CaCl_2 at various concentrations. The salt concentrations were chosen to achieve the same ionic strength for the two electrolytes. Additionally to the wettability, the surface tension of the immersion liquid was also determined before and after the contact with the LB film with an accuracy of $2 \times 10^{-4} \text{ N m}^{-1}$ using a filter paper Wilhelmy plate. Three consecutive cycles of immersion–emersion using fresh immersion liquids at every turn were performed for each plate. The stability of the LB film on the solid support was estimated from both the change in the wettability and the change in the surface tension of the immersion liquids.

As a complementary experiment, the outcome of the contact of liquids with the LB films was also investigated in a sessile drop geometry. Droplets (5 μl) of water or aqueous electrolyte solution

were placed onto the surface of the LB film and the contact angle as well as the surface tension of the liquid were detected using a video-based optical contact angle and surface tension measuring system (OCA15 + Dataphysics, Germany). The two characteristic values of the drop-surface contact were determined on the base of a Laplacian fitting method and were followed for 60 min.

Surface analysis by XPS

X-ray photoelectron spectra were recorded with a Kratos XSAM 800 spectrometer operated in fixed-analyser transmission mode (40 eV pass energy) using $\text{Mg K}\alpha_{1,2}$ (1253.6 eV) excitation. The pressure of the analysis chamber was lower than 10^{-7} Pa . Detailed spectra of the main constituent elements (O1s , C1s , Si2p and Cd3d) were recorded with 0.1 eV steps at 0° takeoff angle. The spectra were referenced to the C1s line of the hydrocarbon-type carbon, set to a binding energy of 284.6 eV.

Spectra were acquired and processed by the Kratos Vision 2000 software package. Quantitative analyses, based on peak area intensity, were done by using the experimentally determined photoionisation cross-section data of Evans et al. [19] and asymmetry parameters of Reilman et al. [20]. The inelastic mean-free-path values of the photoelectrons were calculated by the TPP-2 formula using the NIST electron inelastic-mean-free-path database program [21].

Atomic force microscopy

AFM measurements were carried out by means of a Nanoscope III (Digital Instruments, CA, USA) atomic force microscope in an ambient environment. The instrument was operated in contact mode, by using a $\text{DI Si}_3\text{N}_4$ tip of 0.12 N m^{-1} force constant. Areas of different sizes (linear lengths of the studied area were 2, 5 and $10 \mu\text{m}$) were imaged, giving characteristic morphological features of the surfaces of the LB films. Images were obtained of at least six separate areas on each sample. Cross-section analysis of the surface topography was accomplished by the Nanoscope 4.23r6 software, and the measured thickness of the layer was compared to the thickness of the cadmium arachidate bilayer: 5.6 nm [22]. Average values of the areas at a certain depth were calculated from six images.

Results and discussion

Stability of floating monolayer

The cadmium salt of arachidic acid is formed at the surface of aqueous solution of CdCl_2 when the arachidic acid is spread on the subphase. The shape of the isotherm of the Langmuir layer indicates the salt formation and the condensation of the film compared to the pure arachidic acid film [23, 24]. Nevertheless, the stability of the monolayer is also a crucial point, since the successful transfer of the film requires a constant surface pressure at a given compression area or, in other words, when the film is compressed to the target pressure and the barrier is stopped, a decrease of surface pressure is unfavourable. A marked instability owing to possible nucleation was reported [25] for calcium and magnesium stearate monolayers depending on the pH of the subphase within 1 h. A notable increase of stability and an even higher

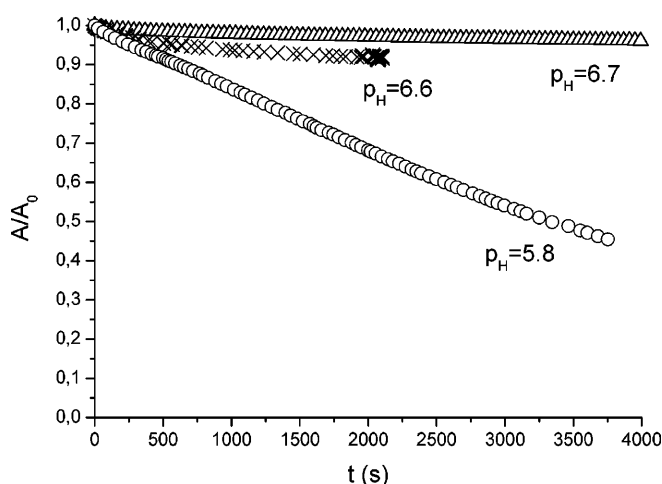


Fig. 1 Relative area, A/A_0 , of a cadmium arachidate Langmuir film at a surface pressure of $3 \times 10^{-2} \text{ N m}^{-1}$ as a function of time. The subphase is an aqueous solution of CdCl_2 without (pH 5.8) or with NaHCO_3 added (pH 6.6 and 6.7)

collapse pressure were achieved by setting the pH of the subphase to 9 with NaOH.

The stability of the cadmium arachidate monolayer could also be enhanced by increasing the pH of the subphase by applying NaHCO_3 at a concentration of $1.7 \times 10^{-4} \text{ M}$ (Fig. 1). The relative area of such a Langmuir monolayer was almost unchanged for hours, making possible the preparation of high-quality LB films. This is consistent with Schwartz's statement [26], whereas the salt formation with cadmium is completed above pH 6.5.

Stability of the LB film

Wettability and surface tension

The cadmium arachidate bilayer, deposited onto the silylated glass plate, with the alkyl chains outward forms a highly hydrophobic surface. The advancing water contact angle measured at the first dip of the LB film was $111.0 \pm 0.8^\circ$, while the corresponding receding angle was $89.5 \pm 1.1^\circ$. Since the surface of the substrate is also hydrophobic but to a lesser extent (see values given in the Sample preparation part), the region of the contact angle between the fully covered and the bare substrate is only about 15° . This fact limits the reasonable estimation of the presence or the integrity of the LB film on the basis of wettability. Nevertheless, in the course of the stability test the wettability of the layer slightly increased (both advancing and receding contact angles were decreased), indicating some loss of the hydrophobic LB material from the surface (Table 1). For the sake of convenience and easier

Table 1 Change of advancing and receding contact angles ($\Sigma\Delta\Theta_A$ and $\Sigma\Delta\Theta_R$) on the cadmium arachidate bilayer and change of surface tension ($\Sigma\Delta\gamma$) of the immersion liquid during the stability test summarised for three immersion cycles

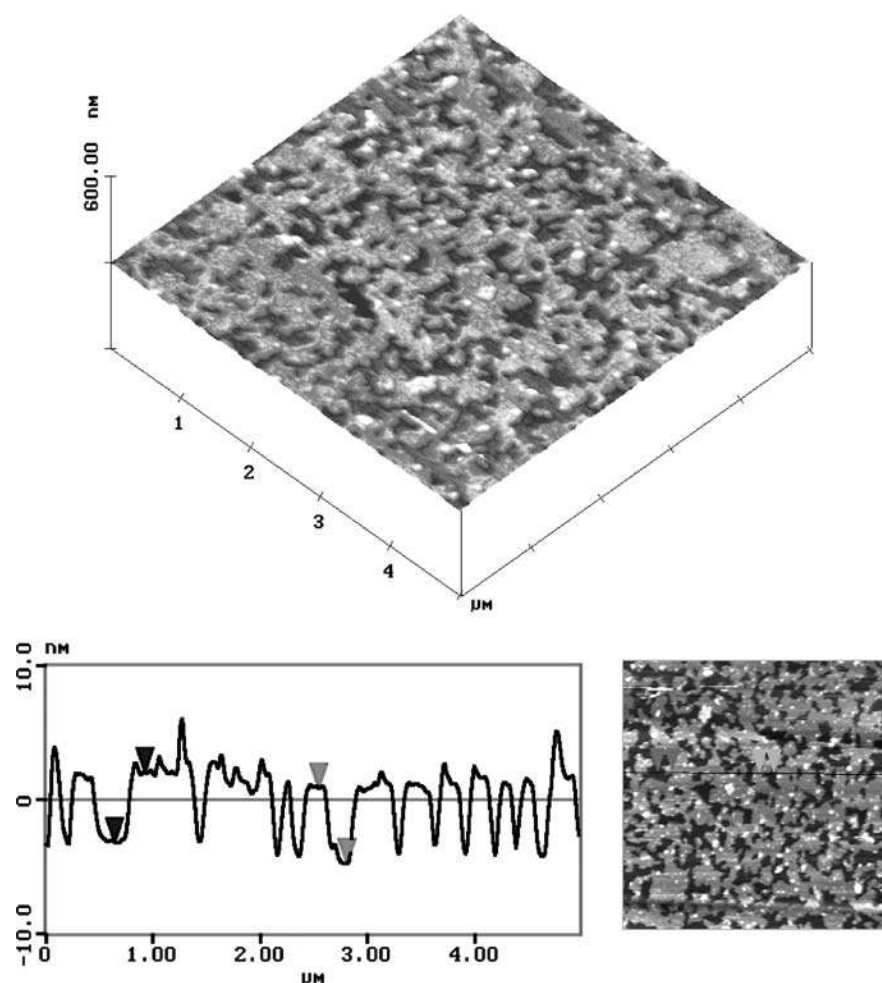
Immersion liquid	Concentration /M	$\Sigma\Delta\Theta_A$	$\Sigma\Delta\Theta_R$	$\Sigma\Delta\gamma /10^{-3} \text{ Nm}^{-1}$
Water		4.8	11.2	1.5
NaCl solution	0.010	7.3	10.4	36
	0.050	2.2	12.3	32
	0.100	1.5	12.7	34
CaCl_2 solution	0.003	2.2	14.8	28
	0.033	4.3	12.3	29

comparison the change in contact angles (and also the change in surface tension values) are summarised for the three immersion cycles. As a result of dipping the LB film three times into water or aqueous electrolyte solutions the decrease in the advancing contact angle is about the same as or is slightly higher than the standard deviation, while a significant decrease in the receding contact angles was found. It is notable that the receding values are close to those obtained on the bare substrate surface. The contact angle data presented in Table 1 suggest, moreover, that the wettability of the surfaces is not influenced by the presence of electrolytes.

In contrast, the surface tension of the immersion liquids (water, NaCl or CaCl_2 solutions) measured before and after the contact with the LB film shows a great difference depending on whether the immersion liquid was water or an electrolyte solution. The change in the surface tension is also summarised for the three consecutive immersion steps, $\Sigma\Delta\gamma$ (Table 1). When the LB film was exposed to water the decrease in the surface tension of the immersion liquid was very low, which corresponds to an amount of cadmium arachidate not more than a few percent of the total amount of material forming the bilayer on the support. From that we can assume that a small, but definite, amount of cadmium arachidate was removed from the LB film during the stability test. On applying aqueous solutions of NaCl or CaCl_2 the decrease in the surface tension is 1 order of magnitude higher than was in the case for water, indicating a considerable release of the LB film from the support. Comparing the results of various electrolytes NaCl proved to be more effective in the displacement of the LB film than CaCl_2 , while as a function of concentration no specific trend was observable.

The liquid was contacted with the LB film in a sessile drop geometry in the other type of stability test. In contrast with the other findings of dipping measurements no significant change was detected in the contact angle or in the surface tension of the liquid within 1 h. This

Fig. 2 Three-dimensional image ($5 \times 5 \mu\text{m}^2$) and a representative cross-sectional profile of the cadmium arachidate bilayer Langmuir–Blodgett (LB) film after immersion treatment in water obtained by atomic force microscopy (AFM). The vertical distances measured are 5.3 and 5.6 nm



contradiction refers to the fact that besides the type of liquid, the way of contact, especially the movement of the three-phase contact line, might be important in the detachment of the LB layer. Consequently, the LB film has considerable stability to the stationary liquid drops, while its sensitivity towards the moving contact line is high in a situation which is reminiscent of the transfer process itself by which the LB film was prepared.

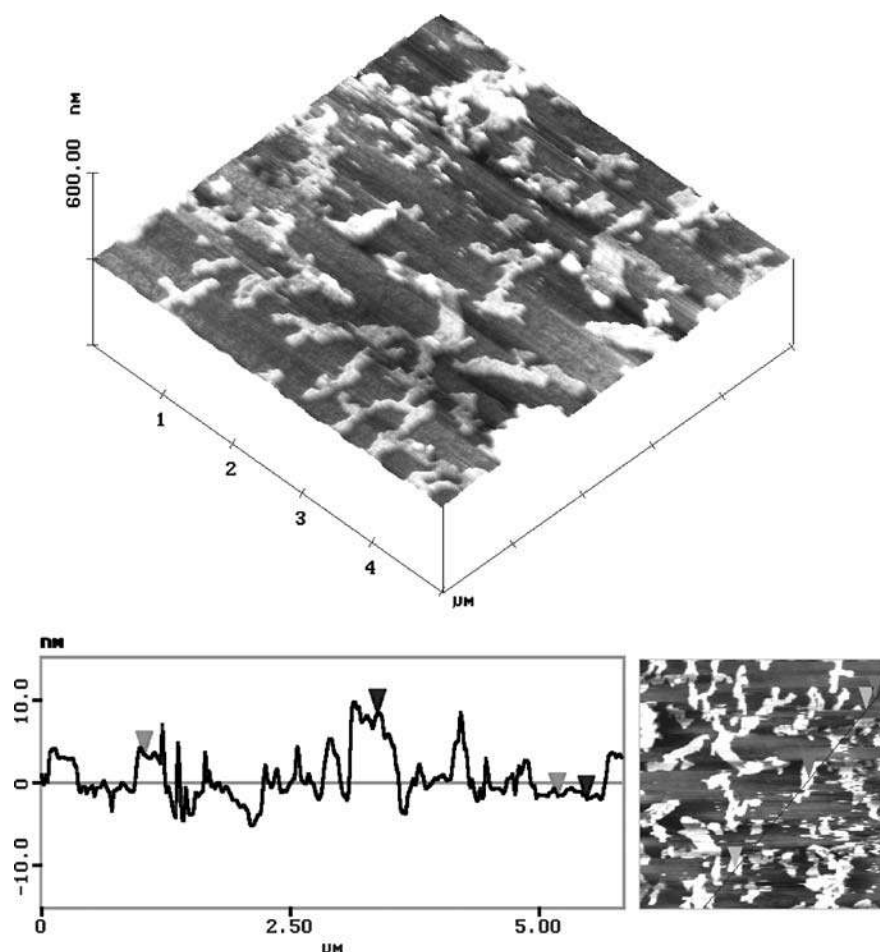
Wettability and surface tension measurements as indirect methods were able to reveal certain instabilities of the LB films in the course of immersion into water or an electrolyte solution; information on the quantitative or structural change of the film, however, can only be obtained using direct methods such as XPS or AFM.

XPS results

Surface analysis of the LB film was accomplished for selected samples following the stability test performed in water, NaCl and CaCl_2 solutions with a concentration of 0.1 and 0.033 M, respectively. The atomic composition

of the surface layer (involving the LB bilayer and a part of the glass support) was evaluated from the intensities of C1s , Cd3d , O1s and Si2p signals and was related to that of a reference sample of the untreated LB film. The composition of the surface layer (given in atomic percent) did not change significantly when the LB film was immersed into water. In contrast, the release of 20–25% of the LB film was assessed from the decreased concentration of carbon and cadmium detected on the surface following the immersion into CaCl_2 solution, while the loss of LB material from the surface was even higher, above 60% on applying NaCl solution in the stability test. The partial detachment of the LB film was also demonstrated by the corresponding increase of oxygen and silicon peaks in the XPS spectra, which is related to the decreased coverage of the substrate surface. These relations could be evaluated in a more precise way using the XPS MultiQuant program [27] incorporating morphological information and applying an adequate model of the layer; however, the strong effect of salts on the adhesional stability of LB films is accurately reflected even in the direct surface composition data.

Fig. 3 Three-dimensional image ($5 \times 5 \mu\text{m}^2$) and a representative cross-sectional profile of the cadmium arachidate bilayer LB film after immersion treatment in an aqueous solution of NaCl (0.1 M) obtained by AFM. The vertical distances measured are 5.0 and 10.5 nm



AFM studies

Two-layer LB films following the treatment in water or aqueous electrolyte solutions were investigated by AFM. Besides the representative three-dimensional images the cross-sections of the layer are also displayed. The surface of the LB film treated in water (Fig. 2) seems to be rather smooth with some holes or hollows of various sizes. From the bearing analysis two depth levels can be identified with a difference between them of about 5.4–5.5 nm. That value is quite close to the thickness of the cadmium arachidate bilayer (5.6 nm), so the depth levels can be supposed to correspond to the bare substrate and to the top of the two-layer LB film. The coverage of the substrate was proved to be more than 90% by calculating it from six images recorded at different areas on the sample.

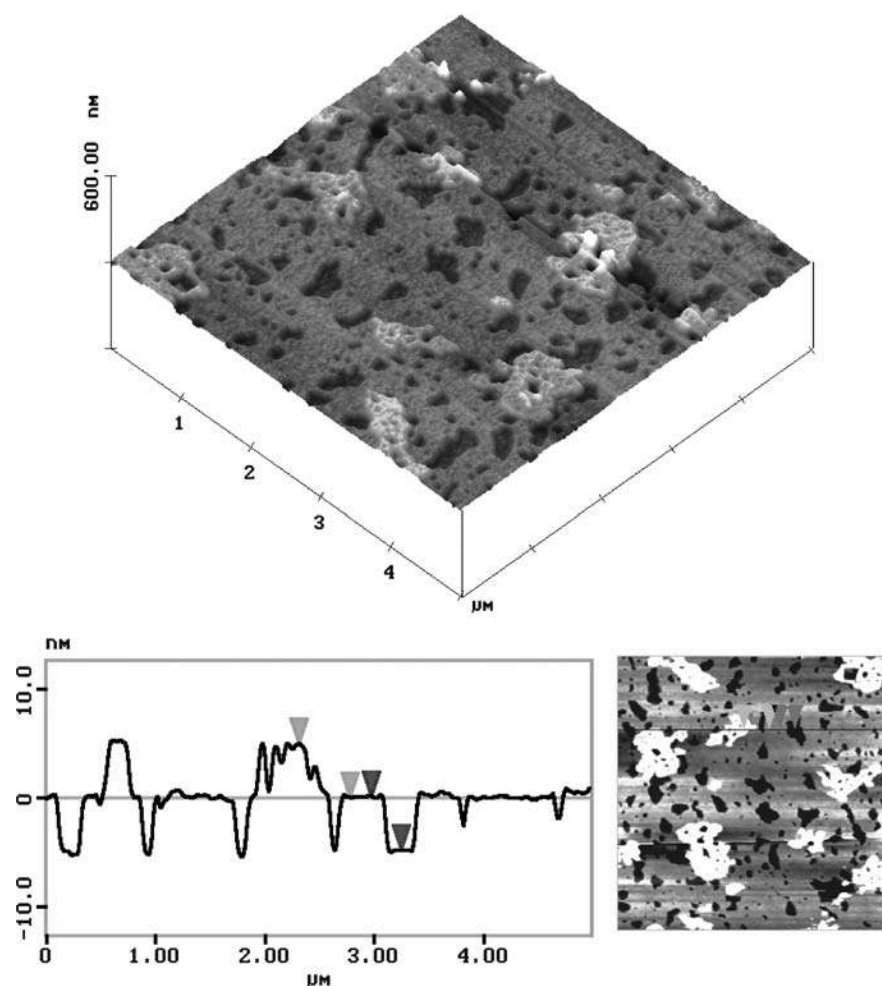
The treatment in NaCl solution (0.1 M) results in a quite different picture of the surface (Fig. 3). The striking feature is that most of the material of the LB film is removed. The coverage of the substrate dropped below 20%. The surface looks rather irregular, the rest of the material apparently lost its ordered structure and formed

random patches. There are no terraces or there are no areas with characteristic thickness as the cross-section profile shows.

The surface of the LB film treated in CaCl_2 solution (0.033 M) is shown in Fig. 4. The height histogram of the image demonstrated that the surface consisted of terraces. Generally three distinct depth levels were observed. The even thickness of the bilayer is more or less preserved, while the bare substrate is also exposed at certain areas. The third depth level corresponds to the surface of additional patches appearing on the top of the bilayer. The difference between these three levels is close to but slightly less than the thickness of the bilayer. The average surface coverage remained about 70%.

It is suggested from the images of the LB film that comparing the two electrolytes their influence originates from different mechanisms. The interaction of an aqueous solution of NaCl with cadmium arachidate is probably a specific dissolution-type effect, which might be initiated at the pinholes or defects of the ordered layer. The results of XPS surface analysis also supported that the removal of cadmium arachidate by NaCl solution is

Fig. 4 Three-dimensional image ($5 \times 5 \mu\text{m}^2$) and a representative cross-sectional profile of the cadmium arachidate bilayer LB film after immersion treatment in an aqueous solution of CaCl_2 (0.033 M) obtained by AFM. Both vertical distances measured are 4.9 nm



much more effective than by a solution of CaCl_2 (applied at the same ionic strength) or by water.

On the other hand, water and a solution of CaCl_2 cause such changes in the LB layer which are similar in nature but different in extent. Both surface tension and surface composition measurements revealed some displacement of the LB film material from the substrate, which was minor in the case of water but more considerable in CaCl_2 solution. As is visualised by AFM studies some parts of the bilayer are detached, leaving bare regions on the substrate. The terraces formed are always separated by a vertical distance which is close to the thickness of a bilayer. The degradation of the LB film by removal of a monolayer was never observed. This fact can be explained by previous results of Kurnaz and Schwartz [24] on the morphology of cadmium arachidate LB films, which implied that structures are correlated in the neighbouring layers.

The bilayer islands which were detached in certain regions from the substrate are characterised by an approximate size of $0.3\text{--}1 \mu\text{m}$. It is interesting to note that domains with ordered structures of cadmium

arachidate films were reported by Choi [28], the characteristic size of which was in the range $0.5\text{--}1 \mu\text{m}$. Besides the morphology of the LB layer following the stability tests, this accordance in the sizes of released islands and domains might suggest that the removal of the LB film (owing to dipping into water or aqueous solution of CaCl_2) is a peeling-type detachment process rather than a molecular scale event. One might speculate that the border of domains are the assailable regions where the peeling can start to operate. Similar phenomena, such as reverse transfer of a lipid layer back to the water surface [14], severe degradation of behenic acid film dipping into water [29], and pure stability of three component LB films at the three-phase contact line [12], were reported previously, although hydrophilic substrates were used in all of those works. That means that the molecular interactions involved in the deposition and adherence of the first layer are different from that in our case, when the attachment of hydrophobic chains of the first layer to the hydrophobic surface is governed by hydrophobic interactions. That kind of interaction usually offers weak adhesion as was found, for example, for a

methylarachidate LB film onto a hydrophobic substrate [13] presenting great sensitivity to “contact line corrosion” [30]. The driving force for the eventual redeposition of the released bilayer patches might be the difference of the hydrophobicity between the substrate and the LB film. On the basis of estimated interaction energies the substrate–water interaction might be energetically more favourable than the LB film–water contact.

Conclusions

The adhesional stability of cadmium arachidate LB films was characterised in an aqueous environment in the geometry of a sessile drop and also by immersing the plate into the liquid. The results demonstrate that the measurement of the surface tension of the immersion liquid provides a sensitive tool to estimate the amount of the LB material removed from the solid substrate. However, the wettability of the LB film was

also found to change during contact with water or aqueous electrolyte solutions; the degree of alteration of the wettability does not allow reliable evaluation of the film stability.

The mechanism of the removal of the cadmium arachidate LB film from a hydrophobic support, as the AFM study reveals, is a peeling-type detachment of a bilayer in water or an aqueous solution of CaCl_2 , while the dissolution of the LB film is more probable in the case of an NaCl solution.

It is noteworthy, however, that the stability of the LB film seems to be dependent on the type of its contact with the liquid. Neither the surface tension of the liquid nor the contact angle showed a detectable change for at least 1 h when the liquid was applied as a sessile drop in contrast to the case of moving contact line in the immersion-type stability test.

Acknowledgement Financial support from the Hungarian Research Fund (OTKA T025789) is acknowledged.

References

- Fendler JH (1987) *Chem Rev* 87:877
- Möhwald H (2000) *Colloids Surf A* 171:25
- Abdelmalek F, Shadaram M, Boushriha H (2001) *Sens Actuators B* 72:208
- Miller LS, McRoberts AM, Walton DJ, Perry DA, Newton AL (1995) *Mater Sci Eng C* 3:257
- Penacorada F, Angelova A, Kamusewitz H, Reiche J, Brehmer L (1995) *Langmuir* 11:612
- Brandl D, Schoppmann Ch, Tomaschko Ch, Schurr M, Voit H (1995) *Thin Solid Films* 256:220
- Girard KP, Quinn JA, Vanderlick TK (2000) *Thin Solid Films* 371:242
- Heens B, Grégoire Ch, Pireaux JJ, Cornelio PA, Gardella JA Jr. (1991) *Appl Surf Sci* 47:163
- Iimura K, Kato T (2000) *Colloids Surf A* 171:249
- Cha J, Shin HS, See Y-K, Lee J, Chang T, Kim SB (2001) *Synth Met* 117:169
- Schwartz DK, Viswanathan R, Zasadzinski JAN (1992) *J Phys Chem* 96:10444
- Berg JM, Eriksson LGT, Claesson PM, Borve KGN (1994) *Langmuir* 10:1225
- Angelova A, Penacorada F, Stiller B, Zetzsche T, Ionov R, Kamusewitz H, Brehmer L (1994) *J Phys Chem* 98:6790
- Yaminski V, Nylander T, Ninham B (1997) *Langmuir* 13:1746
- Marek T, Szeles Cs, Süvegh K, Kiss É, Vértés A, Lynn KG (1999) *Langmuir* 15:8189
- Mohai M, Kiss É, Tóth A, Szalma J, Bertóti I (2002) *Surf Interface Anal* 34:722
- Yaminski VV, Claesson PM, Eriksson JC (1993) *J Colloid Interface Sci* 161:91
- McRitchie F (1990) *Chemistry at interfaces*. Academic, San Diego p 283
- Evans S, Pritchard RG, Thomas JM (1978) *J Electron Spectrosc Relat Phenom* 14:341
- Reilman RF, Msezane A, Mansor ST (1976) *J Electron Spectrosc Relat Phenom* 8:389
- Powell CJ, Jablonski A (2000). NIST electron inelastic-mean-free-oath database, version 1.1. National Institute of Standards and Technology, Gaithersburg, MD
- Peng JB, Barnes GT, Gentle IR (2001) *Adv Colloid Interface Sci* 91:163
- Yazdani M, Yu H, Zografi G (1990) *Langmuir* 6:1093
- Kurnaz ML, Schwartz DK (1996) *J Phys Chem* 100:11113
- Avila LVN, Saraiva SM, Oliveira JF (1999) *Colloids Surf A* 154:209
- Schwartz DK, Viswanathan R, Garnaes J, Zasadzinski JA (1993) *J Am Chem Soc* 115:7374
- Mohai M (2000) XPS MultiQuant for Windows user's manual. Budapest
- Choi J-W, Cho KS, Lee WH, Lee HS (1998) *Thin Solid Films* 327–329:273
- Albrecht O, Matsuda H, Eguchi K, Nakagiri T (1999) *Thin Solid Films* 338:252
- Bikerman JJ (1940) *Trans Faraday Soc* 36:412

János Móczó
Erika Fekete
Béla Pukánszky

Adsorption of surfactants on CaCO_3 and its effect on surface free energy

Abstract A CaCO_3 filler was coated with various mono- and dicarboxylic acids in a dry-blending process. The coated fillers were characterized by various techniques, including dissolution experiments, thermal analysis (differential scanning calorimetry) and inverse gas chromatography (IGC) to determine the amount of surfactant needed to achieve monolayer coverage; IGC proved to be the most convenient, reliable and universal method for this purpose. The dispersion component of the surface tension and the specific interaction potential of the coated filler can be derived from the results, but indirect conclusions can be also drawn from them about the orientation of the molecules on the filler surface and the structure of the layer formed. The coverage of the filler with an organic compound leads to a

decrease both in the dispersion component of the surface tension and in the acid–base character of the filler surface. In the case of monocarboxylic acids the amount needed for monolayer coverage depends on the chemical structure of the surfactant. Linear chains are assumed to orientate vertically to the surface, while increasing chain length, branches as well as unsaturations lead to a less regular arrangement of the molecules, to a looser structure. At the same surface coverage, the surface tension of the filler covered by aliphatic monocarboxylic acids is the same for all compounds. The adsorption of dicarboxylic acids is more complicated and the decrease in surface tension is significantly smaller than for monocarboxylic compounds.

J. Móczó · E. Fekete · B. Pukánszky (✉)
Institute of Chemistry,
Chemical Research Center,
Hungarian Academy of Sciences,
P.O. Box 17, 1525 Budapest,
Hungary
e-mail: pukanszky@muatex.mua.bme.hu

J. Móczó · E. Fekete · B. Pukánszky
Department of Plastics
and Rubber Technology,
Budapest University of Technology
and Economics, P.O. Box 92,
1521 Budapest, Hungary

Introduction

Particulate-filled composites are widely used in many fields of application. The filler used in largest quantity is CaCO_3 , which is added mainly to poly(vinyl chloride), but significant amounts are used also in polypropylene, polyethylene and other polymers. Typical products prepared from CaCO_3 -filled composites are sewer and drainage pipes, garden furniture and breathable films [1]. The properties of particulate-filled polymers are determined by several factors, of which interfacial interactions are extremely important [2, 3]. Particle–particle and

particle–matrix interactions develop in such composites, the first determines the extent of aggregation, while the second the adhesion of the phases. The majority of commercial CaCO_3 fillers are coated with an organic substance, mainly stearic acid, in order to avoid aggregation, which deteriorates composite properties. Surface treatment decreases the surface tension of the filler and thus both kinds of interactions [4, 5]. The decrease of surface tension and the efficiency of the coating are determined by several factors, including the character of the interaction between the surfactant and the filler surface, surface coverage, the structure of the interlayer

formed and the interaction of the adsorbed surfactant molecule with the polymer matrix [5, 6]. The structure of the surfactant layer depends on the orientation of the organic molecules on the filler surface, which, on the other hand, is influenced by their chemical structure and surface coverage [6].

The structure of this layer and the effect of a coating on the surface characteristics of particulate fillers can be studied by numerous techniques [7]. Surface analytic techniques, like X-ray photoelectron spectroscopy, secondary ion mass spectroscopy, Fourier transform IR (FTIR) spectroscopy, solid-state NMR and X-ray diffraction give information about the orientation of the surfactant molecules and about surfactant–filler interaction [5, 6, 7, 8, 9, 10]. Flow microcalorimetry and the determination of adsorption isotherms reveal the amount of surfactant adhering to the surface, the strength of interaction as well as its mechanism [7, 8, 9]. Various other methods may also be applied to draw conclusions about the efficiency of surface coating, like differential scanning calorimetry (DSC), scanning electron microscopy [11], infiltration and adsorption of liquids on the coated filler [12, 13] and the measurement of composite properties [4, 5, 14, 15, 16]. Although inverse gas chromatography (IGC) is often used [17, 18, 19, 20] for the determination of surface free energy, surface coverage and the acid–base character of the coated filler, the measured quantities are rarely related to the structure of the adsorbed layer.

Only a limited number of studies have been carried out to determine the adsorption of carboxylic acids on fillers generally, and even less on CaCO_3 in spite of the practical importance of this filler. Liauw and coworkers [8, 9] investigated the adsorption of various saturated and unsaturated carboxylic acids from heptane on $\text{Mg}(\text{OH})_2$ and $\text{Al}(\text{OH})_3$ and found that the amount and the orientation of the adsorbed acids are affected by the structure of the alkyl tail and the number of double bonds in the surfactant molecule. The double bond participates in the adsorption and a looser surface layer forms than in the case of saturated acids. In a similar study, Ottewil and Tiffany [21] came to practically the same conclusion using rutile titanium dioxide as a filler.

According to them, at monolayer coverage, stearic acid is oriented vertically to the surface, while the orientation of unsaturated carboxylic acids is less regular. Ivanishchenko and Gladkikh [13] studied the adsorption of fatty acids with different chain lengths on CaCO_3 . They pointed out that orientation and surface coverage depend also on the length of the aliphatic chains: more surfactant is needed to achieve monolayer coverage from carboxylic acids with shorter chain lengths. All these studies and our earlier results [5, 22] indicate that the amount of adsorbed surfactant also depends on the specific surface area of the filler. Saturated carboxylic acids are attached to the surface through their acidic functionality, orientated vertically to the surface, and surface coating leads to a decrease in the surface polarity of the filler.

The goal of this study was to use IGC to investigate the adsorption of mono- and dicarboxylic acids on the surface of CaCO_3 as well as the changes in surface free energy as an effect of the coating. In this effort the structure of the surfactant was varied considerably, surfactants with various chain lengths, chemical structures (branched, unsaturated) and with different numbers of acidic moieties were used for the coating of the filler. The amount of acid necessary for monolayer coverage was determined from the measured data and an attempt was made to draw conclusions from the IGC experiments about the orientation of the surfactant molecules and about the structure of the adsorbed layer.

Experimental

A ground-type CaCO_3 with an average particle size of $1.8 \mu\text{m}$ and a specific surface area of $4.0 \text{ m}^2 \text{ g}^{-1}$ was supplied by Omya and was used in the experiments. The most important characteristics of the surfactants studied are listed in Table 1; the compounds include three saturated monocarboxylic acids with different chain lengths, a branched and an unsaturated monocarboxylic acid, as well as two dicarboxylic acids. CaCO_3 was treated with different amounts of surfactant (0–7.0 wt%). The neat CaCO_3 filler was coated with the surfactants in a dry-blending process. The treatment was carried out in a Haake Rheomix 600 internal mixer fitted with blades, which can be used for powder mixing. The mixer was driven by a

Table 1 Characteristics of the surfactants used in the study for the coating of CaCO_3

Compound	Composition	Structure	Molecular weight (g mol^{-1})	Melting temperature ($^{\circ}\text{C}$)	Boiling point ($^{\circ}\text{C}$) ^a
Lauric acid	$\text{C}_{12}\text{H}_{24}\text{O}_2$	$\text{CH}_3(\text{CH}_2)_{10}\text{COOH}$	200.3	44	225^{100}
Stearic acid	$\text{C}_{18}\text{H}_{36}\text{O}_2$	$\text{CH}_3(\text{CH}_2)_{16}\text{COOH}$	284.5	70	291^{100}
Behenic acid	$\text{C}_{22}\text{H}_{44}\text{O}_2$	$\text{CH}_3(\text{CH}_2)_{20}\text{COOH}$	340.6	84	306^{60}
Oleic acid	$\text{C}_{18}\text{H}_{34}\text{O}_2$	$\text{CH}_3(\text{CH}_2)_7\text{CH}=\text{CH}(\text{CH}_2)_7\text{COOH}$	282.5	16	282^{100}
2-Ethylhexanoic acid	$\text{C}_8\text{H}_{16}\text{O}_2$	$\text{CH}_3(\text{CH}_2)_3\text{CH}(\text{C}_2\text{H}_5)\text{COOH}$	144.2	–59	113^{11}
Oxalic acid	$\text{C}_2\text{H}_2\text{O}_4$	$\text{HOOC}-\text{COOH}\cdot\text{H}_2\text{O}$	126.1	101	150^{subl}
Sebacic acid	$\text{C}_{10}\text{H}_{18}\text{O}_4$	$\text{HOOC}(\text{CH}_2)_8\text{COOH}$	202.3	133	

^aThe superscript corresponds to the pressure in torr

Haake Rheocord EU 10-V unit. In this procedure 80 g filler was preblended with the necessary amount of surfactant, then it was introduced into the mixer at various temperatures and was homogenized at 100 rpm for 10 min. Since the compounds used in the project melt over a wide range, the temperature of the coating was selected to be 30 °C higher than the melting temperature of the surfactant in order to create similar conditions in all cases.

The dispersion component of the surface tension of the fillers was determined by linear IGC [23, 24]. Before column preparation the filler was aggregated by suspending it in methanol, then drying at 110 °C in an oven. The ground filler was sieved and the fraction between 800 and 1,000 μm was used as packing. Before the measurement the column was conditioned at 140 °C for 16 h, and the measurements were carried out at 100 °C. High-quality nitrogen was used as a carrier gas with flow rates between 6 and 20 ml min^{-1} . The temperature of both the injector and the flame ionization detector was set to 200 °C. The dispersion component of the surface tension of the fillers was determined from the retention time of normal alkanes with chain lengths between 6 and 10 carbon atoms using the Dorris–Gray method [24]. The specific interaction term was calculated from the retention time of chloroform. The amount of vapor injected into the column changed between 0.5 and 20 μl ; methane was used as a marker. The amount of the irreversibly bonded surfactant was determined by the dissolution technique developed in our laboratory earlier [5, 22]. Coated filler (20 g) was put into 100 cm^3 solvent and stirred for 30 min. As soon as the filler settled, the concentration of the coating agent was determined in the solution by FTIR spectroscopy. The solvent was usually CCl_4 , but occasionally other solvents (tetrahydrofuran, CHCl_3) had to be used. The amount of dissolved surfactant was determined from the absorbance of the carbonyl vibration appearing in the range 1716–1710 cm^{-1} . A calibration curve was prepared and used for quantitative determination. The coated fillers were also studied by DSC. The measurements were done in the DSC 30 cell of a Mettler TA 4000 instrument. Samples of 10 mg were measured under oxygen at a heating rate of 10 °C min^{-1} . The thermograms were evaluated both qualitatively and quantitatively to check the presence of free surfactant; in this way the technique can be used for the determination of monolayer coverage.

Results and discussion

The results of the experiments are presented in three sections. First, monolayer coverages determined by various experimental techniques are compared and the methods are evaluated critically. The adsorption

characteristics of mono- and dicarboxylic acids, respectively, as well as the effect of adsorption on the surface characteristics of the filler are discussed in the following two, separate sections.

Determination of monolayer coverage

The dissolution technique has been described elsewhere [5, 14, 17, 22]; thus, we refrain from its detailed discussion here. The adsorption of organic compounds on the surface of particulate fillers can be studied especially well with the method. Dissolution experiments usually yield an adsorption isotherm with a saturation value. The amount of surfactant needed for monolayer coverage, c_{100} , can be determined from the isotherm as the value deviating from the straight line indicating irreversible bonding. Both the quality of the isotherm and the accuracy of the determination of monolayer coverage depend very much on the particle characteristics of the filler, on the chemical structure of the surfactant and on the solvent used. The adsorption of stearic acid could be determined easily and accurately also in this study; isotherms similar to those reported earlier [5, 14, 22] were also recorded in this case. As the adsorption of other carboxylic acids takes place in more than one step, monolayer coverage was determined from the first step. The c_{100} values determined by the dissolution technique are compiled in Table 2. These values could not be determined unambiguously by this method for dicarboxylic acids, thus they are omitted from the table.

During the detailed investigation of coated fillers we observed that thermal calorimetry gives valuable information about the quality of the coating and the homogeneity of the samples. One or two shoulders or peaks appear on the thermogram recorded by DSC, when the surfactant is overcoated or its distribution is heterogeneous. Further study indicated that these shoulder or peaks belong to the free acid, which is adsorbed on the surface of the filler, but not attached to it by ionic bonds. Moreover, an additional endothermic transition

Table 2 Monolayer coverage (c_{100}) determined by various methods

Carboxylic acid	c_{100} (mmol/100 g filler) determined by				
	Dissolution	Differential scanning calorimetry		Inverse gas chromatography	
		Carboxylic acid melting peak	Oxidation shoulder	Surface tension	Specific interaction term
Lauric	5.0–6.0	6.0	–	5.0	5.0
Stearic	3.5–4.5	3.5	3.5	4.2	4.2
Behenic	2.4–2.9	2.9	2.9	3.5	2.9
Oleic	2.8–3.5	–	3.5	3.5	2.8
2-Ethylhexanoic	–	–	5.6	5.6	5.6

can also be detected for acids having a melting peak above room temperature. Typical thermograms are presented in Fig. 1 for the filler coated with various amounts of stearic acid. The endothermic peak characterizing the melting of the acid appears at around 71 °C, followed by several exothermic transitions. These latter peaks indicate the oxidation of the surfactant, which was proved by measurements carried out in an inert atmosphere. Under such conditions all the exothermic peaks were absent. A closer scrutiny of the thermograms clearly indicates that several peaks appear only above a certain surface coverage. From the analysis of the results we concluded that monolayer coverage could be determined from the appearance of the transitions belonging to the free acid.

In the case of stearic acid the determination of monolayer coverage is demonstrated in Fig. 2. The heat of fusion of the free acid is plotted against the amount of surfactant used for the treatment; the data were taken from the thermograms presented in Fig. 1. The determination of monolayer coverage is clear and unambiguous. Unfortunately the melting peak cannot be used for compounds having a melting temperature lower than room temperature. In this case, the monolayer coverage can be deduced from the appearance of the shoulder related to the oxidation of the free acid. However, the degradation reactions depend very much on the structure of the organic compound; thus, the shape and intensity of these shoulders and peaks vary from compound to compound. As a consequence, in the case of lauric acid, monolayer coverage could not be determined by this second approach at all. Monolayer coverages obtained from the analysis of the thermograms are compiled in Table 2.

IGC is a well-established method for the surface characterization of fillers and fibers. Earlier experiments

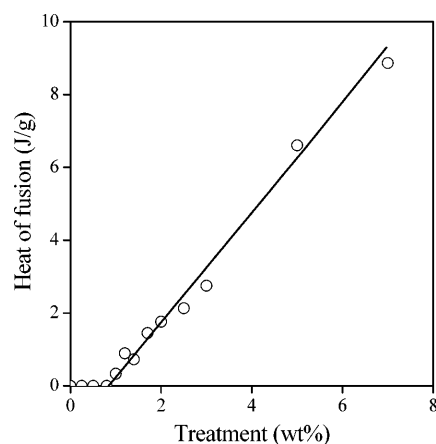


Fig. 2 Heat of fusion of free stearic acid as a function of the amount of surfactant used for the treatment

have shown that the surface tension of fillers treated with stearic acid decreases significantly with increasing surface coverage [4, 5, 14]. A minimum appears in the surface tension as a function of surfactant concentration, then the surface free energy starts to increase again when larger amounts are used for treatment. Measurements carried out by various methods proved that the minimum corresponds to the monolayer coverage of the filler by the given surfactant. In this study, the dispersion component of the surface tension of the filler coated with different mono- and dicarboxylic acids was determined by infinite-dilution IGC. The dispersion component of the surface tension measured on the filler coated with behenic acid is plotted against the amount of acid used for treatment in Fig. 3. As already mentioned, the surface tension decreases, reaches a minimum at about 1.2 wt%, then increases again. If we accept that the minimum corresponds to monolayer coverage, the determination of the

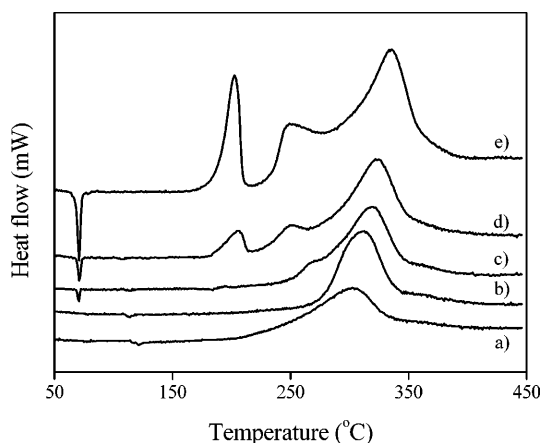


Fig. 1 Differential scanning calorimetry thermograms recorded on CaCO_3 fillers coated by various amounts of stearic acid. *a* 0.5, *b* 0.8, *c* 1.0, *d* 2.0, *e* 5.0 wt%

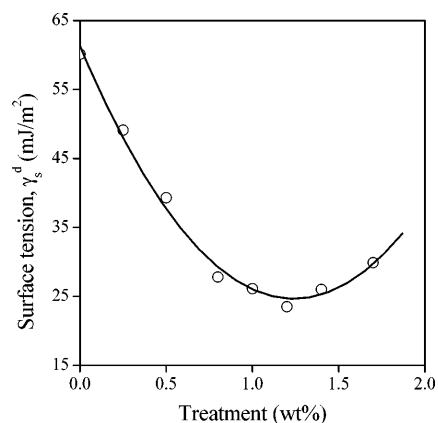


Fig. 3 Changes in the dispersion component of the surface tension of CaCO_3 coated with behenic acid as an effect of the amount of surfactant used for the coating

amount of surfactant necessary to reach this value is easy and accurate. The values obtained in this way are listed in Table 2 for all surfactants.

Polar surfaces enter into acid–base interactions with other materials. Such interactions can be characterized by the free-enthalpy change of adsorption, ΔG^{sp} , of polar probes, which can also be determined by IGC from the retention volume of an appropriate solvent. CaCO_3 is basic in character and its basicity can be determined by using an acidic solvent; CHCl_3 was used in this study. The ΔG^{sp} values obtained on behenic acid coated fillers are plotted in Fig. 4 as a function of the surfactant used for the treatment. The same tendency is observed as in Fig. 3 and the minimum appear practically at the same surfactant content. The free-enthalpy change of adsorption was determined for fillers coated with all the surfactants studied and the results are listed in Table 2.

The comparison of the data compiled in Table 2 allows us to draw several conclusions. We see that the amount of surfactant necessary to reach monolayer coverage is different for most of the surfactants, but the differences are not very large. Moreover, similar values were obtained with all techniques used for determination. On the other hand, the values deduced from the dissolution experiments are not very accurate, in fact only a range could be defined instead of a single value. The possible use of DSC for the determination of monolayer coverage is limited; it depends on the chemical and physical properties of the surfactant used for the treatment. The most reliable method for the determination of monolayer coverage is IGC. The technique could be used in each case, independently of the coating agent applied. Even better agreement can be reached between the values determined from the dispersion component of surface tension and the term characterizing specific acid–base interactions, respectively, if

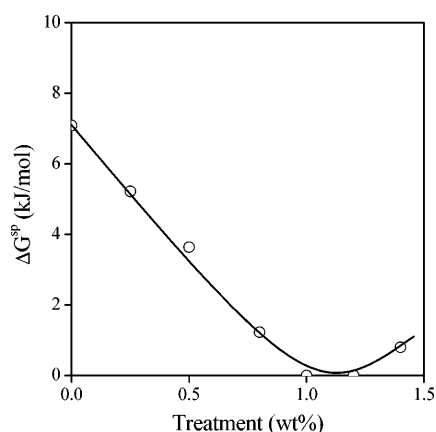


Fig. 4 Acid–base character of the filler coated with behenic acid as a function of the amount of surfactant used for the treatment

these quantities are determined at a larger number of surface coverages than in the present study. Surface tension could also be measured on fillers coated with dicarboxylic acids, but the determination of monolayer coverage was difficult because of the peculiar adsorption character of these acids.

Adsorption of monocarboxylic acids

In the previous section we concluded that IGC is an appropriate technique for the surface characterization of coated fillers. In this section we compare the adsorption of the various surfactants on CaCO_3 and the surface characteristics of the coated fillers. We also try to draw conclusions about the effect of chemical structure on adsorption and on the arrangement of the surfactant molecules on the surface, i.e. about the structure of the adsorbed layer. The dispersion component of the surface tension is plotted in Fig. 5 against the amount of surfactant used for coating for the fillers treated with the three linear, saturated carboxylic acids. The character of the correlation is the same in all three cases. However, the minimum appears at different amounts of surfactant; monolayer coverage is reached with less acid as the length of the aliphatic chain increases. This result is in accordance with literature information and indicates that the arrangement, the orientation of the surfactant on the surface of the filler, changes with chain length [13]. We assume that at monolayer coverage short chains are oriented vertically to the surface, but with increasing chain length the orientation becomes less regular; a single chain occupies a larger area and a looser, less regular structure forms. Naturally, this assumption must be verified by further measurements carried out by appropriate analytical techniques, but this tentative

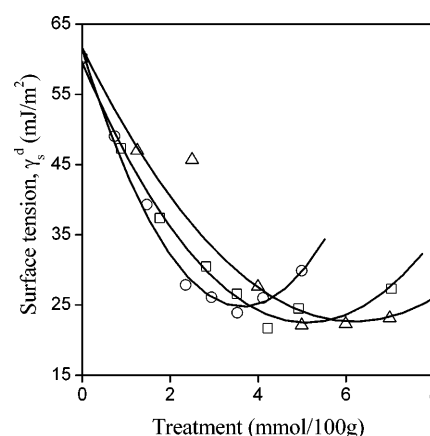


Fig. 5 Effect of the length of the aliphatic chain and the amount of surfactant on the surface tension of CaCO_3 coated with various monocarboxylic acids: behenic (circles), stearic (squares), lauric (triangles)

explanation is in accordance both with the experimental results and with published information.

The conclusion drawn in the previous paragraph is further corroborated by Fig. 6, in which the dispersion component of the surface tension is presented for fillers coated with all the monocarboxylic acids investigated in this study. If the results are plotted on a relative scale, as a function of surface coverage, a single correlation is obtained. The relative scale was created by using the amount of surfactant at which the minimum of surface tension is reached, i.e. monolayer coverage, as a reference value. Although the arrangement of the surfactant molecules on the surface of the filler may depend on their chemical structure, the surface tension of the filler is the same and depends only on coverage, at least in the case of aliphatic monocarboxylic acids. This result has several important practical consequences. It indicates that surface tension cannot be decreased below a certain minimum value with such compounds. If we want to create weaker filler–filler or filler–matrix interactions, we must use a different approach, compounds with a completely dissimilar composition and/or chemical structure. However, the amount of surfactant needed to reach the minimum depends on the chemical structure of the compound used. This opens up possibilities in the selection of the surfactant: the choice can be based on technological aspects as well as on price–performance relations.

The influence of the chemical structure of the surfactant is further emphasized by Fig. 7, where monolayer coverage determined from surface tension, denoted by c^{γ}_{100} , is plotted against the chain length of the carboxylic acid used for the treatment. A well-defined linear correlation is obtained for the saturated acids; the amount needed for monolayer coverage decreases with increasing chain length as discussed earlier. For

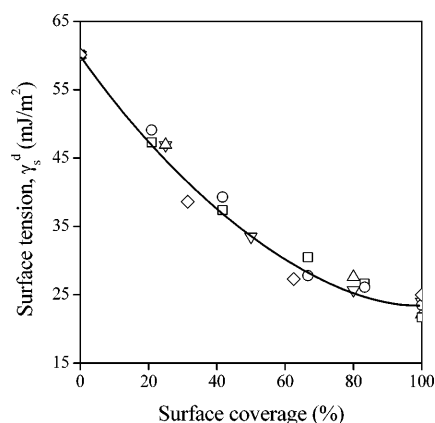


Fig. 6 Universal correlation of surface tension and surface coverage. Oleic acid (*down triangles*), lauric acid (*up triangles*), stearic acid (*squares*), behenic acid (*circles*) and 2-ethylhexanoic acid (*diamonds*)

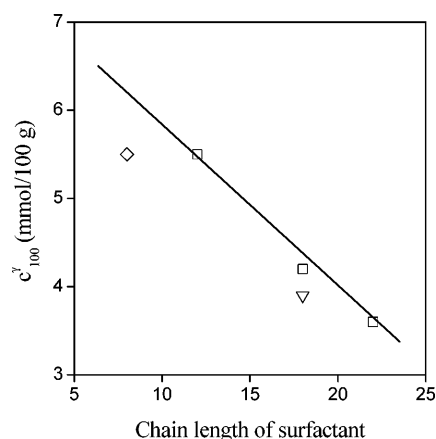


Fig. 7 Effect of chain structure on the amount of aliphatic monocarboxylic acids needed for monolayer coverage. Saturated acids (*squares*), oleic acid (*triangles*), 2-ethylhexanoic acid (*diamonds*)

surfactants with a different structure, i.e. with a branch or unsaturation in the molecule, monolayer coverage is reached at lower amount. This result is again in accordance with literature information [6, 8]. A substituent changes the area occupied by the molecule and the arrangement of the chains on the surface of the filler hinders parallel alignment and creates a looser structure. As we saw already, a looser structure leads to lower surface energy at the same amount of surfactant. Unsaturation has practically the same effect. Double bonds may interact with the surface through induced-dipole interaction, which results in the irregular arrangement of the chains on the surface again. These effects offer further possibilities to choose the proper surfactant for the coating of a filler. However, besides price and performance some other factors, like dosing, homogenization and the stability of the compound, must also be taken into account by the selection.

Adsorption of dicarboxylic acids

The adsorption of dicarboxylic acids is more complicated than that of their monocarboxylic counterparts. They are more polar and the acidic groups situated at both ends of the aliphatic chain offer a variety of possibilities for adsorption. The two groups might be attached to different filler particles, they may be oriented vertically or parallel to the surface or can also form loops. The changes in the dispersion component of surface tension are plotted against the amount of surfactant used for the treatment for fillers coated with the two dicarboxylic acids in Fig. 8. The surface tension of the filler treated with stearic acid is also presented for comparison. Several conclusions can be drawn from the results shown in the figure. A much smaller decrease can be achieved in

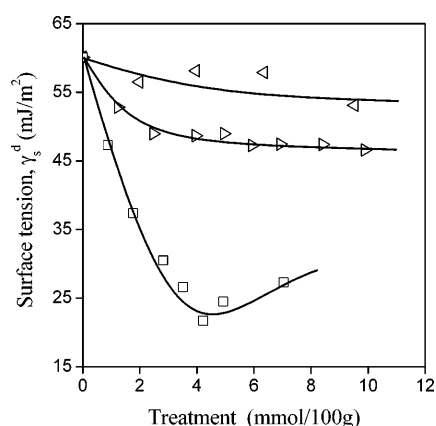


Fig. 8 Coating of CaCO_3 with dicarboxylic acids: effect of the chemical structure and the amount of surfactant used for the treatment. Oxalic acid (left triangles), sebacic acid (right triangles), stearic acid (squares)

surface tension if the filler is coated with dicarboxylic acids than with monocarboxylic acids. The changes in the surface characteristics of the filler are negligible when oxalic acid is used and sebacic acid also has only a moderate effect. In the first case the reason for the limited effect is most probably the high polarity of the acid. On the other hand, the longer aliphatic chain of sebacic acid offers more options for the arrangement of the molecule on the surface. It may bite back to the surface; thus, both functional groups can take part in the adsorption. However, from the available data, we cannot draw definite conclusions about the arrangement of the surfactant on the filler surface and about the structure of the adsorbed layer; further experiments must be carried out to obtain more information about these questions.

Conclusions

The study of a CaCO_3 -filler coated with various mono- and dicarboxylic acids proved that the amount of surfactant which is needed to achieve monolayer coverage can be determined by various techniques, but the most convenient, reliable and universal method is IGC. The dispersion component of the surface tension and the specific interaction term of the coated filler can be determined from the results, but indirect conclusions can be drawn from them about the orientation of the molecules on the filler surface and the structure of the layer formed. The coverage of the filler with an organic compound leads to a decrease both in the surface tension and in the acid-base character of the filler. In the case of monocarboxylic acids the amount needed for monolayer coverage depends on the chemical structure of the surfactant. Linear chains are assumed to be orientated vertically to the surface, and increasing chain length, branches as well as unsaturations, leads to a less regular arrangement of the molecules – to a looser structure. However, at the same surface coverage, the surface tension of the filler covered by aliphatic monocarboxylic acids is the same for all compounds. The adsorption of dicarboxylic acids is more complicated and the decrease in the surface tension is significantly smaller than for monocarboxylic compounds. A further study has to be carried out to verify the tentative conclusions drawn from the IGC results about the orientation of the surfactant and the structure of the layer formed.

Acknowledgements The National Scientific Research Fund of Hungary (grants nos. T 030579 and T 029719), the Institute of Chemistry of the Hungarian Academy of Sciences, as well as the Bolyai Scholarship are acknowledged for their financial support of this study.

References

1. Wypych G (1999) Handbook of fillers. ChemTec, Toronto
2. Pukánszky B (1995) In: Karger-Kocsis J (ed) Polypropylene: structure, blends and composites, vol 3. Chapman and Hall, London, pp 1–70
3. Pukánszky B (2000) In: Vasile C (ed) Handbook of polyolefins. Dekker, New York, pp 689–722
4. Pukánszky B, Fekete E, Tüdös F (1989) Makromol Chem Macromol Symp 28:165–186
5. Fekete E, Pukánszky B, Tóth A, Bertóti I (1990) J Colloid Interface Sci 135:200–208
6. Rothern RN (1995) In: Rothern R (ed) Particulate-filled polymer composites. Longmann, Harlow, pp 123–137
7. Rothern RN (1995) In: Rothern R (ed) Particulate-filled polymer composites. Longmann, Harlow, pp 96–121
8. Liauw CM, Rothern RN, Hurst SJ, Lees GC (1998) Compos Interfaces 5:503–514
9. Liauw CM, Rothern RN, Lees GC, Iqbal Z (2001) J Adhes Sci Technol 15:889–912
10. Gilbert M, Sutherland I, Guest A (2000) J Mater Sci 35:391–397
11. Domka L, Jesionowski T, Morawska A, Kozak M (2002) Tenside Surfactant Detergents 39:33–39
12. Levresse P, Manas-Zloczower I, Fekete DL, Bomal Y, Bortzmeyer D (1999) Powder Technol 106:62–70
13. Ivanishchenko O, Gladkikh Yu P (1979) Colloid J USSR 41:660
14. Pukánszky B, Fekete E (1999) Adv Polym Sci 139:109–154
15. Ashan T, Taylor DA (1998) J Adhes 67:69–79
16. Móczó J, Fekete E, Pukánszky B (2002) J Adhes 78:1–15
17. Papirer E, Schultz J, Turchi C (1984) Eur Polym J 20:1155–1158

-
18. Ashan T, Colenutt BA, Sing KSW (1989) *J Chromatogr* 479:17–25
 19. Ashan T (1992) *Colloid Surf* 64:167–176
 20. Balard H, Papirer E (1993) *Prog Org Coat* 22:1–17
 21. Ottewill RH, Tiffany JM (1967) *J Oil Col Chem Assoc* 50:844
 22. Fekete E, Pukánszky B (1997) *J Colloid Interface Sci* 194:269–275
 23. Conder JR, Young CL (1979) *Physicochemical measurement by gas chromatography*. Wiley, Chichester
 24. Dorris GM, Gray G (1980) *J Colloid Interface Sci* 77:353–362

István Pászli
 Krisztina László

State equation of the boundary layer

I. Pászli
 Department of Colloid Chemistry,
 Lóránd Eötvös University,
 P.O. Box 32,1518 Budapest 112, Hungary
 K. László (✉)
 Department of Physical Chemistry,
 Budapest University of Technology
 and Economics, 1521 Budapest,
 Hungary
 e-mail: klaszlo@mail.bme.hu
 Tel.: + 36-1-4631893
 Fax: + 36-1-4633767

Abstract A surface state equation that is independent of the physical state of the phases is introduced. This relationship exists between individual variables and holds for any phase. Using this equation, quantities that are either inaccessible to measurement or not easily available can be calculated. It can therefore also be applied to the interface of amorphous solid phases or crystal lattices of different Miller indices.

Introduction

Surface tension is a state variable in the collective representation of interfacial thermostatics. Its actual value depends on the chemical behaviour of the adjoining phases. Identical relationships can be obtained if – instead of the collective variables – the individual contributions of the phases are introduced. This is made possible by the individual representation of the capillary theory [1].

The transition between the two representations can be defined by Eq. (1):

$$\gamma_{\varphi\psi} = \chi_{\varphi}\chi_{\psi}, \quad (1)$$

where $\gamma_{\varphi\psi}$ is the interfacial tension of the phase pair $\{\varphi, \psi\}$, and $\{\chi_{\varphi}, \chi_{\psi}\}$ are the tension parameters. Several parameters can be defined by analogous expressions.

Thus, capillary theory can be extended with the transformation given in Eq. (1). Based on the set of tools involving also the material quantities, relationships showing up only in the individual representation can be defined.

State equation of the liquid layer

The surface tension of two fluid phases can be expressed in terms of collective variables as

$$\gamma_{\varphi\psi} = \frac{1}{2} \left| u_{\varphi}^0 - u_{\psi}^0 \right| \cdot \tau_{\varphi\psi}^{\text{eff}}.$$

The $u_{\varphi\psi}^0$ values are the intermolecular potentials of the respective phase, and $\tau_{\varphi\psi}^{\text{eff}}$ is the effective layer thickness. The variables have only positive values and they are symmetrical functions of the physical quantities of the corresponding phases.

If the parameters defining the difference of the potentials and the effective layer thickness are $\{q_{\varphi}, q_{\psi}\}$ and $\{\tau_{\varphi}^{\text{eff}}, \tau_{\psi}^{\text{eff}}\}$, respectively, the previous expression can be given as

$$1 = \frac{1}{q_{\varphi}} \left(\sqrt{2} \frac{\chi_{\varphi}}{\tau_{\psi}^{\text{eff}}} \right) \cdot \frac{1}{q_{\psi}} \left(\sqrt{2} \frac{\chi_{\psi}}{\tau_{\varphi}^{\text{eff}}} \right).$$

As the classical equations of capillary theory can also be applied to a vacuum, the factor q can be defined for the vacuum as well:

Table 1 Liquid-phase parameters from Eqs. (1) and (2)

Liquid	M (g/mol)	ρ (g/cm ³)	λ^{vap} (kJ/mol)	$(u-u_0)\times 10^{12}$ (mN/m ²)	$q\times 10^{-6}$ [(m ² /mN) ^{1/2}]	$\tau^{\text{eff}}\times 10^{-6}$ (m ^{1/2})	$d_{\text{corp}}\times 10^{-1}$ (nm)
Hexane	86.17	0.659	31.56	0.2413	2.2111	71.6942	7.45
Heptane	100.20	0.684	36.57	0.2496	2.2046	68.7687	7.74
Octane	114.22	0.703	41.49	0.2555	2.2000	66.8718	8.01
Nonane	128.13	0.718	46.41	0.2600	2.1963	65.2393	8.27
Decane	142.28	0.730	51.38	0.2636	2.1935	65.5295	8.51
Dodecane	170.33	0.766	61.51	0.2766	2.1832	64.5228	8.90
Tetradecane	198.38	0.765	71.30	0.2749	2.1845	64.0553	9.37
Hexadecane	226.44	0.775	81.38	0.2785	2.1817	65.1352	9.75
Benzene	78.11	0.879	33.83	0.3807	2.1006	43.7784	6.55
Toluene	92.13	0.866	38.01	0.3672	2.1192	45.5006	6.95
Cyclohexane	84.16	0.779	33.01	0.3055	2.1603	56.3353	6.99
Chloroform	119.39	1.489	31.28	0.3901	2.0931	41.6714	6.33
Carbon tetrachloride	153.40	1.565	32.43	0.3372	2.1352	48.3468	6.73
Methanol	32.04	0.792	37.43	0.9252	1.6627	18.8993	5.04
Ethanol	46.07	0.789	42.32	0.7247	1.8253	24.0635	5.70
Propanol	60.09	0.804	47.45	0.6348	1.8976	27.1839	6.18
Butanol	74.12	0.810	52.35	0.5720	1.9479	30.0879	6.62
Pentanol	88.15	0.817	57.02	0.5284	1.9828	32.2262	6.99
Octanol	130.22	0.827	70.98	0.4507	2.0448	35.6594	7.93
Acetone	58.08	0.792	30.99	0.4225	2.0673	39.7624	6.15
Propyl acetate	102.13	0.886	39.92	0.3463	2.1279	49.9665	7.15
Water	18.00	1.000	43.89	2.4139	1.4131	7.1670	3.86
Mercury	200.61	13.546	61.50	4.1528	2.4306	30.8727	3.60

$$q_0 = \sqrt{2} \frac{\chi_0}{\tau_0^{\text{eff}}}.$$

The difference between the potentials depends on the state of the matter. For liquid phases

$$|u_\phi^0 - u_\psi^0| = |(u_\phi^0 - u_0) - (u_\psi^0 - u_0)| = |\Psi_\phi - \Psi_\psi|,$$

where ψ_ϕ and ψ_ψ are the differences between the bulk and vacuum potentials, u_ϕ^0 or u_ψ^0 and u_0 , respectively.

$$\Psi_\phi = |u_\phi^0 - u_0| = \frac{\rho_\phi}{M_\phi} |\lambda_\phi^{\text{vap}}|,$$

where ρ_ϕ and $\lambda_\phi^{\text{vap}}$ are, respectively, the density and the molar heat of evaporation of the bulk phase, and M_ϕ is the molar weight of component ϕ .

The expression containing only those parameters proper to each respective phase therefore also holds:

$$\left(\frac{\tau_0^{\text{eff}}}{\chi_0}\right) = 2 \left(\frac{M_\phi}{\rho_\phi |\lambda_\phi^{\text{vap}}|}\right) \frac{\chi_\phi}{\tau_\phi^{\text{eff}}} = \text{constant}. \quad (2)$$

This relationship exists between individual variables and holds for all the phases. It can be considered as a surface state equation.

Data calculated according to Eqs. (1) and (2) for various liquids are listed in Table 1. d_{corp} is the distance between the spherical particles, and M_ϕ , ρ_ϕ and $\lambda_\phi^{\text{vap}}$ are taken from Ref. [2]. The constant in Eq. (2), which was calculated for the liquids specified in Table 1, was found to be $0.82772 \times 10^{-6} [m/(mN \cdot m^{-1})]^{1/2}$.

By means of Eq. (2) quantities that are not accessible to measurement or not easily available can be calculated.

Conclusion

The surface state equation, Eq. (2), is independent of the state of the phases. It can also be applied to the interface of amorphous solids or to crystal lattices of different Miller indices.

Acknowledgements This research was supported by the National Research Fund (OTKA, grant no. T 025581) and the National Research and Development Programs (NFKP 3/043/2001). The technical assistance of György Bosznai and Emese Fülöp is gratefully acknowledged. Many thanks to Erik Geissler for fruitful discussions.

References

1. Pászli I (1986) Z Phys Chem 267:433
2. CRC (1982) Handbook of chemistry and physics, 63rd edn. CRC, Boca Raton

István Pászli
 Krisztina László

The extended capillary theory

I. Pászli
 Department of Colloid Chemistry,
 Lóránd Eötvös University, P.O. Box 32,
 1518 Budapest 112, Hungary

K. László (✉)
 Department of Physical Chemistry,
 Budapest University of Technology and
 Economics, 1521 Budapest, Hungary
 e-mail: klaszlo@mail.bme.hu
 Tel.: +36-1-4631893
 Fax: +36-1-4633767

Abstract The quantities and relationships of capillary theory are summarized in a consistent formalism. Its constituents are the canonical thermostatics of the excess quantities, the interpretation of the surface tension according to deformation theory, and the formalism of parametric theory. A generalized concept of surface excess quantities is established by introducing the

factors v^ϕ and defining the individual quantities. The deformation quantities can also be incorporated into the theory, but the changes in the phase volumes have to be restricted. The theoretical difficulties of the traditional hypotheses do not arise in this unified approach and quantities that are not open to measurement can be calculated.

Introduction

The capillary equilibrium of a heterogeneous system is characterized by a set of measurable physical quantities defining the interfacial layer and the relations between these quantities. Several quantities belonging to the traditional set of parameters [1, 2, 3, 4, 5, 6, 7, 8, 9, 10, 11, 12, 13, 14, 15, 16] (i.e. the volume or the composition of the layer), however, cannot be given. The empirical relationships (e.g. the exact Kroecker isotherm) cannot be reconstructed in the existing theories [17]. The combination of the corpuscular and phenomenological approaches has spread conceptual confusion from the beginning [18]. Owing to this, important experimental data relevant to adsorption cannot be interpreted, while some of the effects related to wetting cannot be treated theoretically at all. The traditional theory therefore needs to be extended.

The quantities and relationships of capillary theory can be summarized in a consistent formalism. Its constituents are the canonical thermostatics of the excess quantities, the interpretation of the surface tension according to deformation theory, and the formalism of parametric theory. The theoretical difficulties of the

traditional hypotheses do not arise in this unified discipline.

The canonical characteristic functions

In canonical thermostatics a heterogeneous system is characterized by a set of intensive and extensive quantities. However, the state can be unambiguously defined even by a proper subset of the corresponding quantities. The characteristic functions U_λ of a system can be derived from its internal energy function U by a Legendre transformation to satisfy the expression

$$U_\lambda(y_1, \dots, y_\lambda; X_{\lambda+1}, \dots, X_n) := \begin{cases} U(X_1, \dots, X_n) - \sum_1^\lambda y_k X_k \\ \sum_{\lambda+1}^n y_k X_k = \left(\sum_{\lambda+1}^n y_k \bar{\rho}_k \right) V \end{cases} = \text{extr.}! \quad (1)$$

N is the number of interactions, X_n and y_n are the extensive and the corresponding intensive parameters, respectively, and $\bar{\rho}_k$ is the mean density of the extensive

parameter with respect to the volume, V , of the system. According to this definition, the scalar product belonging to a given set of interactions, or even to a single interaction, has an extreme, if each of the independent extensive parameters (extensivities)

$$\iiint_V \rho_k(Q) dV = X_k = \text{const} \quad (2)$$

is conservative. The extremum is attained at a given distribution of the extensity densities. The global extensive and intensive state parameters, $X = \{U_\lambda, \dots, X_k, \dots\}$ and $\{\dots, y_k, \dots\}$, respectively, are, by definition, canonical physical quantities. They can be selected by the energy balance.

The extensive quantities characterizing the geometrical size of the system (surface area or volume of the layer, etc.) are physical parameters that are independent of the chemical/material properties. Therefore, the canonical forms of the characteristic potentials may not contain capillary quantities directly associated with the interfacial layers.

The state of the interfacial layer in the different interactions can also be characterized by various quasi-canonical and noncanonical quantities. The deformation is determined by variables related to the extension of the layer (e.g. the layer volume, V^s , or the surface area A_s) or by derived quantities implicitly containing these parameters.

The characteristic collective and individual variables of the interfacial layers can be introduced into the canonical relationships after identical transformations.

The tools of the generalized excess theory

The general surface excess quantities derived from the canonical characteristic functions of a chemical system define at least one capillary state quantity for each interaction.

The densities \bar{u}_λ of all the characteristic functions of the system can also be expressed by the density of the extensive variables. Thus,

$$\bar{u}_\lambda = \frac{U_\lambda}{V} = \left(\sum_{k=\lambda+1}^n y_k \bar{\rho}_k \right) = \text{extr.}!$$

as well, because U_λ is a homogeneous linear function of the extensive parameters in the equilibrium state. $\{\dots, \bar{\rho}_k, \dots\}$ is the density of the extensive variables of a system with unit volume. Thus, U_λ and \bar{u}_λ are equivalent in their extremum properties. The homogeneous linear function of the variable $\{\dots, X'_k, \dots\}$ and the multiples of \bar{u}_λ and $\bar{\rho}_k$ lead to a similar quantity:

$$U'_\lambda = \frac{V'}{V} \bar{u}_\lambda = v \bar{u}_\lambda = \left(\sum_{k=\lambda+1}^n y_k (v \bar{\rho}_k) \right) = \sum_{k=\lambda+1}^n y_k X'_k.$$

However, the extremum of this function is equal to that of the characteristic function only if the factor v is positive. V' has the dimension of volume. If $V \neq V'$, then V' is different from the volume of the system, and it is therefore permissible to set

$$V' = V - V^{\text{ref}} = V^\sigma > 0,$$

where V , V^{ref} and V^σ are volumes belonging to the same system. However, while V is the true volume, V^{ref} and V^σ can be defined by the corresponding multiplication factors of the following equations:

$$U_\lambda^{\text{ref}} = \sum_{k=\lambda+1}^n (y_k \bar{\rho}_k) V^{\text{ref}} \quad (\text{reference function}),$$

$$U_\lambda^\sigma = \bar{u}_\lambda V^\sigma = \sum_{k=\lambda+1}^n (y_k \bar{\rho}_k) V^\sigma \quad (\text{excess function}).$$

The reference and the excess functions thus characterize the same system. The functions U_λ^{ref} and U_λ^σ are the similarity transformations of the characteristic function, having an extremum of a similar character to U_λ itself, if

$$\{V^{\text{ref}}, V^\sigma\} > 0.$$

Generally, the so-called descriptive multipliers, V^{ref} and V^σ , are fictitious quantities.

In the excess concept the extensive quantities are defined by identical expressions, independently of their conservative or nonconservative feature.

The bulk phase volume V^φ of a static system of a bulk phase $\varphi = \{\alpha; \beta\}$ and interfacial layer $s = s_{\alpha\beta}$ comprise extensive parameters $X^\varphi = \{U_\lambda^\varphi, \dots, X_k^\varphi, \dots\}$. Similarly, the layer with volume V^s has extensive quantities $X^s = \{U_\lambda^s, \dots, X_k^s, \dots\}$. If the average extensity densities are ρ^φ and ρ^s , respectively, then

$$V = \sum_\varphi V^\varphi + V^s$$

and

$$X = \sum_\varphi X^\varphi + X^s = \sum_\varphi \rho^\varphi V^\varphi + \rho^s V^s.$$

If the states of both the symbolic reference and total system are identical, with only their volumes differing by a factor $v^\phi = \{v^\varphi = (v^\alpha, v^\beta); v^s\}$, then

$$V^{\text{ref}} = \sum_\varphi v^\varphi V^\varphi + v^s V^s$$

and

$$X^{\text{ref}} = \sum_{\phi} v^{\phi} X^{\phi} + v^s X^s = \sum_{\phi} v^{\phi} \rho^{\phi} V^{\phi} + v^s \rho^s V^s.$$

Since the mean extensity densities are equal, then for each interaction

$$\bar{\rho} = \frac{X}{V} \equiv \frac{X^{\text{ref}}}{V^{\text{ref}}},$$

hence,

$$\bar{\rho} = \frac{X - X^{\text{ref}}}{V - V^{\text{ref}}} \equiv \frac{X^{\sigma}}{V^{\sigma}}.$$

The excess quantity of both the conservative and the nonconservative extensities can therefore be expressed as

$$X^{\sigma} = \bar{\rho} V^{\sigma} = \sum_{\phi} (1 - v^{\phi}) \rho^{\phi} V^{\phi} + (1 - v^s) \rho^s V^s. \quad (3)$$

The excess volume does not vanish for any choice of reference system. Equation (3) contains the excess quantities V^{σ} and the factors $v^{\phi} = \{v^{\alpha}, v^{\beta}, v^{\sigma}\}$ for a given system at a given algebraic parameter $\bar{\rho}$. They span a hyperplane: the choice of the excess volume, and thus the excess quantities X^{σ} , may be different for the same system.

The excesses of the system can be represented by three-parameter quantities. For the existence of the equation of definition, the value of the factors v^{ϕ} can be chosen arbitrarily. The choice $v^s = 0$ is permitted. When the values of the factors ($v^{\alpha} = 1; v^{\beta} = 1; v^s = 0$) are chosen, the excess adsorption of a multicomponent system is equal to the adsorption capacity of the surface layer, i.e. to the real amount in the layer (Guggenheim excess; if the factors v^{ϕ} are previously given, the relative Gibbs excess or the Findenegg excess, etc., can also be defined). In an inverse procedure the value of v^{ϕ} belonging to a given excess can be obtained. Thus, relationships of quantities that are inaccessible in the traditional set of tools can be derived.

The bulk phases are the similar regions of the system with homogeneous distribution functions. Therefore, the independent factors $\{v^{\alpha}; v^{\beta}\}$ can be deliberately given in symmetrical form, if two conditions are satisfied. Firstly, according to Eq. (3), for the excess volume

$$V^{\sigma} = V^s \quad (4)$$

can be assessed. Then $v = V^{\sigma} = V^s > 0$, i.e. the system is modeled by an excess system of the same state having volume V^s . Secondly, when

$$\sum_i {}^{\phi} n_i^{\sigma} = 0 \quad (5)$$

holds for the adsorption, the number of excess extensities characterizing the “excess system” is not necessarily equal to that of the total system. Equation (5) reduces the number of extensive parameters. Among the $\{..., i, ...\}$ number of variables only $(i-1)$ are independent. Therefore

$$\mu_j n_i^{\sigma} = -\mu_j \sum_i {}^{(j)} n_i^{\sigma}$$

holds as well. Thus, the excess of the characteristic potential,

$$U_{\lambda}^{\sigma} = \begin{cases} U^{\sigma} - \sum_{k=1}^{\lambda} \tilde{y}_k X_k^{\sigma} \\ \sum_{k=\lambda+1}^n \tilde{y}_k X_k^{\sigma} \end{cases} = \text{extr.}!$$

instead of the chemical potential $\{..., \mu, ...\}$, contains

$$\tilde{\mu}_i \equiv \mu_i - \mu_j$$

as the canonical intensity for each of the indices i . For the set of indices $k \notin \{..., i, ...\}$, $\tilde{y}_k \equiv y_k$.

When the excess volume is equal to the layer volume, the general form of the excess quantities of any interaction can be expressed from Eqs. (3) and (5) as

$$X_k^{\sigma} = \left(\frac{\sum_i \rho_i^s}{\sum_i (\rho_i^{\beta} - \rho_i^{\alpha})} \rho_k^{\alpha} + \frac{\sum_i \rho_i^s}{\sum_i (\rho_i^{\alpha} - \rho_i^{\beta})} \rho_k^{\beta} + \rho_k^s \right) V^s \equiv \bar{\rho}_k V^s. \quad (6)$$

The mean extensity density $\bar{\rho}_k$ evidently depends only on the bulk and interfacial densities. The excess quantities relate to an “excess system” having the same mean density as the system and the same volume as the layer. For the reduced number of excess extensities

$$(\mu_i - \mu_j) n_i^{\sigma} = \text{extr.}! \quad (7)$$

but the equation related to the index j is equal to zero. The conservation conditions are valid for the excess extensities as well.

The character of the excess variables corresponding to the existence of the interfaces is unambiguously determined by the restrictions on the factors v^{ϕ} .

Completion of the set of tools of excesses

The state functions necessarily also contain the quantities related to the deformation interaction. Therefore, in the expression for the characteristic potential, the quantity associated with the surface tension does not vanish for any choice of the factor v^{ϕ} .

At a given external pressure, p , the canonical form of the characteristic function of a system having a continuous tension distribution can be given by the Curie equation:

$$\Delta E_{\text{el}} = -p \Delta V + \sum_s \gamma_s \Delta A_s,$$

$$dE_{\text{el}} = - \sum_k X_k dy_k + (\Delta V) p + \sum_s \gamma_s dA_s,$$

where s is the number of interfacial layers, and γ_s and A_s are the surface tension and surface area of each layer, respectively. (Δ represents the deviation from the reference state.) The layers can be created by a continuous deformation of a reference surface with an area A_s^0 , $\Delta A_s = (A_s - A_s^0)$. ΔE_{el} , or its differential value can be included into Eq. (3) only if ΔE_{el}^σ is equal to the fundamental quantity.

The extensity densities of the deformations ε_{ii} (ii are the position coordinates) do not vanish in any of the subsystems. However, the sum of the quantities ε_{ii} with identical dimensions for any homogeneous bulk phase,

$$Sp \hat{\varepsilon}^\varphi = \sum_i \varepsilon_{ii}^\varphi = \frac{\Delta V^\varphi}{V^\varphi},$$

will vanish if there is no change in volume. Therefore, the excess deformation may be identical to the real deformation of the system. The condition for identity is

$$\sum_i \left\{ \sum_\varphi v^\varphi \varepsilon_{ii}^\varphi V^\varphi \right\} = 0$$

and

$$v^\alpha \Delta V^\alpha = -v^\beta \Delta V^\beta.$$

This relation is satisfied, independently from the actual value of the factors, if

$$\Delta V^\varphi = 0$$

since the volume of the system is equal to the sum of the volumes of the bulk phases and the interfacial layers,

$$\Delta V = \sum_s \Delta V^s$$

The volume change arising from a deformation of even a single layer is simply compensated by the volume change of the total system. The product of the latter and the pressure p is negligibly small. At constant bulk volumes the excess of the elastic potential is equal to the eigenpotential of the system. The compatibility of the relations, i.e. the possibility of incorporating the elastic potential into the general excess potential given by Eq. (3) is determined by the conditions of change in the bulk volumes.

The characteristic potential of the deformation does not affect the choice of the volumes of the various regions in the system and is independent of the choice of the factors v^φ determining the type of the excess.

The fundamental relationship for the capillarity is

$$\begin{aligned} dE_{el}^\sigma &= dE_{el}(\{\dots, y_k, \dots\}; \{\dots, [\bar{\varepsilon}_{ii} V \neq 0], \dots\}) \\ &\equiv - \sum_k X_k^\sigma dy_k - \sum_i {}^{(j)} n_i^\sigma d\tilde{\mu}_i + \sum_s \gamma_s d\Delta A_s = 0. \end{aligned} \quad (8)$$

Equation (8) contains both the excess quantities and the surface terms corresponding to the surface tensions,

and it vanishes in the state of equilibrium. This is the fundamental relationship of capillarity.

The linear differential equation given by Eq. (8) uniquely characterizes the interfaces using the surface tension and the various excess quantities. Applying the Young–Schwartz theorem, the Gibbs adsorption equation for a solid/fluid interface $s = \{S; fl\}$ can be deduced directly:

$$-\left(\frac{\partial}{\partial \tilde{\mu}_i} \gamma_{S, fl} \right)_{\tilde{\mu}_i} = \left(\frac{\partial n_i^\sigma}{\partial \Delta A_s} \right) = \Gamma_i^\sigma.$$

The surface tensions are the products of the tension parameters of adjoining phases, which depend only on the bulk properties:

$$\gamma_{S, fl} = \chi_S \chi_{fl}. \quad (9)$$

Thus, all the necessary quantities are accessible.

From the Gibbs adsorption equation and Eq. (9)

$$\Gamma_i^\sigma = \chi_S \left(- \frac{\partial \chi_{fl}}{\partial \tilde{\mu}_i} \right)_{\tilde{\mu}_i} := \chi_S \Gamma_i^{\sigma(0)}.$$

The quantity in parentheses is the so-called fundamental isotherm determined only by the properties of the fluid bulk phases. If the surface area of the solid phase is a_s , then

$$n_i^\sigma = (a_s \chi_S) \Gamma_i^{\sigma(0)},$$

and the effect of the solid and fluid phases can be separated. The shape of the isotherm is defined by the fluid phase, but its absolute value depends on the solid phase.

By unifying the excess concept and the theory of deformation and introducing the individual capillary quantities, the set of tools for capillarity is logically completed. All of the variables and relationships can be defined.

Adsorption on solid surface and the layer quantities

Paradoxically, the choice of factors v^φ proposed earlier guarantees access to all the layer quantities.

The relationships can be directly applied to the adsorption of closed, for example, solid/fluid surface layers. The excess amount of the fluid phase n_i^σ , defined according to Eq. (6), represents a special adsorption case. With $L \rightarrow \alpha$ and $S \rightarrow \beta$, for components $\{1; 2\}$

$$n_1^\sigma = \left(- \frac{\rho_1^s + \rho_2^s}{(\rho_1^L + \rho_2^L)} \rho_1^L + \rho_1^s \right) V^s \equiv -(\rho_1^s + \rho_2^s) V^s x_1 + \rho_1^s V^s \quad (10)$$

can be given. x_1 is the molar fraction in the bulk phase. n_2^σ can be written analogously by exchanging the indices. Using also the mass balance for a closed system, experimentally measurable adsorptions can be defined.

In fact, adsorption from a multicomponent fluid on a solid surface is a kind of perturbation: a new phase boundary is formed. Initially we have a homogeneous fluid phase of n mol. In the final state the adjoining phases $\varphi = \{\alpha; \beta\}$ contain ${}^\alpha n$ and ${}^\beta n$ from the initial n mol of fluid, respectively. ${}^\alpha n$ and ${}^\beta n$ are distributed between their own bulk (V) and surface (s) layers.

$$\varphi n = \varphi n^V + \varphi n^s.$$

This results in a change of the concentration of the various regions. If the initial concentration is x_1^0 and the final ones are φx_i^V and φx_i^s , for each region

$$\sum_i x_i^0 = \sum_i \varphi x_i = \sum_i \varphi x_i^s = 1.$$

The phases contain $\varphi n_i = \varphi n x_i^0$ of each component and $\varphi n_i^V = \varphi n^V x_i^V$ and $\varphi n_i^s = \varphi n^s x_i^s$ in each region. Therefore,

$$\sum_\varphi \left\{ \sum_i [\varphi n (x_i^0 - \varphi x_i) - \varphi n^s (x_i^s - \varphi x_i)] \right\} = 0$$

and mass balance is satisfied. As the difference in the square brackets vanishes, in multicomponent systems

$$\varphi n_i^\sigma = \begin{cases} \varphi n (x_i^0 - \varphi x_i) \\ \varphi n^s (x_i^s - \varphi x_i) \end{cases}$$

can be defined for each component of both phases. For a single component they are equal to the general excess given in Eq. (10). Based on this, the excess adsorption can be defined. The φn^s amount in the closed surface layer of phase φ contains $\varphi n_i^s = \varphi n^s \cdot \varphi x_i^s$ from the i th component. If the same φn^s quantity is found in the bulk phase instead, then its value is $\varphi n_i^V = \varphi n^s \cdot \varphi x_i^V$. Thus, the excess adsorption is the difference for the same component in the two regions of different states, i.e. the real excess of the interfacial layer compared to the bulk phase. The last expression is independent of the number of molecular layers, the cross-sectional area of the molecules, or the actual strength of the interaction. This relationship is at the same time an instruction on how this quantity can be determined experimentally [18]. The mass balance is an invariant equation which by itself satisfies every system in adsorption experiments.

The excess given by Eq. (10) can be measured directly for closed fluid phases. As the various excesses can be converted to each other by the corresponding factors v^ϕ , quantities that are not open to measurement can be calculated. Thus, Eq. (10) has significance in metrology.

The analogous relationships for binary and multiple mixtures offer the possibility of generalization.

Equation 6, describing the independent excesses, can be transformed into

$$n_i^\sigma = \bar{\rho}_i V^s = n x_i^0 \frac{V^s}{V}$$

and from

$$n \sum_i (x_i^0 - x_i) = \sum_i \left[n x_i^0 \left(1 - \frac{x_i}{x_i^0} \right) \right] = \sum_i \left[\bar{\rho}_i V \left(1 - \frac{x_i}{x_i^0} \right) \right]$$

$$V^s = V \left(1 - \frac{x_i}{x_i^0} \right)$$

can be directly deduced.

The layer volume can be calculated from both. As volumes are exclusively positive, in the unperturbed case (net adsorption) the condition $x_1 \leq x_1^0$ is satisfied [19]. The volume V^s and the composition x_1 characterize the result of the adsorption experiment. The same state can be constructed from another, different, system, since V and x_1^0 – when V^s and x_1 are fixed – are in hyperbolic relationship.

The composition of the layer can be deduced from the fundamental isotherm by the extrema of Eq. (7) by using the following expression [20, 21]:

$$x_1^s = x_1 - n_1^\sigma \Delta \mu_{12} \int_0^{x_1} \frac{1}{n_1^\sigma \Delta \mu_{12}} dx_1$$

$$= x_1 - \Gamma_1^{\sigma(0)} \Delta \mu_{12} \int_0^{x_1} \frac{1}{\Gamma_1^{\sigma(0)} \Delta \mu_{12}} dx_1$$

Since the condition $\Gamma_1^{\sigma(0)}(x_1) \geq 0$ holds for all compositions, independently of the number of molecular layers, the inequality

$$\text{sgn} \Gamma_1^{\sigma(0)} \cdot |\Delta \mu_{12}| \int_0^{x_1} \frac{1}{|\Gamma_1^{\sigma(0)}| |\Delta \mu_{12}|} dx_1 \leq 0$$

is satisfied as well. The isotherm is either negative or vanishes for all compositions, and hence $x_1^s \leq x_1$. Relating the last equation to the surface area, the fundamental isotherm of the Guggenheim excess can be expressed as

$$\Gamma_1^{\sigma(0)} = (x_1^s - x_1) (\Gamma^s / \chi_S) := (x_1^s - x_1) \Gamma^{s(0)} \quad (11)$$

and the density of the components in the layer can be derived.

Application of the extended set of tools allows isotherms of binary systems to be computed, on the basis of Eq. (8) and the Gibbs adsorption equation, without any direct adsorption experiment.

The tension parameter of a binary liquid mixture with composition x_1 can be calculated from the fundamental isotherm according to

$$\chi_L(x_1) = \chi_L(0) - \frac{RT}{a_s \chi_S} \int_0^{x_1} n_1^\sigma [\ln(a_1/a_2)]' dx_1$$

$$= \chi_L(0) - RT \int_0^{x_1} \Gamma_1^{\sigma(0)} [\ln(a_1/a_2)]' dx_1$$

Table 1 Adsorption data of acetone and cyclohexane/mercury system calculated from measured surface tension values, 25 °C [24, 25, 26]

x_{acetone}	$\gamma_{\text{Hg/L}}$ (mN/m)	χL ($\sqrt{\text{mN/m}}$)	$\Gamma_{\text{acetone}}^{\sigma(0)}$ (mmol/m ²)	x_{acetone}^s	$\Gamma^{\sigma(0)}$ (mmol/m ²)	$\Gamma_{\text{acetone}}^{\sigma(0)}$ (mmol/m ²)	$\Gamma_{\text{cyclohexane}}^{\sigma(0)}$ (mmol/m ²)
0.0000	378.8	7.1389	0.0000	0	0	0	0
0.0046	378.3	7.1300	-0.0220	0.0046	—	—	—
0.0360	376.4	7.0937	-0.0209	0.0101	0.8107	0.0082	0.8025
0.0690	375.0	7.0673	-0.0346	(-0.0060)	0.4622	(-0.0027)	0.4650
0.1460	373.1	7.0315	-0.0349	0.0221	0.2820	0.0062	0.2758
0.3180	370.9	6.9900	-0.0265	0.1400	0.1492	0.0209	0.1283
0.5080	370.0	6.9730	-0.0130	0.3571	0.0865	0.0308	0.0556
0.7390	369.4	6.9617	-0.0059	0.7155	—	—	—
0.8680	369.2	6.9580	-0.0013	(0.7476)	—	—	—
0.9860	369.1	6.9568	-0.0014	(0.3960)	—	—	—
1.0000	369.1	6.9561	0.0000	1	—	—	—

provided the surface tensions of, for instance, binary mixture/mercury systems are known. The activity coefficient γ_i can also be calculated from the vapour pressure diagrams [22] by the Wilson equations [23]:

$$\ln \gamma_1 = -\ln(x_1 + \Lambda_{12}x_2) + x_2 \left(\frac{\Lambda_{12}}{x_1 + \Lambda_{12}x_2} - \frac{\Lambda_{21}}{x_2 + \Lambda_{21}x_1} \right),$$

$$\ln \gamma_2 = -\ln(x_2 + \Lambda_{21}x_1) - x_1 \left(\frac{\Lambda_{12}}{x_1 + \Lambda_{12}x_2} - \frac{\Lambda_{21}}{x_2 + \Lambda_{21}x_1} \right).$$

The indices $i = \{1;2\}$ relate to the components of the fluid phase, while Λ_{ij} are the Wilson parameters.

Experimental surface tensions from Refs. [24, 25, 26] were used to calculate the excess isotherm of acetone/cyclohexane/mercury at 25 °C. Table 1 lists the computed values and the excess isotherm as well as the concentration of the interfacial layer plotted in Fig. 1. The experimental surface tensions are practically identical in the high acetone concentration range. It cannot be excluded, however, that the surface tension has an extremum comparable to the experimental error of the measurements. The liquid mixture has an azeotropic point at $x_{\text{acetone}} = 0.72$. At this point, therefore, the fundamental isotherm is necessarily zero and changes sign.

By applying extended capillarity theory, quantities that are inaccessible by the traditional theory can be defined as well.

Expressing the basic isotherm as a McLaurin series yields directly the following relationship:

$$m \sum_v a_v x_1^v + x_1 \frac{N}{a_s \chi_s} = x_1^0 \frac{N}{a_s \chi_s},$$

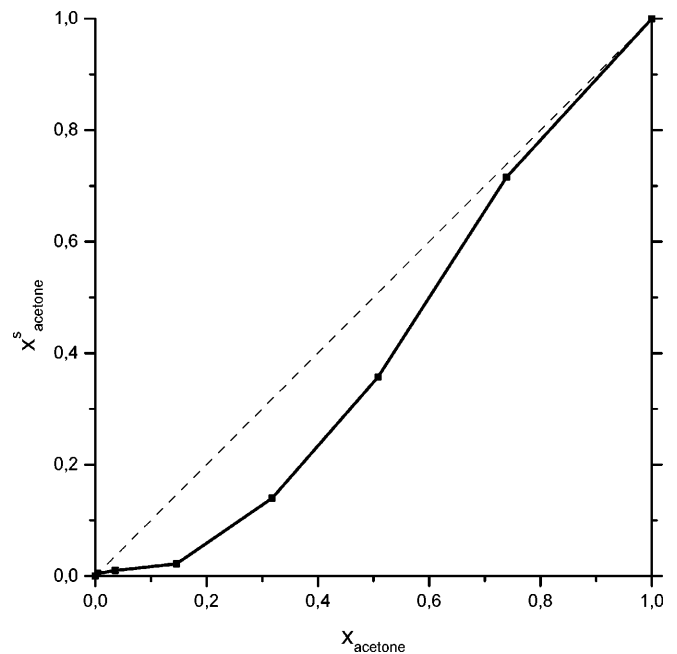
where N is the molar amount of fluid phase added to mass m of solid; $n = N/m$. This equation gives the relation between the input quantities $\{m; N; x_1^0\}$ and the output concentration x_1 . The mass dependence of the sorption – at constant N and x_1^0 – can be obtained when the mass dependence of the equilibrium concentration is

accommodated into the basic isotherm. The function $n_1^\sigma = n_1^\sigma(x_1[m])$ is the recursive Kroecker isotherm.

Consequently, the extended theory of capillarity, in contrast to the traditional one, is fully operational.

Discussion

The closed and logically consistent set of tools of capillary theory is completed by the generalized concept of surface excess quantities, by introducing the factors v^ϕ and defining the individual quantities. It has also to be considered that the deformation quantities can be introduced into the theory only if the changes of the phase volumes are restricted.

**Fig. 1** Equilibrium concentration of acetone in the interfacial layer

The relationships of the extended set of tools are guaranteed by the extremum character of the characteristic excess functions, and are the consequence of Maxwell's relations. However, application of the similarity theory opens the way to defining the fundamental isotherms and new material parameters.

The definition of the general excess quantities is theoretically guaranteed by the similarity transformation, which governs the relationships of the quantities. The mean densities define, on the one hand, the relation of the physical extensities to the volume, and, on the other, the ratio of the excess extensities to the layer volume. The extensities characterizing the whole system and the excess extensities of the interfacial layers are the similarity transformation of each other.

This guarantees both the additivity and the extremum character. The complete analogy existing between the usual and the excess extensities can be extended to the derived relationships as well. As all the layer quantities also contain bulk phase quantities, they are characteristic not of the surface properties but of the whole system.

The generalized theory guarantees access to previously inaccessible quantities and relationships.

Acknowledgements This research was supported by the National Research Fund (OTKA, grant no. T 025581) and the National Research and Development Programs (NKFP 3/043/2001). The technical assistance of György Bosznai and Emese Fülöp is gratefully acknowledged. Many thanks to Erik Geissler for fruitful discussions.

References

- Adamson AW (1990) Physical chemistry of surfaces. Wiley, New York
- Rusanov AI (1978) Phase-nleichgewichte und Grenzflächenerscheinungen. Akademie, Berlin
- Defay R, Prigogine I, Bellemans A, Everett DH (1966) Surface tension and adsorption. Wiley, New York
- Bakker G (1926) In: Wien W, Harms F (eds) Handbuch der Experimentalphysik, vol 6. Akademische Verlagsgesellschaft, Leipzig
- Kirkwood JG, Buff FJ (1949) J Chem Phys 17:338
- Tolman RC (1949) J Chem Phys 17:333
- Goodrich FC (1969) In: Matijevic E (ed) Surface and colloid Science, vol 1. Wiley-Interscience, New York, pp
- Padday JF (1969) In: Matijevic E (ed) Surface and colloid science, vol 1. Wiley-Interscience, New York, pp
- Johnson RE Jr, Dettre R (1969) In: Matijevic E (ed) Surface and colloid science, vol 2. Wiley-Interscience, New York, pp
- Tóth J (1993) Uniform Interpretation of Physical Gas/Solid Adsorption. In: Csempeš F, Hórvölgyi Z, Pászli I (eds) Proceedings of the 6th Conference on Colloid Chemistry, MKE, Budapest
- Hunter RJ (1993) Foundations of colloid science, vol 1. Clarendon, Oxford
- Rowlinson JS, Widom B (1982) Molecular theory of capillarity. Oxford University Press, London
- Stauff J (1960) Kolloidchemie. Springer, Berlin Heidelberg New York
- Lyklema J (2000) Fundamentals of interface and colloid science, vol 3. Liquid–fluid interfaces. Academic, San Diego
- Dörfler HD (1994) Grenzflächen und Kolloidchemie. VCH Weinheim
- Gibbs JW (1928) On the equilibrium of heterogeneous substances. The collected works, vol 1. Thermodynamics. Longmans, New York
- Manegold E (1955) Strassenbau 1:156
- Schay G, Nagy LG (1974) Egyadszorpció folyadék/szilárd és folyadék/gőz határfelületen. Akadémia újabb eredményei. vol 18, Akadémiai, Budapest
- Pászli I, László K (2001) Prog Colloid Polym. Sci 117:51
- Pászli I (1986) Z Phys Chem 267:433
- Pászli I (2000) On the composition of the binary interface layers. Third international conference of the Kolloid-Gesellschaft e.V., Budapest, abstract p 149, poster P 42
- Ohe, Shuzo (ed) (1989) Vapor–liquid equilibrium data. Physical sciences data 37. Kodansha, Tokyo
- Wilson GM (1964) J Am Chem Soc 86:127
- Dunken H (1940) Ann Phy 41:567
- Dunken H (1940) Z Phys Chem Abt B 47:195
- Dunken H, Fredenhagen I, Wolf KL (1941) Kolloid Z 95:186

Imre Varga
Tibor Gilányi
Róbert Mészáros

Experimental investigation of counterion dependence of alkali decyl sulfate adsorption at the air/solution interface

I. Varga (✉) · T. Gilányi · R. Mészáros
Department of Colloid Chemistry,
Loránd Eötvös University, P.O. Box 32,
1518 Budapest 112, Hungary
e-mail: imo@para.chem.elte.hu,
Tel.: +36-1-2090555/1553,
Fax: +36-1-2090602

Abstract Experimental results are presented for the counterion dependence of the adsorption of alkali decyl sulfates (Li^+ , Na^+ , K^+ , Rb^+ and Cs^+) at the air/solution interface. The experimental adsorption isotherms calculated from equilibrium surface tension/concentration data by means of the Gibbs equation

show significant counterion dependence. A new, very efficient and simple method is also proposed for the preparation of surface chemically pure surfactant solutions.

Keywords Adsorption · Ionic surfactant · Counterion · Alkali decyl sulfate · Surface tension

Introduction

The understanding of the interfacial behavior of aqueous surfactant solutions is a major issue in surface science both from a theoretical and from a technological point of view. On the one hand, the interpretation of several colloid phenomena requires detailed knowledge of the adsorption layer of the system [1]; on the other hand, the performance of many commercial products and industrial technologies (e.g. detergents, pharmaceutical applications, food and mineral processing, oil recovery) [2] is based on the adsorption of surfactant molecules. This explains the widespread interest in surfactant adsorption studies and the fact that this phenomenon is still the subject of intensive experimental and theoretical investigation [3].

Surfactant adsorption theories are based on different physical and geometrical models of the adsorbed layer, resulting in a variety of surface equations of state or equivalently in several different adsorption isotherms. The usual approach in the theoretical description of the adsorption of ionic surfactants is the generalization of an adsorption isotherm (or equation of state) of nonionic surfactants by incorporating the electrostatic contribution in the adsorption free energy [4, 5, 6, 7, 8]. The validity of the ionic models derived is usually tested by applying the models for the description of the surface

tension versus surfactant concentration curves either at air/solution or at oil/solution interfaces. The effect of salinity is also often checked and in some cases the surfactant concentration dependence of the surface potential has also been considered. In the case of ionic surfactants the effect of the chemical nature of the counterion on the surfactant adsorption is another parameter that could be used for the testing of ionic surfactant adsorption theories. Despite this there are only a limited number of experimental investigations about the effect of counterion quality [9, 10, 11] and none of the theoretical works have considered the testing of the adsorption theories by this effect. The experimental investigations were performed on alkali dodecyl sulfates. However, owing to the high Krafft point for potassium dodecyl sulfate and rubidium dodecyl sulfate, experimental surface tension data are available only for lithium dodecyl sulfate, sodium dodecyl sulfate and cesium dodecyl sulfate at room temperature.

In this paper we address the role of the counterion quality in the adsorption of an anionic surfactant with different alkali-metal counterions. To achieve our goal we synthesized the whole series of alkali decyl sulfates (Li^+ , Na^+ , K^+ , Rb^+ , Cs^+) and measured the concentration dependence of the surface tension of these surfactant solutions. The adsorption isotherms were calculated from the surface tension data. Since the

surface purity of the surfactant solutions is a crucial point when we consider the reliability of experimental surface tension data we also propose a new, very efficient and simple method for the purification of the surfactant solutions.

Experimental

Materials

Alkali decyl sulfates were prepared from pure *n*-decanol (Jansen, 99 + %) by sulfation with chlorosulfonic acid (Merk) at 0–5 °C. The recipe given in Ref. [11] was slightly modified. The synthesis was performed in CCl₄ medium and the reaction mixture was neutralized by the corresponding alkali carbonates (Aldrich, 99.9%). The salts prepared were recrystallized twice from a hot 1:1 benzene and ethanol mixture. Owing to this recrystallization procedure the amount of contaminants in the purified samples is significantly lower than that in the original alcohol used in the synthesis. Gas chromatographic analysis of the products showed a decanol mole fraction of about 3×10^{-5} in the samples; a combined liquid chromatographic/mass spectrometric analysis showed that the total amount of other homologue salts was less than 5×10^{-3} mole fraction. The solutions were prepared from dried (for 72 h at 40 °C) surfactants and bidistilled water. The critical micelle formation concentrations (cmc) were determined from the intercept in the specific conductance versus concentration functions (Table 1).

Surface purity

The surface purity of the surfactant solutions is an important question in connection with the reliability of the experimental surface tension data [13, 14, 15, 16], though its importance has still not received enough attention. Surfactant solutions always contain impurities, mainly alcohol and longer-chain homologues, with surface activities significantly higher than that of the surfactants investigated. Purification of the surfactant samples by physical methods (extraction, recrystallization) does not provide substances sufficiently pure from a surface chemical point of view.

The aim of the measurements was to determine the equilibrium surface tension of the two-component (surfactant and water) solutions, which is the subject of the thermodynamic analysis. The surfactant solutions can be defined as two-component systems from the surface chemical point of view if the amount of foreign components, always present in any substance, is so low that they do not exert measurable effect on the equilibrium surface tension beyond the error of the method applied. To achieve this goal one has to purify the surfactant solutions and check if the purification was successful.

Since the highly surface active impurities accumulate in the surface layer of the solution the surface purification methods are based on the repeated removal of the contaminated surface layer of the solution by means of single bubbles [17], foaming [14] or by repeated sucking off the surface layer [18]. All these methods are suitable to purify the surface below the cmc and their effectiveness depends on the relative surface activity and concentration of the

contaminants, on the ratio of the solution volume to the total removed surface area and on the time left for the adsorption of contaminants before the removal of the adsorbed layer.

It is difficult to find a general test criterion for checking the surface purity of a surfactant solution. The analysis of the time dependence of the surface tension seems to be the most suitable method for this purpose. Typical cases of the time dependence are shown in Fig. 1 starting from the creation of a fresh surface. The surface tension can be measured with the applied method from time t_0 . Case a is typical for dilute surfactant solutions containing very surface active impurities where both the surfactant and the contaminants decrease the surface tension on a similar time scale. In case b the surfactant and the impurities equilibrate on different time scales and the contaminants adsorb slowly in the experimental time window. Finally, curve c shows the case when the contaminated system reaches its equilibrium before t_0 .

The absence of the time dependence is not an appropriate criterion of purity in itself because it does not work in case a (where even the surface tension of the pure surfactant solution shows a time dependence) and case c (where there is no time dependence in the experimentally available time range). An elegant purity test, suggested by Lunkenheimer et al. [18], is the rapid compression of the surface film, which means a jump in the time scale in Fig. 1 from t_1 to t_2 . The limitation of this method is similar to that of the time-dependence measurements (case b). The combination of an effective surface purification procedure with the analysis of the time dependence can serve as a suitable purity test. In case a, the repeated purification cannot affect the equilibrium surface tension of the pure surfactant solution. In case b, the solution can be considered pure when the repeated purification completely removes the second step from the time-dependence curve. In case c, where the amount of contaminants is high (e.g. the surfactant is a mixture of homologues), the surfactant solution cannot be purified effectively by surface purification methods. In order to exclude this case one must perform a bulk analysis of the surfactant solution and if the amount of foreign components does not exceed a critical level (say it is less than 0.5%) then the time dependence can be analyzed after repeated surface purification.

In this work we used a new surface purification (named gas dispersion) method which is essentially an improved variation of the foam fractionation method. Instead of using macroscopic bubbles, a gas dispersion is formed from the surfactant solution. Dispersing microscopic bubbles in the solution results in a significantly higher gas/solution interface at the same gas volume rate. It is even more important that the average distance between the bubbles is much smaller than in the case of the other methods;

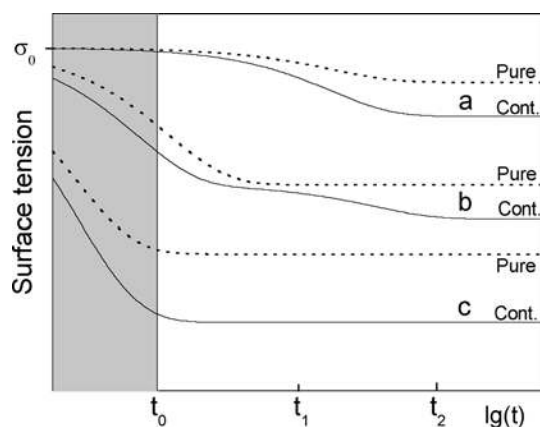


Fig. 1 Schematic representation of the time dependence of contaminated (solid lines) and pure (dotted lines) surfactant solutions

Table 1 The critical micelle formation concentration (cmc) values of the alkali decyl sulfates

Counterion	Li ⁺	Na ⁺	K ⁺	Rb ⁺	Cs ⁺
cmc (mmol/dm ³)	33.5	31.2	27.2	25.5	24.6

consequently, the time needed for the accumulation of the contaminants onto the surface is significantly reduced.

In the real experimental setup the gas dispersion was formed in the surfactant solution by producing microscopic bubbles by pressing nitrogen through a G-5 sintered glass filter into the solution. The solution was stirred and the foam formed above the solution was continuously sucked off. The mean bubble diameter was about 10 μm and the total removed area was approximately 100–200 m^2/hour . In order to validate the gas dispersion method we performed surface tension measurements on sodium dodecyl sulfate solutions. The test solutions were purified at $c \approx \text{cmc}$ and then diluted to 4.0 mM. The experimental procedure was similar to the one we applied for the alkali decyl sulfate solutions (see next section). The measured surface tension was found to be $53.03 \pm 0.05 \text{ mN/m}$, which corresponds to the reference value of the pure 4 mM sodium dodecyl sulfate solution given by Mysels [19].

Surface tension measurements

Prior to the measurements the decyl sulfate stock solutions ($c \approx \text{cmc}$, Table 1) were purified by the gas-dispersion method. The purification procedure lasted for 1–1.5 h and resulted in a 1–2-mM decrease of concentration.

The surface tension was calculated from the maximum force measured by the Wilhelmy plate method using a 2.0-cm-wide and 0.2-mm-thick platinum plate. The purification of the solutions and the dilution were made in a cylindrical cell of 8-cm diameter. The measurements were performed at $25.00 \pm 0.05^\circ\text{C}$. The concentrations of the solutions were determined from electrical conductivity measurements by means of a calibration curve. Five parallel measurements were made at each concentration and between the consecutive measurements the solution surface was sucked off to form a fresh surface and to eliminate the possible effect of contamination from the environment. The measurements were performed 1–2 min after the fresh surface had formed. Time dependence was not observed in the concentration range of the decyl sulfate solutions investigated. The reproducibility of the maximum force was $\pm 2 \times 10^{-6} \text{ N}$ (which corresponds to $\pm 0.05 \text{ mN/m}$ surface tension).

The surface tension measurements were performed on surfactant solutions prepared by the dilution of the purified stock solution. In order to exclude the possibility of contamination caused by the dilution we made test measurements by repeating the purification after each dilution of the surfactant solutions. The results of the two kinds of measurements were identical within the experimental error, indicating the reliability of the applied method.

Results and discussion

The surface tension versus $\log c$ functions are plotted for lithium, sodium, potassium, rubidium and cesium decyl sulfate solutions in Fig. 2. While the surface tension curves of the potassium decyl sulfate, rubidium decyl sulfate and cesium decyl sulfate solutions fall into the same group, the surface tension functions of lithium decyl sulfate and sodium decyl sulfate significantly differ from the others. The effect of the counterions on the σ versus $\log c$ functions is qualitatively similar to that measured for alkali dodecyl sulfate solutions [9, 10, 11].

Using the measured surface tension data summarized in Fig. 2, we calculated the adsorption isotherms by means of the Gibbs equation:

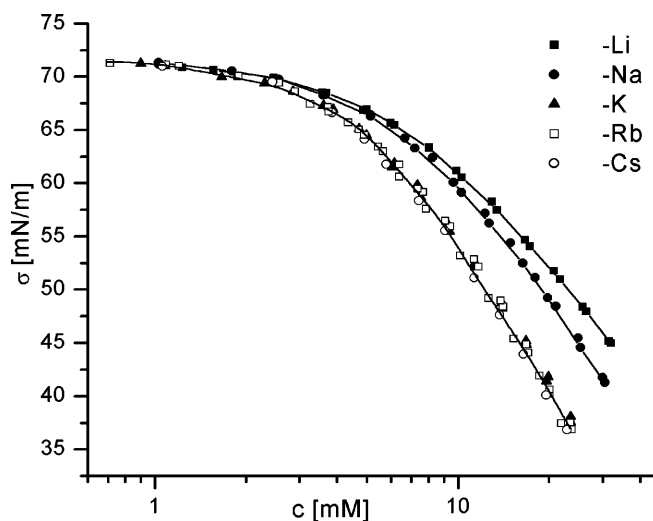


Fig. 2 Surface tension against the concentration of the alkali decyl sulfates

$$\Gamma^{(w)} = -\frac{1}{2RT} \left(\frac{\partial \sigma}{\partial \ln(\gamma_{\pm} c)} \right)_{T,p},$$

where $\Gamma^{(w)}$ is the Gibbs excess relative to the water and γ_{\pm} is the mean activity coefficient of the surfactant. γ_{\pm} was calculated from the Debye–Huckel limiting law. The activity correction was used a little beyond the accepted range of the validity of the Debye–Huckel law, but this may cause a similar systematic error in the case of each counterion investigated. The derivative was calculated by averaging the slopes of two adjacent data points, resulting in a slight smoothing of the experimental adsorption isotherms. Each series of the parallel measurements was evaluated individually.

The experimental adsorption isotherms of the alkali decyl sulfates are plotted in Fig. 3. The standard error of the data points was found to be $7 \times 10^{-12} \text{ mol/cm}^2$ from repeated measurements. As can be expected the isotherms are not simple Langmuir-type ones. The character of the isotherms shows a pronounced change at around $2\text{--}2.5 \times 10^{-10} \text{ mol/cm}^2$ surface excess. Below this concentration range the slope of the adsorption isotherms increases, which reflects that the driving force of the adsorption increases as the surface coverage, Θ , increases.

At $\Theta \rightarrow 0$ the lateral interactions between the hydrocarbon chains of the adsorbed surfactant ions diminish and the hydrophobic driving force contains two major contributions. One of them is the free-energy change accompanying the transfer of an alkyl chain from the aqueous bulk solution to the adsorbed monolayer, while the other one describes the interaction of the alkyl chains with the water surface. With increasing Θ the alkyl chains of the adsorbed surfactant molecules can interact with

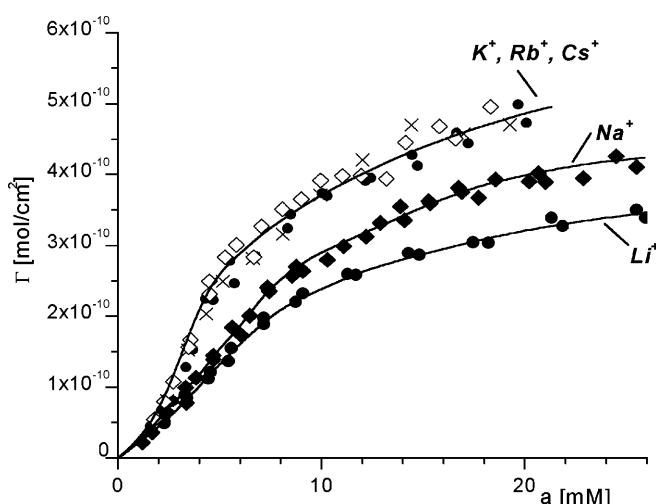


Fig. 3 Experimental adsorption isotherms of alkali decyl sulfates

each other, giving an additional term to the hydrophobic driving force, resulting in a significant increase. Our measurements suggest that the majority of the driving-force increase takes place in the first part of the isotherms ($\Gamma < 2\text{--}2.5 \times 10^{-10} \text{ mol/cm}^2$). This observation is in good agreement with recent sum-frequency spectroscopy and ellipsometry [20] measurements that indicated a monolayer density close to that of a liquid hydrocarbon above a certain surface coverage.

It must also be noted that since the hydrophobic driving force is primarily determined by the alkyl chain length and the lateral interactions of the alkyl chains it should have the same value at a given Γ independent of the type of counterion belonging to the surfactant. This means that the measured differences among the adsorption isotherms can be attributed to the effect of the counterions. The observed counterion effect is similar

to that measured for alkali dodecyl sulfate solutions. These effects are usually explained qualitatively in terms of the hydrated radii of the counterions: the larger the counterion, the less surface active the surfactant is, because the center of the larger counterion is located further away from the plane of the charged headgroups, thus allowing less efficient screening of the electrostatic repulsion among the heads. However, as we have already mentioned, quantitative theoretical calculations have not been performed yet to confirm the physical picture described. Our high-quality surface tension data give the opportunity to test these calculations to get greater insight into the nature of ionic surfactant adsorption.

Conclusions

A new method is proposed for the preparation of surface chemically pure surfactant solutions. Experimental results are presented for the counterion dependence of the adsorption of alkali decyl sulfates at the air/solution interface. The experimental adsorption isotherms calculated from equilibrium surface tension–concentration data show significant counterion dependence. While the adsorption isotherms of potassium decyl sulfate, rubidium decyl sulfate and cesium decyl sulfate fall into the same group, the surface activity of sodium decyl sulfate and lithium decyl sulfate is significantly smaller. The adsorption isotherms do not correspond to the Langmuir isotherm because there is a pronounced change in the shape of the isotherms at around $2\text{--}2.5 \times 10^{-10} \text{ mol/cm}^2$ surface excess.

Acknowledgements This work was supported by the Hungarian Scientific Research Fund (OTKA no. F 034838 and T043621 and by the Ministry of Education (FKFP 0051/2001).

References

- Lyklema J (1995) Fundamentals of interface and colloid science Academic, London
- (1992) In: Gloxhuber C (ed) Surfactant science series, vol 43. Dekker, New York, pp
- Prosser AJ, Franses E I (2001) Colloids Surf A 178:1
- Davies JT, Rideal E K (1963) Interfacial phenomena. Academic, New York
- Borwankar RP, Wasan DT (1986) Chem Eng Sci 1:199
- Nikas YJ, Puvvada S, Blankshtein D (1992) Langmuir 8:2680
- Kalinin VV, Radke CJ (1996) Colloids Surf A 114:337
- Warszynski P, Barzyk W, Lunkenheimer K, Fruhner H (1998) J Phys Chem B 102:10948
- Weil I (1966) J Phys Chem 70:133
- Oh SG, Shah DO (1993) J Phys Chem 97:284
- Lu JR, Marocco A, Su TJ, Thomas RK, Penfold J (1993) J Colloid Interface Sci 158:303
- Dreger EE, Keim GI, Miles GT, Sedlow L, Ross (1944) J Ind Eng Chem 36:610
- Elworthy PH, Mysels KJ (1966) J Colloid Interface Sci 21:331
- Gilányi T, Stergiopoulos C, Wolfram E (1976) Colloid Polym Sci 254:1018
- Lunkenheimer K, Wedler C (1993) Tenside Surfactants Deterg 30:342
- Priester T, Bartoszek M, Lunkenheimer K (1998) J Colloid Interface Sci 208:6
- Mysels KJ, Florence AT (1973) J Colloid Interface Sci 43:577
- Lunkenheimer KJ, Miller R (1987) J Colloid Interface Sci 120:176
- Mysels KJ (1986) Langmuir 2:423
- Bell GR, Manning-Benson S, Bain CD (1998) J Phys Chem B 102:218

L. Halász
 Á. Vincze
 O. Vorster

Relaxation spectrum calculation methods and their use to determine the molecular mass distribution of propylene, ethylene and α -olefin random copolymers

L. Halász (✉) · O. Vorster
 Technikon Pretoria, POB 680,
 Pretoria, Republic of South Africa

Á. Vincze
 Miklós Zrínyi National Defence University,
 146 Pf. 15, Budapest, Hungary

Abstract In the present study a nonlinear regression with regularization and inverse Fourier transformation methods were developed to determine the relaxation spectrum from the frequency-dependent storage and loss modulus data. The spectra obtained were used for the determination of the molecular mass distribution in a calculation process

developed by D.W. Mead [(1994) *Journal of Rheology* 38:1797]. The molecular mass distributions of propylene- α -olefin and ethylene- α -olefin random copolymers have been determined by rheological and gel permeation chromatography methods and the distributions obtained by the two methods agreed quite well with each other.

Introduction

It is well known that the linear viscoelastic properties of polymer melts and concentrated solutions are strong function of molecular structure, average molecular mass and molecular mass distribution (MWD). The relaxation time spectrum is a characteristic quantity describing the viscoelastic properties of polymer melts. Given this spectrum, it is easy to determine a series of rheological parameters. The relaxation time spectrum is not directly accessible by experiments. It is only possible to obtain the spectrum from noisy data.

Experiments can be carried out either in the frequency domain or in the time domain. In the first case, one obtains both storage, $G'(\omega)$, and loss, $G''(\omega)$, moduli, while the second method gives the relaxation modulus, $G(t)$. In any case, the linear viscoelasticity theory predicts that $G'(\omega)$, $G''(\omega)$ or $G(t)$ can be described using a unique function: the relaxation time spectrum, $H(\lambda)$ [1]. $H(\lambda)$ is related to $G(t)$ by

$$G(t) = \int_{-\infty}^{\infty} H(\lambda) \exp(-t/\lambda) d \ln \lambda . \quad (1)$$

Assuming the Maxwellian hypothesis, the relaxation time spectrum can be expressed in a discrete form, leading to

$$G(t) = \sum_{i=1}^n G_i \exp(-t/\lambda_i) . \quad (2)$$

In Eq. (2) the λ_i values are the specific relaxation times and the G_i values are the corresponding weights. The knowledge of the set (G_i, λ_i) is very useful because it allows one to predict the behaviour of the material in any standard experiment. From this set of (G_i, λ_i) values the zero-shear viscosity, η_0 , the plateau modulus, G_N^0 , the zero-shear first normal viscosity, $\Psi_{1,2}^0$ and the weight-average relaxation time, λ_w , can be obtained by the following equations:

$$\eta_0 = \sum_{i=1}^n G_i \lambda_i, \quad (3)$$

$$G_N^0 = \sum_{i=1}^n G_i, \quad (4)$$

$$\Psi_{1,2}^0 = \frac{1}{2} \sum_{i=1}^n G_i \lambda_i^2, \quad (5)$$

$$\lambda_w = \frac{\sum_{i=1}^n G_i \lambda_i^2}{\sum_{i=1}^n G_i \lambda_i} = \frac{\Psi_{1,2}^0}{2\eta_0} \quad (6)$$

Different calculation methods have been developed for the determination of the relaxation spectrum [2, 3, 4, 5, 6, 7, 8, 9].

In this study the relaxation spectrum and MWD have been determined by methods of nonlinear regression and inverse Fourier transformation for some ethylene and propylene homopolymers and α -olefin copolymers.

Methods for obtaining the relaxation spectrum

The experiment most often used to determine the relaxation spectrum of a polymer is small amplitude oscillatory shear. The storage and loss moduli are measured as functions of frequency, and in terms of a discrete relaxation spectrum, they can be expressed as follows at a particular frequency ω_i :

$$G'(\omega_i) = \sum_{i=1}^n G_i \frac{(\omega_i \lambda_i)^2}{1 + (\omega_i \lambda_i)^2}, \quad (7)$$

$$G''(\omega_i) = \sum_{i=1}^n G_i \frac{\omega_i \lambda_i}{1 + (\omega_i \lambda_i)^2}. \quad (8)$$

A typical spectrum is shown in Fig. 1. In materials which obey the time-temperature superposition principle [1], the dynamic moduli are rescaled to master curves at a reference temperature T_0 by using horizontal, a_T , and vertical, b_T , shift factors:

$$\begin{aligned} G'(\omega, T) &= b_T G'(a_T \omega, T_0), \\ G''(\omega, T) &= b_T G''(a_T \omega, T_0). \end{aligned} \quad (9)$$

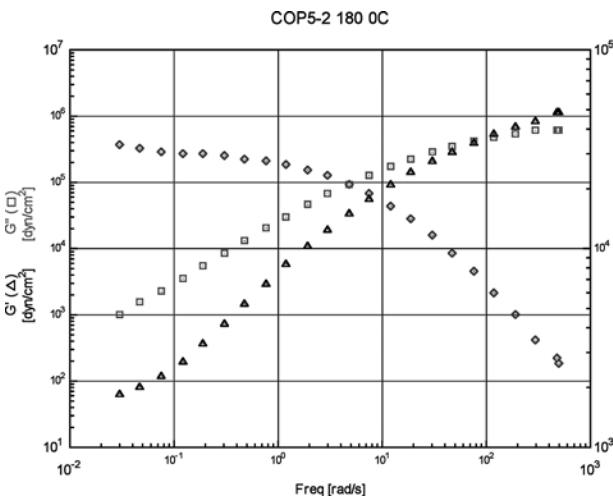


Fig. 1 Storage modulus, loss modulus and complex viscosity curves for propylene-1-pentene copolymer (COP5-2) at 180 °C

Master curves resulting from time-temperature superposition of $G'(\omega)$ and $G''(\omega)$ for the reference temperature $T_0 = 190$ °C are presented in Fig. 2. The behaviour is typical.

Regression

A simple if somewhat arbitrary way using M sets of data [$G'(\omega_i)$, $G''(\omega_i)$] to determine N sets of model parameters (G_i , λ_i) using Eqs. (7) and (8) is to specify N values of λ_i such that they are equally distributed on a logarithmic time scale within the range of experimental frequencies. The values of G_i can then be determined by a least-squares method:

$$\sum_{j=1}^M \left[\left(\sum_{i=1}^N \frac{1}{G'(\omega_j)} G_i \frac{(\omega_j \lambda_i)^2}{1 + (\omega_j \lambda_i)^2} - 1 \right)^2 + \left(\sum_{i=1}^N \frac{1}{G''(\omega_j)} G_i \frac{\omega_j \lambda_i}{1 + (\omega_j \lambda_i)^2} - 1 \right)^2 \right] = \min. \quad (10)$$

The differentiation of Eq. (10) with respect to each G_i gives sets of equations, which are called the normal equations of the linear least-squares problem. These normal equations can be solved by Gauss-Jordan elimination. However, in many cases the normal equations are very close to singular and a zero pivot element may be encountered. In such cases instead of using the normal equations, Eq. (10) can be solved by singular value decomposition.

Regression and regularization

The previous method may not lead to a unique, physically meaningful spectrum, because the value of G_i depends on those of λ_i and N and contains choices, especially as N increases, it can lead to negative values of G_i which are generally thought to be physically unrealistic. To select the true solution from the set of possible solution, Honerkamp and Weese [8, 9] introduced an additional criterion by means of the Tikhonov regularization method. They propose the use of the following condition in place of Eq. (10):

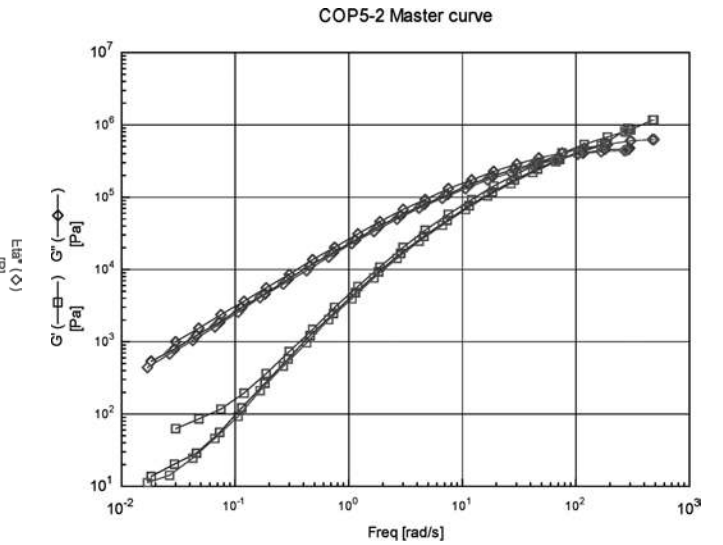


Fig. 2 Storage and loss modulus master curves for COP5-2

$$\sum_{j=1}^M \left[\left(\sum_{i=1}^N \frac{1}{G'(\omega_j)} G_i \frac{(\omega_j \lambda_i)^2}{1 + (\omega_j \lambda_i)^2} - 1 \right)^2 + \left(\sum_{i=1}^N \frac{1}{G''(\omega_j)} G_i \frac{(\omega_j \lambda_i)^2}{1 + (\omega_j \lambda_i)^2} - 1 \right)^2 \right] + \Lambda \sum_{i=1}^N G_i^2 = \min. \quad (11)$$

There are several methods for determining the regularization parameter [10, 11, 12]. The regularization parameter, Λ , can be determined, for example, by minimizing the following function:

$$T(\Lambda) = \sum_{n=1}^N \frac{\Lambda^2}{(w_n^2 + \Lambda)^2} (u_n b)^2 + 2\sigma^2 \sum_{n=1}^M \frac{w_n^2}{w_n^2 + \Lambda}, \quad (12)$$

where σ is the average standard error of the experimental G' and G'' data. Equation (11) suggests a fitting procedure that takes into account not only the mean square deviation of the experimental data from the calculated value but also the norm of G_i . The solution of Eq. (11) is given by [12]

$$G_i = \sum \frac{w_{kk}}{w_{kk}^2 + \Lambda} v_{ik} (u_k b). \quad (13)$$

Direct conversion

The relaxation modulus can also be obtained by direct conversion from the frequency domain to the time domain using the Fourier transform. The complex modulus can be expressed as

$$G^*(\omega) = i\omega \int_{-\infty}^{+\infty} G(t) \exp(-i\omega t) dt \quad (14)$$

and the inverse Fourier integral transform of Eq. (14) is

$$G(t) = \frac{1}{\pi} \int_0^\infty \frac{1}{\omega} (G' \sin \omega t + G'' \cos \omega t) d\omega = \frac{1}{\pi} \int_0^\infty \frac{G^*(\omega)}{i\omega} \exp(i\omega t) d\omega. \quad (15)$$

Since discretely sampled data points are available the continuous integral in Eq. (15) is approximated by the discrete Fourier transform

$$G(t) = \frac{\omega_{\max}}{\pi N} \sum_{m=0}^{N-1} \frac{G^*(\omega)}{i\omega} \exp\left(\frac{i2\pi mk}{N}\right), \quad (16)$$

where $k=0,1,2,\dots,N-1$. The discrete Fourier transform transforms the discretized in ω domain function ($0-\omega_{\max}$, divided into N equal parts) into its fundamental in the time domain ($0-N/\omega_{\max}$, divided into N equal parts). In Eq. (16) $G^*(\omega)/\omega$ values in equally divided intervals are required. A sixth-degree polynomial was used to fit $\log[G^*(\omega)/i\omega]$ as a function of $\log\omega$.

Determination of MWD

Currently the only experimental technique available for the direct determination of the MWD is gel permeation chromatography (GPC). Because of the difficulties involved in GPC measurements, this procedure does

not meet the requirement of a quality control technique. Moreover GPC is known to be insensitive to small amounts of high molecular mass material, which can have significant effects on the processing and product properties. Therefore, GPC data alone often miss important features of the MWD. For these reasons, several authors have attempted to correlate more readily measurable viscoelastic characteristics of polymers [13, 14, 15, 16, 17, 18, 19].

Two general models have been used for MWD determination: the viscosity and the modulus method.

The first method, developed by Malkin and Teishev [15], involves transforming the shear viscosity curve into the MWD using the mixing rule given by Eq. (24):

$$\eta^{1/a} = \sum_i w_i \eta_i^{1/a}, \quad (17)$$

where a is the exponent associated with dependence of the zero-shear viscosity on the weight-average molecular weight and is generally taken to be 3.4. In Eq. (17) w_i is the weight fraction of component i and η_i is its viscosity. Malkin and Tseishev [15] generated a solution by fitting the viscosity data to single-viscosity models and then substituted the parameter from these models directly into the transform equation:

$$W(m) = 1 + \frac{1}{v} \left(\frac{\eta}{\eta_0} \right)^{1/a} \left(\frac{\dot{\gamma}}{\dot{\gamma}_c} \right)^{v/a} \frac{d \ln \eta}{d \ln \dot{\gamma}}; \quad \dot{\gamma} = \dot{\gamma}_c m^{-a/v}, \quad (18)$$

where $W(m)$ is cumulative MWD, v is the slope of the logarithmic viscosity curve in the power-law region and the critical shear rate, $\dot{\gamma}_c$ is the intersection of the extrapolation of the low-shear-rate plateau and the power-law portion of log-log viscosity curve.

Some other methods have been developed to determine the MWD from viscosity curves [16, 17, 18, 19, 20, 21, 22, 23, 24, 25, 26].

The second method uses the dynamic moduli data. To describe the behaviour of polydisperse systems different mixing rules have been proposed in the literature that combine the relaxation features of the monodisperse components. The double-reptation mixing rule proposed by Tsenoglou [27] and des Cloiseaux [28] has been used to calculate the relaxation modulus from known MWDs

$$G(t) = G_N^0 \left[\int_0^\infty W(M \sqrt{F(t, M)}) dM \right]^2, \quad (19)$$

for the continuous distribution, where $G(t)$ is the stress relaxation modulus, G_N^0 is the plateau modulus of the species, $W(M)$ is the MWD function and $F(t, M)$ is the reduced relaxation function for a monodisperse sample at time t of a component of molecular weight M :

Table 1 Average molecular masses, polydispersity and melt flow index (MFI) of the polymers and copolymers investigated

Materials	Type	M_w (g/mol)	M_n (g/mol)	M_w/M_n	MFI (g/min)
PP-2	Homopolymer	440,668	85,277	5.2	7.4
COP5-2	2% 1-pentene	415,298	83,278	5.1	7
COP6-1	0.8% 1-heptene	358,116	50,759	7.1	11
COP9-3	2% 1-nonene	414,032	59,147	7.0	7.5
LDPE	Homopolymer	192,000	50,210	3.8	4.5
COE5-3	3.9% 1-pentene	361,761	67,220	5.4	22
COPET	2% 1-pentene, 3% 1-heptene	104,000	8,250	12.4	5.8

$$\begin{aligned} F(0, M) &= 1, \\ F(\infty, M) &= 0. \end{aligned} \quad (20)$$

Mead [29] developed a method that uses Eq. (19) in the following form:

$$w\left(M=b\sqrt{\frac{t}{K}}\right)=\frac{b}{2}\left[\frac{1}{G_N^0 G(t)}\right]^{1/2}\left[\frac{dG(t)}{dt}\right]K^{1/b}t^{(b-1/b)}|_{t=KM^b}, \quad (21)$$

where $G(t)$ is the stress relaxation modulus, G_N^0 is the plateau modulus, and $w(M)$ is the MWD function. The input parameters are the calculated $G(t)$, the K_λ prefactor, the power exponent b and the plateau modulus.

Experimental and calculations

Polypropylene, low-density polyethylene (LDPE) homopolymers and ethylene- α -olefin and propylene- α -olefin copolymers were prepared by a Ziegler-Natta catalyst system in the slurry phase.

The molecular mass and MWD of all the samples were measured by means of a Waters 150 CV GPC instrument. 1,2-Dichlorobenzene at 140 and 170 °C was used as the eluant. The apparatus was calibrated with polystyrene. Data handling was carried out using Viscotex Trisec version 3.0 software.

The molecular composition of the copolymers was determined by means of PerkinElmer Patagon 2000 FTIR equipment and a ^{13}C standard NMR method.

The rheological measurements were made using a controlled-stress Rheometrics dynamic stress rheometer (SR 500) with a data module and computer acquisition system. The measuring head was a parallel-plate system with diameter 2.5 and 4 cm and a gap of 1 mm. The steady-state viscosity curves, the creep curves and the components of the complex modulus and the complex viscosity were determined in the temperature region between 170 and 230 °C in a dry nitrogen atmosphere. Samples were produced in the form of injection-moulded disks. Orchestrator 6.5.5 software was used to analyse the data. The characteristics of materials investigated are summarized in Table 1.

Calculation of the relaxation modulus function and MWD

In this study we used the iteration method with regularization and the relaxation modulus function was used to determine the linear rheological parameters of the materials. For the use of the regularization equation, the experimental window ($\omega_{\max}-\omega_{\min}$) was divided into several equal intervals on a logarithmic scale. It was assumed that the middle of every logarithmic interval is equal to a relaxation time λ_n . Matlab software was used to programme the methods.

The calculated relaxation modulus curves are shown in Fig. 3. The two methods gave the same results.

In the calculation of the MWD the input parameters are the frequency-dependent G' and G'' values, the K_λ prefactor, the power exponent b and the plateau modulus. We started with the power exponent of the zero-shear viscosity and used $K_\lambda=2.8K/G_N^0$, where K is the proportionality constant in the equation of the relaxation time b and K were determined earlier [30, 31]. The plateau modulus was determined from the maximum value of the loss modulus curves [31].

The MWDs of polypropylene homopolymer calculated from the dynamic data are shown in Fig. 4 compared with data obtained by GPC. The MWD curves of 1-pentene, 1-heptene and 1-nonene propylene copolymers are shown in Figs. 5, 6 and 7. The MWD

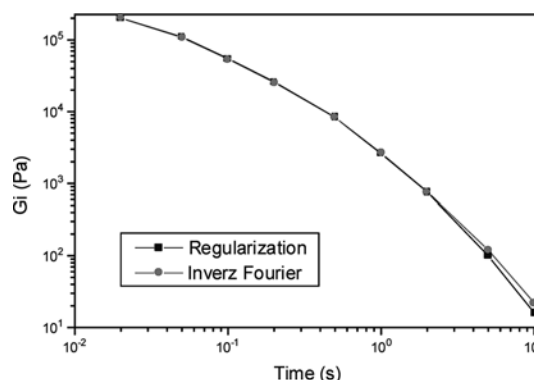


Fig. 3 Calculated relaxation modulus curve for propylene-1-pentene copolymer

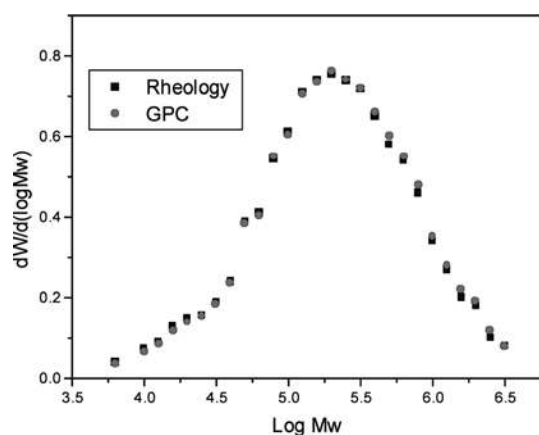


Fig. 4 Molecular mass distributions calculated from gel permeation chromatography (GPC) and rheological data for polypropylene homopolymer

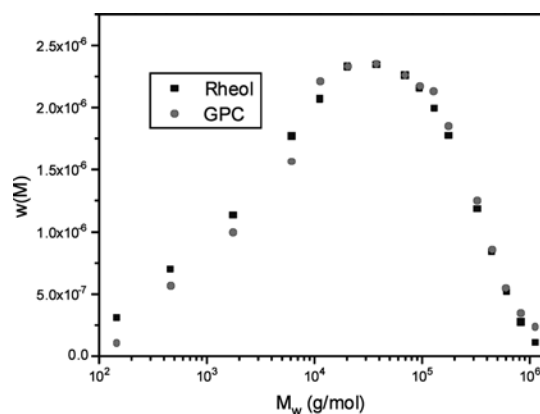


Fig. 7 Molecular mass distributions calculated from GPC and rheological data for a polypropylene-1-nonene copolymer

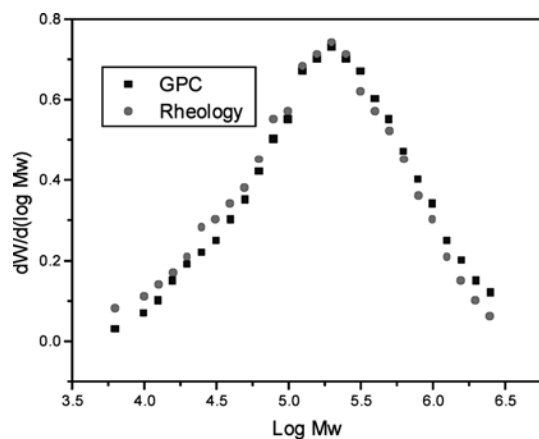


Fig. 5 Molecular mass distributions calculated from GPC and rheological data for a polypropylene-1-pentene copolymer

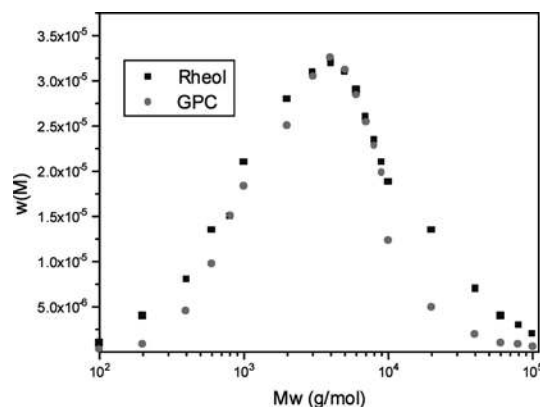


Fig. 8 Molecular mass distributions calculated from GPC and rheological data for a low-density polyethylene homopolymer

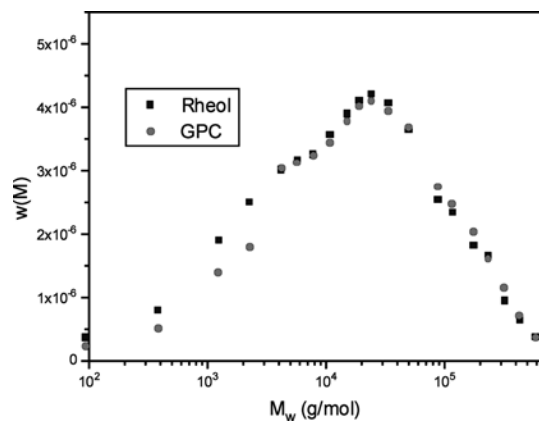


Fig. 6 Molecular mass distributions calculated from GPC and rheological data for a polypropylene-1-heptene copolymer

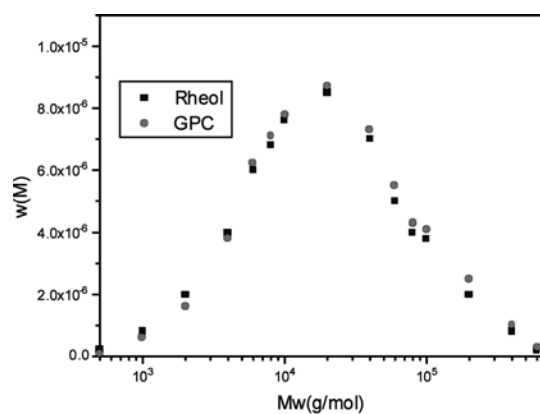


Fig. 9 Molecular mass distributions calculated from GPC and rheological data for an ethylene-1-pentene copolymer

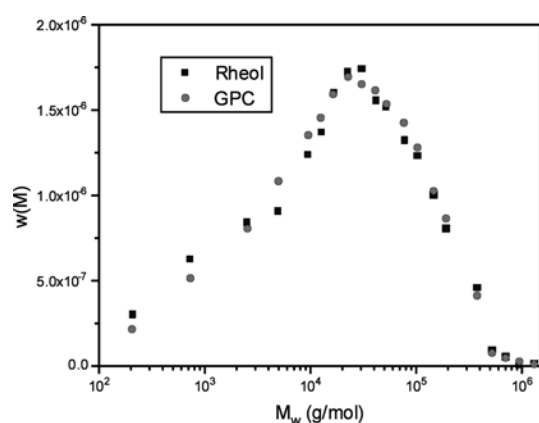


Fig. 10 Molecular mass distributions calculated from GPC and rheological data for an ethylene-1-pentene-1-heptene terpolymer

curves of LDPE homopolymer and ethylene-1-pentene and ethylene-heptene copolymers are shown in Figs. 8, 9 and 10. The rheological and GPC MWD curves agreed well; a small deviation was observed in the low molecular mass region.

Conclusions

The methods for calculating the relaxation spectrum were discussed. The calculated spectra were used to determine the MWD by the Mead method as illustrated in the examples polypropylene, LDPE and propylene- α -olefin and ethylene- α -olefin copolymers. The rheological method is a quick and accurate process to determine the MWD of homopolymers and copolymers.

References

- Ferry JD (1980) Viscoelastic properties of polymer, 3rd edn. Wiley, New York
- Groetch CW (1984) The theory of Tikhonov regularization for Friedholm equations of the first kind. Pitman, London
- Baumgartel M, Winter HH (1992) J Non-Newtonian Fluid Mech 44:15
- Baumgartel M, Schausberger A, Winter HH (1990) Rheol Acta 29:400
- Schausberger A (1991) Rheol Acta 30:197
- Orbey N, Dealy JM (1991) J Rheol 35:1035
- Honerkamp J, Weese J (1990) Continuum Mech Thermodyn 2:17
- Honerkamp J, Weese J (1989) Macromolecules 22:4372
- Malkin AJa, Kuznetsov VV (2000) Rheol Acta 39:379
- Honerkamp J, Elster JC (1992) Rheol Acta 36:911
- Honerkamp J, Weese J, Elster JC (1991) Rheol Acta 30:161
- Honerkamp J (1989) Rheol Acta 28:363
- Bernreiter K, Neissl W (1992) Polym Test 11:99
- Bersted BH, Slee JD (1977) J Appl Polym Eng Sci 21:2631
- Malkin AYa, Teishev AE (1987) Vysokomol Soedin Ser A 29:2230
- Malkin AYa, Teishev AE (1991) Polym Eng Sci 31:1590
- Tuminello WH (1986) Polym Eng Sci 26:1339
- Tuminello WH (1989) Polym Eng Sci 29:645
- Tuminello WH, Cudre-Mauroux N (1991) Polym Eng Sci 31:1496
- Shaw MT, Tuminello WH (1994) Polym Eng Sci 34:159
- Gloor WH (1978) J Appl Polym Sci 22:1177
- Gloor WH (1983) J Appl Polym Sci 28:795
- Nobile MR, Coechni F, Lawler JV (1996) J Rheol 40:363
- Carrot C, Guillet J (1997) J Rheol 41:1203
- Wasserman SH (1995) J Rheol 39:601
- Wasserman SH, Graessley WW (1992) J Rheol 36:543
- Tsenoglou C (1991) Macromolecules 24:1762
- des Cloizeaux J (1992) Macromolecules 25:835
- Mead DW (1994) J Rheol 38:1797
- Halász L, Voster O, Belina K, Tincul I, Potgieter AH (1988) Thermal and rheological properties of some new polypropylene copolymers, IUPAC Macro 98, World Polymer Conference, 12-18 July 1988, Gold Coast, Australia, p 879
- Halász L, Voster O, Belina K, Tincul I (2002) Processing properties of some ethylene- α -olefin copolymers, PPS-18, 16-20 June 2002, Guimaraes, Portugal

Magdolna Kónya
Peter Bohus
Laura Paglino
Ildikó Csóka
Erzsébet Csányi
Istvan Erös

Coherent emulsions containing alkylpolyglucoside esters as emulsifiers

M. Kónya · I. Csóka · E. Csányi
I. Erös (✉)
Department of Pharmaceutical Technology,
University of Szeged, Eötvös Str. 6,
6720 Szeged, Hungary
e-mail: eros@pharma.szote.u-szeged.hu
Tel.: +36-62-545571
Fax: +36-62-545571

P. Bohus · L. Paglino
Cesalpinia Chemicals SpA,
Via Piave 18, 21041 Albizzate, Italy

Abstract During our experimental work a recently developed emulsifier family – Eucarol – was studied by means of producing and examining creams with a high water content. The advantage of these emulsifiers is that principal raw materials of plant origin (fatty alcohol and glucose) are used and these emulsifiers are poly-oxyethylene-chain-free. The effect of these emulsifiers on the relationship

of hydrophilic and lipophilic phases was examined. Moreover, the structure of creams was studied with rheological and thermoanalytical methods. A close correlation was found between the amount of surfactant accumulated on the boundary and the rheological parameters.

Keywords Creams · Rheology · Thermoanalysis · Eucarol

Introduction

The oil-in-water (o/w) type of creams (Fig. 1) are systems of four components: their main elements are the hydrophilic and lipophilic gel phases. Both phases are composed of bilayers of mixed crystals. Water molecules are enclosed between the surfactant and alcoholic groups of the emulsifier molecules. In the gel phase, water molecules in interlamellar binding are in equilibrium with water molecules bound as bulk water. Both aqueous phases constitute the coherent (outer) phase of the system. The surplus of cetostearyl alcohol, which is not part of the hydrophilic gel phase, forms a matrix of lipophilic character called the lipophilic gel phase. The disperse or inner phase is mechanically not removable from the lipophilic gel phase. The lipophilic gel phase is constituted exclusively by cetostearyl alcohol, which can form only a semihydrate water layer [1, 2].

The theory of this four-phase system (hydrophilic gel phase, lipophilic gel phase, filling water phase and disperse inner phase) generally applies to o/w creams prepared with ionic or nonionic emulsifiers and to stearate creams [3].

In pharmaceutical technology surfactant compounds represent the most important and at the same time the

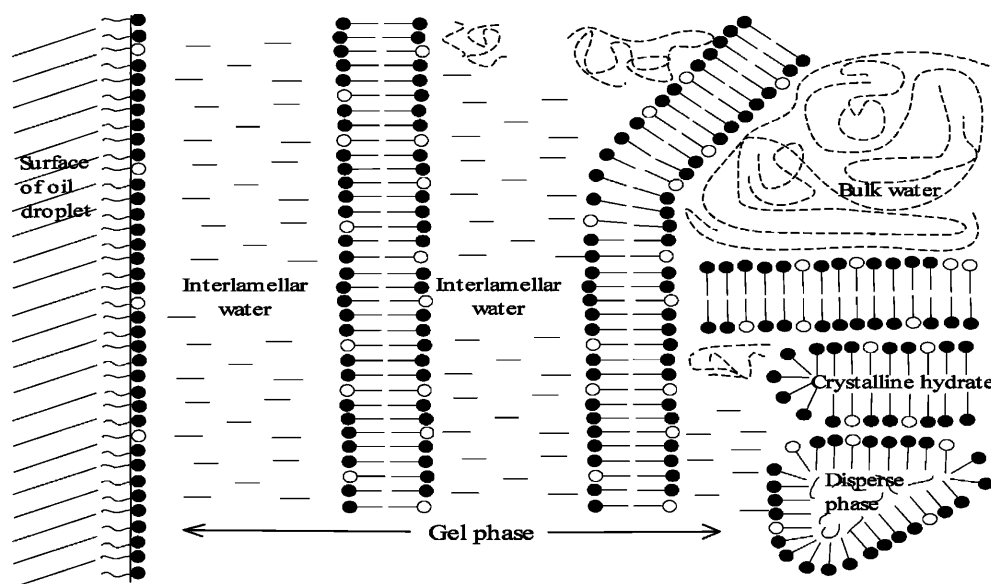
most contradictory group of additives. On the one hand, they are indispensable to the production of dosage forms, and on the other hand, surfactants are additives which cannot be regarded as neutral from the physiological aspect. A major part of surfactants enhances the permeability of the cell membrane; if this effect is irreversible, serious membrane damage will result. This phenomenon depends on concentration, and unfortunately several classic surfactants (fatty alcohol sulphonates, sodium lauryl sulphate) seriously damage the mucosa. If one looks at the development of emulsifiers, it is clear that recently increasing emphasis has been laid by manufactures on the formulation of biodegradable, skin-friendly surfactants, if possible from natural substances of plant origin.

Aims

The aims of our experimental work were:

- To qualify a new emulsifier group.
- To examine the structure and stability of o/w-type coherent emulsions prepared with them from many aspects.

Fig. 1 Typical structure of an oil-in-water cream [2]



- To develop a group of examination methods and to study the relationships between these methods, which can give objective help in the formulation of creams.

Eucarol AGE/EC, ET and SS ionic surfactants have been developed recently by Cesalpinia Chemicals for different applications, for example, cosmetic and pharmaceutical purposes. These surfactants are anionic ester derivatives of alkylpolyglucosides: they do not contain a polyoxyethylene chain, the hydrophilic moiety includes glucose units instead of ethylene oxide, and during their production no ethoxylation is carried out. They do not have an irritating effect as they are free from contaminating components such as dioxane: consequently no irritating effect is expected. After the glucosidation of fatty alcohol, esterification proceeds in order to obtain anionic derivatives. On the basis of the favourable properties listed, they can be used for medicinal purposes.

Materials

Surfactants

In the case of o/w-type systems a so-called mixed emulsifier is frequently used; this helps to eliminate the process of separation, which is essential if the same product is to be prepared with a realistic shelf life and with constant therapeutic properties [4].

Mixed emulsifiers obtained by combining ionic or nonionic surfactants with a structure-forming amphiphilic component were used: ionic surfactants Eucarol AGE/EC (alkylpolyglucoside citrate – Cesalpinia Chemicals, Italy), Eucarol AGE/ET (alkylpolyglucoside tartrate – Cesalpinia Chemicals, Italy) and Eucarol AGE/SS (alkylpolyglucoside sulfosuccinate – Cesalpinia

Chemicals, Italy); nonionic surfactant Tween 60 [polyoxyethylene (20) sorbitan monostearate – Atlas, Germany] was studied for the sake of comparison.

The structure-forming amphiphilic component was cetostearyl alcohol. The lipophilic phase of the creams was white petrolatum. The hydrophilic phase of the coherent emulsions was constituted by distilled water conserved with methyl-*p*-hydroxy benzoate.

- The cetostearyl alcohol, white petrolatum, methyl-*p*-hydroxy benzoate and distilled water used in the studies all corresponded to the quality requirements prescribed by the Fourth European Pharmacopoeia.

The compositions of the coherent emulsions studied are shown in Table 1.

Cream preparation

The white petrolatum and mixed emulsifier were melted in a pan at 70 °C. The preservatives were dissolved in hot distilled water. When the temperature of both phases was 70 °C, the water was added to the melted lipophilic phase and the cream was allowed to cool under continuous stirring. Evaporated water was replaced up to the desired weight. The cream was packaged into aluminium tubes and stored at room temperature.

Methods

During our experimental work the location of surfactants on the boundary was studied and boundary wetting was measured. The structure and properties of the creams were examined with

Table 1 Composition of creams (w/w%)

Surface-active agent	5	5	5	5	5
Cetostearyl alcohol	10	10	10	10	10
White petrolatum	25	20	15	10	5
Distilled water	60	65	70	75	80

rheological and thermoanalytical methods. The latter measurements were performed 1 day after formulation. Each analysis was done at least in triplicate.

Measurement of surface/interfacial tension

Interfacial tension was studied with a Krüss tensiometer on the boundary of liquid petrolatum and water at 25 ± 0.1 °C.

Measurement of wetting

For the examination of wetting, the method of drop spreading based on contact wetting was used. A uniform film was formed from the lipophilic phase on a glass plate. Water containing emulsifier was dropped onto the lipophilic phase from a microburette and the resulting contact angle was determined with Lerk's method and apparatus. The contact angle was calculated with the Weber–Wolfram [5] equation.

Rheological measurements

Rheological measurements were carried out with a computer-controlled Rheometer MC1 (Paar Physica) rotational viscometer, with a Z4 concentric cylindrical measurement system at 25 ± 0.1 °C. The complete flow and viscosity curves of the samples were plotted, and the yield value and the size of the thixotropic area were determined.

The shear rate ranged from 1 to 500 s^{-1} in nine steps both in the ascending and in the descending branches.

Thermoanalytical measurements

Thermogravimetric (TG) measurements were performed with a Derivatograph-C (MOM, Budapest) type apparatus. The TG, its derivative (DTG) and differential thermal analysis curves characterising the samples were drawn. The heating rate was 5 °C min^{-1} , and the measurements were carried out between 25 and 150 °C with linear heating. The weight of the samples was 50 ± 0.1 mg.

Results and evaluation

Interfacial tension and accumulated surfactant

The measurement of interfacial tension revealed that it was markedly decreased by all the three Eucarol emulsifiers. The boundary tension was lower than 10 mN m^{-1} even with 0.1%. The boundary-tension-decreasing effect of the three surfactants did not show a significant difference. When the interfacial tension–concentration functions were plotted separately in a semilogarithmic coordinate system, a linear relationship was found between the logarithm of concentration and interfacial tension in the case of Eucarols in the concentration range of 0.00001 and 0.1.

By using the angular coefficient of the line fitted to the measurement points and with the help of the Gibbs equation, the amount of surfactant accumulated on the boundary was measured. The smallest amount of surfactant accumulated on the boundary in the case of

Tween 60 used as a control, while the greatest extent of accumulation was observed with Eucarol AGE/SS (Table 2).

Examination of wetting

With respect to the quality of surfactants, a basic method is the measurement of interfacial wetting, as this factor has a decisive influence on structure formation and structural stability in creams.

A relationship was searched for between the amount of surfactant on the boundary and wetting. The smallest contact angle and thus the best wetting ability was experienced with Eucarol AGE/SS, while the worst wetting was seen with Tween 60 (Table 3).

Rheological studies

Rheological studies give information about the structure, flow properties and stability of coherent emulsions. With rheological measurements, by plotting flow and viscosity curves the circumstances of structure formation and the changes arising in the structure can be characterised in an exact manner.

The yield value, the value of the linear section of the ascending branch extrapolated to zero shear stress (Bingham's yield value), and the slope of the linear section (plastic viscosity) were determined with the help of flow curves for each sample.

The flow curves of the coherent emulsions show that the consistency typically softens with an increase in water content. The change elicited by emulsified water is the most prominent in the case of the sample containing Eucarol AGE/EC (Fig. 2).

Table 2 Interfacial accumulation of emulsifiers

Surface-active agent	Slope of interfacial tension versus concentration	Γ (mg cm^{-2})
Tween 60	−3.372	1.384
Eucarol AGE/EC	−3.909	1.604
Eucarol AGE/ET	−4.212	1.729
Eucarol AGE/SS	−5.699	2.339

Table 3 Interfacial accumulation and wettability of emulsifiers

Surface active agent	Γ (mg cm^{-2})	Contact angle of wetting
Tween 60	1.384	62.2
Eucarol AGE/EC	1.604	54.3
Eucarol AGE/ET	1.729	51.8
Eucarol AGE/SS	2.339	34.6

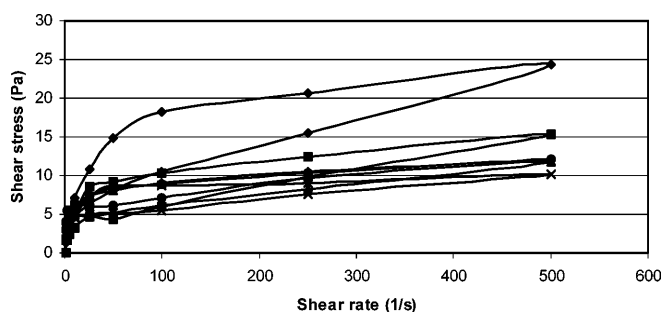


Fig. 2 Flow curves of creams based on Eucarol AGE/EC surfactant. Concentration of water 60 w/w% (diamonds), 65 w/w% (squares), 70 w/w% (triangles), 75 w/w% (crosses), 80 w/w% (circles)

The plastic viscosity and the theoretical yield value decreased gradually. In the case of Eucarol AGE/EC and SS the yield value did not change characteristically above a water content of 65%.

All the systems were thixotropic. Both the ascending and the descending branches of the flow curves had plastic properties. The thixotropic area was determined from the area delimited by the two curves with the trapezoidal method. A certain super-molecular arrangement (structure) is postulated within the system by the theory of thixotropy, and this structure will change owing to the effect of a deforming force.

The size of the thixotropic area showed a continuous and considerable decrease with the increase in water content in the case of emulsifiers Eucarol AGE/EC and ET. In the case of Eucarol AGE/SS the extent of thixotropy decrease was not expressed.

The viscosity of creams is the numerical characteristic of the forces acting in the structure. The greater the structural forces holding together the coherent lipophilic phase are, the greater the viscosity of the cream will be. The viscosity functions of the creams show that the value of structural viscosity determined at various D values decreased measurably with the increase in water content (Table 4). The increasing quantities of water dilute the gel structure, the structure-forming elements move farther from each other and the force holding the structure together decreases.

During our experimental work a relationship was searched between the rheological properties and the amount of surfactant accumulated on the boundary. A relationship was also searched between the structure of the boundary and the viscosity of the creams. It was found that the viscosity typically increased with the increase in the contact angle and decreased measurably with the quantity of the emulsifier accumulated on the boundary. This phenomenon is explained by the hydration of the structure elements. The greater the hydration of the gel structure is, the smaller the contact wetting angle and the softer the consistency of the

Table 4 Relationship between the structural viscosity and the water content ($D = 500 \text{ s}^{-1}$)

Water content (w/w%)	Structural viscosity (mPas)			
	Eucarol AGE/EC	Eucarol AGE/ET	Eucarol AGE/SS	Tween 60
60	48.8	50.1	55.1	51.8
65	30.8	43.5	43.1	47.6
70	24.1	34.6	23.9	37.1
75	23.6	27.8	16.8	30.1
80	20.4	19.8	15.9	26.6

creams will be, and the structural viscosity will be smaller (Fig. 3).

Similarly to our previous research [6, 7], an exponential relationship was found to exist between the water content and the rheological properties of creams (Fig. 4):

$$\eta = \eta_0 \exp(-bc) ,$$

where η is the initial viscosity of creams (mPas), η_0 is the viscosity pertaining to zero water content (w/w%), b is a constant and c is the water content (w/w%)

There is a relationship between the slope of the exponential functions and the incorporation of water into the structure. The greater the viscosity decrease of

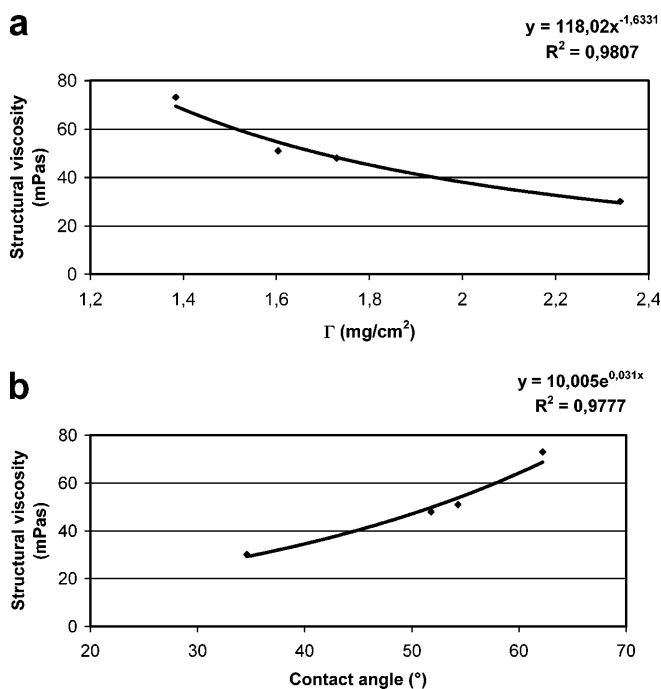


Fig. 3 **a** Relationship between surfactant accumulated on the interface and the structural viscosity of the creams (water content 80 w/w%, $D = 10 \text{ s}^{-1}$). **b** Relationship between contact angle of wetting and the structural viscosity of the creams (water content 80 w/w%)

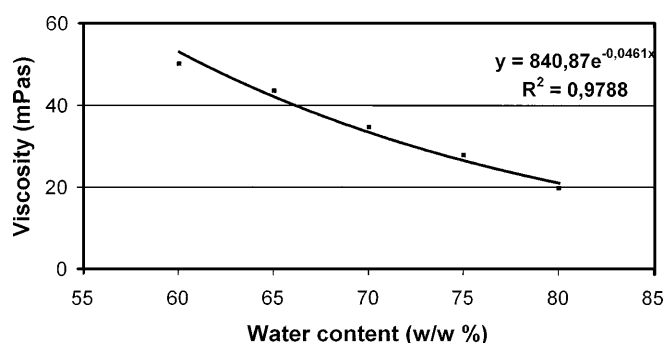


Fig. 4 The effect of water content on the viscosity of creams prepared with Eucarol AGE/ET ($D = 500 \text{ s}^{-1}$)

the creams with the increase in water content is, the binding of the water will be stronger in the lamellar structure. This hypothesis is confirmed by Fig. 5, which presents the relationship between the slope of the exponential functions and the amount of surfactant accumulated on the boundary. The linear relationship is clear from the figure.

TG measurement

The TG curve and its derivative (DTG) are typical characteristics of o/w creams. The TG curve shows the weight loss of the sample as a function of temperature. The DTG curve is the first derivative of the TG curve according to temperature. The DTG curve shows the evaporated part of the incorporated water, which is indicated by an inflection point on the TG curve, with the

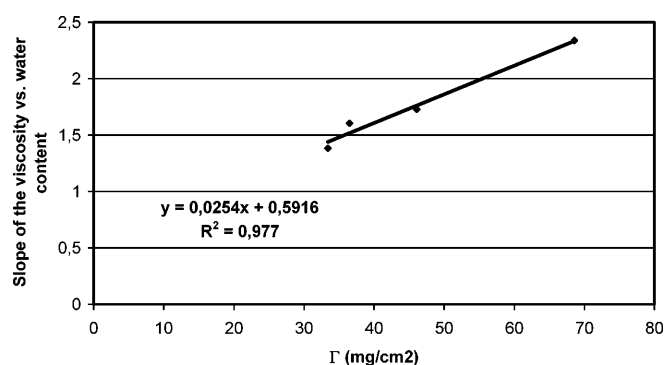


Fig. 5 Relationship between the quantity of surfactant on the interface of the oil/water phases and the slope of the viscosity versus water concentration

simultaneous appearance of a minimum on the DTG curve. Thus the proportion of interlamellarly fixed water and bulk water can be calculated from the area under the DTG curve or from the weight loss with the help of the inflection point of the TG curve [8].

The loss of emulsified water due to the effect of temperature is shown in Fig. 6. Once again, the slope of the exponential functions illustrates the rate of water loss. No significant relationship was found between the properties of the boundary of the creams (surfactant quantity accumulated on the oil/water boundary, wetting) and the evaporation rate of the water phase.

Fig. 6a–d Thermogravimetric (TG) curves of creams with 70% (w/w) water content: **a** Tween 60; **b** Eucarol AGE/EC; **c** Eucarol AGE/ET; **d** Eucarol AGE/SS

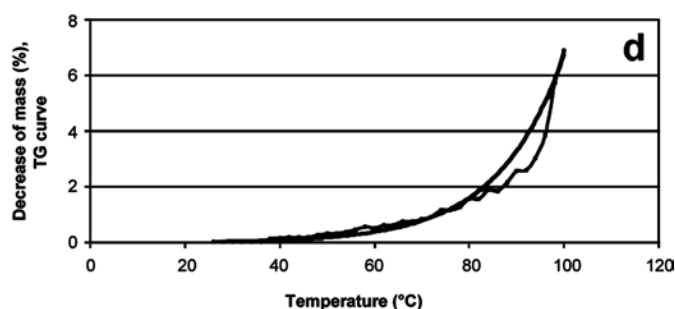
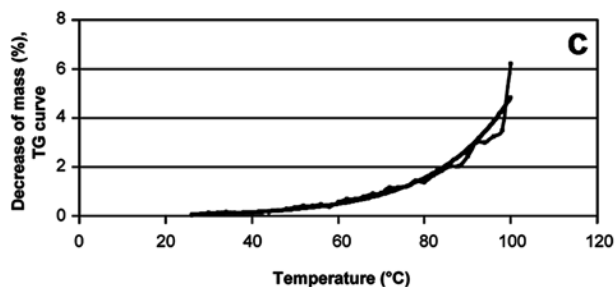
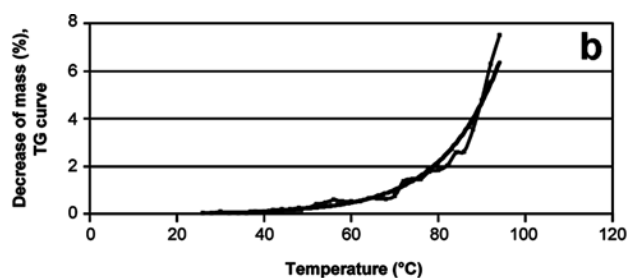
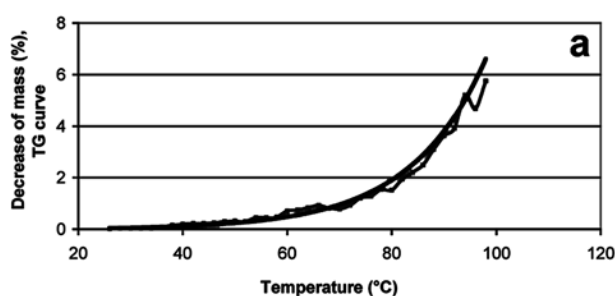


Table 5 Values of the slopes of the thermogravimetric curves

Water content (w/w%)	Slope of the thermogravimetric curve			
	Eucarol AGE/EC	Eucarol AGE/ET	Eucarol AGE/SS	Tween 60
60	0.0564	0.0583	0.0536	0.0683
65	0.0596	0.0572	0.0574	0.0686
70	0.061	0.0589	0.0717	0.0691
75	0.0659	0.0582	0.0731	0.0689
80	0.0767	0.0751	0.0736	0.0681

(The values of the evaporation rate are shown in Table 5.)

On the basis of the data in the figures and the tables it can be stated that the rate of water loss does not depend either on the nature of the emulsifier or on the concentration of water in the composition. This

phenomenon cannot be considered accidental as a considerable part of the water is so-called bulk water, the loss of which does not depend on the size of the binding forces found in the structure.

Conclusions

The results of the experiments can be evaluated as follows. Eucarol emulsifiers proved to be more advantageous with respect to pharmaceutical use than Tween 60, as they are produced with the use of raw materials of plant origin and they do not contain ethoxy groups. They were accumulated on the boundary to a greater extent than Tween 60, they elicited a greater decrease in interfacial tension and also had better wetting properties. These favourable properties were also manifested in better rheological and stability characteristics.

References

1. Junginger HE (1984) Ber Bunsenges Phys Chem 88:1070
2. Swarbrick J, Boylan JC (1988) Encyclopaedia of pharmaceutical technology, vol 5. Dekker, New York, p 171
3. Junginger HE (1984) Pharma Weekblad Sci Ed 6:141
4. Eccleston GM (1997) Colloids Surf A 123–124:169
5. Wolfram E (1971) Kontakt nedvesedés. Akadémiai Kiadó, Budapest, pp 74–78
6. Eros I, Szivoczka-Ferenczi I, Ugri-Hunyadvári E (1980) Pharm Ind 42:944
7. Eros I, Kedvessy G (1984) Acta Chim Hung 115:363
8. Kallionen S, Helenius K, Yliruusi J (1995) Pharmazie 50:478

István Lakatos
Julianna Lakatos-Szabó

Diffusion of H^+ ions in polymer/silicate gels

Abstract General features of H^+ ion diffusion in polymer/silicate gels applied in the hydrocarbon industry and environmental protection were analyzed. It was found that the cumulative mass transport curves of H^+ ions consist of two sections: a transient and a steady-state one. The length of the transient period is strongly dependent on the silicate content of the gel and the concentration gradient of H^+ ions. Using the length and the intersection point of these periods the effective diffusion coefficient and the ion retention capacity of the gel could be calculated. The effective diffusion coefficients obtained were very close to the values characteristic in aqueous solutions. The diffusion mass transport could be described by a modified version of Fick's first law, however, it was stated that on

account of the high ion retention in all the gels the one-dimensional random-walk equation may not be used for prediction of the mean diffusion distance (breakthrough time). Using the formation factor of the gel (effective "porosity" and tortuosity) the effective diffusion coefficient can be predicted with good accuracy and vice versa the gel structure can be determined from the absolute and the effective diffusion coefficients characteristic in the bulk aqueous phase and the gel, respectively. The laboratory experiments provided valuable new information and data to design and formulate industrial "gel" technologies in both enhanced oil recovery and environmental protection.

Keywords Diffusion · Gel · Polymer · Silicate · Hydrogen ion

I. Lakatos (✉) · J. Lakatos-Szabó
Research Institute of Applied Chemistry,
University of Miskolc, P.O. Box 2,
3515 Miskolc-Egyetemváros, Hungary
e-mail: lakatos@me.akk.hu
Tel.: +36-46-565255
Fax: +36-46-363349

Introduction

The use of electrolyte-containing gels in batteries and electric cells goes back to more than a century. Similarly, the application of hydrated gels as profile-correcting agents and barrier-forming materials opened up new vistas in enhanced oil recovery and environmental containment technology. During the past few decades a great variety of gel-forming chemicals have been tested under laboratory and industrial conditions, and some of them proved very useful, indispensable and effective in practice. On analyzing the negative gel properties, however, it became evident that the transport properties being main factors of the gelation, conductivity, block-

forming capacity, long-term usability, etc. are sometime poor and the mass transport mechanism in gels is not completely understood. Consequently, the diffusion of different chemical species in self-conforming phases formed prior to application or in situ in the formation rocks, soils, etc. might be fundamental, and the transport process may influence significantly the efficiency of the different industrial technologies to be applied in relevant areas. Despite these facts, the possible role of diffusion in such procedures – particularly in improved/enhanced oil recovery – are sometimes misunderstood or not mentioned in the literature at all [1], or it is considered as a negative factor resulting in a dilution and a depletion of the reacting species in the mixing zones or the gel itself

[2]. Fortunately, our knowledge of diffusion transport in gels proceeds well and these research areas (in material sciences, electrochemistry, etc.) are often revisited even today [3, 4, 5, 6].

Initiated by the strong industrial demands, a complex gel system containing silicates and water-soluble polymers was developed with the aim of selective fluid shut-off treatments and containment technology. The new methods were tested successfully at different Hungarian oil fields for restriction of water production and gas coning in oil wells. Since multivalent cations were used as cross-linking agents the earlier investigations were concentrated on determination of the diffusion mass transport of different chromium ions in polymer/silicate gels [7, 8]. Independent variables of the laboratory studies were the valency of chromium, and the geometry and composition of the gels. Simultaneously the effective diffusion coefficient, breakthrough time and retention of ions in gels were determined. Since the silicates were polymerized by pH regulation (addition of hydrochloric acid to gel-forming mixtures) the study of H^+ diffusion in gels having different composition also became necessary. The present paper gives a concise summary of the measurements, results and theoretical explanations with the aim at promoting the practical applications.

Experimental

The laboratory studies were focused on a complex gel containing a double network of cross-linked high molecular weight, partially hydrolyzed polyacrylamide and polysilicate. The measurements were carried out in a conventional dual-cell apparatus with cell volume of 400 ml (Fig. 1). The gel phase having 30-mm diameter and 20-mm thickness was fixed into the connecting glass tube of the cells by O-rings. A hydrostatic bypass served to equilibrate the density difference between the test solutions, thus minimizing the hydrodynamic mass transport between the cells. All the measurements were carried out at constant temperature (298 K). The composition of the gel was the following: polyacrylamide 0–2.5 g/l, silicate (SiO_2) 12.5–62.5 g/l, $AlK(SO_4)_2$ 1.0 g/l, $CaCl_2$ 1.0 g/l.

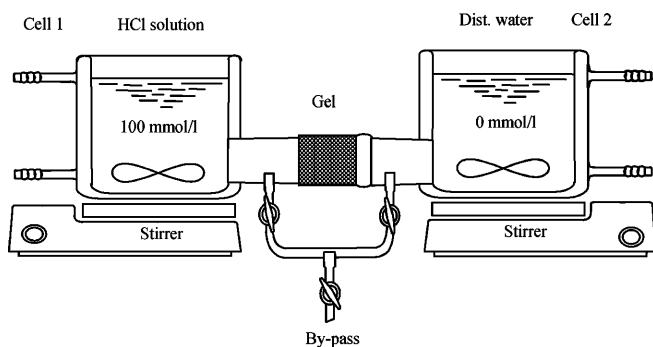


Fig. 1 Schematic of the dual-cell diffusion apparatus

The cross-linking solutions always contained sufficient HCl to set the gelation time within 4–5 min, and to maintain the pH in the range 8.0–8.5. The model tests were performed by H^+ ion added as analytical grade HCl in a concentration of 100 mmol/l. Thus, the initial concentration gradient between the cells was always constant ($50 \mu\text{mol}/\text{cm}^4$). The total diffusion mass transport was evaluated by the actual H^+ ion concentration in the cells determined continuously with a precision pH meter. The total mass balance in the cells was followed by a special computer program developed by us. The diffusion coefficient and the breakthrough time were obtained from the slope and the intersection point of the linear section of the cumulative mass transport curves shown in Fig. 2, while the specific ion retention capacity was calculated by the following relationships:

$$D_{\text{eff}} = \frac{1}{A} \frac{\Delta n}{\Delta t} \frac{x}{\Delta c} \quad (1)$$

and

$$a_n = \frac{1}{V} D_{\text{eff}} A \frac{\Delta c}{x} \int_{t_0}^{t_1} dt = \frac{1}{V} D_{\text{eff}} A \frac{\Delta c}{x} (t_1 - t_0) \quad (2)$$

The reproducibility of this method was determined by repeated measurements and it was better than 5 rel%.

Results and discussion

Effect of silicate content of the gel on transport properties

The basic studies were carried out with a gel containing 1 g/l polymer and 20–70 g/l SiO_2 equivalent orthosilicate. The concentration gradient of H^+ ion was kept constant during the measurements. The results of the primary pH measurements and the derived cumulative mass transport curves of H^+ ions are shown in Figs. 3 and 4.

The conclusions drawn by the experimental findings are as follows:

1. After breakthrough the cumulative transport of diffusing ions increases linearly in time if the absolute change of the original concentration gradient is

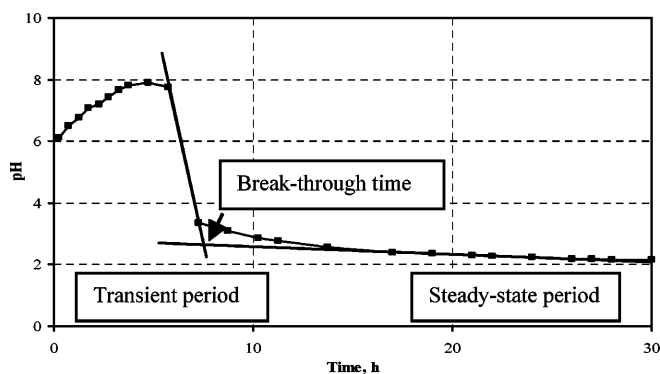


Fig. 2 General shape of the pH change in cell 2 as a function of time

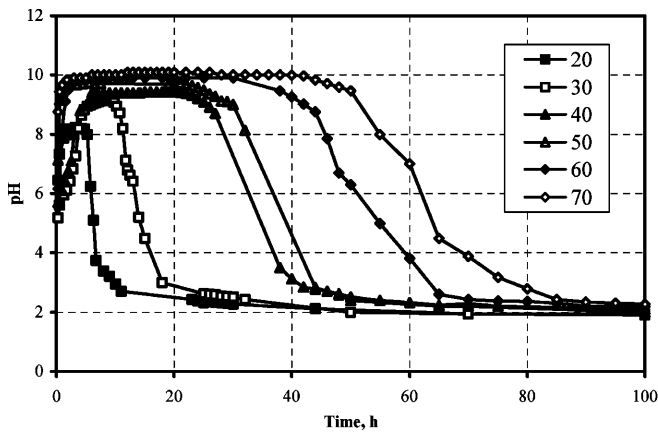


Fig. 3 Time dependency of the pH in cell 2 as a function of SiO_2 content of the gel

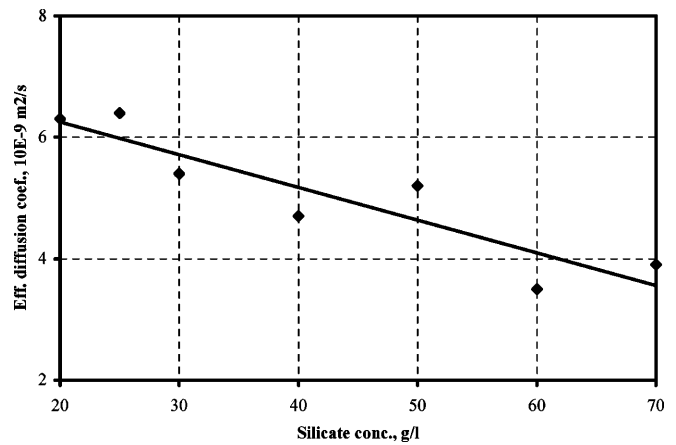


Fig. 5 Effect of SiO_2 content of the gel on the effective diffusion coefficient of H^+ ions

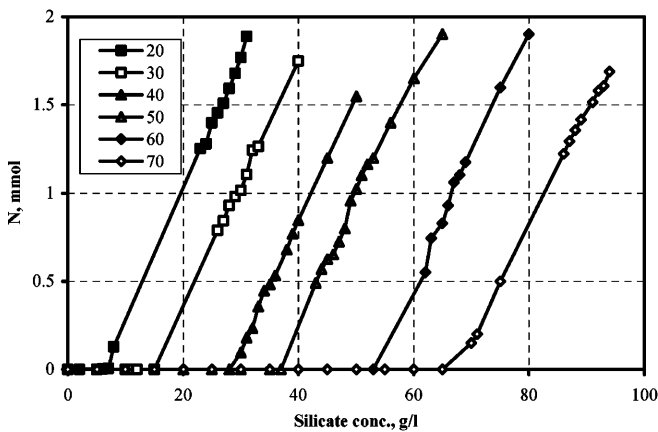


Fig. 4 Time dependency of the cumulative H^+ ion transport as a function of the SiO_2 content of the gel

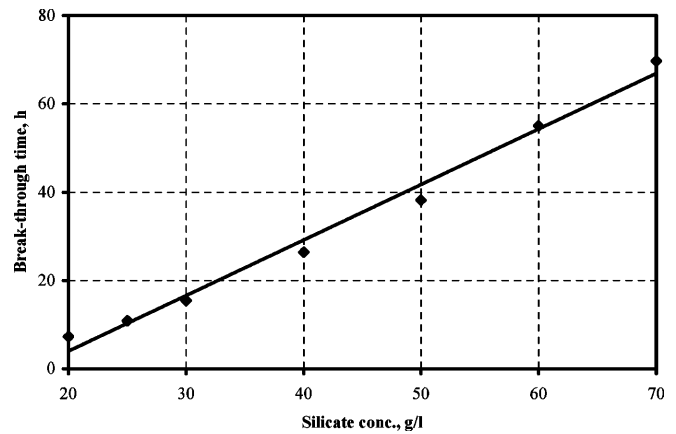


Fig. 6 Effect of SiO_2 content of the gel on the breakthrough time of H^+ ions

negligible (Fig. 4). That fact proves indirectly that the transport phenomena might be described by Fick's first law.

2. The effective diffusion coefficient of H^+ ions significantly depends on the silicate content of the gel. As shown in Fig. 5, the calculated effective diffusion coefficient decreases linearly with the silicate content.
3. Although the effective diffusion coefficients calculated from the slope of the cumulative curves, depending on the SiO_2 content of gel, are different for H^+ ions, they are only 10–50% less than the value ($9.32 \times 10^{-9} \text{ m}^2/\text{s}$) reported by Kollthoff and Lingane [9] for the same species in aqueous solutions.
4. The breakthrough times found for H^+ ions also show remarkable silicate dependency (Fig. 6). This fact can be explained by the original silicate content, and hence the pH of the gels. Since neutralization of the gel needs more acid as the silicate content increases,

the breakthrough time should decrease with the silicate concentration.

5. The ion retention capacity calculated by Eq. (2) changes parallel with the breakthrough time. As predicted, the acid consumption (neutralization or setting the gel pH to 100 mmol/l) also increases with the silicate content of the gel (Fig. 7).

The phenomena converge with the earlier findings of Janke and Radke [10], who stated that the migration of charged ions in gels can be explained jointly by diffusion and in situ reaction/adsorption processes. This idea is correct in the present case, because the main component of the gel, viz. the silicate (water glass), is highly alkaline in its original form, the free alkali present in the gel-forming mixtures is only partially neutralized by acid preaddition and, finally, the silica is well known as an adsorbent containing free $-\text{OH}$ groups on its surface. Here, the governing effect,

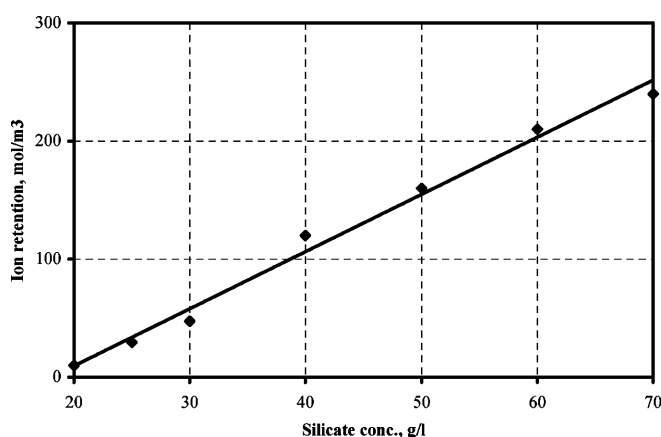


Fig. 7 Effect of SiO_2 content on H^+ ion retention in the gel

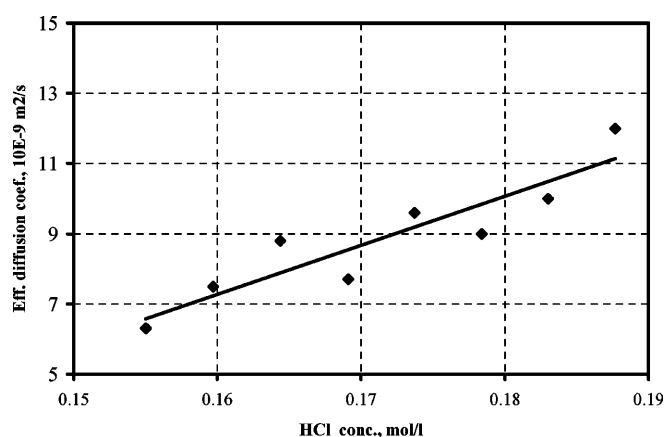


Fig. 9 Effect of the original HCl content of the gel on the effective diffusion coefficient of H^+ ions

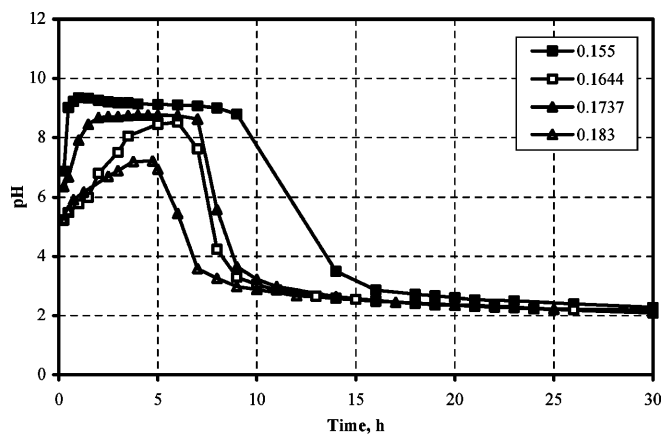


Fig. 8 Time dependency of the pH in cell 2 as a function of the original HCl content of the gel

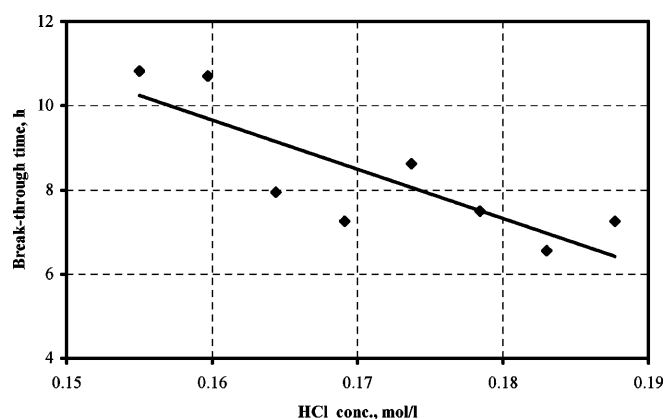


Fig. 10 Effect of the original HCl content of the gel on the breakthrough time of H^+ ions

however, is the neutralization of the free alkali (Na_2O) in the gel.

Effect of HCl content of the gel on transport properties

In the second series of measurements both the polymer and the silicate content of the gel were identical, the same original H^+ concentration gradient was applied but the amount of HCl added to initiate the gelation of the silicates changed between 0.1550 and 0.1877 mol/l. The diffusion tests were carried out at eight different acid concentrations and the same evaluation technique and calculations were used as previously.

The pH changes in cell 2 for selected cases are illustrated in Fig. 8 and the main conclusions concerning the transport properties can be listed as follows:

1. As far as the trends are concerned the effect of the HCl content of the gel has a similar consequences as

the silicate content. On adding HCl to the gel-forming mixture preneutralization takes place, viz. the higher the initial HCl content in the gel, the less additional acid is needed to reach the equilibrium condition or the pH characterizing the gel in the steady-state period.

2. As shown in Fig. 9, the effective diffusion coefficient increases linearly with the original HCl content. This phenomenon is quite obvious when taking the interpretation of Iler [11] and Falcone [12] into account; they reported a definite effect of the pH environment on the structure of silica gels.
3. The original HCl content of the gels also has a substantial impact on the breakthrough time of H^+ ions. As illustrated in Fig. 10 the breakthrough time decreases with the HCl concentration. This observation can easily be explained by the gradual lowering of the pH of the gel, which needs less and less HCl in the transient period to reach the equilibrium condition.

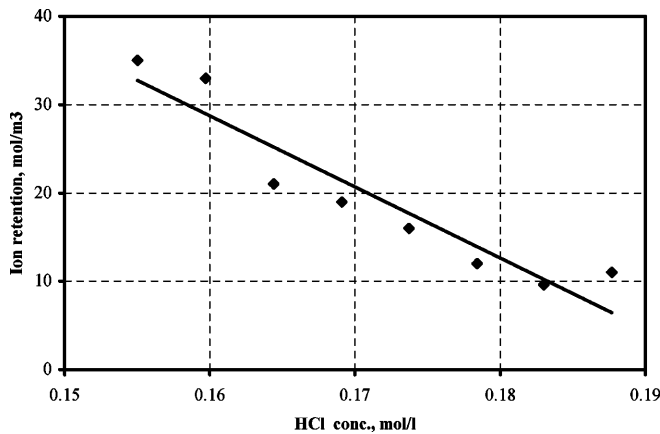


Fig. 11 Effect of the original HCl content of the gel on H^+ ion retention

4. Parallel with the previous statements, the H^+ (and basically HCl) retention also decreases with the original HCl content of the gel (Fig. 11). The reason is the same as mentioned in point 3.

The effect of HCl content on transport properties forecasts a radical structural modification in the gels. Obviously, the permeability of a gel having identical polymer and silicate content significantly increases with the original acid content. In other words, polymerization of water-soluble silicates in a low-pH environment yields fast precipitation in the organic polymer network, and such a composite gel structure is more penetrable by diffusing species than that of those gels which are prepared in neutral or slightly alkaline media.

Characterization of gel structure

The effective diffusion coefficients of H^+ ions found for the composite polymer/silicate gels having less than 10% solid content confirm the earlier findings of Jost [13]. Namely, the effective diffusion coefficient of charged ions might be a maximum of 1 order of magnitude less in gels than in aqueous solutions. Further, the general features of the diffusion transport in gels, particularly the existence of the simultaneous and competitive diffusion and retention processes, also allow us to predict that the one-dimensional random-walk equations cannot be applied for calculation of the mean diffusion distance of chromium ions in gels. The experimental results, however, raise a question: is it possible to draw a correlation between the effective diffusion coefficient and the gel structure or not? Using the “formation factor” concept developed by Pirson [14], Schopper [15], Dullien [16] and others for description of the diffusion mass transport in porous media, a reliable relationship between the effective diffusion coefficients and the

Table 1 Effect of silicate content on gel structure

SiO ₂ concentration (g/l)	D_{eff} (m ² /s, 10 ⁻⁹)	Φ	F	τ
20	6.4	0.9810	1.459	1.193
25	6.3	0.9762	1.482	1.205
30	5.4	0.9715	1.729	1.299
40	5.2	0.9620	1.796	1.308
50	4.7	0.9525	1.987	1.382
60	3.9	0.9430	2.239	1.495
70	3.5	0.9335	2.395	1.586

Table 2 Effect of HCl content on gel structure

HCl concentration (mol/l)	D_{eff} (m ² /s, 10 ⁻⁹)	Φ	F	τ
0.155	6.3	0.9810	1.482	1.205
0.159	7.4	0.9810	1.262	1.112
0.164	7.7	0.9810	1.213	1.091
0.173	8.5	0.9810	1.098	1.037
0.178	9.0	0.9810	1.037	1.008
0.183	9.2	0.9810	0.995	0.998

porosity and tortuosity was derived in earlier studies [7, 8]. Following the same procedure the formation factor was calculated:

$$F = \frac{\tau^2}{\Phi} = \frac{D}{D_{\text{eff}}}, \quad (3)$$

where F is the formation factor, D is the diffusion coefficient in the aqueous phase (meters squared per second), D_{eff} is the effective diffusion coefficient in the gel (meters squared per second), Φ is the “porosity of the gel” and τ is the tortuosity.

Although both the polymer and the silicate or silica exist in the gel as a hydrated double network, the approximate porosity can be calculated from the solid content of the gel. Using this approach the data in Tables 1 and 2 were obtained. The data indicate a disproportionality between the solid content (porosity) of the gel and the tortuosity. For instance, a silicate content between 20 and 70 g/l results in a maximum 7% change in porosity, while the length of the migration path of H^+ ions increases by nearly 40%. Even more stunning is that in gels having the same silicate and polymer content the tortuosity drops by 20% when the original acid concentration increases from 0.155 to 0.183 mol/l. These data indicate a robust structural modification: extensive swelling and coiling (intermolecular interactions) in the former case and shrinkage and ceasing intramolecular and intermolecular interactions in the later one.

The new results obtained by the detailed study of H^+ ions in polymer/silicate gels prove again that the

theoretical approach developed is correct and thus the Fick's first law can be rewritten in the following way:

$$\frac{dn}{dt} = -D_{\text{eff}} A \frac{dc}{dx} = -D \frac{A\Phi}{\tau^2} \frac{dc}{dx} = -D \frac{A_{\text{eff}}}{\tau^2} \frac{dc}{dx}. \quad (4)$$

The special advantage of Eq. (4) is twofold: it provides an easy calculation technique for determination of the approximate effective diffusion coefficient in the gel if its "porosity" and tortuosity are known or having determined the effective diffusion coefficient the gel structure or its modification under special circumstances can be predicted. Consequently, the method presented might be important in both engineering and from the theoretical point of view.

Conclusions

1. Transport properties of H^+ ions were determined in polymer/silicate gels as a function of the silicate and HCl contents.

2. The effective diffusion coefficient of H^+ ions decreased with the silicate content, while the breakthrough time and ion retention increased as the alkaline character of the gels increased.
3. The effective diffusion coefficient increased with the original HCl concentration of the gels, while the breakthrough time and the ion retention changed in the opposite manner.
4. A close correlation was found between the transport properties and the gel structure characterized by the formation factor, the effective porosity and the tortuosity of the gels.
5. The diffusion transport of H^+ ions in polymer/silicate gels could be described by a modified version of Fick's first law and this formula provides an appropriate method for the prediction of the effective diffusion coefficient in gels if the structural parameters of the gels and the absolute diffusion coefficient are known.
6. The laboratory experiments provided valuable new information and data to formulate different industrial "gel" technologies.

References

1. Todd BJ, Willhite GP, Green DW (1993) SPE Reservoir Eng 1:51
2. Seright RS (1991) SPE Reservoir Eng 3:343
3. Takahashi R, Sato S, Sodesowa T, Kamomae Y (2001) J Ceram Soc Jpn 109:840
4. Walcarius A, Etienne M, Bessiere J (2002) Chem Mater 14:2757
5. Takahashi R, Sato S, Sodesowa T, Nishida, H (2002) Phys Chem Chem Phys 4:3800
6. Othman R, Yahaya AH, Arof AK (2002) J New Mater Electrochem Syst 5(177)
7. Lakatos I, Bauer K, Lakatos-Szabó J, Kretzschmar HJ (1997) Land Contamination Reclamation 5:165
8. Lakatos I, Lakatos-Szabó J (1998) Colloids Surf A 141:425
9. Kollthoff IM, Lingane JJ (1952) Polarography, vol. I. Interscience, New York, p 52
10. Janke FM, Radke CJ (1989) Ind Eng Chem Res 28:347
11. Iler RK (1979) The chemistry of silica. Wiley, New York
12. Falcone JS (1982) Soluble silicates, ACS symposium series 194. American Chemical Society, Washington, DC
13. Jost W (1957) Diffusion-Methoden der Messung und Auswertung. Steinkopff, Darmstadt
14. Pirson SJ (1958) Oil reservoir engineering. Mc Graw-Hill, New York
15. Schopper JR (1966) Geophys Prospect 14:301
16. Dullien FAL (1992) Porous media: fluid transport and pore structure. Academic, New York

Atsushi Nohara
Masanori Kageyama
Shigeki Kuroki
Isao Ando

A study of structure and dynamics of water and lysozyme protein in aqueous solution by pulsed-high-field-gradient spin-echo ^1H NMR and ^{17}O NMR methods

Abstract The self-diffusion coefficients of water and lysozyme in aqueous solution have been measured over a wide range of the protein concentration and over a wide range of temperature by means of the pulsed-high-field-gradient spin-echo ^1H NMR method, and also the ^{17}O NMR spectra of water in the protein solutions have been measured by means of a solution ^{17}O NMR method, in order to elucidate the structure and dynamics of water and the protein, and intermolecular interactions between water and the protein. From these experimental results, it is found that there exist two types of water molecules with different diffusion components

in the lysozyme solution. One of them is mobile water with a relatively large diffusion coefficient, and the other is immobile water with a relatively small diffusion coefficient which comes from strong intermolecular interactions between water and the protein. The ^{17}O NMR experiments support such experimental results. Further, detailed discussion on the aggregation of lysozyme molecules is through the diffusion coefficients determined as functions of the protein concentration and temperature.

Keywords Structure · Dynamics · Intermolecular interaction · Lysozyme · Water · Diffusion

A. Nohara · M. Kageyama · S. Kuroki
I. Ando (✉)
Department of Chemistry and Materials
Science, International Research Center
of Macromolecular Science,
Tokyo Institute of Technology,
2-12-1 Ookayama, Meguro-ku,
Tokyo 152-8552, Japan
e-mail: iando@o.cc.titech.ac.jp

Introduction

It is well known that water interacts intermolecularly with proteins in aqueous solution and sometimes forms hydrogen bonds. This leads to significant biochemical activity of proteins. A lot of work on intermolecular interactions between water and proteins from various dimensions as studied from the point of view of their diffusional behavior using the field-gradient NMR method have appeared recently [1, 2, 3, 4, 5, 6, 7, 8, 9, 10, 11, 12, 13].

In our previous works [14, 15, 16, 17, 18], the pulsed-high-field-gradient spin-echo (PHFGSE) ^1H NMR method was used for determining the diffusion coefficient of solvent, probe molecules, and probe polymers in a gel and rodlike polypeptides in the thermotropic liquid-crystalline state. The great strength of the field

gradient has been used to determine relatively small diffusion coefficients with high accuracy. We have designed two kinds of PHFGSE ^1H NMR probe systems for generating strong field gradient pulses with 780 and 2,000 G/cm. Using the great strength of the field gradient pulse, it is possible to determine exactly diffusion coefficients of the order of $10^{-11} \text{ cm}^2/\text{s}$.

From such a background, we aimed to measure self-diffusion coefficients, D , of water and lysozyme in aqueous lysozyme concentrated solution at high concentration and also over a wide range of protein concentrations as a function of temperature by the PHFGSE ^1H NMR method and to measure ^{17}O NMR spectra of aqueous lysozyme concentrated solution, and to elucidate intermolecular interactions between the protein and water through the diffusion coefficient determined and the ^{17}O NMR spectra, in addition to

those obtained in previous works [1, 2, 3, 4, 5, 6, 7, 8, 9, 10, 11, 12, 13].

Experimental

Materials

The hen egg white lysozyme protein sample with molecular weight of 14,300 and nonprosthetic groups used in this work was obtained from Wako Chemical Co.. The aqueous lysozyme solutions with a wide range of protein concentrations from 2 to 200 wt/wt% were prepared in an NMR tube with a diameter of 5 mm. ^{17}O labeled water (20%) was obtained from Cambridge Isotope Laboratories.

Measurements

The self-diffusion coefficient measurements of water and lysozyme in concentrated aqueous solutions were carried out as a function of temperature by means of a JEOL GSX-270 NMR spectrometer operating at 270.1 MHz for ^1H with a homemade pulse gradient generator. As the PHFGSE pulse sequence, two field gradient pulses were added to the $(\pi/2 \text{ pulse} - \tau - \pi \text{ pulse})$ sequence, in which the first field gradient pulse was added at the mid position between the $\pi/2$ and π pulses (i.e., at the position of π^* after the π pulse), and the second at the position of π^* after the π pulse. A homemade pulse gradient generator was designed to generate the strong field gradient pulse (with a maximum field strength of about 2,000 G/cm) and to suppress the eddy currents induced. This was used successfully in our previous works on diffusional behavior in polymer gel systems [10, 11]. In this work, a field gradient strength of about 590 G/cm was used. The spectral width was 4.0 kHz and there were 4,096 data points.

The D value was determined by using the following relationship between the echo signal intensity and the pulsed-field-gradient parameters:

$$\ln[A(\delta)/A(0)] = -\gamma^2 G^2 \delta^2 D (\Delta - \delta/3), \quad (1)$$

where $A(\delta)$ and $A(0)$ are the echo signal intensities at $t = 2\tau$ with and without the magnetic field gradient pulse, respectively, whose length is δ . τ is the pulse interval, γ the gyromagnetic ratio of the proton ($\gamma = 2.675 \times 10^4 \text{ rad/G/s}$), G the field gradient strength, and Δ the gradient pulse interval. The echo signal intensity was measured as a function of δ . The plot of $\ln[A(\delta)/A(0)]$ against $\gamma^2 G^2 \delta^2 (\Delta - \delta/3)$ gives a straight line with a slope $-D$; therefore, D can be determined from this slope. The τ , Δ and δ values employed in these experiments are 4.6 μs , 10 ms and 0.001–2 ms, respectively. A D value of $2.5 \times 10^{-5} \text{ cm}^2/\text{s}$ for deuterium oxide at 300 K was used as the calibration of the field gradient strength. The experimental error for the D value is estimated to be less than around 5%.

^{17}O NMR spectra of water in aqueous lysozyme solution were measured using a JEOL GSX-270 NMR spectrometer operating at 36.6 MHz. The observed frequency range was 100 kHz. The $\pi/2$ and π pulse widths for the ^{17}O nucleus were 4.2 and 8.4 μs , respectively. The spectra are accumulated more than 100 times to achieve a reasonable signal-to-noise ratio.

The ^{17}O spin-lattice relaxation time, T_1 , measurements of ^{17}O labeled water in aqueous lysozyme solution were made by the inversion-recovery pulse sequence $(\pi - \tau - \pi/2)$. The relationship between the signal intensity, $M(\tau)$, at any τ and T_1 is expressed by

$$M(\tau) = M(0)[1 - 2 \exp(-\tau/T_1)], \quad (2)$$

where τ is the waiting time between π and $\pi/2$ pulses. All of the observed ^{17}O chemical shifts were calibrated relative to the ^{17}O chemical shift of pure water ($\delta = 0 \text{ ppm}$) at 300 K.

Results and discussion

Diffusional behavior of water and lysozyme in aqueous solution

Typical PHFGSE ^1H spectra of water in aqueous lysozyme solution at 24 °C are shown in Fig. 1 as a function of field gradient pulse length, δ , where the protein concentration is 200 wt/wt%. A broadened spectrum is observed in the spin-echo ^1H NMR spectra of water in aqueous lysozyme solution. This means that water in aqueous lysozyme solution is strongly bonded with a lysozyme molecule because of the high protein concentration and thus the molecular motion of water is strongly restricted. The plots of $\ln[A(\delta)/A(0)]$ against $\gamma^2 G^2 \delta^2 (\Delta - \delta/3)$ for the previously mentioned peak in the PHFGSE ^1H NMR spectra of bound water consist of two straight lines. This shows that the diffusion of bound water has two components within the observation time and that two types of water with different diffusion coefficients exist around the lysozyme.

The plots of two types of small and large diffusion coefficients of the water in aqueous lysozyme solution against temperature are shown in Fig. 2. The diffusion coefficient of water of the fast diffusion component is

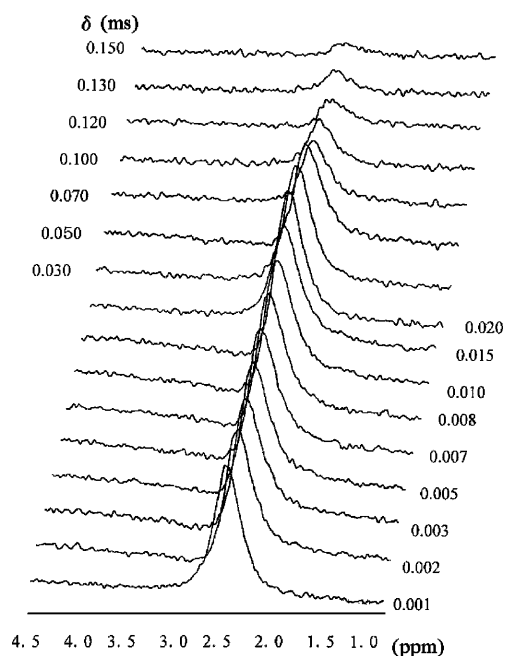


Fig. 1 Typical ^1H pulsed-high-field-gradient spin-echo NMR spectra of water in aqueous lysozyme solution at 24 °C as a function of field gradient pulse length, δ . The lysozyme concentration is 200 wt/wt%

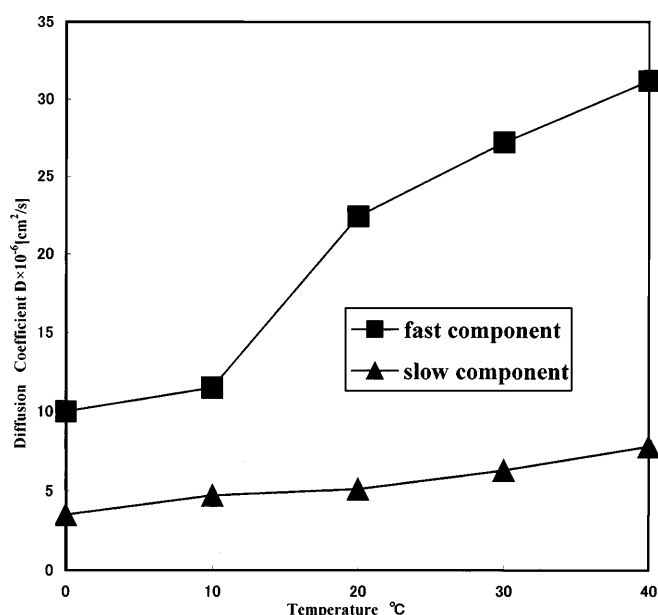


Fig. 2 Temperature dependence of the diffusion coefficient, D

2.2×10^{-5} cm²/s at 20 °C and is very close to that of pure water (2.5×10^{-5} cm²/s at 25 °C). This means that water corresponding to the fast diffusion component is unbound water like pure water. On the other hand, the diffusion coefficient of the other type of water (slow diffusion component) is 0.5×10^{-5} cm²/s at 20 °C and is one fifth of that for pure water. This shows that water corresponding to the slow diffusion component interacts strongly with lysozyme. The diffusion coefficient for the fast diffusion component increases with an increase in temperature, but the temperature dependence of the diffusion coefficient for the slow diffusion component is small.

The weight fractions of the slow diffusion component and the fast diffusion component against temperature are shown in Fig. 3. The weight fraction of the slow diffusion component is above 80% and temperature change of the weight fraction is very small within the temperature range from 10 to 50 °C. As the temperature is decreased from 10 to 0 °C, the weight fraction of the slow diffusion component decreases to below 80% and thus that of the fast diffusion component increases to over 20%. This shows that water bonded with lysozyme is squeezed out by the structural change of the protein at low temperatures and the amount of unbound water increases with a decrease in temperature from 10 to 0 °C.

The plots of the diffusion coefficients of water and lysozyme in aqueous lysozyme solution against the lysozyme concentration at room temperature are shown in Fig. 4. As the lysozyme concentration increases from 5 to 20 wt/wt%, the diffusion coefficient of lysozyme decreases from 1.04×10^{-6} to 7.5×10^{-7} cm²/s. This shows that such a reduction of the diffusion coefficient

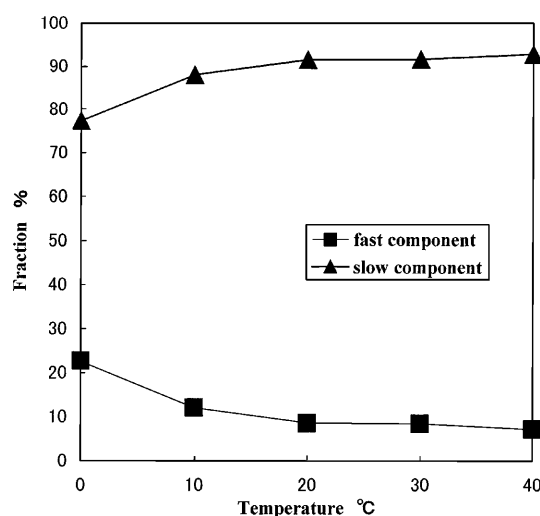


Fig. 3 Weight fraction of water as a function of temperature

comes from the aggregation of lysozyme molecules in aqueous solution. At lysozyme concentrations above 50 wt/wt%, the ¹H NMR signal of lysozyme cannot be observed because of large signal broadening due to the formation of further large clusters. In the lysozyme concentration range from 5 to 100 wt/wt%, the diffusion coefficient of the slow diffusion component of water decreases from 1.7×10^{-5} to 4.9×10^{-6} cm²/s with an

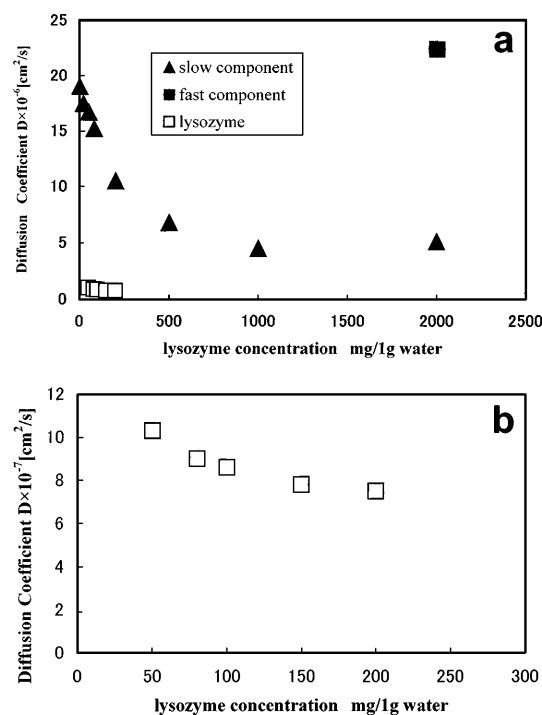


Fig. 4 D of water in aqueous lysozyme solution as a function of concentration

increase in lysozyme concentration. This shows that water is bonded with lysozyme clusters in solution. At 200 wt/wt% lysozyme concentration, two types of water molecules with the slow diffusion component and the fast diffusion component are observed. The water molecules undergo slow exchange between the bound state and the unbound state with lysozyme on the NMR time scale. The diffusion coefficient of the slow component is $5.0 \times 10^{-6} \text{ cm}^2/\text{s}$ and that of the fast diffusion component is $2.25 \times 10^{-5} \text{ cm}^2/\text{s}$. The diffusion coefficient of the fast diffusion component is very close to the diffusion coefficient of pure water and is much larger than that at low lysozyme concentration. At low lysozyme concentration, the water molecules undergo fast exchange between the bound state and the unbound state with lysozyme on the NMR time scale and then the diffusion is observed as one component. Therefore, the apparent diffusion coefficients at low lysozyme concentration are much smaller compared with the diffusion coefficient of water at 200 wt/wt% lysozyme concentration.

The plots of the diffusion coefficients of water in aqueous lysozyme solutions at various concentrations against temperature together with those of pure water determined by Price et al. [8] are shown in Fig. 5. From this figure it can be seen that the temperature dependence of the diffusion coefficient of water at 2 wt/wt% lysozyme concentration is very close to that of pure water. This shows that water at 2 wt/wt% lysozyme concentration is unbound water like pure water. The diffusion coefficient of water at high lysozyme concentrations is much smaller compared with pure water. As already mentioned, this may come from changes of the aggregated state by a temperature change in addition to slow exchange between the bound state and the unbound state with lysozyme on the NMR time scale. This is supported by an increase of the diffusion coefficients of water by temperature elevation. The temperature dependence for the fast diffusion component at 200 wt/wt% is almost

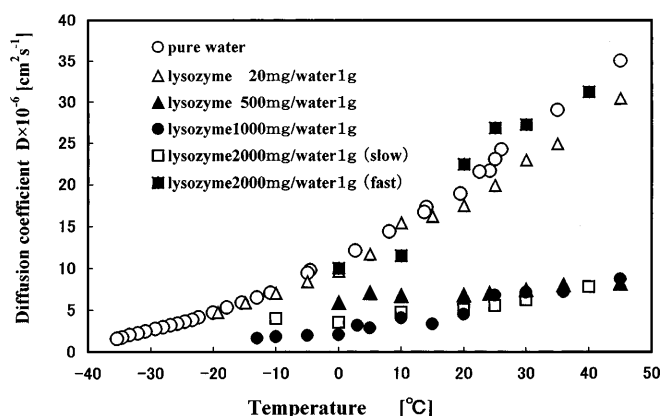


Fig. 5 Temperature dependence of D of water in aqueous lysozyme solution at various concentrations

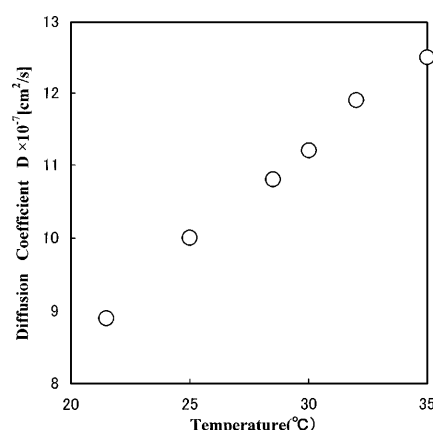


Fig. 6 Temperature dependence of D of lysozyme in aqueous solution at 5 wt/wt% concentration

same as that of pure water, and the temperature dependence for the slow diffusion component is almost same as that of the diffusion coefficient for water at 5–100 wt/wt% lysozyme concentration.

To understand in more detail the aggregation state of lysozyme molecules at high concentrations, let us look at the diffusion coefficients of water and lysozyme at 5 wt/wt% concentration as a function of temperature as shown in Fig. 6. It is found that the diffusion coefficient of lysozyme increases with an increase in temperature and the diffusion coefficient of lysozyme ($1.25 \times 10^{-6} \text{ cm}^2/\text{s}$ at 35 °C) may be close to that of a single lysozyme molecule in aqueous solution. This shows that the lysozyme aggregations dissociate with an increase in temperature and become a single lysozyme molecule. It can be said that an increase in the lysozyme concentration leads to an increase in aggregation of lysozyme molecules.

Structure and dynamics of water in aqueous lysozyme solution by ^{17}O NMR spectral observation

Typical ^{17}O NMR spectra of pure water and bound water in aqueous lysozyme solution at 200 wt/wt% concentration are shown in Fig. 7. The ^{17}O spectrum of bound water consists of two signals. One is a sharp signal which came from the mobile component, and the other is a broadened signal which came from the immobile component. To clarify this, the ^{17}O T_1 values of the two components were measured. The plots of the ^{17}O T_1 values of unbound water (the mobile component) and of bound water (the immobile component) together with pure water against temperature are shown in Fig. 8. These values increase with an increase in temperature. This shows that molecular motion for water with two components is in the fast motion region of Bloembergen–Purcell–Pound theory [19] and the molecules undergo

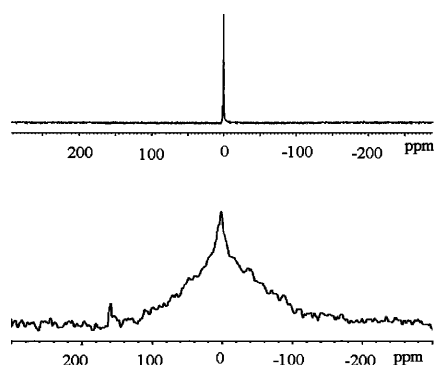


Fig. 7 ^{17}O NMR spectra of pure water (upper) and water (lower) in 200 wt/wt% aqueous lysozyme solution

faster motion than the ^{17}O NMR resonance frequency of 36.6 MHz. The ^{17}O T_1 value for water of the mobile component is much larger than that of the immobile component. This means that water molecules of the mobile component undergo much faster motion than water molecules of the immobile component. The ^{17}O T_1 value for water of the mobile component is very close to that of pure water. The frequencies for the molecular motion are close to each other.

The weight fraction of each of the components is shown in Fig. 9. The weight fraction of the water of the mobile component is about 10% and that of the water of the immobile component is about 90%. This is almost the same as the result obtained by the PHFGSE ^1H NMR method. With a decrease in temperature, the weight fraction of the water of the immobile component decreases slightly and that of the water with the mobile component increases. This tendency is similar to the results obtained by the PHFGSE ^1H NMR method as shown in Fig. 3.

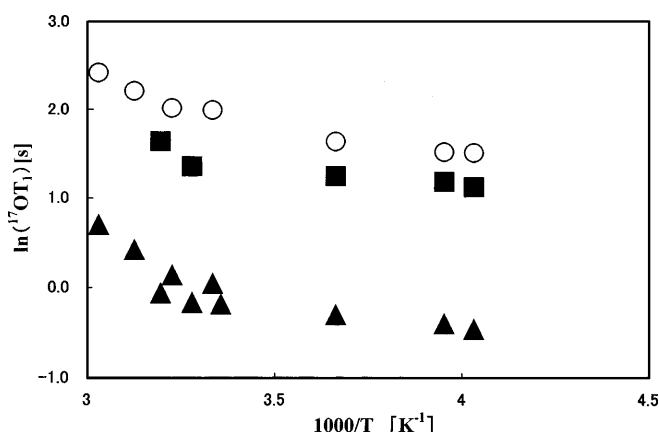


Fig. 8 ^{17}O T_1 of pure water and water in 200 wt/wt% aqueous lysozyme solution against temperature. Immobile water (squares), immobile water (triangles) and pure water (circles)

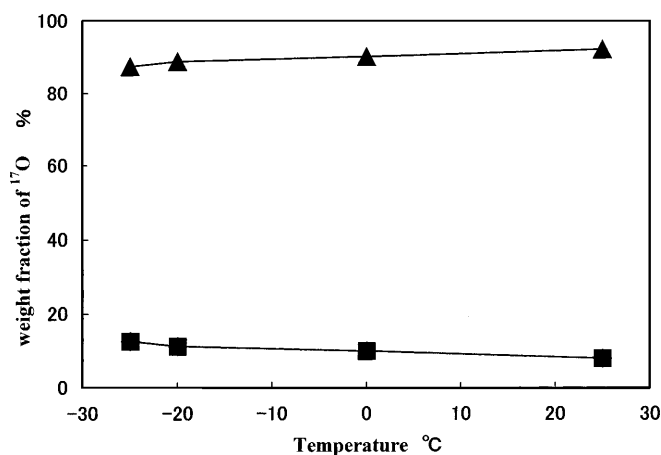


Fig. 9 Weight fraction of water in 200 wt/wt% aqueous lysozyme solution as estimated from the ^{17}O peak intensity. Mobile component (squares) and immobile component (triangles)

In order to understand in more detail the dynamics of water, the correlation time, τ_c , in the molecular motion of water was calculated from the ^{17}O T_1 value by using aqueous lysozyme solution:

$$1/T_1 = 3/40(2I + 3)/I^2(2I - 1)(1 + \eta^2/3)(e^2Qq/h)^2\tau_c, \quad (3)$$

where I is the spin number, η is the asymmetry parameter and $(e^2Qq/h)^2$ is the nuclear quadrupolar constant. The plots of τ_c in the molecular motion of pure water and water in 200 wt/wt% aqueous solution against temperature are shown in Fig. 10. From this figure it can be said that τ_c of immobile water is about 10 times longer than that of mobile water, and the

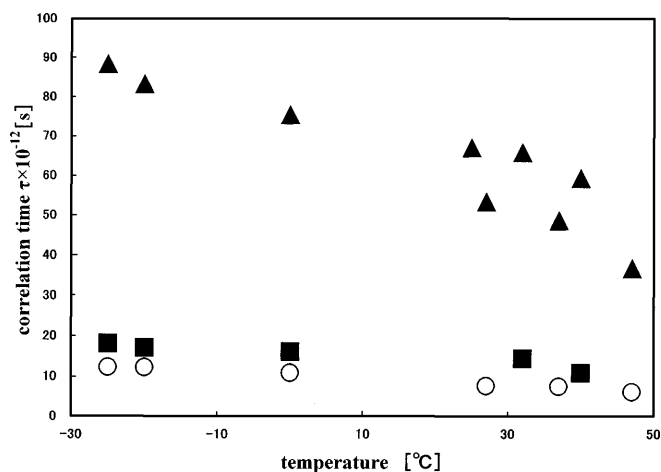


Fig. 10 Correlation time in molecular motion, τ_c , of pure water and water in 200 wt/wt% aqueous solution calculated from ^{17}O T_1 as a function of temperature. Mobile water (squares), immobile water (triangles) and pure water (circles)

temperature change of τ_c of immobile water is larger than that of mobile water. Since τ_c is associated with the rotational motion of water, the rotational motion of immobile water is more sensitive to temperature than mobile water.

Finally, it is concluded that there exist two types of water molecules with different diffusion components in

aqueous lysozyme solution. One of them is normal water with a relatively large diffusion coefficient, and the other is water with a relatively small diffusion coefficient which comes from strong intermolecular interactions between water and lysozyme. The ^{17}O NMR experiments support such experimental results.

References

1. Baranowska HM, Olszewski KJ (1996) *Biochim Biophys Acta* 1289:312
2. Roongta V, Pan H, Woodward C, Mayo KH (1997) *Biochemistry* 36:3383
3. Krishnan VV (1997) *J Magn Reson* 124:468
4. Aso Y, Yoshioka S, Kojima S (1998) *Chem Pharm Bull* 46:1836
5. Tillett ML, Lian L, Norwood TJ (1998) *J Magn Reson* 133:379
6. Nesmelova IV, Fedotov VD (1998) *Biochim Biophys Acta* 1383:311
7. Jones JA, Wilkins DK, Lorna J, Dobson CM (1997) *J Biomol NMR* 10:199
8. Price WS, Tsuchiya F, Arata Y (1999) *J Am Chem Soc* 121:11503
9. Nohara A, Kuroki S, Ando I (2001) *Polym Prepr Jpn* 947
10. Price WS, Tsuchiya F, Arata Y (2001) *Biophys J* 80:1585
11. Nesmelova IV, Skirda VD, Fedotov VD (2002) *Biopolymers* 63:132
12. Zhao H, Pearlstein AJ (2002) *Phys Fluids* 14:2376
13. Huang SY, Lin Y, Lisitz N, Warren WS (2002) *J Chem Phys* 116:10325
14. Yin Y, Zhao C, Kuroki S, Ando I (2000) *J Chem Phys* 113:7635
15. Yin Y, Zhao C, Kuroki S, Ando I (2002) *Macromolecules* 35:2335
16. Yin Y, Zhao C, Sasaki A, Kimura H, Kuroki S, Ando I (2002) *Macromolecules* 35:5910
17. Yamane Y, Kobayashi M, Kuroki S, Ando I (2001) *Macromolecules* 34:5961
18. Yamane Y, Kobayashi M, Kimura H, Kuroki S, Ando I (2002) *Polymer* 43:1767
19. Bloembergen N, Purcell EM, Pound RV (1948) *Phys Rev* 73:679

Tibor Gilányi
Imre Varga
Róbert Mészáros

Molecular interaction model of polymer–surfactant complex formation

Abstract A molecular interaction model of nonionic polymer–surfactant complex formation was developed by modifying the free-energy expression of micelles for interaction with polymer segments. Using the small systems thermodynamics the composition of the surfactant aggregates with respect to the aggregation number, the number of polymer segments involved in the

aggregates, and the distribution of aggregates among the polymer molecules were analysed. The thermodynamic conditions of nonionic polymer–surfactant complex formation were also discussed.

Keywords Polymer–surfactant interaction · Small systems thermodynamic model · Aggregation number

T. Gilányi (✉) · I. Varga · R. Mészáros
Department of Colloid Chemistry,
Loránd Eötvös University, P.O. Box 32,
1518 Budapest 112, Hungary
e-mail: gilanyi@para.chem.elte.hu

Introduction

The current physical picture for the description of the microstructure of polymer–surfactant complexes originated from Shirahama's necklace model [1] in which the polymer chain connects micellelike surfactant aggregates by wrapping around them. This picture was elaborated and qualitatively verified by others [2].

The first molecular interaction model was developed by Nagarajan [3, 4, 5]. For the description of the microstructure of the complex the necklace model was adopted. The free-energy expression developed earlier for micelles was modified in order to incorporate the interaction with the polymer. This interaction was described by two parameters. One of them was the micelle–core area shielded by the polymer and the other one was an interaction parameter due to the hydrophobic contribution of the polymer segments interacting with the core. The shielding of the micelle core has two opposite effects on the micelle formation. On the one hand, it reduces the contact area between the hydrophobic micelle core and water; on the other hand, it increases the polar head group interactions. Since the shielding parameter is some kind of mean value, “at present no *a priori* method for the estimation of this area is available”

[5]. The aggregation number of the most probable micelle was calculated from the modified free-energy expression in which the core area per surfactant was a function of the aggregation number, but the polymer shielded area per surfactant was constant.

Ruckenstein and Huber [6] worked out a different model by trying to eliminate the shielding parameter and the problems associated with it. They introduced a global interaction parameter, $\Delta\sigma$, due to the change of the microenvironment of the micelle in the presence of the polymer. $\Delta\sigma$ was represented by the change of the micelle surface tension and was claimed to be an experimentally determinable parameter from hydrocarbon–polymer solution surface tension measurements. The use of macroscopic parameters such as the surface tension to describe local molecular interactions between the micelle core and its environment has been criticised recently [7]. Furthermore, the surface tension depends on the polymer concentration; therefore, it is not determined unambiguously at which composition the surface tension should be measured.

In this work a new interaction model is introduced to eliminate the mean interaction parameters and to analyse the possibility of complex formation between nonionic polymers and surfactants.

Interaction model

The model calculations utilise a recently developed small systems thermodynamic model for polymer–surfactant complex formation [9]. In the framework of this model the polymer–surfactant macroscopic system is considered as a three-component (water, polymer and surfactant) macroscopic ensemble in which the surfactant can be present in monomer, polymer–surfactant complex and free micelle forms. The polymer–surfactant complex molecules and the micelles are considered as small systems that contain a fluctuating number of building blocks (surfactant molecules in the case of micelles and surfactant aggregate subsystems in the case of the complex molecules). The description of the microstructure of the polymer–surfactant small system is based on Shirahama's necklace model. The subsystem of the polymer–surfactant complex molecules is an individual surfactant aggregate wrapped around by the polymer segments in which both the number of surfactant molecules and the number of polymer segments can fluctuate.

In order to estimate the free energy of the polymer–surfactant subsystem formation a micelle formation model is generalised which successfully predicted the critical micelle formation concentrations and aggregation numbers for surfactant homologous series. The free energy of a resting spherical micelle containing m nonionic surfactant molecules can be given as [10]

$$G_{\text{mic}}^0 = m\mu_{0,\text{ch}} + \sigma_0(A - mA_1) - mkT \ln(p\Gamma_0/\Gamma - 1), \quad (1)$$

where the first term in the right-hand side is the hydrophobic driving force of micellization and $\mu_{0,\text{ch}}$ is the standard state chemical potential of the surfactant alkyl chain in the micelle core. The second term is a correction of the driving force for the contact between the micelle core and water, in which σ_0 is the oil–water surface tension, A is the surface area of the core and A_1 is the cross-sectional area of a methylene group. The last term in Eq. (1) is due to the polar head group interactions on the micelle surface. p is a correction for curvature, $\Gamma = m/A$ and Γ_0 is the limiting value for macroscopic adsorption. The parameters of Eq. (1) can be determined from independent measurements, which means that the model calculations can be performed without parameter-fitting.

In this paper Eq. (1) is modified in order to take into account the interaction between a surfactant aggregate and the polymer segments. The polymer is considered as an ideally flexible coil which covers the surface of a surfactant aggregate with s_2 polymer segments, thus reducing the surface area available for the surfactant polar head groups (s_2A_{seg}). A fraction of the methylene groups of the s_2 of segments (s_1) are immersed into the

core of the micellelike aggregate giving a hydrophobic contribution to the free energy of the subsystem formation ($s_1\Delta\mu_{0,\text{seg}}$). Finally, there is a polymer- and surfactant-specific contribution from the polar interactions and the local conformational change of the s_2 segments in the palisade layer (ΔG_{pol}).

By replacing m with n in Eq. (1) the free energy of the polymer–surfactant subsystem is approximated as

$$G_{\text{sub,ns}}^0 = n\mu_{0,\text{ch}} + s_1\Delta\mu_{0,\text{seg}} + \sigma_0[A - (n + s_1)A_1] - nkT \ln(p\Gamma_0/\Gamma^* - 1) + \Delta G_{\text{pol}}, \quad (2)$$

where $\Gamma^* = n/(A - s_2A_{\text{seg}})$ and $s_2 \geq s_1$.

Equation (2) is similar to the expression introduced by Nagarajan [3] but it contains the number of actually interacting polymer segments instead of a mean value. The distribution of the molecular species is calculated by means of the mentioned small systems thermodynamic model [10]. The probability that the complex contains n surfactants and s polymer segments (P_{ns}) can be expressed as

$$P_{\text{ns}} = \exp[(n\mu^s - G_{\text{sub,ns}}^0)/kT] / \sum_s \sum_n \exp[(n\mu^s - G_{\text{sub,ns}}^0)/kT], \quad (3)$$

where μ^s denotes the chemical potential of the surfactant in the solution. Using this distribution function the mean values of n , s and $G_{\text{sub,ns}}^0$ can be given as

$$\bar{n} = \sum_s \sum_n P_{\text{ns}} n, \quad (4)$$

$$\bar{s} = \sum_s \sum_n P_{\text{ns}} s \quad (5)$$

and

$$\bar{G}_{\text{sub}}^0 = \sum_s \sum_n P_{\text{ns}} G_{\text{sub,ns}}^0 + kT \sum_s \sum_n P_{\text{ns}} \ln P_{\text{ns}}. \quad (6)$$

The probability that the complex contains a subsystems is

$$P_a = x_a / \sum_a x_a, \quad (7)$$

where x_a is the mole fraction of the polymer molecules containing a surfactant aggregates.

Results and discussion

Model calculations were performed for dodecyl polyoxyethylene with 30 ethylene oxide groups using the same parameters as in Ref. [9]. The parameters of the polymer were $s_1 = s_2 = s$, $\Delta\mu_{0,\text{seg}} = -2.5 kT$, $A_{\text{seg}} = 3A_1$ and $\Delta G_{\text{pol}} = 0$, which may be characteristic for vinyl or ethylene oxide type polymers.

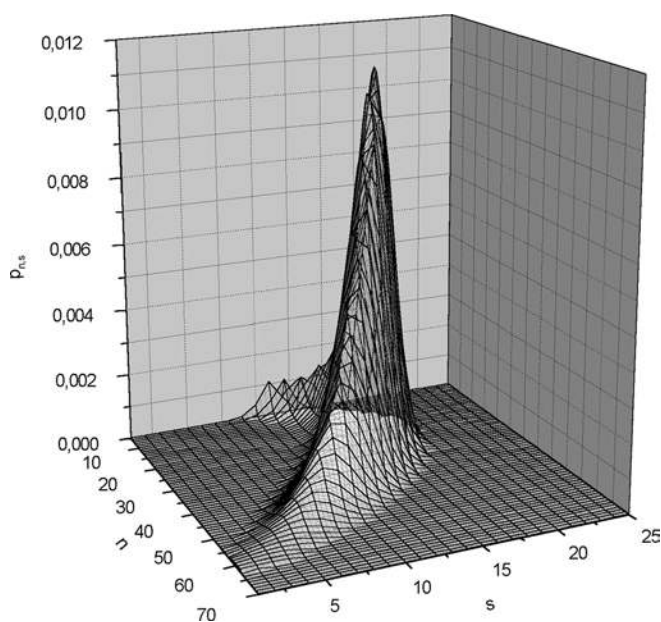


Fig. 1 Distribution function of the surfactant aggregates at $c_e = 0.45$ mM

The distribution function of the surfactant aggregates is plotted in Fig. 1 as a function of the surfactant aggregation number and the number of polymer segments involved in the subsystem at a given equilibrium surfactant concentration ($c_e = 0.45$ mM). With increasing s the probability of the formation of the complex increases and reaches a maximum which is followed by a strong decrease at higher segment numbers. The mean subsystem contains $\bar{n} = 31$ surfactant molecules and $\bar{s} = 13.5$ segments. This means that the mean aggregation number of the surfactant aggregates in the polymer complex is significantly smaller than that of the free micelles ($\bar{m} = 61.7$). The mean composition of the aggregates changes with the equilibrium surfactant (monomer) concentration. \bar{n} increases to 46 ($c_e = 0.53$ mM), while \bar{s} decreases slowly to 9. These changes indicate that there is competition between the surfactants and polymer segments to take part in the subsystem formation.

The distribution of the surfactant aggregates among the complex molecules is plotted at different c_e values in Fig. 2. The distribution is relatively narrow and as expected the mean number of aggregates in a polymer molecule increases with the equilibrium monomer concentration.

The concentration of the surfactant in micellar and in complex form (in monomer units) is plotted against the equilibrium surfactant concentration in Fig. 3. The critical micelle formation concentration is around 0.42 mM. When the total surfactant concentration reaches this value the excess surfactants form micelles at almost constant equilibrium monomer concentration. c_e cannot increase to 0.47–0.48 mM where

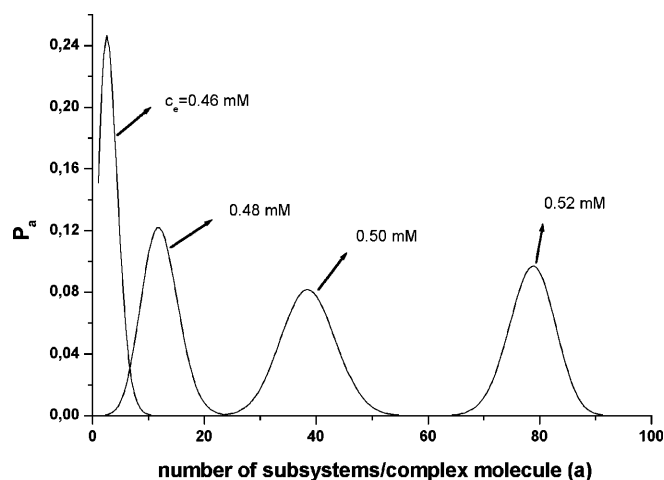


Fig. 2 Distribution functions of the complex molecules with respect to the number of subsystems at different equilibrium surfactant concentrations

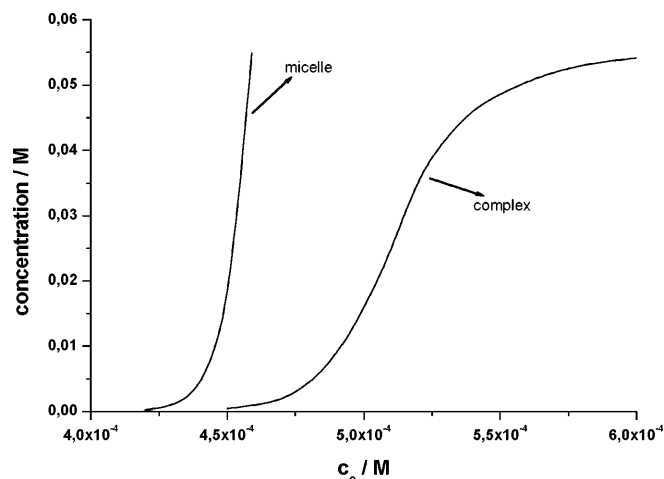


Fig. 3 Concentration of the surfactant in micellar and polymer-complex form against the monomer concentration

polymer-surfactant complex formation could occur to such a large extent that it could be experimentally indicated. Although there is a significant driving force for complex formation the interaction cannot be realised because of the free-micelle formation. From experimental research on a number of neutral polymer and nonionic surfactant systems with a variety of different methods the general conclusion can be drawn that there is very weak, if any, interaction between the electrically uncharged components [8].

The standard free-energy change of the subsystem formation per monomer is plotted in Fig. 4 against the aggregation number. Though, the standard free-energy change is a function of s we used the curves calculated at the mean segment number in order to demonstrate the

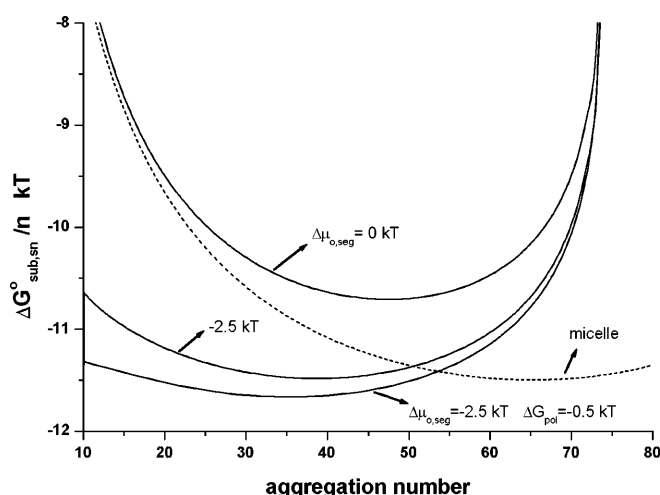


Fig. 4 The standard free-energy change of the subsystem formation per surfactant monomer against the aggregation number ($s = 13.5$)

major trends. The corresponding curve for micelles serves as a reference.

If we assume that there is no hydrophobic interaction between the polymer segment and the core of the surfactant aggregate ($\Delta\mu_{0,seg} = 0$), then the shielding of the aggregate core by the polymer would be the only contribution to the driving force of complex formation. Owing to this effect the minimum of the free-energy function shifts towards smaller aggregation numbers. The extent of this shift is mainly determined by the shielding parameter A_{seg} . On the other hand, the standard free-energy curve of the subsystem runs above that of the micelle. This means that the overall effect of the shielding does not help, but opposes, the complex formation, indicating that the increase of the unfavourable interaction of the polar surfactant head groups overcompensates the favourable effect of the reduction of the contact area between the hydrophobic micelle core and water.

If we assume that the two methylene groups of the monomer are completely immersed into the hydrophobic core of the surfactant aggregate, then the hydrophobic interaction of the segments is the highest possible value ($\Delta\mu_{0,seg} = -2.5 kT$). Using this limiting value for the hydrophobic interaction of the polymer, the minimum of the free-energy function shifts towards even smaller aggregation numbers and $\Delta G^0_{sub,sn}/n \cong \Delta G^0_{mic,m}/m$ at the corresponding minima. The amount of complex is still negligible below the critical micelle concentration as was shown previously for this case. The shielding effect and the hydrophobic contribution of a vinyl or ethylene oxide polymer are not enough for the manifestation of

observable polymer–surfactant complex formation. Complex formation can be expected only if the driving force of the complex formation is further increased. This can be achieved either by increasing the number of methylene groups contained by the polymer segments (e.g. polypropylene [11]), or by introducing a specific attractive interaction between the segments and surfactant head groups. This case is also shown in Fig. 4 with $\Delta G_{pol} = -0.5 kT$. However, except for some specific polymer–surfactant pairs ΔG_{pol} is likely to be a positive contribution to $\Delta G^0_{sub,sn}$ and since $\Delta\mu_{0,seg}$ is overestimated in the model calculations, complex formation between nonionic vinyl polymers and between nonionic surfactants is not predicted. The extension of the model for ionic surfactant–nonionic polymer interaction is in progress.

Conclusions

The general conclusions drawn from the model calculations are summarised as follows.

- There is competition between the segments and surfactants to take part in the aggregate formation.
- The aggregation number of the surfactant in the polymer complex is smaller than that of the micelles.
- The larger the size of the interacting polymer segments the smaller the aggregate is.
- Stronger interaction between the segments and the surfactants also leads to smaller aggregation numbers.
- Despite the fact that the hydrophobic interaction of the polymer segments with the micelle core and the shielding of the core surface from water contact gives rise to significant driving force for polymer–surfactant interaction, complex formation cannot be detected. The reason of this is that the standard free-energy change of complex formation per surfactant is not sufficient in itself to predict the polymer–surfactant complex formation because it is the difference between the driving force of the micelle and the complex formation that determines whether the complex forms in a detectable amount below the critical micelle formation concentration.
- Polymer–surfactant complex formation of nonionic components could be expected if there were specific polar interactions between the surfactants and polymer segments or if the polymer segment had at least three methylene groups per polar group.

Acknowledgement This work was supported by the Hungarian Research Fund (no. T 029780).

References

1. Shirahama K, Tsujii K, Takagi T (1974) *J Biochem* 75:309
2. Cabane B (1977) *J Phys Chem* 81:1639
3. Nagarajan R (1985) *Colloids Surf* 13:1
4. Nagarajan R (1986) *Adv Colloid Interface Sci* 26:205
5. Nagarajan R (1989) *J Chem Phys* 90:1980
6. Ruckenstein E, Huber G, Hoffmann H (1987) *Langmuir* 3:382
7. Wennerström H (1996) *Curr Opin Colloid Interface Sci* 1:370
8. Breuer MM, Robb ID (1970) *Chem Ind* 13:530
9. Gilányi T (1999) *J Phys Chem B* 103:2085
10. Gilányi T (1995) *Colloids Surf* 104:111
11. Brackman JC, van Os NM, Engberts JB (1988) *Langmuir* 4:1266

Tatiana Kharitonova
Alexander Rudnev
Nina Ivanova

Capillary zone electrophoresis for surfactant analysis in aqueous media

Abstract Surfactant mixtures are commonly used in many industrial applications. At the same time, the methods for surfactant analysis are rather laborious and often do not permit the determination of the individual surfactant content in mixed solutions. In the present work capillary zone electrophoresis (CZE) instrumentation was applied for the quantitative analysis of a cationic surfactant (dodecylpyridinium bromide) and a nonionic surfactant (Triton X-100) in aqueous solutions. The linear dependence of the analytical signal (electrophoregram peak area) versus the surfactant concentration was established for both surfactants over a wide concentration range. The analytical signal of an individual surfactant was

found to be independent of the addition of the second surface-active component, making it possible to determine the content of surfactants from both solutions of individual surfactants and mixed solutions. The CZE method was shown to be appropriate for the determination of critical micelle concentrations as the intersection point of two straight lines describing the dependence of analytical signal versus surfactant concentration below and above the critical micelle concentration.

Keywords Capillary electrophoresis · Surfactant analysis · Dodecylpyridinium bromide · Triton X-100 · Critical micelle concentration

T. Kharitonova (✉) · N. Ivanova
Department of Chemistry,
Lomonosov MSU,
Leninskiye Gory, 119899 Moscow, Russia
e-mail: rty@colloid.chem.msu.ru
Tel.: +7-95-9395385
Fax: +7-95-9328846

A. Rudnev
V.I. Vernadsky Institute,
ul. Kosygina 19, 117975 Moscow,
Russia

Introduction

Systems containing two or more surfactants of different types have been investigated intensively for the last few decades [1, 2, 3]. The interest in surfactant mixtures is due to several reasons; the most important is the fact that the properties of the mixtures often drastically differ from those of the individual surfactants of which the mixture consists. Nonideal behavior of surfactant mixtures is the cause of their wide use for many industrial and technological purposes, such as detergency, pharmacy, oil recovery, and waste treatment. In this connection, it has become an important problem to elaborate the convenient methods for surfactant analysis.

Nowadays, numerous methods for the quantitative analysis of systems containing surfactants have been developed: two-phase titration, UV–vis spectroscopy, gravimetry, to name only a few [4]. However, most of them are rather prolonged and laborious; moreover, these methods often do not permit the determination of the individual surfactant content in mixed-surfactant solutions.

In the present work, we propose a technique for the quantitative analysis of the individual surfactants and their mixtures using capillary zone electrophoresis (CZE) instrumentation. CZE is based on the ordered motion of analytes in different media under an applied electric field and is known to be a high-performance and selective method for the analysis of both ionic species and neutral

solutes owing to the possibility of regulation of the migration parameters of the systems under investigation [5].

Experimental

Dodecylpyridinium bromide (DDPB) and Triton X-100 (TX) were used as cationic and nonionic surfactants, correspondingly. DDPB ($M_r = 328.3$), pure grade (Chemapol, Czech Republic), was purified by recrystallization from ethyl acetate according to the method in Ref. [6]. The degree of purity was determined by the absence of the minimum on the surface tension isotherm of the solutions. TX (the average number of ethylene oxide groups is 9.5, $M_r = 646$), pure for analysis (Ferak, Germany), was used as received.

Potassium dihydrophosphate (UZCR, Russia), sodium hydrophosphate (UZCR), potassium bitartrate (RIAP, Ukraine) and ammonium chloride (REAKHIM, Russia) and ammonia (REAKHIM) standards used for preparing the buffer solutions were of analytical grade. Doubly distilled water (conductivity $2 \times 10^{-6} \Omega^{-1} \text{cm}^{-1}$, surface tension 72 mJ m^{-2} , 25°C) was used to prepare all the solutions.

Capillary electrophoresis was carried out with a Capel 105 system (LUMEX, Russia) equipped with a UV monochromator (190–380 nm). A polyimide-coated fused silica capillary with an inner diameter of $75 \mu\text{m}$, an outer diameter of $375 \mu\text{m}$ and a total length of 61.5 cm (52 cm to the detector) was used. Data control was performed with personal computer software for Windows 95. The voltage used in all experiments was 20 kV (cathodic detection side). Between runs, the capillary was rinsed at high pressure for 3 min with 0.5 M NaOH and then with distilled water and flushed with the carrier buffer.

Determination of the surfactant critical micelle concentrations (cmcs) was carried out by means of surface tension, conductivity and Teflon wetting angle. The surface tension of the solutions was measured by the Wilhelmy plate method using a BT-5 tensiometer (TECHNIPROT, Poland). A platinum plate was treated with hot potassium dichromate solution and boiled for 30 min in distilled water to provide complete wetting.

An L-Micro conductometer (SNARK, Russia) was used to measure the specific conductivity of the solutions.

Contact angle measurements were performed with a horizontal microscope. Teflon plates used for the wetting measurements were boiled in dilute potassium dichromate for 20 min and in distilled water for 30 min , and then desiccated over calcium chloride. The contact angle of water on the purified Teflon plates was $115\text{--}120^\circ$.

The temperature of the experiments was maintained at 25°C .

Results and discussion

According to the UV spectra of the surfactants (Fig. 1), we chose $\lambda = 258 \text{ nm}$ and 223 nm for the registration of DDPB and TX signals, correspondingly.

Migration of the zones of the analytes toward the detector is the requisite condition for the CZE separation. The important characteristics are the observed migration time, t_m (the time interval between the beginning of the separation and the passage of an analyte zone through the detection point), the observed velocity of migration, v_{obs} (Eq. 1), and observed electrophoretic mobility, μ_{obs} (Eq. 2):

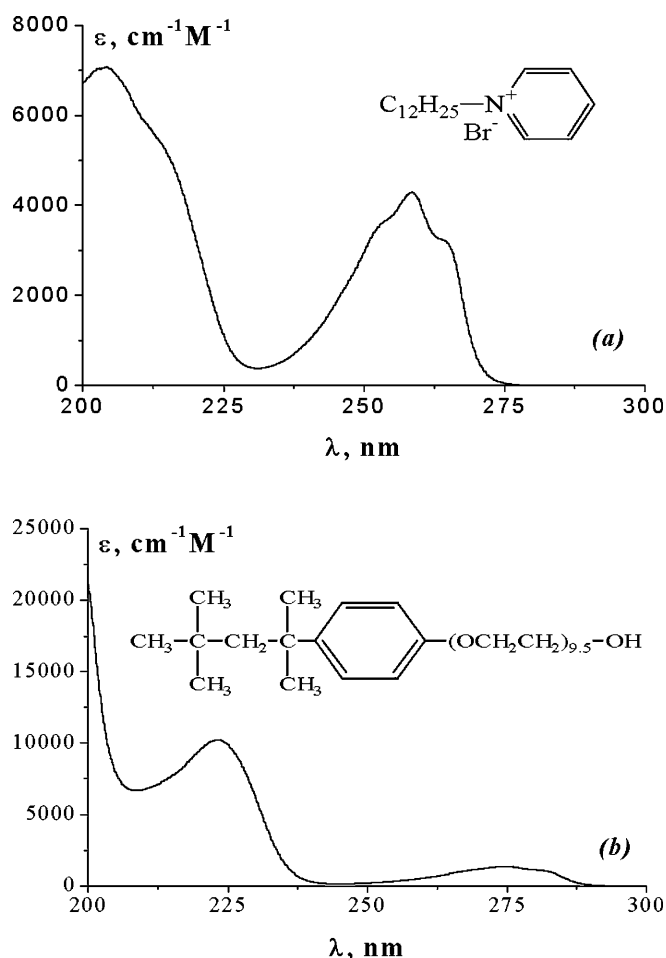


Fig. 1 UV spectra of **a** dodecylpyridinium bromide and **b** Triton X-100 in aqueous solution

$$v_{\text{obs}} = \frac{L_{\text{ef}}}{t_m} (\text{cm s}^{-1}), \quad (1)$$

$$\mu_{\text{obs}} = \frac{v_{\text{obs}}}{E} = \frac{L_{\text{ef}} L_t}{U t_m} (\text{cm}^2 \text{V}^{-1} \text{s}^{-1}). \quad (2)$$

Here E is the applied field strength, L_{ef} is the length to the detector, L_t is the total length of the capillary, and U is the applied voltage. Neglecting the interactions of the analyte with the capillary wall and (or) with other components of the solution, the observed mobility can be considered as the sum of two contributions (Eq. 3) – the mobility contribution of the electroosmotic flow (EOF), μ_{EOF} , and the inherent ionic mobility of ionic analyte, μ_{ion} :

$$\mu_{\text{obs}} = \mu_{\text{EOF}} + \mu_{\text{ion}} \quad (3)$$

For the case of the system under investigation, the migration of DDPB under the applied electric field is due to both its charge and the EOF, while the migration of TX is caused by the EOF only. Since the goal of the

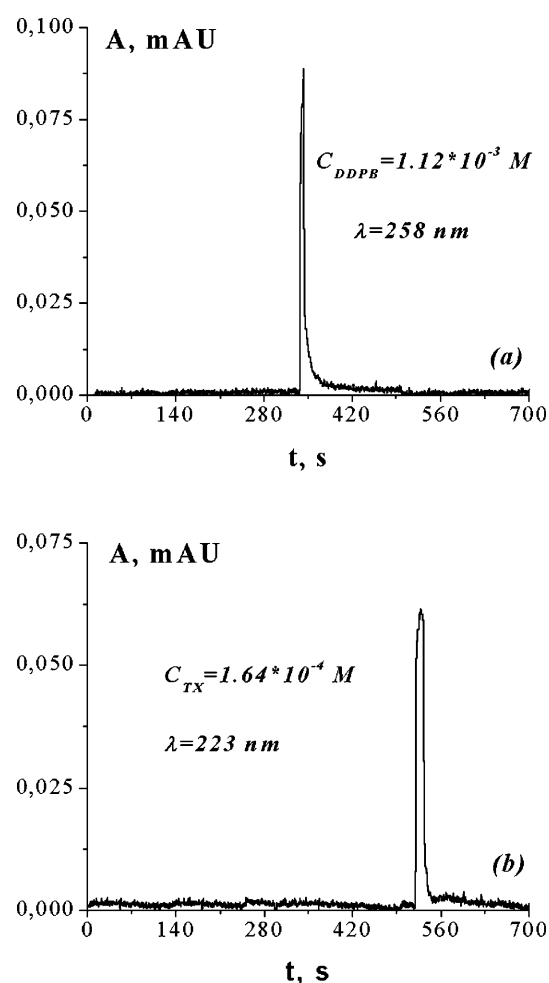
Table 1 Dependence of the observed electrophoretic mobilities of dodecylpyridinium bromide and Triton X-100 on the carrier electrolyte solution pH and ionic strength

pH	<i>I</i> (M)	$\mu_{\text{obs}} \times 10^4 (\text{cm}^2 \text{V}^{-1} \text{s}^{-1})$	
		Triton X-100	Dodecylpyridinium bromide
9.02	0.020	4.07	5.84
	0.002	4.48	6.42
6.86	0.050	2.98	4.67
	0.005	3.77	5.51
3.65	0.020	1.07	3.22

research was to determine the surfactant content not only from a solution of the individual surfactant but also from mixed solutions, it became an important problem to choose suitable conditions for the experiment. The variation of the EOF as the result of surface charge modification is known to be an effective and simple way of regulating movement rate of the analyte [7]. To find the optimal conditions for the surfactant analysis, we investigated the influence of pH and the concentration of the carrier electrolyte solution on the observed mobilities of the surfactants. For these purposes buffer solutions of pH 9.02 ($\text{NH}_3/\text{NH}_4\text{Cl}$), 6.86 ($\text{KH}_2\text{PO}_4/\text{Na}_2\text{HPO}_4$) and 3.65 ($\text{KC}_4\text{H}_5\text{O}_6$) and of different ionic strengths, *I*, were prepared. The results are given in Table 1.

As pH 3.65 is close to the zero point of charge of silica [8], the corresponding EOF becomes small, giving rise to the significant increase in the observed migration times. The buffer solutions of pH 6.86 and 9.02 were found to be more convenient for the analysis since sufficient EOF was observed. However, in spite of the fact that the decrease of the carrier electrolyte solution concentration resulted in the rise of the EOF, the solutions of low concentrations could not be used for the analysis as significant peak broadening and asymmetry were observed for the cationic surfactant. At the same time, in the concentrated buffer solutions the observed migration times corresponding to DDPB and TX became closer and sufficient resolution of the analytical signals was not achieved. Therefore, an ionic strength of 0.02–0.05 M was established to be the optimal condition. It should be pointed out that in the case of the surfactant analysis the effects of surfactant adsorption at the capillary walls should be diminished. Concerning the system of cationic and nonionic surfactants, the change of pH leads to contrary effects with respect to the surfactant adsorption at the silica–solution interface: the increase of the pH values gives rise to an increase of cationic and a decrease of nonionic surfactant adsorption [9]. Thus, the neutral pH values are more preferable for the analysis.

Typical electrophoregrams of the individual surfactants registered at pH 6.86, *I* = 0.05 M are presented in Fig. 2. Corresponding dependencies of the analytical

**Fig. 2** Typical electrophoregrams for **a** dodecylpyridinium bromide and **b** Triton X-100 solutions. Carrier electrolyte $\text{KH}_2\text{PO}_4/\text{Na}_2\text{HPO}_4$, pH 6.86, *I* = 0.05 M

signal (peak area, *S*) versus molar concentration, *C*, for DDPB and TX are given in Fig. 3.

The limit of detection was found to be $4.20 \times 10^{-5} \text{ M}$ for DDPB and $3.50 \times 10^{-6} \text{ M}$ for TX. At fixed concentration ($1.26 \times 10^{-2} \text{ M}$ for DDPB and $2.45 \times 10^{-4} \text{ M}$ for TX) the slope of the linear dependence is changed. Thus, the linear range of the detection of DDPB and TX is $4.20 \times 10^{-5} - 1.00 \times 10^{-2} \text{ M}$ and $3.50 \times 10^{-6} - 2.00 \times 10^{-4} \text{ M}$, correspondingly. The correlation coefficients of the equation $S = aC + b$ determined by the regression analysis for two lines of different slopes were found to be $r = 0.9993 - 0.9998$ for both DDPB and TX, showing a good linear fit within the wide concentration range. Repeatability and reproducibility of the method as well as its accuracy were characterized according to Ref. [10] and were found to be high (relative standard deviations for both surfactants did not exceed 0.03 for repeatability and reproducibility, and 0.05 for accuracy, as the result of six experiments).

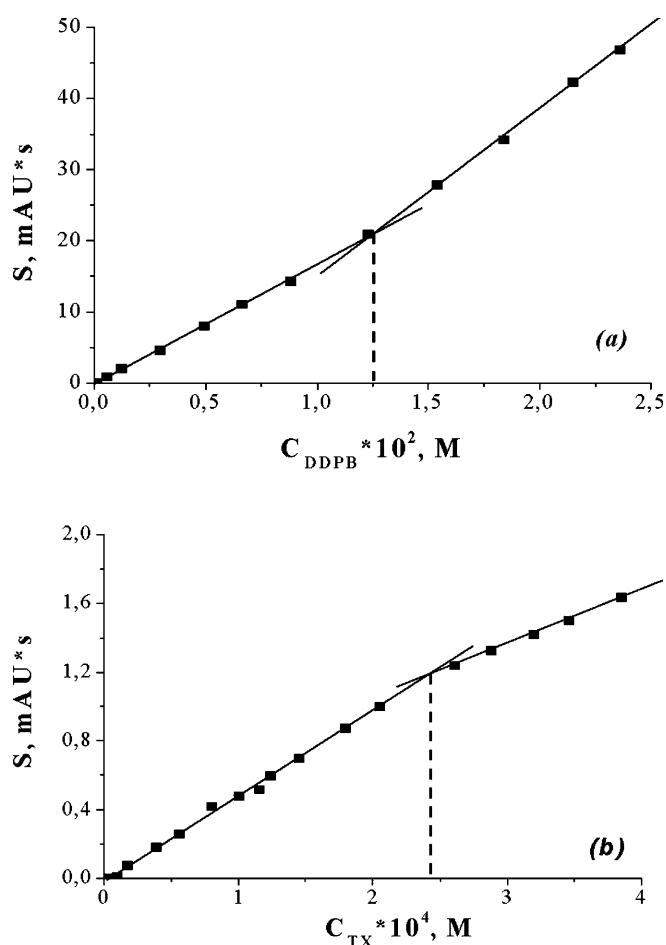


Fig. 3 Dependence of analytical signal (peak area) versus **a** dodecylpyridinium bromide and **b** Triton X-100 concentration. Carrier electrolyte $\text{KH}_2\text{PO}_4/\text{Na}_2\text{HPO}_4$, pH 6.86, $I = 0.05$ M

It is well known that surfactant molecules (ions) can aggregate to form micelles on reaching a fixed concentration (cmc) in the solution [11]. The formation of such aggregates leads to the abrupt changes of physicochemical properties of the surfactant solution. Numerous methods based on the difference between the properties of monomer and micellar solutions can be employed for the estimation of cmc values [12]. We used conductivity and surface tension methods to determine the cmc of DDPB and Teflon wetting and surface tension methods for TX. The results of the cmc estimation are listed in Table 2.

From the data it follows that the values obtained correspond to the intersection point of two straight lines

describing the dependence of peak area versus surfactant concentration, thus making it possible to use the CZE method for the cmc determination. It should be noticed that the CZE technique has already been reported to be useful for the estimation of the cmc values [13]; however, the procedure described was based on electric current measurements and, therefore, it could not be applied for nonionic surfactants. Moreover, the technique employed did not allow quantitative analytical investigations of the surfactant solutions to be carried out.

As already mentioned, it became an important problem to determine the surfactant content not only from the solution of the individual surfactant, but also from the mixed solutions. In this connection, we investigated the influence of the presence of the second component on the analytical signal of the surfactants. For this purpose solutions of DDPB containing a constant amount of TX, and vice versa, were prepared. We showed that the addition of TX ($C = 1.00 \times 10^{-5}$ M, 1.00×10^{-4} M) to the DDPB solutions in the concentration range $5 \times 10^{-5} - 5 \times 10^{-3}$ M as well as the addition of DDPB ($C = 1.00 \times 10^{-4}$ M, 1.00×10^{-3} M) to the $4 \times 10^{-6} - 1 \times 10^{-4}$ M TX solutions did not affect (within the experimental error) the analytical signal of both surfactants.

Conclusions

Solutions of cationic (DDPB) and nonionic (TX) surfactants absorbing in the UV region were analyzed using the CZE method. The influence of pH and ionic strength on the analytical signal of the surfactant solutions was investigated. The optimal conditions of the experiment were found to be pH 6–7 and $I = 0.02-0.05$ M. The CZE method proved to be simple and reliable for the quantitative determination of cationic and nonionic surfactants, showing a linear dependence of the analytical signal versus surfactant concentration over a wide concentration range. The method employed has a number of essential advantages; namely, no pretreatment of the analytical sample is required, a small amount of sample is needed for analysis, the accuracy of the method is high, the method can be used for the analysis of both solutions of individual surfactants and mixed systems of surfactants. Besides analytical applications, the CZE method was shown to be useful for the determination of the surfactant cmc.

Table 2 Critical micelle concentration (cmc) determined by capillary zone electrophoresis (CZE) and compared with those established by other methods (25 °C)

Dodecylpyridinium bromide			
Method	CZE		
cmc (M)	1.26×10^{-2}	Surface tension	1.19×10^{-2}
Triton X-100			
Method	CZE		
cmc (M)	2.45×10^{-4}	Surface tension	2.21×10^{-4}
		Teflon wetting	2.40×10^{-4}

References

1. Rosen MJ (1986) In: Scamehorn JF (ed) Phenomena in mixed surfactant systems. ACS symposium series 311. American Chemical Society, Washington, DC, pp 144–162
2. Aratono M, Villeneuve M, Takiue T, Ikeda N, Iyota H (1998) *J Colloid Interface Sci* 200:161
3. Puvvada S, Blankschtein D (1992) *J Phys Chem* 96:5567
4. Abramzon AA, Zaychenko LP, Faingold SI (1988) *Surfactants*. Khimiya, St. Petersburg
5. Timerbaev AR (2001) *Analyst* 126:964
6. Abdulin AG, Kochurova NN, Rusanov AI (1997) *Kolloidn Zh* 59:725
7. Jandik P, Bonn G (1993) *Capillary electrophoresis of small molecules and ions*. VCH, New York
8. Denoyel R, Rouquerol J (1991) *J Colloid Interface Sci* 143:555
9. Parfitt GD, Rochester CH (1986) *Adsorption from solution at the solid/liquid interface*. Academic, London
10. Panossian A, Mamikonyan G, Torosyan M, Gabrielyan E, Mkhitarian S (2001) *Anal Chem* 73:4379
11. Mukejee P, Mysels KJ (1970) *Critical micelle concentration of aqueous surfactant systems*. National Bureau of Standards, Washington, DC
12. Rusanov AI (1992) *Micellization in surfactant solutions*. Khimiya, St. Petersburg
13. Cifuentes A, Bernal JL, Diez-Masa JC (1997) *Anal Chem* 69:4271

G. Marosi
A. Márton
I. Csontos
S. Matkó
A. Szép
P. Anna
G. Bertalan
É. Kiss

Reactive surfactants – new type of additive for multicomponent polymer systems

G. Marosi (✉) · A. Márton · I. Csontos
S. Matkó · A. Szép · P. Anna · G. Bertalan
Organic Chemical Technology Department,
Budapest University of Technology and
Economics, Muegyetem rkp. 3,
1111 Budapest, Hungary
e-mail: marosi.oct@chem.bme.hu
Tel.: +36-1-4633654
Fax: +36-1-4631150

É. Kiss
Colloid Chemistry Department,
Roland Eötvös University,
Budapest, Hungary

Abstract A new type of interfacial additive has been developed by the authors recently. The molecules of amphiphilic character are capable of forming chemical bonds at both the polar and the apolar sides. These reactive surfactants have been synthesised in a specially designed computer-controlled reactor system. The aim of the development was to combine the advantages of nonreactive surfactants and reactive coupling agents, making possible an

in-line reactive interface modification during the compounding process of the polymer system. The characteristics and effects of the synthesised compounds were determined using methods of analytical and colloid chemistry, like Raman microscopy, surface tension, contact angle and rheological measurements.

Keywords Interface · Composite · Aluminium trihydrate · Polyamide-polyolefin blend

Introduction

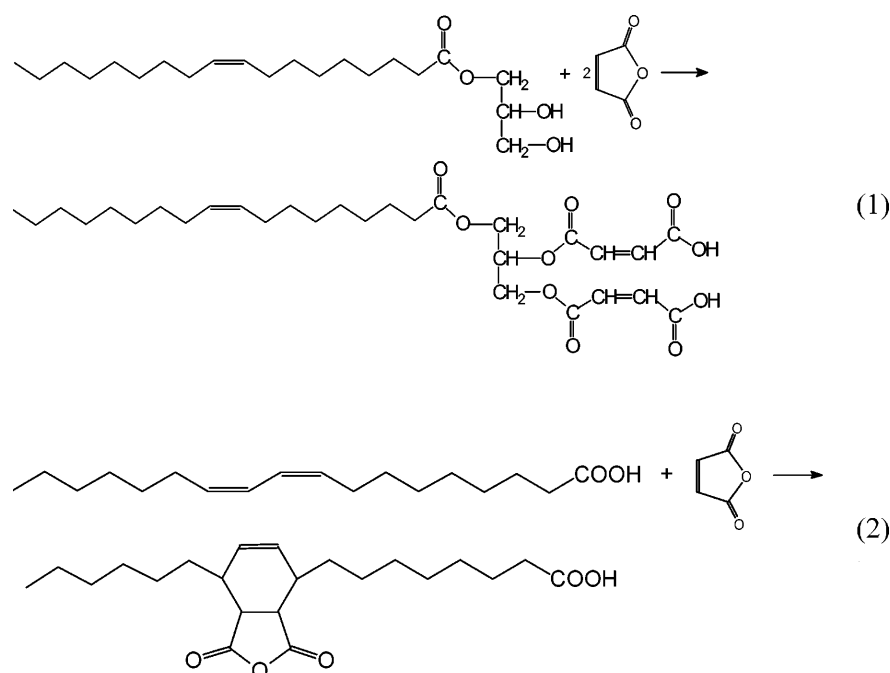
The interfaces formed spontaneously in multicomponent polymer systems need improvement for most applications. On the high-energy surfaces of untreated inorganic additives of polymer systems (fillers or reinforcements) thin layers of adsorbed water and organic molecules are always present (in a common environment), which affect the performance (homogeneity, adhesion etc.) unfavourably. Nonreactive and reactive interface modifications are applied for achieving better interfacial interaction.

The advantageous use of surfactants is well known in multicomponent polymer systems. These additives promote a homogeneous distribution, improve the rheology and wetting, of components and easily reach the interfaces in the polymer disperse systems [1, 2]. On the other hand, surfactants do not give satisfactory results in composites, where considerable improvement of adhesion at the phase boundaries is required. For improving the adhesion coupling, agents can be used instead of surfactants but at the expense of the advantages mentioned because commercial types of these reactive molecules have no amphiphilic character [1]. Layers of

coupling agents on the surface of additive particles are generally formed in complicated solution processes.

A new type of molecule, called reactive surfactants (RS), has been developed for combining the advantages of both additive types [3]. The amphiphilic structure and reactive groups on both sides of the molecule are characteristic for RS. After taking part in the homogenisation process (like traditional surfactants) one side of the RS reacts with the disperse phase and the other reacts with the matrix polymer. The benefits of this behaviour have been utilised in various composites [4]. These molecules are required to form self-assembled layers at interfaces and adsorb preferably on the surface of additive particles. The dispersion of the additive particles in the polymer matrix should be improved owing to this modification. The viscosity of the polymer matrix should be decreased by RS for promoting the wetting process at the interface and thus allowing the polymer melt to penetrate into the pores and other irregularities on the surface of additive particles. The adhesion of the neighbouring phases of polymer systems has been reported to be increased with RS much more considerably than with nonreactive surfactants [3].

Fig. 1 Synthetic routes for forming reactive surfactants (RS): RS1 esterification (1) and RS2 Diels–Alder reaction (2)



In this work the behaviour and the effect of some RS have been studied in various types of multicomponent polymer systems.

Experimental

Materials

The RS molecules applied in this work are shown in Fig. 1.

The synthetic routes of Diels–Alder reaction and esterification were used for producing RS molecules having two reactive sites [5]. The severe control required for the reactions was ensured using a computer-controlled reactor system developed in our laboratory [6]. The preparation of the additives was started with feeding of conjugated unsaturated fatty acid and maleic anhydride into the reactor. The computer raised the temperature, according to the recipe, to 50–120 °C. The products were characterised by Fourier transform IR spectroscopy, differential scanning calorimetry (DSC) and thermogravimetric analysis. The matrix polymer of the various compounds was high-density polyethylene (PE): Stavrolen 276773, density 0.960 g cm⁻³ (Stavropolymer, Russia). Polyamide (PA) used as polymer additive was Danamid FE, a product of Zoltec Magyar Viscosa (Hungary). The anionic surfactant was Disponil AES 63, [alkyl poly(ethylene glycol) ether sulfate] (Henkel), the cationic surfactant was *N*-hexadecyl pyridinium bromide (Caola, Hungary) and the nonionic surfactant was Tegin 4100 palmitic/stearic acid glycerol ester (Th. Goldschmidt, Germany). Al(OH)₃ (ATH), Alolt 60FLS precipitated type, Brunauer–Emmett–Teller area 6 m² g⁻¹, from Ajka Alumina Co. (Hungary) was used.

The work of adhesion was calculated using the equations proposed by Owens and Wendt [7],

$$W_a = 2\sqrt{\gamma_1^d \gamma_2^d} - 2\sqrt{\gamma_1^p \gamma_2^p},$$

and Wu [8],

$$W_a = -\frac{4\gamma_1^d \gamma_2^d}{\gamma_1^d + \gamma_2^d} - \frac{4\gamma_1^p \gamma_2^p}{\gamma_1^p + \gamma_2^p},$$

where W_a is the work of adhesion, and d and p are the dispersive and polar terms of the surface free energy of components 1 and 2. For the purpose of the calculation, the surface free energies of the separate surfaces were determined using methylene iodide and water.

Direct adhesion measurements were performed between a PE film (thickness 20 μm) and a CaCO₃ sheet (a polished section of a piece of calcite from OMYA, France). The films/sheets were treated with the interface modifiers, compressed and then the force of peeling was measured.

The polymer compounds were prepared by homogenisation of the components in the mixing chamber (350) of a Brabender Plastimeter PL2000 with a rotor speed of 50 rpm, at 200 °C. Sheets (100 × 100 × 3 mm) were formed using laboratory compression moulding equipment.

Scanning electron microscopic images of the fractured surface of samples (broken in liquid nitrogen) were taken using a JEOL JSM-35 instrument.

For micro-Raman spectroscopic measurements a Labram Raman microscope system, produced by Jobin Yvon Horiba, was used at 632.81-nm excitation of a HeNe laser.

Results and discussion

RS molecules are designed to accumulate at the interfaces forming a self-assembling layer there and to react with the neighbouring phases. Therefore these characteristics were analysed when the performance of the synthesised RS molecules were evaluated. The applicability of these new additives was tested in various types of polymer composites. The characterisation of the new systems was performed using methods of analytical and colloid chemistry.

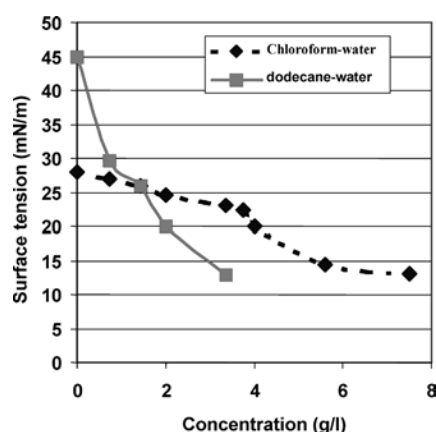


Fig. 2 The surface tension of liquids dissolving poorly in each other against the concentration of RS2

The ability of RS molecules to form self-assembling layers at the interfaces was evaluated by means of surface tension measurements of model systems. The surface tension values determined as a function of the RS concentration at the interface of chloroform–water and dodecane–water are shown in Fig. 2. The significant decrease with increasing RS concentration suggests a surface-active character based on the molecular structure of the interfacial additive.

The formation of the RS layer at the interfaces during homogenisation of the components in a kneading machine or extruder is the condition for replacing the solution process with the more economic (in-line) melt process. The accumulation of RS on the surface of dispersed inorganic particles was analysed for an

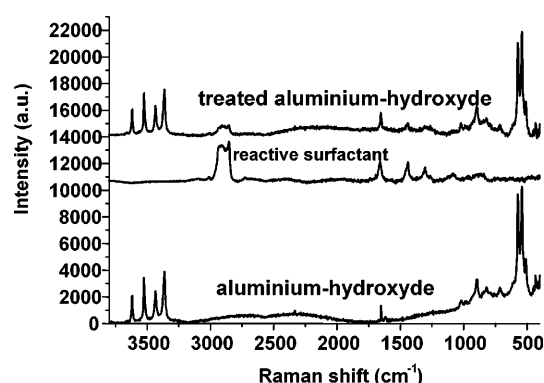


Fig. 3 Raman spectra of $\text{Al}(\text{OH})_3$ (ATH), RS2 and typical ATH particle in RS2-containing polyethylene (PE) systems

ATH-containing polypropylene (PP) system using the Raman microscopy technique. For this purpose ATH of relatively large average particle size, $15\ \mu\text{m}$, was used and the surface of samples, broken under liquid N_2 , was analysed. The Raman spectra of pure ATH, RS and of an ATH particle in the composite of 60%ATH/39%PP/1%RS are shown in Fig. 3.

The appearance of the bands at 2,850–2,950 [$\nu(\text{C-H})$ stretching vibration], 1,448 and $1,304\ \text{cm}^{-1}$ (deformation vibrations), characteristic to RS molecules, in the ATH spectra after compounding is clear evidence of the accumulation of RS at the interface. The $\nu(\text{C}=\text{C})$ stretching vibration of RS at $1,660\ \text{cm}^{-1}$ overlaps with the characteristic band of ATH at $1,653\ \text{cm}^{-1}$.

ATH is generally introduced at high concentration ($\geq 60\%$ or higher) as a flame-retardant filler into polymers. The special advantage of RS has been found

Fig. 4 Torque curves and optical microscope images of 60% pre-precipitated ATH-containing PE systems without treatment (a), with 1% nonreactive surfactant (b) and with 1% RS2 (c)

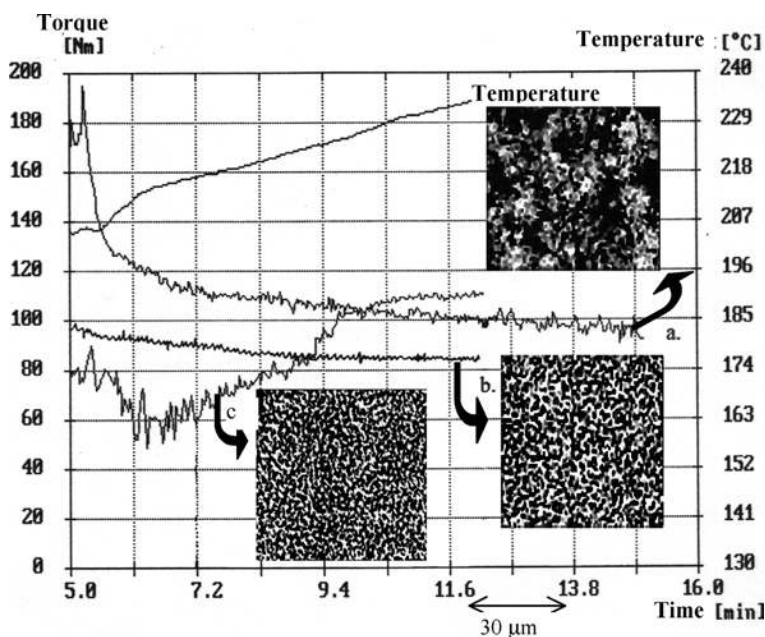


Table 1 Calculated and measured adhesion between polyethylene (PE) and CaCO_3 without modification and with various interfacial additives: nonreactive surfactant (S), reactive surfactant (RS), benzoic peroxide (BP)

Treated side	Untreated side	Thermodynamic work of adhesion, calculated value (mN m^{-1})		Peel strength (N)
		According to Owens–Wendt	According to Wu	
PE untreated (reference)	CaCO_3	76.7	89.9	2.6
Anionic S/PE	CaCO_3	116.5	126.5	
Cationic S/PE	CaCO_3	129.6	137.7	
Nonionic S/PE	CaCO_3	99.3	111.5	
RS1/PE	CaCO_3	151.8	142.0	
RS2/PE	CaCO_3	133.2	141.3	
Anionic S/ CaCO_3	PE	90.0	101.2	3.4
Cationic S/ CaCO_3	PE	85.1	97.1	3.3
Nonionic S/ CaCO_3	PE	83.2	95.5	7.0
RS1/ CaCO_3	PE	87.2	97.3	3.7
RS2/ CaCO_3	PE	86.1	96.8	3.5
RS1 + BP/ CaCO_3	PE			14.5
RS2 + BP/ CaCO_3	PE			14.8

in such systems [9]. The rheological behaviour of an RS-containing system, reflected in the torque of mixing (Fig. 4), is quite complex: low at the stage of homogenisation and then higher owing to the chemical interaction of phases.

The first stage allows a high level of homogeneity to be achieved, while the higher viscosity of the final compound prevents dipping in the case of flame attack. The quality of the dispersion can be seen in the optical microscopic images.

Differences in the value of adhesion between conventional surfactants and RS are expected. The comparison of conventional anionic, cationic and nonionic surfactants with reactive ones was performed with calculations based on wetting experiments and direct adhesion measurements that reflect the real value of adhesion most directly. The well-known Owens–Wendt [7] and Wu [8] methods were used for calculating the work of adhesion. The calculated W_a and the measured peeling force values are given in Table 1.

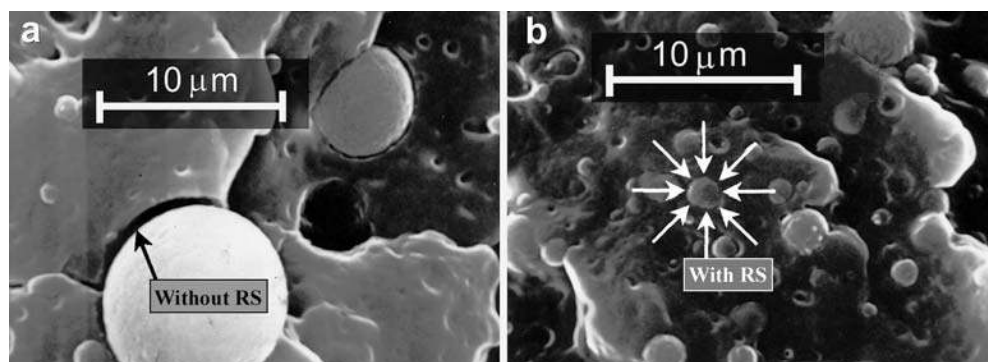
Independent of the type of surfactants and the method of calculation the W_a values (calculated using wetting results on both surfaces) are always lower on the PE

surface. This means that the weak point of adhesion is on the polymer side of the interface. This adhesion has to be improved with chemical reaction. The most important conclusion that can be drawn from Table 1 is the considerably higher peeling strength of RS than any type of nonreactive surfactant. This difference is not predicted by the calculations, which means that the calculated values of W_a are adaptable only for conventional surfactants but are not valid for interfaces containing RS.

The increase of adhesion owing to the RS interfacial layer is reflected in the macroscopic properties of various multicomponent systems [3, 4, 10]. Direct verification of the chemical bonds between RS molecules and the neighbouring phases were carried out using X-ray photoelectron spectroscopy and DSC methods. These results have been published elsewhere [11].

In-line functionalisation of polyolefins with RS resulted in better dispersion and adhesion when blended with PA. Without modification the PA drops, dispersed in a polypropylene matrix, are large and poorly attached to the continuous phase as shown in Fig. 5a. In the presence of RS considerably smaller PA drops and better contact between the phases can be seen in Fig. 5b.

Fig. 5 **a** Scanning electron microscope (SEM) micrographs of polypropylene–polyamide blends without RS (broken under liquid nitrogen). **b** SEM micrographs of polypropylene–polyamide blends with RS (broken under liquid nitrogen)



The smaller particle size means a higher contact area. The improved phase contacts and lower (large-particle induced) local stresses contribute to the better tensile strength and elastic modulus of the blend [4].

Conclusions

The results confirmed that the substances synthesised, called RS,

- Form self-assembled layers at interfaces.
- Reach the surfaces of additive particles during compounding and adsorb there preferably.
- Promote the level of homogeneity in multicomponent polymer systems.

- Reduce the drop size in incompatible polymer blends.
- Decrease the viscosity, allowing the polymer melt to wet the dispersed phase more thoroughly.
- Increase the adhesion at the interfaces through bonding the neighbouring phases to each other with chemical bonds.

Utilisation of the advantages of RS has been shown by examples of an ATH-containing fire-retardant system and blends of polyamide and polyolefin.

Acknowledgements This work was supported financially by the Commission of the European Communities through contract no. G5RD-CT-1999-00120 and by the Hungarian Research Fund through project OTKA T32941.

References

1. Chodak I, Novak I (1999) In: Karger-Kocsis J (ed) Polypropylene, an A–Z reference. Kluwer, Dordrecht, p 790
2. Rätzsch M, Jacobsch H-J, Freitag K-H (1990) *Adv Colloid Interface Sci* 31:225–320
3. Marosi G, Anna P, Csontos I, Márton A, Bertalan G (2001) *Macromol Symp* 176:189–198
4. Bertalan G, Marosi G, Anna P, Ravadits I, Csontos I, Tóth A (2001) *Solid State Ionics* 141–142:211–215
5. Bertalan G, Marosi G, Anna P, Besenyei F (2000) Hungarian Patent 218:016
6. Csontos I, Marosi Gy, Faigl F, Ravadits I, Komives J (1999) *Comput Chem Eng* 23(Suppl): 995–998
7. Owens DK, Wendt RC (1969) *J Appl Polym Sci* 13:1741
8. Wu J (1971) *Polym Sci Part C* 34:19
9. Marosi G, Anna P, Bertalan G, Szabó S, Ravadits I, Papp J (2001) In: Nelson G, Wilkie C (eds) ACS symposium series 797. American Chemical Society, Washington, DC, pp 161–171
10. Marosi G, Bertalan G, Anna P, Rusznák I, Kalafszki L, Szentirmai K (1992) In: Maack (ed) *Polypropylene'92*, Maack, Zurich, p II–1.4
11. Marosi G, Márton A, Szép A, Anna P, Csontos I, Bertalan G, Tóth A *Macromol Symp* (accepted)

Lidija Petrovic
Verica Sovilj
Petar Dokic
Ivan Schäffer

Formation of proanthocyanidin-loaded liposomes under various conditions

L. Petrovic (✉) · V. Sovilj · P. Dokic
I. Schäffer
University of Novi Sad,
Faculty of Technology,
Department of Colloid Chemistry,
Bulevar cara Lazara 1,
21000 Novi Sad, Yugoslavia
e-mail: lidia.p@eunet.yu

Abstract The formation of phosphatidylcholine liposomes loaded with proanthocyanidins isolated from grape (*Vitis vinifera* L.) seeds was studied. Using scanning electron microscopy it was determined that the type and the size of the liposomes depend on various factors: proanthocyanidin concentration and homogenization conditions (time and intensity). Rheological investigations of liposome dispersions

show different types of flow – plastic and pseudoplastic, according to the proanthocyanidin concentration. Liposome dispersions containing 0.25–1.5% proanthocyanidin show satisfactory stability after using a temperature stress test.

Keywords Liposomes · Proanthocyanidins · Scanning electron microscopy · Antioxidant preparations

Introduction

Liposomes composed of one or more concentric bilayers enclosing an aqueous phase are among the most studied systems for drug delivery applications [1, 2, 3]. When made from natural phospholipids, liposomes are completely biocompatible [4, 5]. They can entrap hydrophilic and hydrophobic compounds and usually release their content in a continuous manner [6, 7, 8]. The considerable shortcoming in the use of conventional liposomes is the relatively low physical stability (aggregation and fusion of vesicles may take place) [9]. The kinetic stability of liposomes will largely depend on the physical characteristics of the vesicles (lipid compositions, type and size of vesicles) and the nature of the encapsulated material and its interaction with the liposome components. In that regard, the formation and stability of proanthocyanidin (PRO)-loaded liposomes was studied.

In recent years plant extracts containing flavonoids have attracted increasing attention owing to the wide spectrum of pharmacological applications. The ability of small phenols, including flavonoids, to act as antioxidants has been investigated extensively [10, 11, 12, 13]. It was noticed that flavonoids with more hydroxyl groups

are more easily oxidized [14], and for simple flavonoid oligomers the degree of polymerization is correlated with the ability to scavenge free radicals [15]. But it is also very well known that flavonoids of very high molecular weight have lower bioavailability. PRO from grape seeds, being oligomers in fact, have both of the required abilities: high antioxidative action and good bioavailability [16, 17]. The structure of epicatechin and catechin dimer and trimer is shown in Fig. 1. Other oligomers (tetramers, pentamers and hexamers) are not so important from a pharmacological point of view. In order to improve their bioavailability for topical applications, PRO-loaded liposome formation was investigated.

Experimental

Materials

Soybean phosphatidylcholine (Phospholipon 80, Nattermann Phospholipid, Germany), PRO from grape (*Vitis vinifera* L.) seeds [18] and propylenglycol (Sigma, USA) were used for liposome preparation. Osmium tetroxide and absolute ethanol (Merck, Germany) were used for scanning electron microscopy (SEM) sample preparation. All other chemicals were of analytical grade.

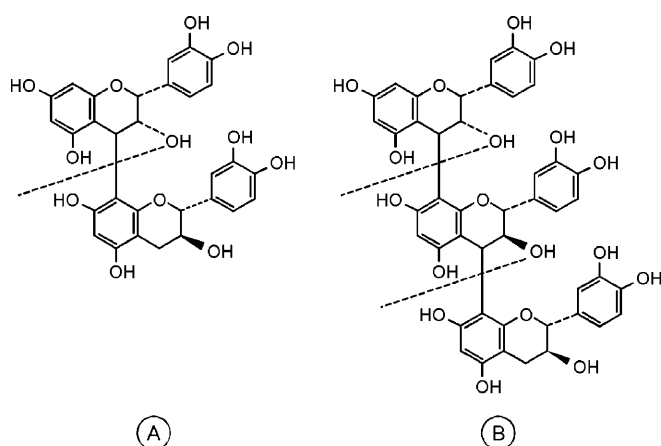


Fig. 1 a Dimer and b trimer of (-) epicatechin and (+) catechin

Methods

Liposome preparation

The liposome dispersions investigated contained 10% Phospholipon 80 and 0.25, 0.5, 1.0, 1.5 and 2.0% (w/w) PRO. At first, Phospholipon 80 was dissolved in propylene glycol (1:0.67 w/w) at 60 °C using a magnetic stirrer, then an ethanolic solution of PRO was added to the phospholipid/propylene glycol mixture in a ratio of 1:1.02 (w/w) at 40 °C. A clear solution containing phospholipids and PRO was mixed with double distilled water in the ratio 1:1.97 (w/w) at 37 °C and homogenized using an ULTRA-TURRAX T25 (Janke & Kunkel, Germany) rotor-stator homogenizer under various conditions: homogenization time (5, 10, 20, 40 and 60 min) and intensity (4,300, 6,300 and 8,000 rpm).

Scanning electron microscopy

The type and size of the liposomes were determined using a JOEL JSM 5300 (Japan) scanning electron microscope and the program package OZARIA for visual information quantification. The samples of liposome dispersions for microscope observation were

Fig. 2 Scanning electron microscope pictures of a liposome dispersion containing 1% proanthocyanidin (PRO)

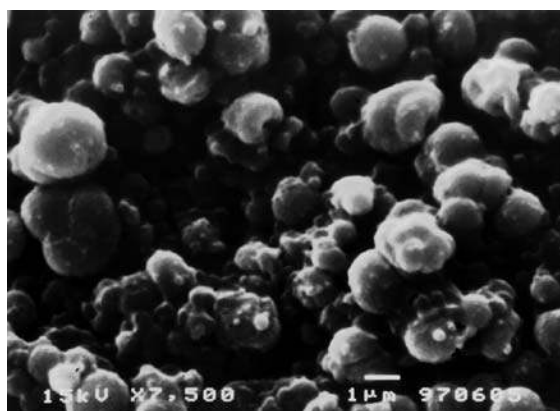


Table 1 Mean vesicle diameter of liposome dispersions containing various proanthocyanidin (PRO) concentrations (homogenized at 4,300 rpm for 60 min)

PRO concentration (%)	Mean vesicle diameter (µm)
0	0.67 ± 0.32
0.25	1.27 ± 0.69
0.50	1.67 ± 0.90
1.00	1.81 ± 0.98
1.50	2.36 ± 1.18
2.00	2.43 ± 1.32

prepared by using a slightly modified standard procedure for tissue preparation: a thin film of liposome dispersion was spread on a type M membrane filter of pore size 0.2 µm (Merck, Germany), and was fixed by keeping it in 1% osmium tetroxide solution for 90 min. After washing it in Millinor buffer (pH 7.2), dehydration of the sample was achieved by immersing it (for 5 min) in the ethanol solutions with increasing concentration starting from 35%, then 50, 70, 95 and 100% (absolute ethanol). The sample was dried in air and covered with platinum on a JOEL JFC-110E ion sputter (Japan). Each sample investigated was scanned several times in order to obtain at least 1,000 vesicles for calculation of the mean diameter.

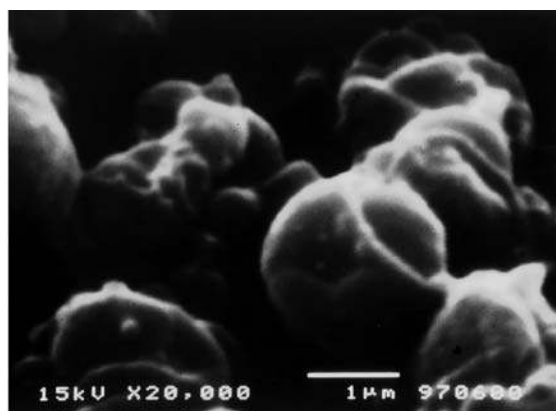
During the preparation procedure of the samples for SEM, certain deviations from the values of the mean vesicle diameters are possible. Referring to a liposome dispersion standard sample (Natipide II), it was concluded that the values of the vesicle diameters are in agreement with the standard sample diameter values within the standard deviation. This could be acceptable, for the aim of this paper was to investigate this influence of various factors (PRO concentration, homogenization terms) on changes in the mean diameter of liposomes.

Rheological investigations

Rheological properties of liposome dispersions were determined using a Rotovisco RV20 (Haake, Germany) with NVSt (outer and inner cylinder radius ratio 1.02) and SVI coaxial cylinders (outer and inner cylinder radius ratio 1.14) at 25 °C.

Stability investigations

All the liposome dispersions investigated were submitted to the temperature stress test, which comprises seven consecutive cycles. Each cycle considers the sample remaining at 4 °C for 24 h, at



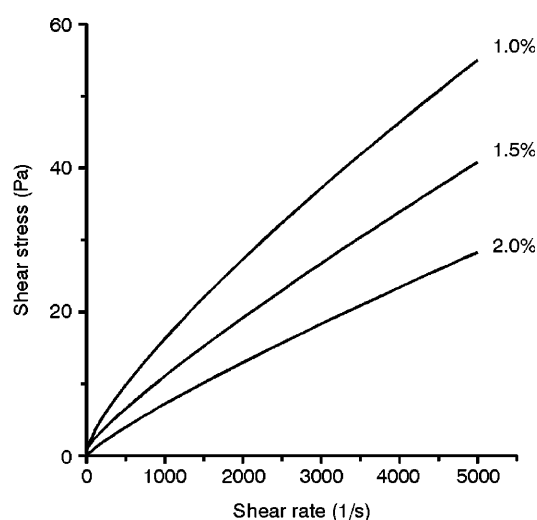
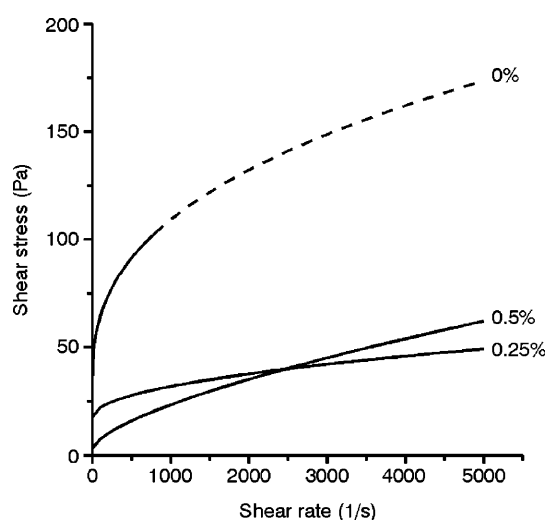


Fig. 3 Flow curves of liposome dispersions containing various PRO concentrations

23 °C (room temperature) for another 24 h and at 40 °C for another 24 h.

Results and discussion

To ascertain the influence of PRO concentration on liposome formation, dispersions containing different PRO concentrations (0–2.0%) prepared at 4,300 rpm and 60-min homogenization time were examined.

The liposomes formed under such conditions were mostly multilamellar vesicles (MLV) as can be seen in Fig. 2. They were characterized by the mean vesicle diameter and their standard deviation, determined by SEM and calculated according to the Gauss distribution equation. From results shown in Table 1 it can be observed that the increase in PRO concentration causes an increase in the mean vesicle diameter. It could be assumed that PRO was mostly located in the aqueous phase of the liposomes, between the lamellas, because of their distinctive polar character and the position of the hydroxyl groups seen in Fig. 1. All the dispersions examined have marked polydispersity of the liposomes.

Rheological investigations of the liposome dispersions showed that the rheological properties change with increasing PRO concentration (Fig. 3). Liposome dispersions containing 0–0.25% PRO show plastic behaviour and dispersions containing 0.5–2.0% PRO show pseudoplastic behaviour. At the same time it can be noticed that the viscosity of liposome dispersions decreases with an increase in PRO concentration. In our opinion, the changes in the rheological behaviour and the viscosity decrease with increasing PRO concentration are the result of changes in the mean diameter and the size distribution. Inner structural reorganization of the vesicles is also assumed. All these changes happen at

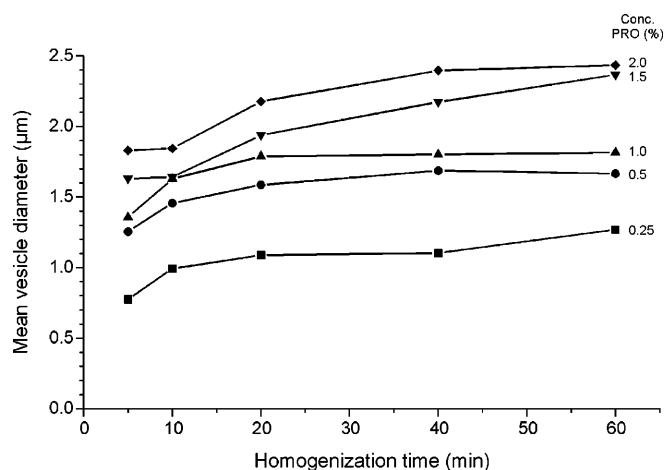


Fig. 4 Effect of homogenization time on changes in the mean vesicle diameter of liposome dispersions at various PRO concentrations

constant Phospholipon 80 concentration in the dispersion.

Beside the active compound concentration, the homogenization conditions (time and intensity) seem to be of great importance for liposome formation and stability. In that regard the influence of the homogenization time on the mean vesicle diameter of liposome dispersions containing various PRO concentrations was investigated (Fig. 4). During the homogenization process a significant increase in the mean vesicle diameter was observed. The smallest liposomes were formed during the first 5 min, independent of the PRO concentration in the liposome dispersions, but prolonged homogenization increased their mean diameter.

The influence of the homogenization intensity on the mean vesicle diameter of the liposomes was also investigated on a liposome dispersion containing 1% PRO. From the results shown in Table 2 it can be seen that with an increase in the homogenization intensity from

Table 2 Effect of homogenization intensity on the mean vesicle diameter (μm) of liposome dispersions containing 1% PRO at various homogenization times

Homogenization intensity (rpm)	Homogenization time (min)		
	20	40	60
4,300	1.79 ± 0.97	1.80 ± 1.10	1.81 ± 0.98
6,300	1.20 ± 0.65	1.93 ± 1.07	1.97 ± 1.05
8,000	1.00 ± 0.55	1.08 ± 0.38	1.15 ± 0.62

Table 3 Mean vesicle diameter measured before and after the temperature stress test

PRO concentration (%)	Mean vesicle diameter (μm)		
	Before test	After test	Increase (%)
0	0.67	0.69	2.38
0.25	1.27	1.31	2.99
0.50	1.67	1.73	3.96
1.00	1.81	1.98	8.93
1.50	2.16	2.45	13.21
2.00	2.43	3.57	46.71

4,300 to 8,000 rpm the mean vesicle diameter of the liposomes decreased in all the liposome dispersions investigated (homogenization time 20, 40 and 60 min). For example, the mean vesicle diameter in a dispersion homogenized for 20 min at 4,300 rpm was $1.79 \mu\text{m}$, at 6,300 rpm it was $1.20 \mu\text{m}$ and at 8,000 rpm it was $1.00 \mu\text{m}$. The same relation was observed with a dispersion homogenized for 40 and 60 min. At the same time, an increase in the mean vesicle diameter during the homogenization process, for all homogenization intensities investigated, was noticed.

In order to examine the long-term stability of the liposomes the samples were submitted to the temperature

stress test. The mean vesicle diameters were measured before and after the test (Table 3). After the test, the mean vesicle diameter was higher in all the liposome dispersions investigated. If the concentration of the active compound (PRO) was higher, a greater increase in diameter was observed, i.e. the stability of the liposomes decreased.

For example, the mean vesicle diameter for "empty" liposomes increases from 0.67 to $0.69 \mu\text{m}$ (increase 2.38%), for liposomes containing 1% PRO it increases from 1.81 to $1.98 \mu\text{m}$ (increase 8.93%) and for liposomes containing 2% PRO it increases from 2.43 to 3.57 (increase 46.71%). Liposome dispersions containing up to 1.5% PRO show an increase in the mean vesicle diameter proportional to the PRO concentration.

Conclusions

Phosphatidylcholine can be applied for PRO-loaded liposome preparation using a mechanical homogenizer. All the liposomes formed were of MLV type and were convenient for topical application. Increasing the PRO concentration and homogenization time enhances the mean vesicle diameter. The smallest vesicles were formed at 5-min homogenization time and 8,000-rpm homogenization intensity. The stability of the liposome dispersion decreases with increasing PRO concentration. Liposome dispersions containing 0.25–1.5% PRO show satisfactory stability.

Acknowledgements The authors thank the Department of Electron Microscopy, University Medical Center of Nis, for assisting with the SEM. The results are from work on Serbian Ministry Science research project BTN.7.1.9.0426.B.

References

- Blume G, Cevc G (1990) *Biochem Biophys Acta* 1029:91
- Crommelin DJA, Schreier H (1994) In: Krauter J (ed) *Colloid drug delivery systems*. Dekker, New York, pp 73–189
- Ganesan MG, Weiner ND, Flynn GL, Ho NFG (1984) *Int J Pharm* 20:139
- Schreier H, Bouwstra J (1994) *J Controlled Release* 30:1
- Tardi C, Brandl M, Schrufer R (1998) *J Controlled Release* 55:261
- Ceruti M, Crosasso P, Brusa P, Arpico S, Dosio F, Cattel L (2000) *J Controlled Release* 63:141
- Albertini G, Dubini B, Gobbi L, Ponzi Bossi MG (1992) *Mol Cryst Liq Cryst* 221:121
- Berrocal MC, Bujan J, Jurado F, Alber A (1998) *J Microencapsulation* 15:341
- Grohmann FL, Csempeš F, Szögyi M (1998) *Colloid Polym Sci* 276:66
- Mattei Faciano R, Carini M, Aldini G, Calloni MT, Bombardelli E, Morazzoni P (1998) *Planta Med* 64:343
- Kaneko T, Baba N (1999) *Biosci Biotechnol Biochem* 63:323
- Hagerman AE, Reidl KM, Jones GA, Sovic KA, Ritchard NT, Hartzfeld PW, Riechel TL (1998) *J Agric Food Chem* 46:1887
- Pekic B, Kovac V, Alonso E, Revilla E (1998) *Food Chem* 61:201
- Hodnick WF, Milosavljevic EB, Nelson JH, Pardini RS (1988) *Biochem Pharmacol* 37:2607
- Ariga T, Hamano M (1990) *Agric Biol Chem* 54:2499
- Bourzeix M, Weiland D, Heredia N, Destenx C (1986) *Bull OIV* 59:1171
- Hollman PCH, Katan MB (1999) *Food Chem Toxicol* 37:937
- Pekic B, Kovac V (1993) *Yugoslavian Patent P-205/93*

H. G. Kilian
R. Kemkemer
H. Gruler

Relaxation processes during cell growth

Abstract According to the law of mass action, stationary states of cell ensembles are identified as open systems, with optimised universal structure properties. “Ingestion” and “digestion” of biomass during a cell cycle stimulate “distortions”. Relaxation processes then reestablish rapidly stationary conditions. Owing to having strictly coordinated processes intracellular relaxation can be described as a Debye-process, the relaxation time of which increases with the cell size. A broad universal relaxation mode distribution comes about. This spectrum is precisely determined by the cell size distribution, evidencing a stringent correlation between structure and

dissipative dynamics. The cell ensemble endures a “collective breathing” with a defined frequency that increased with the ensemble density. Analogously to relaxation, under the action of a periodic external field growing cell ensembles show a typical “frequency dispersion”. Our concept is strongly supported by a consistent description of the cell growth phenomena of two very different systems, i.e. *Escherichia coli* and human melanocytes as representatives of prokaryotic and eukaryotic cell ensembles.

Keywords Cell ensembles · Growth and reduplication · Relaxation

H.-G. Kilian (✉)
Abteilung Experimentelle Physik der
Universität Ulm, Einstein-Alle 11,
89069 Ulm, Germany
e-mail: hanns-georg.kilian@physik.uni-
ulm.de
Tel.: +49-731-5026072
Fax: +49-731-5023036

R. Kemkemer · H. Gruler
Abteilung Biophysik der Universität Ulm,
Einstein-Alle 11, 89069 Ulm, Germany

Introduction

During cell growth and multiplication cell cultures rapidly achieve stationary nonequilibrium patterns with an optimised ensemble structure, for example, the length distribution of the intracellular proteins or the size distribution of the cells [1, 2, 3, 4]. According to the law of mass action, formulated within the framework of irreversible thermodynamics [5, 6], these patterns are self-similar and belong to the same universal type [7]. An intelligent cooperation of genetics and thermodynamics guarantees that the many generations which evolve in the course of time keep their identity with unsurpassed degrees of accuracy (mutations neglected) [1, 7]. This holds true under different external conditions.

Uptake of biomass is supposed to cause fast periodical “distortions” with a characteristic frequency. Stationary conditions should thus continuously be reestablished via

relaxation analogously to classical conceptions [8, 9]. Yet, this idea makes sense only if stationary states operate as temporary states of reference. Because the distortion frequency originates in each cell, it should grow with the density of the cells. Since the ensemble shows a distinct mean relaxation time, cell growth and reduplication should, in principle, be characterised by a “frequency dispersion”.

In the following treatment of these phenomena we focus on the essentials and leave an extended treatment to another paper.

The stationary states

Cell size distributions

Cell ensemble cultures are open systems. The population is usually increased via cell growth and multiplication

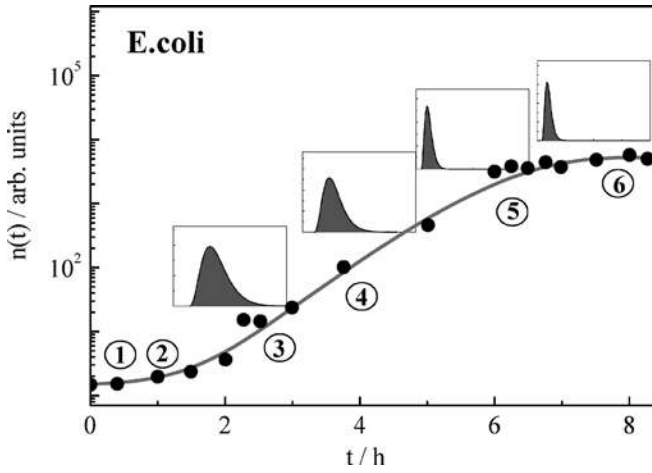


Fig. 1 Density of cells of a culture of *Escherichia coli*, $n(t)$, as a function of the time, t , according to Schlote [3]. The cell size distributions (see also *inserted sketches*) were determined at the times indicated by the *numbers in open circles*

(Fig. 1 [3]). If cells are treated as “aggregates” [10, 11] comprised of equivalent units, a generalised law of mass action can be formulated within the framework of irreversible thermodynamics [6]. It demands that stationary cell size distributions be optimised analogously to the classical situation [12]. The “affinity A ” is the only “nonequilibrium function” that enters into the final equations.

It turns out that the stationary number distribution of cells comprised of y_a units (with $y = y_a - 1$ contacts), n_y , should be equal to [12]

$$n_y = n_0 y^p \exp(-y\beta\Delta u_0) = n_0 y^p \exp[-y\beta(\Delta u_0^* + A)],$$

$$n_0 = \sum_y n_y; \quad \beta = \frac{1}{k_B T}, \quad (1)$$

where n_0 is the normalisation constant. k_B is the Boltzmann constant, and T is the absolute temperature. The standard energy, Δu_0 , is defined by

$$\Delta u_0 = \Delta u_0^* + A. \quad (2)$$

Under stationary conditions the affinity is constant (A is a constant greater than zero) with a value that depends on the external conditions. The front factor in Eq. (1) should account for structurally conditioned extra entropy contributions according to

$$\exp(-\beta\Delta f_0) = \exp\left(\frac{\Delta s_0}{k_B}\right) \exp(-\beta\Delta u_0),$$

$$\exp\left(\frac{\Delta s_0}{k_B}\right) = y^p = \exp(p \ln y), \quad (3)$$

$$\Delta s_0 = k_B p \ln y.$$

The parameter p defines “classes” of dissipative colloid structures. The cell ensembles studied until now

belong to the $p=3$ class. Representative examples are shown in Fig. 2 [7]. The solid lines were computed with Eq. (1) using the parameters indicated.

The universal stationary cell size distribution is obtained by rewriting Eq. (1) in terms of the dimensionless variable η_y :

$$\frac{n_{\eta y}}{n_{\eta 0}} = \eta_y^p \exp(-\eta_y); \quad \eta_y = y\beta\Delta u_0 = y\beta(\Delta u_0^* + A),$$

$$n_{\eta y} = \frac{n_0}{(\beta\Delta u_0)^p}, \quad (4)$$

At constant p the topological identity of cell ensembles is guaranteed on this level. The universal distributions do not, for example, depend on the distance from equilibrium (i.e. on the value of A). The actual distributions are self-similar, i.e. they are related to each other via an affine transformation. All these patterns fit to the master curve defined by Eq. (4). This implies that the many stationary patterns achieved at different growth rates are optimised in the sense of irreversible thermodynamics. Apparently cell ensembles are able to adjust themselves to varying external conditions without losing their global identity.

Saturation

In the increment formulation the affinity of an “aggregation” process is straightforwardly defined by

$$A = -\sum_{y_a} v_{y_a} \mu_{y_a} = -\sum_{y_a} v_{y_a} (u_{y_a} - T s_{y_a}), \quad (5)$$

where v_{y_a} is the stoichiometric coefficient of the cells y_a , μ_{y_a} is the chemical potential. u_{y_a} and s_{y_a} are the partial molar internal energy and entropy. Since at equilibrium $A=0$ we are led to

$$u_{y_a} = T s_{y_a}. \quad (6)$$

By characterizing the equilibrium state of reference analogously the condition of saturation turns out to be given by

$$y_a \Delta u_0 = T \Delta s_{y_a},$$

$$y_a \Delta u_0 = y_a (u_0 - u_1); \quad \Delta s_{y_a} = s_{y_a} - y_a s_1. \quad (7)$$

Standard energy $y_a \Delta u_0$ and $T \Delta s_{y_a}$ should be evenly matched.

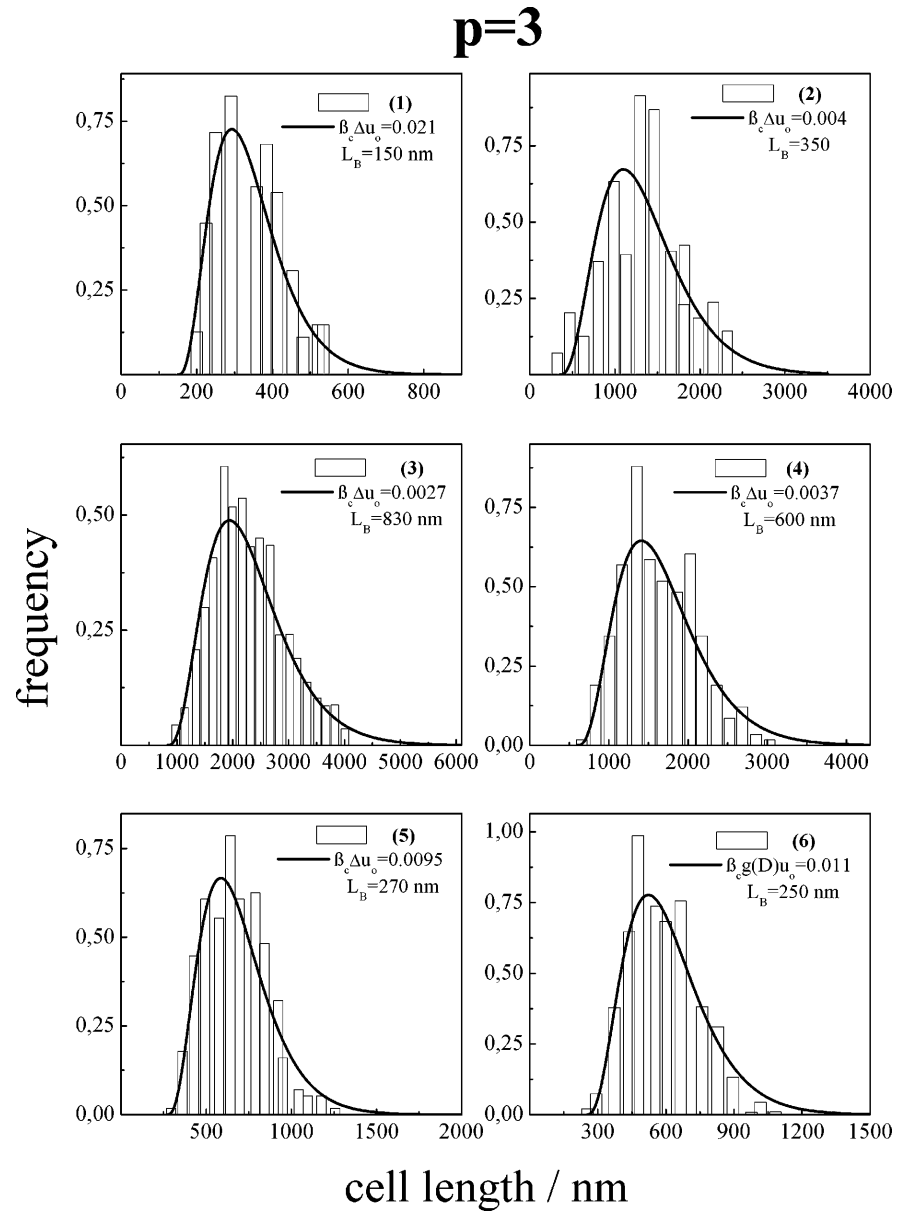
For stationary cell ensembles analogous relations can be formulated straightforwardly (for $y_a=1$ the terms disappear, so y_a can be replaced by y):

$$y(\Delta u_0^* + A) = T \Delta s_y(\xi) = T \ln[\Omega_y(\xi)],$$

$$\Omega_y(\xi) = \frac{\Omega_{cy}(\xi)}{\Omega_{y,\text{ref}}}. \quad (8)$$

ξ is the hidden variable conjugated to the affinity A . Since the standard energy is mainly fixed by the chemical

Fig. 2 Histograms of the cell lengths determined at discrete times shown in Fig. 1. The *solid lines* were computed with Eq. (1) and the parameters indicated. All these patterns belong to the $p = 3$ class



structure of the constituents the previous “condition of saturation” is mostly satisfied by producing or annihilating entropy-relevant molecular conformations and configurations $\Omega_{cy}(\xi)$.

Relaxation

Cell growth and multiplication as a dissipative process

Cells in a medium grow steadily until they become divided. The density of the cells of simple systems thus increases rapidly as demonstrated in Fig. 1 [3]. As

already discussed there are many grounds for suspecting that the continuously running complex processes are accompanied by “relaxation processes”. We have to emphasise two crucial aspects:

1. The assumption must be introduced that an optimised stationary state of the cell population should continuously be distorted when biomass is taken up and “digestion” starts. These processes include the appearance of local concentration gradients or electric potential differences. Distortions are supposed to occur rapidly and “periodically”, inducing fluctuations with a decent frequency ω_c . This characterises the dynamics within the whole growing cell ensemble. Because of the

cell multiplication, ω_c should increase in the course of time proportional to the growing cell density. These processes may be described by defining an “internal distortion field” as a mean-field representation of a complex set of conjugated periodical signals.

2. In classical conceptions weakly distorted systems travel via relaxation towards an equilibrium state [5, 6, 8, 9]. To get the same logistics we have to postulate that in dissipative open systems optimised stationary states operate as temporary states of reference. If sufficiently fast processes are available there is no objection against the hypothesis that relaxation towards such stationary states should exhibit analogous features as in classical models [9]. If the external conditions vary steadily it should also be possible that relaxation is running off while the state of reference passes slowly through a logical sequence of temporary stationary patterns.

With the uptake of biomass, energy is stored whereby this seems to happen periodically. All in all, this energy should depend on the mean cell density. The density should thus characterise the mean-field properties of a cell culture analogously to a “complex viscoelastic modulus”.

The universal relaxation mode spectrum: a correlation between structure and dynamics

We develop now a mathematical formulation of the previous ideas. It is clear that cultivated cell ensembles achieve stationary states via complex processes, including modifications of conformations and configurations, diffusion and enzyme-catalysed chemical reactions [1]. At “small distortions” it is reasonable to assume that relaxation runs via the same set of molecular processes.

All the intracellular events during a cycle are coupled in such a way to achieve strict logistics [1, 2, 4]. For this reason intracellular relaxation is described by a single Debye process [8, 9], the relaxation time of which increases with the size of the cell. Relaxation of a cell ensemble should thus be controlled by directed fluctuations of the whole ensemble structure. If the kinetics is the same everywhere the influence of the colloid structure is explicitly accounted for by introducing the mode factor of a cell composed of y units, τ_{0y} , according to [13]

$$\begin{aligned}\tau_y &= \beta \frac{\zeta(T,p)}{B} \Omega_y = \tau_{0y} \tau_{kin}, \\ \tau_{kin} &= \beta \frac{\zeta(T,p)}{B} : \text{ independent of } y \\ \tau_{0y} &= \Omega_y : \text{ cell - size - dependent}\end{aligned}\quad (9)$$

$\zeta(T,p)$ is the friction coefficient, and B is a constant. The kinetic factor, τ_{kin} , should not depend on the size of the cells (y) and usually changes with temperature or

pressure, for example, according to the Arrhenius law [9]. The nondimensional “relaxation mode” factor, τ_{0y} , of a cell with y contacts should be given by the relative number of “entropy-relevant” configurations per cell Ω_y (Eqs. (8, 9)).

The reduced mass fraction of cells, h_y , should then determine the contribution of cells with y contacts. According to Eq. (4) h_y is equal to

$$h_y = \eta_y^{p+1} \exp(-\eta_y); \quad \eta_y = y\beta\Delta u_0 = y\beta(\Delta u_0^* + A) . \quad (10)$$

In comparison with Eq. (4) the exponent of the front factor is increased by 1 ($p \rightarrow p+1$). As an approximation the mass per cell is set equal to the number of contacts $y = y_a - 1$. By combining Eqs. (8) and (9) we are led to the relevant relation

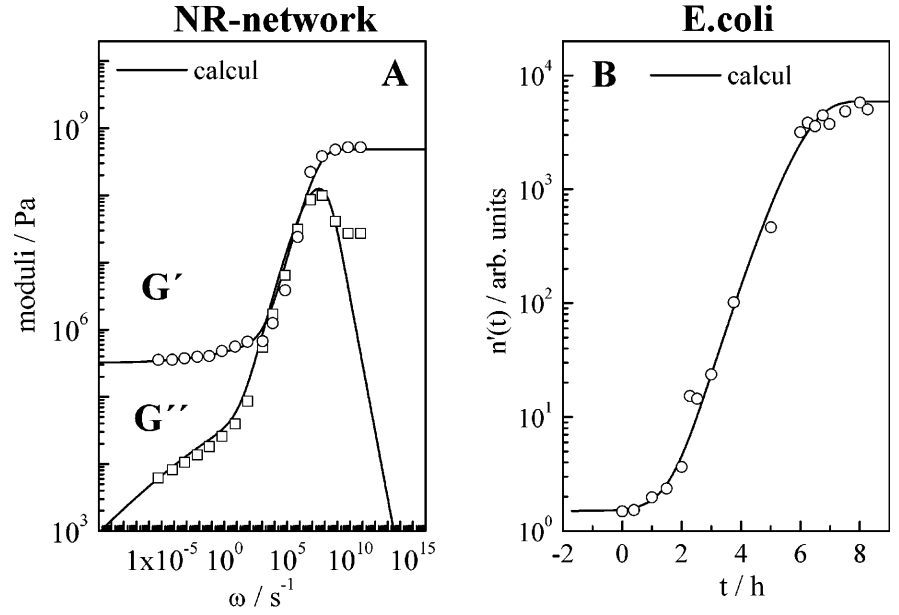
$$\begin{aligned}h_y(\eta_y) &= \eta_y^{p+1} \exp(-\eta_y) = \frac{\ln^{p+1}(\tau_{0y})}{\tau_{0y}} = h_y(\tau_{0y}), \\ n_y &= y\beta\Delta u_0 = \ln \Omega_y = \ln \tau_{0y} .\end{aligned}\quad (11)$$

The relaxation mode distribution $h_y(\tau_{0y})$ is a universal function only depending on the parameter p . Cell cultures typified by $p=3$ should display the same relaxation mode pattern independent of the distance from stationary nonequilibrium conditions. In that way we recognise a mandatory correlation between stationary structure and dynamics.

The frequency dispersion

The above concept implies that relaxation of cell cultures should run like relaxation under periodic distortions enforced from outside at different frequencies [8, 9, 14, 15]. In such experiments one observes a frequency dispersion, the width of which is increased owing to the influence of a relaxation time distribution. The components of the complex shear modulus of a cross-linked network of natural rubber as a function of the frequency ω [14, 16] are shown in Fig. 3a as an example (the solid lines were computed with relations analogous to the ones deduced later). The equilibrium state of reference is typified by the shear modulus at lowest frequencies. The distance from this state of reference grows with increasing frequency. At constant temperature and frequency the system adjusts itself to a stationary nonequilibrium state at a decent distance from equilibrium. “Optimised stationary liquidlike properties” are guaranteed. In the high-frequency regime the distance from equilibrium grows very fast. The maximum losses are observed at $\omega < \tau > = 1$. Finally, at very high frequencies molecular changes of place are frozen in, and the system is “frustrated”, representing a solidified configuration of

Fig. 3 **a** Components $G'(\omega)$ and $G''(\omega)$ of the complex shear modulus of a permanent network of natural rubber (NR) at room temperature [15, 16]. **b** Density of cells of *E. coli* as a function of time according to Schlote [3]



the “aggregate structure of a liquid” [10, 13]. The frequency dispersion is brought about as the result of having a distinct mean relaxation time $\langle \tau \rangle$. At low frequencies any distortion is rapidly repaired, while this is no longer possible at frequencies that are large in comparison with $\langle \tau \rangle$.

A crucial point is now that the $n(t)$ pattern of the cells (Fig. 3b) looks similar to the $G'(\omega)$ (the t -dependency is shown later to be proportional to $\log \omega_c$). Exactly this similarity motivated us to assume that during the growth of cell ensembles relaxation should occur analogously to the mechanical experiment. Accepting this hypothesis we can straightforwardly develop an adequate analytical formulation.

According to Eq. (11) the cell ensemble should be characterised by the universal mean relaxation mode time $\langle \tau_{oy} \rangle$, i.e. by the mean relaxation time $\langle \tau \rangle = \langle \tau_{oy} \rangle \tau_{kin}$ (Eq. 9). Hence, the distortions of ω_c produced during cell growth should bring about a defined and “typical frequency dispersion”. To describe this we define the complex density $n(\omega_c)$ (in analogy to the definition of a complex shear modulus) by

$$n(\omega_c) = n'(\omega_c) + in''(\omega_c) . \quad (12)$$

The real part $n'(\omega_c)$ characterises the energy that can be stored in a growing cell ensemble at defined distances from a stationary state of reference. $n''(\omega_c)$ should describe dissipation during relaxation. Relaxation of the cell ensemble is then consequently considered as a superposition of many Debye processes, the fractions of which are given by the normalised universal mass fraction of the cells of different sizes (see Eq. 11).

$$\begin{aligned} n'(\omega_c) &= n'_0 + \Delta n' \sum h_y(\tau_{0y}) \frac{(\omega_c \tau_y)^2}{1 + (\omega_c \tau_y)^2}, \\ n''(\omega_c) &= \Delta n' \sum h_y(\tau_{0y}) \frac{\omega_c \tau_y}{1 + (\omega_c \tau_y)^2}, \end{aligned} \quad (13)$$

$$\Delta n' = n'_{\max} - n'_0 ,$$

where n'_0 is the value in the state of reference, while n'_{\max} is the maximum value at very large frequencies and mainly determines $\Delta n'$. The frequency ratio ω_c/ω_0 and the time t elapsed from the start of the observations should be related to each other by introducing the cell cycle time t_c according to

$$\log \left(\frac{\omega_c}{\omega_0} \right) = \frac{t}{t_c} \log 2 . \quad (14)$$

ω_0 scales the dimensions of ω_c .

The previous concept is verified if $n(t)$ dispersion curves are reproduced by using in the calculations the universal relaxation mode distribution and the known value of the cell cycle time t_c only. Of course, τ_{kin} must also be adjusted. Owing to the simple rheological conditions τ_{kin} determines only the position of the actual frequency window of the events without affecting the shape of the dispersion pattern.

Results and discussion

Escherichia coli

For batch cultures under different physiological conditions that are ruled by the nutrient supply the cell density

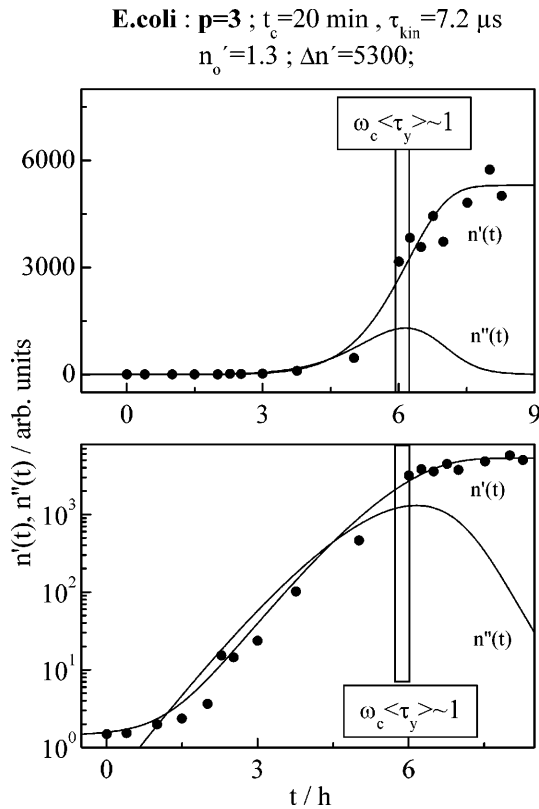


Fig. 4 Fit to the Schlotte data [3] by using Eqs. (13) and (14), $p=3$ and the parameters indicated

increases with the age of the culture [3]. According to Fig. 1 the growth process shows a nonlinear dependency on t . The width of the cell size distributions changes, yet all the patterns belong to the $p=3$ class [7] (Fig. 2), i.e. the ensemble entropy is maximised in each case. The system approaches rapidly stationary states with a constant value of $\Delta u_0 = \Delta u_0^* + A$. If the stationary state of reference is labelled by $\Delta u_0^* = \text{constant}$ the distance to it measured by the value of A should change depending on the experimental conditions to which the culture is exposed.

It is demonstrated by Fig. 4 that $n(t)$ of an *E. coli* culture is fairly well reproduced by using Eq. (13) and the parameters indicated. It is important that the value of the cell cycle time $t_c = 0.33$ h is known. Since n'_0 and $\Delta n'$ follow directly from the measurement, τ_{kin} is left as the only disposable parameter. Assigned to values in the microsecond regime this covers the regime typical for chemical reactions like, for example, the production of proteins [1, 17]. With $\omega_0 = 1/h$ the mean relaxation time $\langle \tau \rangle$ is deduced to be equal to about 9 ms; hence, relaxation seems in all cases to occur so rapidly that in the time window of the measurements all the cell ensembles discussed here can be optimised.

Human melanocytes

Human melanocytes are pigment cells of the skin [18]. A light microscope image of a suspension is depicted in Fig. 5 [19]. It is verified that the shape of these cells, their size distribution, the length distribution of the arms of dendrites as well as the fraction of differently branched cells are optimised in the sense of our model. We will furnish proof of these comments elsewhere.

The cell density as a function of time measured with a flow cytometer within a fixed time window for different initial cell densities is depicted in Fig. 6a [19]. Seeing this pattern we were promptly inspired to draw an analogy to measurements of, for example, the shear modulus within a finite frequency window at different temperatures. Under rheological simple conditions [8, 9, 14, 15] a master curve is constructed by “simple shifts” of the “segments” along the frequency axis. Doing it here in an analogous manner the segments fit in fact together to make the master curve depicted in Fig. 5b. The pattern shows features analogous to those of *E. coli*. Within the limits of accuracy the shift factor exhibits a linear dependence on the reciprocal density (Fig. 5c). The relative growth rate of the density of the cells plotted against the density itself decreases steadily and becomes equal to zero at a maximum frequency beyond which cell multiplication should no longer be possible.

In comparison with *E. coli* (maximum of dissipation at about 6 h) the kinetics of a melanocyte cell ensemble is slower (maximum of dissipation at about 480 h). This might also be due to the condition that activated cells have to have contact with the flat substratum [1]. Nevertheless, in both systems the logistics of the cell growth processes is the same.

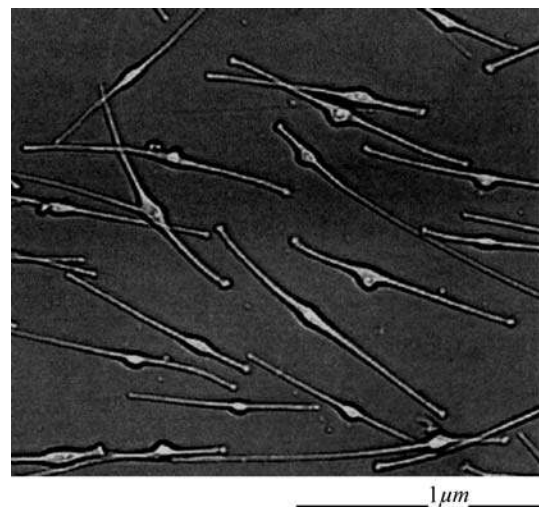


Fig. 5 Light microscope image of cultivated melanocytes [19]

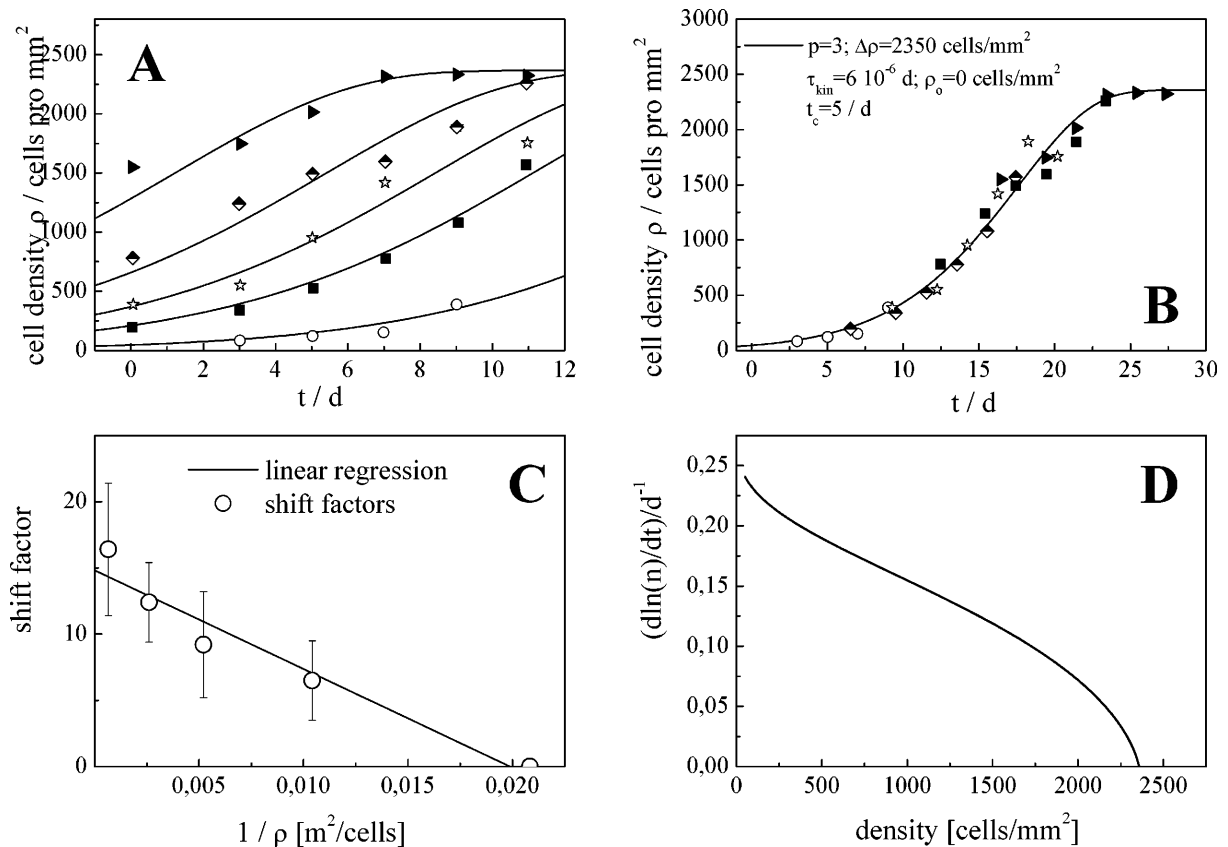


Fig. 6 **a** The cell density of human melanocytes as a function of time covering the same window. The experiments [19] start at systematically increased values of the cell density. **b** Master curve obtained from **a** by shifting each original pattern towards longer times so as to fit to a master curve. **c** The shift factor, δ , against the reciprocal density, $1/\rho$. **d** The relative growth rate of the number of cells, $d\ln n/dt$, against the cell density, ρ

Final comments

Thermodynamics of irreversible processes delivers a complete description of nonequilibrium states by extending the system of coordinates with a set of hidden variables. Following this route an extended version of the law of mass action can be formulated which holds true for stationary states even in open systems. It identifies stationary nonequilibrium states of cell ensembles as optimised patterns with universal features: The reduced version of the cell size distributions of bacteria or yeast belong to the $p=3$ class, while the length distribution of the intracellular proteins is described as $p=1$ type.

Our concept is taken as a platform for extending the classical instruments of describing relaxation, so as to cover time-dependent processes towards stationary states in open systems. Owing to the uptake of biomass followed by complex intracellular processes distortions arise. Cell ensembles are then shown to be “stabilised”

during growth and multiplication via relaxation embracing as dissipative processes, the rates of which are controlled by the distance to the temporary stationary states of reference. De facto, these stationary states should be stable for a while, so optimisation via sufficiently rapid processes is in fact possible.

Processes during a cell cycle are evidenced to be closely controlled cooperative events, including synchronisation within the ensemble. This caused us to describe relaxation within each cell by a Debye process, the relaxation time of which should increase with the size of the cell involved (“finite-size effect”). In that way ensemble structure and relaxation processes of cell ensembles are strictly interrelated. The universal energy density distribution and the universal “relaxation mode distribution” turn out to be copies of each other. Consequently, the spectrum depends only on the universal properties of the ensemble structure, i.e. on the value of p . Since all the cell populations studied here belong to the $p=3$ class, the linear relaxation behaviour should show the same features.

Because of limited working knowledge about the details, we have postulated that uptake of biomass and the later digestion during each cell cycle should excite periodic distortions that enforce a “collective breathing” of the total ensemble. If all cells are active the frequency of the distortions is supposed to grow proportionally to

the cell density. On this basis we deduced relations that describe growth and cell reduplication as a process accompanied by relaxation that shows a peculiar frequency dispersion. The dispersion originates with the existence of a characteristic mean relaxation time. During cell growth the degree of “dynamic frustration” grows systematically with the density of the cells. At very high cell densities cell growth and duplication is fully blocked on account of the “tremendously intensified drumfire of distortions”.

Our concept is strongly supported by the finding that human melanocytes (as relatively large cells) measured within a fixed period of time at different cell concentrations evidence characteristics that strictly correspond to “rheologically simple conditions”: it is an impressive demonstration of the “linear dynamics” of growing cell ensembles, including the superposition of a huge number of Debye processes. A master curve can be constructed in perfect analogy to procedures developed in the classical field of mechanical relaxation. Analogous behaviour is observed when the medium of the culture is suddenly changed [2, 3]. These studies evidence that the cell cycle time can be influenced from outside without modifying the internal logistics. The observations can be described fully within the framework of our approach. Adjustments to the new situations happen “via relaxation under optimum conditions” so as to minimise dissipation of energy. These latest results are not shown here and will be reported elsewhere.

The cell cycle time turns out to characterise in a unique manner the periodical intracellular processes irrespective of individual complexities. It is amazing that the logistics of cell growth and multiplication seems to be

the same for prokaryotic *E. coli* and for eukaryotic melanocytes. In eukaryotic cells many membrane-bound organelles, including the endoplasmic reticulum, Golgi apparatus and mitochondria, are held in their relative locations in the cell by attachment to the cytoskeleton, especially to microtubules [1]. Yet, even the presence of a nucleus and an endomembrane system or the dendritic shape of the melanocyte cells does not seem to annul the imperative competence of thermodynamic principles that control the optimisation of the collective intracellular properties. This is indeed surprising in view of the fluctuating shape of melanocyte cells that are on average more than 10 times larger than *E. coli* cells. Moreover, these cells are active only if they have contact with the substrate. The unique description presented here supports the speculative idea that cell ensembles utilise intelligent strategies of making collective processes within cells in large or in small cells equally efficiently. One might come to the conclusion that unknown “learning” events of cell ensembles lead to self-organisation processes that fit like a key in a lock to the extremum principles of thermodynamics. Hence, growing cell ensembles might be called intelligent living colloid systems with fascinating universal properties.

If we put freely a value on the results presented it is – in our opinion – demonstrated that the extended version of the thermodynamics of irreversible processes seems to explain why in all circumstances genetics and thermodynamics guarantee together in a liberal but imperative manner why within a decent time window optimised stationary nonequilibrium cell ensembles of very different individual features can be achieved in a perfect manner.

References

1. Alberts B, Bray D, Johnson A, Lewis J, Raf FM, Roberts K, Walter P (1997) Essential cell biology. Garland, New York
2. Schlaechter M, Maaloe O, Kjeldgaard N (1958) J Gen Microbiol 19:592
3. Schlote FW (1961) Arch Microbiol 40:283
4. Kjeldgaard NO, Maaloe O, Schaechter M (1958) J Gen Microbiol 19:607
5. Prigogine I (1967) Introduction of thermodynamics of irreversible processes, 3rd edn. Wiley, New York
6. Haase R (1963) Thermodynamik der Irreversiblen Prozesse. Steinkopf, Darmstadt
7. Kilian HG, Koepf M, Vettegren VI (2001) Prog Colloid Polym Sci 117: 172
8. Ferry JD (1970) Viscoelastic properties of polymers. Wiley, New York
9. McCrum NG, Read BE, Williams G (1967) Anelastic and dielectric effects in polymer solids. Wiley, London
10. Kilian HG, Metzler R, Zink B (1997) J Chem Phys 107:8697
11. Kilian HG (2002) Colloid Polym Sci 280:661
12. Kilian HG, Gruler H, Koepf M () Phys Rev E (submitted)
13. Koepf M, Kilian HG (1999) Acta Polym 50:109
14. Metzler R, Schick W, Kilian HG, Nonnenmacher TF (1995) J Chem Phys 103:7180
15. Kilian HG, Glöckle W (1996) Acta Polym 47:150
16. Kraus V, Kilian HG, v Soden W (1992) Prog Colloid Polym Sci 90:27
17. Sheldrake R (2001) Das Gedächtnis der Natur (The presence of the past), 9th edn. Scherz, Frankfurt
18. Whitemann DC, Parsons PG, Green AC (1999) Arch Dermatol Res
19. Kemkemer R (2002) Thesis. University of Ulm

Etelka Tombácz
Tünde Nyilas
Zsuzsanna Libor
Csilla Csanaki

Surface charge heterogeneity and aggregation of clay lamellae in aqueous suspensions

Abstract Montmorillonite (2:1 layer silicate) is the most often studied swelling clay mineral. The faces of the lamellae have permanent negative charges owing to isomorphic substitutions, and pH-dependent charges develop on the surface hydroxyls at the edges. The acid–base titration of sodium montmorillonite suspensions at 0.01, 0.1 and 1 M NaCl was evaluated by fitting of potentiometric data measured between pH 4 and 9 using FITEQL. A surface complexation model assuming ion exchange on faces, and protonation–deprotonation processes at edges in the negative electrostatic field emanating from the particle face were introduced. This model provides excellent fitting of the measured points. The calculated number of edge sites was 3–4 mmol/100 g besides a permanent charge of 100 ± 2 mmol/100 g on the faces. The intrinsic equilibrium constants of the protonation and deprotonation processes were $\log K_{a1}^{\text{int}} = 5.1 \pm 0.1$ and $\log K_{a2}^{\text{int}} = -7.9 \pm 0.1$, respectively. The point of zero charge for edge sites was at $\text{pH} \sim 6.5$, i.e., positive charges can develop on the Al–OH sites of edges only at pHs below around 6.5. Study of the pH-

dependent particle aggregation showed the formation of stable suspensions at low (below 0.01 M NaCl) ionic strength even at low pH, where the edges are positively charged. However, an increase in salt concentration induces edge-to-face aggregation below $\text{pH} \sim 6.5$. X-ray diffraction patterns of montmorillonite films prepared from slightly acidic suspensions proved that the formation of well-ordered lamella packages is hindered by the attraction between edges and faces. Characteristic changes in gel formation and in the plastic, elastic and viscous properties induced by decreasing pH in dense suspensions containing 0.01 M NaCl provided experimental evidence for the structure of the particle network. The significant increase in thixotropy and yield values and also the formation of viscoelastic gels only below $\text{pH} \sim 6.5$ verify that attractive interaction exists between oppositely charged parts of lamellar particles.

Keywords Montmorillonite · Acid–base properties · Surface complexation model · Particle aggregation · Rheology

E. Tombácz (✉) · T. Nyilas · Z. Libor
C. Csanaki
Department of Colloid Chemistry,
University of Szeged, Aradi vt. 1.,
6720 Szeged, Hungary
e-mail: tombacz@chem.u-szeged.hu
Tel.: +36-62-544212
Fax: +36-62-544042

Introduction

Clays are finely divided crystalline aluminosilicates. Swelling clays (e.g. montmorillonite) are widely used as thickening agents in the formulation of, for example,

paints, cosmetics, pharmaceuticals, drilling fluids, and are abundant in natural porous media, such as soils and marls. The extent of swelling depends on the surface charging of clays and the solution condition of the aqueous medium, including ionic composition, ionic strength

and pH. The surface charge properties of clay particles influenced by the solution composition determine the formation, structure and strength of aggregates, and the migration of colloidal clay particles in a porous medium.

Montmorillonite is a 2:1 layer silicate (one octahedral alumina sheet sandwiched between two tetrahedral silica sheets). The main contribution to the surface charge of montmorillonite lamellae is the permanent negative charges on the basal planes owing to the isomorphous substitutions of the central Si and Al ions in the crystal lattice for lower positive valence ions [1, 2]. A negative charge associated with cation replacement in the tetrahedral layer (e.g., Al^{3+} for Si^{4+}) results in a localized charge distribution, whereas a much more diffuse negative charge comes from cation replacement in the octahedral layer (e.g., Mg^{2+} for Al^{3+}) [2]. This excess negative lattice charge is compensated by the exchangeable cations. Additional polar sites, mainly octahedral Al-OH and tetrahedral Si-OH groups, are situated at the broken edges and the exposed hydroxyl-terminated planes of clay lamellae [2]. These amphoteric sites are conditionally charged, and so variable (either positive or negative) charges can develop at the edges by direct proton transfer from the aqueous phase depending on the pH.

The surface charge characterization of clay minerals, when permanent charges from isomorphous substitutions of ions in a clay crystal lattice are present besides the variable edge charges, is more complicated than that of metal oxides. In this case, the intrinsic surface charge density, σ_{in} , can be defined as the sum of the net permanent structural charge density, σ_0 , and the net proton surface charge density, $\sigma_{0,\text{H}}$, i.e., $\sigma_{\text{in}} = \sigma_0 + \sigma_{0,\text{H}}$ [2, 3, 4, 5]. The point of zero charge (PZC), defined as the unique pH where the net surface charge is zero for amphoteric oxides bearing only pH-dependent charges, is not appropriate for clay minerals with both permanent and pH-dependent charges. Additional PZC definitions have to be introduced. The point of zero net proton charge for $\sigma_{0,\text{H}} = 0$ and the point of zero net charge for $\sigma_{\text{in}} = 0$ have been introduced by Sposito [4, 5]. Unfortunately, consistent terminology for points of zero charge has not been used in the literature yet, but nobody argues against their general importance to particle surface characterization.

To date, potentiometric titration is still a main approach to study the surface acid–base chemistry of clay minerals. Only some papers deal with the dissolution of a solid matrix resulting in various hydrolyzed aluminum species, silicic acid and their product – hydrous aluminosilicates, though their interaction with a clay surface should be considered in the modeling description. The surface complexation model (SCM) was successfully applied in a recent paper [6] to interpret surface acid–base reactions involving the dissolution of illite clays during prolonged titration. Voluminous literature on ion adsorption and surface complexation

modeling has appeared since the 1970s [7]. This largely describes the results of well-controlled laboratory investigations with a variety of mineral phases (mainly oxides) and ions. A consistent thermodynamic model (called as clay model) was developed for metal ion adsorption on swelling 2:1 layer clays such as montmorillonite [8]. The montmorillonite was considered as a porous solid bearing a permanent negative charge with an infinite plane interface defined as edges. A cation-exchange process occurred inside the porous solid, resulting in a negative potential of the clay. Surface complexation reactions could take place at the edges whose surface charge and potential are pH-dependent. The negative potential of the clay influenced the surface potential and therefore the surface complexation reactions at the edges. A new, different form of the classic Gouy–Chapman potential–charge relationship was implemented in the calculation. This model fits satisfactorily some experimental data (acid–base titration of montmorillonite at different ionic strengths [8, 9], Zn and Ni ion adsorption on montmorillonite at different pH [8]).

The previously discussed surface charge heterogeneity of clay minerals presented originally by van Olphen [1], then supported and elaborated further in many subsequent and recent investigations [3, 10, 11, 12, 13, 14, 15, 16, 17], governs the particle interactions in clay mineral suspensions. Although the overall particle charge is always negative, both negatively and positively charged parts on the surface of clay mineral particles exist simultaneously under acidic conditions. The attraction between the oppositely charged parts results in aggregates with an edge-to-face heterocoagulated structure below $\text{pH} \sim 7$, while face-to-face homocoagulated structures can form from the interaction of the charge-screened faces of clay lamellae. Not too much work has been published on the theoretical prediction (using Derjaguin–Landau–Verwey–Overbeek, DLVO, theory) of the pH-dependent stability of montmorillonite sols. Significant pH-dependence was found experimentally and explained from the theoretical point of view for an edge-recharged (phosphate-treated) H montmorillonite sample [10]. The effect of pH and permanent charges on the sensitivity of swelling clays to electrolytes was explained [18] on the basis of a theoretical concept similar to that in Ref. [10]. This approach proved to be effective in predicting the permeability reduction in porous media containing swelling clays [18]. Although a theoretical paper by Secor and Radke [19] published more than 20 years ago for spillover of the diffuse double layer on montmorillonite particles showed the exact solution of the Poisson–Boltzmann equation for a thin disc with a positive edge and negative face charges, it has been stated in a recent work [20], however, that DLVO theory is not capable of taking into account the double contribution of the total surface charge, i.e., patchwise surface charge heterogeneity of lamellae.

In any colloiddally stable suspensions the overall particle interaction is repulsive; therefore, particles repel each other and the freely moving primary particles endeavor to place themselves as far from each other as they can. Particles of colloiddally unstable suspensions collide and stick closely together, and so a more or less loose physical network of adhered particles forms in dense suspensions. Whatever the reason, the formation of particle networks strongly affects the mechanical flow properties of clay suspensions, which can be investigated by means of rheology. In general, stable suspensions show liquidlike (viscous) Newtonian flow behavior with shear thinning or thickening character, while the appearance of plastic character frequently together with thixotropy refers to the network formation of aggregated particles. The rheology of clay suspensions has been the subject of a tremendous amount of research for several decades, especially because of the wide-ranging practical application. Although the effects of several variables, i.e., suspension concentration, the quality and quantity of added salts, as well as the effect of thinning agents on the flow properties, have been investigated as seen, for example, in the excellent recent papers [21, 22], the pH-dependence has not been focused on yet.

The objective of the present work is to show how the pH-dependent surface charge heterogeneity of montmorillonite lamellae influences the particle interactions in suspensions, the ordering of lamellae and the structure of the particle network formed in montmorillonite gels, since a prudent determination of pH-dependent charging allowed us to model charge development at edges, and to interpret the pH-dependent surface charge heterogeneity of montmorillonite.

Materials and methods

Montmorillonite was obtained from Wyoming bentonite (USA). A clay mineral fraction smaller than 1 μm was prepared by allowing the larger particles to settle down in a dilute (10 g/l) suspension and then decanting. About 10% of bentonite was discarded. To obtain the monocationic sodium montmorillonite, the suspension was treated with 1 M NaCl. After centrifugation of the suspensions at 3,600 rpm, the supernatant solution was discarded and replaced with fresh solutions. The procedure was repeated three times. The ionic strength of the suspension was lowered progressively, first by washing with Millipore water and then by dialysis against 0.01 M NaCl, to that used in the experiments. The progress of dialysis was controlled by measuring the conductivities of the inner and outer phases daily. The lower electrolyte concentration of the medium was reached by dilution.

The pH-dependent surface charge was determined by potentiometric acid–base titration under a CO_2 -free atmosphere using NaCl electrolyte to maintain a constant ionic strength of 0.01, 0.1 or 1 M. Before titration the suspensions were stirred and bubbled with purified nitrogen for 1 h. Equilibrium titration was performed by means of a self-developed titration system (GIMET1) with 665 Dosimat (Metrohm) burettes, nitrogen bubbling, a magnetic stirrer, and a high-performance potentiometer at 25 ± 1 °C. The whole system (mV measurement, stirring, bubbling, amount and

frequency of titrant) was controlled by an IBM PS/1 computer using AUTOTITR software. A Radelkis OP-0808P (Hungary) combination pH electrode was calibrated for three buffer solutions to check the Nernstian response. The hydrogen ion activity versus concentration relationship was determined from reference electrolyte solution titration, so that the electrode output could be converted directly to hydrogen ion concentration instead of activity. In the first cycle, suspensions were titrated with standard HCl solution down to pH 4, then with standard base solution (NaOH) up to pH 9, then again with acid solution in the second cycle. The titration was reversible within the reproducibility of this method except for the first down curve of the montmorillonite suspensions at each ionic strength.

The net proton surface excess amount ($\Delta n_{\text{H}^+/\text{OH}^-}^\sigma$, moles per gram) is defined as the difference of H^+ ($n_{\text{H}^+}^\sigma$) and OH^- ($n_{\text{OH}^-}^\sigma$) surface excess amounts related to unit mass of solid, $n_{\text{H}^+/\text{OH}^-}^\sigma = n_{\text{H}^+}^\sigma - n_{\text{OH}^-}^\sigma$. The surface excess amount of any solute, like H^+ and OH^- here, can be determined directly from the initial and equilibrium concentration of solute for adsorption from dilute solution [23]. The values of $n_{\text{H}^+}^\sigma$ and $n_{\text{OH}^-}^\sigma$ were calculated at each point of the titration from the electrode output using the actual activity coefficient from the slope of H^+/OH^- activity versus concentration straight lines for background electrolyte titration.

Dynamic light scattering measurements were performed using a ZetaSizer 4 (Malvern, UK) apparatus operating at 633 nm produced by an He–Ne laser at scattering angle 90° at 25 ± 0.1 °C to determine the average particle size in dilute suspensions. The stock montmorillonite dispersion containing 0.01 M NaCl in equilibrium was diluted to reach constant solid content (0.05 g/l) and different (from 0.001 to 0.05 M) final concentrations of NaCl. The pH of the dilute suspensions was adjusted in the range 4–10, and measured directly before a sample was placed in the quartz cell. pH-dependent particle aggregation was measured at constant ionic strength. The correlation functions were evaluated by cumulant analysis [24]. The first-order autocorrelation function, $g^1(t)$, can be given as $|g^1(t)| = \exp(-\Gamma t + (\mu_2/2!)t^2 + (\mu_3/3!)t^3 + \dots)$, where Γ is an average decay rate; Γ characterizes the mean, μ_2 the width and μ_3 the skewness of the distribution. If $qR \ll 1$, translational diffusion is the dominant dynamics, and the diffusion coefficient, D_t , can be calculated, $\Gamma = D_t q^2$, where the scattering vector, \mathbf{q} , is $\mathbf{q} = (4\pi n/\lambda)\sin(\theta/2)$, and from the Stokes–Einstein equation, $D_t = kT/6\pi\eta R_H$, the hydrodynamic radius, R_H , can be obtained. (k is Boltzmann's constant, T is the temperature, η is the viscosity of the medium, n is the refraction index of the solution, λ is the laser wavelength and θ is the scattering angle.)

The X-ray diffraction pattern of oriented clay films on glass plates was determined over the scanning range $2^\circ < 2\theta < 15^\circ$ at room temperature by using a Philips PW 1830 X-ray generator with Cu K α ($\lambda = 0.154$ nm) radiation and a Philips PW 1820 goniometer operating in the reflection mode. The clay films were prepared from dilute sodium montmorillonite suspensions with pH values adjusted to around 9, around 6.5 and around 4 with 0.1 M NaOH or HCl solutions, respectively. The spreading of suspensions was spontaneous on the surface of carefully cleaned glass plates and thin layers were formed; these were dried in a dewatering box at around 100 °C.

The rheological measurements were performed with a Haake RS 150 shear-stress controlled rheometer and a cone–plate sensor (DC60/2° Ti) at 25 ± 0.1 °C controlled by a Haake DC 30/K20 thermostat. Three types of measurements were performed:

- The flow curve (upward) was measured with a shear-rate ramp over 1 min from 0 to 50 1/s, then the ramp was reversed to measure the downward flow curve. The area between the upward and downward curves was calculated as a measure for the thixotropy using the data analysis option of RheoWin software.

- The creep test was performed to determine the viscoelastic behavior under static conditions. A constant stress (0.3 Pa) was applied for 1 min and the resulting strain was measured (creep), then the stress was released and the strain was measured for 1 min (recovery). The shear creep compliance, J (reciprocal pascals), was calculated by dividing the measured shear strain, γ , by the applied stress, τ (pascals).
- The viscoelastic properties of the suspensions were also tested under dynamic conditions. In these measurements, a sinusoidal oscillating strain was applied with an assigned frequency and amplitude. A stress sweep from 0 to 10 Pa in the oscillation mode was applied at constant frequency (1 Hz). The magnitudes of the elastic (G' storage modulus) and viscous (G'' loss modulus) components of the samples tested can be evaluated from the time-dependent stress signal. The phase-shift angle, δ , which is 90° for purely viscous substances and zero for purely elastic substances, can also be calculated using RheoWin software.

Montmorillonite suspensions (4 g/100 g) containing 0.01 M NaCl were measured at pH~8.5, ~6.5 and ~5. The pH of the dense suspensions was adjusted by adding estimated amounts of 1 M NaOH or HCl solutions. The pH of the well-homogenized suspensions was measured, then all were stored in sealed vials under nitrogen for 1 day. The portions of suspensions were carefully placed on the measuring plate of the rheometer, and the measuring position was reached at low speed. The equilibrium pH values of the suspensions were measured after the rheological measurements. The pH shift during standing for 1 day was about 0.2–0.3 pH unit.

Results and discussion

Surface charge heterogeneity of montmorillonite particles

The charge heterogeneity of montmorillonite was characterized by potentiometric acid–base titration. A prudent preparation of montmorillonite suspension provided a well-defined initial state of titration and allowed us to use an evaluation method developed before for oxides [25], which assumes only the mass conservation law for H^+ / OH^- ions during titration. A constant NaCl concentration in the liquid phase and sufficient sodium saturation of ion-exchange sites on the surface was reached in an equilibrium dialysis of montmorillonite suspension against 0.01 M NaCl. The acid–base titration cycles at this ionic strength are shown in Fig. 1. The net proton consumption curves for sodium montmorillonite show a certain hysteresis, the first backward titration curve in the direction of decreasing pH is never repeated in a second backward titration after the forward titration up to pH~9, while these two latter curves seem to be reversible within the reproducibility of this experimental method. To test the reversibility of the acid–base processes, the same titration cycles were performed at higher salt concentrations by titrating sodium montmorillonite suspensions after diluting them with salt solution to adjust the final NaCl concentration to 0.1 and 1 M, respectively. The net proton consumption curves at different salt concentrations can be seen in

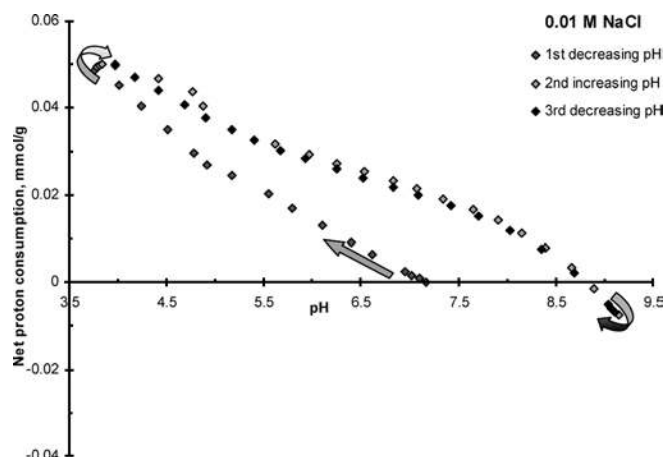


Fig. 1 Experimental net proton consumption curves for sodium montmorillonite dialyzed against and diluted with 0.01 M NaCl solutions at room temperature. The points were calculated from the data of an equilibrium titration cycle to test the reversibility of acid–base processes: first a backward titration (black symbols) with 0.1 M HCl solution, then a forward titration (gray symbols) with 0.1 M NaOH solution, finally a backward titration again

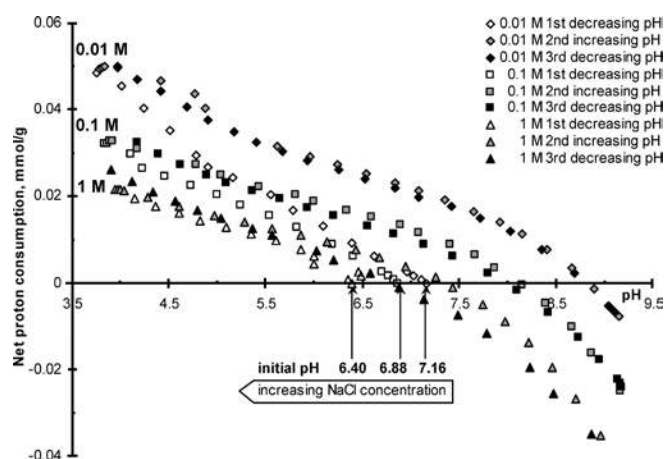


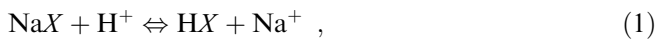
Fig. 2 Experimental net proton consumption curves for sodium montmorillonite dialyzed against 0.01 M NaCl solution then diluted with NaCl solutions to adjust the salt concentrations to 0.01, 0.1 and 1 M, respectively, at room temperature. The points were calculated from the data of an equilibrium titration cycle to test the reversibility of acid–base processes: first a backward titration (black symbols) with 0.1 M HCl solution, then a forward titration (gray symbols) with 0.1 M NaOH solution, finally a backward titration again

Fig. 2. The aforementioned hysteresis experienced to the highest degree at the lowest salt concentration decreases with increasing ionic strength, and almost disappears in the presence of 1 M NaCl. Apart from the first downward curves, the acid–base processes in montmorillonite suspensions under the given experimental condition can be considered as reversible equilibria.

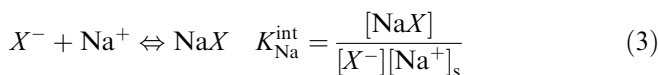
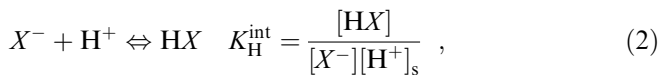
The acid–base titration data exhibit unusual characteristics compared to the “classic” curves usually

obtained for oxides [25, 26]. The reversible net proton surface excess curves at different ionic strengths similarly to those of the clays reported in the literature [8, 9] never intersect, nor can any common intersection point such as a PZC or a point of zero salt effect in the case of oxides [25, 26] be identified, and the extent of proton accumulation on the surface of the solid is always greater at lower ionic strength. It is remarkable how a characteristic decrease in the initial pH of the suspensions with increasing salt concentration was observed. It is indicative of the presence of permanent negative charges on the solid in question according to the basic principles of acid–base surface chemistry of soils [5].

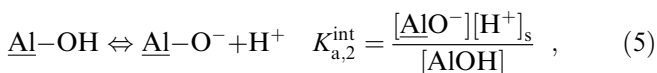
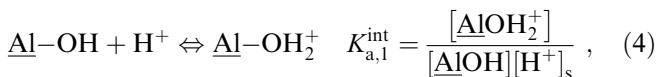
The evaluation of potentiometric data measured in the reversible cycles of acid–base titration at different ionic strengths allows us to calculate the pH-dependent charging of amphoteric edge sites besides the Na^+/H^+ ion-exchange process taking place on permanent charge sites of lamellae. We chose a simple model approach using the principles of the SCM. Our approach was similar to the simple model developed by Kraepiel et al. [9] for kaolinite clay. It was assumed that ion exchange on the particle face and protonation/deprotonation processes at the edges take place simultaneously in the negative electrostatic field emanating from the particle face. The exchange process for H^+ and Na^+ ions can be written as



where X is the solid matrix with permanent negative charges. This cation-exchange reaction can be incorporated into the SCM if X^- is defined as a negatively charged surface site on which the following surface reactions take place, and intrinsic equilibrium constants (K_i^{int}) can be defined:



A simple combination of equations for surface reactions, i.e., subtracting Eq. (3) from Eq. (2), gives the usual form of ion exchange in Eq. (1). The protonation and deprotonation reactions are defined only on the amphoteric Al-OH sites of the edges,



since Si-OH sites of broken edges are not relevant in forming positively charged patches on lamellae considering that only negative charges can be developed on a

silica surface above $\text{pH} \sim 4$ [26, 27]. The effect of a local electrostatic field with potential ψ_0 (below 0) has to be considered. The activity of surface ions, $[\text{H}^+]_s$ and $[\text{Na}^+]_s$, has to be corrected for the energy expended in moving them to the charged surface, where reactions occur. Expressing $[\text{H}^+]_s$ and $[\text{Na}^+]_s$ in term of the bulk solution activity, $[\text{H}^+]$ and $[\text{Na}^+]$,

$$[\text{H}^+]_s = [\text{H}^+] \exp\left(\frac{-e\Psi_0}{kT}\right) , \quad (6)$$

$$[\text{Na}^+]_s = [\text{Na}^+] \exp\left(\frac{-e\Psi_0}{kT}\right) , \quad (7)$$

which shows that concentration of H^+ and Na^+ ions at an electrified interface ($[\text{Na}^+]_s$ and $[\text{H}^+]_s$) is higher than in the bulk solution phase.

The potentiometric data measured in the reversible cycles at different ionic strengths were fitted between pH 4 and 9 by using FITEQL [28]. First, we assumed that the contribution of the ion-exchange process to the net proton consumption is negligible in the presence of the large excess of Na^+ ions, i.e., in 1 M NaCl solution, where the difference between the concentration of Na^+ and H^+ is at least 4 orders of magnitude over the pH range studied. The fitting of data belonging to 1 M NaCl was performed assuming only the surface site Al-OH with the reactions in Eqs. (4) and (5), the surface density of Al-OH was adjusted, and the $\log K$ values of the reactions in Eqs. (4) and (5) were optimized. Second, the surface site X^- with the reactions in Eqs. (2) and (3) was also introduced into the chemical model, and the $\log K$ values of the reactions in Eqs. (2) and (3) were optimized, meanwhile the other parameters (constant $\log K$ values for the reactions in Eqs. 4, 5) were fixed a priori on the basis of previous data optimization, and the surface densities of Al-OH and X^- groups were adjusted in fitting the titration data at 0.01 and 0.1 M NaCl. Finally, the total surface density of Al-OH was fixed to the most probable value and the extent of protonation and deprotonation was fitted at the highest ionic strength again also considering the ion-exchange processes in Eqs. (2) and (3). The permanent charge density was adjusted as an optimization parameter to yield the correct increase in the surface density of protons as the ionic strength decreases. The specific surface area of the clay was taken to be $800 \text{ m}^2/\text{g}$. The results are summarized in Table 1, and shown in Fig. 3.

Despite the great simplicity of this SCM approach, the model provides excellent fitting for the pH-dependent net proton surface excess functions of montmorillonite at all ionic strengths (Fig. 3). In particular, the extent of protonation of the solid is correctly predicted to be always greater at lower ionic strength than at higher salt concentrations. This is the consequence of the negative surface charge, even at low pH, and so the Coulombic

Table 1 Material feature and interfacial acid–base processes assumed in the surface complexation model for montmorillonite, and the results of fitting potentiometric acid–base titration data at different ionic strengths.

Active sites on montmorillonite lamellae		Results	Literature
Constant charges on plates 100 ± 2 mmol/100 g	Terminal Al-OH at edges $< \sim 10$ mmol/100 g	$\text{Al-OH}_{\text{tot}}$ (mmol/100 g) 3–4	5 [20]
Processes		LogK	
Ion exchange $\text{NaX} + \text{H}^+ \rightleftharpoons \text{HX} + \text{Na}^+$			
Modeling $\text{X}^- + \text{H}^+ \rightleftharpoons \text{HX}$		8.77	
$\text{X}^- + \text{Na}^+ \rightleftharpoons \text{NaX}$		0.78	
Protonation/deprotonation $\text{Al-OH} + \text{H}^+ \rightleftharpoons \text{Al-OH}_2^+$		5.1 ± 0.1	
$\text{Al-OH} \rightleftharpoons \text{Al-O}^- + \text{H}^+$		-7.9 ± 0.1 Point of zero charge of edges	
		~ 6.5	
		6.5–7 [8, 9]	

Note: Only deprotonation reactions are assumed on the surface site $=\text{SOH}$ in the clay model [8, 9]:
 $=\text{SOH}_2^+ \rightleftharpoons =\text{SOH} + \text{H}^+$, K_{a1} ,
 $=\text{SOH} \rightleftharpoons =\text{SO}^- + \text{H}^+$, K_{a2}

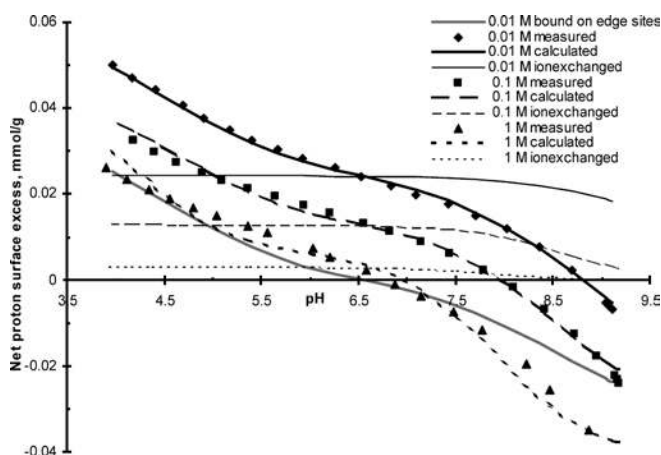


Fig. 3 Experimental points of net proton surface excess amounts from the reversible backward titration cycles of sodium montmorillonite at different NaCl concentrations. The different lines represent the results of numerical fitting (FITEQL [28]) using the diffuse-double-layer option of the surface complexation model assuming reactions of H^+ and Na^+ ions with permanently charged ion-exchange sites in parallel with protonation/deprotonation reactions on amphoteric edge sites

attraction of H^+ is greater at low ionic strength over the whole range of pH. Our model approach predicts that the effect of the ionic strength depends on the relative magnitude of the permanent and variable surface charge densities. Therefore our conclusion for different montmorillonite samples is the same as that of Kraepiel et al. [8, 9], i.e., one should thus expect to observe different behavior among different samples of kaolinite with varying extent of isomorphic substitution.

The calculated number of edge sites was 3–4 mmol/100 g, which is somewhat smaller than that (5 mmol/100 g) for another clay in a recent paper [20], and that (around 10 mmol/100 g) estimated usually as around 10% of the cation-exchange capacity (here 100 ± 2 mmol/100 g). The calculated intrinsic equilibrium

constants of protonation and deprotonation processes are $\log K_{a1}^{\text{int}} = 5.1 \pm 0.1$ and $\log K_{a2}^{\text{int}} = -7.9 \pm 0.1$, respectively, which agree well with the $\log K_{a1} = -5$ and -5.6 and $\log K_{a2} = -8.5$ and -8.7 values of the deprotonation reactions defined as $=\text{SOH}_2^+ \rightleftharpoons =\text{SOH} + \text{H}^+$, K_{a1} , $=\text{SOH} \rightleftharpoons =\text{SO}^- + \text{H}^+$, K_{a2} , in the clay model [8, 9]. The PZC of edge sites can be given at $\text{pH} \sim 6.5$ in good harmony with the recently published values $\text{pH} \sim 6.5$ –7 [8, 9]. Positive charges can develop on the Al-OH sites of edges at pH below around 6.5; however, these are hidden at low electrolyte concentration when the negative electrostatic field emanating from the face of the particles covers them [19].

Particle aggregation in dilute suspension

The pH-dependence of the hydrodynamic radius calculated from the cumulant analysis of first-order correlation functions is shown in Fig. 4. It should be mentioned that the reproducibility of the size data obtained for colloidal stable systems was very good (within $\pm 5\%$), and though the relation $qR \ll 1$ was obviously not fulfilled, the size data obtained at different scattering angles (between 60° and 120°) did not show too large a systematic difference (the average hydrodynamic radius values varied from 460 to 320 nm). The size distribution function of well-stabilized montmorillonite sol was very broad, when a monomodal distribution was assumed, and a multimodal analysis of the data resulted in a bimodal particle size distribution. In the unstable suspensions, however, the particle size measured increased in time, showing the progress of coagulation. Therefore, the larger sizes measured are suitable only to compare a given kinetic state of coagulating systems.

The colloidal stability of charged particles is actually determined by their surface charge state. The pH-dependent aggregation of montmorillonite particles in

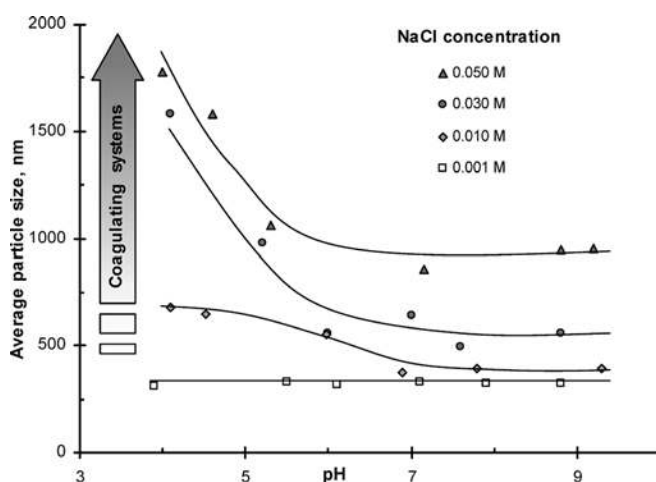


Fig. 4 pH-dependent particle aggregation of montmorillonite particles at different ionic strengths using electrolyte NaCl. (Sizes larger than around 500 nm show a given kinetic state of the coagulating systems.)

dilute suspensions shows that the highly charged particles form stable suspensions at low ionic strength, and the average particle size is almost constant above pH 4 as explained elsewhere [15, 29], independent of the existence of oppositely charged parts on the lamellae. In principle the positively charged edges can interact with the negative basal plates below pH~6.5; however, edge-to-face heterocoagulation does not take place at such a low ionic strength because of the spillover of the negative electrostatic field emanating from the face of montmorillonite plates [19]. Coagulation kinetics studies on montmorillonite sol have shown that diffusion-limited aggregation can be induced by a 1:1 electrolyte (NaCl) concentration higher than 40 mM at pH~4 [30]. This value is in good agreement with the critical coagulation concentration of sodium-rich Wyoming montmorillonite dispersions (critical coagulation concentration of 15–30 mM for coagulating electrolyte NaCl [31]). It correlates well with the theoretical prediction of Secor and Radke [19] for spillover of the diffuse double layer on montmorillonite particles. The exact solution of the Poisson–Boltzmann equation for a thin disc with positive edge and negative face charges revealed that for salt content below about 10 mM the negative electrostatic field emanating from the particle face spills over into the edge region; therefore, the positively charged edge exhibits a negative electrostatic field. This results in a repulsive electrostatic potential for interparticle edge-to-face interaction. At 100 mM, where the diffuse layer is highly compressed and so the edge exhibits a positive electrostatic field, an edge-to-face electrostatic attraction is expected. Therefore, the theoretically predicted region of edge-to-face aggregation falls into 10–100 mM of 1:1 salt concentration.

Ordering of lamellae in a montmorillonite film formed from dilute suspensions

Although the fact that dewatering of montmorillonite suspensions results in a smooth layered solid phase, i.e., montmorillonite lamellae can spontaneously organize themselves into an oriented clay film, is well known and is certainly used in some applications, a systematic study on the why and how questions has not been published yet. We suppose that surface charge heterogeneity of highly anisometric montmorillonite plates influences the ordering of lamellae in the self-oriented films. As mentioned the number of amphoteric edge sites is not significantly related to the total charge of particles; however, pH-dependent charge development (either Al-OH_2^+ or Al-O^-) on the Al-OH sites of broken edges governs the particle interactions. An edge-to-face heterocoagulated assembly of lamellae can form only below pH~6.5, where the edges are positively charged and the parallel orientation of thin lamellae is hindered.

X-ray diffraction patterns of oriented montmorillonite films (Fig. 5) prepared from suspensions with different pH (4, 6.5 and 9) obviously support this assumption. The formation of packets of lamellae ordered parallel to each other is hindered with decreasing pH, since the intensity of the basal plane reflection (d_{001} at around $7^\circ 2\theta$) decreases considerably with decreasing pH. We suppose the formation of random edge-to-face fractal aggregates below pH~7 and an oriented face-to-face structure above pH~8.

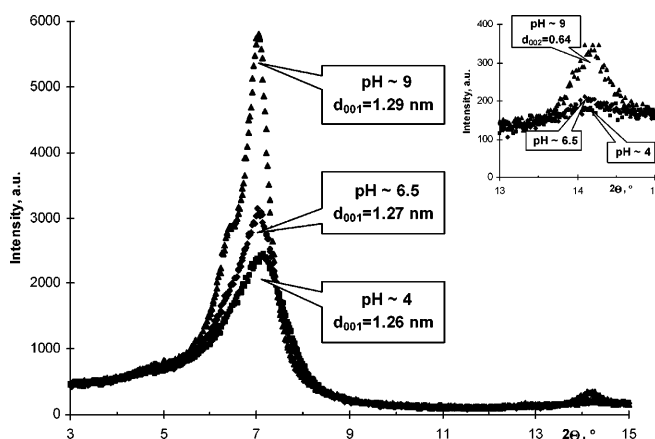


Fig. 5 X-ray diffraction patterns of oriented montmorillonite films on a glass plate prepared from dilute montmorillonite suspensions with different pH at (around 6.5), above (around 9) and below (around 4) the pH of the point of zero charge (PZC) of the edges, where the edges of the lamellae are uncharged, and either similarly or oppositely charged compared to the faces of the particles, respectively

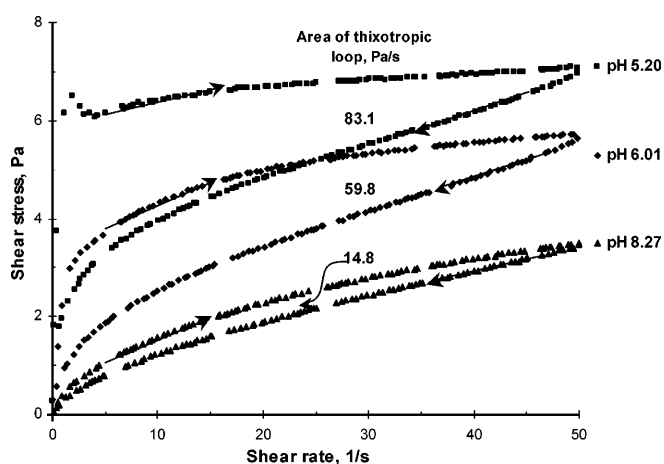


Fig. 6 Flow curves measured with an increasing (upward) then decreasing (downward) shear rate ramp for 4 g/100 g sodium montmorillonite suspensions containing 0.01 M NaCl at different pH above (8.27) and below (6.01 and 5.20) the pH of the PZC of the edges (around 6.5) at 25 ± 0.1 °C

Particle aggregation in dense systems

Formation and mechanical properties of particle network in suspensions can be investigated by means of rheology. Here we investigated the formation of the pH-dependent structure in a montmorillonite suspension.

The results of the most frequently used rheological measurements, the steady-state flow curves of montmorillonite suspensions at different pH, are shown in Fig. 6. The significant change in flow character with decreasing pH is obvious, and it is clearly visible that the upward and downward curves are not identical, especially at pH below the PZC of amphoteric edges. The edges of the lamellae are negatively charged in alkaline suspension; therefore, the whole surface of the lamellae bears similar charges. The uniformly charged particles repel each other, a gel structure cannot form, and so the stable montmorillonite sol shows shear-thinning flow character with a small thixotropy (bottom curve). A decrease in pH slightly below the PZC of the amphoteric edges causes a significant change in flow behavior. A definite plastic character appears and the large thixotropic loop (middle curve) relates to the formation of a time-dependent gel structure in the suspension. In an acidic suspension (uppermost curve at pH~5.2) a strong attractive gel [21], here the edge-to-face heterocoagulated network, can form because of the attraction of oppositely charged edges and faces of montmorillonite platelets. The area of the thixotropic loops increases with decreasing pH, showing the increasing ability of the montmorillonite suspension for gelation. Extrapolation of the downward curves over the plastic flow range (above around 15 1/s) to zero shear rate results in yield values. It increased with decreasing pH, similarly to the effect of increasing salt concentration [21]. The yield is proportional to the

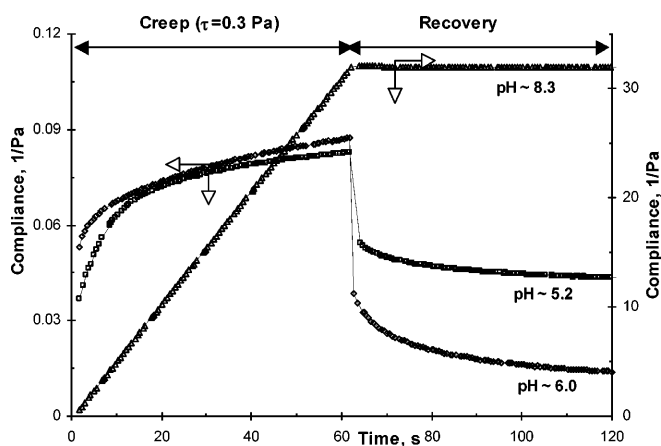


Fig. 7 Creep and recovery results for 4 g/100 g sodium montmorillonite suspensions containing 0.01 M NaCl at different pHs above (8.3) and below 6.0 and 5.2) the pH of the PZC of the edges (around 6.5) at 25 ± 0.1 °C.

mechanical strength of the physical network and depends on the number and the strength of the bonds between particles in unit volume of the suspensions [32]. The lower the pH the greater the number of positive charges on the edges of the clay plates; therefore, the attraction between the positively charged edges and negative basal plates becomes stronger with decreasing pH.

The viscoelastic properties of montmorillonite suspensions were also studied. A series of creep and recovery curves measured at different pH are shown in Fig. 7. The behavior of an alkaline suspension is essentially different from that of acidic ones, in good harmony with the features of the flow curves. Almost ideal Newtonian (liquidlike) behavior was detected for a suspension containing uniformly charged particles at pH~8.3, since deformation continually increased in a linear manner as long as the stress was applied, and there was no restoration at all in the absence of attraction between particles. However, for suspensions below pH~6.5, where the particle network can build in dense suspensions owing to attractive forces between the oppositely charged parts of the lamellae, an elastic response in the jellylike suspensions definitely appears besides viscous deformation at the given shear stress, since a significant part of the deformation was reversible (elastic). The contribution of the elastic component to the viscoelastic deformation of the sample is obvious since the applied stress results in an instantaneous strain jump which is restored after being released; however, a significant nonrecoverable deformation remained owing to the presence of the viscous component. This creep test proved that an attractive gel forms below the pH of edge PZC owing to the electrostatic attraction between positively charged edges and negatively charged plates of montmorillonite lamellae, and has considerable elasticity besides viscous properties. It has to be mentioned that

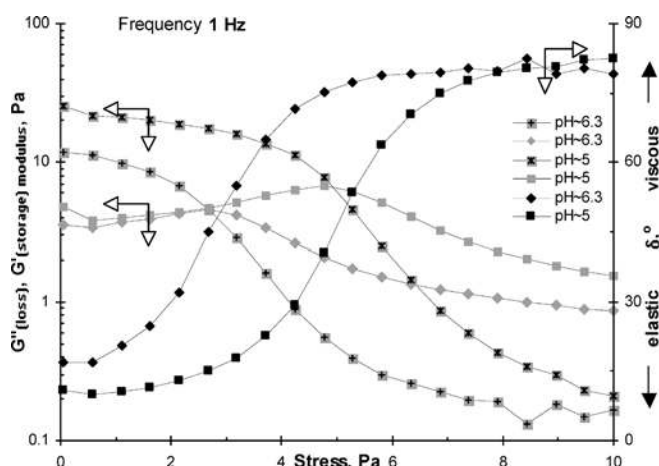


Fig. 8 Storage (G' , crosses) and loss (G'' , gray squares, gray diamonds) moduli, and phase-shift angle (δ° , black squares, black diamonds) of 4 g/100 g montmorillonite suspensions at pH~6.3 and pH~5 as a function of the applied shear stress at $25 \pm 0.1^\circ\text{C}$

there is an elastic response of thixotropic montmorillonite gels only if the applied stress is below the yield values.

The stress sweep in forced oscillation experiments showed (Fig. 8) that the elastic (G' storage) modulus is larger than the viscous (G'' loss) modulus at low stresses. However, when an increasing stress is applied this relation is reversed at stresses of around 2.5 and around 5 Pa for suspensions with pH~6.3 and pH~5, respectively, showing the breakdown of the elastic particle network and the appearance of dominant viscous flow at stronger shear forces. A similar trend is obvious from the change in phase-shift angle (δ) with increasing stress from $10\text{--}20^\circ$ characteristic of a more elastic body to around 80° close to purely viscous substances. The magnitude of the storage moduli measured here is comparable with the values published recently for different montmorillonite suspensions, in which the effect of coagulating electrolytes [21] and liquefying humic acid [22] was investigated. A sharp decay of the storage modulus at a shear stress of around 1 Pa applied in the oscillatory experiment at 1 Hz was measured in 5% w/w sodium montmorillonite suspension (pH~7, 0.01 M NaCl) [22] in accordance with our results at lower pHs. Aggregation by NaCl was accompanied by an increase in yield and storage moduli [21], similarly to the effect of decreasing pH here.

Conclusion

In aqueous systems, the colloidal interactions between clay mineral particles are generally governed by a local

electrostatic field developing around the particles owing to the neutralization of surface charges. The composition of the aqueous solution influences both the surface charging and the charge neutralization. Among clay minerals montmorillonite (2:1 layer silicate) as the most often studied swelling clay was chosen for a comprehensive study to show how the pH-dependent surface charge heterogeneity of clay lamellae influences the particle interactions in suspensions, the ordering of the lamellae and the structure of the particle network formed in montmorillonite gels. A prudent determination of pH-dependent charging allowed us to model charge development at edges, providing an adequate description of acid–base properties of montmorillonite by incorporating an appropriate chemical model into the SCM. Therefore a quantitative interpretation of pH-dependent surface charge heterogeneity of montmorillonite becomes practicable. Montmorillonite particles have both permanent negative charges on faces and pH-dependent charges mainly on Al-OH sites at the broken edges. These clay lamellae have patchwise charge heterogeneity below the pH of the PZC of the edges (around 6.5), where positively charged, protonated Al-OH_2^+ sites exist to a small degree (around 0.03 mmol/g) related to the abundance of permanent charges (around 1 mmol/g) on faces. Edge-to-face heterocoagulation between the oppositely and poorly charged parts of platelets is induced by a relatively low salt concentration (typically between 10 and 50 mM 1:1 electrolyte) at and below the pH of the PZC of edge sites. While well-ordered lamellae packets cannot form in montmorillonite films under these conditions, the gelation of montmorillonite sols is advanced, and the easy formation of semisolid attractive gels with significant thixotropy and viscoelasticity is obvious below pH~6.5. At higher pH, however, the repulsion is the overall interaction between the uniformly charged lamellae, and so rather liquidlike, colloiddally stable montmorillonite sols exist in dilute salt solutions. The homocoagulation of uniformly charged lamellae and the formation of face-to-face aggregates requires a much higher salt concentration to screen the highly charged surface of particles. It would be worth paying greater attention to the role of pH in the behavior of clay suspensions not only in laboratory studies but also in practical applications.

Acknowledgements This work was supported by the grant OTKA T 034755. The authors are grateful to FLORIN Rt. for providing the Haake RS150 rheometer.

References

1. Van Olphen H (1963) An introduction to clay colloid chemistry. Interscience, New York
2. Johnston CT, Tombácz E (2002) In: Dixon JB, Schulze DG (eds) Soil mineralogy with environmental applications. Soil Science Society of America, Madison, WI, pp 37–67
3. Tombácz E (2002) In: Tóth J (ed) Adsorption: theory, modeling, and analysis. Dekker, New York, pp 711–742
4. Sposito G (1992) In: Buffle J, van Leeuwen HP (eds) Environmental particles, vol 1. Lewis, Boca Raton, pp 291–314
5. Sposito G (1984) The surface chemistry of soils. Oxford University Press, New York
6. Liu W (2001) Water Res 35:4111
7. Davis JA, Coston JA, Kent DB, Fuller CC (1998) Environ Sci Technol 32:2820
8. Kraepiel AML, Keller K, Morel FMM (1999) J Colloid Interface Sci 210:43
9. Kraepiel AML, Keller K, Morel FMM (1998) Environ Sci Technol 32:2829
10. Tombácz E, Ábrahám I, Gilde M, Szántó F (1990) Colloids Surf 49:71
11. Zhao H, Low PF, Bradford JM (1991) Soil Sci 151:196
12. Thompson DW, Butterworth JT (1992) J Colloid Interface Sci 154:236
13. Zhou Z, Gunter WD (1992) Clays Clay Miner 40:356
14. (a) Heil D, Sposito G (1993) Soil Sci Soc Am J 57:1241; (b) Heil D, Sposito G (1993) Soil Sci Soc Am J 57:1246
15. Keren R, Sparks DL (1995) Soil Sci Soc Am J 59:430
16. Sondi I, Milat O, Pravdic V (1997) J Colloid Interface Sci 189:66
17. Schroth BK, Sposito G (1997) Clays Clay Miner 45:85
18. Mohan KK, Fogler HS (1997) Langmuir 13:2863
19. Secor RB, Radke CJ (1985) J Colloid Interface Sci 103:237
20. Missana T, Adell A (2000) J Colloid Interface Sci 230:150
21. Abend S, Lagaly G (2000) Appl Clay Sci 16:201
22. Ramos-Tejeda MM, de Vincente J, Ontiveros A, Duran JDG (2001) J Rheol 45:1159
23. Everett DH (1988) Basic principles of colloid science. Royal Society of Chemistry, London
24. Brown W (ed) (1993) Dynamic light scattering. Oxford University Press, New York
25. Tombácz E, Szekeres M (2001) Langmuir 17:1411
26. James RO, Parks GA (1982) In: Matijevic E (ed) Surface colloid science, vol 12. Plenum, New York, pp 119–216
27. Tombácz E, Szekeres M, Kertész I, Turi L (1995) Prog Colloid Polym Sci 98:160
28. Herbelin AL, Westall JC (1996) FITEQL v.3.2. Oregon State University, Corvallis, OR, USA
29. Tombácz E, Csanaky Cs, Illés E (2001) Colloid Polymer Sci 279:484
30. Tombácz E (2003) In: Bárány S (ed) The role of interfaces in environmental protection. NATO ASI series. Kluwer, Dordrecht, pp (in press)
31. Penner D, Lagaly G (2000) Clays Clay Miner 48:246
32. Firth BA, Hunter RJ (1976) J Colloid Interface Sci 57:248

Miklós Vörös
Attila Agod
Péter Basa
Miklós Zrínyi
Zoltán Hórvölgyi

Analysis of the cluster size distribution of two-dimensional aggregates in terms of polydispersity

M. Vörös · A. Agod · P. Basa
M. Zrínyi · Z. Hórvölgyi (✉)
Department of Physical Chemistry,
Budapest University of Technology and
Economics, 1521 Budapest, Hungary
e-mail: zhorvolgyi@mail.bme.hu
Tel: +36-1-4632911
Fax: +36-1-463-3767

Abstract We report a study of the aggregation of silylated glass spheres at the water–air interface. The particle size (75- μm diameter) was selected so that the aggregation could be recorded in situ by a digital camera. Numerous relevant parameters of the aggregation can be expressed as functionals of the cluster size distribution function (e.g. size and number of clusters, polydispersity). Our goal was to find links between these functionals

and measurable quantities such as the surface coverage of the aggregation area. We compared the aggregation of the systems of various starting conditions through the aforementioned functionals in real experiments and computer simulations.

Keywords Interfacial aggregation · Cluster size distribution · Polydispersity · Microbeads · Computer simulation

Introduction

Aggregation phenomena are remarkable topics of recent scientific interest [1, 2, 3, 4, 5, 6, 7, 8, 9, 10, 11, 12, 13, 14, 15, 16, 17, 18, 19, 20, 21, 22]. The 2D aggregation of microparticles at a liquid–fluid interface can serve as a model for the investigation of general aspects of growth [3, 4, 5, 6, 7, 8, 9, 10, 11, 12, 13, 14], particle ordering, phase transitions [23] or surface thermodynamics [24, 25, 26, 27]. The microparticles trapped at the interface are influenced by two relevant attractive forces: short-range (nanometre) colloid and long-range (millimetre) capillary forces [1]. The properties of these forces mainly depend on the sizes and the wettabilities of the particles [1, 28, 29, 30, 31]. In this work we study the aggregation of 75- μm diameter silylated glass spheres at the water–air interface.

The size distribution function of the clusters is a favourable tool to reveal statistical information of the aggregation process. The goal of our work was to find links between the cluster size distribution (CSD), its functionals and other aggregation parameters (aggregation area, initial surface coverage of the

primary particles). We investigated and analysed the time evolution of the size distribution and its functional – the polydispersity. We compared the aggregation of real and simulated systems of different initial surface coverage. In the experiments we used hydrophobic particles having water contact angles of 90° [32].

We present the experimental results of the time evolution of the polydispersity, and the changes in the aggregation mechanism, and discuss the mathematical background of the observed phenomena. In the mathematical analysis we do not limit the dimensionality of the system; thus, the results are readily applicable for 3D aggregating systems as well.

In the next section of the paper we give a description of the experimental methods used in this work.

Materials and methods

For the aggregation experiments distilled water and glass microbeads (Supelco, $75 \pm 5 \mu\text{m}$ diameter, $2,500 \text{ kg m}^{-3}$ density) were used. The surface of the glass beads was rendered hydrophobic by

silylation. The hydrophobicity was characterised by the water contact angle, Θ , which was determined from the optical microscope images of the particles situated at the water–air interface between two plane-parallel glass plates [32]. The aggregation experiments were carried out in a Petri dish (13.0-cm diameter). The glass particles were scattered uniformly through a sieve onto the central and circular area (effective area of aggregation approximately 64 cm²) of the liquid surface. In order to prevent external contamination, the Petri dish was covered by a plane-parallel glass plate, which also provided an equilibrated vapour atmosphere above the liquid. Aggregation experiments of various initial surface coverages (2.2–8.4%) were carried out.

The aggregation phenomena were recorded by a computer-controlled Nikon Coolpix 995 digital camera in 10–15-s intervals. The digital images (24 bit) were sharpened and transformed to binary images (1 bit).

In addition to real experiments, off-lattice molecular dynamics computer simulations [2] were run to get a deeper understanding of the experimental results. The values of the aggregation parameters used in the simulations are given in Table 1.

The output of the simulation was a set of binary images of the same format as those of the real experiments. The images from the two sources were treated identically during the analysis.

The model system

Microscopic glass beads of higher density than water can, owing to the partial wetting of their surface, be trapped at a water–air interface, giving us a way to study 2D aggregations. These particles experience the influence of three forces: the capillary, the colloid, and the drag forces. The long-range interparticle hydrophobic capillary attraction is the driving force of the aggregation. Its emergence is due to gravity and the curved water surfaces. The short-range interparticle colloid attraction locks the relative position of the adjoining particles so that in these systems no significant cluster restructuring can take place. The hydrodynamic drag slows the motion of the particles relative to that of water; thus, on the one hand, it acts as a braking force that slows the formation of clusters and, on the other hand, it intermediates the driving effects of the surface flows induced by thermal inhomogeneities.

Tools of the analysis

First let us define the mathematical tools that we will use throughout this article.

Surface coverage

By the surface coverage, ρ , of the particles we understand the ratio of the area occupied by the aggregating particles and the effective aggregation area. We generally approximate the value of ρ from the experimental images by counting the pixels of particles and divide that number by the total number of pixels in the image of the aggregation area.

Mean size of the clusters

In order to be able to compare different aggregating systems we need a timelike quantity. Simply using the aggregation time is generally useless, since different aggregations can have radically different time evolution. Instead, we used n_m , the number average of the cluster sizes defined as

$$n_m = \frac{\sum_s n_s s}{\sum_s n_s} = \frac{n_p}{n_c} \quad (1)$$

In Eq. (1) n_s is the number of clusters of size s (clusters that contain s primary particles), the summation is for all available s sizes, n_p is the number of the primary particles, and n_c is the number of the clusters in the system. From now we will call n_m the mean size of the clusters.

Polydispersity

Polydispersity shows how broad the CSD is: a low value of π ($\pi \approx 1$) indicates a narrow size distribution, a high value indicates a broad size distribution. The π polydispersity of the CSD function is, by definition, the ratio of its mass and number average:

$$\pi = \frac{\sum_s n_s s^2}{\sum_s n_s s} \bigg/ \frac{\sum_s n_s s}{\sum_s n_s} = \frac{\left(\sum_s n_s\right) \left(\sum_s n_s s^2\right)}{\left(\sum_s n_s s\right)^2}, \quad (2)$$

$$\pi = \frac{n_c \left(\sum_s n_s s^2\right)}{n_p^2} = \frac{\left(\sum_s n_s s^2\right)}{n_m n_p}.$$

If all the clusters are of the same size (there is only a single s for which n_s is nonzero) the sums disappear and $\pi = 1$. For all other cases $\pi > 1$.

If the sizes of all the clusters in an aggregation are multiplied by α ($s' = \alpha s$), or the number of clusters is multiplied by β ($n_s' = \beta n_s$), the polydispersity remains unchanged:

$$\pi' = \frac{\left(\sum_s \beta n_s\right) \left(\sum_s \beta n_s \alpha^2 s^2\right)}{\left(\sum_s \beta n_s \alpha s\right)^2} = \frac{\alpha^2 \beta^2}{\alpha^2 \beta^2} \pi = \pi. \quad (3)$$

Therefore, the polydispersity of a homogeneous system is the same as that of its similar subsystems. Thus, the polydispersity of an infinitely large system can be estimated by using a cell of finite size because it should have a similar size distribution to the original system provided that the finite-size effects can be neglected. The other important consequence is that instead of counting the number of particles in a cluster, one may count the number of its pixels, calculate the polydispersity and reach the same result. This allows us to use simple algorithms, instead of having to deal with complex shape recognition software.

Table 1 Aggregation parameters used in the simulations

Parameter	Default value	Range of modification	Brief description
n_p	3,000	1,000–10,000	The number of aggregating particles
R	10	2–100	Radius of the aggregation area (mm)
erc	1	0.4–1.6	Multiplicative correction of the range of the capillary force (effective range correction)

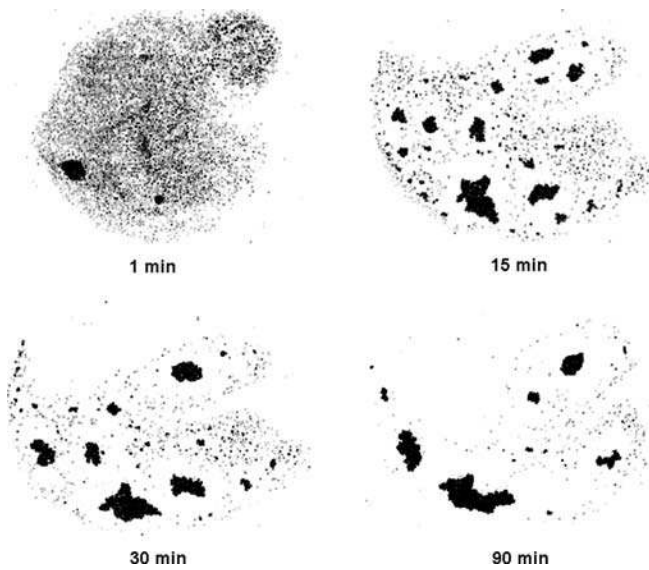


Fig. 1 Aggregation of hydrophobic spheres (90° water contact angle, 8.4% surface coverage) in the 1st, 15th, 30th and 90th minutes

Experimental results

Time evolution

Visual observations

Different stages of a typical aggregation of highly hydrophobic spheres are shown in Fig. 1. It can be seen that many separate large clusters form first, then they make up the final cluster.

Aggregation kinetics

The aggregation kinetics in these systems is generally considered to be of second order [33], at least at the beginning of the aggregation. That is, the following equation holds for the independent kinetic units:

$$\frac{1}{n_c} - \frac{1}{n_p} = kt \quad \text{or} \quad n_m = ktn_p + 1, \quad (4)$$

where k is the kinetic constant that indicates the rate of the aggregation. n_m is plotted as a function of the aggregation time in Fig. 2.

It can be seen that the observed system has second-order aggregation kinetics in the first 90 min. In the later stages (not shown here) the system deviates from the second-order kinetics [2], which can be seen as a significant rise in the kinetic curve.

Polydispersity

Next we investigate the time evolution of the polydispersity functional. At the beginning of the aggregation

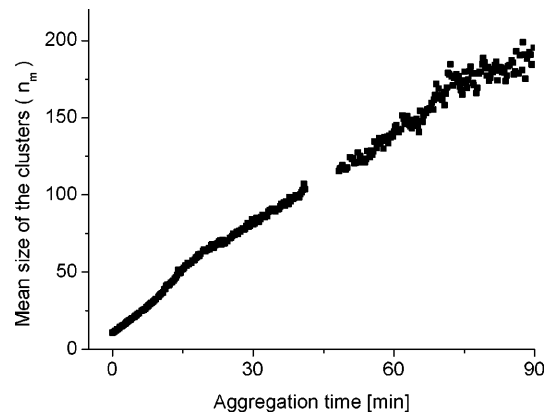


Fig. 2 Aggregation kinetics of the present system (90° water contact angle, 8.4% surface coverage)

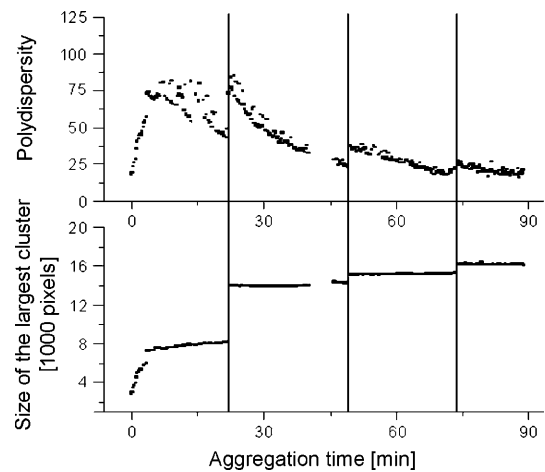


Fig. 3 Time evolution and discontinuities of the polydispersity in the present system (90° water contact angle, 8.4% surface coverage)

only primary particles are in the system, the sum and the number average are the same; thus $\pi = 1$. Also if it comes to that at all, at the end of the irreversible aggregation process all the particles are in the same cluster, making $\pi = 1$. In between we expect the polydispersity to be a maximum curve.

To illustrate the role of $\pi(t)$ in the analysis of the aggregation process, we have plotted the polydispersity together with the size of the greatest cluster in Fig. 3.

It can be seen that $\pi(t)$ starts out as a smooth function, but later it shows large discontinuities that correspond well to major events in the aggregation, such as the fusion of two clusters that contain a significant fraction of the particles. This effect is obviously due to the finite size of the observed system. Through mathematical considerations we learnt that the size of the jump in π is proportional to the product of the sizes of the colliding clusters. The details can be found in Appendix 1.

By plotting the polydispersity of various systems versus the mean size of the clusters on a logarithmic

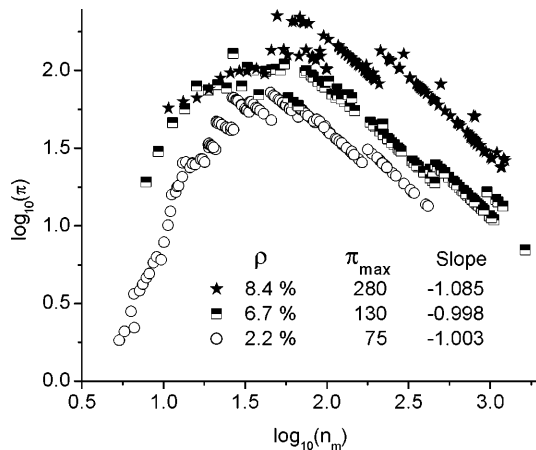


Fig. 4 Polydispersity (π) versus mean size (n_m) of clusters in real systems of various initial surface coverages of particles on a log-log scale; also illustration of the linear sections. ρ is the surface coverage, π_{\max} is the polydispersity maximum, and *slope* is the slope of the linear fit of rightmost part of the curves

graph (Fig. 4), we see that the descending sections of the resulting curves are linear.

The linear fit ($Y = aX + b$) of the graphs yielded slopes ($a = -0.97 \pm 0.09$) that are approximately -1 , i.e. the polydispersity of the system is directly proportional to the number of clusters for all the observed systems (cf. Eq. 1). This region of proportionality is fairly large: it can occupy half of the total aggregation time (measured by the change in the mean cluster size). The linear approximation becomes better towards the end of the aggregation, as the slope converges to -1 . The region of proportionality was observable for all the test systems whether real (Fig. 4) or simulated (Fig. 5).

Simulated systems have another proportional section on the π - n_m diagrams (Fig. 5). At the beginning of the aggregation, while π is smaller than 3 it is well approximated by the mean size of the clusters ($\pi \approx n_m$). Real experiments have not yet shown this behaviour owing to the shortcomings of the experimental setup.

The effects of system parameters on the polydispersity

We assume a link between the maximum of the polydispersity reached by an aggregating system and the aggregation mechanism, and study the effects of changing various starting conditions in real experiments and computer simulations.

The effects of changing the range of the particle-particle interaction (simulations)

To investigate the possible changes in the aggregation mechanisms, we ran computer simulations of a system of

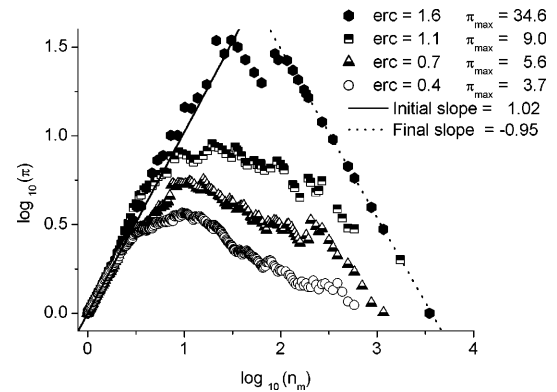


Fig. 5 Polydispersity versus mean size of clusters in simulated systems with different effective ranges for the capillary attraction (3.8% surface coverage)

3,000 particles, with different ranges for the capillary interaction – the driving force of the aggregation. In practice we multiplied the range of the capillary force, F_{cap} , existing in the real system [1] with an effective range correction (erc) coefficient (Eq. 5):

$$F_{\text{cap}}^* = F_{\text{cap}} \left(\frac{r}{\text{erc}} \right), \quad (5)$$

where r is the particle-particle distance.

Figure 5 shows the polydispersity curves and the corresponding erc coefficients. It can be seen that increasing the effective range of the attractive force results in a greater polydispersity maximum and a more polydisperse system.

Initial surface coverage of particles (real experiments and simulations)

If we neglect the size of the particles and time-dependent processes (e.g. restructuring), changing the initial surface coverage of the particles is analogous to changing the effective range of the driving force of the aggregation. Therefore, we also expected a dependence of the polydispersity maximum on the initial surface coverage of the particles. We have already shown the polydispersity functions at various initial surface coverages in Fig. 4, and also reached similar results by computer simulations (not shown here). In the experiments we found that a higher surface coverage of the primary particles gives rise to a higher maximum value of the polydispersity.

In order to clarify to what this rise in polydispersity can be attributed, we ran computer simulations of various initial surface coverages using two methods. First we recreated the real experiments by putting various quantities of particles onto the same reaction area. Next we kept the number of particles constant and varied the size of the reaction plane. The maximums of the polydispersity values are shown in Fig. 6.

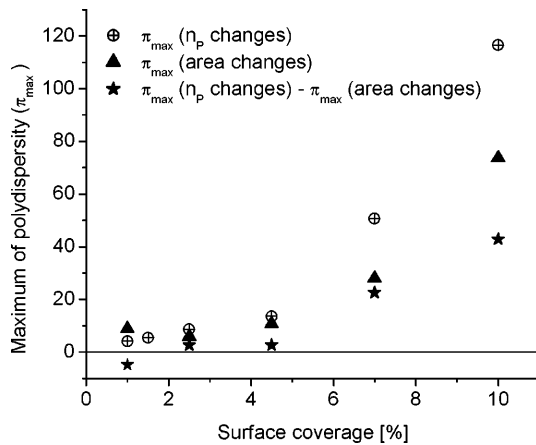


Fig. 6 Maximum value of the polydispersity as a function of the surface coverage of the particles (simulation results – $\text{erc} = 1$)

By subtracting the two curves at the same surface coverages, we found that the difference is monotonous in n_p . All the previously mentioned observations led us to the conclusion that the rise in the polydispersity maximum with the increasing surface coverage can be attributed to two factors. The first is an inherent property of the polydispersity functional – its upper limit is proportional to the number of clusters (Appendix 2). This effect can be eliminated by keeping the number of the particles constant. The other effect is supposedly a shift in the aggregation mechanism that still exists if the number of particles is unchanged.

Finite-size effects

We have seen that the polydispersity maximum is greater if the system has more aggregating particles. In order to clarify what would happen to an infinitely large aggregating system, we had to assess the finite-size effects. In a system of infinite size and number of aggregating particles, the relative weight of any cluster is zero; thus, the polydispersity function will have no noticeable jumps. To tell whether an infinitely large system would have a singular polydispersity maximum we conducted computer simulations in which we successively increased the number of the primary particles and the aggregation area in synchrony to keep the surface coverage constant. Figure 7 shows that with each enlargement of the system, π becomes smoother but the polydispersity maximum changes less and less.

When the system reached a diameter of 30 mm – 1 order of magnitude larger than the range of the capillary attraction – π_{max} did not discernibly change anymore. Therefore, we can presume that if a finite-sized system is much larger than the effective range of the capillary attraction, it can be considered to be free of finite-size effects in terms of the π_{max} ; thus, its polydispersity will be

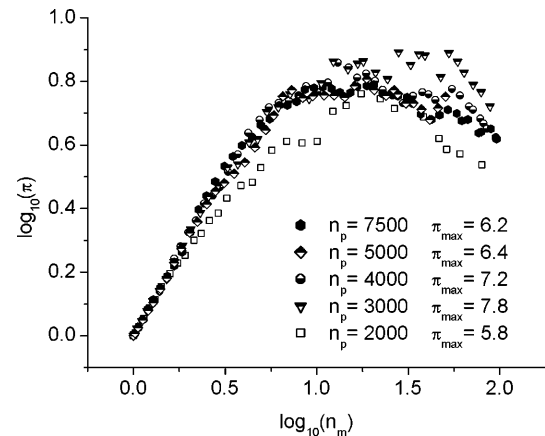


Fig. 7 Polydispersity versus mean cluster size of systems that have different numbers of particles but the same (3%) surface coverage

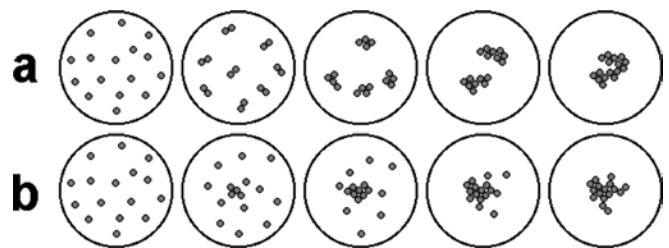


Fig. 8 Two simple models of aggregation mechanisms: **a** monodisperse model; **b** polydisperse model

a good approximation of that of an infinitely large system made up of similar subsystems.

Discussion

Two simplified theoretical systems

We now present a pair of simplified aggregation models to aid us in the calculations.

In Fig. 8, series a shows a monodisperse system where the clusters grow evenly, mainly through cluster–cluster collisions, resulting in a narrow size distribution. Series b is an illustration of the most polydisperse system where only one cluster grows through particle–cluster collisions, and has a broad size distribution. A real aggregating system lies between these two extremities; its particular aggregation mechanism is determined by the relation between the driving force (capillary attraction) and the braking force (hydrodynamic drag), the surface flows, and also the starting conditions: the value, and the homogeneity or inhomogeneity of the initial surface coverage of the particles. One can use the maximum measured polydispersity of a system to judge which model fits the observed aggregation better. In our experiments we found relatively high maximum values

of the polydispersity, and by using the polydisperse aggregation model we could make a reasonable guess at the behaviour of the real, finite-sized systems (see Appendix 2 for model calculations).

Proposed way of the aggregation

We propose a composite model of observed aggregations that has two distinct stages. The first part of the aggregation is ballistic: the motion of the participating particles is mainly determined by interparticle attractions. At this time small-scale inhomogeneities seed the cluster formation, creating a few major clusters with a halo around them (Fig. 1 – first 15 min). If on a large scale the primary particles were spread homogeneously, the resulting major clusters would have roughly similar sizes. During this phase of the aggregation polydispersity is seen to rise sharply (Fig. 5). This aggregation mechanism holds until the separation of the clusters is below the effective range of the interparticle attractive forces. If the separation of the clusters is greater than the range of their interaction, the aggregation cannot be considered ballistic anymore. In this phase, surface flows and other perturbations play major roles, bringing the aforementioned major clusters into interaction range. The flow-driven major clusters perambulate the aggregation area mopping up the rest of the small clusters and primary particles, causing a drop in the polydispersity. (Fig. 1 – after 15 min). At this stage the decreasing π , which becomes proportional to the number of clusters, can be satisfactorily described by the polydisperse aggregation model (Appendix 2). In a finite-sized system the occasional large cluster collisions cause relatively large jumps in the polydispersity, but the course of the aggregation is unaffected.

Increasing the range of the interaction in this model aggregation offsets the crossover point between the two aggregation mechanisms towards larger values of n_m . Increasing the surface coverage of the primary particles has the same effect: it increases the average size of the clusters at the crossover point. The longer the ballistic part of the aggregation is in n_m , the larger the clusters may be at the crossover, and the higher the polydispersity may become. If we wish to use the composite model for a real aggregation, we may define the crossover point at the n_m , where the rise of the polydispersity stalls and permanently deviates from being linear. By reexamining Fig. 5 we can confirm that a higher π_{\max} corresponds to a higher n_m at the now-defined crossover point.

Conclusion

In this work we have investigated the polydispersity (π) – a functional of the CSD function. We have studied the

time dependence of the polydispersity and found that it gives a hint about the aggregation mechanism. In this case the important parameters are its maximum value and discontinuities. The maximum value of the polydispersity rises if the range of the driving force increases, or if the surface coverage of the primary particles rises, indicating a shift in the aggregation mechanism. The discontinuities in π are found to coincide with fusion of the major clusters in the system; thus, for finite systems they contain the history of the aggregation. We have also found that the time-dependent polydispersity functions of all the observed systems obey a proportionality rule in the final stages of the aggregation: π is proportional to the number of clusters (n_c). In simulated systems we have found, but not yet explained, another region of proportionality: at the beginning of the aggregation the polydispersity is well approximated by the value of n_m ; thus, it is inversely proportional to n_c . We have found a composite description of the aggregation mechanism, namely that a transition occurs from the aggregation being dominantly ballistic to flow-driven. These two mechanisms set different evolution paths for the polydispersity functional, allowing us to define a crossover point for simulated systems by examining the deviation of π from the initial linear rise. In the real experiments and computer simulations, altered starting conditions brought the expected changes in the maximum of the polydispersity: increased interaction range or surface coverage resulted in higher π_{\max} values, and in simulated systems a higher n_m at the crossover point.

Appendix 1 – The change in polydispersity during collisions of clusters

If two clusters of size a and b merge, the new value of the polydispersity will be

$$\left. \begin{aligned} \pi_f &= \frac{(n_c \mp 1) \left(\sum_s n_s s^2 \mp (a^2 + b^2) \pm (a+b)^2 \right)}{n_p^2} \\ \pi_f &= \frac{(n_c \mp 1) \left(\sum_s n_s s^2 \pm 2ab \right)}{n_p^2} \\ \pi_f &= \left(\pi_i \pm 2ab \frac{n_c}{n_p} \right) \left(1 \mp \frac{1}{n_c} \right) \end{aligned} \right\}, \quad (6)$$

where π_i is the initial, and π_f is the final polydispersity. The bottom sign signifies the inverse process, namely the shattering of a cluster – containing $a+b$ particles – into two, that is included only for the sake of completeness, but is not a relevant process in this case. To decide whether an event results in higher or lower polydispersity one can derive the threshold in ab for the polydispersity increase from Eq. (6) and considering $\pi_i = \pi_f$ to get

$$ab = \frac{1}{2} \pi_i \frac{n_p^2}{n_c(n_c \mp 1)}. \quad (7)$$

Supposing $n_c \gg 1$, the condition for polydispersity increase for colliding clusters is

$$ab > \frac{1}{2} \pi_i \left(\frac{n_p}{n_c} \right)^2 = \frac{1}{2} \pi_i n_m^2. \quad (8)$$

Appendix 2 – Model calculations for the polydisperse model system

We calculate the polydispersity of a system consisting of one cluster of arbitrary size and a swarm of primary particles as a function of the average cluster size and the number of particles:

$$\pi = \frac{n_c}{n_p^2} \left(\sum_s n_s(t) s^2 \right) = \frac{n_c}{n_p^2} [(n_c - 1) + (n_p - n_c + 1)^2],$$

$$\pi = \left(\frac{n_c}{n_p} - 1 \right)^2 (n_c - 1) + 1, \quad (9)$$

Using the definition of the mean size of the clusters (Eq. 1)

$$\pi = \left(\frac{1}{n_m} - 1 \right)^2 \left(\frac{n_p}{n_m} - 1 \right) + 1. \quad (10)$$

One can see that the polydispersity in this extreme system is directly proportional to the number of particles at a given mean size of the clusters. Real experiments confirmed that the higher number of primary particles in a finite-sized system resulted in a higher maximum polydispersity.

By expanding Eq. (9) we get

$$\pi = \left[\frac{n_c}{n_p} - 2 \left(\frac{n_c}{n_p} \right)^2 + \left(\frac{n_c}{n_p} \right)^3 \right] n_p + \left(\frac{n_c}{n_p} \right)^2. \quad (11)$$

For small n_c/n_p and large n_p – for a sufficiently large system – towards the end of the aggregation

$$\left(\frac{n_c}{n_p} \ll 1, \quad n_p \gg 1 \right) \quad (12)$$

the leading term in this expression is the first one in the bracket: n_c . Thus, the polydispersity is proportional to the number of clusters in the system – a result that has also been found in the real observed systems.

Acknowledgment This work was supported by the Hungarian National Scientific Foundation for Research (OTKA T030457).

References

- Chan DYC, Henry JD Jr, White LR (1981) *J Colloid Interface Sci* 79: 410
- Vincze A, Agod A, Kertész J, Zrínyi M, Hórvölgyi Z (2001) *J Chem Phys* 114:520–529
- Allain C, Joughier B (1983) *J Phys* 44:1
- Hurd AJ, Schaefer DW (1985) *Phys Rev Lett* 54:1043
- Skjeltorp AT (1987) *Phys Rev Lett* 58:1444
- Skjeltorp AT, Helgesen G (1988) *NATO ASI Ser E* 157:56
- Roussel JF, Camoin C, Blanc R (1989) *J Phys* 50:3259
- Roussel JF, Camoin C, Blanc R (1989) *J Phys* 50:3269
- Robinson DJ, Earnshaw JC (1992) *Phys Rev A* 46:2045
- Robinson DJ, Earnshaw JC (1992) *Phys Rev A* 46:2055
- Robinson DJ, Earnshaw JC (1992) *Phys Rev A* 46:2065
- Williams DF, Berg JC (1992) *J Colloid Interface Sci* 152:218
- Kralchevsky PA, Nagayama K (1994) *Langmuir* 10:23
- Robinson DJ, Earnshaw JC (1993) *Langmuir* 9:1436
- Martin JE, Wilcoxon JP, Schaefer D, Odinek (1990) *J Phys Rev A* 41:4379
- Earnshaw JC, Harrison MJB, Robinson DJ (1996) *Phys Rev E* 53:6155
- Earnshaw JC, Robinson DJ (1995) *Physica A* 214:23
- Earnshaw JC, Robinson DJ (1994) *Phys Rev Lett* 72:3682
- Earnshaw JC, Robinson DJ (1993) *Phys Rev Lett* 72:715
- Hidalgo-Alvarez R, Martin A, Fernandez A, Bastos D, Martinez F, de las Nieves FJ (1996) *Adv Colloid Interface Sci* 67:1
- Fernandez-Barbero A, Schmitt A, Cabrerizo-Vilchez M, Martinez-Garcia R (1996) *Physica A* 230:53
- Earnshaw JC, Robinson DJ (1995) *J Phys Condens Matter* 7:397
- Armstrong AJ, Mockler RC, O'Sullivan WJ (1989) *J Phys Condens Matter* 1:1707
- Levine S, Bowen BD (1993) *Colloids Surf A* 70:33
- Aveyard R, Beake BD, Clint JH (1996) *J Chem Soc Faraday Trans* 92:4271
- Aveyard R, Clint JH (1995) *J Chem Soc Faraday Trans* 91:2681
- Menon VB, Nikolov AD, Wasan DT (1988) *J Colloid Interface Sci* 124:317
- Williams DF, Berg JC (1992) *J Colloid Interface Sci* 152:218
- Petkov JT, Denkov ND, Danov KD, Velev OD, Aust R, Durst F (1995) *J Colloid Interface Sci* 172:147
- Onoda GY (1985) *Phys Rev Lett* 55:226
- Hórvölgyi Z, Medveczky M, Zrínyi M (1991) *Colloids Surf* 60:79
- Hórvölgyi Z, Németh S, Fendler JH (1996) *Langmuir* 12:997
- Sonntag H, Strenge K (1987) *Coagulation kinetics and structure formation*. Plenum, New York

- Airolidi M, Boicelli CA, Gennaro G, Giomini M, Giuliani AM, Giustini M, Paci E: Cationic microemulsion hosting polynucleotides: effect of NaCl on host and guest 69
- Alte da Veiga L → Sobral AJFN
- Ambrosone L → Lopez F
- Angelet M → Pérez L
- Antunes FE → Thuresson K
- Ardhammar M, Lincoln P, Nórdén B: Orientation of ruthenium dipyrrophenazine complexes in liposome membranes sensitively controlled by ligand substituents 65
- Arias Garcia C → Terreros Gomez A
- Avramiotis S → Hatzara E
- Baglioni P → Carretti E
- Baptista ALF, Coutinho PJG, Real Oliveira MECD, Rocha Gomes JIN: Lipid interaction with textile fibres in dyeing conditions 88
- Barbosa EFG → Santos MSCS
- Bechinger C → Brunner M
- Behr J-P → Llères D
- Bergström M, Eriksson JC: Synergistic effects in binary surfactant mixtures 16
- Berlot I, Chevalier Y, Coche-Guérente L, Labbé P, Moutet J-C: Interfacial and micellar behaviour of pyrrole-containing surfactants 31
- Bissig H → Scheffold F
- Boicelli CA → Airolidi M
- Bordi F → Di Biasio A
- Boström M, Williams DRM, Ninham BW: Specific ion effects: why colloid science has failed to contribute to biology 110
- Bravo-Díaz C → González-Romero E
- Briscoe WH, Horn RG: Electrical double layer interactions in a non-polar liquid measured with a modified surface force apparatus 147
- Brunner M, Bechinger C: Colloidal systems in intense, two-dimensional laser fields 156
- Buckin V → Lehmann L
- Burrows HD, Kharlamov AA: About energy and electron transfer processes in C₆₀/phthalocyanine films 52
- Burrows HD → Kharlamov AA
- Burrows HD → Hungerford G
- Cabrerizo-Vílchez MÁ → Wege HA
- Cametti C → Di Biasio A
- Cardinaux F → Scheffold F
- Carignano G → Pieri R
- Carretti E, Dei L, Baglioni P: Aqueous polyacrylic acid based gels: physicochemical properties and applications in cultural heritage conservation 280
- Casas M → Miñones Jr J
- Castanheira EMS → Hungerford G
- Castanheira EMS → Céu Rei M
- Ceglie A → Lopez F
- Céu Rei M, Coutinho PJG, Castanheira EMS, Real Oliveira MECD: C_{12E7}-DPPC mixed systems studied by pyrene fluorescence emission 83
- Chevalier Y → Berlot I
- Chevalier Y → Dugas V
- Chittofrati A, Pieri R, D'Aprile F, Lenti D, Maccone P, Visca M: Perfluoropolyether carboxylic salts in micellar solution and O/W microemulsions 23
- Chittofrati A → Pieri R
- Cinelli G → Lopez F
- Cipelletti L → Scheffold F
- Clamme J-P → Llères D
- Clapés P → Pérez L
- Coche-Guérente L → Berlot I
- Colafermina G → Lopez F
- Coutinho PJG → Céu Rei M
- Coutinho PJG → Baptista ALF
- Cuenca A: The role of pre-micellar assemblies and micelles upon the hydrolysis of 2-(2-fluorophenoxy)-quinoxaline 217
- D'Aprile F → Chittofrati A
- D'Aprile F → Pieri R
- Dauty E → Llères D
- Dawson KA → Lawlor A
- de las Nieves FJ → Fernández-Nieves A
- Dei L → Carretti E
- Depret G → Dugas V
- Di Biasio A, Bordi F, Cametti C: Salt-induced aggregation in cationic liposome suspensions 78
- Dugas V, Chevalier Y, Depret G, Nesme X, Souteyrand É: The immobilisation of DNA strands on silica surface by means of chemical grafting 275
- Duguet E → Poncet-Legrand C
- Duportail G → Llères D
- Dynarowicz-Łątka P, Miñones Jr J, Kita K, Milart P: The utility of Brewster angle microscopy in evaluating the origin of the plateau in surface pressure/area isotherms of aromatic carboxylic acids 152
- Dynarowicz-Łątka P → Miñones Jr J
- Dziechciarek Y, van Soest JJG, Philipse AP: Rheology of starch-based colloidal microgels 194
- Edlund H → Persson G
- Eriksson JC → Bergström M
- Esumi K: Adsolubilization by mixtures of ionic and non-ionic surfactants 44
- Fernández-Barbero A → Fernández-Nieves A
- Fernández-Calvar B → González-Romero E
- Fernández-Nieves A, Fernández-Barbero A, de las Nieves FJ: Static light scattering from fractal aggregates of microgel particles 251
- Fischer A → Oligier P
- Foffi G → Lawlor A
- Furukawa H → Uddin MH
- Galera Gomez PA → Terreros Gomez A
- Galisteo-González F → Valle-Delgado JJ
- Galisteo-González F → Martín-Molina A
- Gálvez-Ruiz MJ → Valle-Delgado JJ
- Gennaro G → Airolidi M
- Giomini M → Airolidi M
- Giuliani AM → Airolidi M
- Giustini M → Airolidi M
- González-Romero E, Fernández-Calvar B, Bravo-Díaz C: Electrochemical determination of the stability constant of an aryl radical with β -cyclodextrin 131
- Gzyl B, Paluch M: Langmuir monolayers of lipids at the water/air interface 245
- Harashima A → Uddin MH
- Hato M, Minamikawa H, Salkar RA, Matsutani S: Phase behavior of phytanyl-chained alkylglycoside/water systems 56
- Hatzara E, Karatza E, Avramiotis S, Xenakis A: Spectroscopic mobility probing studies of lecithin organogels 94
- Hauck J, Mika K: Self-assembly of homogeneous systems 98
- Hebrant M → Oligier P
- Hidalgo-Álvarez R → Martín-Molina A
- Hidalgo-Álvarez R → Moncho-Jordá A
- Holgado-Terriza JA → Wege HA

- Horn RG → Briscoe WH
Hrust V, Tomišić V, Kallay N: Characterisation of aqueous solutions of ionic surface active agents by conductometry 127
Hungerford G, Real Oliveira MECD, Castanheira EMS, Burrows HD, Miguel MdG: Transitions in ternary surfactant/alkane/water microemulsions as viewed by fluorescence 1
Infante MR → Pérez L
Iribarnegaray E → Miñones Jr J
Kallay N → Hrust V
Karatza E → Hatzara E
Karavas E → Zoumpanioti M
Kharlamov AA, Burrows HD: Monitoring of the aroma of fruits at their surface by luminescence 178
Kharlamov AA → Burrows HD
Kita K → Dynarowicz-Łątka P
Klich J, Paluch M: Properties of some mixed adsorption films at the water/air interface 231
Kovalchuk NM, Vollhardt D: Direct numerical simulation of the mechanism of surface tension auto-oscillation 123
Kudryashov E → Lehmann L
Kunieda H → Uddin MH
Kurumada K-i, Robinson BH: Viscosity studies of pluronic F127 in aqueous solution 12
Kurumada K-i → Wright M
Labbé P → Berlot I
Lacerda SMV → Santos MSCS
Lawlor A, McCullagh GD, Zaccarelli E, Foffi G, Dawson KA: Interactions in systems with short-range attractions and applications to protein crystallisation 104
Lehmann L, Kudryashov E, Buckin V: Ultrasonic monitoring of the gelatinisation of starch 136
Lenti D → Chittofrati A
Lincoln P → Ardhammar M
Lindblom G → Persson G
Lindman B → Thuresson K
Liu J, Palberg T: Crystal growth and crystal morphology of charged colloidal binary mixtures 222
Liu J → Wette P
Llères D, Clamme J-P, Mély Y, Dauty E, Behr J-P, Duportail G: Oxidisable cationic detergent for gene therapy: condensation of DNA and interaction with model membranes 61
Lopes SH → Sobral AJFN
Lopez Cabarcos E → Terreros Gomez A
Lopez F, Palazzo G, Colafemmina G, Cinelli G, Ambrosone L, Ceglie A: Enzymatic activity of lipase entrapped in CTAB/water/pentanol/hexane reverse micelles: a functional and microstructural investigation 174
Lopez Ruiz B → Terreros Gomez A
Lu JR → Peel LL
Maccone P → Chittofrati A
Martínez-López F → Moncho-Jordá A
Martín-Molina A, Quesada-Pérez M, Galisteo-González F, Hidalgo-Álvarez R: Charge inversion of latex particles in the presence of electrolyte 114
Matos Beja A → Sobral AJFN
Matsutani S → Hato M
McCullagh GD → Lawlor A
Medebach M, Palberg T: Flashing of colloidal crystals in square wave electric fields 260
Melo L → Rosmaninho R
Mély Y → Llères D
Miguel MdG → Hungerford G
Miguel MG → Thuresson K
Mika K → Hauck J
Milart P → Dynarowicz-Łątka P
Minamikawa H → Hato M
Mingotaud C → Poncet-Legrand C
Miñones Jr J, Dynarowicz-Łątka P, Seoane R, Iribarnegaray E, Casas M: Brewster angle microscopy studies of the morphology in dipalmitoyl phosphatidyl glycerol monolayers spread on subphases of different pH 160
Miñones Jr J → Dynarowicz-Łątka P
Molina-Bolívar JA → Valle-Delgado JJ
Moncho-Jordá A, Quesada-Pérez M, Martínez-López F, Hidalgo-Álvarez R: Structure and interaction forces in colloidal monolayers 119
Moutet J-C → Berlot I
Narayanan T → Pontoni D
Nesme X → Dugas V
Ninham BW → Boström M
Nordén B → Ardhammar M
Oliger P, Fischer A, Hebrant M, Tondre C: Probe entrapment by vesicular systems in relation with the properties of the amphiphilic film 48
Paci E → Airoidi M
Paixão JA → Sobral AJFN
Palazzo G → Lopez F
Palberg T → Liu J
Palberg T → Medebach M
Palberg T → Wette P
Paluch M → Klich J
Paluch M → Gzyl B
Peel LL, Lu JR: The interaction of C₁₂E₅ with olive oil films studied by neutron reflection 164
Pérez L, Infante MR, Angelet M, Clapés P, Pinazo A: Glycerolipid arginine-based surfactants: synthesis and surface active properties 210
Persson G, Edlund H, Lindblom G: Phase behaviour of the 1-monooleoyl-*rac*-glycerol/*n*-octyl- β -D-glucoside/water system 36
Petit L → Poncet-Legrand C
Philippe AP → Dziechciarek Y
Pieri R, Carignano G, Chittofrati A, D'Aprile F, Visca M: Wetting of low energy surfaces by perfluoropolyether carboxylic salts in aqueous solution 236
Pieri R → Chittofrati A
Pinazo A → Pérez L
Poncet-Legrand C, Petit L, Reculosa S, Mingotaud C, Duguet E, Ravaine S: Dissymmetrical gold tagging on spherical silica nanoparticles 240
Pontoni D, Narayanan T, Rennie AR: Nucleation and growth kinetics of colloidal silica 227
Quesada-Pérez M → Martín-Molina A
Quesada-Pérez M → Moncho-Jordá A
Ramos Silva M → Sobral AJFN
Ravaine S → Poncet-Legrand C
Real Oliveira MECD → Hungerford G
Real Oliveira MECD → Céu Rei M
Real Oliveira MECD → Baptista ALF
Reculosa S → Poncet-Legrand C
Rennie AR → Pontoni D
Robinson B → Wright M
Robinson BH → Kurumada K-i
Rocha Gomes JIN → Baptista ALF
Rocha Gonsalves AMd → Sobral AJFN
Rojas-Ochoa LF → Scheffold F
Romer S → Scheffold F

- Romsted LS, Zhang J: Determining antioxidant distributions in model food emulsions: development of a new kinetic method based on the pseudophase model in micelles and opaque emulsions 182
- Rosmaninho R, Visser H, Melo L: Influence of the surface tension components of stainless steel on fouling caused by calcium phosphate 203
- Rubio Retama BJ → Terreros Gomez A
- Rueda Rodriguez C → Terreros Gomez A
- Salkar RA → Hato M
- Santos MSCS, Lacerda SMV, Barbosa EFG: Interactions of selected flavonoids with NaDS micelles 73
- Scheffold F, Romer S, Cardinaux F, Bissig H, Stradner A, Rojas-Ochoa LF, Trappe V, Urban C, Skipetrov SE, Cipelletti L, Schurtenberger P: New trends in optical microrheology of complex fluids and gels 141
- Schöpe H-J → Wette P
- Schurtenberger P → Scheffold F
- Seoane R → Miñones Jr J
- Siegel S, Vollhardt D: Phase behaviour and domain structure of 9-hydroxyhexadecanoic acid monolayers 5
- Skipetrov SE → Scheffold F
- Skopelitis C → Zoumpantioti M
- Sobral AJFN, Lopes SH, Rocha Gonsalves AMd'a Ramos Silva M, Matos Beja A, Paixão JA, Alte da Veiga L: Synthesis and crystal structure of new phase-transfer catalysts based on 1,8-diazabicyclo[5.4.0]undec-7-ene and 1,5-diazabicyclo[4.3.0]non-5-ene 28
- Souteyrand É → Dugas V
- Stamatis H → Zoumpantioti M
- Stradner A → Scheffold F
- Terreros Gomez A, Rubio Retama BJ, Lopez Ruiz B, Galera Gomez PA, Rueda Rodriguez C, Arias Garcia C, Lopez Cabarcos E: Encapsulation of alkaline phosphatase in polyacrylamide microparticles using the concentrated emulsion polymerisation method 169
- Thuresson K, Antunes FE, Miguel MG, Lindman B: The association between a non-ionic microemulsion and hydrophobically modified PEG. A rheological investigation 40
- Tomišić V → Hrust V
- Tondre C → Oliger P
- Trappe V → Scheffold F
- Uddin MH, Yamashita Y, Furukawa H, Harashima A, Kunieda H: Phase behavior of poly(oxyethylene)-poly(dimethylsiloxane) surfactant (copolymer) with water or silicone oil 269
- Urban C → Scheffold F
- Valle-Delgado JJ, Molina-Bolívar JA, Galisteo-González F, Gálvez-Ruiz MJ, Molina-Bolívar JA: Stabilisation of an amphoteric latex by hydration forces 255
- van Soest JJG → Dziechciarek Y
- Visca M → Pieri R
- Visca M → Chittofrati A
- Visser H → Rosmaninho R
- Vollhardt D → Kovalchuk NM
- Vollhardt D → Siegel S
- Wege HA, Holgado-Terriza JA, Cabrerizo-Vílchez MÁ: Development of a pressure-controlled pendant-drop surface balance 188
- Wette P, Schöpe H-J, Liu J, Palberg T: Characterisation of colloidal solids 264
- Williams DRM → Boström M
- Wright M, Kurumada K-i, Robinson B: Rates of incorporation of small molecules into pluronic micelles 8
- Xenakis A → Zoumpantioti M
- Xenakis A → Hatzara E
- Yamashita Y → Uddin MH
- Zaccarelli E → Lawlor A
- Zhang J → Romsted LS
- Zoumpantioti M, Karavas E, Skopelitis C, Stamatis H, Xenakis A: Lecithin organogels as model carriers of pharmaceuticals 199

- Absorption 164
Adsolubilization of 44
Adsorption 31, 164, 236
Aggregation 251
Air/water interface 152
Alylglycoside 56
Alkaline 169
Alumina 44
Amino acid 210
Amphiphilic bilayer 48
Amphoteric latex 255
Anionic surfactants 127
Anisotropy 1
Antioxidant distribution 182
Arenediazonium ions 131
Aromatic carboxylic acids 152
Aryl radicals 131
- Binary surfactants 44
Binary systems 52
Biocide 210
Biopolymers 141
Block copolymer micelles 8
Brewster angle microscopy 5, 152, 160
- Calcium phosphate 203
Calorimetry 127
Cationic detergents 61
Cationic surfactant 31
C₁₂E₅ 1
Charged spheres 264
Chemical grafting 275
Circle packings 98
Colloidal crystals 260
Colloidal monolayers 119
Colloids 98, 114, 141, 156, 264
Concentrated emulsion
 polymerisation 169
Concentrated regime 194
Conductivity 69
Conductometry 127
Confined geometry 260
Contact angle 236
Counterion association 127
Counterion-only 147
Critical micelle concentration 73
Crystal growth 264
Crystal growth velocity 222
CTAB 174
Cubic phase 56
Cultural heritage conservation 280
Cyclodextrins 131
- Diffusing wave spectroscopy 141
Diffusion coefficient 222
Dilute regime 194
Dimensional phase transitions 156
Dipalmitoyl phosphatidyl glycerol
 monolayers 160
Dipalmitoylphosphatidylcholine 245
Dipalmitoylphosphatidylcholine 83
Discriminatory adsorption 240
Dissymmetrisation 240
DLVO 110
DNA 275
- DNA chip 275
DNA condensation 61
Dye incorporation 8
- Egg phosphatidylcholine 83
Electric double layer 114
Electrical double layer interactions 147
Electron transfer 52
Electro-osmosis 260
Electrophoresis 260
Electrophoretic mobility 114, 255
Entrapment 8
EPR spectroscopy 94
- Flavonoid 73
Fluorescence 1, 94
Fluorescence spectroscopy 88
Fluorimetry of aroma emission 178
Fouling 203
Fractal 251
FTIR 88
Fullerene C₆₀ 52
Function 119
- Gelatinisation 136
Gels 280
Glucose entrapment 48
Glycerolipid 210
Gold nano-clusters 240
Ground-state aggregation 83
- Hofmeister series 110
Hydration forces 255
Hydrophobicity 73
Hydroxyhexadecanoic acid
 monolayers 5
- Instability 123
Interaction potential 119
Interactions in mixed adsorption
 films 231
Inverse 119
Ionic dispersion potentials 110
- Kinetics 8, 182
Krafft eutectic temperature 56
- Langmuir films 160
Langmuir monolayers 152
Lecithin 88, 94
Light scattering 264
Linear dichroism 65
Lipase 174
Lipid vesicles 61
Lipid 98
Lipid membrane 245
Lipid/surfactant interactions 83
Liquid crystal 269
Living systems 178
Luminescence 178
Luminescence lifetimes 65
- Marangoni effect 123
Membrane mimetic 73
Membrane orientation 65
Mesoscopic effect 52
- 4-Methylumbelliferyl palmitate 245
Micellar solutions 23
Micelles 31, 141, 217
Microemulsion 199
Microgel 251
Microparticles 169
Microrheology 141
Monolayers 98, 245
- 2-naphthol 44
Natural products 98
Neutron reflection 164
Non-ionic emulsions 182
Non-ionic micelles 182
Non-ionic surfactants 83
Non-polar 147
Non-viral 61
Numerical simulation 123
- O/W microemulsions 23
Oligonucleotide 275
Optical 260
Optical Bragg microscopy 222
Optical tweezers 156
Organogels 94, 199
Overcharging 114
- Patterns 98
Pentanol 174
Perfluoropolyether 236
Perfluoropolyethers 23
Permeation kinetics 48
Phase behavior 269
Phase diagram 56
Phase transition 264
phosphatase encapsulation 169
Phytanyl-chained alylglycoside 56
Pluronic 8
Polarography 131
Polyacrylamide 169
Polyacrylic acid 280
Polydispersity 222
Polymer gel 199
Polynucleotides 69
Premicelles 217
Problem 119
Properties 260
Pseudophase model 182
Pyrene 1
Pyrene emission 83
Pyrrole 31
- Quaternary microemulsions 69
Quinoxaline 217
- Radial distribution 119
Reverse micelles 174
Rheology 280
Rhodamine 6G 1
Ruthenium(II) dipyrrophenazine
 complexes 65
- Scattering 251
SEM 88
Setchenow micellisation constant 73

-
- | | | |
|--------------------------------------|---------------------------------------|---------------------------------------|
| Shear flow 260 | Surface 236 | Transition temperature 48 |
| Shear modulus 264 | Surface cleaning 164 | Two-dimensional phase transitions 156 |
| Shear-deformed liposomes 65 | Surface force 147 | |
| Silica 44 | Surface potential 231 | Ultrasonic attenuation 136 |
| Silica nanoparticles 240 | Surface pressure 5 | Ultrasonic spectroscopy 136 |
| Silicone oil 269 | Surface tension 110, 203, 231 | Ultrasonic velocity 136 |
| Silicone surfactant 269 | Surface tension auto-oscillations 123 | |
| Sodium chloride 69 | Surfactant 164, 210 | Vectors 61 |
| Sodium decylsulphonate 127 | System 73 | Vesicles 48 |
| Specific ion effects 110 | | Viscosity 194 |
| Spectroscopy 69 | Textile fibres 88 | Visible chromophores 52 |
| Stability ratio 255 | Tosylate 31 | Volatile compounds 178 |
| Starch 136 | Transdermal drug delivery 199 | |
| Starch-based colloidal microgels 194 | Transfection 61 | Wilson-Frenkel law 222 |